

Introduction to the Equations of Fluid Dynamics and the Finite Element Approximation

1

1.1 General remarks and classification of fluid dynamics problems discussed in this book

The problems of solid and fluid behavior are in many respects similar. In both media stresses occur and in both the material is displaced. There is however one major difference. Fluids cannot support any deviatoric stresses when at rest, where only a pressure or a mean compressive stress can be carried. As we know, in solids general forms of stresses can exist and a solid material can support both deviatoric and pressure stresses.

In addition to pressure, deviatoric stresses can develop when the fluid is in motion and such motion of the fluid will always be of primary interest in *fluid dynamics*. We shall therefore concentrate on problems in which displacement is continuously changing and in which velocity is the main characteristic of the flow. The deviatoric stresses which can now occur will be characterized by a quantity that has great resemblance to the shear modulus of solid mechanics and which is known as *dynamic viscosity* or molecular viscosity.

Up to this point the equations governing fluid flow and solid mechanics appear to be similar with the velocity vector \mathbf{u} replacing the displacement, which often uses the same symbol. However, there is one further difference. Even when the flow has a constant velocity (steady-state), *convective acceleration* effects add terms which make the fluid dynamics equations *non-self-adjoint* (see Appendix A). Therefore, in most cases, unless the velocities are very small so that the convective acceleration is negligible, the treatment has to be somewhat different from that of solid mechanics. The reader should note that for self-adjoint forms, approximating the equations by the Galerkin method gives the minimum error in the energy norm and thus such approximations are in a sense optimal. In general, this is no longer true in fluid mechanics, though for slow flows such as creeping flows where the convective acceleration terms are negligible the situation is somewhat similar.

With a fluid which is in motion, conservation of mass is always essential and, unless the fluid is highly compressible, we require that the divergence of the velocity vector be zero. Similar problems are encountered in the context of incompressible elasticity and the *incompressibility constraint* can introduce difficulties in the formulation

(viz. Ref. [1]). In fluid dynamics the same difficulty again arises and all fluid dynamics approximations have to be such that, even if compressibility is possible, the limit of incompressibility can be modeled. This precludes the use of many elements which are otherwise acceptable.

In this book we shall introduce the reader to finite element treatment of the equations of motion for various problems of fluid dynamics. Much of the earlier activity in fluid dynamics has however pursued a *finite difference* formulation and later a derivative of this known as the *finite volume* technique. Competition between finite element methods and techniques of finite differences has appeared and led to a much slower adoption of the finite element process in fluid dynamics than in structures. The reasons for this are perhaps simple. In solid mechanics or structural problems, the treatment of continua often arises in combination with other structural forms, e.g., trusses, beams, plates, and shells. The engineer often dealing with structures composed of structural elements does not need to solve continuum problems. In addition when continuum problems are encountered, the system can lead to use of many different material models which are easily treated using a finite element formulation. In fluid mechanics, practically all situations of flow require a two- or three-dimensional treatment and here approximation is required. This accounts for the early use of finite differences in the 1950s before the finite element process was made available. However, as pointed out in Ref. [1], there are many advantages of using the finite element process. This not only allows a fully unstructured and arbitrary domain subdivision to be used but also provides an approximation which in self-adjoint problems is always superior to or at least equal to that provided by finite differences.

A methodology which appears to have gained an intermediate position is that of finite volumes, which were initially derived as a subclass of finite difference methods. As shown later in this chapter, these are simply another kind of finite element form in which subdomain collocation is used. We do not see much advantage in using this form of approximation; however, there is one point which seems to appeal to some investigators. That is the fact the finite volume approximation explicitly satisfies conservation conditions for each finite volume [2]. In full finite element analysis, however, satisfaction of conservation conditions is implicitly achieved [3–10]. Explicit satisfaction of the conservation conditions on an individual element is not an advantage if the general finite element approximation gives results which are superior.

In this book we will discuss various classes of problems, each of which has a certain behavior in the numerical solution. Here we start with incompressible flows or flows where the only change of volume is elastic and associated with transient changes of pressure (Chapters 4 and 5). For such flows full incompressible constraints must be available.

Further, with very slow speeds, convective acceleration effects are often negligible and the solution can on occasion be reached using identical methods to those derived for linear incompressible elasticity. This indeed was the first venture of finite element developers into the field of fluid mechanics, thus transferring the direct knowledge from solid mechanics to fluids. In particular the so-called linear Stokes flow is the case where fully incompressible but elastic behavior occurs. A particular variant of Stokes

flow is that used in metal forming where the material can no longer be described by a constant viscosity but possesses a viscosity which is non-Newtonian and depends on the strain rates and temperature. [Chapter 5](#) is devoted to such problems. Here the fluid (flow formulation) can be applied directly to problems such as the forming of metals or plastics and we shall discuss this extreme situation in [Chapter 5](#). However, even in incompressible flows, when the speed increases convective acceleration terms become important. Here often steady-state solutions do not exist or at least are extremely unstable. This leads us to such problems as vortex shedding. Vortex shedding indicates the start of instability which becomes very irregular and indeed random when high-speed flow occurs in viscous fluids. This introduces the subject of turbulence, which occurs frequently in fluid dynamics. In turbulent flows random fluctuation of velocity occurs at all points and the problem is highly time dependent. With such turbulent motion, it is possible to obtain an averaged solution using time-averaged equations. Details for some available time-averaged models are summarized in [Chapter 8](#).

[Chapter 6](#) deals with incompressible flow in which free surface and other gravity controlled effects occur. In particular we show three different approaches for dealing with free surface flows and explain the necessary modifications to the general formulation.

The next area of fluid dynamics to which much practical interest is devoted is of course that of flow of gases for which the compressibility effects are much larger. Here compressibility is problem dependent and generally obeys gas laws which relate the pressure to temperature and density. It is now often necessary to add the energy conservation equation to the system governing the motion so that the temperature can be evaluated. Such an energy equation can of course be written for incompressible flows but this shows only a weak or no coupling with the dynamics of the flow. This is not the case in compressible flows where coupling between all equations is very strong. In such compressible flows the flow speed may exceed the speed of sound and this may lead to shock development. This subject is of major importance in the field of aerodynamics and we shall devote [Chapter 7](#) to this particular problem.

In a real fluid, viscosity is always present but at high speeds such viscous effects are confined to a narrow zone in the vicinity of solid boundaries (the so-called *boundary layer*). In such cases, the remainder of the fluid can be considered to be inviscid. There we can return to the fiction of an ideal fluid in which viscosity is not present and here various simplifications are again possible. Such simplifications have been used since the early days of aerodynamics and date back to the work of Prandtl and Schlichting [11]. One simplification is the introduction of potential flow and we shall mention this later in this chapter. Potential flows are indeed the topic of many finite element investigators, but unfortunately such solutions are not easily extendible to realistic problems.

A particular form of viscous flow problem occurs in the modeling of flow in porous media. This important field is discussed in [Chapter 9](#). In the topic of flow through porous media, two extreme situations are often encountered. In the first, the porous medium is stationary and the fluid flow occurs only in the narrow passages between solid grains. Such an extreme is the basis of porous medium flow modeling in

applications such as geo-fluid dynamics where the flow of water or oil through porous soils or rocks occurs. The other extreme of porous media flow is the one in which the solid occupies only a small part of the total volume (for example, representing thermal insulation systems, heat exchangers, etc.). In such problems flow is almost the same as that occurring in fluids without the solid phase which only applies an added, distributed, resistance to flow. Both extremes are discussed in [Chapter 9](#).

Another major field of fluid mechanics of interest to us is that of shallow-water flows that occur in coastal estuaries or elsewhere. In this class of problems the depth dimension of flow is very much less than the horizontal ones. [Chapter 10](#) deals with such problems in which essentially the distribution of pressure in the vertical direction is almost hydrostatic. For such shallow-water problems a free surface also occurs. This dominates the flow characteristics and here we note that shallow-water flow problems result in a formulation which is closely related to gas flow.

Whenever a free surface occurs it is possible for transient phenomena to happen, generating waves such as those occurring in oceans or other bodies of water. [Chapters 11](#) and [12](#) deal with this particular aspect of fluid dynamics. Such wave phenomena are also typical of some other physical problems. For instance, acoustic and electromagnetic waves can be solved using similar approaches. Indeed, one can show that the treatment for this class of problems is very similar to that of surface wave problems.

The interaction of two or more distinctive disciplines is often an integral part of many engineering problems. One such example is the subject of fluid and structure interaction. This topic is the primary focus in many offshore and biomedical engineering problems. In [Chapter 13](#), we have introduced some fundamental approaches to modeling the fluid-solid interaction using the finite element method.

The treatments used for fluid dynamics and fluid-structure interaction problems have a dramatic influence on the biofluid dynamics problems. Although biofluid dynamics is a topic of applied fluid dynamics, there are many situations that require additional knowledge and treatment. [Chapter 14](#) describes some treatments that are important in the solution of biofluid dynamics problems.

In what remains of this chapter we shall introduce the general equations of fluid dynamics valid for most compressible and incompressible flows, showing how a particular simplification occurs in some categories of problems mentioned above. However, before proceeding with the recommended discretization procedures, which we present in [Chapter 3](#), we must introduce the treatment of problems in which convection and diffusion occur simultaneously. This we shall do in [Chapter 2](#) using the scalar convection-diffusion equation. Based on concepts given in [Chapter 2](#), [Chapter 3](#) will introduce a general algorithm capable of solving most of the fluid mechanics problems encountered in this book. There are many possible algorithms and very often specialized ones are used in different areas of applications. However the general algorithm of [Chapter 3](#) produces results which are at least as good as others achieved by more specialized means. We feel that this will give a certain unification to the whole subject of fluid dynamics and, without apology, we will omit reference to many other methods or discuss them only in passing.

For completeness we shall show in the present chapter some detail of the finite element process to avoid the repetition of basic finite element presentations which we assume are known to the reader either from Ref. [1] or from any of the numerous texts available.

1.2 The governing equations of fluid dynamics [2, 11–17]

1.2.1 Velocity, strain rates, and stresses in fluids

As noted above, the essential characteristic of a fluid is its inability to sustain deviatoric stresses when at rest. Here only hydrostatic “stress” or pressure is possible. Any analysis must therefore concentrate on the motion, and the essential independent variable is the velocity \mathbf{u} or, if we adopt indicial notation (with the coordinate axes referred to as x_i , $i = 1, 2, 3$),

$$u_i, i = 1, 2, 3 \quad \text{or} \quad \mathbf{u} = [u_1, u_2, u_3]^T \quad (1.1)$$

This replaces the displacement variable which is of primary importance in solid mechanics. The rates of strain are the primary cause of the general stresses, σ_{ij} , and these are defined in a manner analogous to that of infinitesimal strain in solid mechanics as

$$\dot{\varepsilon}_{ij} = \frac{1}{2} \left(\frac{\partial u_i}{\partial x_j} + \frac{\partial u_j}{\partial x_i} \right) \quad (1.2)$$

This is a well-known tensorial definition of strain rates but for use later in variational forms is written as a vector, which is more convenient in finite element analysis. Details of such matrix forms are given fully in Ref. [1] but for completeness we summarize them here. Thus, the strain rate is written as a vector ($\dot{\boldsymbol{\varepsilon}}$) and is given by the form

$$\dot{\boldsymbol{\varepsilon}} = [\dot{\varepsilon}_{11}, \dot{\varepsilon}_{22}, \dot{\varepsilon}_{33}, 2\dot{\varepsilon}_{12}, 2\dot{\varepsilon}_{23}, 2\dot{\varepsilon}_{31}]^T \quad (1.3a)$$

in three dimensions with the form in two dimensions given by*

$$\dot{\boldsymbol{\varepsilon}} = [\dot{\varepsilon}_{11}, \dot{\varepsilon}_{22}, 2\dot{\varepsilon}_{12}]^T \quad (1.3b)$$

In the above $2\dot{\varepsilon}_{ij}$, $i \neq j$ is an engineering shear strain rate which we will write as

$$\dot{\varepsilon}_{ij} = \dot{\gamma}_{ij} \quad \text{for } i \neq j \quad (1.3c)$$

When such vector forms are used we can write the strain rate vector in the form

$$2\dot{\boldsymbol{\varepsilon}} = \boldsymbol{\mathcal{S}}\mathbf{u} \quad (1.4)$$

where $\boldsymbol{\mathcal{S}}$ is known as the strain rate operator and \mathbf{u} is the velocity given in Eq. (1.1).

Similarly, we will write the tensor components of stress as σ_{ij} and express this in matrix form as

$$\boldsymbol{\sigma} = [\sigma_{11} \ \sigma_{22} \ \sigma_{33} \ \sigma_{12} \ \sigma_{23} \ \sigma_{31}]^T \quad (1.5)$$

*In plane flows $\dot{\varepsilon}_{33} = 0$ and we solve in the x_1, x_2 plane.

1.2.2 Constitutive relations for fluids

The stress-strain rate relations for a linear (Newtonian) isotropic fluid require the definition of two constants. The first of these links the *deviatoric stresses* τ_{ij} to the *deviatoric strain rates*:

$$\tau_{ij} \equiv \sigma_{ij} - \frac{1}{3}\delta_{ij}\sigma_{kk} = 2\mu\left(\dot{\varepsilon}_{ij} - \frac{1}{3}\delta_{ij}\dot{\varepsilon}_{kk}\right) \quad (1.6)$$

In the above equation the quantity in brackets is known as the deviatoric strain rate, δ_{ij} is the Kronecker delta,

$$\delta_{ij} = \begin{cases} 1, & \text{for } i = j \\ 0, & \text{for } i \neq j \end{cases}$$

and a repeated index implies summation over the range of the index; thus

$$\sigma_{kk} \equiv \sigma_{11} + \sigma_{22} + \sigma_{33} \quad \text{and} \quad \dot{\varepsilon}_{kk} \equiv \dot{\varepsilon}_{11} + \dot{\varepsilon}_{22} + \dot{\varepsilon}_{33} \quad (1.7)$$

The coefficient μ is known as the dynamic (shear) viscosity or simply viscosity and is analogous to the shear modulus G in linear elasticity.

The second relation is that between the mean stress changes and the volumetric strain rate. This defines the pressure as

$$p = -\frac{1}{3}\sigma_{kk} = -\kappa\dot{\varepsilon}_{kk} + p_0 \quad (1.8)$$

where κ is a *volumetric viscosity* coefficient analogous to the bulk modulus K in linear elasticity and p_0 is the initial hydrostatic pressure independent of the strain rate (note that p and p_0 are invariably defined as positive when compressive).

We can immediately write the “constitutive” relation for fluids from Eqs. (1.6) and (1.8) as

$$\begin{aligned} \sigma_{ij} &= \tau_{ij} - \delta_{ij}p \\ &= 2\mu\left(\dot{\varepsilon}_{ij} - \frac{1}{3}\delta_{ij}\dot{\varepsilon}_{kk}\right) + \kappa\delta_{ij}\dot{\varepsilon}_{kk} - \delta_{ij}p_0 \end{aligned} \quad (1.9a)$$

or

$$\sigma_{ij} = 2\mu\dot{\varepsilon}_{ij} + \delta_{ij}(\kappa - \frac{2}{3}\mu)\dot{\varepsilon}_{kk} - \delta_{ij}p_0 \quad (1.9b)$$

There is little evidence about the existence of volumetric viscosity and, in what follows, we shall take

$$\kappa\dot{\varepsilon}_{kk} \equiv 0 \quad (1.10)$$

giving the essential constitutive relation as (now dropping the suffix on p_0)

$$\sigma_{ij} = 2\mu\left(\dot{\varepsilon}_{ij} - \frac{1}{3}\delta_{ij}\dot{\varepsilon}_{kk}\right) - \delta_{ij}p \equiv \tau_{ij} - \delta_{ij}p \quad (1.11a)$$

without necessarily implying incompressibility $\dot{\varepsilon}_{kk} = 0$.

In the above,

$$\tau_{ij} = 2\mu \left(\dot{\varepsilon}_{ij} - \frac{1}{3} \delta_{ij} \dot{\varepsilon}_{kk} \right) = \mu \left[\left(\frac{\partial u_i}{\partial x_j} + \frac{\partial u_j}{\partial x_i} \right) - \frac{2}{3} \delta_{ij} \frac{\partial u_k}{\partial x_k} \right] \quad (1.11b)$$

The above relationships are identical to those of isotropic linear elasticity as we will note again later for incompressible flow. However, in solid mechanics we often consider anisotropic materials where a larger number of parameters (i.e., more than 2) are required to define the stress-strain relations. In fluid mechanics use of such anisotropy is rare and in this book we will limit ourselves to purely isotropic behavior.

Nonlinearity of some fluid flows is observed with a coefficient μ depending on strain rates and/or other variables such as temperature. We shall term such flows “non-Newtonian.”

We now consider the basic conservation principles used to write the equations of fluid dynamics. These are *mass conservation*, *momentum conservation*, and *energy conservation*.

1.2.3 Mass conservation

If ρ is the fluid density then the balance of mass flow ρu_i entering and leaving an infinitesimal control volume (Fig. 1.1) is equal to the rate of change in density as expressed by the relation

$$\frac{\partial \rho}{\partial t} + \frac{\partial}{\partial x_i} (\rho u_i) \equiv \frac{\partial \rho}{\partial t} + \nabla^T (\rho \mathbf{u}) = 0 \quad (1.12)$$

where $\nabla^T = [\partial/\partial x_1, \partial/\partial x_2, \partial/\partial x_3]$ is known as the gradient operator.

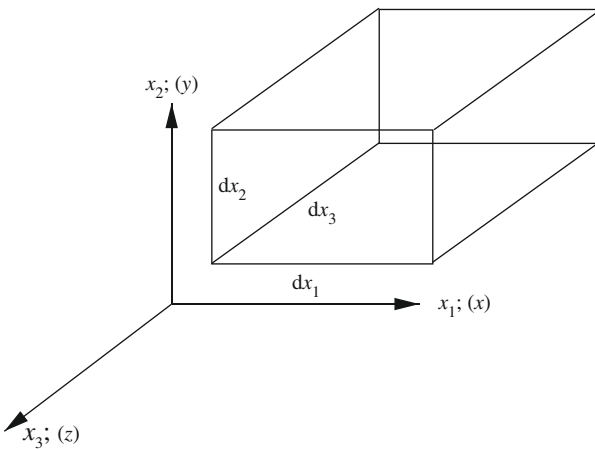
It should be noted that in this section, and indeed a majority of subsequent ones, the control volume remains fixed in space. This is known as the “Eulerian form” and displacements of a particle are ignored. This is in contrast to the usual treatment in solid mechanics where displacement is a primary dependent variable.

It is possible to recast the above equations in relation to a moving frame of reference and, if the motion follows the particle, the equations will be named “Lagrangian.” Such Lagrangian frame of reference is occasionally used in fluid dynamics and briefly discussed in [Chapter 6](#).

1.2.4 Momentum conservation: Dynamic equilibrium

In the j th direction the balance of linear momentum leaving and entering the control volume (Fig. 1.1) is to be in dynamic equilibrium with the stresses σ_{ij} and body forces ρg_j . This gives a typical component equation

$$\frac{\partial(\rho u_j)}{\partial t} + \frac{\partial}{\partial x_i} [(\rho u_j) u_i] - \frac{\partial}{\partial x_i} (\sigma_{ij}) - \rho g_j = 0, \quad j = 1, 2, 3 \quad (1.13)$$

**FIGURE 1.1**

Coordinate direction and the infinitesimal control volume.

or using (1.11a),

$$\frac{\partial(\rho u_j)}{\partial t} + \frac{\partial}{\partial x_i}[(\rho u_j)u_i] - \frac{\partial \tau_{ij}}{\partial x_i} + \frac{\partial p}{\partial x_j} - \rho g_j = 0, \quad j = 1, 2, 3 \quad (1.14)$$

with (1.11b) implied.

The conservation of angular momentum merely requires the stress to be symmetric, i.e.,

$$\sigma_{ij} = \sigma_{ji} \quad \text{or} \quad \tau_{ij} = \tau_{ji}$$

In the sequel we will use the term *momentum conservation* to imply both linear and angular forms.

1.2.5 Energy conservation and equation of state

We note that in the equations of Sections 1.2.3 and 1.2.4 the dependent variables are u_i (the velocity components), p (the pressure), and ρ (the density). The deviatoric stresses, of course, are defined by Eq. (1.11b) in terms of velocities and hence are dependent variables.

Obviously, there is one variable too many for this equation system to be capable of solution. However, if the density is assumed constant (as in incompressible fluids) or if a single relationship linking pressure and density can be established (as in isothermal flow with small compressibility) the system becomes complete and solvable.

More generally, the pressure (p), density (ρ), and absolute temperature (T) are related by an *equation of state* of the form

$$\rho = \rho(p, T) \quad (1.15a)$$

For an *ideal gas* this takes the form

$$\rho = \frac{p}{RT} \quad (1.15b)$$

where R is the universal gas constant.

In such a general case, it is necessary to supplement the governing equation system by the equation of *energy conservation*. This equation is of interest even if it is not coupled with the mass and momentum conservation, as it provides additional information about the behavior of the system.

Before proceeding with the derivation of the energy conservation equation we must define some further quantities. Thus we introduce e , the *intrinsic energy* per unit mass. This is dependent on the state of the fluid, i.e., its pressure p and temperature T or

$$e = e(T, p) \quad (1.16)$$

The total energy per unit mass, E , includes of course the kinetic energy per unit mass and thus

$$E = e + \frac{1}{2} u_i u_i \quad (1.17)$$

Finally, we can define the *enthalpy* as

$$h = e + \frac{p}{\rho} \quad \text{or} \quad H = h + \frac{1}{2} u_i u_i = E + \frac{p}{\rho} \quad (1.18)$$

and these variables are found to be convenient to express the conservation of energy relation.

Energy transfer can take place by convection and by conduction (radiation generally being confined to boundaries). The conductive heat flux q_i for an isotropic material is defined as

$$q_i = -k \frac{\partial T}{\partial x_i} \quad (1.19)$$

where k is thermal conductivity.

To complete the relationship it is necessary to determine heat source terms. These can be specified per unit volume as q_H due to chemical reaction (if any) and must include the energy dissipation due to internal stresses, i.e., using Eq. (1.11a),

$$\frac{\partial}{\partial x_i} (\sigma_{ij} u_j) = \frac{\partial}{\partial x_i} (\tau_{ij} u_j) - \frac{\partial}{\partial x_j} (p u_j) \quad (1.20)$$

The balance of energy in an infinitesimal control volume can now be written as

$$\frac{\partial(\rho E)}{\partial t} + \frac{\partial}{\partial x_i} (\rho u_i E) - \frac{\partial}{\partial x_i} \left(k \frac{\partial T}{\partial x_i} \right) + \frac{\partial}{\partial x_i} (p u_i) - \frac{\partial}{\partial x_i} (\tau_{ij} u_j) - \rho g_i u_i - q_H = 0 \quad (1.21a)$$

or using Eq. (1.18) more simply

$$\frac{\partial(\rho E)}{\partial t} + \frac{\partial}{\partial x_i} (\rho u_i H) - \frac{\partial}{\partial x_i} \left(k \frac{\partial T}{\partial x_i} \right) - \frac{\partial}{\partial x_i} (\tau_{ij} u_j) - \rho g_i u_i - q_H = 0 \quad (1.21b)$$

Here, the penultimate term represents the rate of work done by body forces.

1.2.6 Boundary conditions

On the boundary of a typical fluid dynamics problem *boundary conditions* need to be specified to make the solution possible. These are given simply as follows:

- a. The velocities can be described as

$$u_i = \bar{u}_i \quad \text{on } \Gamma_u \quad (1.22a)$$

or traction as

$$t_i = n_j \sigma_{ij} = \bar{t}_i \quad \text{on } \Gamma_t \quad (1.22b)$$

where $\Gamma_u \cup \Gamma_t = \Gamma$ and $\Gamma_u \cap \Gamma_t = 0$. Generally traction is resolved into normal and tangential components to the boundary.

- b. In problems for which consideration of energy is important the temperature on the boundary is expressed as

$$T = \bar{T} \quad \text{on } \Gamma_T \quad (1.23a)$$

or thermal flux

$$q_n = -n_i k \frac{\partial T}{\partial x_i} = -k \frac{\partial T}{\partial n} = \bar{q}_n \quad \text{on } \Gamma_q \quad (1.23b)$$

where $\Gamma_T \cup \Gamma_q = \Gamma$ and $\Gamma_T \cap \Gamma_q = 0$.

- c. For problems of compressible flow the input density is specified as

$$\rho = \bar{\rho} \quad \text{on } \Gamma_\rho \quad (1.24)$$

1.2.7 Navier-Stokes and Euler equations

The governing equations derived in the preceding sections can be written in a general conservative form as

$$\frac{\partial \Phi}{\partial t} + \frac{\partial \mathbf{F}_i}{\partial x_i} + \frac{\partial \mathbf{G}_i}{\partial x_i} + \mathbf{Q} = \mathbf{0} \quad (1.25)$$

in which Eqs. (1.12), (1.14), or (1.21b) provide the particular entries to the vectors.

Thus, using indicial notation the vector of independent unknowns is

$$\Phi = \begin{Bmatrix} \rho \\ \rho u_1 \\ \rho u_2 \\ \rho u_3 \\ \rho E \end{Bmatrix} \quad (1.26a)$$

The convective flux is expressed as

$$\mathbf{F}_i = \begin{Bmatrix} \rho u_i \\ \rho u_1 u_i + p \delta_{1i} \\ \rho u_2 u_i + p \delta_{2i} \\ \rho u_3 u_i + p \delta_{3i} \\ \rho H u_i \end{Bmatrix} \quad (1.26b)$$

Similarly, the diffusive flux is expressed as

$$\mathbf{G}_i = \begin{Bmatrix} 0 \\ -\tau_{1i} \\ -\tau_{2i} \\ -\tau_{3i} \\ -(\tau_{ij} u_j) - k \frac{\partial T}{\partial x_i} \end{Bmatrix} \quad (1.26c)$$

and the source terms as

$$\mathbf{Q} = \begin{Bmatrix} 0 \\ -\rho g_1 \\ -\rho g_2 \\ -\rho g_3 \\ -\rho g_i u_i - q_H \end{Bmatrix} \quad (1.26d)$$

with

$$\tau_{ij} = \mu \left[\left(\frac{\partial u_i}{\partial x_j} + \frac{\partial u_j}{\partial x_i} \right) - \frac{2}{3} \delta_{ij} \frac{\partial u_k}{\partial x_k} \right]$$

The complete set of (1.25) is known as the *Navier-Stokes equation*. A particular case when viscosity is assumed to be zero and no heat conduction exists is known as the “Euler equation” (where $\tau_{ij} = 0$ and $q_i = 0$).

The above equations are the basis from which all fluid dynamics studies start and it is not surprising that many alternative forms are given in the literature obtained by combinations of the various equations [13].

The above set is, however, convenient and physically meaningful, defining the conservation of important quantities. It should be noted that only equations written in conservation form will yield the correct, physically meaningful, results in problems where shock or other forms of discontinuities are present.

In Appendix B, we show a particular set of nonconservative equations which are frequently used. The reader is cautioned not to extend the use of nonconservative equations to problems of high-speed flow.

In many actual situations one or another feature of the flow is predominant. For instance, frequently the viscosity is only of importance close to the boundaries at which velocities are specified. In such cases the problem can be considered separately in two parts: one as a *boundary layer* near such boundaries and another as *inviscid flow* outside the boundary layer.

Further, in many cases a steady-state solution is not available with the fluid exhibiting *turbulence*, i.e., a random fluctuation of velocity. Here it is still possible to use the general Navier-Stokes equations now written in terms of the mean flow with an additional *Reynolds stress* term. Turbulent instability is inherent in the Navier-Stokes equations. It is in principle always possible to obtain the transient, turbulent, solution modeling of the flow, provided the mesh size is capable of reproducing the small eddies which develop in the problem. Such computations, although possible, are extremely costly and hence the Reynolds averaging approach is of practical importance.

Two further points have to be made concerning *inviscid flow* (ideal fluid flow as it is sometimes known). Firstly, the Euler equations are of a purely convective form

$$\frac{\partial \Phi}{\partial t} + \frac{\partial \mathbf{F}_i}{\partial x_i} + \mathbf{Q} = \mathbf{0} \quad \mathbf{F}_i = \mathbf{F}_i(\Phi) \quad (1.27)$$

and hence very special methods for their solutions will be necessary. These methods are applicable and useful mainly in *compressible flow*, as we shall discuss in [Chapter 7](#). Secondly, for incompressible (or nearly incompressible) flows it is of interest to introduce a *potential* that converts the Euler equations to a simple self-adjoint form (see [Appendix A](#)). We shall discuss this potential approximation in [Section 1.3](#). Although potential forms are applicable also to compressible flows we shall not use them as they fail in complex situations.

1.3 Inviscid, incompressible flow

In the absence of viscosity and compressibility, ρ is constant and [Eq. \(1.12\)](#) can be written as

$$\frac{\partial u_i}{\partial x_i} = 0 \quad (1.28)$$

and [\(1.14\)](#) as

$$\frac{\partial u_i}{\partial t} + \frac{\partial}{\partial x_j}(u_j u_i) + \frac{1}{\rho} \frac{\partial p}{\partial x_i} - g_i = 0 \quad (1.29)$$

1.3.1 Velocity potential solution

The Euler equations given above may be simplified by introducing a potential, ϕ , and defining velocities as

$$u_1 = -\frac{\partial \phi}{\partial x_1} \quad u_2 = -\frac{\partial \phi}{\partial x_2} \quad u_3 = -\frac{\partial \phi}{\partial x_3}$$

or

$$u_i = -\frac{\partial \phi}{\partial x_i} \quad (1.30)$$

If such a potential exists then insertion of [Eq. \(1.30\)](#) into [\(1.28\)](#) gives a single governing equation

$$\frac{\partial^2 \phi}{\partial x_i \partial x_i} \equiv \nabla^2 \phi = 0 \quad (1.31)$$

which, with appropriate boundary conditions, can be readily solved. [Equation \(1.31\)](#) is a classical Laplacian equation. For contained flow we can of course impose the normal velocity u_n on the boundaries:

$$u_n = -\frac{\partial \phi}{\partial n} = \bar{u}_n \quad (1.32)$$

As we shall see later, this provides a *natural* boundary condition for a weighted residual or finite element solution.

Of course we must be assured that the potential function ϕ exists, and indeed determine what conditions are necessary for its existence. Here we observe that so far in the definition of the problem we have not used the momentum conservation equation (1.29), to which we shall now return. However, we first note that a single-valued potential function implies that

$$\frac{\partial^2 \phi}{\partial x_j \partial x_i} = \frac{\partial^2 \phi}{\partial x_i \partial x_j} \quad (1.33)$$

Defining vorticity as rotation rate per unit area

$$\omega_{ij} = \frac{1}{2} \left(\frac{\partial u_i}{\partial x_j} - \frac{\partial u_j}{\partial x_i} \right) \quad (1.34)$$

we note that the use of the velocity potential in (1.34) gives

$$\omega_{ij} = 0 \quad (1.35)$$

and the flow is therefore named *irrotational*.

Inserting the definition of potential into the first term of Eq. (1.29) and using Eqs. (1.28) and (1.34) we can rewrite Eq. (1.29) as

$$-\frac{\partial}{\partial x_i} \left(\frac{\partial \phi}{\partial t} \right) + \frac{\partial}{\partial x_i} \left[\frac{1}{2} u_j u_j + \frac{p}{\rho} + P \right] = 0 \quad (1.36)$$

in which P is a potential of the body forces given by

$$g_i = -\frac{\partial P}{\partial x_i} \quad (1.37)$$

In problems involving constant gravity forces in the x_3 direction the body force potential is simply

$$P = g x_3 \quad (1.38)$$

Equation (1.36) is alternatively written as

$$\nabla \left(-\frac{\partial \phi}{\partial t} + H + P \right) = 0 \quad (1.39)$$

where H is the *enthalpy*, given by (1.18).

If isothermal conditions pertain, the specific energy is constant and (1.39) implies that

$$-\frac{\partial \phi}{\partial t} + \frac{1}{2} u_i u_i + \frac{p}{\rho} + P = \text{constant} \quad (1.40)$$

over the whole domain. This can be taken as a corollary of the existence of the potential and indeed is a condition for its existence. In steady-state flows it provides the well-known Bernoulli equation that allows the pressures to be determined throughout the whole potential field once the value of the constant is established.

We note that the governing potential [equation \(1.31\)](#) is self-adjoint (see [Appendix A](#)) and that the introduction of the potential has sidestepped the difficulties of dealing with convective terms. It is also of interest to note that the Laplacian equation, which is obeyed by the velocity potential, occurs in other contexts. For instance in two-dimensional flow it is convenient to introduce a *stream function* the contours of which lie along the streamlines. The stream function, ψ , defines the velocities as

$$u_1 = \frac{\partial \psi}{\partial x_2} \quad \text{and} \quad u_2 = -\frac{\partial \psi}{\partial x_1} \quad (1.41)$$

which satisfy the incompressibility condition [\(1.28\)](#):

$$\frac{\partial u_i}{\partial x_i} = \frac{\partial}{\partial x_1} \left(\frac{\partial \psi}{\partial x_2} \right) + \frac{\partial}{\partial x_2} \left(-\frac{\partial \psi}{\partial x_1} \right) = 0 \quad (1.42)$$

For an existence of a unique potential for irrotational flow we note that $\omega_{12} = 0$ gives a Laplacian equation

$$\frac{\partial^2 \psi}{\partial x_i \partial x_i} = \nabla^2 \psi = 0 \quad (1.43)$$

The stream function is very useful in getting a pictorial representation of flow. In [Appendix C](#) we show how the stream function can be readily computed from a known distribution of velocities.

1.4 Incompressible (or nearly incompressible) flows

We observed earlier that the Navier-Stokes equations are completed by the existence of a state relationship giving [[Eq. \(1.15a\)](#)]

$$\rho = \rho(p, T)$$

In (nearly) incompressible relations we shall frequently assume that

- a. The problem is isothermal.
- b. The variation of ρ with p is very small, i.e., such that in product terms of velocity and density the latter can be assumed constant.

The first assumption will be relaxed, as we shall see later, allowing some thermal coupling via the dependence of the fluid properties on temperature. In such cases we shall introduce the coupling iteratively. For such cases the problem of density-induced currents or temperature-dependent viscosity will be typical (see [Chapters 5 and 6](#)).

If the assumptions introduced above are used we can still allow for small compressibility, noting that density changes are, as a consequence of elastic deformability, related to pressure changes. Thus we can write

$$d\rho = \frac{\rho}{K} dp \quad (1.44a)$$

where K is the elastic bulk modulus. This also can be written as

$$d\rho = \frac{1}{c^2} dp \quad (1.44b)$$

or

$$\frac{\partial \rho}{\partial t} = \frac{1}{c^2} \frac{\partial p}{\partial t} \quad (1.44c)$$

with $c = \sqrt{K/\rho}$ being the acoustic wave velocity.

[Equations \(1.25\)](#) and [\(1.26a\)–\(1.26d\)](#) can now be rewritten omitting the energy transport equation (and condensing the general form) as

$$\frac{1}{c^2} \frac{\partial p}{\partial t} + \rho \frac{\partial u_i}{\partial x_i} = 0 \quad (1.45a)$$

$$\frac{\partial u_j}{\partial t} + \frac{\partial}{\partial x_i} (u_j u_i) + \frac{1}{\rho} \frac{\partial p}{\partial x_j} - \frac{1}{\rho} \frac{\partial \tau_{ij}}{\partial x_i} - g_j = 0 \quad (1.45b)$$

In three dimensions $j = 1, 2, 3$ and the above represents a system of four equations in which the variables are u_j and p . Here

$$\frac{1}{\rho} \tau_{ij} = \nu \left(\frac{\partial u_i}{\partial x_j} + \frac{\partial u_j}{\partial x_i} - \frac{2}{3} \delta_{ij} \frac{\partial u_k}{\partial x_k} \right)$$

where $\nu = \mu/\rho$ is the kinematic viscosity.

The reader will note that the above equations, with the exception of the convective acceleration terms, are *identical to those governing the problem of incompressible (or slightly compressible) elasticity* (e.g., see Chapter 10 of [Ref. \[1\]](#)).

1.5 Numerical solutions: Weak forms, weighted residual, and finite element approximation

1.5.1 Strong and weak forms

We assume the reader is already familiar with basic ideas of finite element and finite difference methods. However, to avoid a constant cross reference to other texts (e.g., [\[1\]](#)), we provide here a brief introduction to *weighted residual* (or Galerkin) and *finite element methods*.

The Laplace equation, which we introduced in [Section 1.3](#), is a very convenient example for the start of numerical approximations. We shall generalize slightly and discuss in some detail the quasi-harmonic (Poisson) equation

$$-\frac{\partial}{\partial x_i} \left(k \frac{\partial \phi}{\partial x_i} \right) + Q = 0 \quad (1.46)$$

where k and Q are specified functions. These equations together with appropriate boundary conditions define the problem uniquely. The boundary conditions can be Dirichlet type,

$$\phi = \bar{\phi} \quad \text{on } \Gamma_\phi \quad (1.47a)$$

or Neumann type,

$$q_n = -k \frac{\partial \phi}{\partial n} = \bar{q}_n \quad \text{on } \Gamma_q \quad (1.47b)$$

where a bar denotes a specified quantity.

[Equations \(1.46\)](#) to [\(1.47b\)](#) are defined as the *strong form* of the problem.

1.5.1.1 Weak form of equations

We note that direct use of [Eq. \(1.46\)](#) requires computation of second derivatives to solve a problem using approximate techniques. This requirement may be weakened by considering an integral expression for [Eq. \(1.46\)](#) written as

$$\int_{\Omega} v \left[-\frac{\partial}{\partial x_i} \left(k \frac{\partial \phi}{\partial x_i} \right) + Q \right] d\Omega = 0 \quad (1.48)$$

in which v is an arbitrary function. A proof that [Eq. \(1.48\)](#) is equivalent to [Eq. \(1.46\)](#) is simple.

If we assume [Eq. \(1.46\)](#) is not zero at some point x_i in Ω then we can also let v be a positive parameter times the same value resulting in a positive result for the integral of [Eq. \(1.48\)](#). Since this violates the equality we conclude that [Eq. \(1.46\)](#) must be zero for every x_i in Ω hence proving its equality with [Eq. \(1.48\)](#).

We may integrate by parts the second derivative terms in [Eq. \(1.48\)](#) to obtain

$$\int_{\Omega} \frac{\partial v}{\partial x_i} \left(k \frac{\partial \phi}{\partial x_i} \right) d\Omega + \int_{\Omega} v Q d\Omega - \int_{\Gamma} v n_i \left(k \frac{\partial \phi}{\partial x_i} \right) d\Gamma = 0 \quad (1.49)$$

We now split the boundary into two parts, Γ_ϕ and Γ_q , with $\Gamma = \Gamma_\phi \cup \Gamma_q$, and $\Gamma_\phi \cap \Gamma_q = 0$, and use [\(1.47b\)](#) in [\(1.49\)](#) to give

$$\int_{\Omega} \frac{\partial v}{\partial x_i} \left(k \frac{\partial \phi}{\partial x_i} \right) d\Omega + \int_{\Omega} v Q d\Omega + \int_{\Gamma_q} v \bar{q}_n d\Gamma = 0 \quad (1.50)$$

which is valid only if v vanishes on Γ_ϕ . Hence we must impose [Eq. \(1.47a\)](#) for equivalence.

[Equation \(1.50\)](#) is known as the *weak form* of the problem since only first derivatives are necessary in constructing a solution. Such forms are the basis for the finite element solutions we use throughout this book.

1.5.2 Weighted residual approximation

In a weighted residual scheme an approximation to the independent variable ϕ is written as a sum of known *trial functions* (basis functions) $N_a(x_i)$ and unknown parameters $\tilde{\phi}^a$. Thus we can always write

$$\begin{aligned}\phi \approx \hat{\phi} &= N_1(x_i)\tilde{\phi}^1 + N_2(x_i)\tilde{\phi}^2 + \dots \\ &= \sum_{a=1}^n N_a(x_i)\tilde{\phi}^a = \mathbf{N}(x_i)\tilde{\phi}\end{aligned}\quad (1.51)$$

where

$$\mathbf{N} = [N_1, \quad N_2, \dots, \quad N_n] \quad (1.52a)$$

and

$$\tilde{\phi} = [\tilde{\phi}^1, \quad \tilde{\phi}^2, \dots, \quad \tilde{\phi}^n]^T \quad (1.52b)$$

In a similar way we can express the arbitrary variable v as

$$\begin{aligned}v \approx \hat{v} &= W_1(x_i)\tilde{v}^1 + W_2(x_i)\tilde{v}^2 + \dots \\ &= \sum_{a=1}^n W_a(x_i)\tilde{v}^a = \mathbf{W}(x_i)\tilde{\mathbf{v}}\end{aligned}\quad (1.53)$$

in which W_a are *test functions* and \tilde{v}^a arbitrary parameters. Using this form of approximation will convert (1.50) to a set of algebraic equations.

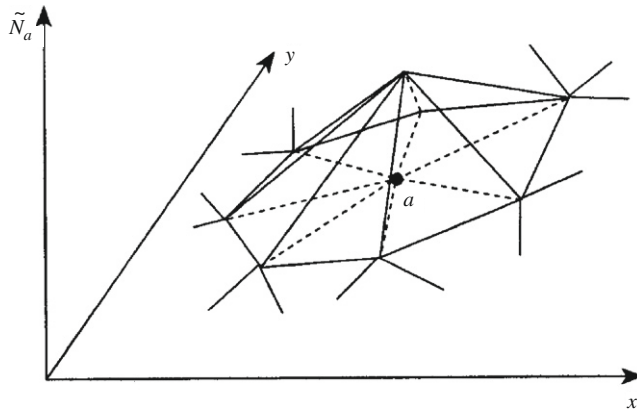
In the finite element method and indeed in all other numerical procedures for which a computer-based solution can be used, the test and trial functions will generally be defined in a local manner. It is convenient to consider each of the test and basis functions to be defined in partitions Ω_e of the total domain Ω . This division is denoted by

$$\Omega \approx \Omega_h = \bigcup \Omega_e \quad (1.54)$$

and in a finite element method Ω_e are known as *elements*. The very simplest uses lines in one dimension, triangles in two dimensions, and tetrahedra in three dimensions in which the basis functions are usually linear polynomials in each element and the unknown parameters are *nodal values* of ϕ . In Fig. 1.2 we show a typical set of such linear functions defined in two dimensions.

In a weighted residual procedure we first insert the approximate function $\hat{\phi}$ into the governing differential equation creating a residual, $R(x_i)$, which of course should be zero at the exact solution. In the present case for the quasi-harmonic equation we obtain

$$R = -\frac{\partial}{\partial x_i} \left(k \sum_a \frac{\partial N_a}{\partial x_i} \tilde{\phi}^a \right) + Q \quad (1.55)$$

**FIGURE 1.2**

Basis function in linear polynomials for a patch of triangular elements.

and we now seek the best values of the parameter set $\tilde{\phi}^a$ which ensures that

$$\int_{\Omega} W_b R d\Omega = 0, \quad b = 1, 2, \dots, n \quad (1.56)$$

Note that this is the term multiplying the arbitrary parameter \tilde{v}^b . As noted previously, integration by parts is used to avoid higher-order derivatives (i.e., those greater than or equal to two) and therefore reduce the constraints on choosing the basis functions to permit integration over individual elements using Eq. (1.54). In the present case, for instance, the weighted residual after integration by parts and introducing the natural boundary condition becomes

$$\int_{\Omega} \frac{\partial W_b}{\partial x_i} \left(k \sum_a \frac{\partial N_a}{\partial x_i} \tilde{\phi}^a \right) d\Omega + \int_{\Omega} W_b Q d\Omega + \int_{\Gamma_q} W_b \bar{q}_n d\Gamma = 0 \quad (1.57)$$

where b denotes a specific node where the residual is evaluated.

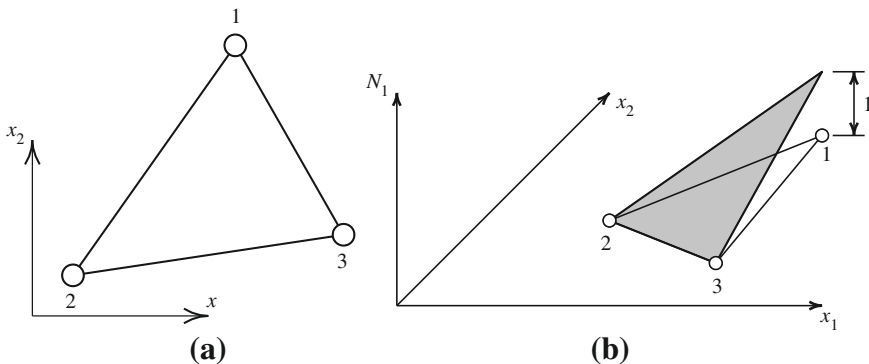
1.5.3 The Galerkin finite element method

In the Galerkin method we simply take $W_b = N_b$, which gives the assembled system of equations

$$\sum_{a=1}^n K_{ba} \tilde{\phi}^a + f_b = 0, \quad b = 1, 2, \dots, n - r \quad (1.58)$$

where r is the number of nodes appearing in the approximation to the Dirichlet boundary condition [i.e., Eq. (1.47a)] and K_{ba} is assembled from element contributions K_{ba}^e with

$$K_{ba}^e = \int_{\Omega_e} \frac{\partial N_b}{\partial x_i} k \frac{\partial N_a}{\partial x_i} d\Omega \quad (1.59)$$

**FIGURE 1.3**(a) Three-node triangular element and (b) shape function for N_1 .

Similarly, f_b is computed from the element as

$$f_b^e = \int_{\Omega_e} N_b Q \, d\Omega + \int_{\Gamma_{eq}} N_b \bar{q}_n \, d\Gamma \quad (1.60)$$

To impose the Dirichlet boundary condition we set

$$\tilde{\phi}^b = \bar{\phi}^b \text{ at each boundary node} \quad (1.61)$$

and replace $\tilde{\phi}^a$ by given $\bar{\phi}^a$ for the r boundary nodes.

It is evident in this example that the Galerkin method results in a symmetric set of algebraic equations (e.g., $K_{ba} = K_{ab}$). However this only happens if the differential equations are *self-adjoint* (see [Appendix A](#)). Indeed the existence of symmetry provides a test for self-adjointness and for steady-state problems existence of a variational principle whose stationarity is sought [1].

It is necessary to remark here that if we were considering a pure convection equation

$$u_i \frac{\partial \phi}{\partial x_i} + Q = 0 \quad (1.62)$$

with u_i being the velocity components, symmetry would not exist and the equations can often become unstable if the Galerkin method is used. We will discuss this matter further in the next chapter.

Example 1.1. Shape functions for triangle with three nodes

A typical finite element with a triangular shape is defined by the local nodes 1, 2, 3 and straight line boundaries between nodes as shown in [Fig. 1.3a](#) and will yield the shape of N_a of the form shown in [Fig. 1.3b](#). Writing a scalar variable as

$$\phi = \alpha_1 + \alpha_2 x_1 + \alpha_3 x_2 \quad (1.63)$$

we may evaluate the three constants by solving a set of three simultaneous equations which arise if the nodal coordinates are inserted and the scalar variable equated to the appropriate nodal values. For example, nodal values may be written as

$$\begin{aligned}\tilde{\phi}^1 &= \alpha_1 + \alpha_2 x_1^1 + \alpha_3 x_2^1 \\ \tilde{\phi}^2 &= \alpha_1 + \alpha_2 x_1^2 + \alpha_3 x_2^2 \\ \tilde{\phi}^3 &= \alpha_1 + \alpha_2 x_1^3 + \alpha_3 x_2^3\end{aligned}\quad (1.64)$$

We can easily solve for α_1 , α_2 , and α_3 in terms of the nodal values $\tilde{\phi}^1$, $\tilde{\phi}^2$, and $\tilde{\phi}^3$ and substituting into Eq. 1.63 gives

$$\phi = \frac{1}{2\Delta} \left[(a_1 + b_1 x_1 + c_1 x_2) \tilde{\phi}^1 + (a_2 + b_2 x_1 + c_2 x_2) \tilde{\phi}^2 + (a_3 + b_3 x_1 + c_3 x_2) \tilde{\phi}^3 \right] \quad (1.65)$$

in which

$$\begin{aligned}a_1 &= x_1^2 x_2^3 - x_1^3 x_2^2 \\ b_1 &= x_2^2 - x_2^3 \\ c_1 &= x_1^3 - x_1^2\end{aligned}\quad (1.66)$$

where x_i^a is the i-direction coordinate of node a and other coefficients are obtained by cyclic permutation of the subscripts in the order 1, 2, 3, and

$$2\Delta = \det \begin{vmatrix} 1 & x_1^1 & x_2^1 \\ 1 & x_1^2 & x_2^2 \\ 1 & x_1^3 & x_2^3 \end{vmatrix} = 2 \cdot (\text{area of triangle 123}) \quad (1.67)$$

From Eq. (1.65) we see that the shape functions are given by

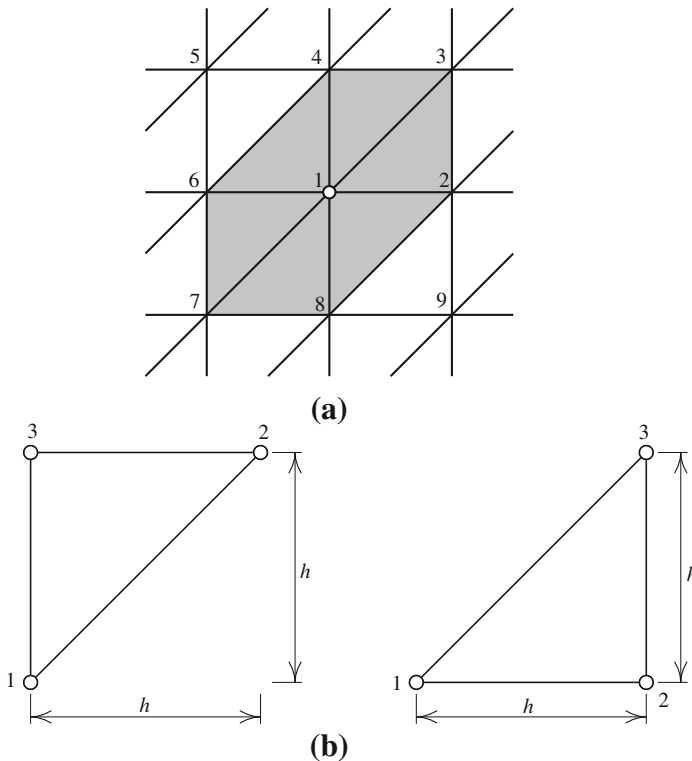
$$N_a = (a_a + b_a x_1 + c_a x_2)/(2\Delta), \quad a = 1, 2, 3 \quad (1.68)$$

Since the unknown nodal quantities defined by these shape functions vary linearly along any side of a triangle the interpolation equation (1.65) guarantees continuity between adjacent elements and, with identical nodal values imposed, the same scalar variable value will clearly exist along an interface between elements. We note, however, that in general the derivatives will not be continuous between element assemblies [1].

Example 1.2. Poisson equation in two dimensions: Galerkin formulation with triangular elements

The relations for a Galerkin finite element solution have been given in (1.58)–(1.60). The components of K_{ba} and f_b can be evaluated for a typical element or subdomain and the system of equations built by standard methods.

For instance, considering the set of nodes and elements shown shaded in Fig. 1.4a, to compute the equation for node 1 in the assembled patch, it is only necessary to

**FIGURE 1.4**

Linear triangular elements for Poisson equation example: (a) “connected” equations for node 1; (b) Type 1 and Type 2 element shapes in mesh.

compute the K_{ba}^e for two element shapes as indicated in Fig. 1.4b. For the Type 1 element (left element in Fig. 1.4b) the shape functions evaluated from (1.68) using (1.66) and (1.67) and placing the origin of coordinates at node 1 give

$$N_1 = 1 - \frac{x_2}{h}, \quad N_2 = \frac{x_1}{h}, \quad N_3 = \frac{x_2 - x_1}{h}$$

Thus, the derivatives are given by

$$\frac{\partial \mathbf{N}}{\partial x_1} = \begin{Bmatrix} \frac{\partial N_1}{\partial x_1} \\ \frac{\partial N_2}{\partial x_1} \\ \frac{\partial N_3}{\partial x_1} \end{Bmatrix} = \begin{Bmatrix} 0 \\ \frac{1}{h} \\ -\frac{1}{h} \end{Bmatrix} \quad \text{and} \quad \frac{\partial \mathbf{N}}{\partial x_2} = \begin{Bmatrix} \frac{\partial N_1}{\partial x_2} \\ \frac{\partial N_2}{\partial x_2} \\ \frac{\partial N_3}{\partial x_2} \end{Bmatrix} = \begin{Bmatrix} -\frac{1}{h} \\ 0 \\ \frac{1}{h} \end{Bmatrix}$$

Similarly, for the Type 2 element the shape functions are expressed by

$$N_1 = 1 - \frac{x_1}{h}, \quad N_2 = \frac{x_1 - x_2}{h}, \quad N_3 = \frac{x_2}{h}$$

and their derivatives by

$$\frac{\partial \mathbf{N}}{\partial x_1} = \begin{Bmatrix} \frac{\partial N_1}{\partial x_1} \\ \frac{\partial N_2}{\partial x_1} \\ \frac{\partial N_3}{\partial x_1} \end{Bmatrix} = \begin{Bmatrix} -\frac{1}{h} \\ \frac{1}{h} \\ 0 \end{Bmatrix} \quad \text{and} \quad \frac{\partial \mathbf{N}}{\partial x_2} = \begin{Bmatrix} \frac{\partial N_1}{\partial x_2} \\ \frac{\partial N_2}{\partial x_2} \\ \frac{\partial N_3}{\partial x_2} \end{Bmatrix} = \begin{Bmatrix} 0 \\ -\frac{1}{h} \\ \frac{1}{h} \end{Bmatrix}$$

Evaluation of the matrix K_{ba}^e and f_b^e for Type 1 and Type 2 elements gives (refer to [Appendix F](#) for integration formulae)

$$\mathbf{K}^e \tilde{\boldsymbol{\phi}}^e = \frac{1}{2} k \begin{bmatrix} 1 & 0 & -1 \\ 0 & 1 & -1 \\ -1 & -1 & 2 \end{bmatrix} \begin{Bmatrix} \tilde{\phi}^{1e} \\ \tilde{\phi}^{2e} \\ \tilde{\phi}^{3e} \end{Bmatrix} \quad \text{and} \quad \mathbf{K}^e \tilde{\boldsymbol{\phi}}^e = \frac{1}{2} k \begin{bmatrix} 1 & -1 & 0 \\ -1 & 2 & -1 \\ 0 & -1 & 1 \end{bmatrix} \begin{Bmatrix} \tilde{\phi}^{1e} \\ \tilde{\phi}^{2e} \\ \tilde{\phi}^{3e} \end{Bmatrix}$$

respectively. The force vector for a constant Q over each element is given by

$$\mathbf{f}^e = \frac{1}{6} Q h^2 \begin{Bmatrix} 1 \\ 1 \\ 1 \end{Bmatrix}$$

for both types of elements. Assembling the patch of elements shown in [Fig. 1.4a](#) gives the equation with nonzero coefficients for node 1 as (refer to [1] and [18] for assembly procedure)

$$k \begin{bmatrix} 4 & -1 & -1 & -1 & -1 \end{bmatrix} \begin{Bmatrix} \tilde{\phi}^1 \\ \tilde{\phi}^2 \\ \tilde{\phi}^4 \\ \tilde{\phi}^6 \\ \tilde{\phi}^8 \end{Bmatrix} + Q h^2 = 0$$

Using a central finite difference approximation directly in the differential equation (1.46) gives the approximation

$$\frac{k}{h^2} \begin{bmatrix} 4 & -1 & -1 & -1 & -1 \end{bmatrix} \begin{Bmatrix} \tilde{\phi}^1 \\ \tilde{\phi}^2 \\ \tilde{\phi}^4 \\ \tilde{\phi}^6 \\ \tilde{\phi}^8 \end{Bmatrix} + Q = 0$$

and we note that the assembled node is identical to the finite difference approximation though presented slightly differently. If all the boundary conditions are forced (i.e., $\phi = \bar{\phi}$) no differences arise between a finite element and a finite difference solution for the regular mesh assumed. However, if any boundary conditions are of natural type or the mesh is irregular, differences will arise, with the finite element solution

generally giving superior answers. Indeed, no restrictions on shape of elements or assembly type are imposed by the finite element approach.

Example 1.3. Local and global conservation of the finite element method

As mentioned before the finite element method can be locally and globally conservative. The local conservation is achieved by considering a patch of elements surrounding a node a as shown in Fig. 1.2. Rewriting a conservation equation in terms of flux gives

$$-\frac{\partial \mathbf{F}_i}{\partial x_i} + Q = 0 \quad (1.69)$$

Here \mathbf{F}_i contains all fluxes including the diffusive and convective fluxes normally encountered in fluid dynamics. Subjecting the above to the Galerkin finite element process explained in the previous section results in

$$\int_{\Omega} \frac{\partial N_b}{\partial x_i} \hat{\mathbf{F}}_i d\Omega + \int_{\Omega} N_b Q d\Omega - \int_{\Gamma_q} N_b \hat{\mathbf{F}}_i n_i d\Gamma = 0 \quad (1.70)$$

where $\hat{\mathbf{F}}_i$ is the approximation for the flux. Since the sum of the trial function derivatives for an inside node surrounded by an element patch is zero, the equation for an inside patch becomes

$$\int_{\Omega^P} N_b Q d\Omega - \int_{\Gamma_q^P} N_b \hat{\mathbf{F}}_i n_i d\Gamma = 0 \quad (1.71)$$

where Ω^P and Γ_q^P respectively indicate the volume and surface of an inner patch.

The above equation clearly shows that net production (source) is equal to net flux leaving the patch, demonstrating the local conservation of quantities. Now, assuming this is true for all inner patches and assuming a uniform source, the above equation is valid for the entire domain of the problem as long as Neumann boundaries surround the domain. If Dirichlet boundary conditions are applied, the global conservation is not directly demonstrable as these boundary conditions require the weighting functions to vanish on the boundaries. To make the finite element globally conservative, an extra flux boundary condition may be applied along the boundaries.

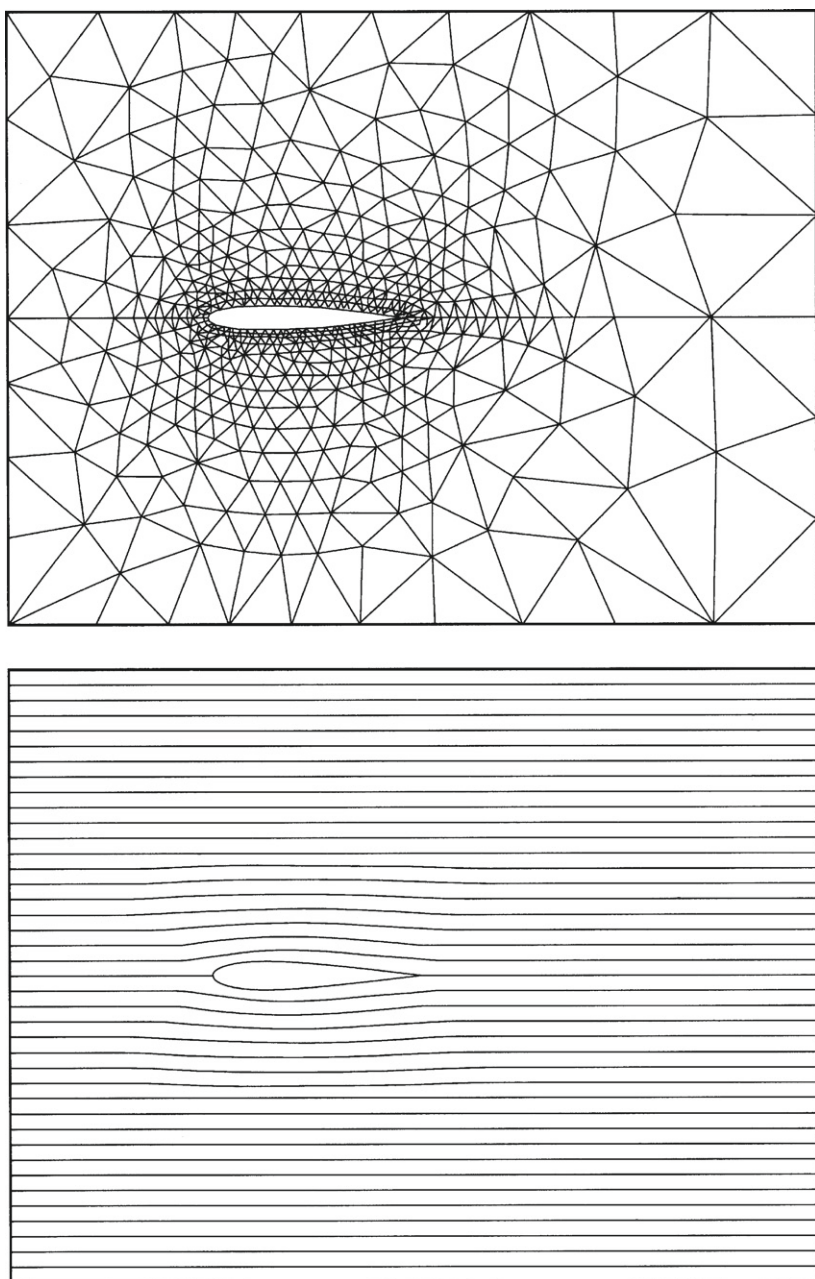
Example 1.4. In Fig. 1.5 an example of a typical potential solution as described in Section 1.3 is given. Here we show the finite element mesh and streamlines for a domain of flow around a symmetric aerofoil.

Example 1.5. Some problems of specific interest are those of flow with a free surface [19–21]. Here the governing Laplace equation for the potential remains identical, but the free surface position has to be found iteratively. In Fig. 1.6 an example of such a free surface flow solution is given [20].

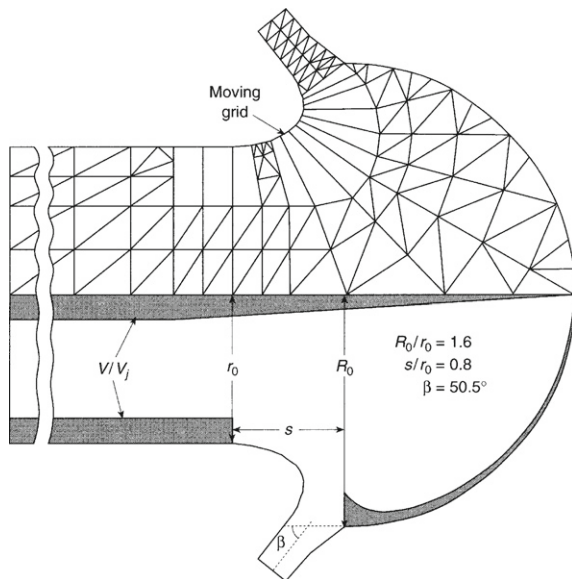
For gravity forces given by (1.38) the free surface condition in two dimensions (x_1, x_2) requires

$$\frac{1}{2}(u_1^2 + u_3^2) - gx_2 = 0$$

Solution of such conditions involves an iterative, nonlinear algorithm, as illustrated by examples of overflows in Ref. [19].

**FIGURE 1.5**

Potential flow solution around an aerofoil. Mesh and streamline plots.

**FIGURE 1.6**

Free surface potential flow, illustrating an axisymmetric jet impinging on a hemispherical thrust reverser (from Sarpkaya and Hiriart [20]).

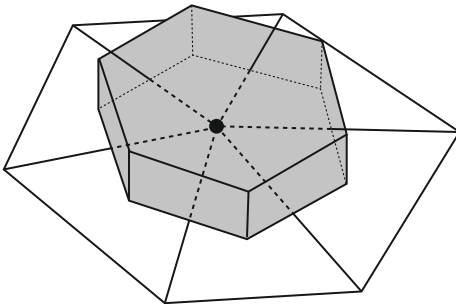
1.5.4 A finite volume approximation

Many choices of basis and weight functions are available. A large number of procedures are discussed in Ref. [1]. An approximation which is frequently used in fluid dynamics is the *finite volume* process which many consider to be a generalized finite difference form. Here the weighting function is often taken as unity over a specified subdomain Ω_b and two variants are used: (a) an element (cell) centered approach and (b) a node (vertex) centered approach. Here we will consider only a node centered approach with basis functions as given in Eq. (1.51) for each triangular subdomain and the specified integration cell (dual cell) for each node as shown in Fig. 1.7. For a solution of the Poisson equation discussed above, integration by parts of (1.56) for a unit W_b gives

$$\int_{\Omega_b} Q d\Omega - \int_{\Gamma_b} n_i \frac{\partial \phi}{\partial x_i} d\Gamma = 0 \quad (1.72)$$

for each subdomain Ω_b with boundary Γ_b . In this form the integral of the first term gives

$$\int_{\Omega_b} Q d\Omega = Q \Omega_b \quad (1.73)$$

**FIGURE 1.7**

Finite volume weighting. Vertex centered method.

when Q is constant in the domain. Introduction of the basis functions into the second term gives

$$\int_{\Gamma_b} n_i \frac{\partial \phi}{\partial x_i} d\Gamma \approx \int_{\Gamma_b} n_i \frac{\partial \hat{\phi}}{\partial x_i} d\Gamma = \int_{\Gamma_b} n_i \frac{\partial N_a}{\partial x_i} d\Gamma \tilde{\phi}^a \quad (1.74)$$

requiring now only boundary integrals of the shape functions. In order to make the process clearer we again consider the case for the patch of elements shown in Fig. 1.4a.

Example 1.6. Poisson equation in two dimensions: Finite volume formulation with triangular elements

The subdomain for the determination of the equation for node 1 using the finite volume method is shown in Fig. 1.8a. The shape functions and their derivatives for the Type 1 and Type 2 elements shown in Fig. 1.8b are given in Example 1.1. We note especially that the derivatives of the shape functions in each element type are constant. Thus, the boundary integral terms in Eq. (1.74) become

$$\int_{\Gamma_b} n_i \frac{\partial N_a}{\partial x_i} d\Gamma = \sum_e \int_{\Gamma_e} n_i^e d\Gamma \frac{\partial N_a^e}{\partial x_i}$$

where e denotes the elements surrounding node a . The integrals on Γ_e may be evaluated by computing I_1 , I_2 and I_3 as shown for Type 1 and Type 2 elements. It is simple to show for the x_1 derivative we obtain

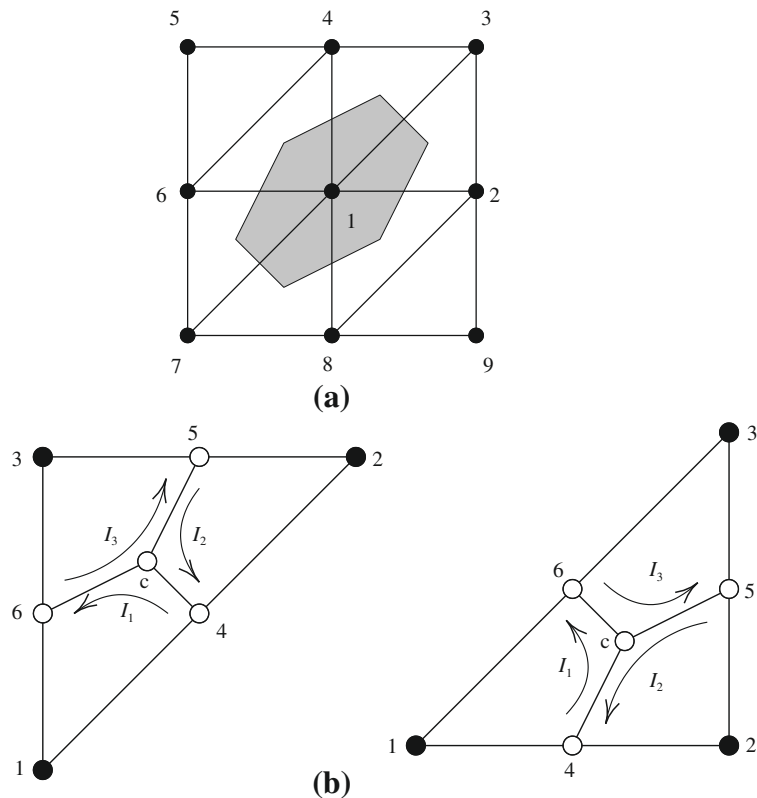
$$I_1^1 = \int_{\Gamma_e} n_1^e d\Gamma = \int_4^c n_1^e d\Gamma + \int_c^6 n_1^e d\Gamma = x_2^6 - x_2^4$$

where x_2^4, x_2^6 are mid-edge coordinates of the triangle as shown in Fig. 1.8b. Similarly, for the x_2 derivative we obtain

$$I_1^2 = \int_{\Gamma_e} n_2^e d\Gamma = \int_4^c n_2^e d\Gamma + \int_c^6 n_2^e d\Gamma = x_1^4 - x_1^6$$

Thus, for the integral I_1 we obtain

$$I_1 = \int_{\Gamma_e} n_i \frac{\partial N_a}{\partial x_i} d\Gamma = \frac{\partial N_a}{\partial x_1} (x_2^6 - x_2^4) + \frac{\partial N_a}{\partial x_2} (x_1^4 - x_1^6)$$

**FIGURE 1.8**

Finite volume domain and integrations for vertex centered method: “connected” equations for node 1; (b) Type 1 and Type 2 element boundary integrals.

The results for I_2 and I_3 are likewise obtained as

$$\begin{aligned} I_2 &= \frac{\partial N_a}{\partial x_1}(x_2^4 - x_2^5) + \frac{\partial N_a}{\partial x_2}(x_1^5 - x_1^4) \\ I_3 &= \frac{\partial N_a}{\partial x_1}(x_2^5 - x_2^6) + \frac{\partial N_a}{\partial x_2}(x_1^6 - x_1^5) \end{aligned}$$

Using the above we may write the finite volume result for the subdomain shown in Fig. 1.8a as

$$k \begin{bmatrix} 4 & -1 & -1 & -1 & -1 \end{bmatrix} \begin{Bmatrix} \tilde{\phi}^1 \\ \tilde{\phi}^2 \\ \tilde{\phi}^4 \\ \tilde{\phi}^6 \\ \tilde{\phi}^8 \end{Bmatrix} + Q h^2 = 0$$

We note that for the regular mesh the result is identical to that obtained using the standard Galerkin approximation. This identity does not generally hold when irregular meshes are considered and we find that the result from the finite volume approach applied to the Poisson equation will not yield a symmetric coefficient matrix [due to the fact that first derivative of shape functions appears in Eq. (1.72)]. As we know, the Galerkin method is optimal in terms of energy error and, thus, has more desirable properties than either the finite difference or the finite volume approaches.

Using the integrals defined on “elements,” as shown in Fig. 1.8b, it is possible to implement the finite volume method directly in a standard finite element program. The assembled matrix is computed elementwise by assembly for each node on an element. The unit weight will be “discontinuous” in each element, but otherwise all steps are standard.

1.6 Concluding remarks

We have observed in this chapter that a full set of Navier-Stokes equations can be written incorporating both compressible and incompressible behavior. At this stage it is worth remarking that

1. More specialized sets of equations such as those which govern shallow-water flow or surface wave behavior (Chapters 10–12) will be of similar forms and need not be repeated here.
2. The essential difference from solid mechanics equations involves the non-self-adjoint convective terms.
3. For simplified problems on structured meshes, the finite element, finite volume, and finite difference methods give identical solutions.

Before proceeding with discretization and indeed the finite element solution of the full fluid equations, it is important to discuss in more detail the finite element procedures which are necessary to deal with such convective transport terms.

We shall do this in the next chapter where a standard scalar convective-diffusive-reactive equation is discussed.

References

- [1] O.C. Zienkiewicz, R.L. Taylor, J.Z. Zhu, *The Finite Element Method: Its Basis and Fundamentals*, seventh ed., Elsevier, Oxford, 2013.
- [2] C. Hirsch, *Numerical Computation of Internal and External Flows*, vol. 1, John Wiley & Sons, New York, 1992.
- [3] A. Mizukami, A mixed finite element method for boundary flux computation , *Comput. Methods Appl. Mech. Eng.* 57 (1986) 239–243.

- [4] P.M. Gresho, R.L. Lee, R.L. Sani, M.K. Maslanik, B.E. Eaton, The consistent Galerkin FEM for computing derived boundary quantities in thermal and/or fluids problems, *Int. J. Numer. Methods Fluids* 7 (1987) 371–394.
- [5] M. Oshima, T.J.R. Hughes, K. Jansen, Consistent finite element calculation of boundary and internal fluxes , *Int. J. Comp. Fluid. Dyn.* 9 (1998) 227–235.
- [6] T.R.J. Hughes, G. Engel, L. Mazzei, M.G. Larson, The continuous Galerkin method is locally conservative, *J. Comput. Phy.* 163 (2000) 467–488.
- [7] T.R.J. Hughes, G.N. Wells, Conservation properties for the Galerkin and stabilised forms of the advection-diffusion and incompressible Navier-Stokes equations, *Comput. Methods Appl. Mech. Eng.* 194 (2005) 1141–1159.
- [8] P. Nithiarasu, A simple locally conservative Galerkin (LCG) finite-element method for transient conservation equations, *Numer. Heat Transfer B—Fund.* 46 (2004) 357–370.
- [9] C.G. Thomas, P. Nithiarasu, R.L.T. Bevan, The locally conservative Galerkin (LCG) method for solving the incompressible Navier-Stokes equations, *Int. J. Numer. Methods Fluids* 57 (2008) 1771–1792.
- [10] C.G. Thomas, P. Nithiarasu, An element-wise, locally conservative Galerkin (LCG) method for solving diffusion and convection-diffusion problems, *Int. J. Numer. Methods Eng.* 73 (2008) 642–664.
- [11] H. Schlichting, *Boundary Layer Theory*, Pergamon Press, London, 1955.
- [12] C.K. Batchelor, *An Introduction to Fluid Dynamics*, Cambridge University Press, Cambridge, 1967.
- [13] H. Lamb, *Hydrodynamics*, sixth ed., Cambridge University Press, Cambridge, 1932.
- [14] P.J. Roach, *Computational Fluid Mechanics*, Hermosa Press, Albuquerque, New Mexico, 1972.
- [15] L.D. Landau, E.M. Lifshitz, *Fluid Mechanics*, Pergamon Press, London, 1959.
- [16] R. Temam, *The Navier-Stokes Equation*, North-Holland, Dordrecht, 1977.
- [17] I.G. Currie, *Fundamental Mechanics of Fluids*, McGraw-Hill, New York, 1993.
- [18] R.W. Lewis, P. Nithiarasu, K.N. Seetharamu, *Fundamentals of the Finite Element Method for Heat and Fluid Flow*, John Wiley and Sons, 2004.
- [19] P. Bettess, J.A. Bettess, Analysis of free surface flows using isoparametric finite elements, *Int. J. Numer. Methods Eng.* 19 (1983) 1675–1689.
- [20] T. Sarpkaya, G. Hiriart, Finite element analysis of jet impingement on axisymmetric curved deflectors, in: J.T. Oden, O.C. Zienkiewicz, R.H. Gallagher, C. Taylor (Eds.), *Finite Elements in Fluids*, vol. 2, John Wiley & Sons, New York, 1976, pp. 265–279.
- [21] M.J. O'Carroll, A variational principle for ideal flow over a spillway, *Int. J. Numer. Methods Eng.* 15 (1980) 767–789.

2

Convection-Dominated Problems: Finite Element Approximations to the Convection-Diffusion-Reaction Equation

2.1 Introduction

In this chapter we are concerned with steady-state and transient solutions for equations of the type

$$\frac{\partial \Phi}{\partial t} + \frac{\partial \mathbf{F}_i}{\partial x_i} + \frac{\partial \mathbf{G}_i}{\partial x_i} + \mathbf{Q} = \mathbf{0} \quad (2.1)$$

where in general Φ is the basic dependent, vector-valued variable, \mathbf{Q} is a source or reaction term vector, and the *flux* matrices \mathbf{F} and \mathbf{G} are such that

$$\begin{aligned} \mathbf{F}_i &= \mathbf{F}_i(\Phi) \\ \mathbf{G}_i &= \mathbf{G}_i\left(\frac{\partial \Phi}{\partial x_j}\right) \end{aligned} \quad (2.2a)$$

and in general

$$\mathbf{Q} = \mathbf{Q}(x_i, \Phi) \quad (2.2b)$$

In the above, x_i and i refer, in the indicial manner, to Cartesian coordinates and quantities associated with these. A linear relationship between the source and the scalar variable in Eq. (2.2b) is frequently referred to as a reaction term.

The general equation (2.1) can be termed the *transport equation* with \mathbf{F} standing for the *convective* and \mathbf{G} for the *diffusive* flux quantities.

Equation (2.1) is a set of *conservation laws* arising from a balance of the quantity Φ with its fluxes \mathbf{F} and \mathbf{G} entering and leaving a control volume. Such equations are typical of fluid mechanics which we have discussed in Chapter 1. As such equations may also arise in other physical situations, this chapter is devoted to a general discussion of their approximate solution.

The simplest form of Eqs. (2.1), (2.2a), and (2.2b) is one in which the unknown is a scalar. Most of this chapter is devoted to the solution of such equations. Throughout this book we shall show that there is no need of dealing with convection of vector-type

quantities. Thus for the scalar form we have

$$\begin{aligned}\Phi &\rightarrow \phi & \mathbf{Q} &\rightarrow Q(x_i, \phi) \\ \mathbf{F}_i &\rightarrow F_i = U_i \phi & \mathbf{G}_i &\rightarrow G_i = -k \frac{\partial \phi}{\partial x_i}\end{aligned}\quad (2.3)$$

We also now have in Cartesian coordinates a scalar equation of the form

$$\frac{\partial \phi}{\partial t} + \frac{\partial(U_i \phi)}{\partial x_i} - \frac{\partial}{\partial x_i} \left(k \frac{\partial \phi}{\partial x_i} \right) + Q = 0 \quad (2.4)$$

In the above equation, U_i is a known velocity field and ϕ is a *scalar* quantity being transported by this velocity. However diffusion can also exist and here k is the diffusion coefficient.

The term Q represents any external sources of the quantity ϕ being admitted to the system and the reaction loss or gain which itself is dependent on the function ϕ .

A simple linear relation for the reaction may be written as

$$Q = c \phi \quad (2.5)$$

where c is a scalar parameter. The equation can be rewritten in a slightly modified form in which the convective term has been differentiated as

$$\underline{\frac{\partial \phi}{\partial t} + U_i \frac{\partial \phi}{\partial x_i}} + \phi \frac{\partial U_i}{\partial x_i} - \frac{\partial}{\partial x_i} \left(k \frac{\partial \phi}{\partial x_i} \right) + Q = 0 \quad (2.6)$$

We note that the above form of the problem is self-adjoint with the exception of a convective term which is underlined. The reader is referred to [Appendix A](#) for the definition of self-adjoint problems. The third term in [Eq. \(2.6\)](#) disappears if the flow itself is such that its divergence is zero, i.e., if

$$\frac{\partial U_i}{\partial x_i} = 0 \quad (2.7)$$

In what follows we shall discuss the scalar equation in much more detail as many of the finite element remedies are only applicable to such scalar problems and are not directly transferable to the vector form. In the CBS scheme, which we shall introduce in [Chapter 3](#), the equations of fluid dynamics will be split so that only scalar transport occurs, where the treatment considered here is sufficient.

From [Eqs. \(2.6\)](#) and [\(2.7\)](#) we have

$$\frac{\partial \phi}{\partial t} + U_i \frac{\partial \phi}{\partial x_i} - \frac{\partial}{\partial x_i} \left(k \frac{\partial \phi}{\partial x_i} \right) + Q = 0 \quad (2.8)$$

With the variable ϕ approximated in the usual way,

$$\phi \approx \hat{\phi} = \mathbf{N} \tilde{\Phi} = \sum N_a \tilde{\phi}_a \quad (2.9)$$

the problem may be presented following the usual (weighted residual) semi-discretization process as

$$\mathbf{M}\dot{\tilde{\Phi}} + \mathbf{H}\tilde{\Phi} + \mathbf{f} = \mathbf{0} \quad (2.10)$$

where

$$\begin{aligned} M_{ab} &= \int_{\Omega} W_a N_b d\Omega \\ H_{ab} &= \int_{\Omega} \left[W_a U_i \frac{\partial N_b}{\partial x_i} + \frac{\partial W_a}{\partial x_i} k \frac{\partial N_b}{\partial x_i} \right] d\Omega \\ f_a &= \int_{\Omega} W_a Q d\Omega + \int_{\Gamma_q} W_a \bar{q}_n d\Omega \end{aligned}$$

Now even with standard Galerkin weighting the matrix \mathbf{H} will not be symmetric. However, this is a relatively minor computational problem compared with inaccuracies and instabilities in the solution which follow the arbitrary use of the weighting function.

This chapter will discuss the manner in which these difficulties can be overcome and the approximation improved.

We shall discuss in the main address the problem of solving Eq. (2.8), i.e., the scalar form, and to simplify matters further we shall start with the idealized one-dimensional equation:

$$\frac{\partial \phi}{\partial t} + U \frac{\partial \phi}{\partial x} - \frac{\partial}{\partial x} \left(k \frac{\partial \phi}{\partial x} \right) + Q = 0 \quad (2.11)$$

The term $\phi \partial U / \partial x$ has been removed for simplicity, which of course is true if U is constant. The above reduces in steady state to an ordinary differential equation:

$$\begin{aligned} U \frac{d\phi}{dx} - \frac{d}{dx} \left(k \frac{d\phi}{dx} \right) + Q &= 0 \\ \mathcal{L}(\phi) + Q &= 0 \end{aligned} \quad (2.12)$$

in which we shall often assume U , k , and Q to be constant. The basic concepts will be evident from the above and will later be extended to multidimensional problems, still treating ϕ as a scalar variable.

Indeed the methodology of dealing with the first space derivatives occurring in differential equations governing a problem, which lead to non-self-adjointness, opens the way for many new physical situations.

The present chapter will be divided into three parts. Part I deals with *steady-state situations* starting from Eq. (2.12), Part II with *transient solutions* starting from Eq. (2.11), and Part III with treatment of boundary conditions for convective-diffusive problems where use of “weak forms” is shown to be desirable.

Although the scalar problem will mainly be dealt with here in detail, the discussion of the procedures can indicate the choice of optimal ones, which will have much bearing on the solution of the general case of Eq. (2.1). The extension of some procedures to the vector case is presented in Appendix D.

Part I: Steady-State Problems

2.2 The steady-state problem in one dimension

2.2.1 General remarks

We consider the discretization of Eq. (2.12) with

$$\phi \approx \hat{\phi} = \sum N_a \tilde{\phi}_a = \mathbf{N} \tilde{\phi} \quad (2.13)$$

where N_a are shape functions and $\tilde{\phi}$ represents a set of still unknown parameters. Here we shall take these to be the nodal values of ϕ . The weighted residual form of the one-dimensional problem is written as (see Chapter 1)

$$\int_{\Omega} W_a \left[U \frac{d\hat{\phi}}{dx} - \frac{d}{dx} \left(k \frac{d\hat{\phi}}{dx} \right) + Q \right] d\Omega = 0 \quad (2.14)$$

Integrating the second term by parts gives

$$\int_{\Omega} W_a \left[U \frac{d\hat{\phi}}{dx} + Q \right] d\Omega + \int_{\Omega} \frac{dW_a}{dx} k \frac{d\hat{\phi}}{dx} d\Omega = \int_{\Gamma_q} W_a \bar{q}_n d\Gamma \quad (2.15)$$

where

$$\bar{q}_n = -k \frac{\partial \hat{\phi}}{\partial n} \quad \text{on } \Gamma_q$$

and

$$\hat{\phi} = \bar{\phi} \quad \text{on } \Gamma_{\phi}$$

is assumed. For a typical internal node a the approximating equation becomes

$$K_{ab} \tilde{\phi}_b + f_a = 0 \quad (2.16)$$

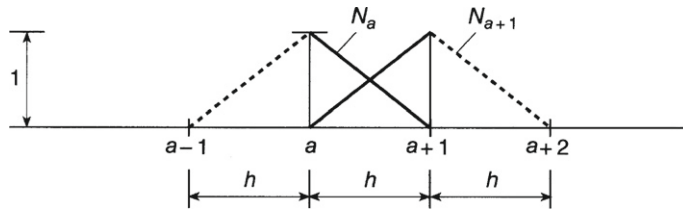
where

$$\begin{aligned} K_{ab} &= \int_0^L W_a U \frac{dN_b}{dx} dx + \int_0^L \frac{dW_a}{dx} k \frac{dN_b}{dx} dx \\ f_a &= \int_0^L W_a Q dx + W_a \bar{q}_n \Big|_{\Gamma_q} \end{aligned} \quad (2.17)$$

and the domain of the problem is $0 \leq x \leq L$.

For linear shape functions (Fig. 2.1), Galerkin weighting ($W_a = N_a$), and elements of equal size h , we have for *constant* values of U , k , and Q (see Appendix E)

$$\begin{aligned} \mathbf{K}^e &= \frac{U}{2} \begin{bmatrix} -1 & 1 \\ -1 & 1 \end{bmatrix} + \frac{k}{h} \begin{bmatrix} 1 & -1 \\ -1 & 1 \end{bmatrix} \\ \mathbf{f}^e &= \frac{Q}{2} \begin{Bmatrix} 1 \\ 1 \end{Bmatrix} \end{aligned}$$

**FIGURE 2.1**

A linear shape function for a one-dimensional problem.

which yields a typical assembled equation (after multiplying by h/k) for an inside node “ a ”

$$(-Pe - 1)\tilde{\phi}_{a-1} + 2\tilde{\phi}_a + (Pe - 1)\tilde{\phi}_{a+1} + \frac{Qh^2}{k} = 0 \quad (2.18)$$

where

$$Pe = \frac{Uh}{2k} \quad (2.19)$$

is the element *Peclet* number. Incidentally, for the case of constant Q the above is identical to the usual central finite difference approximation obtained by putting

$$\frac{d\phi}{dx} \approx \frac{\tilde{\phi}_{a+1} - \tilde{\phi}_{a-1}}{2h} \quad (2.20a)$$

and

$$\frac{d^2\phi}{dx^2} \approx \frac{\tilde{\phi}_{a+1} - 2\tilde{\phi}_a + \tilde{\phi}_{a-1}}{h^2} \quad (2.20b)$$

The algebraic [equations](#) (2.18) are obviously nonsymmetric and their accuracy deteriorates as the parameter Pe increases, i.e., when convective terms are of primary importance. Indeed as $Pe \rightarrow \infty$, the solution is purely oscillatory and bears no relation to the underlying problem. This may be ascertained by considering [Eq. \(2.18\)](#) for different element Peclet numbers and it is easy to show that with the standard Galerkin procedure oscillations in $\tilde{\phi}_a$ occur when

$$|Pe| > 1 \quad (2.21)$$

To illustrate this point we consider a simple example.

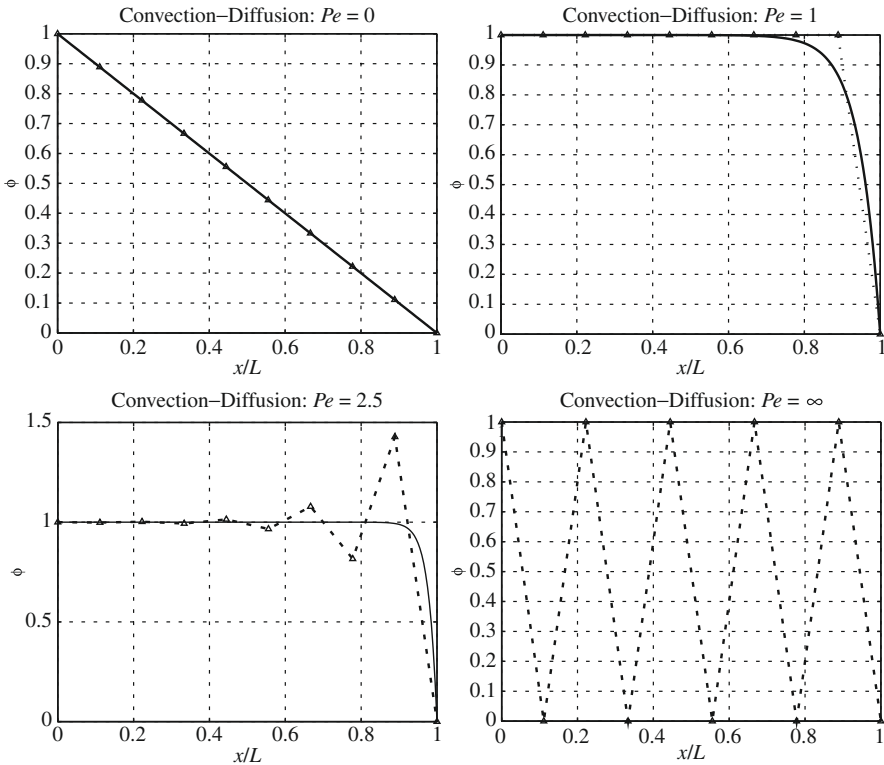
Example 2.1. One-dimensional convection-diffusion ($Q = 0$)

The domain of the problem considered is $0 \leq x \leq L$ and the boundary conditions are both of Dirichlet type and given by

$$\phi(0) = 1 \quad \text{and} \quad \phi(L) = 0$$

We approximate the solution using nine equal size linear elements and the Galerkin form of (2.15):

$$\left[\int_0^L \left(\frac{dN_a}{dx} k + N_a U \right) \frac{dN_b}{dx} dx \right] \tilde{\phi}_b = 0$$

**FIGURE 2.2**

Approximations to $Ud\phi/dx - kd^2\phi/dx^2 = 0$ for $\phi(0) = 1$ and $\phi(L) = 0$ for various Peclet numbers. Solid line: exact solution; dotted line with triangular symbol: standard Galerkin solution.

The solution shown in Fig. 2.2 with curves labeled with triangles gives results for element Peclet numbers [given by (2.19)] $Pe = 0, 1, 2.5$, and ∞ (the solution for this problem with $Pe = \infty$ is only possible for an odd number of elements). We see that as the Pe number increases above 1 the solution becomes oscillatory and progressively departs from the smooth exact solution (solid line in Fig. 2.2):

$$\phi = \frac{e^{Ux/k} - e^{UL/k}}{1 - e^{UL/k}}$$

Of course the above is partly a problem of boundary conditions. When diffusion is omitted ($k = 0$) only a single boundary condition can be imposed and when the diffusion is small we note that the downstream boundary condition ($\phi(L) = 0$) is felt in only a very small region of a *boundary layer*.

The above example clearly demonstrates that the standard Galerkin method in which $W_a = N_a$ cannot be used to solve problems in which convective terms are large compared with those of diffusion. Of course, one can consider replacing the

weight functions N_a by other more general ones W_a (commonly called a Petrov-Galerkin weighting). Indeed for the linear one-dimensional steady-state problem we can always find weight functions which give exact solutions at the interelement nodes.

Example 2.2. Weight function for exact nodal solutions

Here we consider the problem of [Example 2.1](#) where the weak form including Q is given by

$$\int_{x_1}^{x_2} v \left[U \frac{d\phi}{dx} - \frac{d}{dx} \left(k \frac{d\phi}{dx} \right) + Q \right] dx = 0$$

where $x_1 \leq x \leq x_2$ denotes the domain. After integration by parts for all derivatives on ϕ we obtain

$$\begin{aligned} & \int_{x_1}^{x_2} \left[-U \frac{dv}{dx} - \frac{d}{dx} \left(k \frac{dv}{dx} \right) \right] \phi dx + \int_{x_1}^{x_2} v Q dx \\ & + v \left(U \phi - k \frac{d\phi}{dx} \right) \Big|_{x_1}^{x_2} + \frac{dv}{dx} k \phi \Big|_{x_1}^{x_2} = 0 \end{aligned}$$

in which

$$-U \frac{dv}{dx} - \frac{d}{dx} \left(k \frac{dv}{dx} \right)$$

is the *adjoint equation* for the original problem and the sign of the first derivative is opposite to that of the original operator. We note that the presence of the first derivative term makes the problem *non-self-adjoint* (see [Appendix A](#)).

Motivated by the fact that the propagation of information is in the direction of the velocity U , finite difference practitioners were the first to overcome the bad approximation problem of the central difference method. They used *one-sided* finite differences to approximate the first derivative [1–4]. Thus in place of [Eq. \(2.20a\)](#) and with positive U , the approximation was put as

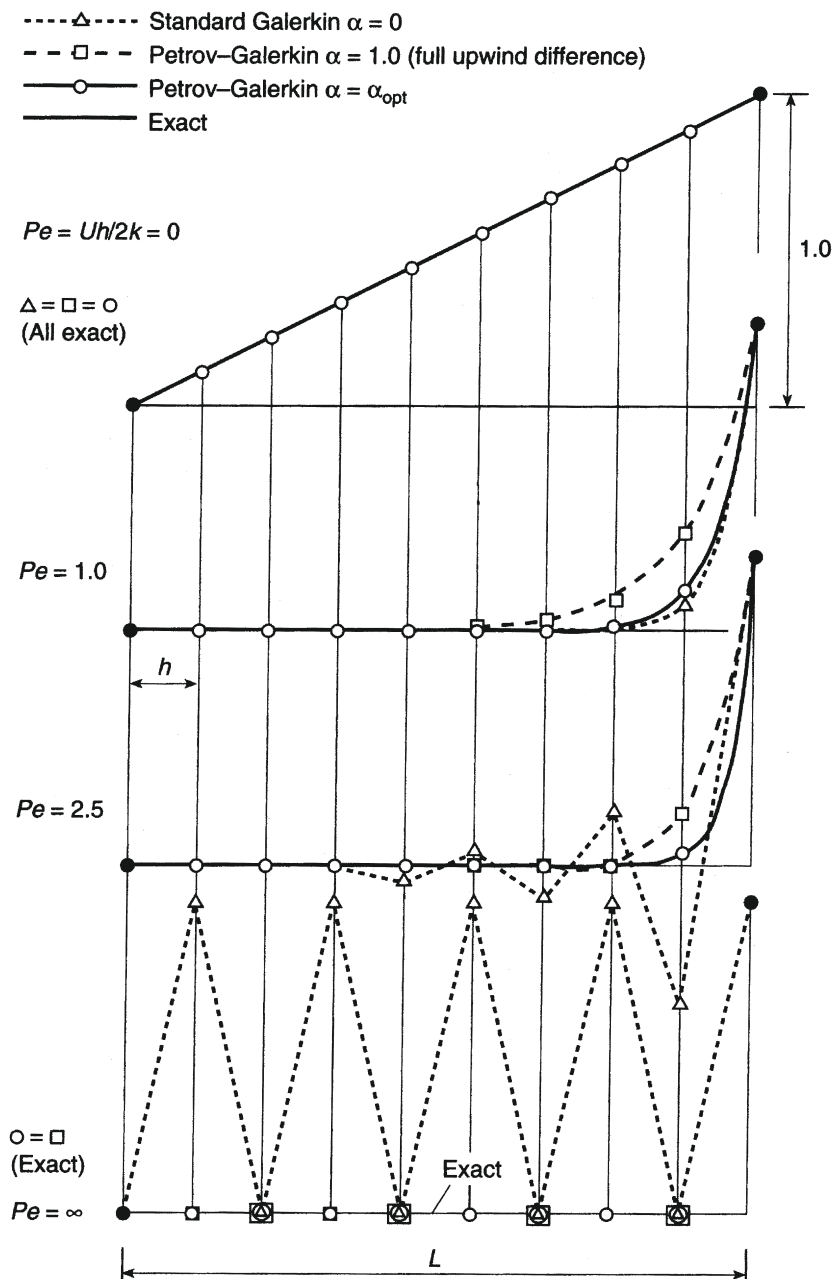
$$\frac{d\phi}{dx} \approx \frac{\tilde{\phi}_a - \tilde{\phi}_{a-1}}{h} \quad (2.22)$$

changing the central finite difference form of the governing equation approximation [as given by [Eq. \(2.18\)](#)] to

$$(-2Pe - 1)\tilde{\phi}_{a-1} + (2 + 2Pe)\tilde{\phi}_a - \tilde{\phi}_{a+1} + \frac{Qh^2}{k} = 0 \quad (2.23)$$

With this *upwind* difference approximation, nonoscillatory solutions are obtained through the whole range of Peclet numbers as shown in [Fig. 2.3](#) by curves labeled $\alpha = 1$. Now exact *nodal solutions* are obtained for pure diffusion ($Pe = 0$) and for pure convection ($Pe = \infty$); however, results for other values of Pe are generally not accurate.

How can such upwind differencing be introduced into a finite element scheme and generalized to more complex situations? This is the problem that we now address and indeed show that, for linear one-dimensional elements, this form of finite element solution also can result in exact nodal values for all Peclet numbers.

**FIGURE 2.3**

Approximations to $U d\phi/dx - k d^2\phi/dx^2 = 0$ for $\phi = 0$ at $x = 0$ and $\phi = 1$ at $x = L$ for various Peclet numbers.

2.2.2 Petrov-Galerkin methods for upwinding in one dimension

The first possibility is that of the use of a Petrov-Galerkin type of weighting in which $W_a \neq N_a$ [5–8]. Such weighting was first suggested by Zienkiewicz et al. [5] in 1976 and used by Christie et al. [6]. In particular, again for elements with linear shape functions N_a , shown in Fig. 2.1, we shall take weighting functions constructed as shown in Fig. 2.4 so that

$$W_a = N_a + \alpha W_a^* \quad (2.24)$$

where W_a^* is such that (to obtain finite difference equivalent)

$$\int_{\Omega_e} W_a^* dx = \pm \frac{h}{2} \quad (2.25)$$

with the sign depending on whether U is a velocity directed toward or away from the node. With this approximation (2.15) becomes

$$\begin{aligned} \int_{\Omega} (N_a + \alpha W_a^*) \left[U \frac{d\hat{\phi}}{dx} + Q \right] d\Omega + \int_{\Omega} \left(\frac{dN_a}{dx} + \alpha \frac{dW_a^*}{dx} \right) k \frac{d\hat{\phi}}{dx} d\Omega \\ - (N_a + \alpha W_a^*) \bar{q}_n \Big|_{\Gamma_q} = 0 \end{aligned} \quad (2.26)$$

Various forms of W_a^* are possible, but the most convenient is the following simple definition which is, of course, a discontinuous function (continuity requirements are discussed below):

$$W_a^* = \frac{h}{2} \frac{U}{|U|} \frac{dN_a}{dx} \quad (2.27)$$

where $|U|$ denotes the absolute value.

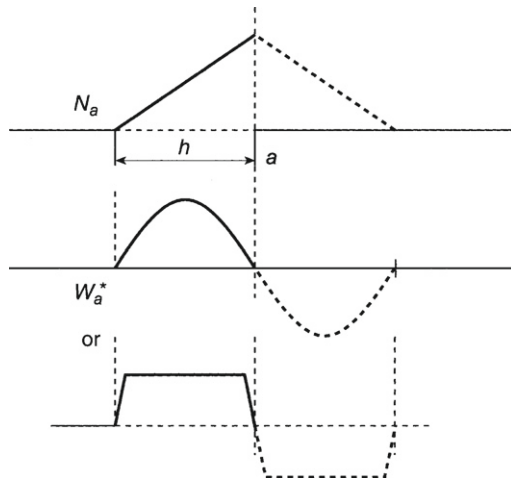


FIGURE 2.4

Petrov-Galerkin weight function $W_a = N_a + \alpha W_a^*$. Continuous and discontinuous definitions.

With the above weighting functions the approximation from Eq. (2.15) for a typical node a becomes

$$[-Pe(\alpha + 1) - 1]\tilde{\phi}_{a-1} + [2 + 2\alpha(Pe)]\tilde{\phi}_a + [-Pe(\alpha - 1) - 1]\tilde{\phi}_{a+1} + \frac{Qh^2}{k} = 0 \quad (2.28)$$

where Q is assumed constant for the whole domain and equal length elements are used.

Immediately we see that with $\alpha = 0$ the standard Galerkin approximation is recovered [Eq. (2.18)] and that with $\alpha = 1$ the full upwind form [Eq. (2.23)] is available, each giving exact nodal values for purely diffusive or purely convective cases respectively (Fig. 2.3).

Now if the value of α is chosen as

$$\alpha = \alpha_{\text{opt}} = \coth |Pe| - \frac{1}{|Pe|} \quad (2.29)$$

then exact nodal values will be given for all values of Pe . The proof of this is given in Refs. [6] and [9] for the present, one-dimensional, case where it is also shown that if

$$\alpha > \alpha_{\text{crit}} = 1 - \frac{1}{|Pe|} \quad (2.30)$$

oscillatory solutions never arise. Figure 2.5 shows the variation of α_{opt} and α_{crit} with Pe .

Although the proof of optimality for the upwinding parameter was given for the case of constant coefficients and constant size elements, nodally exact values will also be given if $\alpha = \alpha_{\text{opt}}$ is chosen for each element individually. We show some typical solutions in Fig. 2.6 for a variable source term $Q = Q(x)$ and variable element sizes.

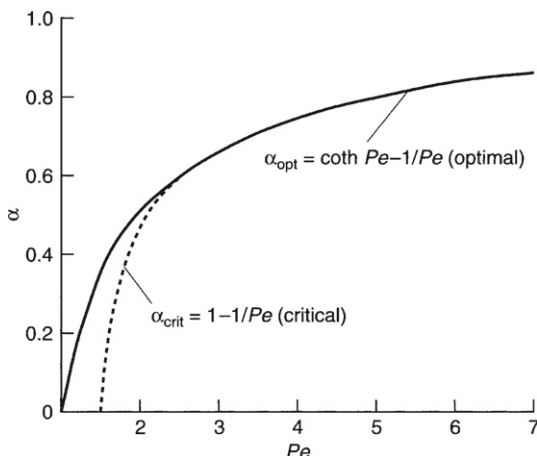
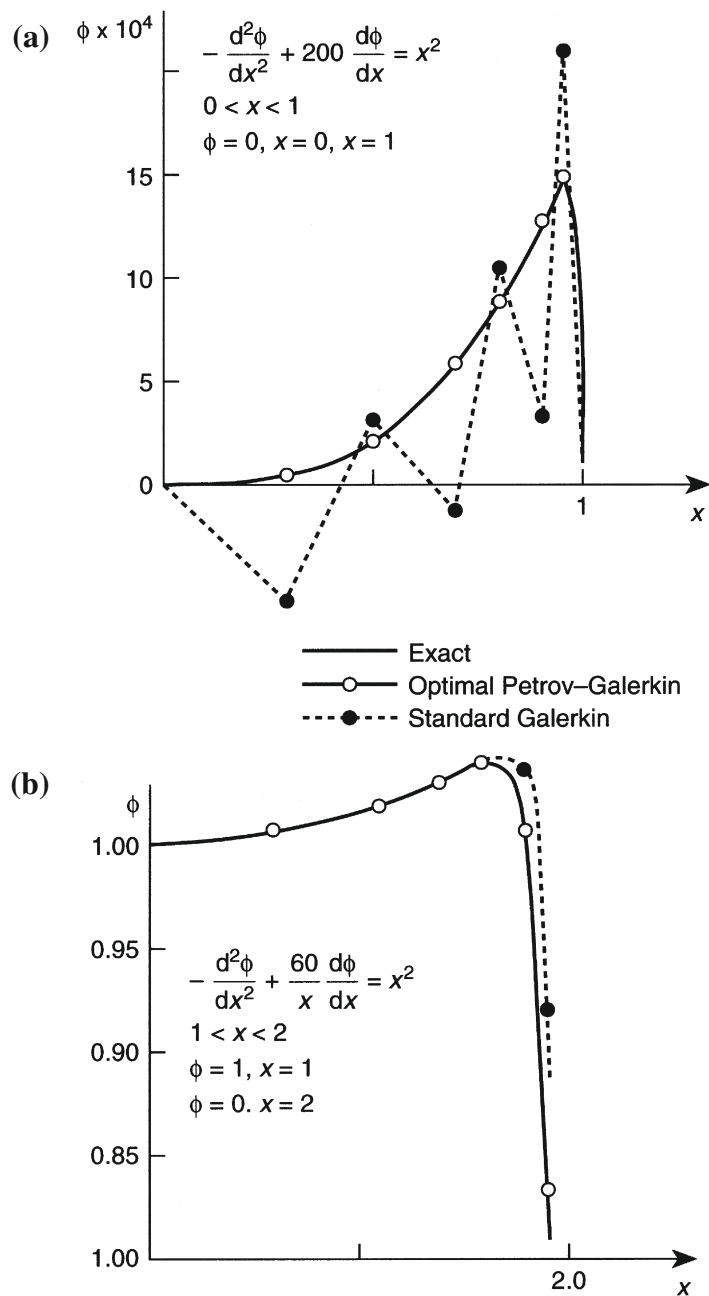
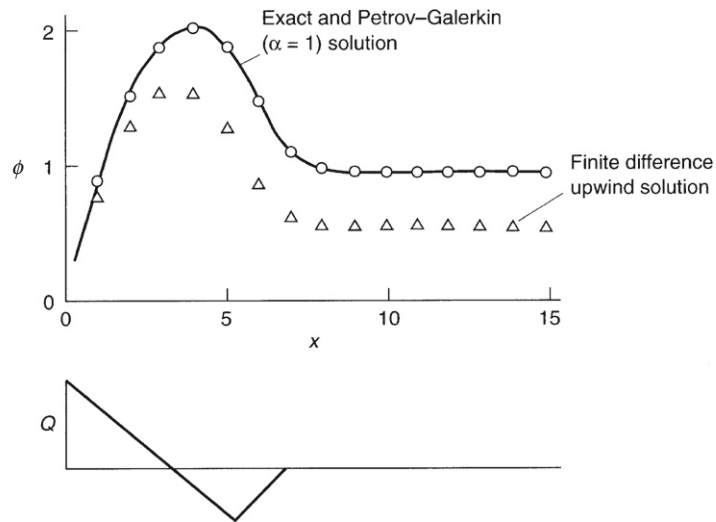


FIGURE 2.5

Critical (stable) and optimal values of the “upwind” parameter α for different values of $Pe = Uh/2k$.

**FIGURE 2.6**

Application of standard Galerkin and Petrov-Galerkin (optimal) approximation: (a) variable source term equation with constants k and h ; (b) variable source term with a variable U .

**FIGURE 2.7**

A one-dimensional pure convective problem ($k = 0$) with a variable source term Q and constant U . The Petrov-Galerkin procedure results in an exact solution but simple finite difference upwinding gives substantial error.

Figure 2.6(a) uses a constant convection velocity while Fig. 2.6(b) has a variable velocity [10]. Each of these is compared with a standard Galerkin solution, showing that even when the latter does not result in oscillations the accuracy is improved. Of course in the above examples the Petrov-Galerkin weighting must be applied to all terms of the equation. When this is not done (as in simple finite difference upwinding) totally wrong results will be obtained, as shown in the finite difference results of Fig. 2.7, which was used in Ref. [11] to discredit upwinding methods. The effect of α on the source term is not apparent in Eq. (2.28) where Q is constant in the whole domain, but its influence is strong when $Q = Q(x)$.

2.2.2.1 Continuity requirements for weighting functions

The weighting function W_a (or W_a^*) introduced in Fig. 2.4 can of course be discontinuous as far as the contributions to the convective terms are concerned [see Eq. (2.17)], i.e.,

$$\int_0^L W_a \frac{d(U N_b)}{dx} dx \quad \text{or} \quad \int_0^L W_a U \frac{dN_b}{dx} dx$$

Clearly no difficulty arises at the discontinuity in the evaluation of the above integrals. However, when evaluating the diffusion term, we generally introduce integration by parts and evaluate such terms as

$$\int_0^L \frac{dW_a}{dx} k \frac{dN_b}{dx} dx$$

in place of the form

$$-\int_0^L W_a \frac{d}{dx} \left(k \frac{dN_b}{dx} \right) dx$$

Here a local infinity will occur with discontinuous W_a . To avoid this difficulty we *mollify* or *smooth* the discontinuity of the W_a^* so that this occurs within the element [12] and thus avoid the discontinuity at the node in the manner shown in Fig. 2.4. Now direct integration can be used, showing in the present case zero contributions to the diffusion term.

2.2.3 Balancing diffusion in one dimension

The comparison of the nodal equations (2.18) and (2.28) obtained on a uniform mesh and for a constant Q shows that the effect of using the Petrov-Galerkin procedure is equivalent to the use of a standard Galerkin process with the addition of a diffusion

$$k_b = \frac{1}{2} \alpha U h \quad (2.31)$$

to the original differential equation (2.12). The reader can easily verify that with this substituted into the original equation, thus writing now in place of Eq. (2.12)

$$U \frac{d\phi}{dx} - \frac{d}{dx} \left[(k + k_b) \frac{d\phi}{dx} \right] + Q = 0 \quad (2.32)$$

we obtain an identical expression to that of Eq. (2.28) providing Q is constant and a standard Galerkin procedure is used.

Such *balancing diffusion* is easier to implement than Petrov-Galerkin weighting, particularly in two or three dimensions, and has some physical merit in the interpretation of the Petrov-Galerkin methods. However, it does not provide the required modification of source terms, and for instance in the example of Fig. 2.7 will give erroneous results identical with a simple finite difference, upwind, approximation.

The concept of *artificial diffusion* introduced frequently in finite difference models suffers of course from the same drawbacks and in addition cannot be logically justified.

It is of interest to observe that a central difference approximation, when applied to the original equations (or the use of the standard Galerkin process), fails by introducing a *negative diffusion* [13] into the equations. This “negative” diffusion is countered by the present, balancing, one.

2.2.4 A variational principle in one dimension

Equation (2.12), which we are considering here, is not self-adjoint and hence is not directly derivable from any variational principle. However, it was shown by Guymon et al. [14] that it is a simple matter to derive a variational principle (or ensure self-adjointness, which is equivalent) if the operator is premultiplied by a suitable function p . Thus we write a weak form of Eq. (2.12) as

$$\int_0^L vp \left[U \frac{d\phi}{dx} - \frac{d}{dx} \left(k \frac{d\phi}{dx} \right) + Q \right] dx = 0 \quad (2.33)$$

where $p = p(x)$ is as yet undetermined. This gives, on integration by parts,

$$\int_0^L \left[v \frac{d\phi}{dx} \left(pU + k \frac{dp}{dx} \right) + \frac{dv}{dx} (k p) \frac{d\phi}{dx} + v p Q \right] dx + v k p \frac{d\phi}{dx} \Big|_0^L = 0 \quad (2.34)$$

Immediately we see that the operator can be made self-adjoint and a symmetric approximation achieved if the first term in square brackets is made zero [15]. This requires that p be chosen so that

$$pU + k \frac{dp}{dx} = 0 \quad (2.35a)$$

or that

$$p = C e^{-Ux/k} = C e^{-2Pe x/h} \quad (2.35b)$$

For such a form corresponding to the existence of a variational principle the “best” approximation is that of the Galerkin method with

$$v = \sum N_a \tilde{v}_a \quad \text{and} \quad \phi = \sum N_b \tilde{\phi}_b \quad (2.36)$$

where \tilde{v}_a is an arbitrary parameter.

Indeed, such a formulation will, in one dimension, yield exact answers at nodes [15, 16]. It must therefore be equivalent to that obtained earlier by weighting in the Petrov-Galerkin manner. Inserting the approximation of Eq. (2.36) into Eq. (2.34), with Eqs. (2.35a) and (2.35b) defining p using an origin at $x = x_a$, we have for the a th equation of the uniform mesh

$$\int_{-h}^h \left[\frac{dN_a}{dx} (ke^{-2Pe x/h}) \frac{dN_b}{dx} \tilde{\phi}_b + N_a e^{-2Pe x/h} Q \right] dx = 0 \quad (2.37)$$

with $b = a - 1, a, a + 1$. This gives, after some algebra, a typical nodal equation:

$$\begin{aligned} & \left(1 - e^{2Pe} \right) \tilde{\phi}_{a-1} + \left(e^{2Pe} - e^{-2Pe} \right) \tilde{\phi}_a - \left(1 - e^{-2Pe} \right) \tilde{\phi}_{a+1} \\ & + \frac{Qh^2}{2Pe k} \left(e^{Pe} - e^{-Pe} \right)^2 = 0 \end{aligned} \quad (2.38)$$

which can be shown to be identical with the expression (2.28) into which $\alpha = \alpha_{\text{opt}}$ given by Eq. (2.29) has been inserted.

Here we have a somewhat more convincing proof of the optimality of the proposed Petrov-Galerkin weighting [17, 18] introduced in the previous subsection. However, serious drawbacks exist. The numerical evaluation of the integrals is difficult and the equation system, though symmetric overall, is not well conditioned if p is taken as a continuous function of x through the whole domain. The second point is easily overcome by taking p to be *locally* defined, for instance taking the origin of x at point a for all assemblies as we did in deriving Eq. (2.38). This is permissible by arguments

given in [Section 2.2.1](#) and is equivalent to scaling the full equation system row by row [[17](#)]. Now of course the total equation system ceases to be symmetric.

The numerical integration difficulties disappear, of course, if the simple weighting functions previously derived are used. However, the proof of equivalence is important as the problem of determining the optimal weighting is no longer necessary.

2.2.5 Galerkin least-squares approximation (GLS) in one dimension

In the preceding sections we have shown that many, apparently different, approaches have resulted in identical (or almost identical) approximations. Here another procedure is presented which again will produce similar results. In this a combination of standard Galerkin and least-squares approximation is made [[19,20](#)].

If [Eq. \(2.12\)](#) is rewritten as

$$\mathcal{L}(\phi) + Q = 0 \quad \phi \approx \hat{\phi} = \mathbf{N}\tilde{\phi} \quad (2.39a)$$

with

$$L = U \frac{d}{dx} - \frac{d}{dx} \left(k \frac{d}{dx} \right) \quad (2.39b)$$

the standard Galerkin approximation gives for the a th equation

$$\int_{\Omega} N_a [\mathcal{L}(\hat{\phi}) + Q] dx = 0 \quad (2.40)$$

with boundary conditions omitted for simplicity.

Similarly, a least-squares minimization of the residual $R = \mathcal{L}(\hat{\phi}) + Q$ results in

$$\frac{1}{2} \frac{d}{d\tilde{\phi}^a} \int_{\Omega} R^2 dx = \int_{\Omega} \frac{d\mathcal{L}(\hat{\phi})}{d\tilde{\phi}^a} [\mathcal{L}(\hat{\phi}) + Q] dx \quad (2.41)$$

or

$$\int_{\Omega} \left[U \frac{dN_a}{dx} - \frac{d}{dx} \left(k \frac{dN_a}{dx} \right) \right] (\mathcal{L}(\hat{\phi}) + Q) dx = \int_{\Omega} \mathcal{L}(N_a) [\mathcal{L}(\hat{\phi}) + Q] dx \quad (2.42)$$

If the final approximation is written as a linear combination of [Eqs. \(2.40\)](#) and [\(2.42\)](#), we have

$$\begin{aligned} \int_{\Omega} \left[N_a + \lambda \left(U \frac{dN_a}{dx} - \frac{d}{dx} \left(k \frac{dN_a}{dx} \right) \right) \right] (\mathcal{L}(\hat{\phi}) + Q) dx &= 0 \\ \text{or} \\ \int_{\Omega} \left[N_a + \lambda \mathcal{L}(N_a) \right] (\mathcal{L}(\hat{\phi}) + Q) dx &= 0 \end{aligned} \quad (2.43)$$

If the second-derivative term on N_a is omitted (as could be done assuming linear N_a and a mollification as in [Fig. 2.4](#)), [Eq. \(2.43\)](#) is the same as the Petrov-Galerkin

approximation with an undetermined parameter λ . Indeed, if we take

$$\lambda = \frac{\alpha h}{2|U|} \quad (2.44)$$

the approximation is identical to that of the Petrov-Galerkin method with the weighting given by Eqs. (2.24) and (2.25).

Once again we see that a Petrov-Galerkin form written as

$$\int_{\Omega} \left(N_a + \frac{\alpha h}{2} \frac{U}{|U|} \frac{dN_a}{dx} \right) \left(U \frac{d\bar{\phi}}{dx} - \frac{d}{dx} \left(k \frac{d\bar{\phi}}{dx} \right) + Q \right) dx = 0 \quad (2.45)$$

is a result that follows from diverse approaches, though only the variational form of Section 2.2.4 and that using an exact solution of the adjoint differential equation explicitly determine the value of α that should optimally be used. In all the other derivations this value is determined by an *a posteriori* analysis.

2.2.6 Subgrid scale (SGS) approximation

The SGS method was originally introduced by Hughes [21,22] following the principles of turbulence modeling. More details on the method as applied to convection-diffusion problems are available in Ref. [23]. In this method the scalar quantity is divided into two parts $\bar{\phi}$ and ϕ' , and Eq. (2.12) is written as

$$\begin{aligned} U \frac{d}{dx} (\bar{\phi} + \phi') - \frac{d}{dx} \left[k \frac{d}{dx} (\bar{\phi} + \phi') \right] + Q &= 0 \\ \text{or} \\ \mathcal{L}(\bar{\phi}) + \mathcal{L}(\phi') + Q &= 0 \end{aligned} \quad (2.46)$$

In the above split $\bar{\phi}$ is assumed to be the solution given by a finite element discretization (the so-called resolved scale) and ϕ' the unresolved, fine-scale part of the solution.

If we construct a weak form for the problem, we have

$$\int_{\Omega} v [\mathcal{L}(\bar{\phi}) + \mathcal{L}(\phi') + Q] dx = 0 \quad (2.47)$$

where Ω is the domain considered. After integration by parts and assuming boundary conditions for ϕ' are zero at the boundaries of each element (i.e., assuming that $\bar{\phi}$ has values at element boundaries which are accurate and oscillation free) we obtain

$$\int_{\Omega} v \left[U \frac{d\bar{\phi}}{dx} + Q \right] dx + \int_{\Omega} \frac{dv}{dx} k \frac{d\bar{\phi}}{dx} dx + \int_{\Omega} \mathcal{L}^*(v) \phi' dx + v \bar{q}_n \Big|_{\Gamma_q} = 0 \quad (2.48)$$

where

$$\mathcal{L}^*(v) = -U \frac{dv}{dx} - \frac{d}{dx} \left(k \frac{dv}{dx} \right) \quad (2.49)$$

is the adjoint differential equation. As shown before, the solution using $\bar{\phi}$ alone with a standard Galerkin method leads to oscillatory results when convection effects are significant. Here we wish to take account of effects from the unresolved part when computing $\bar{\phi}$. From (2.46) we obtain

$$\mathcal{L}(\phi') = -(\mathcal{L}(\bar{\phi}) + Q) \quad (2.50)$$

for which the Green's function solution gives

$$\phi'(x) = - \int g(x, y) [\mathcal{L}(\bar{\phi}(y)) + Q] dy \quad (2.51)$$

What we need here, however, is a simple approximation which does not require such a complex solution (and the Green's function). Using the simple approximation

$$\phi'(x) = -\beta [\mathcal{L}(\bar{\phi}(x)) + Q] \quad (2.52)$$

with *beta* appropriately defined has been shown by Codina to give accurate results [23]. Substitution of (2.52) into (2.48) gives

$$\begin{aligned} & \int_{\Omega} v \left[U \frac{d\bar{\phi}}{dx} + Q \right] dx + \int_{\Omega} \frac{dv}{dx} k \frac{d\bar{\phi}}{dx} dx \\ & - \int_{\Omega} \mathcal{L}^*(v) \beta [\mathcal{L}(\bar{\phi}) + Q] dx + v \bar{q}_n \Big|_{\Gamma_q} = 0 \end{aligned} \quad (2.53)$$

If higher-order derivative terms are neglected in the above equation and $\beta = \alpha h / 2|U|$, the formulation is identical to that of the Petrov-Galerkin method and the Galerkin least-squares method. However, if Q contains reaction terms such equivalence is lost and some differences occur [23].

2.2.7 The finite increment calculus (FIC) for stabilizing the convective-diffusion equation in one dimension

As mentioned in the previous sections, there are many procedures which give nearly identical results to those of the Petrov-Galerkin approximation. We shall also find a number of such procedures arising directly from the transient formulations discussed in Part II of this chapter; however, there is one further process that can be applied directly to the steady-state equation. This process was suggested by Onate in 1998 [24] and we describe its basis below.

We start at the stage where the conservation equation of the type given by Eq. (2.6) is derived. Now instead of considering an infinitesimal control volume of length “ dx ,” we consider a finite length δ . Expanding to one higher order by Taylor series (backwards), we obtain instead of Eq. (2.12)

$$U \frac{d\phi}{dx} - \frac{d}{dx} \left(k \frac{d\phi}{dx} \right) + Q - \frac{\delta}{2} \frac{d}{dx} \left[U \frac{d\phi}{dx} - \frac{d}{dx} \left(k \frac{d\phi}{dx} \right) + Q \right] = 0 \quad (2.54)$$

with δ being the finite distance which is smaller than or equal to that of the element size h . Rearranging terms and substituting $\delta = \alpha h$ we have (assuming positives U)

$$U \frac{d\phi}{dx} - \frac{d}{dx} \left[\left(k + \frac{\alpha h U}{2} \right) \frac{d\phi}{dx} \right] + Q - \frac{\delta}{2} \frac{dQ}{dx} = 0 \quad (2.55)$$

In the above equation we have omitted the higher-order expansion for the diffusion term as in the previous sections. The final equations are now obtained by applying the Galerkin method with $W_a = N_a$.

From the last equation we see immediately that a stabilizing term has been recovered and the additional term $\alpha h U / 2$ is identical to that of the Petrov-Galerkin form (Eq. 2.28).

There is no need to discuss further and we see how the finite increment procedure has again yielded exactly the same result by directly modifying the conservation differential equations. In Ref. [24] it is shown further that arguments can be brought to determine α as being precisely the optimal value we have already obtained by studying the Petrov-Galerkin method.

2.2.8 Higher-order approximations

The derivation of accurate Petrov-Galerkin procedures for the convective-diffusion equation is of course possible for any order of finite element expansion. In Ref. [8] Heinrich and Zienkiewicz show how the procedure of studying exact discrete solutions can yield optimal upwind parameters for quadratic shape functions. However, here the simplest approach involves the procedures of Section 2.2.4, which are available of course for any element expansion and, as shown before, will always give an optimal approximation at nodes.

We thus recommend the reader pursue the example discussed in that section and, by extending Eq. (2.37), arrive at an appropriate equation linking the two quadratic elements of Fig. 2.8. For higher-order elements the solution gives exact values at interior nodes.

For practical purposes it is possible to extend the Petrov-Galerkin weighting of the type given in Eqs. (2.24)–(2.27) now using

$$\alpha_{\text{opt}} = \coth Pe - \frac{1}{Pe} \quad (2.56a)$$

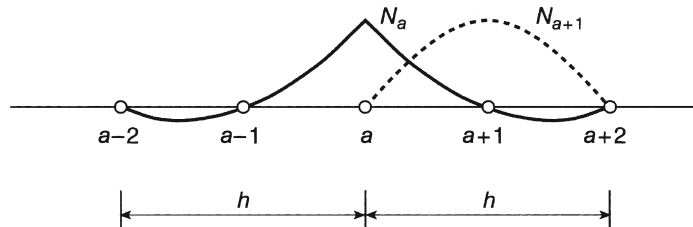


FIGURE 2.8

Assembly of one-dimensional quadratic elements.

for the midside node and

$$\alpha_{\text{opt}} = \frac{(\coth Pe - 1/Pe) - (\cosh Pe)^2(\coth 2Pe - 1/(2Pe))}{1 - (\cosh Pe)^2/2} \quad (2.56b)$$

for side nodes. A simplified procedure, though not as exact as that for linear elements, is very effective and has been used with success for solution of Navier-Stokes equations [25].

The subject of optimal upwinding for higher-order approximations has been studied further and Refs. [9, 26, 27] show the developments.

2.3 The steady-state problem in two (or three) dimensions

2.3.1 General remarks

It is clear that the application of standard Galerkin discretization to the steady-state scalar convection-diffusion equation in several space dimensions is similar to the problem discussed previously in Section 2.2.1 in one dimension and will again yield unsatisfactory answers with high oscillation for local Peclet numbers greater than unity.

The equation now considered is the steady-state version of Eq. (2.8) in multidimensions, i.e.,

$$U_i \frac{\partial \phi}{\partial x_i} - \frac{\partial}{\partial x_i} \left(k \frac{\partial \phi}{\partial x_i} \right) + Q = 0 \quad (2.57)$$

Obviously the problem is now of greater practical interest than the one-dimensional case so far discussed, and a satisfactory solution is important. Again, all of the possible numerical approaches we have discussed are applicable.

2.3.2 Streamline (upwind) Petrov-Galerkin weighting (SUPG)

The most obvious procedure is to use again some form of Petrov-Galerkin method of the type introduced in Section 2.2.2 and Eqs. (2.24)–(2.29), seeking optimality of α in some heuristic manner. Restricting attention here to two dimensions, we note immediately that the Peclet parameter

$$\mathbf{Pe} = \frac{\mathbf{U}h}{2k} \quad \mathbf{U} = \begin{Bmatrix} U_1 \\ U_2 \end{Bmatrix} \quad (2.58)$$

is now a “vector” quantity and hence that upwinding needs to be “directional.”

The first reasonably satisfactory attempt to do this consisted of determining the optimal Petrov-Galerkin formulation using αW^* based on components of \mathbf{U} associated to the *sides of elements* and obtaining the final weight functions by a blending procedure [7, 8].

A better method was soon realized when the analogy between balancing diffusion and upwinding was established, as shown in Section 2.2.3. In two (or three) dimensions the convection is only active in the direction of the resultant element velocity \mathbf{U} ,

and hence the corrective, or *balancing diffusion* introduced by upwinding should be anisotropic with a coefficient different from zero only in the direction of the resultant velocity. This innovation introduced simultaneously by Hughes and Brooks [28,29] and Kelly et al. [10] can be readily accomplished by taking the individual weighting functions as

$$\begin{aligned} W_a &= N_a + \alpha W_a^* \\ &\equiv N_a + \frac{\alpha h}{2} \frac{U_i}{|\mathbf{U}|} \frac{\partial N_a}{\partial x_i} \end{aligned} \quad (2.59)$$

with this last form being applicable to two and three dimensions. Here α is determined for each element by the previously found expression (2.25) written as follows:

$$\alpha = \alpha_{\text{opt}} = \coth Pe - \frac{1}{Pe} \quad (2.60)$$

where

$$Pe = \frac{|\mathbf{U}|h}{2k} \quad \text{with} \quad |\mathbf{U}| = \sqrt{U_i U_i} \quad (2.61)$$

The above expressions presuppose that the velocity components U_i in a particular element are substantially constant and that the element size h can be reasonably defined.

Figure 2.9 shows an assembly of a linear triangle and bilinear quadrilateral for each of which the mean resultant velocity \mathbf{U} is indicated. Determination of the element size h to use in expression (2.61) is of course somewhat arbitrary. In Fig. 2.9 we show it simply as the size in the direction of the velocity vector.

The form of Eq. (2.59) is such that the “nonstandard” weighting W^* has a zero effect in the direction where the velocity is zero. Thus the balancing diffusion is only introduced in the direction of the resultant (convective) velocity vector \mathbf{U} .

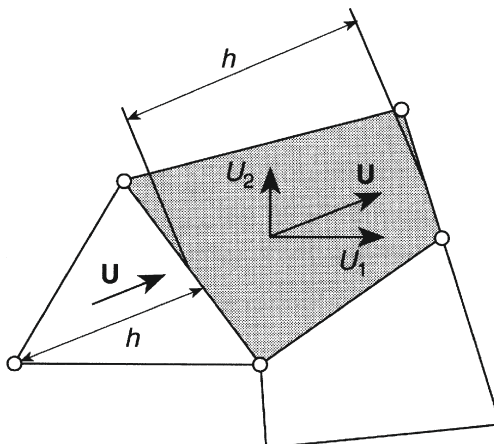


FIGURE 2.9

A two-dimensional, streamline assembly. Element size h and streamline directions.

Introducing the approximation

$$\phi \approx \hat{\phi} = \sum_a N_a(x_i) \tilde{\phi}_a \quad (2.62)$$

and using the weights given by Eq. (2.59) the SUPG method is computed from the weighted residual form

$$\int_{\Omega} \left[N_a + \frac{\alpha h}{2} \frac{U_i}{|\mathbf{U}|} \frac{\partial N_a}{\partial x_i} \right] [\mathcal{L}(\hat{\phi}) + Q] d\Omega = 0 \quad (2.63)$$

or after integration by parts and introduction of the natural boundary condition on Γ_q

$$\begin{aligned} & \int_{\Omega} \left[N_a \left(U_i \frac{\partial \hat{\phi}}{\partial x_i} + Q \right) + \frac{\partial N_a}{\partial x_i} k \frac{\partial \hat{\phi}}{\partial x_i} + \frac{\alpha h}{2} \frac{U_i}{|\mathbf{U}|} \frac{\partial N_a}{\partial x_i} (\mathcal{L}(\hat{\phi}) + Q) \right] d\Omega \\ & + \int_{\Gamma_q} N_a \bar{q}_n d\Gamma = 0 \end{aligned} \quad (2.64)$$

where $\bar{q}_n = -k \partial \hat{\phi} / \partial n$. In the discretized form the “balancing diffusion” term becomes

$$\int_{\Omega} \frac{\partial N_a}{\partial x_i} \tilde{k}_{ij} \frac{\partial N_b}{\partial x_j} d\Omega \quad (2.65)$$

with

$$\tilde{k}_{ij} = \frac{\alpha U_i U_j}{|\mathbf{U}|} \frac{h}{2} \quad (2.66)$$

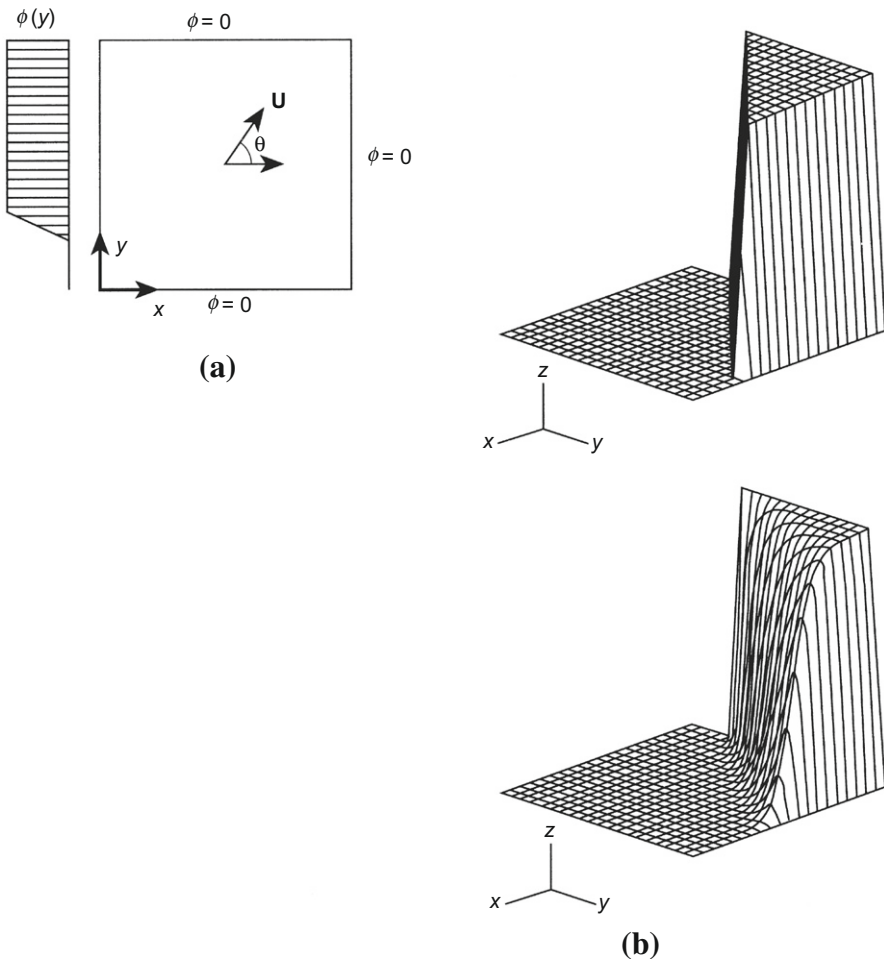
This indicates a zero coefficient normal to the convective velocity vector direction. It is therefore named the *streamline balancing diffusion* [10,28,29] or streamline upwind Petrov-Galerkin process.

The streamline diffusion should allow discontinuities in the direction normal to the streamline to travel without appreciable distortion. However, with the standard finite element approximations actual discontinuities cannot be modeled and in practice some oscillations may develop. For this reason some investigators add a smoothing diffusion in the direction normal to the streamlines (crosswind diffusion) [30–33].

The mathematical validity of the procedure introduced in this section has been established by Johnson et al. [34] for $\alpha = 1$, showing convergence improvement over the standard Galerkin process. However, the proof does not include any optimality in the selection of α values as shown by Eq. (2.60).

Figure 2.10 shows a typical solution of Eq. (2.57), indicating the very small amount of “crosswind diffusion,” i.e., allowing discontinuities to propagate in the direction of flow without substantial smearing [35].

A more convincing “optimality” can be achieved by applying the exponential modifying function, making the problem self-adjoint. This of course follows precisely the procedures of Section 2.2.4 and is easily accomplished if the velocities are constant

**FIGURE 2.10**

“Streamline” procedures in a two-dimensional problem of pure convection. Bilinear elements [35]: (a) boundary conditions for test problem; solutions for $\theta = 45^\circ$ (top) and $\theta = 65^\circ$.

in the element assembly domain. If velocities vary from element to element, again the exponential functions

$$p = e^{-Ux'/k} \quad (2.67)$$

with x' oriented in the velocity direction in each element can be taken. This appears to have been first implemented by Sampaio [35] but problems regarding the origin of coordinates, etc., have once again to be addressed. However, the results are similar to those achieved here by the streamline upwind Petrov-Galerkin procedure.

2.3.3 Galerkin least squares (GLS) and finite increment calculus (FIC) in multidimensional problems

It is of interest to observe that the somewhat intuitive approach to the generation of the “streamline” Petrov-Galerkin weight functions of Eq. (2.59) can be avoided if the least-squares Galerkin procedure of Section 2.2.5 is extended to deal with the multi-dimensional equation. Simple extension of the reasoning given in Eqs. (2.39a)–(2.45) will immediately yield the weighting of Eq. (2.59).

Extension of the GLS to two or three dimensions gives (again using indicial notation)

$$\int_{\Omega} \left(N_a + \lambda \mathcal{L}(N_a) \right) \left(U_j \frac{\partial \hat{\phi}}{\partial x_j} - \frac{\partial}{\partial x_j} \left(k \frac{\partial \hat{\phi}}{\partial x_j} \right) + Q \right) d\Omega = 0 \quad (2.68)$$

where

$$\mathcal{L}(N_a) = U_i \frac{\partial N_a}{\partial x_i} + \frac{\partial}{\partial x_i} \left(k \frac{\partial N_a}{\partial x_i} \right) \quad (2.69)$$

In the above equation after integration by parts, higher-order derivative terms of two or more are omitted for the sake of simplicity. As in one dimension [Eq. (2.43)] we have an additional weighting term. Now assuming

$$\lambda = \frac{\alpha h}{2|\mathbf{U}|} \quad (2.70)$$

we obtain an identical stabilizing term to that of the streamline Petrov-Galerkin procedure [Eq. (2.64)].

The finite increment calculus method in multidimensions can be written as [24]

$$\begin{aligned} U_j \frac{\partial \phi}{\partial x_j} - \frac{\partial}{\partial x_j} \left(k \frac{\partial \phi}{\partial x_j} \right) + Q - \frac{\delta_i}{2} \frac{\partial}{\partial x_i} \left[U_j \frac{\partial \phi}{\partial x_j} - \frac{\partial}{\partial x_j} \left(k \frac{\partial \phi}{\partial x_j} \right) + Q \right] &= 0 \\ \text{or} \\ \mathcal{L}(\phi) + Q - \frac{\delta_i}{2} [\mathcal{L}(\phi) + Q] &= 0 \end{aligned} \quad (2.71)$$

Note that the value of δ_i is now dependent on the coordinate direction. To obtain streamline-oriented stabilization, we simply assume that δ_i is the projection oriented along the streamlines. Now

$$\delta_i = \delta \frac{U_i}{|\mathbf{U}|} \quad (2.72)$$

With $\delta = \alpha h$ and again omitting the higher-order derivative terms in k , the streamline Petrov-Galerkin form of stabilization is obtained [Eq. (2.64)]. The reader can verify that both the GLS and FIC produce the correct weighting for the source term Q as of course is required by the Petrov-Galerkin method.

The extension of the SGS procedure to multidimensions is straightforward and follows the approach explained in Section 2.2.6.

2.4 Steady state: Concluding remarks

In Sections 2.2 and 2.3 we presented several currently used procedures for dealing with the steady-state convection-diffusion equation with a scalar variable. All of these translate essentially to the use of streamline Petrov-Galerkin discretization, though of course the modification of the basic equations to a self-adjoint form given in Section 2.2.4 provides the *full justification* of the special weighting. Which of the procedures is best used in practice is largely a matter of taste, as all can give excellent results.

The generalized representation of all the stabilization methods discussed in this part may be written as

$$\int_{\Omega} \left(N_a + \gamma_i \frac{\partial N_a}{\partial x_i} \right) \left[U \frac{\partial N_a}{\partial x} \hat{\phi}^a + \frac{\partial N_1}{\partial x} k \frac{\partial N_b}{\partial x} \hat{\phi}^b + Q \right] d\Omega = 0 \quad (2.73)$$

where γ_i is a stabilizing parameter.

In the second part of this chapter dealing with transient problems it will be found that similar stabilizing forms arise directly when steady state is reached or assumed.

In this case the parameter γ_i is now replaced by another one involving the length of the time step Δt . We shall show at the end of the next section a comparison between various procedures for stabilization and will note essentially the same forms in the steady-state situation.

Part II: Transients

2.5 Transients: Introductory remarks

2.5.1 Mathematical background

The objective of this section is to develop procedures of general applicability for the solution by direct time-stepping methods of Eq. (2.1) written for scalar values of ϕ , F_i , and G_i . Starting from the scalar form Eq. (2.8)

$$\frac{\partial \phi}{\partial t} + \frac{\partial (U_i \phi)}{\partial x_i} - \frac{\partial}{\partial x_i} \left(k \frac{\partial \phi}{\partial x_i} \right) + Q = 0 \quad (2.74)$$

though consideration of the procedure for dealing with a vector-valued function is included in Appendix D. To allow a simple interpretation of the various methods and of behavior patterns the scalar equation in one dimension in nonconservation form [see Eq. (2.11)], i.e.,

$$\frac{\partial \phi}{\partial t} + U \frac{\partial \phi}{\partial x} - \frac{\partial}{\partial x} \left(k \frac{\partial \phi}{\partial x} \right) + Q = 0 \quad (2.75)$$

will be considered. The problem so defined is nonlinear unless U is independent of ϕ . However, the nonconservative equation (2.75) admits a spatial variation of U and is quite general.

In the general form (2.74) the main behavior patterns can be determined by a change of the independent variable x to x' such that

$$dx' = dx - Udt \quad (2.76)$$

Noting that for $\phi = \phi(x', t)$ we have

$$\frac{\partial \phi}{\partial t} \Big|_{x \text{ const}} = \frac{\partial \phi}{\partial x'} \frac{\partial x'}{\partial t} + \frac{\partial \phi}{\partial t} \Big|_{x' \text{ const}} = -U \frac{\partial \phi}{\partial x'} + \frac{\partial \phi}{\partial t} \Big|_{x' \text{ const}} \quad (2.77)$$

The one-dimensional equation (2.75) now becomes simply

$$\frac{\partial \phi}{\partial t} - \frac{\partial}{\partial x'} \left(k \frac{\partial \phi}{\partial x'} \right) + Q(x') = 0 \quad (2.78)$$

and equations of this type can be readily discretized with self-adjoint spatial operators and solved by standard finite element Galerkin procedures [15].

The coordinate system of Eq. (2.76) describes *characteristic directions* and the moving nature of the coordinates must be noted. A further corollary of the coordinate change is that with no conduction or source terms, i.e., when $k = 0$ and $Q = 0$, we have simply

$$\frac{\partial \phi}{\partial t} = 0 \quad (2.79a)$$

or, for the one-dimensional case,

$$\phi(x') = \phi(x - Ut) = \text{constant} \quad (2.79b)$$

along a characteristic (assuming U to be constant). This is a typical equation of a wave propagating with a velocity U in the x direction, as shown in Fig. 2.11. The wave nature is evident in the problem even if the conduction (diffusion) is not zero, and in this case we shall have solutions showing a wave that attenuates with the distance traveled.

2.5.2 Possible discretization procedures

In Part I of this chapter we have concentrated on the essential methods applicable directly to the steady-state equations. These procedures started off from somewhat heuristic considerations. The Petrov-Galerkin method was perhaps the most rational

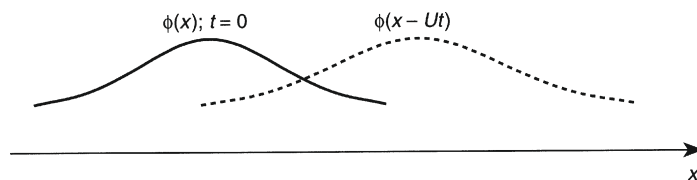


FIGURE 2.11

The wave nature of a solution with no conduction. Constant wave velocity U .

but even here the amount and the nature of the weighting functions were a matter of guesswork which was subsequently justified by consideration of the numerical error at nodal points. The Galerkin least-squares (GLS) method in the same way provided no absolute necessity for improving the answers though of course the least-squares method would tend to increase the symmetry of the equations and thus could be proved useful. It was only by results which turned out to be remarkably similar to those obtained by the Petrov-Galerkin method that we have deemed this method to be a success. The same remark could be directed at the finite increment calculus (FIC) method and indeed to other methods suggested to deal with the problems of steady-state equations.

For the transient solutions the obvious first approach would be to try again the same types of methods used in steady-state calculations and indeed much literature has been devoted to this [23,30–47]. Petrov-Galerkin methods have been used here quite extensively. However, it is obvious that the application of Petrov-Galerkin methods will lead to nonsymmetric mass matrices and these will be difficult to use for any explicit method as mass lumping is not by any means obvious.

Serious difficulty will also arise with the Galerkin least-squares (GLS) procedure even if the temporal variation is generally included by considering space-time finite elements in the whole formulation. This approach to such problems was made by Nguen and Reynen [36], Carey and Jieng [37,38], Johnson and coworkers [34,39,40], and others [41,42]. However the use of space-time elements is expensive as explicit procedures are not available.

Which way, therefore, should we proceed? Is there any other obvious approach which has not been mentioned? The answer lies in the wave nature of the equations which indeed not only permits different methods of approach but in many senses is much more direct and fully justifies the numerical procedures which we shall use later for the full fluid dynamics equations. We shall therefore concentrate on such methods and we will show that they lead to stabilizing diffusions which in form are very similar to those obtained previously by the Petrov-Galerkin method but in a much more direct manner which is consistent with the equations.

The following discussion will therefore be centered on two main directions: we will start with (1) the procedures based on the use of the *characteristics* and the wave nature directly, leading to so-called characteristic-Galerkin methods which we shall discuss in [Section 2.6](#); and then (2) we shall proceed to approach the problem through the use of higher-order time approximations called Taylor-Galerkin methods.

Of the two approaches the first one based on the characteristics is in our view more important. However, for historical and other reasons we shall discuss both methods which for a scalar variable can be shown to give identical answers.

The solutions of convective scalar equations can be given by both approaches very simply. This will form the basis of our treatment for the solution of the full fluid mechanics equations in [Chapter 3](#), where both explicit (time iteration) processes as well as implicit methods can be used.

Many of the methods for solving the transient scalar equations of convective diffusion have been applied to the full fluid mechanics equations, i.e., solving the full vector-valued convective-diffusive equations we presented at the beginning of the

chapter [Eq. (2.1)]. This applies in particular to the Taylor-Galerkin method which has proved to be quite successful in the treatment of high-speed compressible gas flow problems. Indeed this particular approach was the first one adopted to solve such problems. However, the simple wave concepts which are evident in the scalar form of the equations do not translate to such multivariant problems and make the procedures largely heuristic. The same can be said of the direct application of the SUPG and GLS methods to multivariant problems. The procedures such as GLS can provide a useful stabilization of difficulties encountered with incompressible behavior [15]. This does not justify their use on the full equations and we therefore recommend the alternatives to be discussed in Chapter 3.

2.6 Characteristic-based methods

2.6.1 Mesh updating and interpolation methods

We have already observed that, if the spatial coordinate is “convected” in the manner implied by Eq. (2.76), i.e., along the problem *characteristics*, then the convective, first-order, terms disappear. The remaining problem is that of simple diffusion for which discretization procedures with the standard Galerkin spatial approximation are optimal (in an energy norm sense). The most obvious use of this in the finite element context is to update the position of the mesh points in an incremental Lagrangian manner. In Fig. 2.12a we show such an update for the one-dimensional problem of Eq. (2.75) occurring in an interval Δt .

For a constant x' coordinate

$$dx = U dt \quad (2.80)$$

and for a typical nodal point a , we have

$$x_a^{n+1} = x_a^n + \int_{t_n}^{t_{n+1}} U dt \quad (2.81)$$

where in general the “velocity” U may be dependent on x .

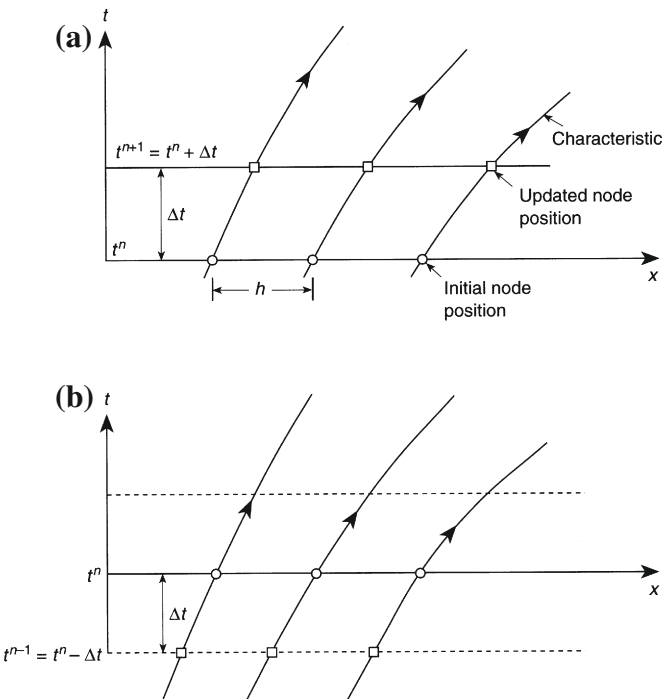
For a constant U we have simply

$$x_a^{n+1} = x_a^n + U \Delta t \quad (2.82)$$

for the updated mesh position. This is not always the case and updating generally has to be done with variable U .

On the updated mesh only the time-dependent diffusion problem needs to be solved using the Galerkin method [15].

The process of continuously updating the mesh and solving the diffusion problem on the new mesh is, of course, impractical. When applied to two- or three-dimensional configurations very distorted elements would result and difficulties will always arise near the boundaries of the domain. For these reasons it seems obvious that after completion of a single step a return to the original mesh should be made by interpolating from the updated values to the original mesh positions.

**FIGURE 2.12**

Mesh updating and interpolation: (a) forward and (b) backward.

This procedure can of course be reversed and characteristic origins traced backwards, as shown in Fig. 2.12b using appropriate interpolated starting values.

The method described is somewhat intuitive but has been used with success for solution of transport equations by Adey and Brebbia [48] and others as early as 1974. The procedure can be formalized and presented more generally and gives the basis of so-called characteristic-Galerkin methods [49].

The diffusion part of the computation is carried out either on the original or on the final mesh, each representing a certain approximation. Intuitively we imagine in the updating scheme that the *operator is split* with the diffusion changes occurring separately from those of convection. This idea is explained in the procedures of the next section.

2.6.2 Characteristic-Galerkin procedures

We shall consider that the equation of convective diffusion in its one-dimensional form (2.75) is split into two parts such that

$$\phi = \phi^* + \phi^{**} \quad (2.83)$$

and separate the differential equation into two additive parts. Accordingly,

$$\frac{\partial \phi^*}{\partial t} + U \frac{\partial \phi}{\partial x} = 0 \quad (2.84a)$$

is a purely convective system while

$$\frac{\partial \phi^{**}}{\partial t} - \frac{\partial}{\partial x} \left(k \frac{\partial \phi}{\partial x} \right) + Q = 0 \quad (2.84b)$$

represents the self-adjoint terms [here Q contains the source, reaction, and term $(\partial U / \partial x)\phi$].

Both ϕ^* and ϕ^{**} now are approximated by expansions

$$\hat{\phi}^* = N_a \tilde{\phi}_a^* \quad \hat{\phi}^{**} = N_a \tilde{\phi}_a^{**} \quad (2.85)$$

and in a single time step t^n to $t^n + \Delta t = t^{n+1}$ we shall assume that the initial conditions are

$$t = t^n \quad \phi^* = 0 \quad \phi^{**} = \phi^{*n} \quad (2.86)$$

Standard Galerkin discretization of the diffusion equation allows $\tilde{\phi}^{**n+1}$ to be determined on the given fixed mesh by solving an equation of the form

$$\mathbf{M} \Delta \tilde{\phi}^{**n} = \Delta t \left[\mathbf{H} (\tilde{\phi}^n + \theta \Delta \tilde{\phi}^{**n}) + \mathbf{f} \right] \quad (2.87)$$

with

$$\tilde{\phi}^{**n+1} = \tilde{\phi}^{**n} + \Delta \tilde{\phi}^{**n}$$

and

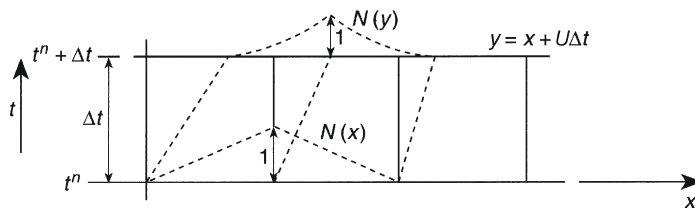
$$\begin{aligned} M_{ab} &= \int_{\Omega} N_a N_b d\Omega \\ H_{ab} &= \int_{\Omega} \frac{\partial N_a}{\partial x_i} k \frac{\partial N_b}{\partial x_i} d\Omega \\ f_a &= \int_{\Omega} N_a Q d\Omega \end{aligned}$$

In solving the convective problem we assume that ϕ^* remains unchanged along the characteristic. However, Fig. 2.13 shows how the initial value of ϕ^{*n} interpolated by standard linear shape functions at time n [see Eq. (2.85)] becomes shifted and distorted. The new value is given by

$$\phi^{*n+1} = N_a(y) \tilde{\phi}_a^{*n} \quad y = x + U \Delta t \quad (2.88)$$

As we require ϕ^{*n+1} to be approximated by standard shape functions, we shall write a projection for smoothing of these values as

$$\int_{\Omega} \mathbf{N}^T (\mathbf{N} \tilde{\phi}^{*n+1} - \mathbf{N}(y) \tilde{\phi}^{*n}) dx = 0 \quad (2.89)$$

**FIGURE 2.13**

Distortion of convected shape function.

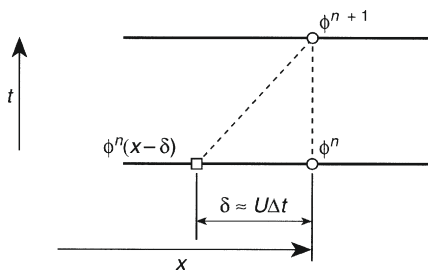
giving

$$\mathbf{M}\tilde{\phi}^{*n+1} = \int_{\Omega} [\mathbf{N}^T \mathbf{N}(y) dx] \tilde{\phi}^{*n} \quad (2.90)$$

The evaluation of the above integrals is of course still complex, especially if the procedure is extended to two or three dimensions. This is generally performed numerically and the stability of the formulation is dependent on the accuracy of such integration [49]. The scheme is stable and indeed exact as far as the convective terms are concerned if the integration is performed exactly (which of course is an unreachable goal). However, stability and indeed accuracy will even then be controlled by the diffusion terms where several approximations have been involved.

2.6.3 A simple explicit characteristic-Galerkin procedure

Many variants of the schemes described in the previous section are possible and were introduced quite early. References [48–59] present some successful versions. However, all methods then proposed are somewhat complex in programming and are time consuming. For this reason a simpler alternative was developed in which the difficulties are avoided at the expense of conditional stability. This method was first published in 1984 [60] and is fully described in numerous publications [61–64]. Its derivation involves a local Taylor expansion and we illustrate this in Fig. 2.14.

**FIGURE 2.14**

A simple characteristic-Galerkin procedure.

We can write Eq. (2.75) along the characteristic as

$$\frac{\partial \phi}{\partial t}(x'(t), t) - \frac{\partial}{\partial x'} \left(k \frac{\partial \phi}{\partial x'} \right) - Q(x') = 0 \quad (2.91)$$

As we can see, in the moving coordinate x' , the convective acceleration term disappears and source and diffusion terms are averaged quantities along the characteristic. Now the equation is self-adjoint and the Galerkin spatial approximation is optimal. The time discretization of the above equation along the characteristic (Fig. 2.14) gives

$$\begin{aligned} \frac{1}{\Delta t} (\phi^{n+1} - \phi^n|_{(x-\delta)}) &\approx \theta \left[\frac{\partial}{\partial x} \left(k \frac{\partial \phi}{\partial x} \right) - Q \right]^{n+1} \\ &+ (1 - \theta) \left[\frac{\partial}{\partial x} \left(k \frac{\partial \phi}{\partial x} \right) - Q \right]^n |_{(x-\delta)} \end{aligned} \quad (2.92)$$

where θ is equal to zero for explicit forms and between zero and unity for semi-implicit and fully implicit forms. As we know, the solution of the above equation in moving coordinates leads to mesh updating and presents difficulties, so we will suggest alternatives. From the Taylor expansion we have

$$\phi^n|_{(x-\delta)} \approx \phi^n - \delta \frac{\partial \phi^n}{\partial x} + \frac{\delta^2}{2} \frac{\partial^2 \phi^n}{\partial x^2} + O(\Delta t^3) \quad (2.93)$$

and assuming $\theta = 0.5$

$$\begin{aligned} \frac{1}{2} \frac{\partial}{\partial x} \left(k \frac{\partial \phi}{\partial x} \right) |_{(x-\delta)} &\approx \frac{1}{2} \frac{\partial}{\partial x} \left(k \frac{\partial \phi}{\partial x} \right)^n - \frac{\delta}{2} \frac{\partial}{\partial x} \left[\frac{\partial}{\partial x} \left(k \frac{\partial \phi}{\partial x} \right)^n \right] + O(\Delta t^2) \\ \text{and } \frac{1}{2} Q |_{(x-\delta)} &\approx \frac{Q^n}{2} - \frac{\delta}{2} \frac{\partial Q^n}{\partial x} \end{aligned} \quad (2.94)$$

where δ is the distance traveled by a particle in the x -direction (Fig. 2.14) which is

$$\delta = \bar{U} \Delta t \quad (2.95)$$

where \bar{U} is an average value of U along the characteristic. Different approximations of \bar{U} lead to different stabilizing terms. The following relation is commonly used [65,66]:

$$\bar{U} = U^n - U^n \Delta t \frac{\partial U^n}{\partial x} \quad (2.96)$$

Inserting Eqs. (2.93)–(2.96) into Eq. (2.92) we have

$$\begin{aligned} \phi^{n+1} - \phi^n &= -\Delta t \left\{ U \frac{\partial \phi^n}{\partial x} - \frac{\partial}{\partial x} \left(k \frac{\partial \phi}{\partial x} \right)^{n+1/2} + Q^{n+1/2} \right\} \\ &+ \Delta t \left\{ \frac{\Delta t}{2} \frac{\partial}{\partial x} \left[U^2 \frac{\partial \phi}{\partial x} \right] - \frac{\Delta t}{2} U \frac{\partial^2}{\partial x^2} \left(k \frac{\partial \phi}{\partial x} \right) + \frac{\Delta t}{2} U \frac{\partial Q}{\partial x} \right\} \end{aligned} \quad (2.97a)$$

where

$$\frac{\partial}{\partial x} \left(k \frac{\partial \phi}{\partial x} \right)^{n+1/2} = \frac{1}{2} \frac{\partial}{\partial x} \left(k \frac{\partial \phi}{\partial x} \right)^{n+1} + \frac{1}{2} \frac{\partial}{\partial x} \left(k \frac{\partial \phi}{\partial x} \right)^n \quad (2.97b)$$

and

$$Q^{n+1/2} = \frac{1}{2}(Q^{n+1} + Q^n) \quad (2.97c)$$

In the above equation, higher-order terms are neglected. If $n + 1/2$ terms in the above equations are replaced with n terms, the equations become explicit in time. This, as already mentioned, is of a similar form to those resulting from Taylor-Galerkin procedures which will be discussed fully in the next section, and the additional terms ($\Delta t^2/2$ terms) add the stabilizing diffusion in the streamline direction. For multidimensional problems, Eq. (2.97a) can be written in indicial notation and approximating $n + 1/2$ terms with n terms (for the fully explicit form)

$$\begin{aligned} \phi^{n+1} - \phi^n &= -\Delta t \left\{ U_j \frac{\partial \phi}{\partial x_j} - \frac{\partial}{\partial x_i} \left(k \frac{\partial \phi}{\partial x_i} \right) + Q \right\}^n \\ &\quad + \Delta t \left\{ \frac{\Delta t}{2} \frac{\partial}{\partial x_i} \left[U_i U_j \frac{\partial \phi}{\partial x_j} \right] \right. \\ &\quad \left. - \frac{\Delta t}{2} U_k \frac{\partial}{\partial x_k} \left[\frac{\partial}{\partial x_i} \left(k \frac{\partial \phi}{\partial x_i} \right) \right] + \frac{\Delta t}{2} U_i \frac{\partial Q}{\partial x_i} \right\}^n \end{aligned} \quad (2.98)$$

An alternative approximation for \bar{U} is [65]

$$\bar{U} = \frac{1}{2} (U^{n+1} + U^n|_{(x-\delta)}) \quad (2.99)$$

Using the Taylor expansion

$$U^n|_{(x-\delta)} \approx U^n - \Delta t U^n \frac{\partial U^n}{\partial x} + O(\Delta t^2) \quad (2.100)$$

from Eqs. (2.92)–(2.95) and Eqs. (2.99) and (2.100) with θ equal to 0.5 we have

$$\begin{aligned} \frac{1}{\Delta t} (\phi^{n+1} - \phi^n) &= -U^{n+1/2} \frac{\partial \phi^n}{\partial x} + \frac{\Delta t}{2} U^n \frac{\partial U^n}{\partial x} \frac{\partial \phi^n}{\partial x} + \frac{\Delta t}{2} U^{n+1/2} U^{n+1/2} \frac{\partial^2 \phi}{\partial x^2} \\ &\quad + \frac{\partial}{\partial x} \left(k \frac{\partial \phi}{\partial x} \right)^{n+1/2} - \frac{\Delta t}{2} U^{n+1/2} \frac{\partial}{\partial x} \left[\frac{\partial}{\partial x} \left(k \frac{\partial \phi}{\partial x} \right)^n \right] \\ &\quad - Q + \frac{\Delta t}{2} U^{n+1/2} \frac{\partial Q}{\partial x} \end{aligned} \quad (2.101)$$

where

$$U^{n+1/2} = \frac{1}{2}(U^{n+1} + U^n) \quad (2.102)$$

As mentioned earlier, we can further approximate $n + 1/2$ terms using n to get the fully explicit version of the scheme. Thus we have

$$U^{n+1/2} = U^n + O(\Delta t) \quad (2.103)$$

and similarly the diffusion term is approximated. The final form of the explicit characteristic-Galerkin method in one dimension can be written as

$$\begin{aligned}\Delta\phi = \phi^{n+1} - \phi^n &= -\Delta t \left[U^n \frac{\partial\phi}{\partial x} - \frac{\partial}{\partial x} \left(k \frac{\partial\phi}{\partial x} \right) + Q \right]^n \\ &\quad + \frac{\Delta t^2}{2} U^n \frac{\partial}{\partial x} \left[U^n \frac{\partial\phi}{\partial x} - \frac{\partial}{\partial x} \left(k \frac{\partial\phi}{\partial x} \right) + Q \right]^n\end{aligned}\quad (2.104)$$

Generalization to multidimensions is direct and can be written in indicial notation for equations of the form Eq. (2.6):

$$\begin{aligned}\Delta\phi &= -\Delta t \left[\frac{\partial(U_j\phi)}{\partial x_j} - \frac{\partial}{\partial x_i} \left(k \frac{\partial\phi}{\partial x_i} \right) + Q \right]^n \\ &\quad + \frac{\Delta t^2}{2} U_k^n \frac{\partial}{\partial x_k} \left[\frac{\partial(U_j\phi)}{\partial x_j} - \frac{\partial}{\partial x_i} \left(k \frac{\partial\phi}{\partial x_i} \right) + Q \right]^n\end{aligned}\quad (2.105)$$

The reader will notice the difference in the stabilizing terms obtained by two different approximations for \tilde{U} [Eqs. (2.98) and (2.105)]. However, as we can see the difference between them is small and when U is constant both approximations give identical stabilizing terms. In the rest of the book we shall follow the latter approximation and always use the conservative form of the equations [Eq. (2.105)].

As we proved earlier, the Galerkin spatial approximation is justified when the characteristic-Galerkin procedure is used. We can thus write the approximation

$$\phi = \mathbf{N}\tilde{\phi} \quad (2.106)$$

and use the weighting \mathbf{N}^T in the integrated residual expression. Thus we obtain

$$\mathbf{M}(\tilde{\phi}^{n+1} - \tilde{\phi}^n) = -\Delta t[(\mathbf{C}\tilde{\phi}^n + \mathbf{K}\tilde{\phi}^n + \mathbf{f}^n) - \Delta t(\mathbf{K}_u\tilde{\phi}^n + \mathbf{f}_s^n)] \quad (2.107)$$

In the above equation

$$\begin{aligned}\mathbf{M} &= \int_{\Omega} \mathbf{N}^T \mathbf{N} d\Omega \quad \mathbf{C} = \int_{\Omega} \mathbf{N}^T \frac{\partial}{\partial x_i} (U_i \mathbf{N}) d\Omega \\ \mathbf{K} &= \int_{\Omega} \frac{\partial \mathbf{N}^T}{\partial x_i} k \frac{\partial \mathbf{N}}{\partial x_i} d\Omega \quad \mathbf{f} = \int_{\Omega} \mathbf{N}^T Q d\Omega + \text{b.t.}\end{aligned}\quad (2.108)$$

and \mathbf{K}_u and \mathbf{f}_s^n come from the new term introduced by the discretization along the characteristics. After integration by parts, the expression of \mathbf{K}_u and \mathbf{f}_s is

$$\begin{aligned}\mathbf{K}_u &= -\frac{1}{2} \int_{\Omega} \frac{\partial}{\partial x_i} \left(U_i \mathbf{N}^T \right) \frac{\partial}{\partial x_i} (U_i \mathbf{N}) d\Omega \\ \mathbf{f}_s &= -\frac{1}{2} \int_{\Omega} \frac{\partial}{\partial x_i} \left(U_i \mathbf{N}^T \right) Q d\Omega + \text{b.t.}\end{aligned}\quad (2.109)$$

where b.t. stands for integrals along region boundaries. Note that the higher-order (third and above) derivatives are not included in the above equation. The boundary terms from the discretization of stabilizing terms are ignored because the original residual is zero.

The approximation is valid for any scalar convected quantity even if that is the velocity component U_i itself, as is the case with momentum-conservation equations. For this reason we have elaborated above the full details of the spatial approximation as the matrices will be repeatedly used.

It is of interest to note that the explicit form of Eq. (2.107) is only conditionally stable. For one-dimensional problems, the stability condition is given as (neglecting the effect of sources)

$$\Delta t \leq \Delta t_{\text{crit}} = \frac{h}{|U|} \quad (2.110)$$

for linear elements in the absence of diffusion. If the diffusion is present a new critical time step has to be calculated as [65, 66]

$$\Delta t_{\text{crit}} = \frac{\Delta t_u \Delta t_k}{\Delta t_u + \Delta t_k} \quad (2.111)$$

where Δt_u is given by Eq. (2.110) and $\Delta t_k = h^2/2k$ is the diffusive limit for the critical one-dimensional time step. In two and three dimensions the nodal element size h is taken as the minimum of element sizes surrounding a node. In practice, however,

$$\Delta t_{\text{crit}} = \min(\Delta t_u, \Delta t_k) \quad (2.112)$$

is more suitable.

Further, with $\Delta t = \Delta t_{\text{crit}}$ the steady-state solution results in an (almost) identical balancing diffusion change to that obtained by using the optimal streamline upwinding procedures discussed in Part I of this chapter. Thus if steady-state solutions are the main objective of the computation such a value of Δt should be used in connection with the \mathbf{K}_u term.

A fully implicit form of solution is an expensive one involving unsymmetric matrices. However it is often convenient to apply $\theta \geq 1/2$ to the diffusive term only. We call this a *nearly* (or *quasi*) *implicit form* and if it is employed we return to the stability condition

$$\Delta t_{\text{crit}} = \frac{h}{|U|} \quad (2.113)$$

which can present an appreciable benefit.

It is of considerable interest to examine the behavior of the solution when the steady state is reached—for instance, if we use the time-stepping algorithm of Eq. (2.107) as an iterative process. Now the final solution is given by taking

$$\tilde{\phi}^{n+1} = \tilde{\phi}^n = \tilde{\phi}$$

which gives

$$[(\mathbf{C} + \mathbf{K} - \Delta t \mathbf{K}_u) \tilde{\phi} + \mathbf{f} - \Delta t \mathbf{f}_s] = 0 \quad (2.114)$$

Inspection of Sections 2.2 and 2.3 shows that the above is identical in form with the use of the Petrov-Galerkin approximation. In the latter the matrix \mathbf{C} is identical and the matrix \mathbf{K}_u includes balancing diffusion of the amount given by $\frac{1}{2}\alpha Uh$. However, if we take

$$\frac{1}{2}\alpha Uh = \frac{U^2 \Delta t}{2} \quad (2.115)$$

the identity of the two schemes results. This can be written as a requirement that

$$\alpha = \frac{U \Delta t}{h} = C \quad (2.116)$$

where C is the Courant number. If $C_{critical}$ is calculated from Eq. (2.111), $C_{critical} = \sqrt{1/Pe + 1} - 1/Pe$.

In Fig. 2.15 we therefore plot the optimal value of α as given in Eq. (2.29) against Pe . We note immediately that if the time-stepping scheme is operated at or near the critical stability limit of the lumped scheme the steady-state solution reached will be close to that resulting from the optimal Petrov-Galerkin process for the steady state. However, if smaller time steps than the critical ones are used, the final solution, though stable, will tend toward the standard Galerkin steady-state discretization and may show oscillations if boundary conditions are such that boundary layers are created. Nevertheless, such small time steps result in very accurate transients so we can conclude that it is unlikely that optimality for transients and steady state can be reached simultaneously.

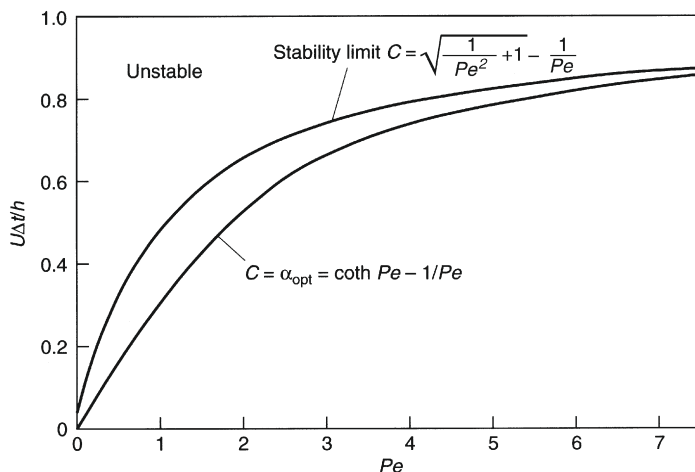


FIGURE 2.15

Stability limit for lumped mass approximation and optimal upwind parameter.

Examination of Eqs. (2.107) shows that the characteristic-Galerkin algorithm could have been obtained by applying a Petrov-Galerkin weighting

$$\left(\mathbf{N}^T + \frac{\Delta t}{2} U_i \frac{\partial \mathbf{N}^T}{\partial x_i} \right)$$

to the various terms of the governing Eq. (2.74) excluding the time derivative $\partial\phi/\partial t$ to which the standard Galerkin weighting of \mathbf{N}^T is attached. Comparing the above with the steady-state problem and the weighting given in Eq. (2.59) the connection is obvious.

A two-dimensional application of the characteristic-Galerkin process is illustrated in Fig. 2.16 in which we show pure convection of a disturbance in a circulating flow. It is remarkable to note that almost no dispersion occurs after a complete revolution. The present scheme is here contrasted with the solution obtained by the finite difference scheme of Lax and Wendroff [67] which for a regular one-dimensional mesh gives a scheme identical to the characteristic-Galerkin except for the mass matrix, which is always diagonal (lumped) in the finite difference scheme.

It seems that here the difference is entirely due to the proper form of the mass matrix \mathbf{M} now used and we note that for transient response the importance of the consistent mass matrix is crucial. However, the numerical convenience of using the lumped form is overwhelming in an explicit scheme. It is easy to recover the performance of the consistent mass matrix by using a simple iteration. In this we write Eq. (2.107) as

$$\mathbf{M}\Delta\tilde{\phi}^n = \Delta t \mathbf{S}^n \quad (2.117)$$

with \mathbf{S}^n being the right-hand side of Eq. (2.107) and

$$\tilde{\phi}^{n+1} = \tilde{\phi}^n + \Delta\tilde{\phi}^n$$

Substituting a lumped mass matrix \mathbf{M}_L to ease the solution process we can iterate as follows:

$$\left(\Delta\tilde{\phi} \right)_l^n = \mathbf{M}_L^{-1} [\Delta t \mathbf{S}^n + (\mathbf{M}_L - M) \left(\Delta\tilde{\phi} \right)_{l-1}^n] \quad (2.118)$$

where l is the iteration number. The process converges very rapidly and in Fig. 2.17 we show the dramatic improvements of results in the solution of a one-dimensional wave propagation with three such iterations done at each time step. At this stage the results are identical to those obtained with the consistent mass matrix.

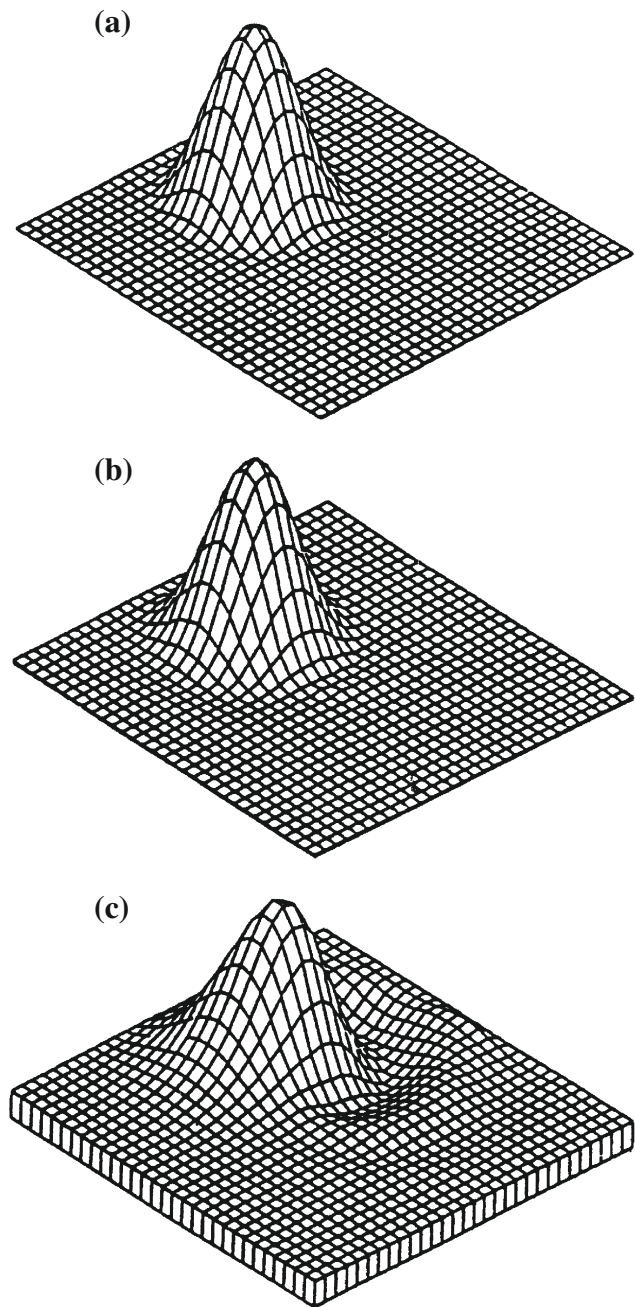
2.6.4 Boundary conditions: Radiation

As we have already indicated the convection-diffusion problem allows one of the conditions

$$\phi = \bar{\phi} \quad \text{on } \Gamma_u \quad (2.119a)$$

or

$$-k \left(\frac{\partial \phi}{\partial n} \right) = \bar{q} \quad \text{on } \Gamma_q \quad (2.119b)$$

**FIGURE 2.16**

Advection of a Gaussian cone in a rotating fluid by characteristic-Galerkin method: (a) original form; (b) form after one revolution using consistent \mathbf{M} matrix; and (c) form after one revolution using lumped mass (Lax-Wendroff).

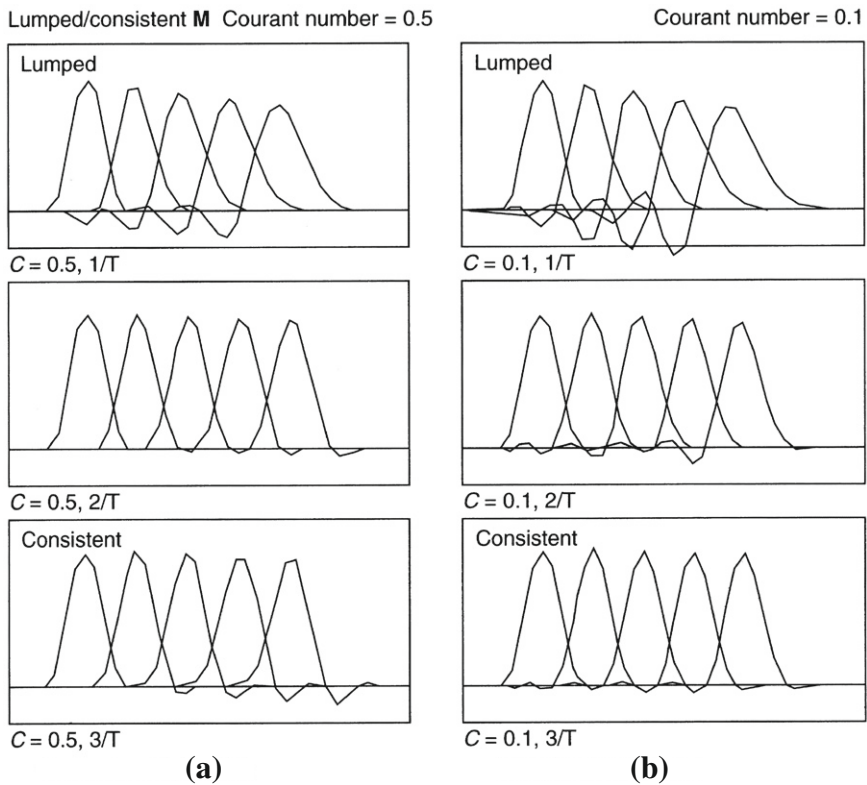


FIGURE 2.17

Characteristic-Galerkin method in the solution of a one-dimensional wave progression. Effect of using a lumped mass matrix and one of consistent iteration: (a) Courant number = 0.5; (b) Courant number = 0.1.

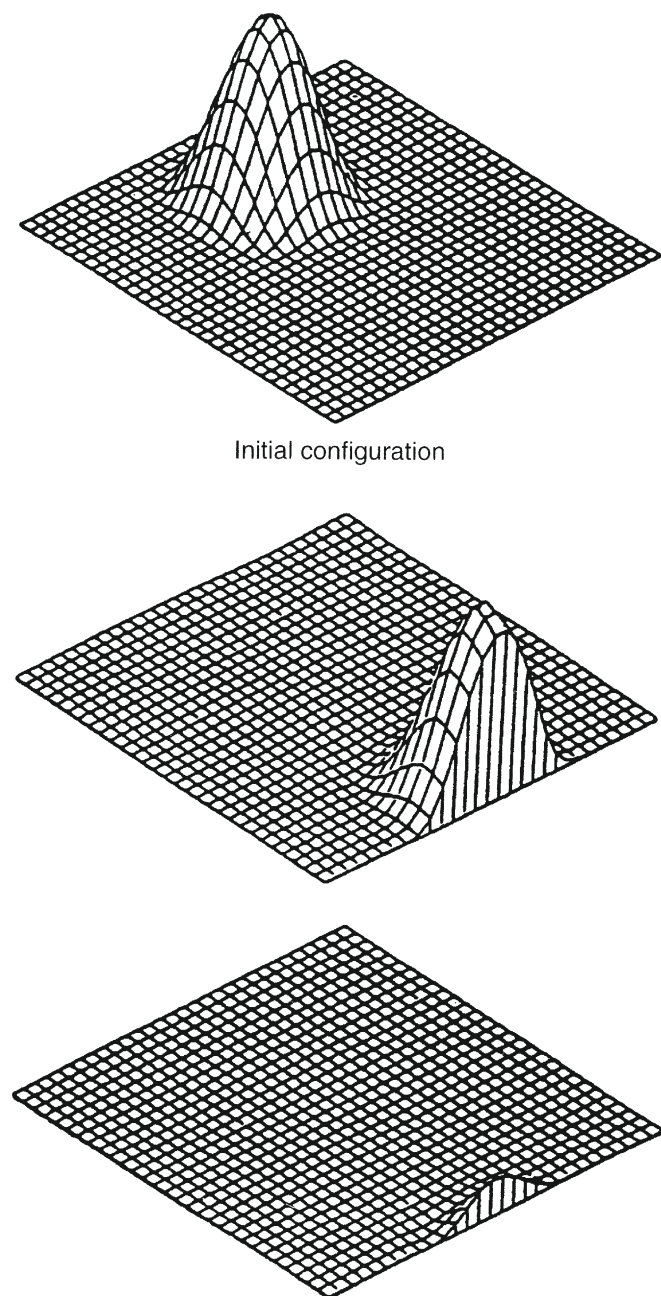
(where $\Gamma = \Gamma_u \cup \Gamma_q$) to be imposed on the boundary, providing the equation is of second order and diffusion is present.

In the case of pure convection this is no longer the case as the differential equation is of first order. Indeed this was responsible for the difficulty of obtaining a solution in the example of Fig. 2.2 when $Pe \rightarrow \infty$ and an exit boundary condition of the type given by Eq. (2.119a) was imposed. In this one-dimensional case for pure convection only the inlet boundary condition can be given; at the exit no boundary condition needs to be prescribed if U , the wave velocity, is positive.

For multidimensional problems of pure convection the same wave specification depends on the value of the normal component of U . Thus if

$$U_i n_i > 0 \quad (2.120)$$

where n_i is the outward normal vector to the boundary, the wave is leaving the problem and then no boundary condition is specified. If the problem has some diffusion, the

**FIGURE 2.18**

A Gaussian distribution advected in a constant velocity field. Boundary condition causes no reflection.

same specification of “no boundary condition” is equivalent to putting

$$-k\left(\frac{\partial \phi}{\partial n}\right) = 0 \quad (2.121)$$

at the exit boundary.

In Fig. 2.18 we illustrate, following the work of Peraire [68], how cleanly the same wave as that specified in the problem of Fig. 2.15 leaves the domain in the uniform velocity field [64, 68] when the correct boundary condition is imposed.

2.7 Taylor-Galerkin procedures for scalar variables

In the Taylor-Galerkin process, the Taylor expansion in time precedes the Galerkin space discretization. Firstly, the scalar variable ϕ is expanded by the Taylor series in time [61, 69]:

$$\phi^{n+1} = \phi^n + \Delta t \frac{\partial \phi^n}{\partial t} + \frac{\Delta t^2}{2} \frac{\partial^2 \phi^n}{\partial t^2} + O(\Delta t^3) \quad (2.122)$$

From Eq. (2.75) we have

$$\frac{\partial \phi^n}{\partial t} = \left[-U \frac{\partial \phi}{\partial x} + \frac{\partial}{\partial x} \left(k \frac{\partial \phi}{\partial x} \right) - Q \right]^n \quad (2.123a)$$

and

$$\frac{\partial^2 \phi^n}{\partial t^2} = \frac{\partial}{\partial t} \left[-U \frac{\partial \phi}{\partial x} + \frac{\partial}{\partial x} \left(k \frac{\partial \phi}{\partial x} \right) - Q \right]^n \quad (2.123b)$$

Substituting Eqs. (2.123a) and (2.123b) into Eq. (2.122) we have

$$\begin{aligned} \phi^{n+1} - \phi^n &= -\Delta t \left[U \frac{\partial \phi}{\partial x} - \frac{\partial}{\partial x} \left(k \frac{\partial \phi}{\partial x} \right) + Q \right]^n \\ &\quad - \frac{\Delta t^2}{2} \frac{\partial}{\partial t} \left[U \frac{\partial \phi}{\partial x} - \frac{\partial}{\partial x} \left(k \frac{\partial \phi}{\partial x} \right) + Q \right]^n \end{aligned} \quad (2.124)$$

Assuming U and k to be constant we have

$$\begin{aligned} \phi^{n+1} - \phi^n &= -\Delta t \left[U \frac{\partial \phi}{\partial x} - \frac{\partial}{\partial x} \left(k \frac{\partial \phi}{\partial x} \right) + Q \right]^n \\ &\quad - \frac{\Delta t^2}{2} \frac{\partial}{\partial x} \left[U \frac{\partial \phi}{\partial t} - \frac{\partial}{\partial x} \left(k \frac{\partial \phi}{\partial t} \right) + \frac{\partial x}{\partial t} Q \right]^n \end{aligned} \quad (2.125)$$

Inserting Eq. (2.123a) into Eq. (2.125) and neglecting higher-order terms gives

$$\begin{aligned} \phi^{n+1} - \phi^n &= -\Delta t \left[U \frac{\partial \phi}{\partial x} - \frac{\partial}{\partial x} \left(k \frac{\partial \phi}{\partial x} \right) + Q \right]^n \\ &\quad + \frac{\Delta t^2}{2} \frac{\partial}{\partial x} \left[U^2 \frac{\partial \phi}{\partial x} - U \frac{\partial}{\partial x} \left(k \frac{\partial \phi}{\partial x} \right) + U Q \right]^n + O(\Delta t^3) \end{aligned} \quad (2.126)$$

As we can see the above equation, having assumed constants U and k , is identical to Eq. (2.104) derived from the characteristic approach. Clearly for scalar variables both characteristic- and Taylor-Galerkin procedures give identical stabilizing terms. Thus selection of a method for a scalar variable is a matter of taste. However, *the sound mathematical justification of the characteristic-Galerkin method should be emphasized here and for this reason the characteristic-Galerkin procedure forms the fundamental basis for the remainder of this text.*

The Taylor-Galerkin procedure for the convection-diffusion equation in multidimensions can be written as

$$\begin{aligned}\phi^{n+1} - \phi^n = & -\Delta t \left\{ U_j \frac{\partial \phi}{\partial x_j} - \frac{\partial}{\partial x_i} \left(k \frac{\partial \phi}{\partial x_i} \right) + Q \right. \\ & \left. - \frac{\Delta t}{2} \frac{\partial}{\partial x_i} \left[U_i U_j \frac{\partial \phi}{\partial x_j} - U_i \frac{\partial}{\partial x_j} \left(k \frac{\partial \phi}{\partial x_j} \right) + U_i Q \right] \right\}^n\end{aligned}\quad (2.127)$$

again showing the complete similarity with the appropriate characteristic-Galerkin form and identity when U_i and k are constant. The Taylor-Galerkin method is the finite element equivalent of the Lax-Wendroff method developed in the finite difference context [67].

The Taylor-Galerkin process has one important feature. The idea can be used directly for dealing with the vector form of the convection-diffusion equation, such as we have mentioned at the beginning of this chapter [viz. (2.1)]. This method was used with reasonable success to solve problems of high-speed gas flow. For this reason we have explained the treatment of vector valued-functions in Appendix D.

2.8 Steady-state condition

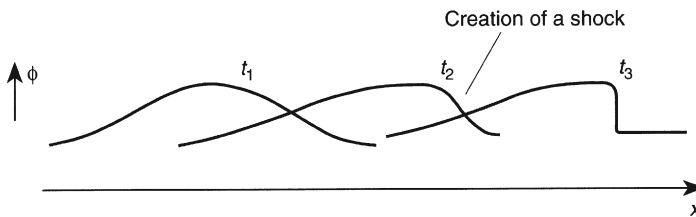
Both the Taylor-Galerkin and characteristic-Galerkin methods give an answer which compares directly with SUPG and GLS giving additional streamline diffusion (higher-order derivatives are omitted) and sources

$$\frac{\Delta t^2}{2} \frac{\partial}{\partial x_i} \left[U_i U_j \frac{\partial \phi}{\partial x_j} \right] \quad \text{and} \quad \frac{\Delta t}{2} \frac{\partial}{\partial x_i} \left[U_i Q \right] \quad (2.128)$$

with Δt replacing the coefficient αh . With the characteristic-Galerkin method being the only method that has a full mathematical justification, we feel that even for steady-state problems this should be considered as an appropriate solution technique.

2.9 Nonlinear waves and shocks

The procedures developed in the previous sections are in principle of course available for both linear and nonlinear problems (with explicit procedures of time stepping being particularly efficient for the latter). Quite generally the convective part of the

**FIGURE 2.19**

Progression of a wave with velocity $U = \phi$.

equation, i.e.,

$$\frac{\partial \phi}{\partial t} + \frac{\partial F_i}{\partial x_i} \equiv \frac{\partial \phi}{\partial t} + U_i \frac{\partial \phi}{\partial x_i} = 0 \quad (2.129)$$

will have the vector U_i dependent on ϕ . Thus

$$U_i \equiv \frac{\partial F_i}{\partial \phi} = U_i(\phi) \quad (2.130)$$

In the one-dimensional case with a scalar variable we shall have equations of the type

$$\frac{\partial \phi}{\partial t} + \frac{\partial F}{\partial x} \equiv \frac{\partial \phi}{\partial t} + U(\phi) \frac{\partial \phi}{\partial x} = 0 \quad (2.131)$$

corresponding to waves moving with a nonuniform velocity U . A typical problem in this category is that due to Burger, which is defined by

$$\frac{\partial \phi}{\partial t} + \frac{\partial}{\partial x} \left(\frac{1}{2} \phi^2 \right) = \frac{\partial \phi}{\partial t} + \phi \frac{\partial \phi}{\partial x} = 0 \quad (2.132)$$

In Fig. 2.19 we illustrate qualitatively how different parts of the wave moving with velocities proportional to their amplitude cause it to steepen and finally develop into a shock form. This behavior is typical of many nonlinear systems and in Chapter 7 we shall see how shocks develop in compressible flow at transonic and supersonic speeds.

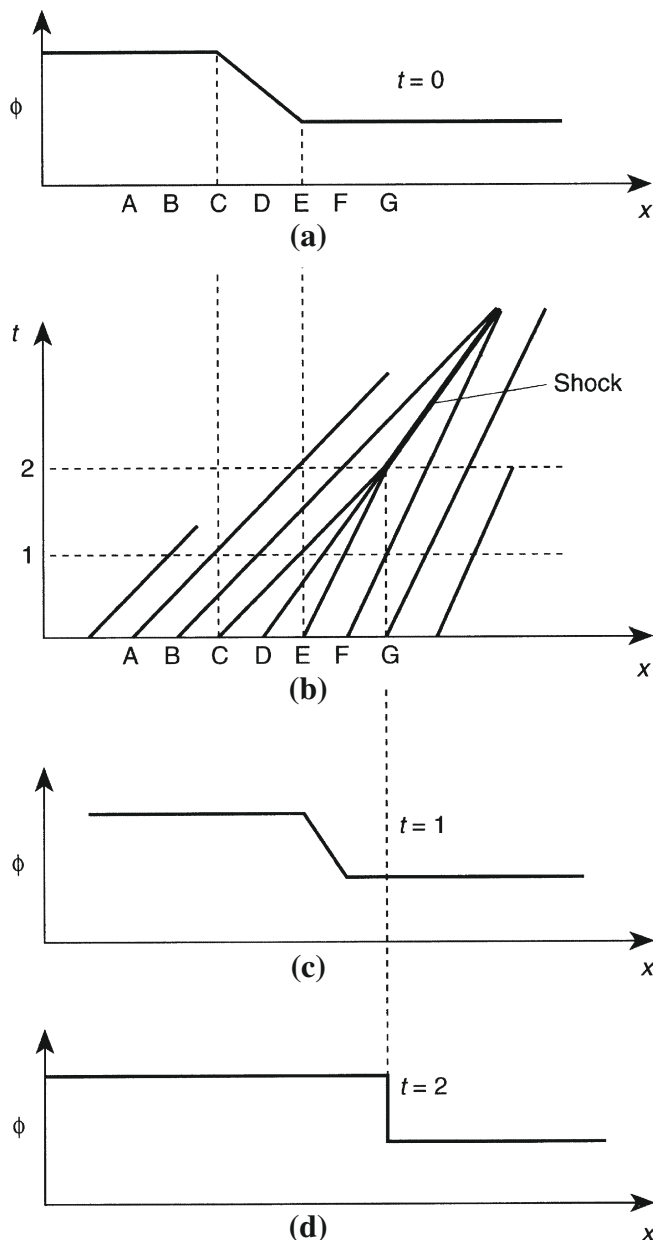
To illustrate the necessity for the development of the shock, consider the propagation of a wave with an originally smooth profile illustrated in Fig. 2.20a. Here as we know the characteristics along which ϕ is constant are straight lines shown in Fig. 2.20b (in $x - t$ plane). These show different propagation speeds intersecting at time $t = 2$ when a discontinuous shock appears. This shock propagates at a finite speed (which here is the average of the two extreme values).

In such a shock the differential equation is no longer valid but the conservation integral is. We can thus write for a small length Δs around the discontinuity

$$\frac{\partial}{\partial t} \int_{\Delta s} \phi \, ds + F(s + \Delta s) - F(s) = 0 \quad (2.133a)$$

or

$$C \Delta \phi + \Delta F = 0 \quad (2.133b)$$

**FIGURE 2.20**

Development of a shock (Burger equation): (a) profile at time $t = 0$; (b) characteristics; (c) profile at time $t = 1$; (d) profile at time $t = 2$.

where $C = \lim \Delta s / \Delta t$ is the speed of shock propagation and $\Delta\phi$ and ΔF are the discontinuities in ϕ and F respectively. Eq. (2.133b) is known as the Rankine-Hugoniot condition.

We shall find that such shocks develop frequently in the context of compressible gas flow and shallow-water flow (Chapters 7 and 10) and can often exist even in the presence of diffusive terms in the equation. Indeed, such shocks are not specific to transients but can persist in the steady state. Clearly, approximation of the finite element kind in which we have postulated in general a C_0 continuity to $\hat{\phi}$ can at best *smear* such a discontinuity over an element length, and generally oscillations near such a discontinuity arise even when the best algorithms of the preceding sections are used.

Figure 2.21 illustrates the difficulties of modeling such steep waves occurring even in linear problems in which the physical dissipation contained in the equations is incapable of smoothing the solution out reasonably, and to overcome this problem artificial diffusivity is frequently used. This artificial diffusivity must have the following characteristics:

1. It must vanish as the element size tends to zero.
2. It must not affect substantially the smooth domain of the solution.

A typical diffusivity often used is a finite element version of that introduced by Lapidus [70] for finite differences, but many other forms of local smoothing have been proposed [71, 72]. The additional Lapidus-type diffusivity is of the form

$$\tilde{k} = C_{\text{Lap}} h^2 \left| \frac{\partial \phi}{\partial x} \right| \quad (2.134)$$

In the above equation C_{Lap} is a coefficient and h is the element size.

In Fig. 2.22 we show a problem of discontinuous propagation in the Burger equation (2.132) and how a progressive increase of the C_{Lap} coefficient kills spurious oscillation, but at the expense of rounding of a steep wave.

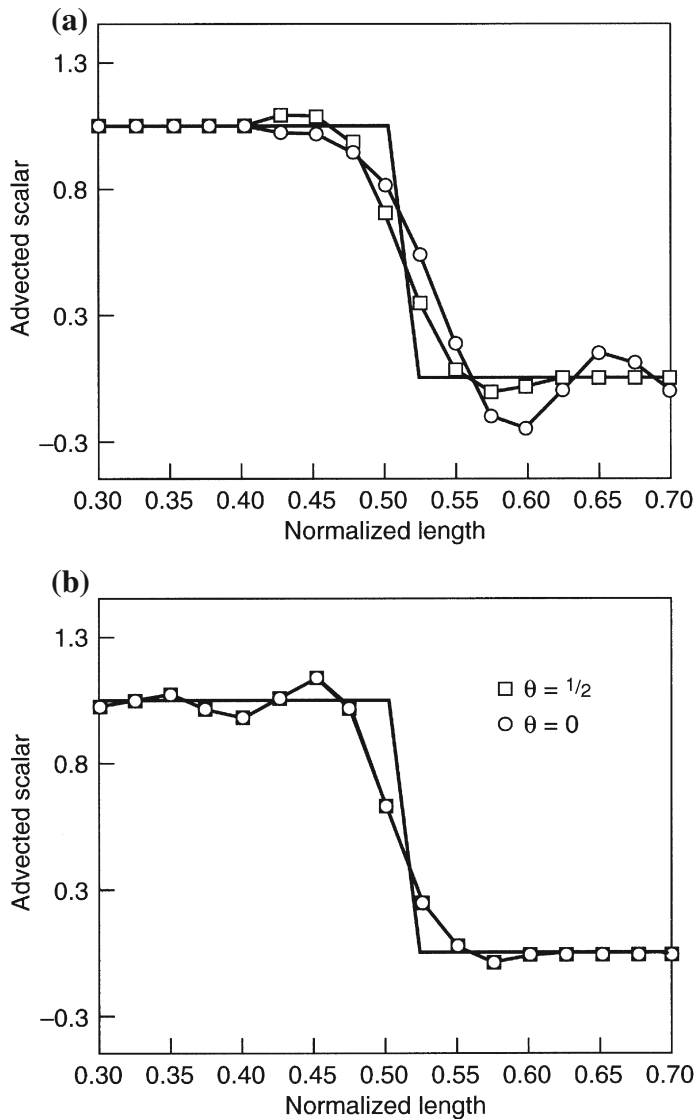
For a multidimensional problem, a degree of anisotropy can be introduced and a possible expression generalizing (2.134) is

$$\tilde{k}_{ij} = C_{\text{Lap}} h^2 \frac{|V_i V_j|}{|\mathbf{V}|} \quad (2.135)$$

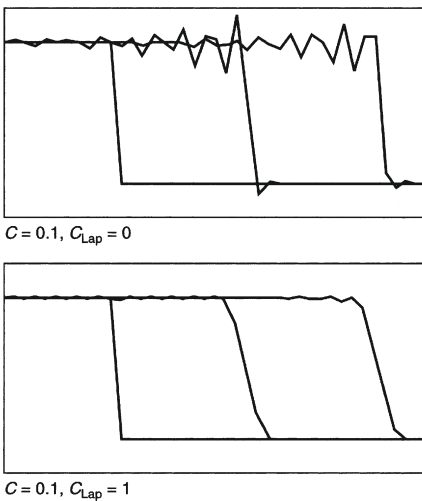
where

$$V_i = \frac{\partial \phi}{\partial x_i}$$

Other possibilities are open here and numerous papers have been devoted to the subject of “shock capture.” We will return to this problem in Chapter 7 where its importance in the high-speed flow of gases is paramount.

**FIGURE 2.21**

Propagation of a steep wave by Taylor-Galerkin process: (a) explicit methods $C = 0.5$, step wave at $Pe = 12,500$ and (b) explicit methods $C = 0.1$, step wave at $Pe = 12,500$.

**FIGURE 2.22**

Propagation of a steep front in Burger's equation with solution obtained using different values of C_{Lap} .

Part III: Boundary Conditions

2.10 Treatment of pure convection

In pure convection problems the equation reduces to

$$\frac{\partial \phi}{\partial t} + U_i \frac{\partial \phi}{\partial x_i} + Q = 0 \quad (2.136)$$

It is clear that only the “inlet” values of ϕ can be set. By inlet we mean those where

$$U_i n_i < 0 \quad (2.137)$$

for n_i an outward pointing normal to the boundary.

This is particularly obvious when we consider the one-dimensional form of Eq. (2.136) in steady state:

$$U \frac{d\phi}{dx} + Q = 0 \quad (2.138)$$

This ordinary differential equation can only have conditions imposed on ϕ at one end of the domain. Let us consider the example where

$$U \frac{d\phi}{dx} + Q = 0, \quad \phi(0) = 1$$

with a constant u and Q . The Galerkin solution to Eq. (2.138) is given by

$$\int_{\Omega} N_a \left[U \frac{d\phi}{dx} + Q \right] dx = 0 \quad (2.139)$$

As shown in Section 2.2.1 where this type of problem is solved as the limit case $Pe = \infty$ and for one-dimensional problems in which boundary conditions are imposed at both ends a purely oscillatory solution occurs. However, when properly solved with only one boundary condition imposed, i.e.,

$$\phi(0) = 1 \quad \text{for } 0 < x < L$$

the correct result for the example shown in Fig. 2.2 is obtained. The same result will be obtained no matter what order finite element approximation is used.

The reader should note the solution “develops” from the inlet in an elementwise manner when Eq. (2.137) is considered. The element-by-element process eliminates the need to solve a large set of simultaneous equations (which is not a serious matter in one-dimensional problems). For two- and three-dimensional problems these savings can be quite substantial if proper boundary conditions are imposed and the process was described by Lesaint and Raviart [73].

Let us consider a one-dimensional domain as shown in Fig. 2.23a with linear elements. Since the flow direction is from the left to right, the solution at node a is influenced only by the node or element upstream. Thus the need for assembly is eliminated and the resulting discrete Galerkin finite element form of Eq. (2.139) at node a is

$$u \left(\frac{u_a - u_{a-1}}{2} \right) + \frac{Ql}{2} = 0 \quad (2.140)$$

This expression is identical to the upwind finite difference approximation discussed previously. In two-dimensional problems (Fig. 2.23b) a similar rule applies and the solution at node a is only affected by the solutions of nodes b and c as shown in

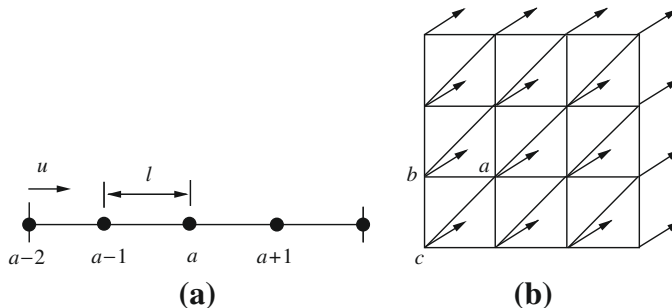


FIGURE 2.23

Solution of pure convection in element-by-element manner. Source term Q and constant u : (a) one-dimensional solution sequence; (b) tow-dimensional solution sequence.

Fig. 2.23b. The calculation can proceed using small groups of elements as illustrated in [Fig. 2.23b](#).

The problem of pure convection is a common one in neutron transport where reaction effects are included [[73, 74](#)]. We note that for compressible flow without viscosity we shall later use the so-called Euler equations [viz. [Chapter 7](#)]. Once again the values of the unknown functions will only be specified at the inlet boundaries if supersonic conditions exist.

2.11 Boundary conditions for convection-diffusion

If diffusion occurs, boundary conditions must be imposed on all boundaries. Thus, in the one-dimensional case we return to the situation discussed at the beginning of this chapter. We see immediately that the standard Galerkin process breaks down near the outlet boundary when we try to specify the value of the unknown ϕ in a “strong” (Dirichlet) manner when convection effects are important (i.e., $Pe > 1$). In such a case we shall try to impose the Dirichlet boundary condition in a “weak” manner to balance the solution between the interior and the boundary treatments. Such a weak imposition of the Dirichlet condition was presented by Nitsche in 1971 [[75](#)] and is used frequently when discontinuous Galerkin methods are discussed.

We again start with the Galerkin equation in which the diffusive term is integrated by parts yielding

$$-\int_{\Gamma} N_a n_i \left(k \frac{\partial \phi}{\partial x_i} \right) d\Gamma = -\int_{\Gamma_\phi} N_a n_i \left(k \frac{\partial \phi}{\partial x_i} \right) d\Gamma + \int_{\Gamma_q} N_a \bar{q}_n d\Gamma \quad (2.141)$$

where the natural boundary condition has been imposed on Γ_q . When the approximate solution is used in [Eq. \(2.141\)](#) a contribution to the coefficient matrix arises and is given by

$$K_{ab} = -\int_{\Gamma_\phi} N_a n_i k \frac{\partial N_b}{\partial x_i} d\Gamma \quad (2.142)$$

This term is clearly unsymmetric and to restore symmetry Nitsche adds two terms:

$$-\int_{\Gamma_\phi} \frac{\partial N_a}{\partial x_i} n_i k (\phi - \bar{\phi}) d\Gamma + \kappa \int_{\Gamma_\phi} N_a (\phi - \bar{\phi}) d\Gamma = 0$$

where κ is a parameter. In the above equation the desired value of the Dirichlet condition appears. The second term is a least-squares type term used to maintain stability of the solution. This gives the final form for the boundary integrals as

$$-\int_{\Gamma_\phi} \left[N_a n_i k \frac{\partial \phi}{\partial x_i} + \frac{\partial N_a}{\partial x_i} n_i k (\phi - \bar{\phi}) \right] d\Gamma + \kappa \int_{\Gamma_\phi} N_a (\phi - \bar{\phi}) d\Gamma \quad (2.143)$$

We observe as $\kappa \rightarrow \infty$ we recover the penalty method. However, Nitsche shows that choosing

$$\kappa = O(k/h)$$

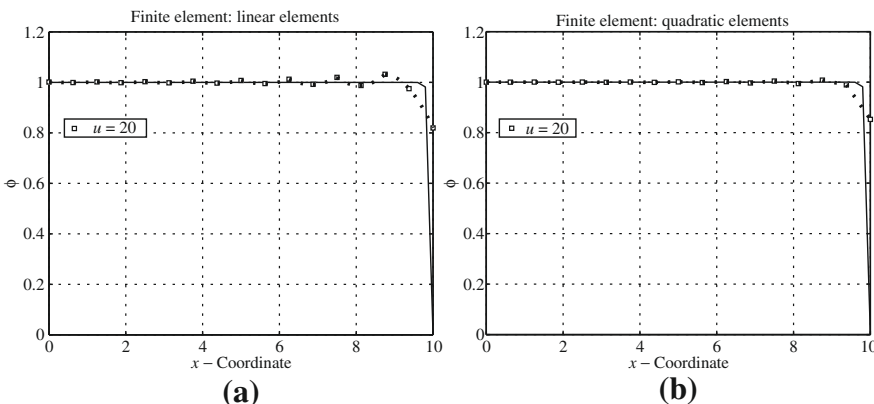


FIGURE 2.24

Solution of one-dimensional convection-diffusion problem: (a) one-dimensional linear element solution; (b) one-dimensional quadratic element solution.

where h is an element size of the mesh, an effective solution results without strong imposition of the boundary condition. In Fig. 2.24 we show results for the problem originally given in Fig. 2.2 for a large Peclet number. The overall good results are obtained *without any modification of the standard Galerkin process in the interior of the domain*.

From results shown in Fig. 2.24 using linear and quadratic elements we see immediately that the results obtained by weakening the Dirichlet condition at the outlet are quite acceptable. If we contrast these results with those obtained by using the procedures of Part I we observe that no longer are exact values obtained at nodes but the solution is accurate in the “mean.” The oscillations are almost nonexistent and yet the standard Galerkin procedure is used throughout the whole domain with the special treatment confined to the outlet boundary.

2.12 Summary and concluding remarks

The reader may well be confused by the variety of apparently unrelated approaches given in this chapter. This may be excused by the fact that optimality guaranteed by the finite element approaches in elliptic, self-adjoint problems does not automatically transfer to hyperbolic non-self-adjoint ones.

The major part of this chapter is concerned with a scalar variable in the convection-diffusion reaction equation. The several procedures presented for steady-state and transient equations yield almost identical results. However the characteristic-Galerkin method is the most logical one for transient problems and gives identical stabilizing terms to that derived by the use of Petrov-Galerkin, GLS, and other procedures when the time step used is near the stability limit. For such a problem the optimality is assured simply by splitting the problem into the self-adjoint part where the direct

Galerkin approximation is optimal and an advective motion where the unknown variable remains fixed in the characteristic space.

Extension of the various procedures presented to vector variables has been made in the past and here we relegate such procedures to [Appendix D](#) as they present special problems. For this reason we recommend that when dealing with equations such as those arising in the motion of a fluid a split is made in a manner separating several scalar convection-diffusion problems for which the treatment described is used. We shall do so in the next chapter when we introduce the CBS algorithm using the *characteristic-based split*.

References

- [1] E. Isaacson, R. Courant, M. Rees, On the solution of non-linear hyperbolic differential equations by finite differences, *Commun. Pure Appl. Math.* V (1952) 243–255.
- [2] A.K. Runchall, M. Wolfstein, Numerical integration procedure for the steady state Navier–Stokes equations, *J. Mech. Eng. Sci.* 11 (1969) 445–453.
- [3] D.B. Spalding, A novel finite difference formulation for differential equations involving both first and second derivatives, *Int. J. Numer. Methods Eng.* 4 (1972) 551–559.
- [4] K.E. Barrett, The numerical solution of singular perturbation boundary value problem, *Quart. J. Mech. Appl. Math.* 27 (1974) 57–68.
- [5] O.C. Zienkiewicz, R.H. Gallagher, P. Hood, Newtonian and non-Newtonian viscous incompressible flow. Temperature induced flows and finite element solutions, in: J. Whiteman (Ed.), *The Mathematics of Finite Elements and Applications*, vol. II, Academic Press, London, 1976.
- [6] I. Christie, D.F. Griffiths, A.R. Mitchell, O.C. Zienkiewicz, Finite element methods for second order differential equations with significant first derivatives, *Int. J. Numer. Methods Eng.* 10 (1976) 1389–1396.
- [7] O.C. Zienkiewicz, J.C. Heinrich, P.S. Huyakorn, A.R. Mitchell, An upwind finite element scheme for two dimensional convective transport equations, *Int. J. Numer. Methods Eng.* 11 (1977) 131–144.
- [8] J.C. Heinrich, O.C. Zienkiewicz, Quadratic finite element schemes for two dimensional convective-transport problems, *Int. J. Numer. Methods Eng.* 11 (1977) 1831–1844.
- [9] J. Donea, A. Huerta, *Finite Element Methods for Flow Problems*, John Wiley & Sons, Chichester, 2003.
- [10] D.W. Kelly, S. Nakazawa, O.C. Zienkiewicz, A note on anisotropic balancing dissipation in the finite element method approximation to convective diffusion problems, *Int. J. Numer. Methods Eng.* 15 (1980) 1705–1711.
- [11] B.P. Leonard, A survey of finite differences of opinion on numerical modeling of the incompressible defective convection equation, in: T.J.R. Hughes

- (Ed.), Finite Elements for Convection Dominated Flows, vol. AMD 34, ASME, New York, 1979.
- [12] A.N. Brooks, T.J.R. Hughes, Streamline upwind/Petrov-Galerkin formulation for convection dominated flows with particular emphasis on the incompressible Navier Stokes equation, *Comput. Methods Appl. Mech. Eng.* 32 (1982) 199–259.
 - [13] C.A. Fletcher, Computational Techniques for Fluid Dynamics: Fundamentals and General Techniques, Springer-Verlag, Berlin, 1988, vol. 1.
 - [14] G.L. Guymon, V.H. Scott, L.R. Herrmann, A general numerical solution of the two-dimensional diffusion-convection equation by the finite element method, *Water Resour.* 6 (1970) 1611–1615.
 - [15] O.C. Zienkiewicz, R.L. Taylor, J.Z. Zhu, The Finite Element Method: Its Basis and Fundamentals, seventh ed., Elsevier, Oxford, 2013.
 - [16] P. Tong, Exact solution of certain problems by the finite element method, *J. AIAA* 7 (1969) 179–180.
 - [17] T.J.R. Hughes, J.D. Atkinson, A variational basis of ‘upwind’ finite elements, in: S. Nemat-Nasser (Ed.), Variational Methods in the Mechanics of Solids, Pergamon Press, Oxford, 1980, pp. 387–390.
 - [18] G.F. Carey, Exponential upwinding and integrating factors for symmetrization, *Commun. Appl. Numer. Methods* 1 (1985) 57–60.
 - [19] J. Donea, T. Belytschko, P. Smolinski, A generalized Galerkin method for steady state convection-diffusion problems with application to quadratic shape function, *Comput. Methods Appl. Mech. Eng.* 48 (1985) 25–43.
 - [20] T.J.R. Hughes, L.P. Franca, G.M. Hulbert, Z. Johan, F. Sakhid, The Galerkin least square method for advective diffusion equations, in: T.E. Tezduyar, T.J.R. Hughes (Eds.), Recent Developments in Computational Fluid Mechanics, vol. AMD 95, ASME, New York, 1988.
 - [21] T.J.R. Hughes, Multiscale phenomena: Green’s function, subgrid scale models, bubbles, and the origins of stabilized formulations, in: M. Morandi Cecchi, K. Morgan, J. Periaux, B.A. Schrefler, O.C. Zienkiewicz (Eds.), Proc. Ninth Int. Conf. Finite Elements Fluids – New Trends and Applications, Venezia, October 1995.
 - [22] T.J.R. Hughes, Multiscale phenomena: Green’s function, Dirichlet-to-Neumann formulation, subgrid scale models, bubbles and the origins of stabilized formulations, *Comput. Methods Appl. Mech. Eng.* 127 (1995) 387–401.
 - [23] R. Codina, A comparison of some finite element methods for solving the diffusion-convection-reaction equation, *Comput. Methods Appl. Mech. Eng.* 156 (1998) 185–210.
 - [24] E. Oñate, Derivation of stabilized equations for numerical solution of advective-diffusive transport and fluid flow problems, *Comput. Methods Appl. Mech. Eng.* 151 (1998) 233–265.
 - [25] S. Nakazawa, J.F. Pittman, O.C. Zienkiewicz, Numerical solution of flow and heat transfer in polymer melts, in: R.H. Gallagher et al. (Eds.), Finite Elements in Fluids, vol. 4, John Wiley & Sons, Chichester, 1982, pp. 251–283, Chapter 13.

- [26] R. Codina, E. Oñate, M. Cervera, The intrinsic time for the streamline upwind Petrov-Galerkin formulation using quadratic elements, *Comput. Methods Appl. Mech. Eng.* 94 (1992) 239–262.
- [27] R. Codina, Stability analysis of forward Euler scheme for convection diffusion equation using the SUPG formulation in space, *Int. J. Numer. Methods Eng.* 36 (1993) 1445–1464.
- [28] T.J.R. Hughes, A. Brooks, A multi-dimensional upwind scheme with no cross wind diffusion, in: T.J.R. Hughes (Ed.), *Finite Elements for Convection Dominated Flows*, vol. AMD 34, ASME, New York, 1979.
- [29] T.J.R. Hughes, A.N. Brooks, A theoretical framework for Petrov-Galerkin methods with discontinuous weighting function, in: R.H. Gallagher et al. (Eds.), *Finite Elements in Fluids*, vol. 4, John Wiley & Sons, Chichester, 1982, pp. 47–65.
- [30] C. Johnson, A. Szepessy, On the convergence of a finite element method for a nonlinear hyperbolic conservation law, *Math. Comput.* 49 (1987) 427–444.
- [31] F. Shakib, T.R.J. Hughes, Z. Johan, A new finite element formulation for computational fluid dynamics: X. The compressible Euler and Navier–Stokes equations, *Comput. Methods Appl. Mech. Eng.* 89 (1991) 141–219.
- [32] R. Codina, A discontinuity capturing crosswind-dissipation for the finite element solution of convection diffusion equation, *Comput. Methods Appl. Mech. Eng.* 110 (1993) 325–342.
- [33] P. Nithiarasu, O.C. Zienkiewicz, B.V.K.S. Sai, K. Morgan, R. Codina, M. Vázquez, Shock capturing viscosities for the general fluid mechanics algorithm, *Int. J. Numer. Methods Fluids* 28 (1998) 1325–1353.
- [34] C. Johnson, U. Nävert, J. Pitkäranta, Finite element methods for linear hyperbolic problems, *Comput. Methods Appl. Mech. Eng.* 45 (1984) 285–312.
- [35] P.A.B. de Sampaio, A modified operator analysis of convection diffusion problems, in: Proc. II National Meeting on Thermal Sciences, Aguas de Lindoia (Brazil), 1988, pp. 180–183.
- [36] N. Nguen, J. Reynen, A space–time least square finite element scheme for advection–diffusion equations, *Comput. Methods Appl. Mech. Eng.* 42 (1984) 331–342.
- [37] G.F. Carey, B.N. Jiang, Least square finite elements for first order hyperbolic systems, *Int. J. Numer. Methods Eng.* 26 (1988) 81–93.
- [38] B.N. Jiang, G.F. Carey, A stable least-square finite element method for non-linear hyperbolic problems, *Int. J. Numer. Methods Fluids* 8 (1988) 933–942.
- [39] C. Johnson, Streamline diffusion elements for problems in fluid mechanics, in: R.H. Gallagher et al. (Eds.), *Finite Elements in Fluids*, vol. 6, John Wiley & Sons, Chichester, 1986, pp. 251–261.
- [40] C. Johnson, *Numerical Solutions of Partial Differential Equations by the Finite Element Method*, Cambridge University Press, Cambridge, 1987.
- [41] C.C. Yu, J.C. Heinrich, Petrov-Galerkin methods for the time dependent convective transport equation, *Int. J. Numer. Methods Eng.* 23 (1986) 883–901.

- [42] C.C. Yu, J.C. Heinrich, Petrov-Galerkin methods for multidimensional, time dependent convective diffusion equation, *Int. J. Numer. Methods Eng.* 24 (1987) 2201–2215.
- [43] C.E. Baumann, M.A. Storti, S.R. Idelsohn, A Petrov-Galerkin technique for the solution of transonic and supersonic flows, *Comput. Methods Appl. Mech. Eng.* 95 (1992) 49–70.
- [44] P.A.B. de Sampaio, P.R.M. Lyra, K. Morgan, N.P. Weatherill, Petrov-Galerkin solutions of the incompressible Navier–Stokes equations in primitive variables with adaptive remeshing, *Comput. Methods Appl. Mech. Eng.* 106 (1993) 143–178.
- [45] J.A. Cardle, A modification of the Petrov-Galerkin method for the transient convection diffusion equation, *Int. J. Numer. Methods Eng.* 38 (1995) 171–181.
- [46] S.R. Idelsohn, J.C. Heinrich, E. Oñate, Petrov-Galerkin methods for the transient advective–diffusive equation with sharp gradients, *Int. J. Numer. Methods Eng.* 39 (1996) 1455–1473.
- [47] P.K. Maji, G. Biswas, Analysis of flow in the spiral casing using a streamline upwind Petrov-Galerkin method, *Int. J. Numer. Methods Eng.* 45 (1999) 147–174.
- [48] R.A. Adey, C.A. Brebbia, Finite element solution of effluent dispersion, in: C.A. Brebbia, J.J. Connor (Eds.), *Numerical Methods in Fluid Mechanics*, Pentech Press, Southampton, 1974, pp. 325–354.
- [49] K.W. Morton, Generalised Galerkin methods for hyperbolic problems, *Comput. Methods Appl. Mech. Eng.* 52 (1985) 847–871.
- [50] R.E. Ewing, T.F. Russell, Multistep Galerkin methods along characteristics for convection–diffusion problems, in: R. Vichnevetsky, R.S. Stepleman (Eds.), *Advances in Computation Methods for PDEs*, vol. IV, IMACS, Rutgers University, Brunswick, NJ, 1981, pp. 28–36.
- [51] J. Douglas Jr, T.F. Russell, Numerical methods for convection dominated diffusion problems based on combining the method of characteristics with finite element or finite difference procedures, *SIAM J. Numer. Anal.* 19 (1982) 871–885.
- [52] O. Pironneau, On the transport diffusion algorithm and its application to the Navier–Stokes equation, *Numer. Math.* 38 (1982) 309–332.
- [53] M. Bercovier, O. Pironneau, Y. Harbani, E. Levine, Characteristics and finite element methods applied to equations of fluids, in: J. Whiteman (Ed.), *The Mathematics of Finite Elements and Applications*, vol. V, Academic Press, London, 1982, pp. 471–478.
- [54] J. Goussebaile, F. Hecht, C. Labadie, L. Reinhart, Finite element solution of the shallow water equations by a quasi-direct decomposition procedure, *Int. J. Numer. Methods Fluids* 4 (1984) 1117–1136.
- [55] M. Bercovier, O. Pironneau, V. Sastri, Finite elements and characteristics for some parabolic–hyperbolic problems, *Appl. Math. Model.* 7 (1983) 89–96.
- [56] J.P. Benque, J.P. Gregoire, A. Hauguel, M. Maxant, Application des méthodes de décomposition aux calculs numériques en hydraulique industrielle, in: INRIA,

6th Coll. Inst. Methodes de Calcul Sci. et Techn., Versailles, 12–16 December 1983.

- [57] A. Bermudez, J. Durany, M. Posse, C. Vazquez, An upwind method for solving transport–diffusion–reaction systems, *Int. J. Numer. Methods Eng.* 28 (1984) 2021–2040.
- [58] P.X. Lin, K.W. Morton, E. Suli, Characteristic Galerkin schemes for scalar conservation laws in two and three space dimensions, *SIAM J. Numer. Anal.* 34 (1997) 779–796.
- [59] O. Pironneau, J. Liou, T.T.I. Tezduyar, Characteristic Galerkin and Galerkin least squares space-time formulations for the advection–diffusion equation with time dependent domain, *Comput. Methods Appl. Mech. Eng.* 100 (1992) 117–141.
- [60] O.C. Zienkiewicz, R. Löhner, K. Morgan, S. Nakazawa, Finite elements in fluid mechanics – a decade of progress, in: R.H. Gallagher et al. (Eds.), *Finite Elements in Fluids*, vol. 5, John Wiley & Sons, Chichester, 1984, pp. 1–26.
- [61] R. Löhner, K. Morgan, O.C. Zienkiewicz, The solution of non-linear hyperbolic equation systems by the finite element method, *Int. J. Numer. Methods Fluids* 4 (1984) 1043–1063.
- [62] O.C. Zienkiewicz, R. Löhner, K. Morgan, J. Peraire, High speed compressible flow and other advection dominated problems of fluid mechanics, in: R.H. Gallagher et al. (Eds.), *Finite Elements in Fluids*, vol. 6, John Wiley & Sons, Chichester, 1986, pp. 41–88.
- [63] R. Löhner, K. Morgan, O.C. Zienkiewicz, An adaptive finite element procedure for compressible high speed flows, *Comput. Methods Appl. Mech. Eng.* 51 (1985) 441–465.
- [64] O.C. Zienkiewicz, R. Löhner, K. Morgan, High speed inviscid compressive flow by the finite element method, in: J. Whiteman (Ed.), *The Mathematics of Finite Elements and Applications*, vol. VI, Academic Press, London, 1985, pp. 1–25.
- [65] O.C. Zienkiewicz, R. Codina, A general algorithm for compressible and incompressible flow – Part I. The split, characteristic based scheme, *Int. J. Numer. Methods Fluids* 20 (1996) 869–885.
- [66] O.C. Zienkiewicz, P. Nithiarasu, R. Codina, M. Vazquez, P. Ortiz, The characteristic-based-split (CBS) procedure: an efficient and accurate algorithm for fluid problems, *Int. J. Numer. Methods Fluids* 31 (1999) 359–392.
- [67] P.D. Lax, B. Wendroff, Systems of conservative laws, *Commun. Pure Appl. Math.* 13 (1960) 217–237.
- [68] J. Peraire, A finite method for convection dominated flows, Ph.D. Thesis, University of Wales, Swansea, 1986.
- [69] J. Donea, A Taylor-Galerkin method for convective transport problems, *Int. J. Numer. Methods Eng.* 20 (1984) 101–119.
- [70] A. Lapidus, A detached shock calculation by second order finite differences, *J. Comput. Phys.* 2 (1967) 154–177.
- [71] J.P. Boris, D.L. Brook, Flux corrected transport I. Shasta – a fluid transport algorithm that works, *J. Comput. Phys.* 11 (1973) 38–69.

- [72] S.T. Zalesak, Fully multidimensional flux corrected transport algorithm for fluids, *J. Comput. Phys.* 31 (1979) 335–362.
- [73] P. Lesaint, P.-A. Raviart, On a finite element method for solving the neutron transport equation, in: C. de Boor (Ed.), *Mathematical Aspects of Finite Elements in Partial Differential Equations*, Academic Press, New York, 1974.
- [74] W.H. Reed, T.R. Hill, Triangular mesh methods for the neutron transport equation, Technical Report LA-UR-73-479, Los Alamos Scientific Laboratory, 1973.
- [75] J.A. Nitsche, Über ein Variationsprinzip zur Lösung Dirichlet-Problemen bei Verwendung von Teilräumen, die keinen Randbedingungen unerworfene sind, *Abh. Math. Sem. Univ. Hamburg* 36 (1971) 9–15.

3

The Characteristic-Based Split (CBS) Algorithm: A General Procedure for Compressible and Incompressible Flow

3.1 Introduction

In the first chapter we have written the fluid dynamics equations in a very general format applicable to both incompressible and compressible flows. The equations included that of energy which for compressible situations are fully coupled with equations for conservation of mass and momentum. However, of course, the equations, with small modifications, are applicable for specialized treatment in scenarios from incompressible flow where the energy coupling disappears, to the problems of shallow-water equations where the variables describe a somewhat different flow regime. Chapters 4–6 and 10 deal with such specialized forms.

The equations have been written in Chapter 1 in fully conservative, standard form [Eqs. (1.25) and (1.26a)–(1.26d)] but all the essential features can be captured by writing the three sets of equations as below.

Mass conservation

$$\frac{\partial \rho}{\partial t} = -\frac{\partial U_i}{\partial x_i} \quad (3.1)$$

For flows with small compressibility (see Eq. 1.44c)

$$\frac{\partial \rho}{\partial t} = \frac{1}{c^2} \frac{\partial p}{\partial t} = -\frac{\partial U_i}{\partial x_i} \quad (3.2)$$

where c is the speed of sound and depends on E , p , and ρ and, assuming constant entropy,

$$c^2 = \frac{\partial p}{\partial \rho} = \frac{\gamma p}{\rho} \quad (3.3)$$

where γ is the ratio of specific heats equal to c_p/c_v , where c_p is the specific heat at constant pressure and c_v is the specific heat at constant volume, and we define the mass flow flux as

$$U_i = \rho u_i \quad (3.4)$$

For a fluid with a small compressibility, the speed of sound may be written as

$$c^2 = \frac{K}{\rho} \quad (3.5)$$

in which K is the elastic bulk modulus. Depending on the application we use an appropriate relation for c^2 .

Momentum conservation

$$\frac{\partial U_i}{\partial t} = -\frac{\partial}{\partial x_j}(u_j U_i) + \frac{\partial \tau_{ij}}{\partial x_j} - \frac{\partial p}{\partial x_i} + \rho g_i \quad (3.6)$$

Energy conservation

$$\frac{\partial(\rho E)}{\partial t} = -\frac{\partial}{\partial x_i}(u_i \rho E) + \frac{\partial}{\partial x_i}\left(k \frac{\partial T}{\partial x_i}\right) - \frac{\partial}{\partial x_i}(u_i p) + \frac{\partial}{\partial x_i}(\tau_{ij} u_j) + \rho g_i u_i \quad (3.7)$$

In all of the above u_i are the velocity components, ρ is the density, E is the specific energy, p is the pressure, T is the absolute temperature, ρg_i represents body forces and other source terms, k is the thermal conductivity, and τ_{ij} are the deviatoric stress components given by (Eq. 1.11b)

$$\tau_{ij} = \mu \left(\frac{\partial u_i}{\partial x_j} + \frac{\partial u_j}{\partial x_i} - \frac{2}{3} \delta_{ij} \frac{\partial u_k}{\partial x_k} \right) \quad (3.8)$$

where δ_{ij} is the Kronecker delta and equals 1 if $i = j$ and 0 if $i \neq j$. In general, μ , the dynamic viscosity, in the above equation is a function of temperature, $\mu(T)$, and appropriate relations will be used if necessary. The equations are completed by a relationship that relates the pressure and density. One of the popular choices of this relation is the universal gas law when the flow is coupled and compressible, i.e.,

$$p = \rho R T \quad (3.9)$$

where R is the universal gas constant.

The reader will observe that the major difference in the momentum-conservation equation (3.6) and the corresponding ones describing the behavior of solids (see Ref. [1]) is the presence of a convective acceleration term.

This does not lend itself to the optimal Galerkin approximation as the equations are now non-self-adjoint in nature (see Appendix A). However, it will be observed that if a certain split is made, the characteristic-Galerkin procedure can be applied to the part of the system which is not self-adjoint but has an identical form to the convection-diffusion equation. We have shown in the previous chapter that the characteristic-Galerkin procedure is excellent for dealing with such equations. However, we have also shown that many alternatives will lead to precisely the same convection stabilizing terms. The choice of the name CBS is thus somewhat subjective indicating simply that the characteristic process is, for us, the most basic justification.

It is important to state again here that the equations given above are of the conservation forms. As it is possible for nonconservative equations (Appendix B) to yield multiple and/or inaccurate solutions, this fact is very important.

We believe that the algorithm introduced in this chapter is currently the most general one available for fluids, as it can be directly applied to almost all physical situations. We shall show such applications ranging from low Mach number viscous or indeed inviscid flow to the solution of hypersonic flows. In all applications the algorithm proves to be at least as good as other procedures developed. Further, in problems of very slow viscous flow we find that the treatment can be almost identical to that of incompressible elastic solids and here we shall often find it expedient to use higher-order approximations satisfying the incompressibility conditions (the so-called Babuška-Brezzi restriction) [2,3]. Indeed on certain occasions the direct use of incompressibility stabilizing processes is as described in Chapter 10 of Ref. [1].

3.2 Nondimensional form of the governing equations

The governing equations described above, Eqs. (3.1)–(3.9), are often written in nondimensional form. The scales used to nondimensionalize these equations vary depending on the nature of the flow. We describe below the scales frequently used in flow computations, though of course many alternatives are possible:

$$\begin{aligned}\bar{t} &= \frac{tu_\infty}{L}, \quad \bar{x}_i = \frac{x_i}{L}, \quad \bar{\rho} = \frac{\rho}{\rho_\infty}, \quad \bar{p} = \frac{p}{\rho_\infty u_\infty^2} \\ \bar{u}_i &= \frac{u_i}{u_\infty}, \quad \bar{E} = \frac{E}{u_\infty^2}, \quad \bar{T} = \frac{T c_p}{u_\infty^2}, \quad \bar{c}^2 = \frac{c^2}{u_\infty^2}\end{aligned}\tag{3.10}$$

where an overbar indicates a nondimensional quantity, subscript ∞ represents a free stream quantity, and L is a reference length. Applying the above scales to the governing equations and rearranging we have the following form:

Conservation of mass

$$\frac{\partial \bar{\rho}}{\partial \bar{t}} = -\frac{\partial \bar{U}_i}{\partial \bar{x}_i}\tag{3.11}$$

Conservation of momentum

$$\frac{\partial \bar{U}_i}{\partial \bar{t}} = -\frac{\partial}{\partial \bar{x}_j}(\bar{u}_j \bar{U}_i) + \frac{1}{Re} \frac{\partial(\bar{v} \bar{\tau}_{ij})}{\partial \bar{x}_j} - \frac{\partial \bar{p}}{\partial \bar{x}_i} + \bar{\rho} \bar{g}_i\tag{3.12}$$

where

$$Re = \frac{u_\infty L}{v_\infty}, \quad \bar{g}_i = \frac{g_i L}{u_\infty^2}, \quad \bar{v} = \frac{v}{v_\infty}\tag{3.13}$$

are the Reynolds number, nondimensional body forces, and viscosity ratio, respectively. In the above equation v is the kinematic viscosity equal to μ/ρ with μ being the dynamic viscosity.

Conservation of energy

$$\frac{\partial(\bar{\rho}\bar{E})}{\partial\bar{t}} = -\frac{\partial}{\partial\bar{x}_i}(\bar{u}_i\bar{\rho}\bar{E}) + \frac{1}{RePr}\frac{\partial}{\partial\bar{x}_i}\left(k^*\frac{\partial\bar{T}}{\partial\bar{x}_i}\right) - \frac{\partial}{\partial\bar{x}_i}(\bar{u}_j\bar{p}) + \frac{1}{Re}\frac{\partial}{\partial\bar{x}_i}(\bar{v}\bar{\tau}_{ij}\bar{u}_j) \quad (3.14)$$

where Pr is the Prandtl number and k^* is the conductivity ratio given by the relations

$$Pr = \frac{\mu_\infty c_p}{k_\infty}, \quad k^* = \frac{k}{k_\infty} \quad (3.15)$$

where k_∞ is a reference thermal conductivity.

Equation of state

$$\bar{p} = \frac{\bar{\rho}R\bar{T}}{c_p} = \bar{\rho}\bar{R}\bar{T} = \bar{\rho}\frac{(\gamma-1)}{\gamma}\bar{T} \quad (3.16)$$

In the above equation $R = c_p - c_v$ and $\bar{R} = (c_p - c_v)/c_p$ are used. The following forms of nondimensional equations are useful to relate the speed of sound, temperature, pressure, energy, etc.

$$\begin{aligned} \bar{E} &= \frac{\bar{T}}{\gamma} + \frac{1}{2}\bar{u}_i\bar{u}_i \\ \bar{c}^2 &= (\gamma-1)\bar{T} \\ \bar{p} &= (\gamma-1)\left(\bar{\rho}\bar{E} - \frac{1}{2}\frac{\bar{U}_i\bar{U}_i}{\bar{\rho}}\right) \end{aligned} \quad (3.17)$$

The above nondimensional equations are convenient when coding the CBS algorithm. However, the dimensional form will be retained in this and other chapters for clarity.

3.3 Characteristic-based split (CBS) algorithm

3.3.1 The split: General remarks

The split follows the process initially introduced by Chorin [4,5] for incompressible flow problems in a finite difference context. A similar extension of the split to a finite element formulation for different applications of incompressible flows has been carried out by many authors [6–34]. However, in this chapter we extend the split to solve the fluid dynamics equations of both compressible and incompressible forms using the characteristic-Galerkin procedure [35–87]. The algorithm in its full form was first introduced in 1995 by Zienkiewicz and Codina [35,36] and followed several years of preliminary research [88–92].

Although the original Chorin split [4,5] could never be used in a fully explicit algorithm, the new form is applicable for fully compressible flows in both explicit and semi-implicit forms. The split provides a fully explicit algorithm even in the

incompressible case for steady-state problems now using an “artificial” compressibility which does not affect the steady-state solution; unsteady state can be recovered through so-called dual time stepping [57]. When real compressibility exists, such as in gas flows, the computational advantages of the explicit form compare well with those of other currently used schemes and the additional cost due to splitting is insignificant. Generally for an identical cost, results are considerably improved throughout a large range of aerodynamic problems. However, a further advantage is that both subsonic and supersonic problems can be solved by the same algorithm.

3.3.2 The split: Temporal discretization

At this stage we will only consider the solution of (3.1) and (3.6) with variables u_i and p . The extension to include energy and any other variables will be treated after these are available. We can discretize Eq. (3.6) in time using the characteristic-Galerkin process. Except for the pressure term this equation is similar to the convection-diffusion equation (2.11). This term can however be treated as a known (source type) quantity provided we have an independent way of evaluating the pressure. Before proceeding with the algorithm, we repeat Eq. (3.6) below for use with the characteristic-Galerkin method:

$$\frac{\partial U_i}{\partial t} = -\frac{\partial}{\partial x_j}(u_j U_i) + \frac{\partial \tau_{ij}}{\partial x_j} - \frac{\partial p}{\partial x_i} + \rho g_i \quad (3.18)$$

At this stage we have to introduce the “split” in which we substitute a suitable approximation. In all procedures the values of the solution (U_i^{n+1}, p^{n+1}) at time t^{n+1} must be determined from the known values (U_i^n, p^n) at time t^n . Two alternative approximations are useful and we shall describe these as *Split A* and *Split B*, respectively. In each we assume during the time increment $\Delta t = t^{n+1} - t^n$

$$U_i^{n+1} = U_i^n + \Delta U_i^* + \Delta U_i^{**} \quad (3.19)$$

We also discretize in time using the approximation for the time interval $t^n \leq t \leq t^{n+1}$

$$\frac{\partial U_i}{\partial t} = \frac{U_i^{n+1} - U_i^n}{\Delta t} = \frac{\Delta U_i^*}{\Delta t} + \frac{\Delta U_i^{**}}{\Delta t} \quad (3.20)$$

Using Eq. (2.105) from the previous chapter and replacing ϕ by U_i , we can write

$$\begin{aligned} U_i^{n+1} - U_i^n &= \Delta t \left[-\frac{\partial}{\partial x_j}(u_j U_i)^n + \frac{\partial \tau_{ij}^n}{\partial x_j} + (\rho g_i)^n \right] - \Delta t \frac{\partial p^{n+\theta_2}}{\partial x_i} \\ &\quad + \frac{\Delta t^2}{2} u_k \frac{\partial}{\partial x_k} \left[\frac{\partial}{\partial x_j}(u_j U_i) - \frac{\partial \tau_{ij}^n}{\partial x_j} - \rho g_i \right]^n \\ &\quad + \frac{\Delta t^2}{2} u_k \frac{\partial}{\partial x_k} \left(\frac{\partial p^{n+\theta_2}}{\partial x_i} \right) \end{aligned} \quad (3.21)$$

In the above equation

$$\frac{\partial p^{n+\theta_2}}{\partial x_i} = (1 - \theta_2) \frac{\partial p^n}{\partial x_i} + \theta_2 \frac{\partial p^{n+1}}{\partial x_i} \quad (3.22)$$

or

$$\frac{\partial p^{n+\theta_2}}{\partial x_i} = \frac{\partial p^n}{\partial x_i} + \theta_2 \frac{\partial \Delta p}{\partial x_i} \quad (3.23)$$

where

$$\Delta p = p^{n+1} - p^n \quad (3.24)$$

The reader should note that the velocity and deviatoric stress terms are evaluated at t^n , whereas the pressure is evaluated at $t^{n+\theta_2}$. This is certainly permitted as the method may be shown to be fully consistent.

Using the auxiliary variables ΔU_i^* and ΔU_i^{**} we split Eq. (3.21) into two parts.

In the first form we remove all the pressure gradient terms from Eq. (3.21); in the second we retain in that equation the pressure gradient corresponding to the beginning of the step, i.e., $\partial p^n / \partial x_i$. Though it appears that the second split might be more accurate, there are other reasons for the success of the first split which we shall refer to later. Indeed Split A is the one which we shall universally recommend for steady-state problems. For transient problems however Split B with additional pressure stability or Split A with dual time stepping may give a slightly better result [83, 87, 93].

Split A

In this form we introduce an auxiliary variable ΔU_i^* such that (removing third-order terms)

$$\Delta U_i^* = \Delta t \left[-\frac{\partial}{\partial x_j} (u_j U_i) + \frac{\partial \tau_{ij}}{\partial x_j} + \rho g_i + \frac{\Delta t}{2} u_k \frac{\partial}{\partial x_k} \left(\frac{\partial}{\partial x_j} (u_j U_i) - \rho g_i \right) \right]^n \quad (3.25)$$

We note that this equation is solved by an explicit time step applied to the discretized form and a complete solution is now possible. The “correction” given below is available once the pressure increment is evaluated:

$$\Delta U_i^{**} = -\Delta t \frac{\partial p^{n+\theta_2}}{\partial x_i} + \frac{\Delta t^2}{2} u_k \frac{\partial^2 p^n}{\partial x_k \partial x_i} \quad (3.26)$$

From Eq. (3.1) we have

$$\Delta \rho = -\Delta t \frac{\partial U_i^{n+\theta_1}}{\partial x_i} = -\Delta t \left[\frac{\partial U_i^n}{\partial x_i} + \theta_1 \frac{\partial \Delta U_i}{\partial x_i} \right] \quad (3.27)$$

Replacing ΔU_i by the known intermediate, auxiliary variable ΔU_i^* , using Eqs. (3.20) and (3.26) and rearranging and neglecting third- and higher-order terms we obtain

$$\Delta \rho = -\Delta t \left[\frac{\partial U_i^n}{\partial x_i} + \theta_1 \frac{\partial \Delta U_i^*}{\partial x_i} - \Delta t \theta_1 \left(\frac{\partial^2 p^n}{\partial x_i \partial x_i} + \theta_2 \frac{\partial^2 \Delta p}{\partial x_i \partial x_i} \right) \right] \quad (3.28)$$

The above equation is fully self-adjoint in the variable $\Delta \rho$ which is the unknown. Now, therefore, a standard Galerkin-type procedure can be optimally used for spatial

approximation of Eq. (3.28). It is clear that the governing equations can be solved after spatial discretization in the following order:

- (a) Eq. (3.25) to obtain ΔU_i^*
- (b) Eq. (3.28) to obtain $\Delta \rho$
- (c) Eq. (3.26) to obtain ΔU_i^{**} thus establishing the values of U_i and p from the energy and gas law at t^{n+1}

After completing the calculation to establish ΔU_i and $\Delta \rho$ the energy equation is dealt with independently and the value of $(\rho E)^{n+1}$ is obtained by the characteristic-Galerkin process applied to Eq. (3.7).

It is important to remark that this sequence allows us to solve the governing equations (3.1), (3.6), and (3.7) in an efficient manner and with adequate convection stabilization. Note that these equations are written in conservation form. Therefore, this algorithm is well suited for dealing with supersonic and hypersonic problems, in which the conservation form ensures that shocks will be placed at the right position and a unique solution achieved. However, we must remark that near the actual shocks, additional numerical damping will always be needed.

Split B

In this split we also introduce an auxiliary variable ΔU_i^* now retaining the known values of $\partial p^n / \partial x_i$, i.e.,

$$\begin{aligned} \Delta U_i^* = \Delta t & \left[-\frac{\partial}{\partial x_j} (u_j U_i) + \frac{\partial \tau_{ij}}{\partial x_j} - \frac{\partial p}{\partial x_i} + \rho g_i \right. \\ & \left. + \frac{\Delta t}{2} u_k \frac{\partial}{\partial x_k} \left(\frac{\partial}{\partial x_j} (u_j U_i) + \frac{\partial p}{\partial x_i} - \rho g_i \right) \right]^n \end{aligned} \quad (3.29)$$

It would appear that now U_i^* is a better approximation than that from Split A in (3.25).

We can now write the correction as

$$\Delta U_i^{**} = -\theta_2 \Delta t \frac{\partial \Delta p}{\partial x_i} \quad (3.30)$$

i.e., the correction to be applied is smaller than that assuming Split A, Eq. (3.26). Further, if we use the fully explicit form with $\theta_2 = 0$, no mass velocity (ΔU_i^{**}) correction is necessary. We proceed to calculate the density changes as in Split A:

$$\Delta \rho = -\Delta t \left[\frac{\partial U_i^n}{\partial x_i} + \theta_1 \frac{\partial \Delta U_i^*}{\partial x_i} - \Delta t \theta_1 \theta_2 \frac{\partial^2 \Delta p}{\partial x_i^2} \right] \quad (3.31)$$

The solution stages follow the same steps as in Split A. Later we will see that Split B does not possess the self-pressure stabilizing properties of Split A when incompressibility (or near incompressibility) is encountered (Section 3.6).

3.3.3 Spatial discretization and solution procedure

In all of the equations given below the standard Galerkin procedure is used for spatial discretization as this was fully justified for the characteristic-Galerkin method in [Chapter 2](#). We now approximate spatially using standard finite element shape functions as

$$\begin{aligned} U_i &= \mathbf{N}_u \tilde{\mathbf{U}}_i & \Delta U_i &= \mathbf{N}_u \Delta \tilde{\mathbf{U}}_i & \Delta U_i^* &= \mathbf{N}_u \Delta \tilde{\mathbf{U}}_i^* & \Delta U_i^{**} &= \mathbf{N}_u \Delta \tilde{\mathbf{U}}_i^{**} \\ u_i &= \mathbf{N}_u \tilde{\mathbf{u}}_i & p &= \mathbf{N}_p \tilde{\mathbf{p}} & \rho &= \mathbf{N}_\rho \tilde{\boldsymbol{\rho}} \end{aligned} \quad (3.32)$$

In the above equation

$$\begin{aligned} \tilde{\mathbf{U}}_i &= [U_i^1 \quad U_i^2 \quad \dots \quad U_i^a \quad \dots \quad U_i^m]^T \\ \mathbf{N} &= [N^1 \quad N^2 \quad \dots \quad N^a \quad \dots \quad N^m] \end{aligned} \quad (3.33)$$

where a is the node (or variable) identifying number (and varies between 1 and m).

Split A

We have the following weak form of [Eq. \(3.25\)](#) for the standard Galerkin approximation (weighting functions are the shape functions):

$$\begin{aligned} &\int_{\Omega} N_u^a \Delta U_i^* d\Omega \\ &= -\Delta t \left[\int_{\Omega} N_u^a \frac{\partial}{\partial x_j} (u_j U_i) d\Omega + \int_{\Omega} \frac{\partial N_u^a}{\partial x_j} \tau_{ij} d\Omega - \int_{\Omega} N_u^a (\rho g_i) d\Omega \right]^n \\ &\quad + \frac{\Delta t^2}{2} \left[\int_{\Omega} \frac{\partial}{\partial x_k} (u_k N_u^a) \left(-\frac{\partial}{\partial x_j} (u_j U_i) + \rho g_i \right) d\Omega \right]^n \\ &\quad + \Delta t \left[\int_{\Gamma} N_u^a \tau_{ij} n_j d\Gamma \right]^n \end{aligned} \quad (3.34)$$

Here, the viscous and stabilizing terms are integrated by parts and the last term is the boundary integral arising from integrating by parts the viscous contribution. Since the residual on the boundaries can be neglected, other boundary contributions from the stabilizing terms are negligible. Note from [Eq. \(2.105\)](#) that the whole residual appears in the stabilizing term. However, we have omitted diffusion terms in the above equation since they are of higher order.

As mentioned in [Chapter 1](#), it is convenient to use matrix notation when the finite element formulation is carried out. We start here from [Eq. \(1.6\)](#) of [Chapter 1](#) and repeat the deviatoric stress and strain rate relations below:

$$\tau_{ij} = 2\mu (\dot{\varepsilon}_{ij} - \frac{1}{3} \delta_{ij} \dot{\varepsilon}_{kk}) \quad (3.35)$$

where the quantity in brackets is the deviatoric strain rate. In the above

$$\dot{\varepsilon}_{ij} = \frac{1}{2} \left(\frac{\partial u_i}{\partial x_j} + \frac{\partial u_j}{\partial x_i} \right) \quad (3.36)$$

and

$$\dot{\varepsilon}_{kk} = \frac{\partial u_k}{\partial x_k} \quad (3.37)$$

We now define the strain rate in three dimensions by a six-component vector as given below:¹

$$\dot{\boldsymbol{\varepsilon}} = [\dot{\varepsilon}_{11} \quad \dot{\varepsilon}_{22} \quad \dot{\varepsilon}_{33} \quad 2\dot{\varepsilon}_{12} \quad 2\dot{\varepsilon}_{23} \quad 2\dot{\varepsilon}_{31}]^T \quad (3.38)$$

With a matrix \mathbf{m} defined as

$$\mathbf{m} = [1 \quad 1 \quad 1 \quad 0 \quad 0 \quad 0]^T \quad (3.39)$$

we find that the volumetric strain rate is

$$\dot{\varepsilon}_v = \dot{\varepsilon}_{ii} = \dot{\varepsilon}_{11} + \dot{\varepsilon}_{22} + \dot{\varepsilon}_{33} = \mathbf{m}^T \dot{\boldsymbol{\varepsilon}} \quad (3.40)$$

The deviatoric strain rate can now be written simply as [see Eq. (3.33)]

$$\dot{\boldsymbol{\varepsilon}}^d = \dot{\boldsymbol{\varepsilon}} - \frac{1}{3}\mathbf{m}\dot{\varepsilon}_v = (\mathbf{I} - \frac{1}{3}\mathbf{m}\mathbf{m}^T)\dot{\boldsymbol{\varepsilon}} = \mathbf{I}_d \dot{\boldsymbol{\varepsilon}} \quad (3.41)$$

where

$$\mathbf{I}_d = (\mathbf{I} - \frac{1}{3}\mathbf{m}\mathbf{m}^T) \quad (3.42)$$

and thus

$$\mathbf{I}_d = \frac{1}{3} \begin{bmatrix} 2 & -1 & -1 & 0 & 0 & 0 \\ -1 & 2 & -1 & 0 & 0 & 0 \\ -1 & -1 & 2 & 0 & 0 & 0 \\ 0 & 0 & 0 & 3 & 0 & 0 \\ 0 & 0 & 0 & 0 & 3 & 0 \\ 0 & 0 & 0 & 0 & 0 & 3 \end{bmatrix} \quad (3.43)$$

The stresses are similarly written in vector form as

$$\boldsymbol{\sigma} = [\sigma_{11} \quad \sigma_{22} \quad \sigma_{33} \quad \sigma_{12} \quad \sigma_{23} \quad \sigma_{31}]^T \quad (3.44)$$

where of course σ_{11} is equal to $\tau_{11} - p$ while σ_{12} is identical to τ_{12} , etc.

Immediately we can assume that the deviatoric stresses are proportional to the deviatoric strain rates and write directly from Eq. (3.35)

$$\boldsymbol{\sigma}^d = \mathbf{I}_d \boldsymbol{\sigma} = \mu \mathbf{I}_0 \dot{\boldsymbol{\varepsilon}}^d = \mu (\mathbf{I}_0 - \frac{2}{3}\mathbf{m}\mathbf{m}^T) \dot{\boldsymbol{\varepsilon}} \quad (3.45)$$

where the diagonal matrix \mathbf{I}_0 is

$$\mathbf{I}_0 = \begin{bmatrix} 2 & & & & & \\ & 2 & & & & \\ & & 2 & & & \\ & & & 1 & & \\ & & & & 1 & \\ & & & & & 1 \end{bmatrix} \quad (3.46)$$

¹In two dimensions we use a three-component vector $\dot{\boldsymbol{\varepsilon}} = [\dot{\varepsilon}_{11} \quad \dot{\varepsilon}_{22} \quad 2\dot{\varepsilon}_{12}]^T$, noting that $\dot{\varepsilon}_{33}$ is zero.

To complete the matrix derivation the velocities and strain rates have to be appropriately related and the reader can verify that using the tensorial strain definitions we can write

$$\dot{\boldsymbol{\epsilon}} = \mathcal{S}\mathbf{u} \quad (3.47)$$

where

$$\mathbf{u} = [u_1 \quad u_2 \quad u_3]^T \quad (3.48)$$

and \mathcal{S} is an appropriate strain rate matrix (operator) defined below:

$$\mathcal{S} = \begin{bmatrix} \frac{\partial}{\partial x_1} & 0 & 0 \\ 0 & \frac{\partial}{\partial x_2} & 0 \\ 0 & 0 & \frac{\partial}{\partial x_3} \\ \frac{\partial}{\partial x_2} & \frac{\partial}{\partial x_1} & 0 \\ 0 & \frac{\partial}{\partial x_3} & \frac{\partial}{\partial x_2} \\ \frac{\partial}{\partial x_3} & 0 & \frac{\partial}{\partial x_1} \end{bmatrix} \quad (3.49)$$

Finally the reader will note that the direct link between the strain rates and velocities will involve a matrix \mathbf{B} defined simply by

$$\mathbf{B} = \mathcal{S}\mathbf{N}_u \quad (3.50)$$

Now from Eqs. (3.32), (3.34), and (3.45), the solution for ΔU_i^* in matrix form is

Step 1

$$\Delta \tilde{\mathbf{U}}^* = -\mathbf{M}_u^{-1} \Delta t \left[(\mathbf{C}_u \tilde{\mathbf{U}} + \mathbf{K}_t \tilde{\mathbf{u}} - \mathbf{f}) - \Delta t (\mathbf{K}_u \tilde{\mathbf{U}} + \mathbf{f}_s) \right]^n \quad (3.51)$$

where the quantities with a \sim indicate nodal values and all the discretization matrices are similar to those defined in Chapter 2 for convection-diffusion equations (Eqs. 2.108 and 2.109) and are given as

$$\begin{aligned} \mathbf{M}_u &= \int_{\Omega} \mathbf{N}_u^T \mathbf{N}_u d\Omega & \mathbf{C}_u &= \int_{\Omega} \mathbf{N}_u^T (\nabla(\mathbf{u} \mathbf{N}_u)) d\Omega \\ \mathbf{K}_t &= \int_{\Omega} \mathbf{B}^T \mu (\mathbf{I}_0 - \frac{2}{3} \mathbf{m} \mathbf{m}^T) \mathbf{B} d\Omega & \mathbf{f} &= \int_{\Omega} \mathbf{N}_u^T \rho \mathbf{g} d\Omega + \int_{\Gamma} \mathbf{N}_u^T \mathbf{t}^d d\Gamma \end{aligned} \quad (3.52)$$

where \mathbf{g} is $[g_1 \ g_2 \ g_3]^T$ and \mathbf{t}^d is the traction corresponding to the deviatoric stress components.

In Eq. (3.51) \mathbf{K}_u and \mathbf{f}_s come from the terms introduced by the discretization along the characteristics. After integration by parts [i.e., from (3.34)], the expressions for \mathbf{K}_u and \mathbf{f}_s are

$$\mathbf{K}_u = -\frac{1}{2} \int_{\Omega} [\nabla^T(\mathbf{u} \mathbf{N}_u)]^T [\nabla^T(\mathbf{u} \mathbf{N}_u)] d\Omega \quad (3.53)$$

and

$$\mathbf{f}_s = -\frac{1}{2} \int_{\Omega} [\nabla^T(\mathbf{u}\mathbf{N}_u)]^T \rho \mathbf{g} d\Omega \quad (3.54)$$

where $\nabla^T = [\partial/\partial x_1, \partial/\partial x_2, \partial/\partial x_3]$.

The weak form of the density-pressure equation is

$$\begin{aligned} \int_{\Omega} N_p^a \Delta \rho d\Omega &= -\Delta t \int_{\Omega} N_p^a \frac{\partial}{\partial x_i} \left(U_i^n + \theta_1 \Delta U_i^* - \theta_1 \Delta t \frac{\partial p^{n+\theta_2}}{\partial x_i} \right) d\Omega \\ &= \Delta t \int_{\Omega} \frac{\partial N_p^a}{\partial x_i} \left[U_i^n + \theta_1 \left(\Delta U_i^* - \Delta t \frac{\partial p^{n+\theta_2}}{\partial x_i} \right) \right] d\Omega \quad (3.55) \\ &\quad - \Delta t \int_{\Gamma} N_p^a \left[U_i^n + \theta_1 \left(\Delta U_i^* - \Delta t \frac{\partial p^{n+\theta_2}}{\partial x_i} \right) \right] n_i d\Gamma \end{aligned}$$

In the above, all the RHS terms are integrated by parts. Further we shall discretize ρ directly only in problems of compressible gas flows and therefore below we retain p as the main variable. Spatial discretization of the above equation gives

Step 2

$$(\mathbf{M}_p + \Delta t^2 \theta_1 \theta_2 \mathbf{H}) \Delta \tilde{\mathbf{p}} = \Delta t [\mathbf{G} \tilde{\mathbf{U}}^n + \theta_1 \mathbf{G} \Delta \tilde{\mathbf{U}}^* - \Delta t \theta_1 \mathbf{H} \tilde{\mathbf{p}}^n - \mathbf{f}_p] \quad (3.56)$$

which can be solved for $\Delta \tilde{\mathbf{p}}$.

The new matrices arising here are

$$\begin{aligned} \mathbf{H} &= \int_{\Omega} (\nabla \mathbf{N}_p)^T \nabla \mathbf{N}_p d\Omega \quad \mathbf{M}_p = \int_{\Omega} \mathbf{N}_p^T \left(\frac{1}{c^2} \right)^n \mathbf{N}_p d\Omega \\ \mathbf{G} &= \int_{\Omega} (\nabla \mathbf{N}_p)^T \mathbf{N}_u d\Omega \quad \mathbf{f}_p = \Delta t \int_{\Gamma} \mathbf{N}_p^T \mathbf{n}^T [\tilde{\mathbf{U}}^n + \theta_1 (\Delta \tilde{\mathbf{U}}^* - \Delta t \nabla p^{n+\theta_2})] d\Gamma \end{aligned} \quad (3.57)$$

In the above \mathbf{f}_p contains boundary conditions as shown. We shall discuss these forcing terms fully in a later section as this form is vital to the success of the solution process. The weak form of the correction step from Eq. (3.26) is

$$\begin{aligned} \int_{\Omega} N_u^a \Delta U_i^{**} d\Omega &= \int_{\Omega} N_u^a \Delta U_i d\Omega - \int_{\Omega} N_u^a \Delta U_i^* d\Omega \\ &= -\Delta t \int_{\Omega} N_u^a \left(\frac{\partial p^n}{\partial x_i} + \theta_2 \frac{\partial \Delta p}{\partial x_i} \right) d\Omega \\ &\quad - \frac{\Delta t^2}{2} \int_{\Omega} \frac{\partial}{\partial x_j} (u_j N_u^a) \frac{\partial p^n}{\partial x_i} d\Omega \end{aligned} \quad (3.58)$$

The final stage of the computation of the mass flow vector U_i^{n+1} is completed by the following matrix form:

Step 3

$$\Delta \mathbf{U}^{**} = \Delta \tilde{\mathbf{U}} - \Delta \tilde{\mathbf{U}}^* = -\mathbf{M}_u^{-1} \Delta t \left[\mathbf{G}^T (\tilde{\mathbf{p}}^n + \theta_2 \Delta \tilde{\mathbf{p}}) + \frac{\Delta t}{2} \mathbf{P} \tilde{\mathbf{p}}^n \right] \quad (3.59)$$

where

$$\mathbf{P} = \int_{\Omega} (\nabla(\mathbf{u}\mathbf{N}_u))^T \nabla \mathbf{N}_p d\Omega \quad (3.60)$$

At the completion of this stage the values of $\tilde{\mathbf{U}}^{n+1}$ and $\tilde{\mathbf{p}}^{n+1}$ are fully determined but the computation of the energy $(\rho E)^{n+1}$ is needed for gas flow problems so that pressure and density can be related through temperature.

Once again the energy equation (3.7) is identical in form to that of the scalar problem of convection-diffusion if we observe that p , U_i , etc., are known. The weak form of the energy equation is written using the characteristic-Galerkin approximation of Eq. (2.105) as

$$\begin{aligned} & \int_{\Omega} N_E^k \Delta(\rho E)^{n+1} d\Omega \\ &= \Delta t \left[- \int_{\Omega} N_E^k \frac{\partial}{\partial x_i} (u_i(\rho E + p)) d\Omega - \int_{\Omega} \frac{\partial N_E^k}{\partial x_i} \left(\tau_{ij} u_j + k \frac{\partial T}{\partial x_i} \right) d\Omega \right]^n \\ &+ \frac{\Delta t^2}{2} \left[\int_{\Omega} \frac{\partial}{\partial x_j} (u_j N_E^k) \left[\frac{\partial}{\partial x_i} (-u_i(\rho E + p)) \right] d\Omega \right]^n \\ &+ \Delta t \left[\int_{\Gamma} N_E^k \left(\tau_{ij} u_j + k \frac{\partial T}{\partial x_i} \right) n_i d\Gamma \right]^n \end{aligned} \quad (3.61)$$

Step 4

With the additional approximations

$$\rho E = \mathbf{N}_E \tilde{\mathbf{E}} \quad \text{and} \quad T = \mathbf{N}_T \tilde{\mathbf{T}} \quad (3.62)$$

we have

$$\Delta \tilde{\mathbf{E}} = -\mathbf{M}_E^{-1} \Delta t \left[\mathbf{C}_E \tilde{\mathbf{E}} + \mathbf{C}_p \tilde{\mathbf{p}} + \mathbf{K}_T \tilde{\mathbf{T}} + \mathbf{K}_{\tau E} \tilde{\mathbf{u}} + \mathbf{f}_e - \Delta t (\mathbf{K}_{uE} \tilde{\mathbf{E}} + \mathbf{K}_{up} \tilde{\mathbf{p}} + \mathbf{f}_{es}) \right]^n \quad (3.63)$$

where $\tilde{\mathbf{E}}$ contains the nodal values of ρE and again the matrices and forcing vectors are similar to those previously obtained and given as

$$\begin{aligned} \mathbf{M}_E &= \int_{\Omega} \mathbf{N}_E^T \mathbf{N}_E d\Omega \quad \mathbf{C}_E = \int_{\Omega} \mathbf{N}_E^T \nabla^T (\mathbf{u} \mathbf{N}_E) d\Omega \quad \mathbf{C}_p = \int_{\Omega} \mathbf{N}_E^T \nabla^T (\mathbf{u} \mathbf{N}_p) d\Omega \\ \mathbf{K}_T &= \int_{\Omega} (\nabla \mathbf{N}_E)^T k \nabla \mathbf{N}_T d\Omega \quad \mathbf{K}_{\tau E} = \int_{\Omega} \mathbf{B}^T \mu \mathbf{u}_{av} (\mathbf{I}_0 - \frac{2}{3} \mathbf{m} \mathbf{m}^T) \mathbf{B} d\Omega \\ \mathbf{K}_{uE} &= -\frac{1}{2} \int_{\Omega} (\nabla^T (\mathbf{u} \mathbf{N}_E))^T (\nabla \mathbf{N}_E) d\Omega \quad \mathbf{f}_e = \int_{\Gamma} \mathbf{N}_E^T \mathbf{n}^T (\mathbf{t}^d \mathbf{u} + k \nabla T) d\Gamma \\ \mathbf{K}_{up} &= -\frac{1}{2} \int_{\Omega} (\nabla^T (\mathbf{u} \mathbf{N}_E))^T (\nabla \mathbf{N}_p) d\Omega \end{aligned} \quad (3.64)$$

The forcing term \mathbf{f}_{es} contains source terms. For a three dimensional flow problem

$$\tau = \begin{bmatrix} \tau_{11} & \tau_{12} & \tau_{13} \\ \tau_{21} & \tau_{22} & \tau_{23} \\ \tau_{31} & \tau_{32} & \tau_{33} \end{bmatrix}, \text{ if no source terms are available this term is equal to zero.}$$

It is of interest to observe that the process of Step 4 can be extended to include in an identical manner the equations describing the transport of quantities such as turbulence parameters [43], chemical concentrations, etc., once the essential Steps 1–3 have been completed.

For isothermal compressible flows the first three steps of the CBS scheme are sufficient. However, for incompressible flows all four steps are required and the pressure should be related to density and temperature (energy) via a gas law (for example, the ideal gas law presented in this chapter).

Split B

With Split B, the discretization and solution procedures have to be modified slightly. Leaving the details of the derivation to the reader and using identical discretization processes, the final steps can be summarized as follows:

Step 1

$$\Delta \tilde{\mathbf{U}}_i^* = -\mathbf{M}_u^{-1} \Delta t \left[(\mathbf{C}_u \tilde{\mathbf{U}} + \mathbf{K}_\tau \tilde{\mathbf{u}} + \mathbf{G}^T \tilde{\mathbf{p}} - \mathbf{f}) - \Delta t \left(\mathbf{K}_u \tilde{\mathbf{U}} + \mathbf{f}_s + \frac{\Delta t}{2} \mathbf{P} \tilde{\mathbf{p}} \right) \right]^n \quad (3.65)$$

where all matrices are the same as in Split A except the forcing term \mathbf{f} which is

$$\mathbf{f} = \int_{\Omega} \mathbf{N}_u^T \rho \mathbf{g} d\Omega + \int_{\Gamma} \mathbf{N}_u^T \bar{\mathbf{t}} d\Gamma \quad (3.66)$$

since the pressure term has now been integrated by parts.

Step 2

$$(\mathbf{M}_p + \Delta t^2 \theta_1 \theta_2 \mathbf{H}) \Delta \tilde{\mathbf{p}} = \Delta t [\mathbf{G} \tilde{\mathbf{U}}^n + \theta_1 \mathbf{G} \Delta \tilde{\mathbf{U}}^* - \mathbf{f}_p]^n \quad (3.67)$$

and

Step 3

$$\Delta \tilde{\mathbf{U}}^{**} = -\mathbf{M}_u^{-1} \Delta t [\theta_2 \mathbf{G}^T \Delta \tilde{\mathbf{p}}] \quad (3.68)$$

Step 4, calculation of the energy, is unchanged. The reader can notice the differences in the above equations from those of Split A.

3.3.4 Mass diagonalization (lumping)

In Steps 1 to 3 of the split algorithm the solution often only requires the inversion (or solution) of mass matrices \mathbf{M}_u and \mathbf{M}_p . Such steps are called explicit and generally are accomplished using approximation by a diagonal (lumped) form. Procedures for such diagonalization are described in Ref. [1]. Here we quote one which is generally efficient. In this the matrix form \mathbf{M}_u is replaced by \mathbf{M}^L computed as

$$M_{ab}^L = \delta_{ab} \int_{\Omega} N_a d\Omega \quad \text{no sum}$$

which the reader will recognize as the *row sum* of the full (consistent) mass matrix.

Such lumping for steady-state problems makes Steps 1 to 3 trivial and the errors involved are of no consequence as terms involving time variation disappear at a converged (steady-state) solution. However, for transient problems, quite serious errors can occur and in such cases an additional iteration is used to obtain a consistent solution. This already was discussed for the scalar equation in [Section 2.6.3](#) [viz. [Eq. \(2.118\)](#)].

3.4 Explicit, semi-implicit, and nearly implicit forms

The split algorithm A or B will contain an explicit portion in the first characteristic-Galerkin step. However the second step, i.e., that of the determination of the pressure increment, can be made either explicit or implicit depending on the choice of θ_2 and speed of sound. Now different stability criteria will apply (θ_1 will always be taken to satisfy $1/2 \leq \theta_1 \leq 1$ and, thus, stability does not depend on it). We refer to schemes as being fully explicit or semi-implicit depending on the choice of the parameter θ_2 as zero or nonzero, respectively. It is necessary at this point to mention that the fully explicit form is possible only for compressible flows for which $c \neq \infty$; however, later we will show that this restriction may be removed by introducing an “artificial compressibility.”

It is also possible to solve the first step in a partially implicit manner to avoid severe time step restrictions. Now the viscous term is the one for which an implicit solution is sought. We refer to such schemes as quasi- (nearly) implicit schemes.

3.4.1 Fully explicit form

In fully explicit forms, $\frac{1}{2} \leq \theta_1 \leq 1$ and $\theta_2 = 0$. In general the time step limitations explained for the convection-diffusion equations are applicable, i.e.,

$$\Delta t \leq \frac{h}{c + |\mathbf{u}|} \quad (3.69)$$

if the viscosity effects are negligible. In the above equation h is the element size, assuming linear elements only and one-dimensional behavior. For two- and three-dimensional flow problems determination of the element size is difficult. We shall discuss some possibilities in [Section 3.4.4](#).

This particular form is very successful in compressible flow computations and has been widely used by the authors for solving many complex problems (see [Chapter 7](#)). More recently the algorithm has also been successfully used in conjunction with artificial compressibility to solve many other flow situations, including those in which incompressibility is involved (see [Chapter 4](#)).

3.4.2 Semi-implicit form

In semi-implicit form the following values apply:

$$\frac{1}{2} \leq \theta_1 \leq 1 \quad \text{and} \quad \frac{1}{2} \leq \theta_2 \leq 1 \quad (3.70)$$

Again the CBS algorithm is conditionally stable. The permissible time step is governed by the critical step of the characteristic-Galerkin explicit relation solved in Step 1 of the algorithm. This is the standard convection-diffusion problem discussed in [Chapter 2](#) and the same stability limits apply, i.e.,

$$\Delta t \leq \Delta t_u = \frac{h}{|\mathbf{u}|} \quad (3.71a)$$

and/or

$$\Delta t \leq \Delta t_v = \frac{h^2}{2\nu} \quad (3.71b)$$

where ν is the kinematic viscosity. A convenient form incorporating both limits can be written as

$$\Delta t = \min(\Delta t_u, \Delta t_v) \quad (3.72)$$

The reader can verify that the above relation will give appropriate time step limits with and without the domination of viscosity.

For slightly compressible or incompressible problems in which \mathbf{M}_p is small or zero, the semi-implicit form is efficient and it should be noted that the matrix \mathbf{H} of [Eqs. \(3.56\)](#) and [\(3.67\)](#) does not vary during the computation process. Therefore \mathbf{H} can be factored into its triangular parts once leading to an economical direct procedure.

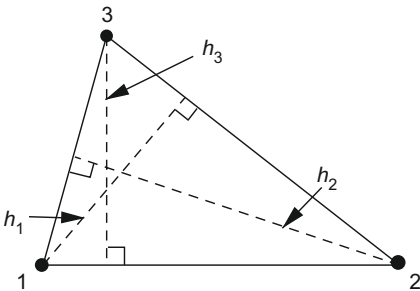
The implicit equation is usually solved either by direct solvers or by iterative (conjugate gradient) methods.

3.4.3 Quasi- (nearly) implicit form

To overcome the severe time step restriction made by the diffusion terms (e.g., viscosity or thermal conductivity), these terms can be treated implicitly. This involves solving separately an implicit form connecting the viscous terms with ΔU_i^* . Here, at each step, simultaneous equations need to be solved and this procedure can be of great advantage in certain cases such as high-viscosity flows and low Mach number flows [[16, 18, 26, 48](#)]. Now the only time step limitation is $\Delta t \leq h/|\mathbf{u}|$ which appears to be a very reasonable and physically meaningful restriction.

3.4.4 Evaluation of time step limits: Local and global time steps

Though they are defined in terms of element sizes the time step values are established. In [Fig. 3.1](#) the manner in which the size of the element is easily established at nodes is shown. In such cases, as seen, the element size is not unique for each node. In the calculation, we shall specify, if the scheme is conditionally stable, the time step limit at each node by assigning the minimum value for such nodes calculated from all elements connected to that node. When a problem is being solved in true time then obviously the smallest time step of all nodal values has to be adopted for the solution. However, in many problems it is possible to use *local time stepping* if steady-state solution is the only interest. In such problems local “nodal” time step values are conveniently used.

**FIGURE 3.1**

Element sizes at different nodes of a linear triangle.

This of course is equivalent to assuming identical time steps for the whole problem and simply adjusting the lumped masses. Such a problem with adjusted lumped masses is still physically and mathematically meaningful and we know that the convergence will be achieved as it invariably is. If only convective problems are considered, the time step needs only the element size in the direction of the streamline. This may very well be different from the minimum h . The procedure has been shown to be efficient by Thomas and Nithiarasu [94]. This is particularly important if the elements are elongated as we shall later mention in the case of supersonic flows with shocks.

Many steady-state problems have used such localized time stepping in the calculations.

In the context of local and global time stepping it is interesting to note that the stabilizing terms introduced by the characteristic-Galerkin process will not take on the optimal value for any element in which the time step differs from the critical one; that is of course if we use local time stepping we shall automatically achieve this optimal value often throughout all elements at least for steady-state problems. However, on other occasions it may be useful to make sure that (a) in all elements we introduce optimal damping and (b) that the progressive time step for all elements is identical. The latter of course is absolutely necessary if for instance we deal with transient problems where all time steps are real. For such cases it is possible to consider the Δt as being introduced in two stages: (1) as the Δt_{ext} which has of course to preserve stability and must be left at a minimum Δt calculated from any element; and (2) to use in the calculation of each individual element the Δt_{int} which is optimal for an element, as of course exceeding the stability limit does not matter there and we are simply adding better damping characteristics. Here the Δt_{int} is the only one occurring in convection stabilizing terms.

This internal-external subdivision is of some importance when incompressibility effects are considered. As shown in the next section, the stabilizing diagonal term occurs in steady-state problems depending on the size of the time step. If the mesh is graded and very small elements dictate the time step over the whole domain, we might find that the diagonal term introduced overall is not sufficient to preserve

incompressibility. For such problems we recommend the use of internal and external time steps which differ and we introduced these in Ref. [53]. In this case the internal time step Δt_{int} is the one multiplying the second-order pressure terms at Step 2.

3.5 Artificial compressibility and dual time stepping

3.5.1 Artificial compressibility for steady-state problems

When the real compressibility is small, it is often assumed that the fluid is incompressible with the speed of sound approaching infinity. Even if the speed of sound is finite, its value will have to be large and hence a very severe time step limitation arises. However, an artificial compressibility method can be employed to eliminate the restrictions posed by the speed of sound at Step 2 by taking an artificial value for the speed of sound which is sufficiently low. This of course only possible if steady-state conditions exist and therefore in that limit the transient term disappears. Step 2 of the CBS scheme may be rewritten in its semi-discrete form as [57]

$$\begin{aligned}\Delta\rho &= \left(\frac{1}{c^2}\right)^n \Delta p \approx \left(\frac{1}{\beta^2}\right)^n \Delta p \\ &= -\Delta t \left[\frac{\partial U_i^n}{\partial x_i} + \theta_1 \frac{\partial \Delta U_i^\star}{\partial x_i} - \Delta t \theta_1 \left(\frac{\partial^2 p^n}{\partial x_i \partial x_i} + \theta_2 \frac{\partial^2 \Delta p}{\partial x_i \partial x_i} \right) \right] \quad (3.73)\end{aligned}$$

where β is an artificial parameter with the dimensions of velocity. This parameter may be either given as a constant throughout the domain or determined based on the convective or diffusive time step restrictions. We recommend the latter option, as this results in manageable local and global time step sizes. The β value may be locally computed using the following relation so that the convective and viscous time steps are represented:

$$\beta = \max(\varepsilon, u_{\text{conv}}, u_{\text{diff}}) \quad (3.74)$$

where ε is a small constant and it makes sure that the β is not approaching zero under any circumstances. u_{conv} and u_{diff} are respectively the convection and diffusion velocities given as

$$\begin{aligned}u_{\text{conv}} &= |\mathbf{u}| = \sqrt{u_i u_i} \\ u_{\text{diff}} &= \frac{\nu}{h} \quad (3.75)\end{aligned}$$

where h is the element size and ν is the kinematic viscosity.

The three steps of the CBS scheme follow exactly the procedure discussed in the preceding sections. However, the difference here is that no coupling exists between the energy and the rest of the governing equations. Note that the time step limitation for the artificial compressibility method may be written as

$$\Delta t = \frac{h}{|\mathbf{u}| + \beta} \quad (3.76)$$

The above relation includes the viscous effect via the artificial parameter. The artificial compressibility method explained here is valid for steady flows. However, an appropriate dual time-stepping method, explained in the following subsection, should be employed to recover a true transient solution.

3.5.2 Artificial compressibility in transient problems (dual time stepping)

A transient formulation for the artificial compressibility method is easy to derive within the CBS framework. Unlike standard artificial compressibility methods, the present formulation is stable for both convection and pressure effects [57,58]. The main difference between the CBS formulation presented before and the artificial compressibility formulation is that the time step Δt here is treated as a pseudo iterative time step to reach an instantaneous steady state within a real time step $\Delta\tau$. This requires addition of a real time term to the semi-discrete form of the momentum equation, i.e., [from Eq. (3.21)],

$$\begin{aligned} U_i^{n+1} - U_i^n = & \Delta t \left[-\frac{\partial}{\partial x_j} (u_j U_i)^n + \frac{\partial \tau_{ij}^n}{\partial x_j} + (\rho g_i)^n - \frac{\Delta U_i^m}{\Delta \tau} \right] - \Delta t \frac{\partial p^{n+\theta_2}}{\partial x_i} \\ & + \frac{\Delta t^2}{2} u_k \frac{\partial}{\partial x_k} \left[\frac{\partial}{\partial x_j} (u_j U_i) - \frac{\partial \tau_{ij}^n}{\partial x_j} - \rho g_i + \frac{\Delta U_i^m}{\Delta \tau} \right]^n \\ & + \frac{\Delta t^2}{2} u_k \frac{\partial}{\partial x_k} \left(\frac{\partial p^{n+\theta_2}}{\partial x_i} \right) \end{aligned} \quad (3.77)$$

where ΔU_i^m is the real time variation of the variable U_i . This term may be approximated depending on the transient accuracy requirement. The second-order accuracy may be obtained by approximating

$$\Delta U_i^m = \frac{3U_i^n - 4U_i^m + U_i^{m-1}}{2} \quad (3.78)$$

Here superscript m refers to the real time variation. It is easy to understand from Eq. (3.77) that at pseudo-steady state $U_i^{n+1} = U_i^n$ and this leads to the recovery of the semi-discrete form of the momentum equation in real time. Incorporating the above changes into the CBS formulation, the three semi-discrete steps of the CBS scheme may be written for Split A as

$$\begin{aligned} \Delta U_i^* = & \Delta t \left[-\frac{\partial}{\partial x_j} (u_j U_i) + \frac{\partial \tau_{ij}}{\partial x_j} + \rho g_i \right. \\ & \left. + \frac{\Delta t}{2} u_k \frac{\partial}{\partial x_k} \left(\frac{\partial}{\partial x_j} (u_j U_i) - \frac{\partial \tau_{ij}}{\partial x_j} - \rho g_i \right) \right]^n \end{aligned} \quad (3.79)$$

is the first step. We note that this equation is solved by an explicit time step. As before, the “correction” given below is available once the pressure increment is evaluated

(Step 3):

$$\begin{aligned}\Delta U_i^{**} = \Delta U_i - \Delta U_i^* &= -\Delta t \frac{\partial p^{n+\theta_2}}{\partial x_i} - \frac{\Delta U_i^m}{\Delta \tau} + \frac{\Delta t^2}{2} u_k \frac{\partial^2 p^n}{\partial x_k \partial x_i} \\ &+ \frac{\Delta t^2}{2} u_k \frac{\partial}{\partial x_k} \left(\frac{\Delta U_i^m}{\Delta \tau} \right)\end{aligned}\quad (3.80)$$

The modified form of Eq. (3.1) is now written as

$$\Delta \rho = \frac{1}{\beta^2} \Delta p = -\Delta t \frac{\partial U_i^{n+\theta_1}}{\partial x_i} = -\Delta t \left[\frac{\partial U_i^n}{\partial x_i} + \theta_1 \frac{\partial \Delta U_i}{\partial x_i} \right] \quad (3.81)$$

Replacing ΔU_i with $\Delta U_i^* + \Delta U_i^{**}$ and rearranging after neglecting third- and higher-order terms we obtain (final form of Step 2)

$$\begin{aligned}\frac{1}{\beta^2} \Delta p &= -\Delta t \left[\frac{\partial U_i^n}{\partial x_i} + \theta_1 \frac{\partial \Delta U_i^*}{\partial x_i} - \Delta t \theta_1 \left(\frac{\partial^2 p^n}{\partial x_i \partial x_i} + \theta_2 \frac{\partial^2 \Delta p}{\partial x_i \partial x_i} \right) \right. \\ &\quad \left. - \theta_1 \frac{\partial}{\partial x_i} \left(\frac{\Delta U_i^m}{\Delta \tau} \right) \right]\end{aligned}\quad (3.82)$$

The method described above brings together all three steps several times within a real time step $\Delta \tau$. This strongly couples the three steps within every real time step $\Delta \tau$ and produces a one-step monolithic type approximation. As a result, the splitting errors faced by standard fractional step methods do not apply here. To demonstrate this, all three steps should be considered at a pseudo steady state, i.e., when $\Delta U_i = 0$. Combining Steps 1 [Eq. (3.79)] and 3 [Eq. (3.80)] gives

$$\begin{aligned}- \left[\frac{\Delta U_i^m}{\Delta \tau} + \frac{\partial}{\partial x_j} (u_j U_i) + \frac{\partial p}{\partial x_i} - \frac{\partial \tau_{ij}}{\partial x_j} - (\rho g_i) \right]^n \\ + \frac{\Delta t}{2} u_k \frac{\partial}{\partial x_k} \left[\frac{\partial}{\partial x_j} (u_j U_i) - \frac{\partial \tau_{ij}}{\partial x_j} - \rho g_i + \frac{\Delta U_i^m}{\Delta \tau} + \frac{\partial p}{\partial x_i} \right]^n = 0\end{aligned}\quad (3.83)$$

Substituting Step 1 [Eq. (3.79)] into Step 2 [Eq. (3.82)], neglecting third- and higher-order terms, and rearranging (assuming $\theta_1 = 0.5$, $\theta_2 = 0$ and pseudo steady state with $\Delta p = 0$)

$$\frac{\partial U_i^n}{\partial x_i} + \frac{\Delta t}{2} \frac{\partial}{\partial x_i} \left[\frac{\partial (u_j U_i)}{\partial x_j} - \frac{\partial \tau_{ij}}{\partial x_j} - \rho g + \frac{\partial p}{\partial x_i} + \frac{\Delta U_i^m}{\Delta \tau} \right]^n = 0 \quad (3.84)$$

Equations (3.83) and (3.84) clearly show that the equations are consistent. As shown the conservation of momentum and conservation of mass equations for incompressible flows in their semi-discrete form are recovered along with the convection and pressure stabilization terms. It is also obvious from these equations that the stabilization terms are functions of the residual and the stabilization coefficient is proportional to pseudo time step Δt . Since $n = m + 1$ at instantaneous steady state, this scheme is equivalent to a stabilized implicit monolithic method [87].

3.6 “Circumvention” of the Babuška-Brezzi (BB) restrictions

In the previous sections we have not restricted the nature of the interpolation functions for shape functions \mathbf{N}_u and \mathbf{N}_p . If we choose these interpolations in a manner satisfying the mixed patch test conditions [1, 95, 96] or the Babuška-Brezzi (BB) restriction for incompressibility [2, 3] (also see Chapter 4 for some permissible interpolations) then of course completely incompressible problems can be dealt with without any special difficulties by both Split A and Split B formulations. However Split A introduces an important bonus which permits us to avoid any restrictions on the nature of the two shape functions used for velocity and pressure. Let us examine here the structure of the equations obtained in steady-state conditions. For simplicity we shall consider here only the Stokes form of the governing equations in which the convective terms disappear. Further we shall take the fluid as incompressible (e.g., $c = \infty$) and thus uncoupled from the energy equations. Now the three steps of Split A given in Eqs. (3.51), (3.56), and (3.59) are written as

$$\begin{aligned}\Delta\tilde{\mathbf{U}}^* &= -\Delta t \mathbf{M}_u^{-1} [\mathbf{K}_\tau \tilde{\mathbf{u}}^n - \mathbf{f}] \\ \Delta\tilde{\mathbf{p}} &= \frac{1}{\Delta t \theta_1 \theta_2} \mathbf{H}^{-1} [\mathbf{G}\tilde{\mathbf{U}}^n + \theta_1 \mathbf{G}\Delta\tilde{\mathbf{U}}^* - \Delta t \theta_1 \mathbf{H}\tilde{\mathbf{p}}^n - \mathbf{f}_p] \\ \Delta\tilde{\mathbf{U}}^{**} &= \Delta\tilde{\mathbf{U}} - \Delta\tilde{\mathbf{U}}^* = -\Delta t \mathbf{M}_u^{-1} \mathbf{G}^T (\tilde{\mathbf{p}}^n + \theta_2 \Delta\tilde{\mathbf{p}})\end{aligned}\quad (3.85)$$

At steady state we have $\Delta\tilde{\mathbf{p}} = \Delta\tilde{\mathbf{U}} = \mathbf{0}$ and eliminating $\Delta\tilde{\mathbf{U}}^*$ and $\Delta\tilde{\mathbf{U}}^{**}$ we can write (dropping now the superscript n) from the first and third of Eqs. (3.85)

$$\mathbf{K}_\tau \tilde{\mathbf{u}} + \mathbf{G}^T \tilde{\mathbf{p}} = \mathbf{f} \quad (3.86)$$

and

$$\mathbf{G}\tilde{\mathbf{U}} + \theta_1 \Delta t \mathbf{G}\mathbf{M}_u^{-1} \mathbf{G}^T \tilde{\mathbf{p}} - \Delta t \theta_1 \mathbf{H}\tilde{\mathbf{p}} - \mathbf{f}_p = 0 \quad (3.87)$$

from the second and third of Eqs. (3.85)

We finally have a system which can be written in the form

$$\begin{bmatrix} \mathbf{K}_\tau/\rho & \mathbf{G}^T \\ \mathbf{G} & \Delta t \theta_1 [\mathbf{G}\mathbf{M}_u^{-1} \mathbf{G}^T - \mathbf{H}] \end{bmatrix} \begin{Bmatrix} \tilde{\mathbf{U}} \\ \tilde{\mathbf{p}} \end{Bmatrix} = \begin{Bmatrix} \mathbf{f}_1 \\ \mathbf{f}_2 \end{Bmatrix} \quad (3.88)$$

Here \mathbf{f}_1 and \mathbf{f}_2 arise from the forcing terms.

The system is now always positive definite [41] and therefore leads to a non-singular solution for *any interpolation functions* \mathbf{N}_u , \mathbf{N}_p chosen. In most of the examples discussed in this book and elsewhere equal interpolation is used for both the U_i and p variables, i.e., $\mathbf{N}_u = \mathbf{N}_p$. We must however stress that any other interpolation can be used without violating the stability. This is an important reason for the preferred use of the Split A form.

If the pressure gradient term is retained as in Eq. (3.29), (i.e., if we use Split B) the lower diagonal term of Eq. (3.88) is identically zero and the BB conditions in the

full scheme cannot be avoided. To show this we start from Eqs. (3.65), (3.67), and (3.68). For incompressible Stokes flow we have

$$\begin{aligned}\Delta\tilde{\mathbf{U}}_i^* &= -\mathbf{M}_u^{-1}\Delta t [\mathbf{K}_\tau \tilde{\mathbf{u}} + \mathbf{G}^T \tilde{\mathbf{p}} - \mathbf{f}]^n \\ \Delta\tilde{\mathbf{p}} &= \frac{1}{\Delta t \theta_1 \theta_2} \mathbf{H}^{-1} \Delta t [\mathbf{G}\tilde{\mathbf{U}}^n + \theta_1 \mathbf{G}\Delta\tilde{\mathbf{U}}^* - \mathbf{f}_p] \\ \Delta\tilde{\mathbf{U}}^{**} &= -\mathbf{M}_u^{-1}\Delta t [\theta_2 \mathbf{G}^T \Delta\tilde{\mathbf{p}}]\end{aligned}\quad (3.89)$$

At steady state $\Delta\tilde{\mathbf{p}} = \Delta\tilde{\mathbf{U}} = \mathbf{0}$, which gives the following two equations:

$$\mathbf{K}_\tau \tilde{\mathbf{u}} + \mathbf{G}^T \tilde{\mathbf{p}} = \mathbf{f} \quad (3.90)$$

and

$$\mathbf{G}\tilde{\mathbf{U}} = \mathbf{f}_p \quad (3.91)$$

Note that $\Delta\mathbf{U}_i^{**}$ is zero from the third of Eq. (3.89). As in Split A we can write the following system:

$$\begin{bmatrix} \mathbf{K}_\tau/\rho & \mathbf{G}^T \\ \mathbf{G} & \mathbf{0} \end{bmatrix} \begin{Bmatrix} \tilde{\mathbf{U}} \\ \tilde{\mathbf{p}} \end{Bmatrix} = \begin{Bmatrix} \mathbf{f}_1 \\ \mathbf{f}_2 \end{Bmatrix} \quad (3.92)$$

where \mathbf{f}_1 and \mathbf{f}_2 arise from the forcing terms as in the Split A form. Clearly here the BB restrictions are not circumvented.

It is interesting to observe that the lower diagonal term which appeared in Eq. (3.88) is equivalent to the difference between the so-called fourth-order and second-order finite difference approximations of the Laplacian. This justifies the use of similar terms introduced into the computation by Jameson and Mavriplis [97].

3.7 A single-step version

If the $\Delta\mathbf{U}_i^*$ term in Eq. (3.28) is omitted, the intermediate variable \mathbf{U}_i^* need not be determined. Instead we can directly calculate ρ (or p), \mathbf{U}_i , and $\rho\mathbf{E}$. This of course introduces an additional approximation.

The approximation of Eq. (3.1) is not necessary in any expected fully explicit scheme as the density increment is directly obtained if we note that

$$\mathbf{M}_p \Delta\tilde{\mathbf{p}} = \mathbf{M}_u \Delta\tilde{\mathbf{p}} \quad (3.93)$$

With the above simplifications Split A becomes

$$\Delta\tilde{\Phi} = -\mathbf{M}_u^{-1} \Delta t \left[\int_\Omega \mathbf{N}^T \left(\frac{\partial \mathbf{F}_i}{\partial x_i} + \frac{\partial \mathbf{G}_i}{\partial x_i} \right) d\Omega - \frac{1}{2} \Delta t \int_\Omega \mathbf{N}^T \mathbf{D} d\Omega \right]^n \quad (3.94)$$

omitting the source terms for clarity [\mathbf{F}_i and \mathbf{G}_i are explained in Chapter 1, Eqs. (1.26b) and (1.26c)] and noting that now $\tilde{\Phi}$ denotes all the variables. The added stabilizing

terms \mathbf{D} are defined below and have to be integrated by parts in the usual manner:

$$\left\{ \begin{array}{l} 2\theta_1 \frac{\partial p^2}{\partial x_i \partial x_i} \\ u_i \frac{\partial}{\partial x_i} \left[\frac{\partial}{\partial x_j} (u_j \rho u_1) + \frac{\partial p}{\partial x_1} \right] \\ u_i \frac{\partial}{\partial x_i} \left[\frac{\partial}{\partial x_j} (u_j \rho u_2) + \frac{\partial p}{\partial x_2} \right] \\ u_i \frac{\partial}{\partial x_i} \left[\frac{\partial}{\partial x_j} (u_j \rho u_3) + \frac{\partial p}{\partial x_3} \right] \\ u_i \frac{\partial}{\partial x_i} \left[\frac{\partial}{\partial x_j} (u_j \rho E + u_j p) \right] \end{array} \right\} \quad (3.95)$$

The added “diffusions” are simple and are streamline oriented, and thus do not mask the true effects of viscosity as it happens in some schemes (e.g., the Taylor-Galerkin process).

If only steady-state results are sought it would appear that Δt multiplying the matrix \mathbf{D} should be set at its optimal value of $\Delta t_{\text{crit}} \approx h/|\mathbf{u}|$ and we generally recommend, providing the viscosity is small, this value for the full scheme [37].

However the oversimplified scheme of Eq. (3.94) can lose some accuracy and even when steady state is reached it will give slightly different results than those obtained using the full sequential updating [37]. However at low Mach numbers the difference is negligible as we shall show later in Section 3.10. The small additional cost involved in computing the two-step sequence $\Delta \tilde{\mathbf{U}}^* \rightarrow \Delta \mathbf{p} \rightarrow \Delta \tilde{\mathbf{U}} \rightarrow \Delta \tilde{\mathbf{E}}$ will have to be balanced against the accuracy increase. In general, we have found that the two-step version is preferable.

However it is interesting to consider once again the performance of the single-step scheme in the case of Stokes equations as we did for the other schemes in the previous section. After discretization we have, omitting convective terms, only one additional diffusion term which arises [Eq. (3.82)] in the mass conservation equation. After discretization, in steady state

$$\begin{bmatrix} \mathbf{K}_\tau / \rho & \mathbf{G}^T \\ \mathbf{G} & \theta_1 \Delta t \mathbf{H} \end{bmatrix} \begin{Bmatrix} \tilde{\mathbf{U}} \\ \tilde{\mathbf{p}} \end{Bmatrix} = \begin{Bmatrix} \mathbf{f}_1 \\ \mathbf{f}_2 \end{Bmatrix} \quad (3.96)$$

Clearly the single-step algorithm retains the capacity of dealing with full incompressibility without stability problems but of course can only be used for the nearly incompressible range of problems for which \mathbf{M}_p exists. We should remark here that this formulation now achieves precisely the same stabilization as that suggested by Brezzi and Pitkäranta [98], see Chapter 10 in Ref. [1].

We shall note the performance of single- and two-step algorithms in Section 3.10 of this chapter.

3.8 Splitting error

As shown previously the CBS algorithm with Split A provides conditional pressure stability and thus spurious pressure modes can be reduced. However, due to the three-step procedure introduced within the CBS procedure it is prone to a “so-called” splitting error. One such error is the first-order error temporal in pressure. This is a widely discussed topic in the literature with application to the quasi-implicit form of the CBS or similar splitting methods (often referred to as the semi-implicit fractional step method) [93, 99–102]. This is mainly a topic in incompressible flows. In order to explain the splitting error, we need to first consider the pressure Poisson equation of Step 2. When using the quasi-implicit form of the algorithm, the pressure Poisson equation is reduced to [substitute $\Delta\rho = 0$, $\theta_1 = \theta_2 = 1$ into Eq. (3.28)]

$$\frac{\partial^2 p^{n+1}}{\partial x_i^2} = \frac{\rho}{\Delta t} \left(\frac{\partial u_i^*}{\partial x_i} \right) \quad (3.97)$$

However, if the momentum equation for incompressible flow is differentiated with respect to x_i (divergence) and the incompressibility constrain is applied, we obtain

$$\frac{\partial^2 p}{\partial x_i^2} = -\rho \frac{\partial}{\partial x_i} \left(\frac{\partial(u_i u_j)}{\partial x_j} \right) \quad (3.98)$$

Since the discrete form of Eq. (3.97) and continuous form of Eq. (3.98) are equal only to first order in time, a first-order pressure error is introduced into the three-step split procedure. This error can be demonstrated by substituting the intermediate velocity field of the quasi-implicit form (without source)

$$\begin{aligned} \rho \Delta u_i^* &= \Delta t \left[-\rho \frac{\partial}{\partial x_j} (u_j u_i) + \mu \frac{\partial^2 u_i^*}{\partial x_j \partial x_j} \right. \\ &\quad \left. + \frac{\delta t}{2} u_k \frac{\partial}{\partial x_k} \left(\rho \frac{\partial}{\partial x_j} (u_j u_i) - \mu \frac{\partial^2 u}{\partial x_j \partial x_i} \right)^n \right] \end{aligned} \quad (3.99)$$

into Eq. (3.97). Substituting $u^* = (u + \Delta t \partial p / \partial x_i)^{n+1}$ into the RHS of Eq. (3.99) (neglecting the stabilization terms for simplicity) gives

$$\rho u_i^* = \rho u_i^n - \Delta t \left[\rho \frac{\partial(u_i u_j)^n}{\partial x_j} - \mu \frac{\partial^2}{\partial x_j \partial x_j} \left(u + \Delta t \frac{\partial p}{\partial x_i} \right)^{n+1} \right] \quad (3.100)$$

Substituting Eq. (3.100) into Eq. (3.97) and applying conservation of mass and simplifying (note that $u^{n+1} = u^n + \Delta t \frac{\partial u^n}{\partial t}$), we obtain

$$\begin{aligned} \frac{\partial^2 p^{n+1}}{\partial x_i^2} &= -\frac{\partial}{\partial x_i} \left[\rho \frac{\partial(u_i u_j)^n}{\partial x_j} \right] + \Delta t \mu \frac{\partial}{\partial x_i} \left[\frac{\partial^2}{\partial x_j \partial x_j} \left(\frac{\partial u}{\partial t} \right)^n \right] \\ &\quad + \Delta t \mu \frac{\partial}{\partial x_i} \left[\frac{\partial^2}{\partial x_j \partial x_j} \left(\frac{\partial p}{\partial x_i} \right)^{n+1} \right] \end{aligned} \quad (3.101)$$

Comparison of Eqs. (3.101) and (3.98) clearly shows that the discrete form of Eq. (3.97) leads to first-order error terms in time. Note that the second term on the RHS of the above equation is equal to zero for incompressible flows.

3.8.1 Elimination of first-order pressure error

One of the early methods proposed [99] to remove the first-order pressure error was to first calculate the approximate pressure p_{old} from Eq. (3.97) and then use the correction

$$p_{new} = p_{old} - \mu \Delta t \frac{\partial^2 p_{old}}{\partial x_i^2} \quad (3.102)$$

This correction eliminates the last term in Eq. (3.101).

At low Reynolds numbers and for Stokes flow, adding dual time stepping to the CBS scheme is an alternative way of reducing the first-order pressure error. Adding dual time stepping as explained in Section 3.5.2 replaces the first-order pressure error with the following form at the instantaneous steady state ($\Delta u / \Delta t \approx 0$):

$$\begin{aligned} \frac{\partial^2 p^{n+1}}{\partial x_i^2} &= -\frac{1}{\Delta t} \frac{\partial}{\partial x_i} \left[\rho \Delta t \frac{\partial(u_i u_j)^n}{\partial x_j} \right] \\ &\quad + \Delta t \mu \frac{\partial}{\partial x_i} \left[\frac{\partial^2}{\partial x_j \partial x_j} \left(\frac{\partial p}{\partial x_i} + \frac{\Delta u^m}{\Delta \tau} \right)^{n+1} \right] \end{aligned} \quad (3.103)$$

Substituting for $\Delta u^m / \Delta \tau$ at instantaneous steady state from Section 3.5.2, we get

$$\begin{aligned} \frac{\partial^2 p^{n+1}}{\partial x_i^2} &= -\frac{1}{\Delta t} \frac{\partial}{\partial x_i} \left[\rho \Delta t \frac{\partial(u_i u_j)^n}{\partial x_j} \right] \\ &\quad + \Delta t \mu \frac{\partial}{\partial x_i} \left[\frac{\partial^2}{\partial x_j \partial x_j} \left(-\rho \frac{\partial u_i u_j}{\partial x_j} + \mu \frac{\partial^2 u_i}{\partial x_j \partial x_j} \right)^{m+1} \right] \end{aligned} \quad (3.104)$$

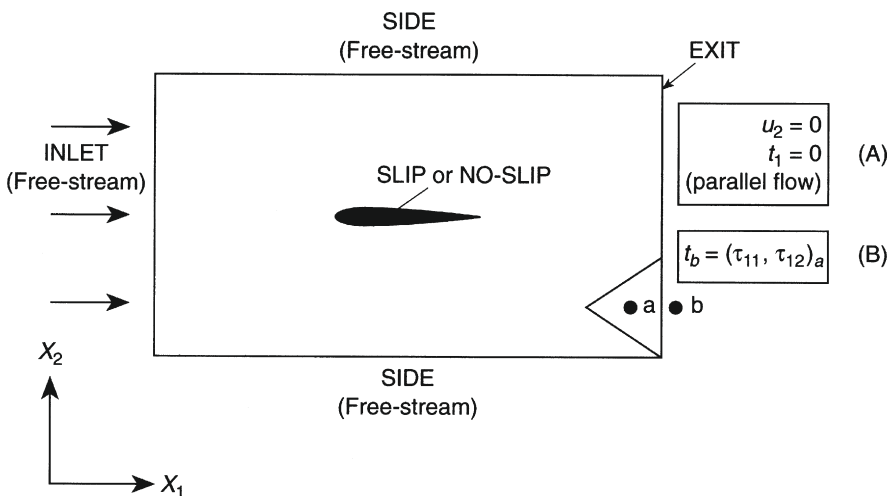
The error now is a function of Δt , the pseudo time step, not the real time step $\Delta \tau$.

3.9 Boundary conditions

3.9.1 Fictitious boundaries

In a large number of fluid mechanics problems the flow in open domains is considered. A typical open domain describing flow past an aircraft wing is shown in Fig. 3.2. In such problems the boundaries are simply limits of computation and they are therefore fictitious. With suitable values specified at such boundaries, however, accurate solution for the flow inside the isolated domain can be achieved.

Generally as the distance from the object grows, the boundary values tend to those encountered in the free domain flow or the flow at infinity. This is particularly true at

**FIGURE 3.2**

Fictitious and real boundaries.

the entry and side boundaries shown in Fig. 3.2. At the exit, however, the conditions are different and here the effect of the introduced disturbance can continue for a very large distance denoting the wake of the problem. We shall from time to time discuss problems of this nature but now we shall simply make the following remarks.

1. If the flow is subsonic the specification of all quantities except the density (or pressure) can be made on both the side and entry boundaries.
2. Whereas for supersonic flows all the variables can be prescribed at the inlet or side boundaries, at the exit boundary however no conditions can be imposed simply because by definition no disturbance in a supersonic stream can travel upstream.

With subsonic exit conditions the situation is somewhat more complex and here various possibilities exist. We again illustrate such conditions in Fig. 3.2.

Condition A: Denoting the most obvious assumptions with regard to the traction and velocities.

Condition B: A more sophisticated condition of zero gradient of traction and stresses existing there. Such conditions will of course always apply to the exit domains for incompressible flow. Condition B was first introduced by Zienkiewicz et al. [88] and is discussed fully by Papanastasiou et al. [103]. This condition is of some importance as it gives remarkably good answers.

We shall refer to these open boundary conditions in various classes of problems dealt with later in this book and shall discuss them in detail.

Of considerable importance, especially in view of the CBS scheme, are conditions which we will encounter on real boundaries.

3.9.2 Real boundaries

By real boundaries we mean limits of fluid domains which are physically defined and here three different possibilities exist.

1. *Solid boundaries with no-slip conditions*: On such boundaries the fluid is assumed to stick or attach itself to the boundary and thus all velocity components become zero. Obviously this condition is only possible for viscous flows.
2. *Solid boundaries in inviscid flow (slip conditions)*: When the flow is inviscid we will always encounter slipping boundary conditions where only the normal velocity component is specified. This will generally be zero if the boundaries are stationary. Such boundary conditions will invariably be imposed for problems of Euler flow whether it is compressible or incompressible.
3. *Prescribed traction boundary conditions*: The last category is that of boundaries on which tractions are prescribed. This includes zero traction in the case of free surfaces of fluids or any prescribed tractions such as those caused by wind being imposed on the surface.

These three basic kinds of boundary conditions have to be imposed on the fluid and special consideration has to be given to these when split operator schemes are used.

3.9.3 Application of real boundary conditions in the discretization using the CBS algorithm

We shall first consider the treatment of boundaries described under (1) or (2) of the previous section. On such boundaries

$$u_n = 0, \quad \text{normal velocity zero} \quad (3.105)$$

and either

$$t_s = 0, \quad \text{tangential traction zero for inviscid flow}$$

or

$$u_s = 0, \quad \text{tangential velocity zero for viscous flow}$$

In early applications of the CBS algorithm it appeared correct that when computing $\Delta\tilde{U}_i^*$ no velocity boundary conditions be imposed and to use instead the value of boundary tractions which corresponds to the deviatoric stresses and pressures computed at time t_n . We note that if the pressure is removed as in Split A these pressures could also be removed from the boundary traction component. However, in Split B no such pressure removal is necessary. This requires, in viscous problems, evaluation of the boundary τ_{ij} 's and this point is explained further later.

When computing $\Delta\rho$ or Δp we integrate by parts obtaining [Eq. (3.55)]

$$\begin{aligned} \int_{\Omega} N_p^k \frac{1}{c^2} \Delta p \, d\Omega &= -\Delta t \int_{\Omega} N_p^k \frac{\partial}{\partial x_i} \left(U_i^n + \theta_1 \Delta U_i^* - \theta_1 \Delta t \frac{\partial p^{n+\theta_2}}{\partial x_i} \right) \, d\Omega \\ &= \Delta t \int_{\Omega} \frac{\partial N_p^k}{\partial x_i} \left[U_i^n + \theta_1 \left(\Delta U_i^* - \Delta t \frac{\partial p^{n+\theta_2}}{\partial x_i} \right) \right] \, d\omega \\ &\quad - \Delta t \int_{\Gamma} N_p^k n_i \left[U_i^n + \theta_1 \left(\Delta U_i^* - \Delta t \frac{\partial p^{n+\theta_2}}{\partial x_i} \right) \right] \, d\Gamma \end{aligned} \quad (3.106)$$

Here n_i is the outward drawn normal. The last term in the above equation is identically equal to zero on boundaries in which slip and no-slip conditions are applied from the condition of Eq. (3.26):

$$U_n = n_i U_i = n_i \left[U_i^n + \theta_1 \left(\Delta U_i^* - \Delta t \frac{\partial p^{n+\theta_2}}{\partial x_i} \right) \right] = 0 \quad (3.107)$$

For nonzero normal velocity this would simply become the specified normal velocity. This point seems to have baffled some investigators who simply assume

$$\frac{\partial p}{\partial n} = n_i \frac{\partial p}{\partial x_i} = 0 \quad (3.108)$$

on solid boundaries although this is not exactly true as shown by Codina et al. [46].

Returning to the traction on the boundaries, the traction on the surface can be defined as

$$t_i = \tau_{ij} n_j - p n_i \quad (3.109)$$

Prescribing the above traction using Split A, we replace the stress components in Step 1 [last term in Eq. (3.34)] as follows:

$$\int_{\Gamma} N_u^k \tau_{ij} n_j \, d\Gamma = \int_{\Gamma - \Gamma_t} N_u^k \tau_{ij} n_j \, d\Gamma + \int_{\Gamma_t} N_u^k (t_i + p n_i) \, d\Gamma \quad (3.110)$$

where Γ_t represents the part of the boundary where the traction is prescribed.

The above calculation may involve a substantial error in “projecting” deviatoric stresses onto the boundary.

The last step requires the solution for the velocity correction terms to obtain finally the \tilde{U}_i^{n+1} . Clearly correct velocity boundary values must always be imposed in this step.

Although the above-described procedure is theoretically correct and instructive, it is complex to implement. For this reason we will recommend the use of a much simpler procedure which relies on the fact that when summation is made of the CBS components correct velocity and traction conditions should be satisfied by the sum. Thus in the recommended procedure we apply all the specified tractions.

3.10 The performance of two- and single-step algorithms on an inviscid problem

In this section we demonstrate the performance of the single- and two-step algorithms via an inviscid problem of subsonic and supersonic flow past a NACA0012 aerofoil. The problem domain and finite element mesh used are shown in Fig. 3.3a and b. The discretization near the aerofoil surface is finer than that of other places and a total number of 969 nodes and 1824 elements are used in the mesh.

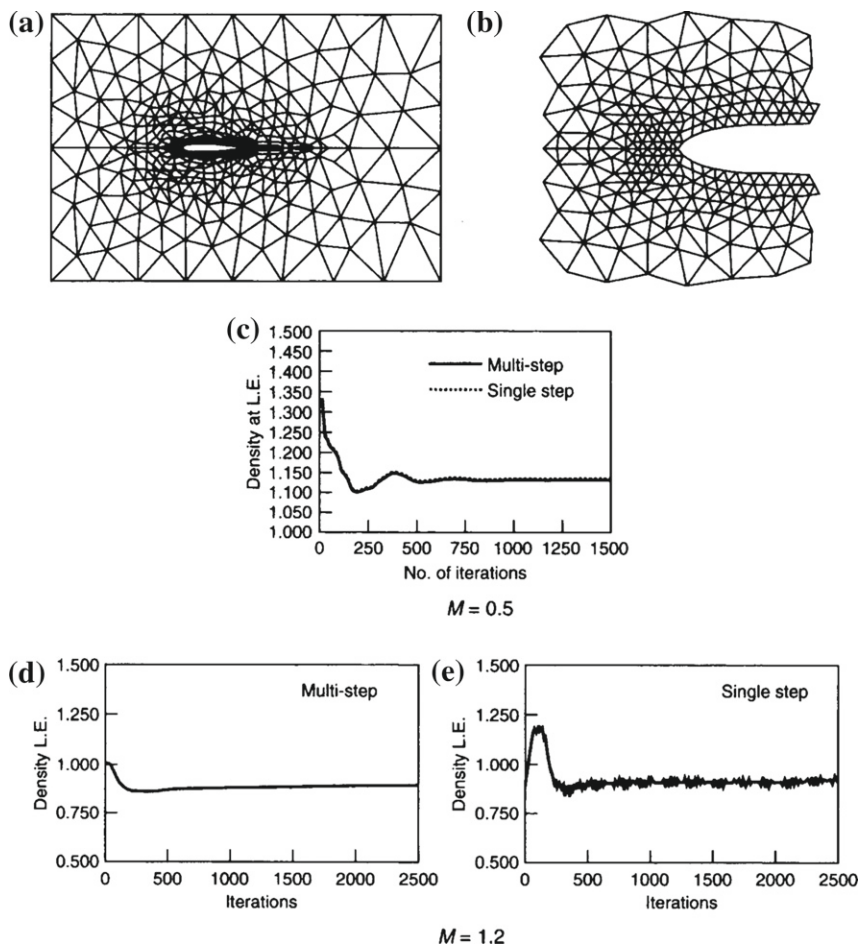


FIGURE 3.3

Inviscid flow past a NACA0012 aerofoil $\alpha = 0$: (a) unstructured mesh with 1824 elements and 969 nodes; (b) details of mesh near stagnation point; (c) steady-state convergence for $M = 0.5$ with two- and single-step schemes, fully explicit form; (d) steady-state convergence for $M = 1.2$ for two-step scheme; (e) steady-state convergence for $M = 1.2$ for single-step scheme.

The inlet Mach number is assumed to be equal to 0.5 and all variables except the density are prescribed at the inlet. The density is imposed at the exit of the domain. Both the top and bottom sides are assumed to be symmetric with normal component of velocity equal to zero. A slipping boundary is assumed on the surface of the aerofoil. No real or additional viscosity in any form is used in this problem when we use the CBS algorithm. However other schemes do need additional diffusions to get a reasonable solution.

Figure 3.3c shows the comparison of the density evolution at the stagnation point of the aerofoil. It is observed that the difference between the single- and two-step schemes is negligibly small. Further tests on these schemes were carried out at a higher inlet Mach number of 1.2 with the flow being supersonic, and a different mesh with a higher number of nodes (3753) and elements (7351). Here all the variables at the inlet were specified and the exit was free. As we can see from Fig. 3.3d and e, the single-step scheme gives spurious oscillations in density values at the stagnation

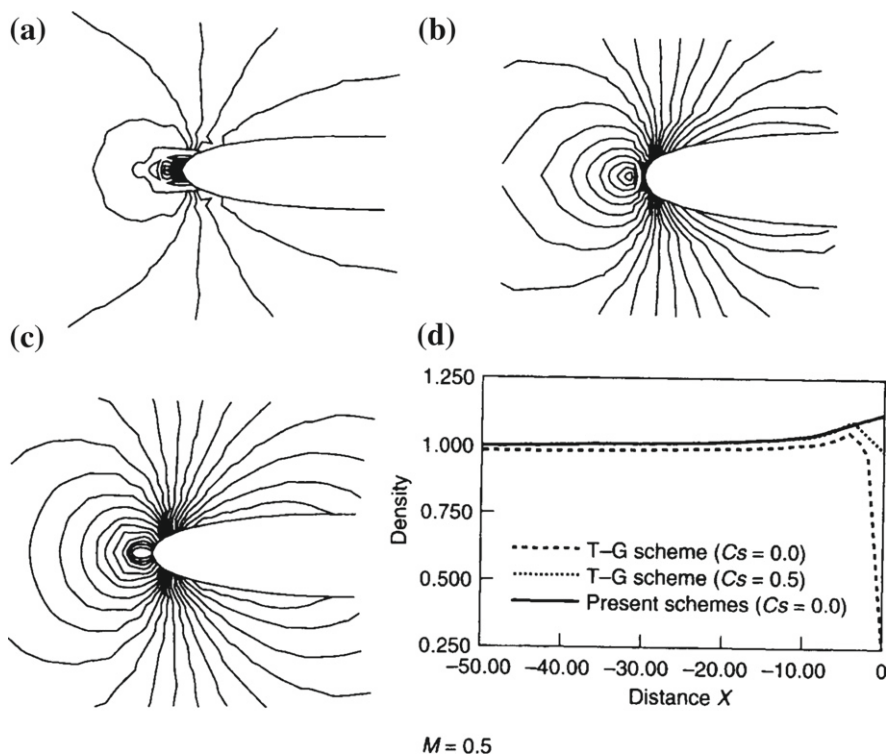


FIGURE 3.4

Subsonic inviscid flow past a NACA0012 aerofoil with $\alpha = 0$ and $M = 0.5$: (a) density contours with TG scheme with no additional viscosity; (b) density contours with TG scheme with additional viscosity; (c) density contours with CBS scheme with no additional viscosity; (d) comparison of density along the stagnation line.

point. Therefore we conclude that here the two-step algorithm is valid for any range of Mach numbers and the single-step algorithm is limited to low Mach numbers flows with small compressibility.

In Fig. 3.4 we compare the two-step algorithm results of the subsonic inviscid ($M = 0.5$) results with those obtained by the Taylor-Galerkin scheme for the same mesh. It is observed that the CBS algorithm gives a smooth solution near the stagnation point even though no additional artificial diffusion is introduced. However the Taylor-Galerkin scheme gives spurious solutions and a reasonable solution is obtained from this scheme only with a considerable amount of additional diffusion. Comparison of density distribution along the stagnation line shows (Fig. 3.4d) that the Taylor-Galerkin scheme gives an incorrect solution even with additional diffusion. However, the CBS algorithm again gives an accurate solution without the use of any additional artificial diffusion.

3.11 Performance of dual time stepping to remove pressure error

The problem considered here is to demonstrate that the performance of a quasi-implicit scheme with dual time stepping is vortex decay within a unit square domain. This analytical benchmark allows for a quantitative assessment of the relative temporal properties of the standard quasi-implicit scheme compared to that of dual time stepping-based approach. This two-dimensional problem has the following analytical solution:

$$\begin{aligned} u(x, y, t) &= -\cos \pi x \sin \pi y \exp^{-2\pi^2 t / Re} \\ v(x, y, t) &= \sin \pi x \cos \pi y \exp^{-2\pi^2 t / Re} \\ p(x, y, t) &= -\frac{1}{4} (\cos 2\pi x + \cos 2\pi y) \exp^{-4\pi^2 t / Re} \end{aligned} \quad (3.111)$$

where $Re = 20$ and $-0.5 \leq x, y \leq 0.5$. The initial and boundary conditions are computed using the analytical solution. The initial time history that is needed to enact the dual time stepping is also calculated using the analytical solution. A uniformly structured mesh of 115,200 linear triangular elements was employed in the calculations. The instantaneous steady-state convergence within the pseudo time stepping iteration loop was determined via a normalized L2 norm of the velocity and pressure differences between two consecutive pseudo time steps. In both cases, a tolerance of 1×10^{-11} was employed.

In order to assess the temporal convergence behavior, the difference between the analytical solution and the predicted numerical solution was examined at a total time of unity. The difference between the analytical and predicted solutions was determined (e.g., for pressure) using

$$error = \frac{\|p - p_{analytical}\|}{\|p_{analytical}\|} \quad (3.112)$$

where $\|.\|$ denotes the Euclidean norm. Once the error was determined for a range of transient time step values ($\Delta\tau$ values), a least-squares technique was utilized to determine the rate of convergence.

The convergence of the dual time-stepping approach is demonstrated in Fig. 3.5. In this figure, both velocity and pressure temporal behavior is identical. The calculated convergence in time is presented in Table 3.1 for both the classical and dual time-stepping approaches. As seen all calculated convergence gradients have a Pearson coefficient greater than 0.9992, demonstrating that a negligible error exists within the calculated convergence rates. It is very clear from Fig. 3.5 and Table 3.1 that dual time stepping gives the expected formal accuracy in time. This behavior demonstrates the monolithic equivalence of the dual time-stepping-based quasi-implicit scheme. However, since the scheme does not require a monolithic solution procedure, the computational cost is reduced.

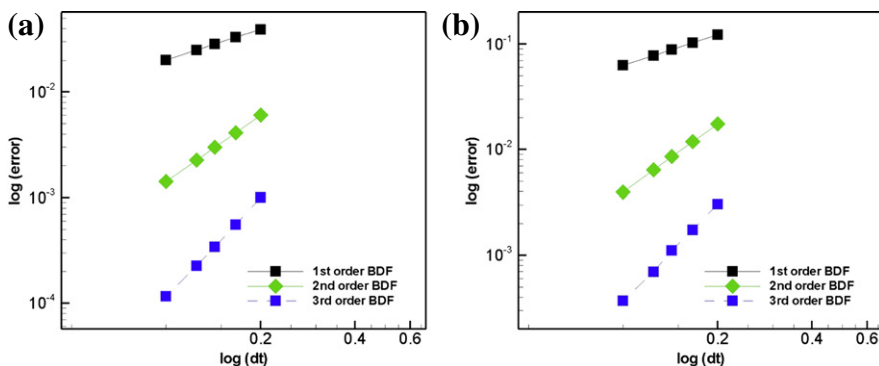


FIGURE 3.5

Vortex decay. Temporal convergence of the dual time-stepping quasi-implicit scheme with first-, second-, and third-order backward difference formula for $\Delta u^n / \Delta \tau$: (a) velocity; (b) pressure.

Table 3.1 Vortex Decay: Calculated Rates of Convergence and Associated Pearson Coefficient

Method	Order	Velocity	Pearson Coefficient (V)	Pressure	Pearson Coefficient (P)
Standard	1st	0.9038	0.9992	0.9561	1.0000
Dual time	1st	0.9657	1.0000	0.9670	1.0000
Standard	2nd	2.0339	0.9996	1.1512	0.9993
Dual time	2nd	2.1426	1.0000	2.1334	0.9999
Dual time	3rd	3.1146	0.9997	3.0608	0.9992

3.12 Concluding remarks

The general CBS algorithm is discussed in detail in this chapter for the equations of fluid dynamics in their conservation form. Comparison between the single- and two-step algorithms in section 3.10 shows that the latter scheme is valid for all ranges of flows. In later chapters, we generally apply the two-step algorithm for different flow applications. Another important conclusion made from this chapter is about the accuracy of the present scheme. As observed in section 3.10, the present CBS algorithm gives excellent performance when the flow is slightly compressible compared to the Taylor-Galerkin algorithm. In the following chapters we show further tests on the algorithm for a variety of problems including general compressible and incompressible flow problems, shallow-water problems, etc.

References

- [1] O.C. Zienkiewicz, R.L. Taylor, J.Z. Zhu, *The Finite Element Method: Its Basis and Fundamentals*, seventh ed., Elsevier, Oxford, 2013.
- [2] I. Babuška, The finite element method with Lagrangian multipliers, *Numer. Math.* 20 (1973) 179–192.
- [3] F. Brezzi, On the existence, uniqueness and approximation of saddle-point problems arising from Lagrange multipliers, *Rev. Française d'Automatique Inform. Rech. Opér., Ser. Rouge Anal. Numér.* 8 (R-2) (1974) 129–151.
- [4] A.J. Chorin, Numerical solution of Navier-Stokes equations, *Math. Comput.* 22 (1968) 745–762.
- [5] A.J. Chorin, On the convergence of discrete approximation to the Navier-Stokes equations, *Math. Comput.* 23 (1969) 341–353.
- [6] G. Comini, S. Del Guidice, Finite element solution of incompressible Navier-Stokes equations, *Numer. Heat Transfer, Part A* 5 (1972) 463–478.
- [7] G.E. Schneider, G.D. Raithby, M.M. Yovanovich, Finite element analysis of incompressible flow incorporating equal order pressure and velocity interpolation, in: C. Taylor, K. Morgan, C.A. Brebbia (Eds.), *Numerical Methods in Laminar and Turbulent Flow*, Pentech Press, Plymouth, 1978.
- [8] J. Donea, S. Giuliani, H. Laval, L. Quartapelle, Finite element solution of unsteady Navier-Stokes equations by a fractional step method, *Comput. Methods Appl. Mech. Eng.* 33 (1982) 53–73.
- [9] P.M. Gresho, S.T. Chan, R.L. Lee, C.D. Upson, A modified finite element method for solving incompressible Navier-Stokes equations. Part I: Theory, *Int. J. Numer. Methods Eng.* 4 (1984) 557–598.
- [10] M. Kawahara, K. Ohmiya, Finite element analysis of density flow using the velocity correction method, *Int. J. Numer. Methods Eng.* 5 (1985) 981–993.
- [11] J.G. Rice, R.J. Schnipke, An equal-order velocity-pressure formulation that does not exhibit spurious pressure modes, *Comput. Methods Appl. Mech. Eng.* 58 (1986) 135–149.

- [12] B. Ramaswamy, M. Kawahara, T. Nakayama, Lagrangian finite element method for the analysis of two dimensional sloshing problems, *Int. J. Numer. Methods Fluids* 6 (1986) 659–670.
- [13] B. Ramaswamy, Finite element solution for advection and natural convection flows, *Comput. Fluids* 16 (1988) 349–388.
- [14] M. Shimura, M. Kawahara, Two dimensional finite element flow analysis using the velocity correction procedure, *Earthq. Eng. Struct. Dyn.* 5 (1988) 255–263.
- [15] S.G.R. Kumar, P.A.A. Narayana, K.N. Seetharamu, B. Ramaswamy, Laminar flow and heat transfer over a two dimensional triangular step, *Int. J. Numer. Methods Fluids* 9 (1989) 1165–1177.
- [16] B. Ramaswamy, T.C. Jue, J.E. Akin, Semi-implicit and explicit finite element schemes for coupled fluid thermal problems, *Int. J. Numer. Methods Eng.* 34 (1992) 675–696.
- [17] R. Rannacher, On Chorin's projection method for the incompressible Navier-Stokes equations, *Lect. Notes Math.* 1530 (1993) 167–183.
- [18] B. Ramaswamy, Theory and implementation of a semi-implicit finite element method for viscous incompressible flows, *Comput. Fluids* 22 (1993) 725–747.
- [19] C.B. Yiang, M. Kawahara, A three step finite element method for unsteady incompressible flows, *Comput. Mech.* 11 (1993) 355–370.
- [20] G. Ren, T. Utne, A finite element solution of the time dependent incompressible Navier-Stokes equations using a modified velocity correction method, *Int. J. Numer. Methods Fluids* 17 (1993) 349–364.
- [21] B.V.K.S. Sai, K.N. Seetharamu, P.A.A. Narayana, Solution of transient laminar natural convection in a square cavity by an explicit finite element scheme, *Numer. Heat Transfer, Part A* 25 (1994) 593–609.
- [22] M. Srinivas, M.S. Ravisanker, K.N. Seetharamu, P.A. Aswathanarayana, Finite element analysis of internal flows with heat transfer, *Sadhana - Acad. Proc. Eng.* 19 (1994) 785–816.
- [23] P.M. Gresho, S.T. Chan, M.A. Christon, A.C. Hindmarsh, A little more on stabilized Q1Q1 for transient viscous incompressible flow, *Int. J. Numer. Methods Fluids* 21 (1995) 837–856.
- [24] Y.T.K. Gowda, P.A.A. Narayana, K.N. Seetharamu, Mixed convection heat transfer past in-line cylinders in a vertical duct, *Numer. Heat Transfer, Part A* 31 (1996) 551–562.
- [25] A.R. Chaudhuri, K.N. Seetharamu, T. Sundararajan, Modelling of steam surface condenser using finite element methods, *Commun. Appl. Numer. Methods* 13 (1997) 909–921.
- [26] P. Nithiarasu, T. Sundararajan, K.N. Seetharamu, Finite element analysis of transient natural convection in an odd-shaped enclosure, *Int. J. Num. Methods Heat Fluid Flow* 8 (1998) 199–220.
- [27] P.K. Maji, G. Biswas, Three-dimensional analysis of flow in the spiral casing of a reaction turbine using a differently weighted Petrov Galerkin method, *Comput. Methods Appl. Mech. Eng.* 167 (1998) 167–190.

- [28] P.D. Minev, P.M. Gresho, A remark on pressure correction schemes for transient viscous incompressible flow, *Commun. Appl. Numer. Methods* 14 (1998) 335–346.
- [29] J. Blasco, R. Codina, A. Huerta, A fractional-step method for the incompressible Navier-Stokes equations related to a predictor-multicorrector algorithm, *Int. J. Numer. Methods Fluids* 28 (1998) 1391–1419.
- [30] B.S.V.P. Patnaik, P.A.A. Narayana, K.N. Seetharamu, Numerical simulation of vortex shedding past a cylinder under the influence of buoyancy, *Int. J. Heat Mass Transfer* 42 (1999) 3495–3507.
- [31] J.L. Guermond, Result of convergence of order two in time for approximation of Navier-Stokes equations by means of an incremental projection method, *RAIRO - Mathematical Modelling and Numerical Analysis* 33 (1999) 169–189.
- [32] J.L. Guermond, J. Shen, Velocity-correction projection methods for incompressible flows, *SIAM J. Numer. Anal.* 41 (2003) 112–134.
- [33] J.L. Guermond, P. Minev, J. Shen, An overview of projection methods for incompressible flows, *Comput. Methods Appl. Mech. Eng.* 195 (44–47) (2006) 6011–6045.
- [34] S. Dong, J. Shen, An unconditionally stable rotational velocity-correction scheme for incompressible flows, *J. Comput. Phys.* 229 (19) (2010) 7013–7029.
- [35] O.C. Zienkiewicz, R. Codina, Search for a general fluid mechanics algorithm, in: D.A. Caughey, M.M. Hafez (Eds.), *Frontiers of Computational Fluid Dynamics*, John Wiley & Sons, New York, 1995, pp. 101–113.
- [36] O.C. Zienkiewicz, R. Codina, A general algorithm for compressible and incompressible flow—Part I: The split, characteristic-based scheme, *Int. J. Numer. Methods Fluids* 20 (1995) 869–885.
- [37] O.C. Zienkiewicz, B.V.K.S. Sai, K. Morgan, R. Codina, M. Vázquez, A general algorithm for compressible and incompressible flow—Part II: Tests on the explicit form, *Int. J. Numer. Methods Fluids* 20 (1995) 887–913.
- [38] O.C. Zienkiewicz, P. Ortiz, A split characteristic based finite element model for shallow water equations, *Int. J. Numer. Methods Fluids* 20 (1995) 1061–1080.
- [39] P. Ortiz, O.C. Zienkiewicz, Modelizacin por elementos finitos en hidrulica e hidrodinmica costera, Technical report, Centro de Estudios y Experimentation de Obras Pblicas, CEDEX, Madrid, 1995.
- [40] O.C. Zienkiewicz, A new algorithm for fluid mechanics. Compressible and incompressible behaviour, in: M. Morandi Cecchi, K. Morgan, J. Periaux, B.A. Schrefler, O.C. Zienkiewicz (Eds.), *Proceedings of the 9th International Conference on Finite Elements Fluids—New Trends and Applications*, Venezia, October 1995, pp. 49–55.
- [41] R. Codina, M. Vázquez, O.C. Zienkiewicz, A fractional step method for compressible flows: boundary conditions and incompressible limit, in: M. Morandi Cecchi, K. Morgan, J. Periaux, B.A. Schrefler, O.C. Zienkiewicz (Eds.), *Proceedings of the 9th International Conference on Finite Elements Fluids—New Trends and Applications*, Venezia, October 1995, pp. 409–418.

- [42] P. Ortiz, O.C. Zienkiewicz, Tide and bore propagation in the Severn Estuary by a new algorithm, in: M. Morandi Cecchi, K. Morgan, J. Periaux, B.A. Schrefler, O.C. Zienkiewicz (Eds.), Proceedings of the 9th International Conference on Finite Elements Fluids—New Trends and Applications, Venezia, October 1995, pp. 1543–1552.
- [43] O.C. Zienkiewicz, B.V.K.S. Sai, K. Morgan, R. Codina, Split characteristic based semi-implicit algorithm for laminar/turbulent incompressible flows, *Int. J. Numer. Methods Fluids* 23 (1996) 1–23.
- [44] P. Ortiz, O.C. Zienkiewicz, An improved finite element model for shallow water problems, in: G.F. Carey (Ed.), *Finite Element Modeling of Environmental Problems*, John Wiley & Sons, New York, 1996, pp. 61–84.
- [45] P. Nithiarasu, O.C. Zienkiewicz, B.V.K.S. Sai, K. Morgan, R. Codina, M. Vázquez, Shock capturing viscosities for the general fluid mechanics algorithm, *Int. J. Numer. Methods Fluids* 28 (1998) 1325–1353.
- [46] R. Codina, M. Vázquez, O.C. Zienkiewicz, General algorithm for compressible and incompressible flows, Part III—A semi-implicit form, *Int. J. Numer. Methods Fluids* 27 (1998) 13–32.
- [47] B.V.K.S. Sai, O.C. Zienkiewicz, M.T. Manzari, P.R.M. Lyra, K. Morgan, General purpose vs. special algorithms for high speed flows with shocks, *Int. J. Numer. Methods Fluids* 27 (1998) 57–80.
- [48] R. Codina, M. Vázquez, O.C. Zienkiewicz, A fractional step method for the solution of compressible Navier-Stokes equations, in: M. Hafez, K. Oshima (Eds.), *Computational Fluid Dynamics Review 1998*, vol. 1, World Scientific Publishing, 1998, pp. 331–347.
- [49] N. Massarotti, P. Nithiarasu, O.C. Zienkiewicz, Characteristic-based-split (CBS) algorithm for incompressible flow problems with heat transfer, *Int. J. Numer. Methods Heat Fluid Flow* 8 (1998) 969–990.
- [50] O.C. Zienkiewicz, P. Nithiarasu, R. Codina, M. Vázquez, P. Ortiz, Characteristic-based-split algorithm, Part I: The theory and general discussion, in: K.D. Papailou et al. (Eds.), *Proceedings of the ECCOMAS CVD 1998*, vol. 2, 1998, Greece, Athens
- [51] N. Massarotti, P. Nithiarasu, O.C. Zienkiewicz, Characteristic-based-split algorithm, Part II: Incompressible flow problems with heat transfer, in: K.D. Papailou et al. (Eds.), *Proceedings of ECCOMAS CFD 1998*, vol. 2, 1998, Greece, Athens
- [52] O.C. Zienkiewicz, P. Ortiz, The CBS (characteristic-based-split) algorithm in hydraulic and shallow water flow, in: *Proceedings of the Second International Symposium on Environmental Hydraulics*, University of Hong Kong, December 1998, pp. 3–12.
- [53] P. Nithiarasu, O.C. Zienkiewicz, On stabilization of the CBS algorithm. Internal and external time steps, *Int. J. Numer. Methods Eng.* 48 (2000) 875–880.
- [54] O.C. Zienkiewicz, J. Rojek, R.L. Taylor, M. Pastor, Triangles and tetrahedra in explicit dynamic codes for solids, *Int. J. Numer. Methods Eng.* 43 (1999) 565–583.

- [55] O.C. Zienkiewicz, P. Nithiarasu, R. Codina, M. Vázquez, The characteristic based split procedure: an efficient and accurate algorithm for fluid problems, *Int. J. Numer. Methods Fluids* 31 (1999) 359–392.
- [56] P. Nithiarasu, Boundary conditions for the characteristic based split (CBS) algorithm for fluid dynamics, *Int. J. Numer. Methods Eng.* 54 (2002) 523–536.
- [57] P. Nithiarasu, An efficient artificial compressibility (AC) scheme based on the characteristic based split (CBS) method for incompressible flows, *Int. J. Numer. Methods Eng.* 56 (2003) 1815–1845.
- [58] P. Nithiarasu, J.S. Mathur, N.P. Weatherill, K. Morgan, Three-dimensional incompressible flow calculations using the characteristic based split (CBS) scheme, *Int. J. Numer. Methods Fluids* 44 (2004) 1207–1229.
- [59] P. Nithiarasu, N. Massarotti, J.S. Mathur, Forced convection heat transfer heat from solder balls on a printed circuit board using the characteristic based split (CBS) scheme, *Int. J. Numer. Methods Heat Fluid Flow* 15 (1) (2005) 73–95.
- [60] P. Nithiarasu, An arbitrary Lagrangian Eulerian (ALE) formulation for free surface flows using the characteristic-based split (CBS) scheme, *Int. J. Numer. Methods Fluids* 48 (2005) 1415–1428.
- [61] P. Nithiarasu, C.-B. Liu, Steady and unsteady incompressible flow in a double driven cavity using the artificial compressibility (AC)-based characteristic-based split (CBS) scheme, *Int. J. Numer. Methods Eng.* 63 (2005) 380–397.
- [62] P. Nithiarasu, R. Codina, Special issue: Characteristic-based split (CBS) procedure, *Int. J. Numer. Methods Eng.* 66 (2006) 1511–1512.
- [63] X. Li, Q. Duan, Meshfree iterative stabilized Taylor-Galerkin and characteristic-based split (CBS) algorithms for incompressible N-S equations, *Comput. Methods Appl. Mech. Eng.* 195 (2006) 6125–6145.
- [64] P. Nithiarasu, C.-B. Liu, An artificial compressibility based characteristic based split (CBS) scheme for steady and unsteady turbulent incompressible flows, *Comput. Methods Appl. Mech. Eng.* 195 (2006) 2961–2982.
- [65] O.C. Zienkiewicz, Special issue: Characteristic-based split (CBS) procedure—Foreword, *Int. J. Numer. Methods Eng.* 66 (2006) 1513.
- [66] V.M. Kulkarni, K.N. Seetharamu, I.A. Azid, P.A.A. Narayana, G.A. Quadir, Numerical simulation of underfill encapsulation process based on characteristic split method, *Int. J. Numer. Methods Eng.* 66 (2006) 1658–1671.
- [67] M. Morandi-Cecchi, M. Venturin, Characteristic-based split (CBS) algorithm finite element modelling for shallow waters in the Venice lagoon, *Int. J. Numer. Methods Eng.* 66 (2006) 1641–1657.
- [68] P. Nithiarasu, R. Codina, O.C. Zienkiewicz, The characteristic-based split (CBS) scheme—a unified approach to fluid dynamics, *Int. J. Numer. Methods Eng.* 66 (2006) 1514–1546.
- [69] P. Nithiarasu, C.-B. Liu, N. Massarotti, Laminar and turbulent flow calculations through a model human upper airway using unstructured meshes, *Commun. Numer. Methods Eng.* 23 (12) (2007) 1057–1069.

- [70] C.-B. Liu, P. Nithiarasu, The characteristic-based split (CBS) scheme for viscoelastic flow past a circular cylinder, *Int. J. Numer. Methods Fluids* 57 (2008) 157–176.
- [71] C.-B. Liu, P. Nithiarasu, An artificial-dissipation-based fractional step scheme for upper-conveyed Maxwell (UCM) fluid flow past a circular cylinder, *Int. J. Numer. Methods Fluids* 57 (2008) 1171–1187.
- [72] P. Nithiarasu, O. Hassan, K. Morgan, N.P. Weatherill, C. Fielder, H. Whittet, P. Ebden, K.R. Lewis, Steady flow through a realistic human upper airway geometry, *Int. J. Numer. Methods Fluids* 57 (2008) 631–651.
- [73] K. Chitra, S. Vengadesan, T. Sundararajan, P. Nithiarasu, An investigation of pulsatile flow in a model cavo-pulmonary vascular system, *Commun. Numer. Methods Eng.* 25 (2009) 1061–1083.
- [74] Y. Bao, D. Zhou, C. Huang, Numerical simulation of flow over three circular cylinders in equilateral arrangements at low Reynolds number by a second-order characteristic-based split finite element method, *Comput. Fluids* 39 (2010) 882–899.
- [75] R.L.T. Bevan, P. Nithiarasu, R. Van Loon, I. Sazonov, H. Luckraz, A. Garnham, Application of a locally conservative Galerkin (LCG) method for modelling blood flow through a patient-specific carotid bifurcation, *Int. J. Numer. Methods Fluids* 64 (2010) 1274–1295.
- [76] X. H Zhang, J. Ouyang, L. Zhang, The characteristic-based split (CBS) mesh-free method for free surface flow problems in ALE formulation, *Int. J. Numer. Methods Fluids* 65 (2011) 798–811.
- [77] A. Mauro, P. Nithiarasu, N. Massarotti, F. Arpino, The finite element method: discretization and application to heat convection problems, in: R.S. Amano, B. Sundén (Eds.), *Computational Fluid Dynamics and Heat Transfer: Emerging Topics*, International Series on Developments in Heat Transfer, WIT Press, Billerica, MA, 2011, pp. 129–170.
- [78] R.L.T. Bevan, I. Sazonov, P.H. Saksono, P. Nithiarasu, R. van Loon, H. Luckraz, S. Ashraf, Patient-specific blood flow simulation through an aneurysmal thoracic aorta with a folded proximal neck, *Int. J. Numer. Methods Biomed. Eng.* 27 (2011) 1167–1184.
- [79] P.H. Saksono, P. Nithiarasu, I. Sazonov, S.Y. Yeo, Computational flow studies in a subject-specific human upper airway using a one-equation turbulence model. Influence of the nasal cavity, *Int. J. Numer. Methods Eng.* 87 (2011) 96–114.
- [80] K. Chitra, T. Sundararajan, S. Vengadesan, P. Nithiarasu, Non-Newtonian blood flow study in a model cavopulmonary vascular system, *Int. J. Numer. Methods Fluids* 66 (2011) 269–283.
- [81] P. Nithiarasu, R. Bevan, I. Sazonov, R. van Loon, H. Luckraz, M. Collins, A. Garnham, Influences of domain extensions to a moderately stenosed patient-specific carotid bifurcation: Investigation of wall quantities, *Int. J. Numer. Methods Heat Fluid Flow* 21 (2011) 952–979.

- [82] P.H. Saksono, P. Nithiarasu, I. Sazonov, Numerical prediction of heat transfer patterns in a subject-specific human upper airway, *J. Heat Transfer—Trans. ASME* 134 (2012).
- [83] R.L.T. Bevan, P. Nithiarasu, Accelerating incompressible flow calculations using a quasi-implicit scheme: local and dual time stepping approaches, *Comput. Mech.* 50 (6, SI) (2012) 687–693.
- [84] R.L.T. Bevan, R.W. Lewis, P. Nithiarasu, Forced convection heat transfer within a moderately-stenosed, patient-specific carotid bifurcation, *Int. J. Numer. Methods Heat Fluid Flow* 22 (2012) 1120–1134.
- [85] C.A. Klettner, I. Eames, Viscous free surface simulations with the characteristic based split scheme, *Comput. Fluids* 71 (2013) 487–495.
- [86] F. Arpino, N. Massarotti, A. Mauro, P. Nithiarasu, Artificial compressibility based CBS solutions for double diffusive natural convection in cavities, *Int. J. Numer. Methods Heat Fluid Flow* 23 (2013) 205–225.
- [87] P. Nithiarasu, R.L.T. Bevan, K. Murali, An artificial compressibility based fractional step method for solving time dependent incompressible flow equations. Temporal accuracy and similarity with a monolithic method, *Comput. Mech.* 51 (3) (2013) 255–260.
- [88] O.C. Zienkiewicz, J. Szmelter, J. Peraire, Compressible and incompressible flow: an algorithm for all seasons, *Comput. Methods Appl. Mech. Eng.* 78 (1990) 105–121.
- [89] O.C. Zienkiewicz, Explicit or semi-explicit general algorithm for compressible and incompressible flows with equal finite element interpolation, Technical Report 90/5, Chalmers Technical University, Gothenburg, 1990.
- [90] O.C. Zienkiewicz, Finite elements and computational fluid mechanics, in: SEMNI Congress, Metodos Numericos en Ingenieria, Gran Canaria, 1991, pp. 51–61.
- [91] O.C. Zienkiewicz, J. Wu, Incompressibility without tears! How to avoid restrictions of mixed formulations, *Int. J. Numer. Methods Eng.* 32 (1991) 1184–1203.
- [92] O.C. Zienkiewicz, J. Wu, A general explicit or semi-explicit algorithm for compressible and incompressible flows, *Int. J. Numer. Methods Eng.* 35 (1992) 457–479.
- [93] P. Nithiarasu, O.C. Zienkiewicz, Analysis of an explicit and matrix free fractional step method for incompressible flows, *Comput. Methods Appl. Mech. Eng.* 195 (41–43) (2006) 5537–5551.
- [94] C. Thomas, P. Nithiarasu, The characteristic based split (CBS) approach for inviscid compressible flow problems. Effect of element size calculation in the streamline direction, in: Netanmaki et al. (Eds.), ECCOMAS, 2004, Jyväskylä, Finland, 24–28 July, 2004.
- [95] O.C. Zienkiewicz, S. Qu, R.L. Taylor, S. Nakazawa, The patch test for mixed formulations, *Int. J. Numer. Methods Eng.* 23 (1986) 1873–1883.
- [96] O.C. Zienkiewicz, R.L. Taylor, The finite element patch test revisited: a computer test for convergence, validation and error estimates, *Comput. Methods Appl. Mech. Eng.* 149 (1997) 523–544.

- [97] A. Jameson, D.J. Mavriplis, Finite volume solution of the two dimensional Euler equations on a regular triangular mesh, in: AIAA 23th Aerospace Sciences Meeting, Reno, NV, 1985, Paper AIAA-85-0435.
- [98] F. Brezzi, J. Pitkäranta, On the stabilization of finite element approximations of the Stokes problem, in: W. Hackbusch (Ed.), Efficient Solution of Elliptic Problems, Notes on Numerical Fluid Mechanics, vol. 10, Vieweg, Wiesbaden, 1984.
- [99] J. Kim, P. Moin, Application of a fractional step method to incompressible Navier-Stokes equations, *J. Comput. Phys.* 59 (1985) 308–323.
- [100] J.B. Perot, An analysis of the fractional step method, *J. Comput. Phys.* 108 (1993) 51–58.
- [101] R. Codina, Pressure stability in fractional step finite element methods for incompressible flows, *J. Comput. Phys.* 170 (2001) 112–140.
- [102] T.M. Burton, J.K. Eaton, Analysis of a fractional-step method on overset grids, *J. Comput. Phys.* 177 (2002) 336–364.
- [103] T.C. Papanastasiou, N. Malamataris, K. Ellwood, A new outflow boundary condition, *Int. J. Numer. Methods Fluids* 14 (1992) 587–608.

Incompressible Newtonian Laminar Flows

4

4.1 Introduction and the basic equations

The problems of incompressible flows dominate a large part of the fluid mechanics scene. For this reason, they are given special attention in this book and we devote three chapters to this subject. In the present chapter we deal with various laminar steady-state and transient Newtonian situations in which the flow is forced by appropriate pressure gradients and boundary forces. In the next chapter we shall consider non-Newtonian flows including metal forming and viscoelastic flows. Free surface flows in which gravity establishes appropriate free surface patterns as well as the so-called buoyancy force in which the only driving forces are density changes caused by temperature variations are discussed in [Chapter 6](#).

It is mentioned in [Ref. \[1\]](#) that certain difficulties are encountered with incompressibility when this is present in the equations of solid mechanics. We shall find that exactly the same problems arise again in fluids especially with very slow flows where the acceleration can be neglected and viscosity is dominant (so-called Stokes flow). Complete identity with linear elasticity is found here.

The essential difference in the governing equations for incompressible flows from those of compressible flows is that the coupling between the equations of energy and the other equations is very weak and thus frequently the energy equations can be considered completely independently.

To proceed further we return to the original equations of fluid dynamics which have been given in [Chapters 1](#) and [3](#); we repeat these below for problems of small compressibility.

Conservation of mass

$$\frac{\partial \rho}{\partial t} = \frac{1}{c^2} \frac{\partial p}{\partial t} = - \frac{\partial U_i}{\partial x_i} \quad (4.1)$$

and $c^2 = K/\rho$ where K is the bulk modulus. Here in the incompressible limit, the density ρ is assumed to be constant and in this situation the term on the left-hand side is simply zero.

Conservation of momentum

$$\frac{\partial U_i}{\partial t} = - \frac{\partial}{\partial x_j} (u_j U_i) + \frac{\partial \tau_{ij}}{\partial x_j} - \frac{\partial p}{\partial x_i} + \rho g_i \quad (4.2)$$

In the above we define the mass flow fluxes as

$$U_i = \rho u_i \quad (4.3)$$

Conservation of energy

$$\frac{\partial(\rho E)}{\partial t} = -\frac{\partial}{\partial x_j}(u_j \rho E) + \frac{\partial}{\partial x_i} \left(k \frac{\partial T}{\partial x_i} \right) - \frac{\partial}{\partial x_j}(u_j p) + \frac{\partial}{\partial x_i}(\tau_{ij} u_j) \quad (4.4)$$

This is now uncoupled and can be solved independently. In the above u_i are the velocity components, E is the specific energy ($c_v T$), p is the pressure, T is the absolute temperature, ρg_i represents the body force and other source terms, and τ_{ij} are the deviatoric stress components given by (1.11b):

$$\tau_{ij} = \mu \left(\frac{\partial u_i}{\partial x_j} + \frac{\partial u_j}{\partial x_i} \right) \quad (4.5)$$

With the substitution made for density changes we note that the essential variables in the first two equations become those of pressure and velocity. In exactly the same way as these, we can specify the variables linking displacements and pressure in the case of incompressible solids. It is thus possible to solve these equations in one of many ways described in Chapter 10 of Ref. [1] though, of course, the use of the CBS algorithm is obvious.

Unless the viscosity and in fact the bulk modulus have a strong dependence on temperature the problem is very weakly linked with the energy equation which can be solved independently.

The energy equation for incompressible materials is best written in terms of the absolute temperature T avoiding the specific energy. The equation now becomes simply (neglecting source terms)

$$c_v \rho \left[\frac{\partial T}{\partial t} + u_j \frac{\partial T}{\partial x_j} \right] = \frac{\partial}{\partial x_i} \left(k \frac{\partial T}{\partial x_i} \right) + \frac{\partial}{\partial x_i}(\tau_{ij} u_j) - \frac{\partial}{\partial x_j}(u_j p) \quad (4.6)$$

and we note that this is now a scalar convection-diffusion equation of the type we have already encountered in [Chapter 2](#), written in terms of the variable temperature as the unknown. In the above equation, the last two work dissipation terms are often neglected for fully incompressible flows. Note that the above equation is derived assuming the density and c_v (specific heat at constant volume) to be constants.

In this chapter we shall in general deal with problems for which the coupling is weak and the temperature equations do not present any difficulties. However, in [Chapter 6](#) we shall encounter buoyancy effects caused by atmospheric or general circulation induced by small density changes due to temperature differences.

If viscosity is a function of temperature, it is very often best to proceed simply by iterating over a cycle in which the velocity and pressure are solved with the assumption of known viscosity, followed by the solution of temperature. Many practical problems have been so treated very satisfactorily. We shall show some of these applications in the field of metal forming in the next chapter.

In the main part of this chapter we shall consider the solution of viscous, Newtonian fluids and we shall generally use the CBS algorithm described in [Chapter 3](#), though

on occasion we shall depart from this due to the similarity with the equations of solid mechanics and use a more direct approach either by satisfying the BB stability conditions of Chapter 10 in [1] for the velocity and pressure variables, or by using reduced integration in the context of a pure velocity formulation with a penalty parameter.

4.2 Use of the CBS algorithm for incompressible flows

4.2.1 The fully explicit artificial compressibility form

The fully explicit scheme for incompressible flow approximation is obtained by substituting $0.5 \leq \theta_1 \leq 1.0$ and $\theta_2 = 0$ into Eqs. (3.56) and (3.59). It is obvious that $c \rightarrow 0$ in incompressible flow approximations and therefore needs to be replaced with an artificial parameter β as discussed in Section 3.5.1 [2,3]. With such an approximation, the steady-state solutions will be straightforward. However, for unsteady state the dual time-stepping procedure described in Section 3.5.2 needs to be followed. We consider both steady and unsteady state solutions here. The artificial compressibility-based CBS scheme is generally referred to as the CBS-AC scheme in the present text.

4.2.2 The semi-implicit form

For problems of incompressibility with K being equal to infinity or indeed when K is very large, we have a choice of using the fully explicit procedure with artificial compressibility as discussed in the above section and we have a second choice of using the CBS algorithm in its semi-implicit form with $0.5 \leq \theta_1 \leq 1.0$ and $0.5 \leq \theta_2 \leq 1$ (Chapter 3, Section 3.4.2) [4]. This of course will use an explicit solution for the momentum equation followed by solution of the pressure Laplacian form (the Poisson equation). The solution which has to be obtained implicitly involves only the pressure variable [Eq. (3.56)] and we will further notice that, from the contents of Chapter 3, at each step the basic equation remains unchanged and therefore the solution can be repeated simply with different right-hand side vectors.

The convergence rate to steady state of course depends on the time step used and here we have the time step limitation given by the Courant number

$$\Delta t_1 \leq \Delta t_{\text{crit}} = \frac{h}{|\mathbf{u}|} \quad (4.7)$$

for inviscid problems and for viscous problems

$$\Delta t_2 \leq \Delta t_{\text{crit}} = \frac{h^2}{2\nu} \quad (4.8)$$

is an additional limitation. Here we note immediately that the viscosity lowers the limit quite substantially and therefore convergence to steady state may not be exceedingly rapid. The examples which we shall show nevertheless indicate its good performance.

Example 4.1. Incompressible flow in a lid-driven cavity

The classical problem on which we shall judge the performance is that of the closed cavity driven by the motion of a lid [5–9]. There are various ways of assuming

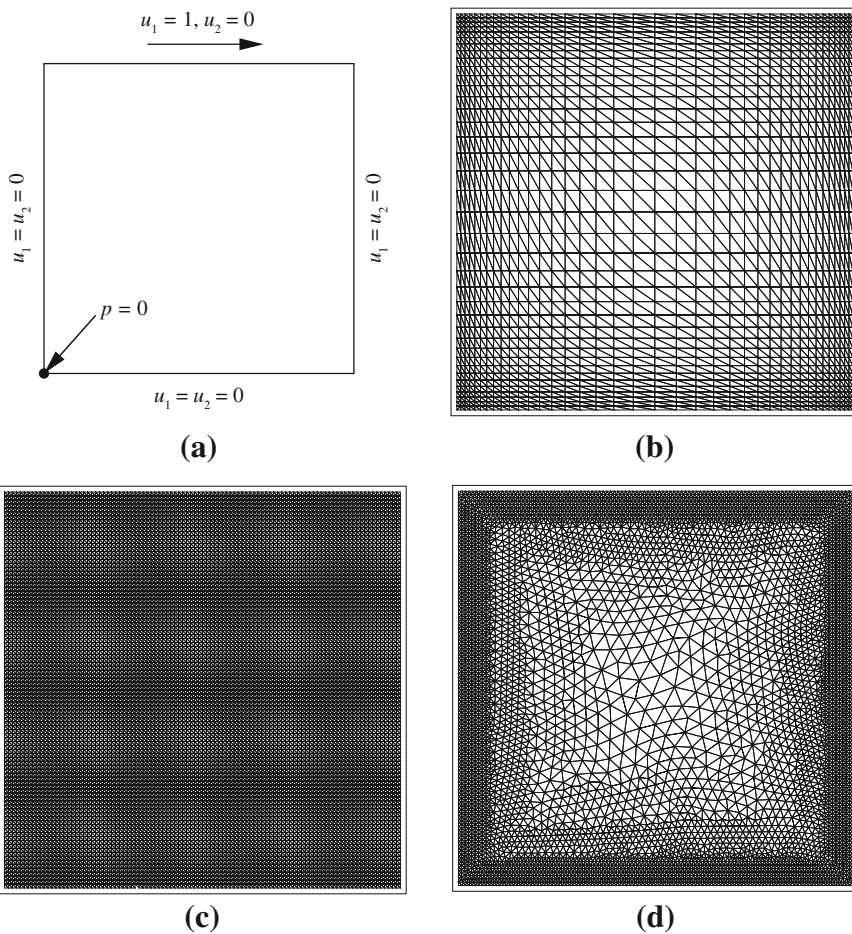
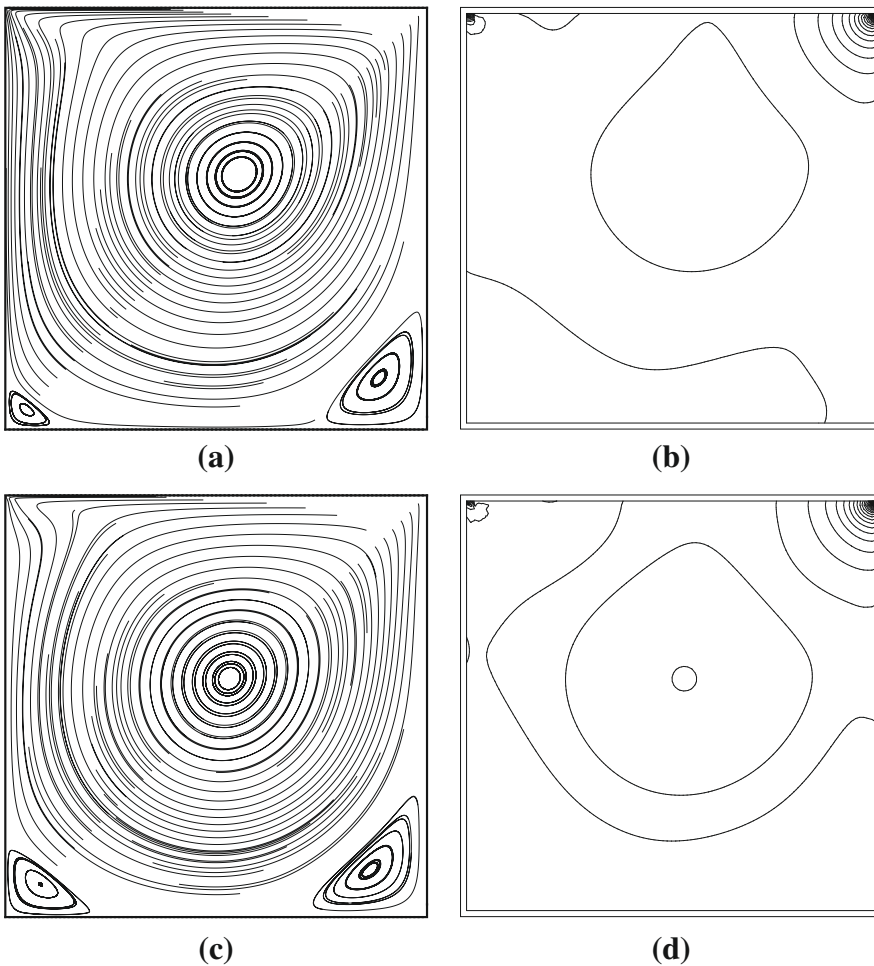


FIGURE 4.1

Incompressible flow in a lid-driven cavity. Geometry and meshes. (a) Geometry and boundary conditions; (b) nonuniform structured mesh (elements: 2888, nodes: 1521); (c) uniform structured mesh (elements: 20,000, nodes: 10,201); (d) nonuniform unstructured mesh (elements: 10,596, nodes: 5515).

the boundary conditions but the most common is one in which the velocity along the top surface increases from the corner node to the driven value in the length of one element (so-called ramp conditions).¹ The solution was obtained for different values of Reynolds number thus testing the performance of the viscous formulation.

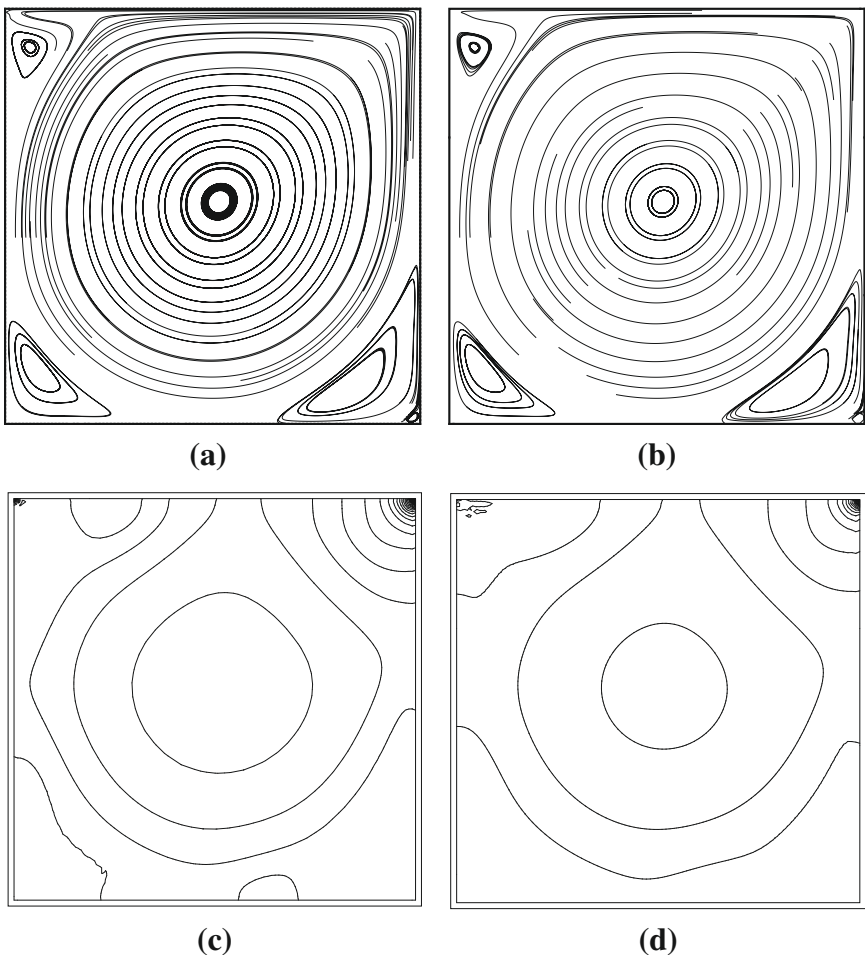
¹Some investigators use the leaking lid formulation in which the velocity along the top surface is constant and varies to zero within an element in the sides. It is preferable however to use the formulation where velocity is zero on all nodes of the vertical sides.

**FIGURE 4.2**

Incompressible flow in a lid-driven cavity: (a) $Re = 100$, stream traces; (b) $Re = 100$, pressure contours; (c) $Re = 400$, stream traces, (d) $Re = 400$, pressure contours.

The problem has been studied by many investigators but probably the most detailed early investigation was that of Ghia et al. [5] in which they quote many solutions and data for different Reynolds numbers. We shall use those results for comparison.

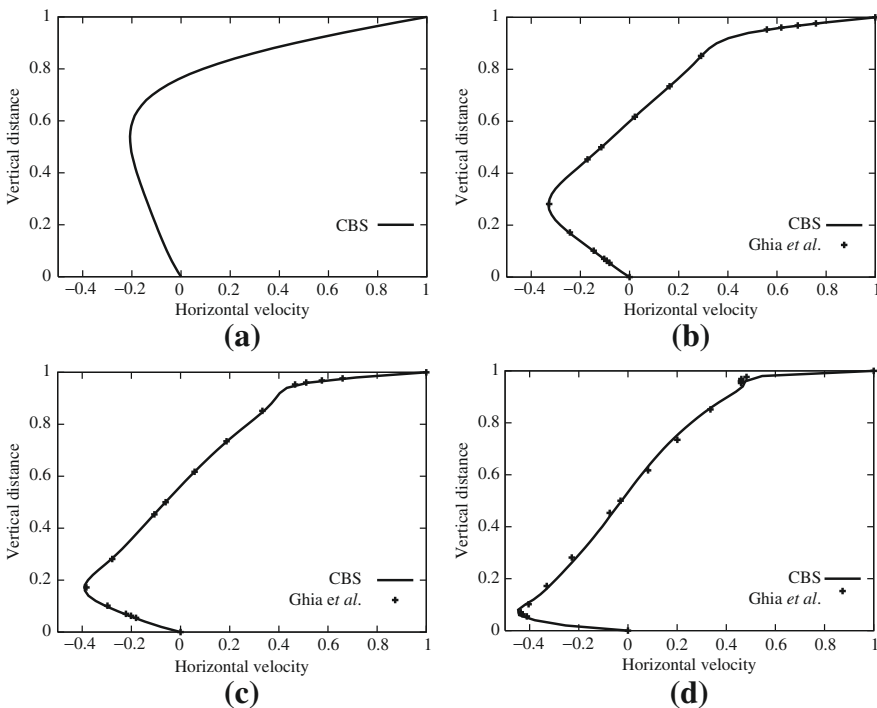
In the first figure, Fig. 4.1, we show the geometry, boundary conditions, and finite element meshes. The problem definition is shown in Fig. 4.1a. The top lid of the cavity is assumed to move with a prescribed velocity in one direction and all other walls are stationary. No-slip conditions for velocity are applied on all solid walls. Pressure is prescribed at one point as shown in Fig. 4.1a. Several meshes have been tested in the past [2] but only three meshes are shown in Fig. 4.1. The first mesh is

**FIGURE 4.3**

Incompressible flow in a lid-driven cavity: (a) $Re = 5000$, stream traces on the unstructured mesh; (b) $Re = 5000$, stream traces on the uniform structured mesh; (c) $Re = 5000$, pressure contours on the unstructured mesh; (d) $Re = 5000$, pressure contours on the uniform structured mesh.

a nonuniform structured mesh with smaller elements close to the walls. The second mesh is a uniform structured mesh of 100×100 size and the last mesh given in Fig. 4.1 is a nonuniform unstructured mesh with higher resolution close to the cavity walls.

Figure 4.2 shows the stream traces and pressure contours for $Re = 100$ and 400 generated from the unstructured mesh shown in Fig. 4.1d. As seen the results are smooth and free of oscillations. Expected secondary vortices on both bottom corners are predicted excellently by the scheme. In Fig. 4.3 the results produced by the

**FIGURE 4.4**

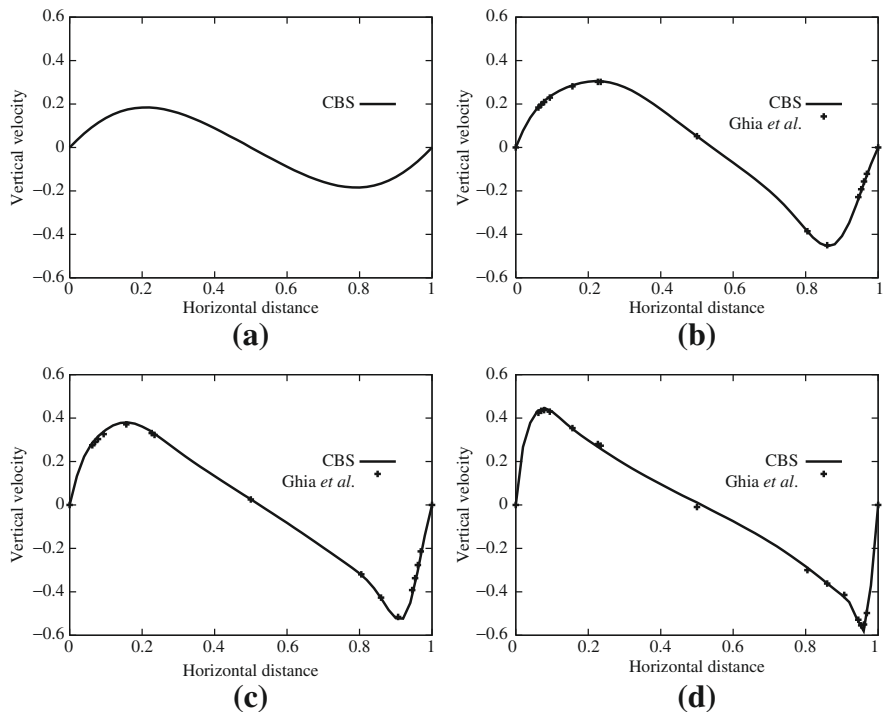
Incompressible flow in a lid-driven cavity. Horizontal velocity distribution at different Reynolds numbers: (a) $Re = 0$; (b) $Re = 400$; (c) $Re = 1000$; (d) $Re = 5000$.

unstructured mesh (Fig. 4.1d) and uniform structured mesh (Fig. 4.1c) are compared for a Reynolds number of 5000. As noticed both the results are smooth and in good agreement with the other reported results. The important aspect of this figure is that a small corner vortex at the bottom right corner, which normally requires a very high mesh resolution, has been predicted by the CBS scheme.

The horizontal and vertical velocity component distributions are shown in Figs. 4.4 and 4.5. All the results in these figures are produced using the unstructured mesh (Fig. 4.1d). As noted the results are in excellent agreement with the benchmark fine mesh (121×121) solutions reported by Ghia et al. [5].

A three-dimensional lid-driven cavity solution is shown in Fig. 4.6 at $Re = 400$. As seen the solutions obtained are smooth and the velocity distribution is in good agreement with the 2D results. However, it should be noted that at higher Reynolds numbers (>1000) no steady state exists and the results show a fully three-dimensional solution [3, 8, 9].

Figure 4.7 gives the steady-state convergence histories of the lid-driven cavity problem for semi-implicit and fully explicit schemes. The L_2 norm of velocity residual

**FIGURE 4.5**

Incompressible flow in a lid-driven cavity. Vertical velocity distribution at different Reynolds numbers: (a) $Re = 0$; (b) $Re = 400$; (c) $Re = 1000$; (d) $Re = 5000$.

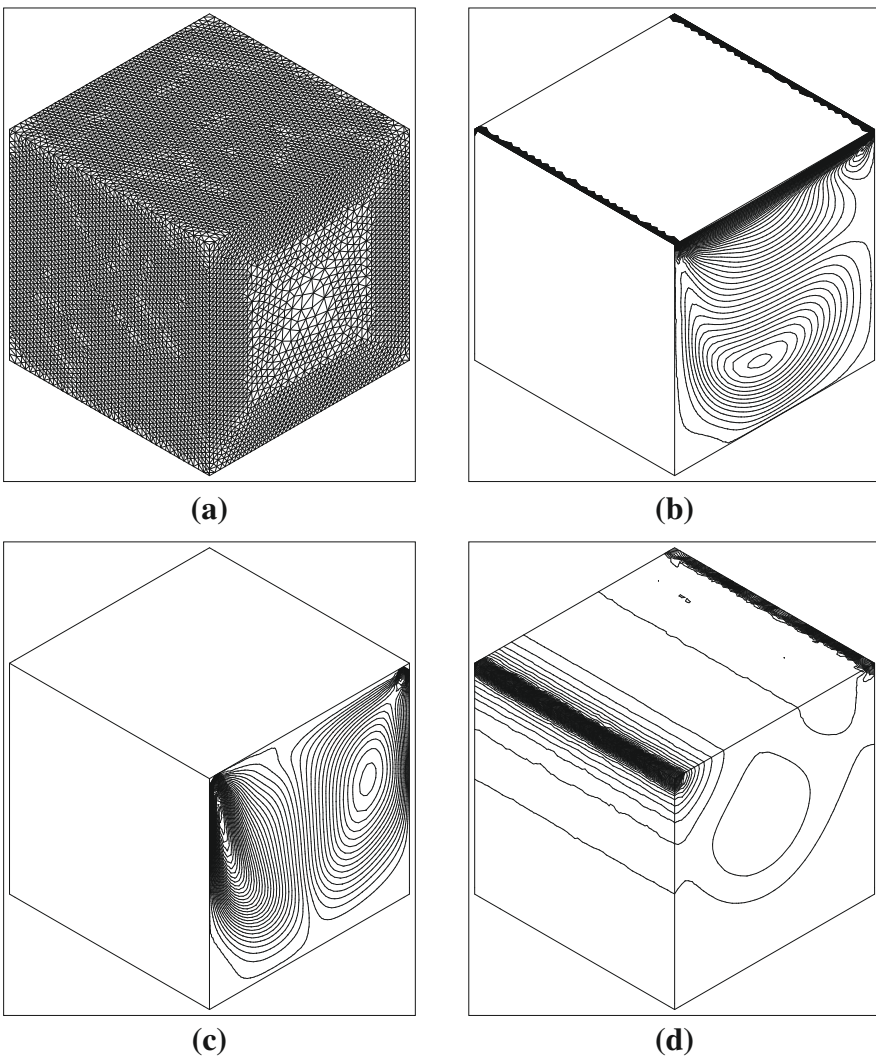
is calculated as

$$\frac{\sum_{i=1}^{No.\,Nodes} \sqrt{(|\mathbf{u}|^{n+1} - |\mathbf{u}|^n)^2}}{\sum_{i=1}^{No.\,Nodes} \sqrt{(|\mathbf{u}|^{n+1})^2}} \quad (4.9)$$

A steady state was assumed when the above L_2 norm reached a value below 10^{-5} . It is clear from Fig. 4.7 that both the fully explicit and semi-implicit schemes converge almost at the same rate at $Re = 5000$. However, at $Re = 400$, the convergence rate of the semi-implicit form is slightly better than that of the fully explicit scheme. Both the results were produced using local time stepping.

Example 4.2. Steady flow past a backward facing step

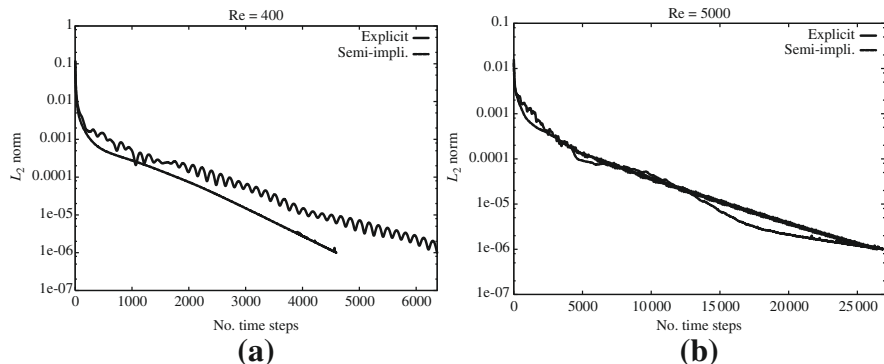
In this example, another widely used benchmark problem of flow past a backward facing step is considered [10]. The problem definition is shown in Fig. 4.8. The inlet is situated at a distance of four times the step height from the step. The inlet height is twice the height of the step itself. The total length is 40 times the height of the step. The inlet Reynolds number based on the step height and the average inlet velocity is 229.

**FIGURE 4.6**

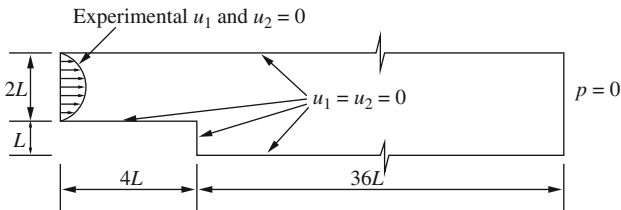
Incompressible flow in a 3D lid-driven cavity. Mesh and contours at $\text{Re} = 400$: (a) unstructured mesh; (b) u_1 contours; (c) u_3 contours; (d) pressure contours.

At the inlet a nearly parabolic horizontal velocity profile (experimental) is assumed and the vertical velocity component is assumed to be equal to zero. On the walls no-slip boundary conditions apply and at the exit constant (zero) pressure conditions are prescribed.

In Fig. 4.9, the unstructured mesh used and the contours of the horizontal velocity component and pressure are given. The mesh is finer near the walls and coarser away

**FIGURE 4.7**

Lid-driven cavity. Steady-state convergence histories for (a) $Re = 400$ and (b) 5000. Comparison between fully explicit and semi-implicit schemes.

**FIGURE 4.8**

Incompressible flow past a backward facing step. Geometry and boundary conditions.

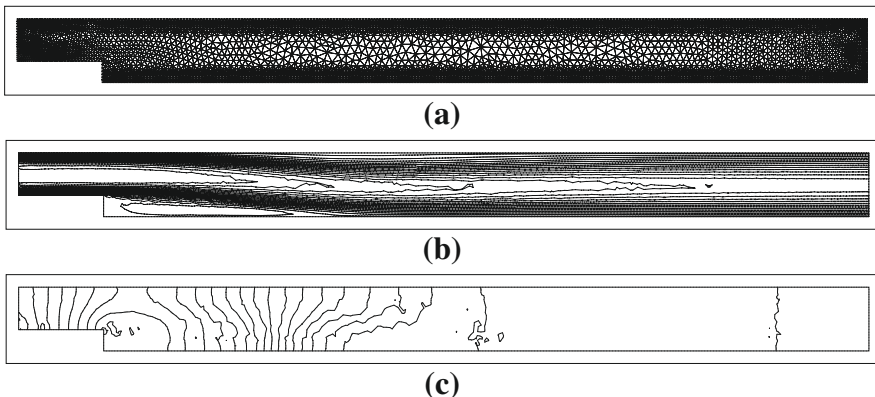
from the walls. The variable distribution shown in Fig. 4.9b and c is in good agreement with the available data.

In Fig. 4.10, the numerical data are compared against the experimental data in the recirculation zone. As seen the agreement between the numerical and experimental data [10] is excellent.

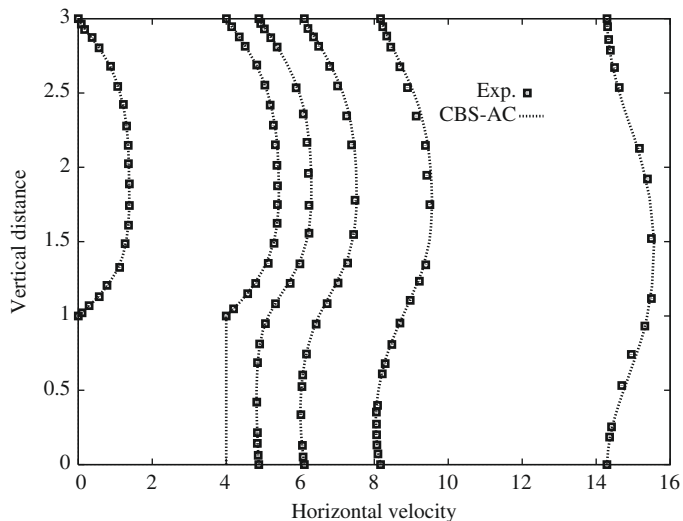
Example 4.3. Steady flow past a sphere

The next problem considered is fully three-dimensional and shows flow past a sphere. The computational domain is a rectangular imaginary box of length $25D$, where D is the diameter of the sphere, with the downstream boundary located $20D$ from the center of the sphere. The four side walls are located at a distance of $5D$ from the center of the sphere. All four confinement walls are assumed to be slip walls with normal velocity equal to zero. The inlet velocity is assumed to be uniform and the no-slip condition prevails on the sphere surface. This problem is solved using the fully explicit form of the CBS scheme.

For this problem, an unstructured grid containing 953,025 tetrahedral elements has been used. This mesh is generated using the mesh generator developed in Swansea [11–14]. Figure 4.11a shows a portion of the surface mesh and Fig. 4.11b shows a

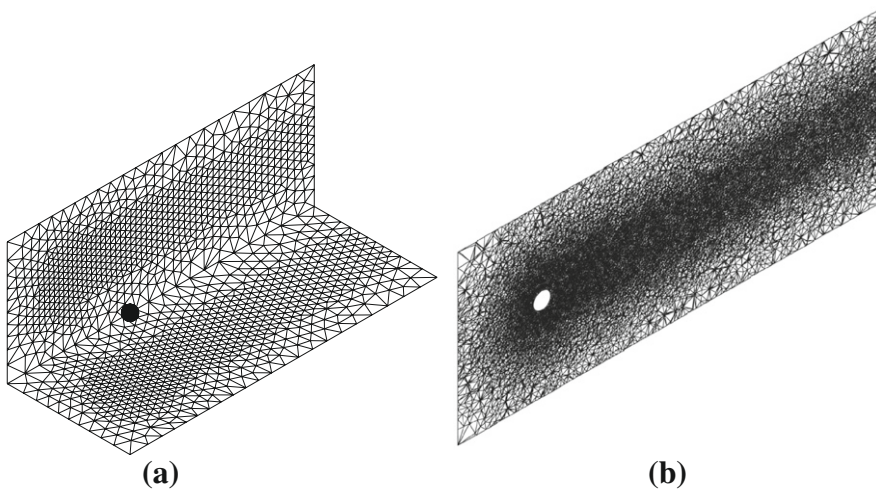
**FIGURE 4.9**

Incompressible flow past a backward facing step: (a) unstructured mesh; (b) u_1 velocity contours; (c) pressure contours ($Re = 229$).

**FIGURE 4.10**

Incompressible flow past a backward facing step. Comparison between experimental [10] and numerical data, $Re = 229$.

sectional view. The mesh is refined close to the sphere surface and in the rear where recirculation is expected. Figure 4.12 shows the contours of the u_1 component of the velocity and the pressures computed at Reynolds numbers of 100 and 200. The coefficient of pressure, C_p , values on the surface along the flow axis are shown in

**FIGURE 4.11**

Incompressible flow past a sphere: (a) unstructured mesh; (b) unstructured mesh, cross section.

Fig. 4.13. The nondimensional C_p is calculated as

$$C_p = 2(p - p_{ref}) \quad (4.10)$$

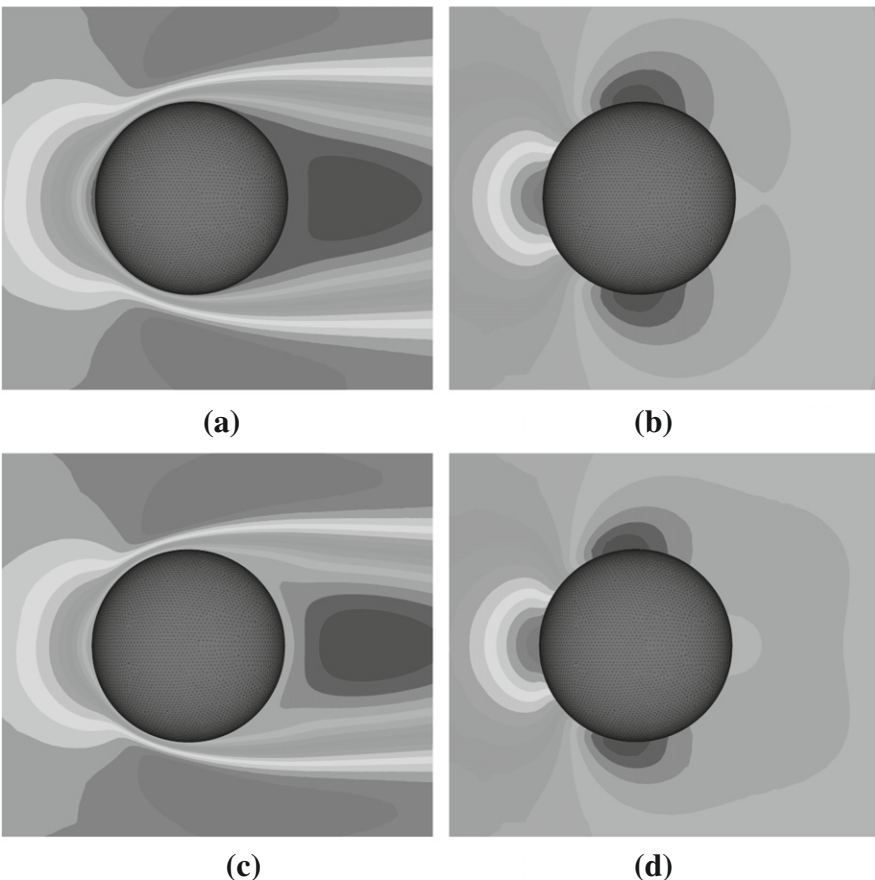
Note that the results used for comparison were generated using very fine structured meshes [15, 16]. It should also be noted that all the results differ from each other close to any separation zone.

Example 4.4. Transient flow past a circular cylinder

This is a popular test case for validating the transient part of numerical schemes. Many other problems of interest can also be solved for transient accuracy but in this section only flow over a single circular cylinder is considered.

Problem definition is standard. The inlet flow is uniform and the cylinder is placed at the centerline between two slip walls. The distances from the inlet and slip walls to the center of the cylinder are $4D$, where D is the diameter of the cylinder. The total length of the domain is $16D$. A no-slip condition is applied on the cylinder surface. The initial values of horizontal velocity were assumed to be unity and the vertical component of velocity was assumed to be zero all over the domain.

Figure 4.14 shows the mesh used in two dimensions and the solution obtained. As seen the mesh close to the cylinder is very fine in order to capture the boundary layer and separation. **Figure 4.14b** and c show the time history of the vertical velocity component at the mid-exit point and the drag coefficient. Both the histories are in good agreement with many reported results.

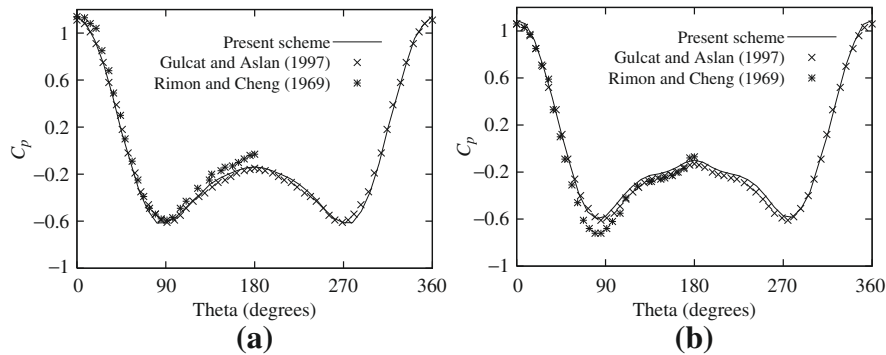
**FIGURE 4.12**

Incompressible flow past sphere: (a) u_1 contours, $Re = 100$; (b) pressure contours, $Re = 100$; (c) u_1 contours, $Re = 200$; pressure contours, $Re = 200$.

4.2.3 Quasi-implicit solution

We have already remarked in [Chapter 3](#) that the reduction of the explicit time step due to viscosity can be very inconvenient and may require a larger number of time steps. The example of the cavity is precisely in that category and at higher Reynolds numbers the reader will certainly note a very large number of time steps which have to be performed before results become reasonably steady. In quasi-implicit form, the viscous terms of the momentum equations are treated implicitly [18]. Here the time step is governed only by the relation given in [Eq. \(4.7\)](#).

It is also possible to incorporate dual time stepping into the quasi-implicit method (or semi-implicit method) as discussed in [Chapter 3](#). Such a formulation allows us

**FIGURE 4.13**

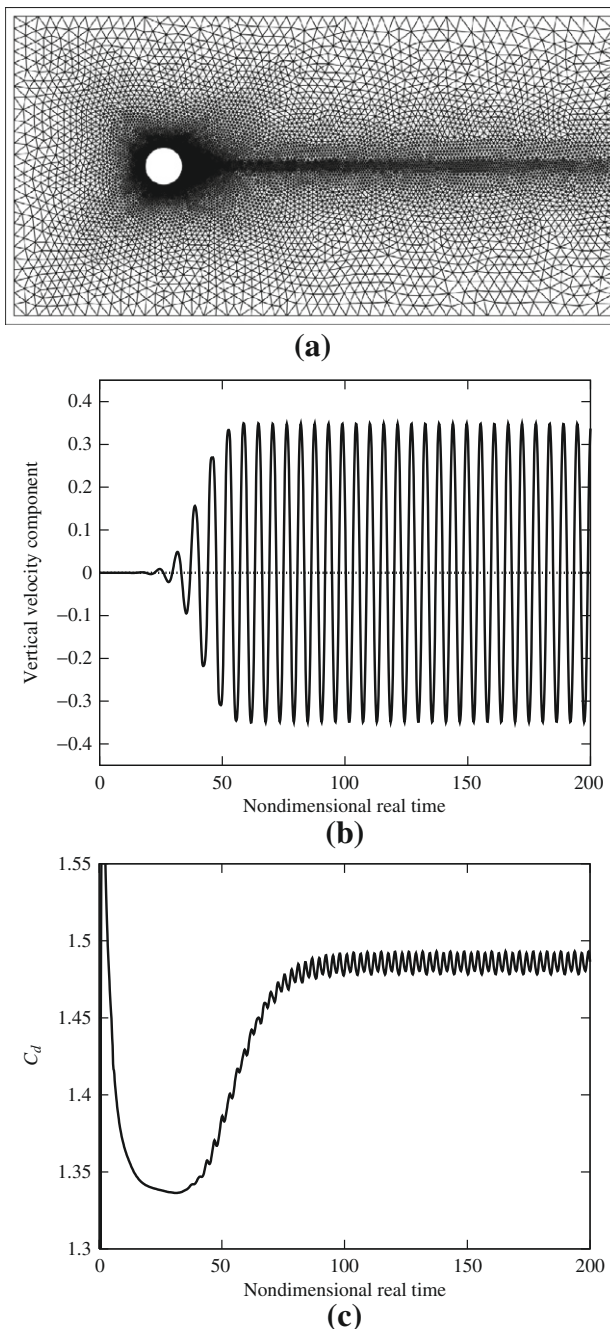
Incompressible flow past a sphere. Coefficient of pressure distribution on the surface along the flow direction [15–17]: (a) $\text{Re} = 100$; (b) $\text{Re} = 200$.

to use a locally defined pseudo time step to accelerate the solution to instantaneous or final steady state. Calculations show that a substantial savings in computational time can be achieved using such a formulation for both steady and unsteady problems [19]. To demonstrate this, steady flow in the lid-driven cavity is reconsidered here at a Reynolds number of 1000 [5]. The nonuniform structured mesh employed consists of 28,800 linear triangular elements and 14,641 nodes. The mesh is refined in the vicinity of the boundaries, with an area ratio of 365 between the largest and smallest elements. Figure 4.15 presents the horizontal and vertical velocity distributions along mid-vertical and mid-horizontal cuts, respectively. As seen, the results from both the global and local time stepping schemes are in excellent agreement with each other and with those predicted by Ghia et al. [5].

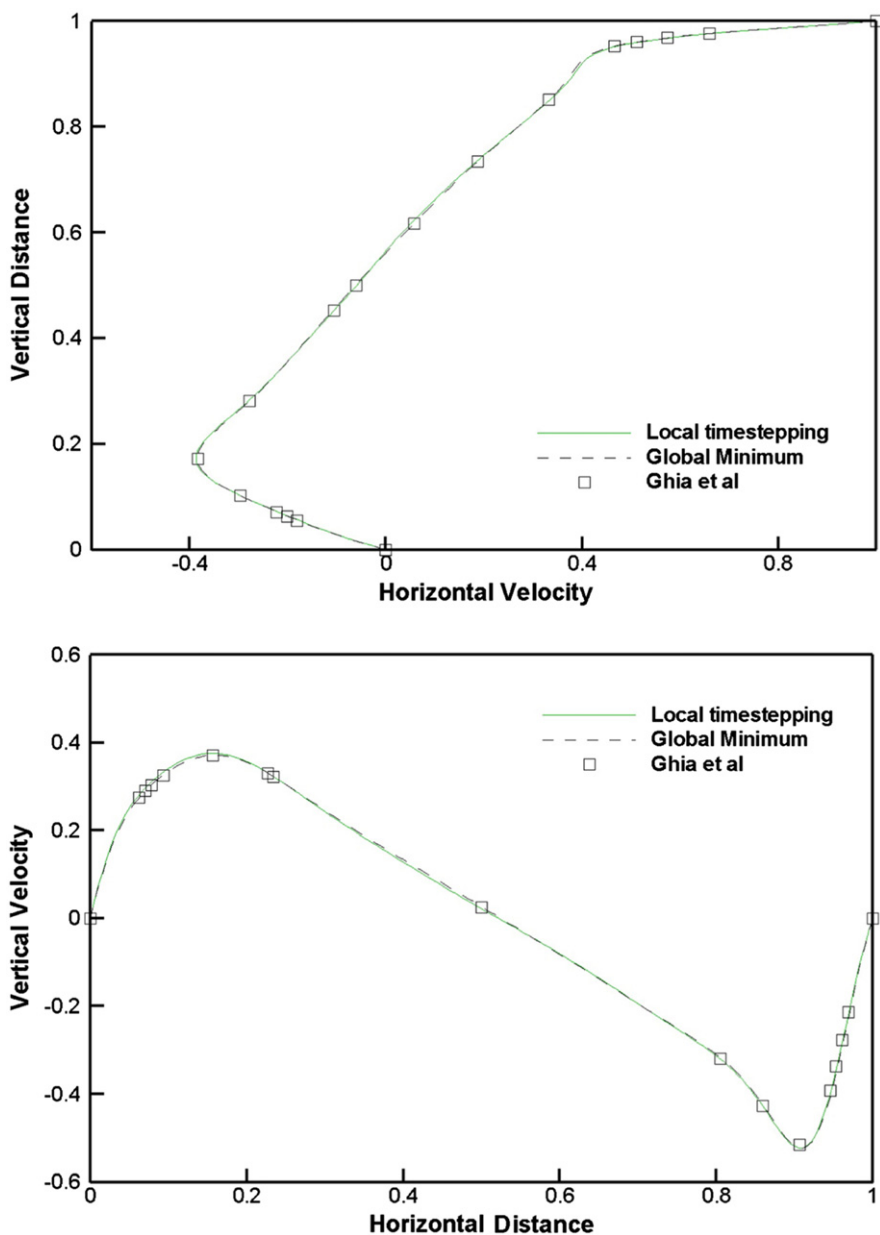
From the quantitative results in Fig. 4.15 and Table 4.1, it is clear that the local time-stepping approach provides almost identical results to that of the global time-stepping approach. However, the computational cost is significantly different as presented in Table 4.2. A single core of an Intel Nehalem quad-core (3 GHz) CPU was employed. From the table, the local time stepping-based quasi-implicit scheme requires only 18.5% of the computational cost. Thus, the speed-up advantage of the local time stepping is clear in this case. Such a reduction in computational time is also possible for transient problems [19].

4.3 Adaptive mesh refinement

We have discussed the matter of adaptive refinement in Chapters 15 and 16 of Ref. [1] in some detail. In that reference generally an attempt is made to keep energy norm error constant within all elements. The same procedures concerning the energy norm error can be extended of course to viscous flow especially when this is relatively slow and the problem is nearly elliptic. However, the energy norm has little significance

**FIGURE 4.14**

Transient flow past a circular cylinder, $Re = 100$: (a) unstructured mesh; (b) vertical velocity fluctuation at the exit mid-point; (c) drag history.

**FIGURE 4.15**

Lid-driven cavity. Horizontal and vertical velocity distributions along the centerline cross-sections, $Re = 1000$.

Table 4.1 Lid-Driven Cavity Problem: Predicted Vortex Locations and Comparison with the Simulation of Ghia et al. [5], Re = 1000

Location	Primary Vortex		Bottom Right (First Vortex)	
	x	y	x	y
Ghia et al.	0.531	0.562	0.859	0.109
Global minimum	0.532	0.566	0.865	0.112
Local time stepping	0.531	0.566	0.862	0.114

Table 4.2 Lid-Driven Cavity: Computational Cost, Re = 1000

	Run Time (s)
Global minimum	7532.1
Local time stepping	1396.2

at high speeds and here we revert to other considerations which simply give an *error indicator* rather than an error estimator. Two procedures are available and will be used in this chapter as well as later when dealing with compressible flows. References [11, 12, 14, 20–82] list some of the many contributions to the field of adaptive procedures and mesh generation in fluid dynamics.

4.3.1 Second gradient (curvature) based refinement

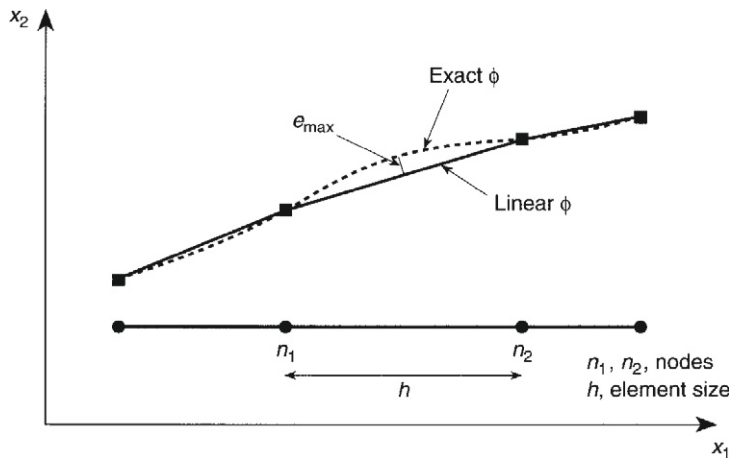
Here the meaning of error analysis is somewhat different from that of the energy norm and we follow an approach where the error value is constant in each element. In what follows we shall consider first-order (linear) elements and the so-called h refinement process in which increased accuracy is achieved by variation of element size. The p refinement in which the order of the element polynomial expression is changed is of course possible. Many studies are available on hp refinements where both h and p refinements are carried out simultaneously. This has been widely studied by Oden et al. [27, 28, 43, 44] but we believe that such refinements impose many limitations on mesh generation and solution procedures and as most fluid mechanics problems involve an explicit time marching algorithm, the higher-order elements are not popular.

The determination of error indicators in linear elements is achieved by consideration of the so-called *interpolation error*. Thus if we take a one-dimensional element of length h and a scalar function ϕ , it is clear that the error in ϕ is of order $O(h^2)$ and that it can be written as (see Ref. [21] for details)

$$e = \phi - \phi^h = ch^2 \frac{d^2\phi}{dx^2} \approx ch^2 \frac{d^2\phi^h}{dx^2} \quad (4.11)$$

where ϕ^h is the finite element solution and c is a constant.

If, for instance, we further assume that $\phi = \phi^h$ at the nodes, i.e., that the nodal error is zero, then e represents the values on a parabola with a curvature of $d^2\phi^h/dx^2$. This

**FIGURE 4.16**

Interpolation error in a one-dimensional problem with linear shape functions.

allows c , the unknown constant, to be determined, giving for instance the maximum interpolation error as (see Fig. 4.16)

$$e_{\max} = \frac{1}{8}h^2 \frac{d^2\phi^h}{dx^2} \quad (4.12)$$

or an RMS departure error as

$$e_{\text{RMS}} = \frac{1}{\sqrt{120}}h^2 \frac{d^2\phi^h}{dx^2} \quad (4.13)$$

In deducing Eqs. (4.12) and (4.13), we have assumed that the nodal values of the function ϕ are exact. As is shown in Ref. [1] this is true only for some types of interpolating functions and equations. However the nodal values are always more accurate than those noted elsewhere and it would be sensible even in one-dimensional problems to strive for equal distribution of such errors. This would mean that we would now seek an element subdivision in which

$$h^2 \frac{d^2\phi^h}{dx^2} = C \quad (4.14)$$

To appreciate the value of the arbitrary constant C occurring in Eq. (4.14) we can interpret this as giving a permissible value of the limiting interpolation error and simply insisting that

$$h^2 \frac{d^2\phi^h}{dx^2} \leq e_p \quad (4.15)$$

where $e_p = C$ is the user-specified error limit.

If we consider the shape functions of ϕ to be linear then of course second derivatives are difficult quantities to determine. These are clearly zero inside every element and infinity at the element nodes in the one-dimensional case or element interfaces in two or three dimensions. Some averaging process has therefore to be used to determine the curvatures from nodally computed values. Before discussing, however, the procedures used for this, we must note the situation which will occur in two or three dimensions.

The extension to two or three dimensions is of course necessary for practical engineering problems. In two and three dimensions the second derivatives (or curvatures) are tensor valued and given as

$$\frac{\partial^2 \phi}{\partial x_i \partial x_j} \quad (4.16)$$

and such definitions require the determination of the *principal values* and directions. These principal directions are necessary for element elongation, which is explained in the following section.

The determination of the curvatures (or second derivatives) of ϕ^h needs of course some elaboration. With linear elements (e.g., simple triangles or tetrahedra) the curvatures of ϕ^h which are interpolated as

$$\phi^h = \mathbf{N}\tilde{\phi} \quad (4.17)$$

are zero within the elements and become infinity at element boundaries. There are two convenient methods available for the determination of curvatures of the approximate solution which are accurate and effective. Both of these follow some of the matter discussed in Chapter 15 of Ref. [1] and are concerned with recovery. We shall describe them separately.

4.3.2 Local patch interpolation: Superconvergent values

In the first method we simply assume that the values of the function such as pressure or velocity converge at a rate which is one order higher at nodes than that achieved at other points of the element. If indeed such values are more accurate it is natural that they should be used for interpreting the curvatures and the gradients. Here the simplest way is to assume that a second-order polynomial is used to interpolate the nodal values in an element patch which uses linear elements. Such a polynomial can be applied in a least-squares manner to fit the values at all nodal points occurring within a patch which assembles the approximation at a particular node. For triangles this rule requires at least five elements that are assembled in a patch and this is a matter easily achieved. The procedure of determining such least squares is given fully in Chapter 15 of Ref. [1] and will not be discussed here. However once a polynomial distribution of say ϕ is available then immediately the second derivatives of that function can be calculated at any point, the most convenient one being of course the point referring to the node which we require.

On occasion, as we shall see in other processes of refinement, it is not the curvature which is required but the gradient of the function. Again the maximum value of the gradient, for instance of ϕ , can easily be determined at any point of the patch and in particular at the nodes.

4.3.3 Estimation of second derivatives at nodes

In this method we assume that the second derivative is interpolated in exactly the same way as the main function and write the approximation as

$$\left(\frac{\partial^2 \phi}{\partial x_i \partial x_j} \right)^h = \mathbf{N} \overline{\left(\frac{\partial^2 \phi}{\partial x_i \partial x_j} \right)^*} \quad (4.18)$$

This approximation is made to be a weighted residual approximation to the actual distribution of curvatures, i.e.,

$$\int_{\Omega} \mathbf{N}^T \left[\mathbf{N} \overline{\left(\frac{\partial^2 \phi}{\partial x_i \partial x_j} \right)^*} - \frac{\partial^2 \phi^h}{\partial x_i \partial x_j} \right] d\Omega = 0 \quad (4.19)$$

and integrating by parts to give

$$\overline{\left(\frac{\partial^2 \phi}{\partial x_i \partial x_j} \right)^*} = \mathbf{M}^{-1} \left(\int_{\Omega} \mathbf{N}^T \frac{\partial^2 \phi^h}{\partial x_i \partial x_j} \right) d\Omega = -\mathbf{M}^{-1} \left(\int_{\Omega} \frac{\partial \mathbf{N}^T}{\partial x_i} \frac{\partial \mathbf{N}}{\partial x_j} d\Omega \right) \tilde{\boldsymbol{\phi}} \quad (4.20)$$

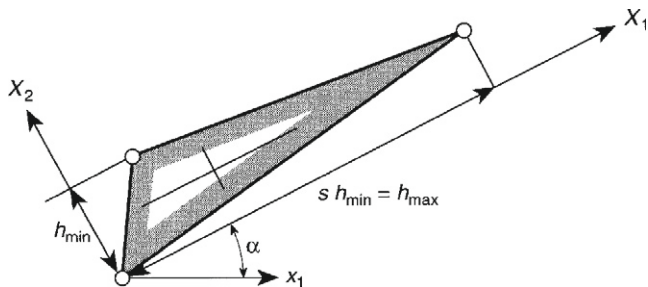
where \mathbf{M} is the mass matrix given by

$$\mathbf{M} = \int_{\Omega} \mathbf{N}^T \mathbf{N} d\Omega \quad (4.21)$$

which of course can be “lumped.”

4.3.4 Element elongation

Elongated elements are frequently introduced to deal with “one-dimensional” phenomena such as shocks, boundary layers, etc. The first paper dealing with such elongation was presented as early as 1987 by Peraire et al. [21]. But the possible elongation was limited by practical considerations if a general mesh of triangles was to be used. An alternative to this is to introduce a locally structured mesh in shocks and boundary layers which connects to the completely unstructured triangles. This idea has been extensively used by Hassan et al. [11, 47, 48], Zienkiewicz and Wu [42], and Marchant et al [56] in the compressible flow context. In both procedures it is necessary to establish the desired elongation of elements. Obviously in completely parallel flow phenomena no limit on elongation exists but in a general field the elongation ratio defining the maximum to minimum size of the element can be derived by considering curvatures of the contours. Thus the local error is proportional to the curvature and making h^2 times the curvature equal to a constant, we immediately derive the ratio h_{\max}/h_{\min} .

**FIGURE 4.17**

Element elongation δ and minimum and maximum element sizes.

In Fig. 4.17, X_1 and X_2 are the directions of the minimum and maximum principal values of the curvatures. Thus for an equal distribution of the interpolation error we can write for each node²

$$h_{\min}^2 \left| \frac{\partial^2 \phi}{\partial X_2^2} \right| = h_{\max}^2 \left| \frac{\partial^2 \phi}{\partial X_1^2} \right| = C \quad (4.22)$$

which gives us the stretching ratio s as

$$s = \frac{h_{\max}}{h_{\min}} = \sqrt{\frac{\left| \frac{\partial^2 \phi}{\partial X_2^2} \right|}{\left| \frac{\partial^2 \phi}{\partial X_1^2} \right|}} \quad (4.23)$$

With the relations given above, we can formulate the following steps to adaptively refine a mesh:

1. Find the solution using an initial coarse mesh.
2. Select a suitable representative scalar variable and calculate the local maximum and minimum curvatures and directions of these at all nodes.
3. Calculate the new element sizes at all nodes from the maximum and minimum curvatures using the relation in Eq. (4.22).
4. Calculate the stretching ratio from the ratio of the calculated maximum to minimum element sizes [Eq. (4.23)]. If this is very high, limit it by a maximum allowable value.
5. Remesh the whole domain based on the new element size, stretching ratios, and the direction of stretching.

²Principal curvatures and directions can be found in a manner analogous to that of the determination of principal stresses and their directions. Procedures are described in standard engineering texts.

To use the above procedure, an efficient unstructured mesh generator is essential. We normally use the advancing front technique operating on the background mesh principle [21] in most of the examples presented here.³ The information from the previous solution in the form of local mesh sizes, stretching ratio, and stretching direction are stored in the previous mesh and this mesh is used as a background mesh for the new mesh.

In the above steps of anisotropic mesh generation, to avoid very small and large elements (especially in compressible flows), the minimum and maximum allowable sizes of the elements are given as inputs. The maximum allowable stretching ratio is also supplied to the code to avoid bad elements in the vicinity of discontinuities. It is generally useful to know the minimum element size used in a mesh as many flow solvers are conditionally stable. In such solvers the time step limitation depends very much on the element size.

The procedure just described for an elongated element can of course be applied for the generation of isotropic meshes simply by taking the maximum curvature at every point.

The matter to which we have not yet referred is that of suitably choosing the variable ϕ to which we will wish to assign the error. We shall come back to this matter later but it is clear that this has to be a well-representative quantity available from the choice of velocities, pressures, temperature, etc.

4.3.5 First derivative (gradient) based refinement

The nature of the fluid flow problems is elliptic in the vicinity of the boundaries often forming so-called viscous boundary layers though some distance from the boundaries the equations become almost hyperbolic. For such hyperbolic problems it is possible to express the propagation type error in terms of the gradient of the solution in the domain. In such cases the error can be considered as

$$h \frac{\partial \phi}{\partial n} = C \quad (4.24)$$

where n is the direction of maximum gradient and h is the element size (minimum size) in the same direction. The above expression can be used to determine the minimum element size at all nodes or other points of consideration in exactly the same manner as was done when using the curvature. However the question of stretching is less clear. At every point a maximum element size should be determined. One way of doing this is of course to return to the curvatures and find the curvature ratios. Another procedure to determine the maximum element size is described by Zienkiewicz and Wu [42]. In this the curvature of the streamlines is considered and h_{\max} is calculated as

$$h_{\max} \leq \delta R \quad (4.25)$$

³Another successful unstructured mesh generator is based on Delaunay triangulation. The reader can obtain more information by consulting Refs. [12, 14, 51–53, 74, 76, 79–81].

where R is the radius of curvature of the streamline and δ is a constant that varies between 0 and 1. Immediately the ratio between the maximum and minimum element size gives the stretching ratio.

4.3.6 Choice of variables

In both methods of mesh refinement, i.e., those following curvatures and those following gradients, a particular scalar variable needs to be chosen to define the mesh. The simplest procedure is to consider only one of the many variables and here the one which is efficient is simply the absolute value of the velocity vector, i.e., $|\mathbf{u}|$. Such a velocity is convenient both for problems of incompressible flow and, as we shall see later, for problems of compressible flow where local refinement is even more important than here. (Very often in compressible flows the Mach number, which in a sense measures the same quantity, has been used.)

Of course other variables can be chosen or any combination of variables such as velocities, pressures, temperatures, etc., can be used. Certainly in this chapter the absolute velocity is the most reasonable criterion. Some authors have considered using each of the problem variables to generate a new mesh [45, 52, 53, 60, 83]. However this is rather expensive and we believe velocity alone can give accurate results in most cases.

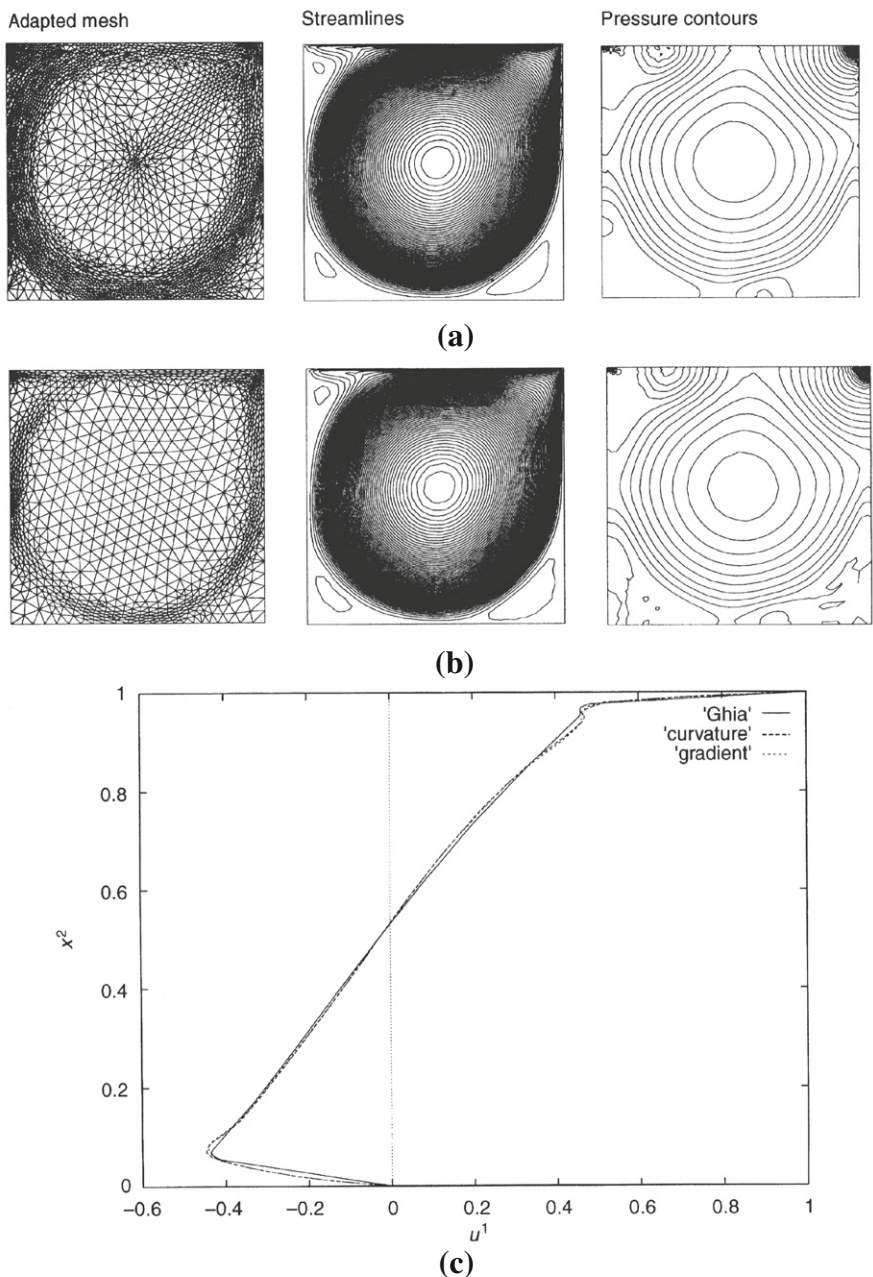
4.3.7 An example

Here we show an example of an incompressible flow problem solved using the above-mentioned adaptive mesh generation procedures. In the first problem of driven flow in a cavity which we have previously examined is again used. We use an initial uniform mesh with 481 nodes and 880 elements. Final meshes and solutions obtained by both curvature- and gradient-based procedures are shown in Fig. 4.18. In general the curvature-based procedure gives a wide band of refined elements along the circulation path (Fig. 4.18a). However, the number of refined elements along the circulation path is smaller when the gradient-based refinement is used (Fig. 4.18b). Both the meshes give excellent comparison with the benchmark solution of Ghia et al. [5] (Fig. 4.18c).

In the adaptive solutions shown here we have not used any absolute value of the desired error norm as the definition of a suitable norm presents certain difficulties, though of course the use of an energy norm in the manner suggested in Ref. [1] could be adopted. We shall use such an error requirement in some later problems.

4.4 Adaptive mesh generation for transient problems

In the preceding sections we have indicated various adaptive methods using complete mesh regeneration with error indicators of the interpolation kind. Obviously other methods of mesh refinement can be used (mesh enrichment or r refinement) and other procedures of error estimation can be employed if the problem is nearly elliptic. One such study in which the energy norm is quite effectively used is reported by Wu

**FIGURE 4.18**

Lid-driven cavity, $Re = 5000$. Adapted meshes using curvature- and gradient-based refinements and solutions: (a) curvature-based procedure (nodes: 2389, elements: 4599); (b) gradient-based procedure (nodes: 1034, elements: 1962); (c) comparison of velocity at mid-vertical plane.

et al. [32]. In that study the full transient behavior of the *Von Karman* vortex street behind a cylinder was considered and the results are presented in Fig. 4.19.

In this problem, the mesh is regenerated at fixed time intervals using the energy norm error and the methodologies largely described in Chapter 16 of Ref. [1].

Similar procedures have been used by others and the reader can refer to these works [33,34].

4.5 Slow flows: Mixed and penalty formulations

4.5.1 Analogy with incompressible elasticity

Slow, viscous incompressible flow represents the extreme situation at the other end of the scale from the inviscid problem of Section 1.3. Here all dynamic (acceleration) forces are, *a priori*, neglected and Eqs. (4.1) and (4.2) reduce, in indicial form, to

$$\frac{\partial u_i}{\partial x_i} \equiv \dot{\varepsilon}_v = 0 \quad (4.26)$$

and

$$\frac{\partial \tau_{ij}}{\partial x_j} - \frac{\partial p}{\partial x_i} + \rho g_i = 0 \quad (4.27)$$

The above are completed of course by the constitutive relation

$$\tau_{ij} = \mu \left(\frac{\partial u_i}{\partial x_j} + \frac{\partial u_j}{\partial x_i} \right) \quad (4.28)$$

which is identical to the problem of incompressible elasticity in which we replace

- (a) The displacements by velocities
- (b) The shear modulus G by the viscosity μ
- (c) The mean stress by negative pressure

4.5.2 Mixed and penalty discretization

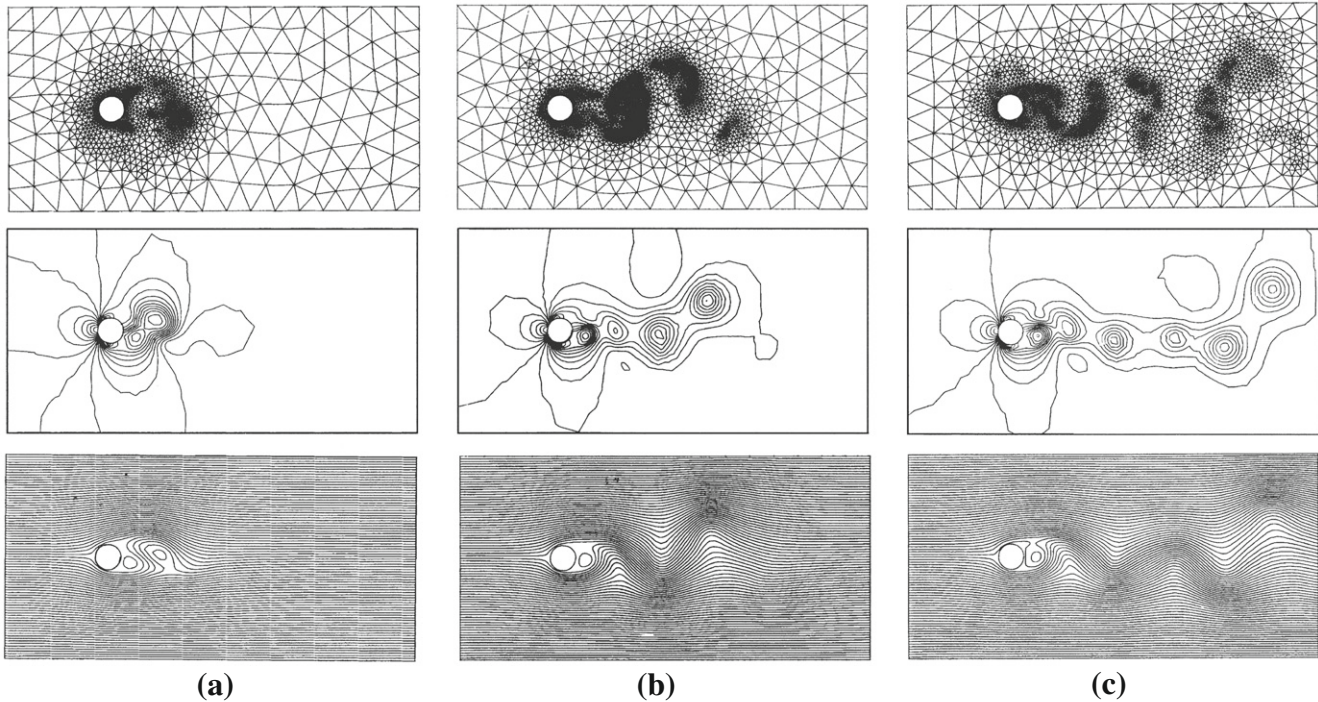
The discretization can be started from the *mixed form* with independent approximations of \mathbf{u} and p , i.e.,

$$\mathbf{u} = \mathbf{N}_u \tilde{\mathbf{u}} \quad p = \mathbf{N}_p \tilde{\mathbf{p}} \quad (4.29)$$

or by a penalty form in which Eq. (4.26) is augmented by p/γ where γ is a large penalty parameter

$$\mathbf{m}^T \mathcal{S} \mathbf{u} + \frac{p}{\gamma} = 0 \quad (4.30)$$

When suitable discontinuous \mathbf{N}_p are used, penalty terms computed using reduced integration are equivalent to the mixed form [84] (see Chapter 9 of Ref. [1] for details).

**FIGURE 4.19**

Transient incompressible flow around a cylinder at $Re = 250$. Adaptively refined mesh. Pressure contours and streamlines at various times after initiation of “vortex shedding”: (a) $t = 6$ s; (b) $t = 11.5$ s; (c) $t = 16.5$ s.

The use of penalty forms in fluid mechanics was introduced early in the 1970s [85–87] and is fully discussed elsewhere [88–90]. As computationally it is advantageous to use the mixed form and introduce the penalty parameter only to eliminate the $\tilde{\mathbf{p}}$ values at the element levels, we shall presume such penalization to be done after the mixed discretization.

The discretized equations will always be of the form

$$\begin{bmatrix} \mathbf{K} & -\mathbf{G} \\ -\mathbf{G}^T & -\mathbf{V}/\gamma \end{bmatrix} \begin{Bmatrix} \tilde{\mathbf{u}} \\ \tilde{\mathbf{p}} \end{Bmatrix} = \begin{Bmatrix} \bar{\mathbf{f}} \\ \mathbf{0} \end{Bmatrix} \quad (4.31)$$

in which

$$\begin{aligned} \mathbf{K} &= \int_{\Omega} \mathbf{B}^T \mu \mathbf{I}_0 \mathbf{B} d\Omega \quad \text{where } \mathbf{B} \equiv \mathcal{S} \mathbf{N}_u \\ \mathbf{G} &= \int_{\Omega} \mathbf{B}^T \mathbf{m} \mathbf{N}_p d\Omega, \quad \mathbf{V} = \int_{\Omega} \mathbf{N}_p^T \mathbf{N}_p d\Omega \\ \bar{\mathbf{f}} &= \int_{\Omega} \mathbf{N}_u^T \rho \mathbf{g} d\Omega + \int_{\Gamma_t} \mathbf{N}_u^T \bar{\mathbf{t}} d\Gamma \end{aligned} \quad (4.32)$$

and the penalty number, γ , is introduced purely as a numerical convenience. This is taken generally as [88, 90]

$$\gamma = (10^7 - 10^8) \mu$$

There is little more to be said about the solution procedures for creeping incompressible flow with constant viscosity. The range of applicability is of course limited to low velocities of flow or high viscosity fluids such as oil, blood in biomechanics applications, etc. It is, however, important to recall here that the mixed form allows only certain combinations of \mathbf{N}_u and \mathbf{N}_p interpolations to be used without violating the convergence conditions. This is discussed in detail in Chapter 10 of Ref. [1], but for completeness Fig. 4.20 lists some of the available elements together with their asymptotic convergence rates [91]. Many other elements useful in fluid mechanics are documented elsewhere [92–94], but those of proven performance are given in the table.

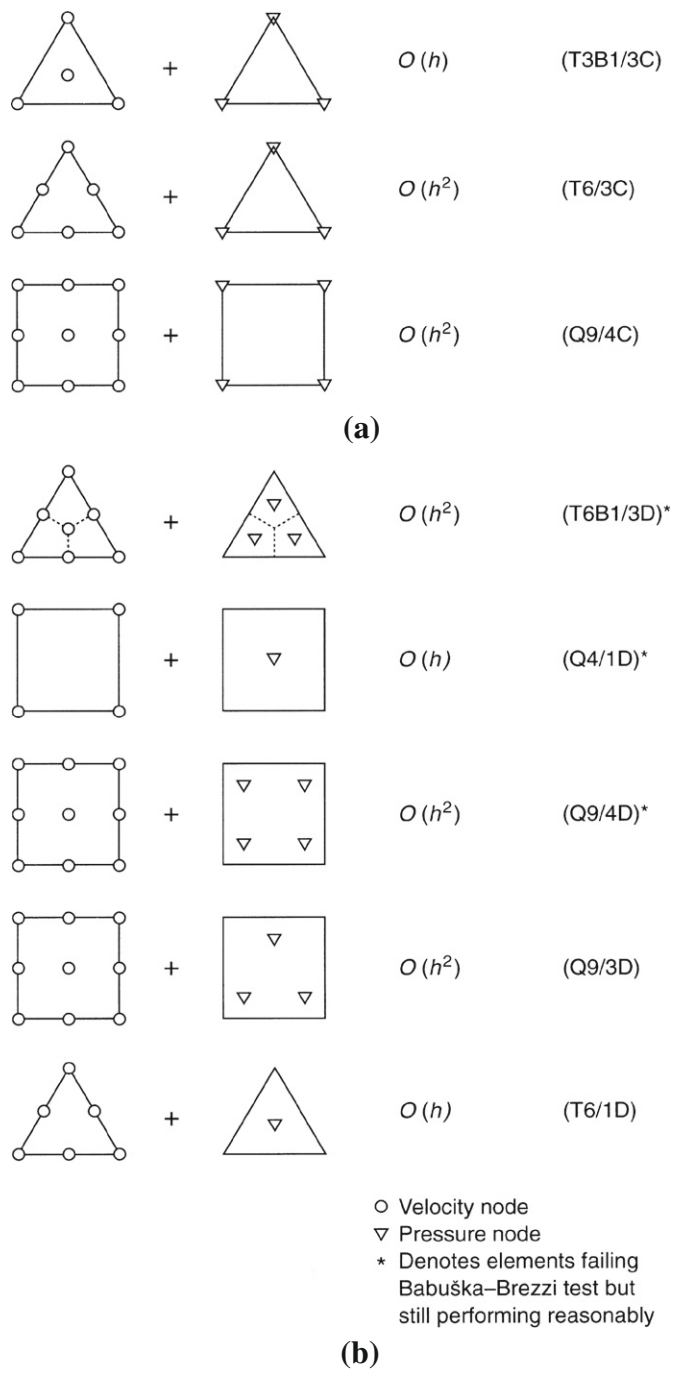
It is of general interest to note that frequently elements with C_0 continuous pressure interpolations are used in fluid mechanics and indeed that their performance is generally superior to those with discontinuous pressure interpolation on a given mesh, even though the cost of solution is marginally greater.

It is important to note that the recommendations concerning the element types for the Stokes problem carry over unchanged to situations in which dynamic terms are of importance.

The fairly obvious extension of the use of incompressible elastic codes to Stokes flow is undoubtedly the reason why the first finite element solutions of fluid mechanics were applied in this area.

4.6 Concluding remarks

The incompressible Newtonian fluid dynamics has been discussed in this chapter. Several more two- and three-dimensional problems can be found in recent publica-

**FIGURE 4.20**

Some useful velocity-pressure interpolations and their asymptotic, energy norm convergence rates: (a) continuous p interpolation; (b) discontinuous p interpolation.

tions on the CBS scheme. In addition to covering several benchmark problems of incompressible flows, we also have discussed several adaptive procedures for fluid dynamics problems. The chapter finally concludes by briefly describing the penalty methods.

References

- [1] O.C. Zienkiewicz, R.L. Taylor, J.Z. Zhu, *The Finite Element Method: Its Basis and Fundamentals*, seventh ed., Elsevier, Oxford, 2013.
- [2] P. Nithiarasu, An efficient artificial compressibility (AC) scheme based on the characteristic based split (CBS) method for incompressible flows, *Int. J. Numer. Methods Eng.* 56 (2003) 1815–1845.
- [3] P. Nithiarasu, J.S. Mathur, N.P. Weatherill, K. Morgan, Three-dimensional incompressible flow calculations using the characteristic based split (CBS) scheme, *Int. J. Numer. Methods Fluids* 44 (2004) 1207–1229.
- [4] R. Codina, M. Vázquez, O.C. Zienkiewicz, General algorithm for compressible and incompressible flows, Part III – a semi-implicit form, *Int. J. Numer. Methods Fluids* 27 (1998) 13–32.
- [5] U. Ghia, K.N. Ghia, C.T. Shin, High-resolution for incompressible flow using the Navier-Stokes equations and multigrid method, *J. Comput. Phys.* 48 (1982) 387–411.
- [6] P.N. Shankar, M.D. Deshpande, Fluid mechanics in the driven cavity, *Annu. Rev. Fluid Mech.* 32 (2000) 93–136.
- [7] A. Yeckel, J.W. Smith, J.J. Derby, Parallel finite element calculation of flow in a three-dimensional lid-driven cavity using the CM-5 and T3D, *Int. J. Numer. Methods Fluids* 24 (1997) 1449–1461.
- [8] L.Q. Tang, T.W. Cheng, T.T.H. Tsang, Transient solutions for 3-dimensional lid-driven cavity flows by a least-squares finite element method, *Int. J. Numer. Methods Fluids* 21 (1995) 413–432.
- [9] J. Kim, P. Moin, Application of a fractional step method to incompressible Navier-Stokes equations, *J. Comput. Phys.* 59 (1985) 308–323.
- [10] M.K. Denham, M.A. Patrik, Laminar flow over a downstream-facing step in a two-dimensional flow channel, *Trans. Inst. Chem. Eng.* 52 (1974) 361–367.
- [11] O. Hassan, E.J. Probert, K. Morgan, J. Peraire, Mesh generation and adaptivity for the solution of compressible viscous high speed flows, *Int. J. Numer. Methods Eng.* 38 (1995) 1123–1148.
- [12] N.P. Weatherill, O. Hassan, Efficient 3-dimensional Delaunay triangulation with automatic point generation and imposed boundary constraints, *Int. J. Numer. Methods Eng.* 37 (1994) 2005–2039.
- [13] K. Morgan, J. Peraire, Unstructured grid finite element methods for fluid mechanics, *Rep. Prog. Phys.* 61 (1998) 569–638.

- [14] N.P. Weatherill, O. Hassan, D.L. Marcum, Compressible flow field solutions with unstructured grids generated by Delaunay triangulation, *J. AIAA* 33 (1995) 1196–1204.
- [15] Ü. Gülcat, A.R. Aslan, Accurate 3D viscous incompressible flow calculations with FEM, *Int. J. Numer. Methods Fluids* 25 (1997) 985–1001.
- [16] Y. Rimon, S.I. Cheng, Numerical solution of a uniform flow over a sphere at intermediate reynolds numbers, *Phys. Fluids* 12 (1969) 949–959.
- [17] P. Nithiarasu, N. Massarotti, J.S. Mathur, Forced convection heat transfer from solder balls on a printed circuit board using the characteristic based split (CBS) scheme, *Int. J. Numer. Methods Heat Fluid Flow* 15 (1) (2005) 73–95.
- [18] R. Codina, M. Vázquez, O.C. Zienkiewicz, A fractional step method for the solution of compressible Navier-Stokes equations, in: M. Hafez, K. Oshima (Eds.), *Computational Fluid Dynamics Review*, vol. 1, World Scientific Publishing, 1998, pp. 331–347.
- [19] R.L.T. Bevan, P. Nithiarasu, Accelerating incompressible flow calculations using a quasi-implicit scheme: local and dual time stepping approaches, *Comput. Mech.* 50 (6, SI) (2012) 687–693.
- [20] R. Löhner, K. Morgan, O.C. Zienkiewicz, An adaptive finite element procedure for compressible high speed flows, *Comput. Methods Appl. Mech. Eng.* 51 (1985) 441–465.
- [21] J. Peraire, M. Vahdati, K. Morgan, O.C. Zienkiewicz, Adaptive remeshing for compressible flow computations, *J. Comput. Phys.* 72 (1987) 449–466.
- [22] J.T. Oden, T. Strouboulis, P. Devloo, Adaptive finite element methods for high speed compressible flows, *Int. J. Numer. Methods Eng.* 7 (1987) 1211–1228.
- [23] J. Peraire, K. Morgan, O.C. Zienkiewicz, Convection dominated problems, *Numerical Methods for Compressible Flows – Finite Difference, Element and Volume Techniques*, vol. AMD 78, ASME, New York, 1987.
- [24] O.C. Zienkiewicz, J.Z. Zhu, Y.C. Liu, K. Morgan, J. Peraire, Error estimates and adaptivity. From elasticity to high speed compressible flow, in: J. Whiteman (Ed.), *The Mathematics of Finite Elements and Applications*, vol. VII, Academic Press, London, 1988, pp. 483–512.
- [25] B. Palmerio, A two-dimensional FEM adaptive moving-node method for steady Euler flow simulation, *Comput. Methods Appl. Mech. Eng.* 71 (1988) 315–340.
- [26] R. Löhner, Adaptive remeshing for transient problems, *Comput. Methods Appl. Mech. Eng.* 75 (1989) 195–214.
- [27] L. Demkowicz, J.T. Oden, W. Rachowicz, O. Hardy, Toward a universal $h - p$ adaptive finite element strategy. Part 1: Constrained approximation and data structure, *Comput. Methods Appl. Mech. Eng.* 77 (1989) 79–112.
- [28] J.T. Oden, L. Demkowicz, W. Rachowicz, T.A. Westermann, Toward a universal h-p adaptive finite element strategy. Part 2: A posteriori error estimation, *Comput. Methods Appl. Mech. Eng.* 77 (1989) 113–180.
- [29] O.C. Zienkiewicz, Adaptivity-fluids-localization – the new challenge to computational mechanics, *Tran. Can. Soc. Mech. Eng.* 15 (1991) 137–145.

- [30] E.J. Probert, O. Hassan, K. Morgan, J. Peraire, An adaptive finite element method for transient compressible flows with moving boundaries, *Int. J. Numer. Methods Eng.* 32 (1991) 751–765.
- [31] A. Evans, M.J. Marchant, J. Szmelter, N.P. Weatherill, Adaptivity for compressible flow computations using point embedding on 2-D structured multiblock meshes, *Int. J. Numer. Methods Eng.* 32 (1991) 895–919.
- [32] J. Wu, J.Z. Zhu, J. Szmelter, O.C. Zienkiewicz, Error estimation and adaptivity in Navier-Stokes incompressible flows, *Comput. Mech.* 61 (1991) 30–39.
- [33] J.F. Hetu, D.H. Pelletier, Adaptive remeshing for viscous incompressible flows, *AIAA J.* 30 (1992) 1986–1992.
- [34] J.F. Hetu, D.H. Pelletier, Fast, adaptive finite element scheme for viscous incompressible flows, *AIAA J.* 30 (1992) 2677–2682.
- [35] J. Peraire, J. Peiro, K. Morgan, Adaptive remeshing for 3-dimensional compressible flow computations, *J. Comput. Phys.* 103 (1992) 269–285.
- [36] E.J. Probert, O. Hassan, K. Morgan, J. Peraire, Adaptive explicit and implicit finite element methods for transient thermal analysis, *Int. J. Numer. Methods Eng.* 35 (1992) 655–670.
- [37] J. Szmelter, M.J. Marchant, A. Evans, N.P. Weatherill, 2-dimensional Navier-Stokes equations with adaptivity on structured meshes, *Comput. Methods Appl. Mech. Eng.* 101 (1992) 355–368.
- [38] R. Löhner, J.D. Baum, Adaptive h -refinement on 3D unstructured grid for transient problems, *Int. J. Numer. Methods Fluids* 14 (1992) 1407–1419.
- [39] M.J. Marchant, N.P. Weatherill, Adaptivity techniques for compressible inviscid flows, *Comput. Methods Appl. Mech. Eng.* 106 (1993) 83–106.
- [40] W. Rachowicz, An anisotropic h -type mesh refinement strategy, *Comput. Methods Appl. Mech. Eng.* 109 (1993) 169–181.
- [41] P.A.B. de Sampaio, P.R.M. Lyra, K. Morgan, N.P. Weatherill, Petrov-Galerkin solutions of the incompressible Navier-Stokes equations in primitive variables with adaptive remeshing, *Comput. Methods Appl. Mech. Eng.* 106 (1993) 143–178.
- [42] O.C. Zienkiewicz, J. Wu, Automatic directional refinement in adaptive analysis of compressible flows, *Int. J. Numer. Methods Eng.* 37 (1994) 2189–2219.
- [43] J.T. Oden, W. Wu, M. Ainsworth, An a posteriori error estimate for finite element approximations of the Navier-Stokes equations, *Comput. Methods Appl. Mech. Eng.* 111 (1994) 185–202.
- [44] J.T. Oden, W. Wu, V. Legat, An hp adaptive strategy for finite element approximations of the Navier-Stokes equations, *Int. J. Numer. Methods Fluids* 20 (1995) 831–851.
- [45] M.J. Castro-Díaz, H. Borouchaki, P.L. George, F. Hecht, B. Mohammadi, Anisotropic adaptive mesh generation in two dimensions for CFD, in: *Computational Fluid Dynamics '96*, 1996, pp. 181–186.
- [46] R. Löhner, Mesh adaptation in fluid mechanics, *Eng. Frac. Mech.* 50 (1995) 819–847.

- [47] O. Hassan, K. Morgan, E.J. Probert, J. Peraire, Unstructured tetrahedral mesh generation for three dimensional viscous flows, *Int. J. Numer. Methods Eng.* 39 (1996) 549–567.
- [48] O. Hassan, K. Morgan, E.J. Probert, J. Peraire, Unstructured tetrahedral mesh generation for three dimensional viscous flows, *Int. J. Num. Methods Eng.* 39 (1996) 549–567.
- [49] D.D.D. Yahia, W.G. Habashi, A. Tam, M.G. Vallet, M. Fortin, A directionally adaptive methodology using an edge based error estimate on quadrilateral grids, *Int. J. Numer. Methods Fluids* 23 (1996) 673–690.
- [50] M. Fortin, M.G. Vallet, J. Dompierre, Y. Bourgault, W.G. Habashi, Anisotropic mesh adaption: theory, validation and applications, in: *Computational Fluid Dynamics '96*, 1996, pp. 174–180.
- [51] K.S.V. Kumar, A.V.R. Babu, K.N. Seetharamu, T. Sundararajan, P.A.A. Narayana, A generalized Delaunay triangulation algorithm with adaptive grid size control, *Commun. Appl. Numer. Methods* 13 (1997) 941–948.
- [52] H. Borouchaki, P.L. George, F. Hecht, P. Laug, E. Saltel, Delaunay mesh generation governed by metric specifications. Part I. Algorithms, *Finite Elem. Anal. Des.* 25 (1997) 61–83.
- [53] H. Borouchaki, P.L. George, B. Mohammadi, Delaunay mesh generation governed by metric specifications. Part II. Applications, *Finite Elem. Anal. Des.* 25 (1997) 85–109.
- [54] W. Rachowicz, An anisotropic h -adaptive finite element method for compressible Navier-Stokes equations, *Comput. Methods Appl. Mech. Eng.* 146 (1997) 231–252.
- [55] J. Peraire, K. Morgan, Unstructured mesh generation including directional refinement for aerodynamic flow simulation, *Finite Elem. Anal. Des.* 25 (1997) 343–356.
- [56] M.J. Marchant, N.P. Weatherill, O. Hassan, The adaptation of unstructured grids for transonic viscous flow simulation, *Finite Elem. Anal. Des.* 25 (1997) 199–218.
- [57] H. Borouchaki, F. Hecht, P.J. Frey, Mesh gradation control, *Int. J. Numer. Methods Fluids* 43 (1998) 1143–1165.
- [58] H. Borouchaki, P.J. Frey, Adaptive triangular-quadrilateral mesh generation, *Int. J. Numer. Methods Eng.* 41 (1998) 915–934.
- [59] H. Jin, S. Prudhomme, A posteriori error estimation of steady-state finite element solution of the Navier-Stokes equations by a subdomain residual method, *Comput. Methods Appl. Mech. Eng.* 159 (1998) 19–48.
- [60] P. Nithiarasu, O.C. Zienkiewicz, Adaptive mesh generation procedure for fluid mechanics problems, *Int. J. Numer. Methods Eng.* 47 (2000) 629–662.
- [61] P. Nithiarasu, An adaptive finite element procedure for solidification problems, *Heat Mass Transfer* 36 (3) (2000) 223–229.
- [62] E. De Santiago, K.H. Law, A distributed implementation of an adaptive finite element method for fluid problems, *Comput. Fluids* 74 (2000) 97–119.

- [63] P. Saramito, N. Roquet, An adaptive finite element method for viscoplastic fluid flows in pipes, *Comput. Methods Appl. Mech. Eng.* 190 (40–41) (2001) 5391–5412.
- [64] P. Nithiarasu, An adaptive remeshing technique for laminar natural convection problems, *Heat Mass Transfer* 38 (3) (2002) 243–250.
- [65] N. Roquet, P. Saramito, An adaptive finite element method for Bingham fluid flows around a cylinder, *Comput. Methods Appl. Mech. Eng.* 192 (2003) 3317–3341.
- [66] P. Yue, C. Zhou, J.J. Feng, C.F. Ollivier-Gooch, H.H. Hu, Phase-field simulations of interfacial dynamics in viscoelastic fluids using finite elements with adaptive meshing, *J. Comput. Phys.* 219 (2006) 47–67.
- [67] D.R. Davies, J.H. Davies, O. Hassan, K. Morgan, P. Nithiarasu, Investigations into the applicability of adaptive finite element methods to two-dimensional infinite Prandtl number thermal and thermochemical convection, *Geochem. Geophys. Geosyst.* 8 (2007).
- [68] J. Narski, M. Picasso, Adaptive finite elements with high aspect ratio for dendritic growth of a binary alloy including fluid flow induced by shrinkage, *Comput. Methods Appl. Mech. Eng.* 196 (2007) 3562–3576.
- [69] D.R. Davies, J.H. Davies, O. Hassan, K. Morgan, P. Nithiarasu, Adaptive finite element methods in geodynamics: convection dominated mid-ocean ridge and subduction zone simulations, *Int. J. Numer. Methods Heat Fluid Flow* 18 (7–8) (2008) 1015–1035.
- [70] F. Bengzon, M.G. Larson, Adaptive finite element approximation of multi-physics problems: a fluid-structure interaction model problem, *Int. J. Numer. Methods Eng.* 84 (2010) 1451–1465.
- [71] M.G. Armentano, C. Padra, R. Rodriguez, M. Scheble, An hp finite element adaptive scheme to solve the Laplace model for fluid-solid vibrations, *Comput. Methods Appl. Mech. Eng.* 200 (2011) 178–188.
- [72] X. Garcia, D. Pavlidis, G.J. Gorman, J.L.M.A. Gomes, M.D. Piggott, E. Aristodemou, J. Mindel, J.-P. Latham, C.C. Pain, H. ApSimon, A two-phase adaptive finite element method for solid-fluid coupling in complex geometries, *Int. J. Numer. Methods Fluids* 66 (2011) 82–96.
- [73] P.J. Green, R. Sibson, Computing Dirichlet tessellations in the plane, *Comput. J.* 21 (1978) 168–173.
- [74] D.F. Watson, Computing the n -dimensional Delaunay tessellation with application to Voronoi polytopes, *Comput. J.* 24 (1981) 167–172.
- [75] J.C. Cavendish, D.A. Field, W.H. Frey, An approach to automatic three dimensional finite element mesh generation, *Int. J. Numer. Methods Eng.* 21 (1985) 329–347.
- [76] W.J. Schroeder, M.S. Shephard, A combined octree Delaunay method for fully automatic 3-d mesh generation, *Int. J. Numer. Methods Eng.* 29 (1990) 37–55.
- [77] N.P. Weatherill, Mesh generation for aerospace applications, *Sadhana Acc. Proc. Eng. Sci.* 16 (1991) 1–45.

- [78] N.P. Weatherill, P.R. Eiseman, J. Hause, J.F. Thompson, Numerical Grid Generation in Computational Fluid Dynamics and Related Fields, Pineridge Press, Swansea, 1994.
- [79] G. Subramanian, V.V.S. Raveendra, M.G. Kamath, Robust boundary triangulation and Delaunay triangulation of arbitrary planar domains, *Int. J. Numer. Methods Eng.* 37 (1994) 1779–1789.
- [80] R.W. Lewis, Y. Zhang, A.S. Usmani, Aspects of adaptive mesh generation based on domain decomposition and Delaunay triangulation, *Finite Elem. Anal. Des.* 20 (1995) 47–70.
- [81] H. Borouchaki, P.L. George, Aspects of 2-D Delaunay mesh generation, *Int. J. Numer. Methods Eng.* 40 (1997) 1957–1975.
- [82] J.F. Thompson, B.K. Soni, N.P. Weatherill (Eds.), *Handbook of Grid Generation*, CRC Press, January 1999.
- [83] M.J. Castro-Diaz, H. Borouchaki, P.L. George, F. Hecht, B. Mohammadi, Error interpolation minimization and anisotropic mesh generation, in: M. Morandi Cecchi, K. Morgan, J. Periaux, B.A. Schrefler, O.C. Zienkiewicz (Eds.), *Proceedings of 9th International Conference Finite Elements Fluids – New Trends and Applications*, Venezia, October 1995, pp. 139–148.
- [84] D.S. Malkus, T.J.R. Hughes, Mixed finite element methods in reduced and selective integration techniques: a unification of concepts, *Comput. Methods Appl. Mech. Eng.* 15 (1978) 63–81.
- [85] O.C. Zienkiewicz, P.N. Godbole, Viscous incompressible flow with special reference to non-Newtonian (plastic) flows, in: R.H. Gallagher et al. (Eds.), *Finite Elements in Fluids*, vol. 1, John Wiley & Sons, 1975, pp. 25–55, (Chapter 2)
- [86] T.J.R. Hughes, R.L. Taylor, J.F. Levy, A finite element method for incompressible flows, in: *Proceedings 2nd International Symposium on Finite Elements in Fluid Problems ICCAD*, Santa Margherita Ligure, Italy, 1976, pp. 1–6.
- [87] O.C. Zienkiewicz, P.N. Godbole, A penalty function approach to problems of plastic flow of metals with large surface deformation, *J. Strain Anal.* 10 (1975) 180–183.
- [88] O.C. Zienkiewicz, S. Nakazawa, The penalty function method and its applications to the numerical solution of boundary value problems, *ASME, AMD* 51 (1982) 157–179.
- [89] J.T. Oden, R.I.P. methods for Stokesian flow, in: R.H. Gallagher, D.N. Norrie, J.T. Oden, O.C. Zienkiewicz (Eds.), *Finite Elements in Fluids*, vol. 4, John Wiley & Sons, 1982, pp. 305–318 (Chapter 15)
- [90] O.C. Zienkiewicz, J.P. Vilotte, S. Toyoshima, S. Nakazawa, Iterative method for constrained and mixed approximation. An inexpensive improvement of FEM performance, *Comput. Methods Appl. Mech. Eng.* 51 (1985) 3–29.
- [91] O.C. Zienkiewicz, Y.C. Liu, G.C. Huang, Error estimates and convergence rates for various incompressible elements, *Int. J. Numer. Methods Eng.* 28 (1989) 2191–2202.
- [92] M. Fortin, Old and new finite elements for incompressible flow, *Int. J. Numer. Methods Fluids* 1 (1981) 347–364.

- [93] M. Fortin, N. Fortin, Newer and newer elements for incompressible flow, in: R.H. Gallagher, G.F. Carey, J.T. Oden, O.C. Zienkiewicz (Eds.), Finite Elements in Fluids, vol. 6, John Wiley & Sons, 1985, pp. 171–188 (Chapter 7).
- [94] M.S. Engleman, R.L. Sani, P.M. Gresho, H. Bercovier, Consistent vs. reduced integration penalty methods for incompressible media using several old and new elements, Int. J. Numer. Methods Fluids 2 (1982) 25–42.

Incompressible Non-Newtonian Flows

5

5.1 Introduction

In this chapter we discuss briefly the non-Newtonian effect in flow problems. In non-Newtonian flow cases, the viscosity of the material is nonlinearly dependent on the stress or strain rate and their magnitudes. There are several models available for non-Newtonian fluids. The simplest and widely used among these models is the one based on the *power law*. We start with such a formulation for metal and polymer forming in [Section 5.2](#). Fluids that partially return to the original form when applied stress is released are called *viscoelastic*. The models for viscoelastic fluids can be quite complicated. In [Section 5.3](#) we provide such models and discuss their numerical solution using the CBS procedure described in [Chapter 3](#). In [Section 5.4](#) we briefly discuss a direct displacement method based on the CBS approach to impact problems.

5.2 Non-Newtonian flows: Metal and polymer forming

5.2.1 Non-Newtonian flows including viscoplasticity and plasticity

In many fluids the viscosity, though isotropic, may be dependent on the rate of strain $\dot{\varepsilon}_{ij}$ as well as on the state variables such as temperature or total deformation. Typical here is, for instance, the behavior of many polymers, hot metals, blood in small arteries, etc., where a power law of the type

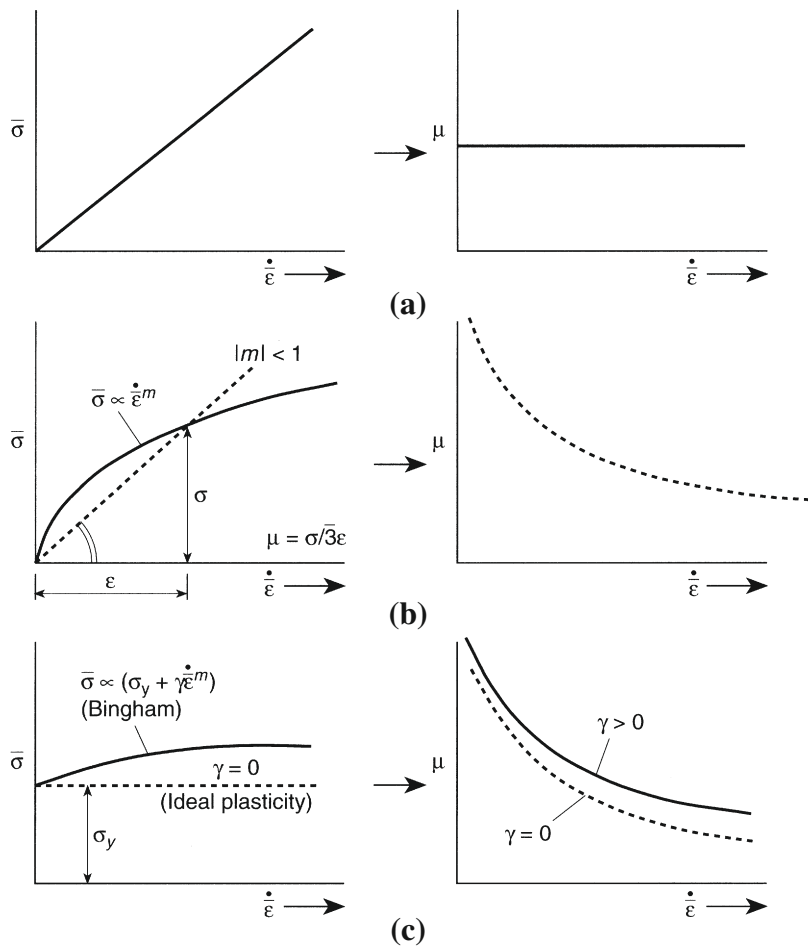
$$\mu = \mu_0 \dot{\varepsilon}^{(m-1)} \quad (5.1)$$

with

$$\mu_0 = \mu_0(T, \bar{\varepsilon})$$

governs the viscosity-strain rate dependence where m is a physical constant. In the above $\dot{\varepsilon}$ is the second invariant of the deviatoric strain rate tensor defined from [Eq. \(3.36\)](#), T is the (absolute) temperature, and $\bar{\varepsilon}$ is the total strain invariant.

This *secant* viscosity can of course be obtained by plotting the relation between the deviatoric stresses and deviatoric strains or their invariants, as [Eq. \(3.35\)](#) simply defines the viscosity by the appropriate ratio of the stress to strain rate. Such plots are shown in [Fig. 5.1](#) where $\bar{\sigma}$ denotes the second deviatoric stress invariant. The above power law relation of [Eq. \(5.1\)](#) is known as the Oswald de Wahle law (or power law) and is illustrated in [Fig. 5.1b](#).

**FIGURE 5.1**

Stress $\bar{\sigma}$, viscosity μ , and strain rate $\dot{\varepsilon}$ relationships for various materials: (a) linear, Newtonian, fluid; (b) non-Newtonian polymers; (c) viscoplastic-plastic metals.

In a similar manner viscosity laws can be found for viscoplastic and indeed purely plastic behavior of an incompressible kind. For instance, in Fig. 5.1c we show a viscoplastic Bingham fluid in which a threshold or yield value of the second stress invariant has to be exceeded before any strain rate is observed. Thus for the viscoplastic fluid illustrated it is evident that a highly nonlinear viscosity relation is obtained. This can be written as

$$\mu = \frac{\bar{\sigma}_y + \gamma \dot{\varepsilon}^m}{\dot{\varepsilon}} \quad (5.2)$$

where $\bar{\sigma}_y$ is the value of the second stress invariant at yield.

The special case of pure plasticity follows of course as a limiting case when the fluidity parameter $\gamma = 0$, and now we have simply

$$\mu = \frac{\bar{\sigma}_y}{\dot{\varepsilon}} \quad (5.3)$$

Of course, once again $\bar{\sigma}_y$ can be dependent on the *state* of the fluid, i.e.,

$$\bar{\sigma}_y = \bar{\sigma}_y(T, \bar{\varepsilon}) \quad (5.4)$$

The solutions (at a given state of the fluid) can be obtained by various iterative procedures, noting that Eq. (4.31) continues to be valid but now with the matrix \mathbf{K} being dependent on viscosity, i.e.,

$$\mathbf{K} = \mathbf{K}(\mu) = \mathbf{K}(\dot{\varepsilon}) = \mathbf{K}(\mathbf{u}) \quad (5.5)$$

thus being dependent on the solution.

The total iteration process can be used simply here (see Ref. [1]). Thus rewriting Eq. (4.31) as

$$\mathbf{A} \begin{Bmatrix} \tilde{\mathbf{u}} \\ \tilde{\mathbf{p}} \end{Bmatrix} = \begin{Bmatrix} \bar{\mathbf{f}} \\ \mathbf{0} \end{Bmatrix} \quad (5.6)$$

and noting that

$$\mathbf{A} = \mathbf{A}(\tilde{\mathbf{u}}, \tilde{\mathbf{p}})$$

we can write

$$\begin{Bmatrix} \tilde{\mathbf{u}} \\ \tilde{\mathbf{p}} \end{Bmatrix}^{n+1} = \mathbf{A}_n^{-1} \begin{Bmatrix} \bar{\mathbf{f}} \\ \mathbf{0} \end{Bmatrix} \quad \mathbf{A}_n = \mathbf{A}(\tilde{\mathbf{u}}, \tilde{\mathbf{p}})^n \quad (5.7)$$

Starting with an arbitrary value of μ we repeat the solution until convergence is obtained.

Such an iterative process converges rapidly (even when, as in pure plasticity, μ can vary from zero to infinity), providing that the forcing $\bar{\mathbf{f}}$ is due to *prescribed boundary velocities* and thus immediately confines the variation of all velocities in a narrow range. In such cases, five to seven iterations are generally required to bring the difference of the n th and $(n + 1)$ th solutions to within the 1% (Euclidian) norm.

The first non-Newtonian flow solutions were applied to polymers and to hot metals in the early 1970s [2, 3]. Application of the same procedures to the forming of metals was introduced at the same time and has subsequently been widely developed [4–33].

It is perhaps difficult to visualize steel or aluminum behaving as a fluid, being conditioned to use these materials as structural members. If, however, we note that during the forming process the elastic strains are of the order of 10^{-6} while the plastic strain can reach or exceed a value of unity, neglect of the former (which is implied in the viscosity definition) seems justifiable. This is indeed born out by comparison of computations based on what we now call *flow formulation* with elastoplastic computation or experiment. The process has alternatively been introduced as a “rigid-plastic” form [12, 14], though such modeling is more complex and less descriptive.

Today the methodology is widely accepted for the solution of metal and polymer forming processes, and only a limited selection of references of application can be

cited. The reader would do well to consult Refs. [20, 34–38] for a complete survey of the field.

5.2.2 Steady-state problems of forming

Two categories of problems arise in forming situations. *Steady-state flow* is the first of these. In this, a real, continuing, flow is modeled, as shown in Fig. 5.2a and here velocity and other properties can be assumed to be fixed in a particular point of space. In Fig. 5.2b the more usual *transient* processes of forming are illustrated and we shall deal with these later. In a typical steady-state problem if the state parameters T and $\bar{\epsilon}$ defining the temperature and total strain invariant are known in the whole field, the solution can be carried out in the manner previously described. We could, for instance, assume that the “viscous” flow of the problem of Fig. 5.3 is that of an ideally plastic material under isothermal conditions modeling an extrusion process and obtain the solution shown in Table 5.1. For such a material exact extrusion forces can be calculated [39] and the table shows the errors obtained with the flow formulation using the different triangular elements of Fig. 5.3 and two meshes [40]. The fine mesh here was arrived at by using error estimates and a single adaptive remeshing.

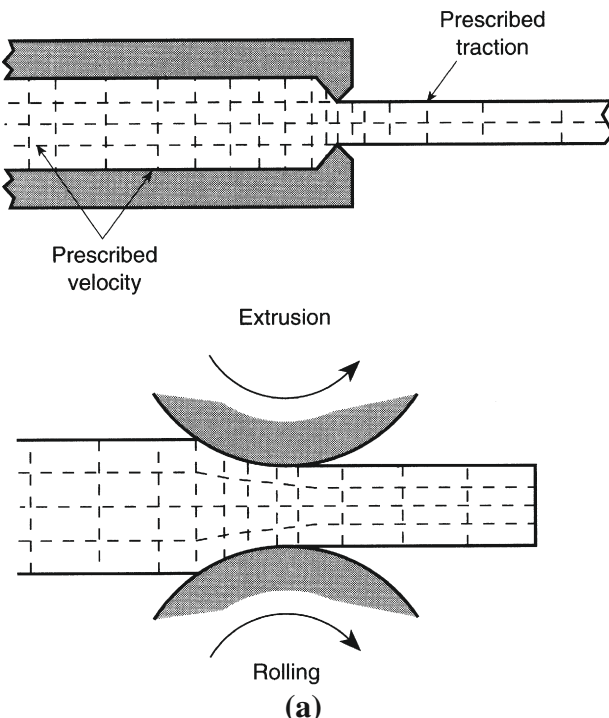


FIGURE 5.2

Forming processes typically used in manufacture: (a) steady rate; (b) transient.

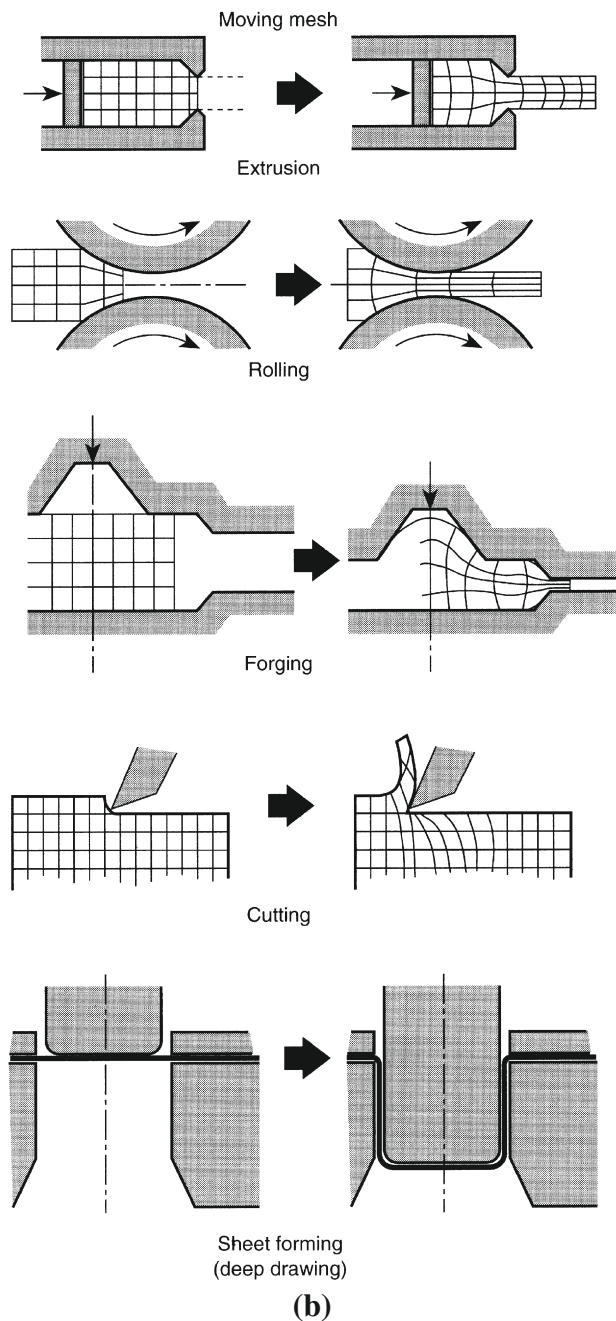
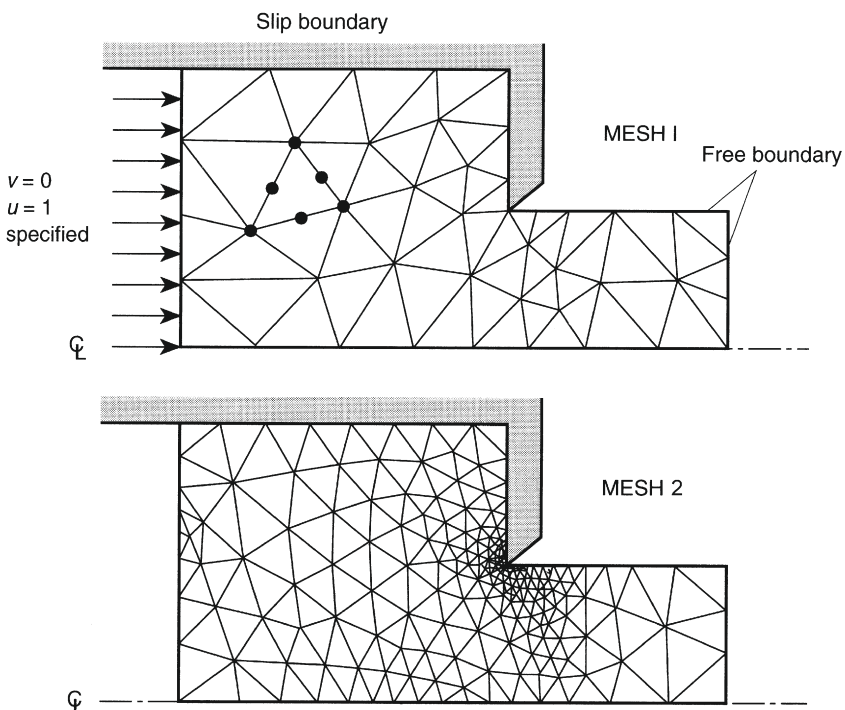


FIGURE 5.2
(Continued).

**FIGURE 5.3**

Plane strain extrusion (extrusion ratio 2:1) with ideal plasticity assumed.

Table 5.1 Comparisons of Performance of Several Triangular Mixed Elements of Fig. 5.3 in a Plane Extrusion Problem (ideal plasticity assumed) [40]

Element Type	Mesh 1 (coarse)			Mesh 2 (fine)		
	Ext. Force	Force Error	CPU(s)	Ext. Force	Force Error	CPU(s)
T6/1D	28,901.0	12.02	67.81	25,990.0	0.73	579.71
T6B1/3D	31,043.0	20.32	75.76	26,258.0	1.78	780.13
T6B1/3D*	29,031.0	12.52	73.08	26,229.0	1.66	613.92
T6/3C	27,902.5	8.15	87.62	25,975.0	0.67	855.38
Exact	25,800.0	0.00	—	25,800.0	0.00	—

In general the problem of steady-state flow is accompanied by the evolution of temperature (and other state parameters such as the total strain invariant $\bar{\epsilon}$) and here it is necessary to couple the solution with the heat balance and possibly other evolution equations. The evolution of heat has already been discussed and the appropriate conservation equations such as Eq. (4.6) can be used. It is convenient now to rewrite this equation in a modified form.

Firstly, we note that the kinetic energy is generally negligible in the problems considered and that with a constant heat capacity \hat{c} per unit volume we can write

$$\rho E \approx \rho e = \hat{c}T \quad (5.8a)$$

Secondly, we observe that the internal work dissipation can be rewritten by the identity

$$\frac{\partial}{\partial x_i}(pu_i) - \frac{\partial}{\partial x_j}(\tau_{ji}u_i) \equiv -\sigma_{ji}\dot{\varepsilon}_{ji} \quad (5.8b)$$

where, by Eq. (1.9a),

$$\sigma_{ji} = \tau_{ji} - \delta_{ji}p \quad (5.8c)$$

and, by Eq. (1.2),

$$\dot{\varepsilon}_{ji} = \frac{1}{2} \left(\frac{\partial u_j}{\partial x_i} + \frac{\partial u_i}{\partial x_j} \right) \quad (5.8d)$$

We note in passing that in general the effect of the pressure term in Eq. (5.8b) is negligible and can be omitted if desired.

Using the above and inserting the incompressibility relation we can write the energy conservation as [for an alternative form see Eq. (4.6)]

$$\left(\hat{c} \frac{\partial T}{\partial t} + \hat{c}u_i \frac{\partial T}{\partial x_i} \right) - \frac{\partial}{\partial x_i} \left(k \frac{\partial T}{\partial x_i} \right) - (\sigma_{ij}\dot{\varepsilon}_{ij} + \rho g_i u_i) = 0 \quad (5.9)$$

The solution of the coupled problem can be carried out iteratively. Here the term in the last bracket can be evaluated repeatedly from the known velocities and stresses from the flow solution. We note that the first bracketed term represents a total derivative of the convective kind which, even in the steady state, requires the use of the special weighting procedures discussed in Chapter 2.

Such coupled solutions were carried out for the first time as early as 1973 and later in 1978 [7, 13], but are today practiced routinely.

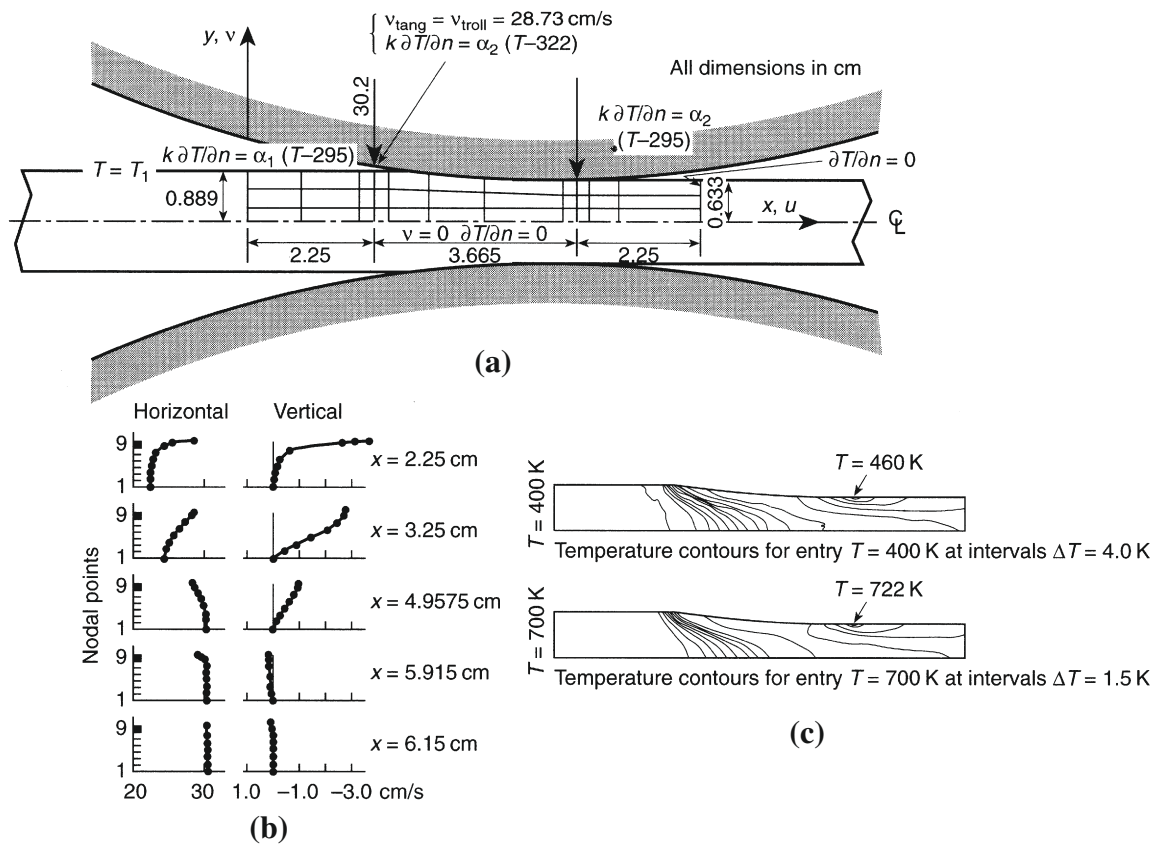
Example 5.1. Steady-state rolling problem

Figure 5.4 shows a typical thermally coupled solution for a steady-state rolling problem from Ref. [13]. It is of interest to note that in this problem boundary friction plays an important role and that this is modeled by using thin elements near the boundary, making the viscosity coefficient in that layer pressure dependent [21]. This procedure is very simple and although not exact gives results of sufficient practical accuracy.

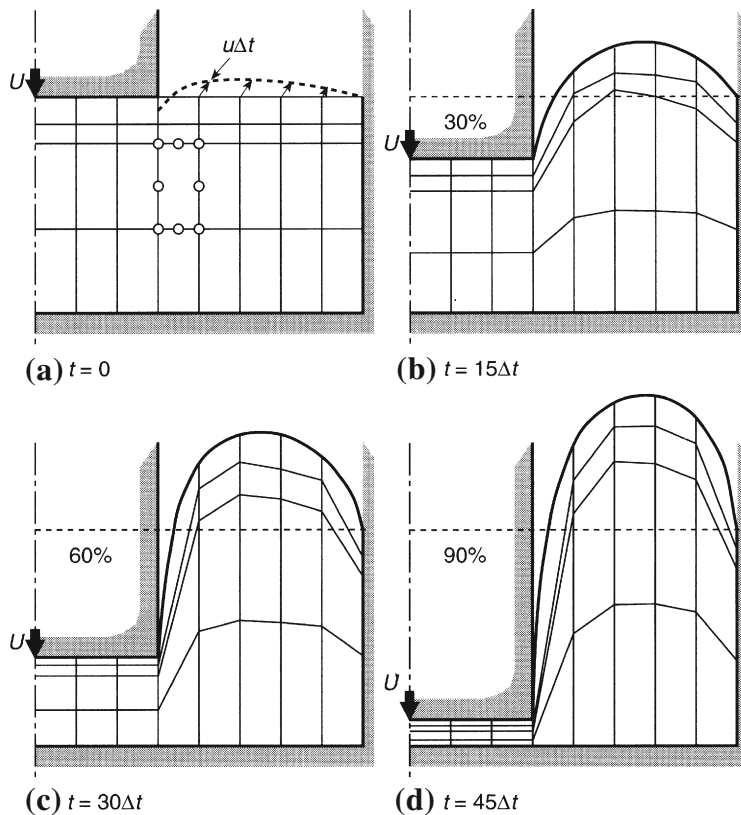
5.2.3 Transient problems with changing boundaries

These represent the second, probably larger, category of forming problems. Typical examples here are those of forging, indentation, etc., and again thermal coupling can be included if necessary. Figures 5.5 and 5.6 illustrate typical applications.

The solution for velocities and internal stresses can be readily accomplished at a given configuration, provided the temperatures and other state variables are known at that instant. This allows the new configuration to be obtained both for the boundaries

**FIGURE 5.4**

Steady-state rolling process with thermal coupling [40]: (a) geometry; (b) velocity profiles; (c) temperature distribution for different entry temperatures.

**FIGURE 5.5**

Punch indentation problem (penalty function approach) [4]. Updated mesh and surface profile with 24 isoparametric elements. Ideally plastic material; (a), (b), (c), and (d) show various depths of indentation (reduced integration is used here).

and for the mesh by writing explicitly

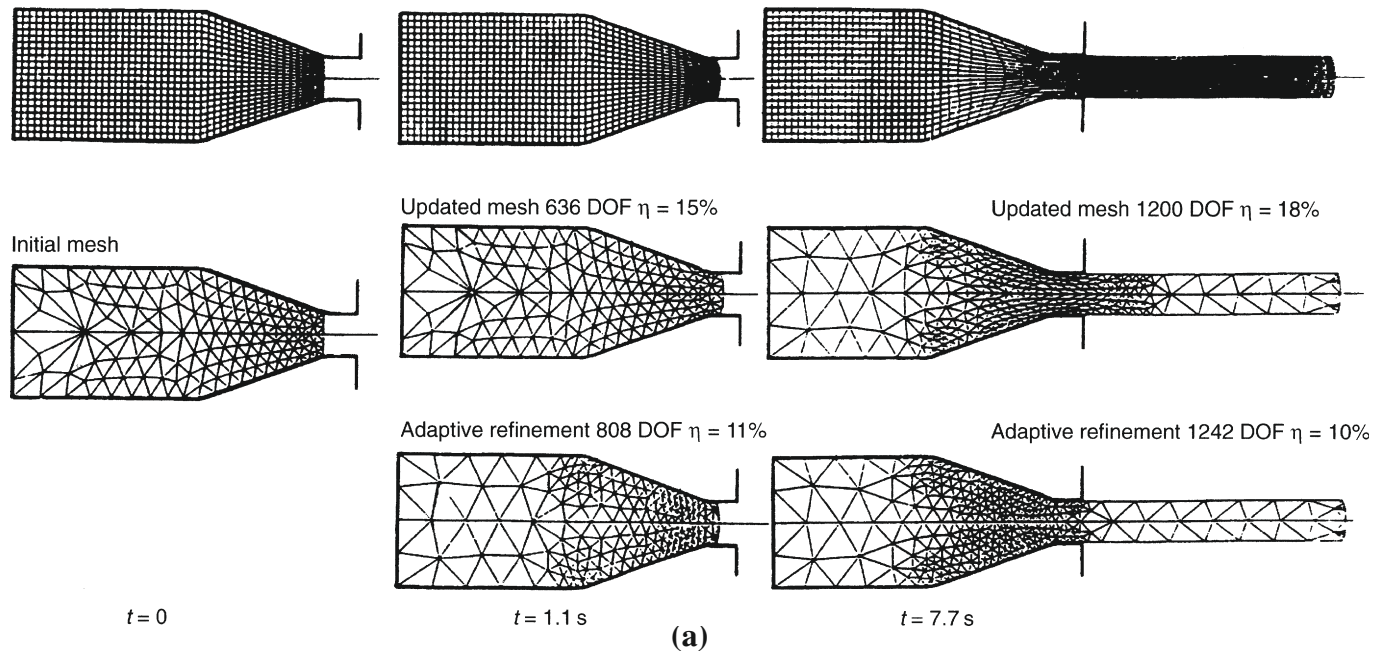
$$\Delta x_i = u_i \Delta t \quad (5.10)$$

as the incremental relation.

If thermal coupling is important increments of temperature need also to be evaluated. However, we note that for convected coordinates Eq. (5.9) is simplified as the convected terms disappear. We can now write

$$\hat{c} \frac{\partial T}{\partial t} - \frac{\partial}{\partial x_i} \left(k \frac{\partial T}{\partial x_i} \right) - (\sigma_{ij} \dot{\epsilon}_{ij} + \rho g_i u_i + g_h) = 0 \quad (5.11)$$

where the last term is the heat input known at the start of the interval and computation of temperature increments is made using either explicit or implicit procedures discussed in Chapter 3.

**FIGURE 5.6**

(a) A material grid and updated and adapted meshes with material deformation (η percentage in energy norm). A transient extrusion problem with temperature and strain-dependent yield [42]. Adaptive mesh refinement uses T6/1D elements of Fig. 4.20; (b) Contours of state parameters at $t = 2.9 \text{ s}$; (c) load versus time.

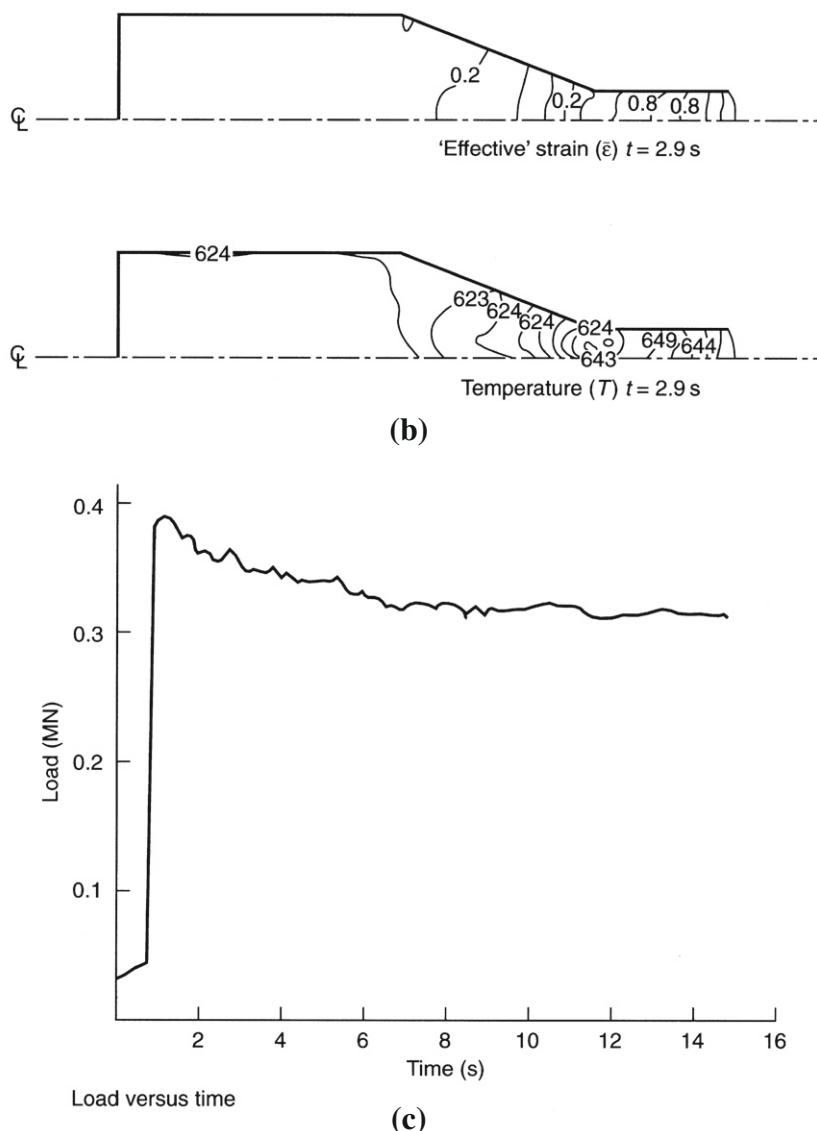


FIGURE 5.6
(Continued).

Indeed, both the coordinate and thermal updating can make use iteratively of the solution on the updated mesh to increase accuracy. However, it must be noted that any continuous mesh updating will soon lead to unacceptable meshes and some form of remeshing is necessary.

Example 5.2. Punch indentation problem

In the example of Fig. 5.5 [4], in which ideal plasticity was assumed together with isothermal behavior, it is necessary only to keep track of boundary movements. As temperature and other state variables do not enter the problem the remeshing can be done simply—in the case shown by keeping the same vertical lines for the mesh position.

Example 5.3. Transient extrusion problem

In the example of Fig. 5.6 showing a more realistic problem [41,42], when a new mesh is created an interpolation of all the state parameters from the old to the new mesh positions is necessary. In such problems it is worthwhile to strive to obtain discretization errors within specified bounds and to remesh adaptively when these errors are too large.

We have discussed the problem of adaptive remeshing for linear problems in Chapter 16 of Ref. [1]. In the present examples similar methods have been adopted with success [43,44] and in Fig. 5.6 we show how remeshing proceeds during the forming process. It is of interest simply to observe that here the *energy norm* of the error is the measure used.

The details of various applications can be found in the extensive literature on the subject. This also deals with various sophisticated mesh updating procedures. One particularly successful method is the so-called ALE (arbitrary Lagrangian-Eulerian) method [45–49]. Here the original mesh is given some prescribed velocity \bar{v} in a manner fitting the moving boundaries, and the convective terms in the equations are retained with reference to this velocity. In Eq. (5.9), for instance, in place of

$$\hat{c}u_i \frac{\partial T}{\partial x_i} \quad \text{we write} \quad \hat{c}(u_i - \bar{v}_i) \frac{\partial T}{\partial x_i}$$

etc., and the solution can proceed in a manner similar to that of steady state (with convection disappearing of course when $\bar{v}_i = u_i$, i.e., in the pure updating process). For more details on the ALE framework, readers are referred to Chapter 6.

It is of interest to observe that the flow methods can equally well be applied to the forming of thin sections resembling shells. Here of course all the assumptions of shell theory and corresponding finite element technology are applicable. Because of this, incompressibility constraints are no longer a problem but other complications arise. The literature of such applications is large, but much of the relevant information can be found in Refs. [50–62]. Practical applications ranging from the forming of beer cans to those of car bodies abound. Figures 5.7 and 5.8 illustrate some typical problems.

5.2.4 Elastic springback and viscoelastic fluids

In Section 5.2.1 we have argued that omission of elastic effects in problems of metal or plastic forming can be justified because of the small amount of elastic straining. This is undoubtedly true when we wish to consider the forces necessary to initiate large deformations and to follow these through. There are however a number of problems in which the inclusion of elasticity is important. One such problem is for instance that

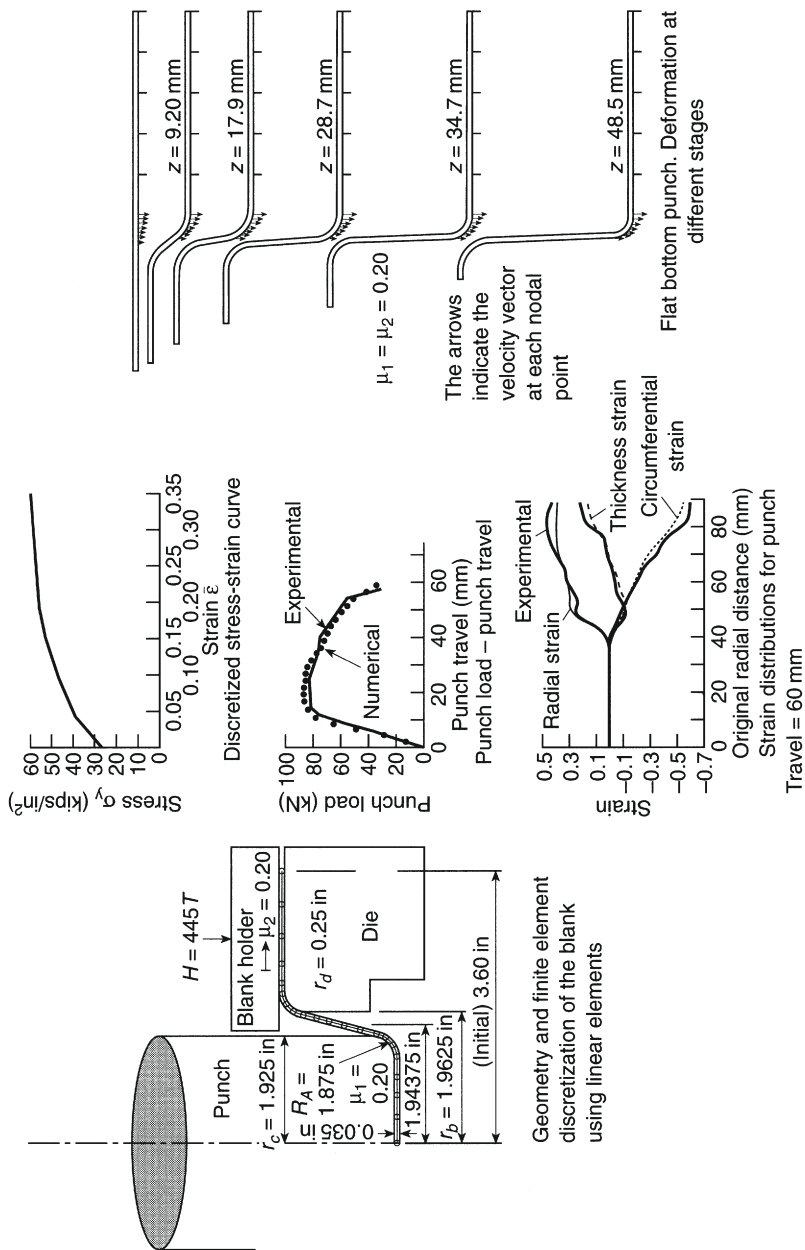


FIGURE 5.7
Deep drawing by a flat-nosed punch [50].

of “spring-back” occurring particularly in metal forming of complex shapes. Here it is important to determine the amount of elastic recovery which may occur after removing the forming loads. Some possible suggestions for the treatment of such effects have been presented in Ref. [21] as early as 1984. However since that time much attention has been focused on the flow of viscoelastic fluids, which is relevant to the above problem as well to the problem of transportation of fluids such as synthetic rubbers, etc. The procedures used in the study of such problems are quite complex and belong to the subject of numerical rheology [63–86]. Obviously the subject is vast and here we shall give a brief summary of the topic.

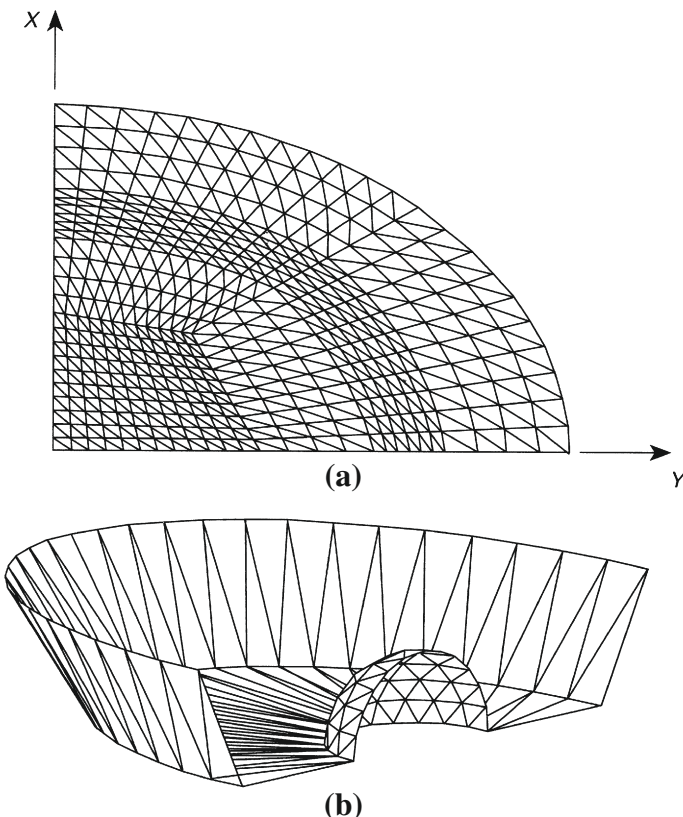


FIGURE 5.8

Finite element simulation of the superplastic forming of a thin sheet component by air pressure application. This example considers the superplastic forming of a truncated ellipsoid with a spherical indent. The original flat blank was 150 × 100 mm. The truncated ellipsoid is 20 mm deep. The original thickness was 1 mm. The minimum final thickness was 0.53 mm; 69 time steps were used with a total of 285 Newton-Raphson iterations (complete equation solutions) [53]: (a) mesh of 856 elements for sheet idealization; (b) mesh for establishing die geometry; (c) deformed sheets at various times.

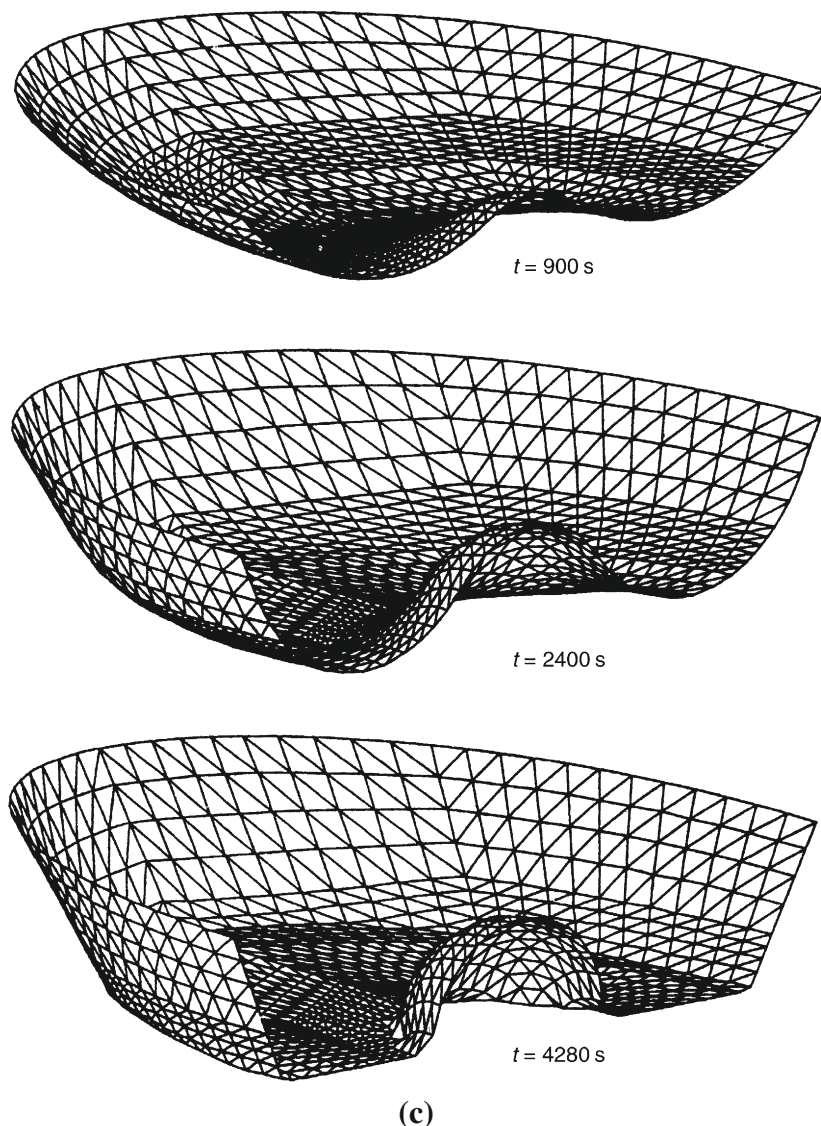
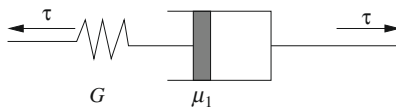


FIGURE 5.8
(Continued).

5.3 Viscoelastic flows

In this section we present a brief introduction to viscoelastic flow equations and their finite element solution using the CBS scheme. A good example of viscoelastic fluid is a polymeric liquid. Because of the memory (or spring-back) effect such fluids behave like an elastic material. A viscoelastic fluid can be represented by a number

**FIGURE 5.9**

Physical representation of Maxwell model using spring and dashpot.

of springs and dashpots connected appropriately. In such a system, springs represent elastic effect and dashpots represent viscous behavior. One such system in series is shown in Fig. 5.9. Assuming $\dot{\gamma}$ to be the strain rate of the series, the stress τ will satisfy the following relation:

$$\tau + \lambda \frac{\delta \tau}{\delta t} = \mu_1 \dot{\gamma} \quad (5.12)$$

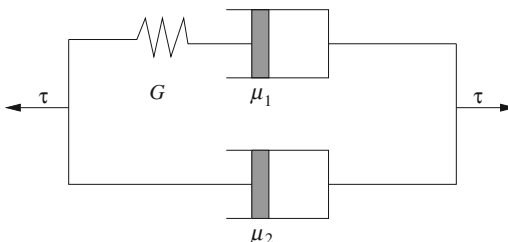
where μ_1 is the viscosity and λ is the relaxation time $= \mu_1/G$, with G being the spring constant. The above equation is widely known as the Maxwell equation. The above equation can easily be generalized to three dimensions. However, Eq. (5.12) does not obey the “objectivity rule.” The generalization of the Maxwell model to satisfy the objectivity rule is carried out by replacing the time derivative with the upper convected time derivative, i.e., replace Eq. (5.12) with

$$\tau + \lambda \left(\frac{\partial \tau}{\partial t} + u \frac{\partial \tau}{\partial x} \right) = \mu_1 \dot{\gamma} \quad (5.13)$$

In multidimensions the constitutive equation becomes

$$\tau_{ij} + \lambda \left(\frac{\partial \tau_{ij}}{\partial t} + u_k \frac{\partial \tau_{ij}}{\partial x_k} \right) = \mu_1 \left(\frac{\partial u_i}{\partial x_j} + \frac{\partial u_j}{\partial x_i} \right) \quad (5.14)$$

In viscoelastic flows, τ_{ij} calculated from constitutive equations generally replace the deviatoric stress in the momentum equation. Another popular model used by many researchers is the Oldroyd-B model. Here, stresses generated by a Newtonian solvent and polymer solution are combined. In addition to the spring and dashpot shown in Fig. 5.9, a Newtonian dashpot is connected to the system in parallel when deriving the Oldroyd-B model as shown in Fig. 5.10. If we assume τ_v to be the stress developed

**FIGURE 5.10**

Physical representation of Oldroyd-B model using spring and dashpots.

by the polymer solution and τ_n is the stress developed by the Newtonian solvent, the Oldroyd-B model may be written as

$$\tau_v + \lambda \frac{\delta \tau_v}{\delta t} = \mu_1 \left(\frac{\partial u_i}{\partial x_j} + \frac{\partial u_j}{\partial x_i} \right) + \tau_n + \lambda \frac{\delta \tau_n}{\delta t} \quad (5.15)$$

With $\tau_n = \mu_2 \dot{\gamma}$ we get

$$\tau_v + \lambda \frac{\delta \tau_v}{\delta t} = \mu_1 \left(\frac{\partial u_i}{\partial x_j} + \frac{\partial u_j}{\partial x_i} \right) + \mu_2 \left(\frac{\partial u_i}{\partial x_j} + \frac{\partial u_j}{\partial x_i} \right) + \mu_2 \lambda \frac{\delta \dot{\gamma}}{\delta t} \quad (5.16)$$

where μ_2 is the viscosity of the Newtonian solvent. Rearranging and substituting $\mu = \mu_1 + \mu_2$, we get

$$\tau_v + \lambda \frac{\delta \tau_v}{\delta t} = \mu \left[\left(\frac{\partial u_i}{\partial x_j} + \frac{\partial u_j}{\partial x_i} \right) + \lambda_R \frac{\delta \dot{\gamma}}{\delta t} \right] \quad (5.17)$$

In the above equation λ_R is the retardation time given as $\mu_2 \lambda / \mu$. In order to satisfy the objectivity rule the $\delta/\delta t$ terms need to be replaced with the upper convected derivatives as in Eq. (5.14). In the following subsection we present a generalized form of the Maxwell and Oldroyd-B models together with the equilibrium equations to solve viscoelastic flows. Further details on constitutive modeling of viscoelastic flows may be found in Refs. [63, 87].

5.3.1 Governing equations

The governing equations of viscoelastic flow can be written as follows:

Continuity equation

$$\frac{\partial \rho}{\partial t} + \frac{\partial}{\partial x_i} (U_i) = 0 \quad (5.18)$$

Momentum equation

$$\frac{\partial U_i}{\partial t} + \frac{\partial}{\partial x_j} (u_j U_i) = - \frac{\partial p}{\partial x_i} + \frac{\partial \tau_{ij}^n}{\partial x_j} + \frac{\partial \tau_{ij}^v}{\partial x_j} \quad (5.19)$$

where $U_i = \rho u_i$, ρ is the density, u_i are the velocity components, p is the pressure, and x_i are the coordinate directions. The superscript n in the above momentum equation indicates the Newtonian stress and superscript v indicates the non-Newtonian viscoelastic part of the stress. The Newtonian part of the stress relation can be written as

$$\tau_{ij}^n = \mu_2 \left(\frac{\partial u_i}{\partial x_j} + \frac{\partial u_j}{\partial x_i} \right) \quad (5.20)$$

In the above equation μ_2 is the Newtonian dynamic viscosity. The non-Newtonian extra stress tensor is expressed in conservation form as

$$\tau_{ij}^v + \lambda \left(\frac{\partial \tau_{ij}^v}{\partial t} + \frac{\partial}{\partial x_k} (u_k \tau_{ij}^v) \right) = \lambda \left(\tau_{ik}^v \frac{\partial u_j}{\partial x_k} + \tau_{jk}^v \frac{\partial u_i}{\partial x_k} \right) + \mu_1 \left(\frac{\partial u_i}{\partial x_j} + \frac{\partial u_j}{\partial x_i} \right) \quad (5.21)$$

In the above equation, μ_1 is the viscosity of viscoelastic contribution and λ is the relaxation time. It should be noted that the transient density term in the continuity equation can be replaced by the following pseudo pressure term for incompressible flows as discussed in Chapter 3:

$$\frac{\partial \rho}{\partial t} = \frac{1}{\beta^2} \frac{\partial p}{\partial t} \quad (5.22)$$

where β is an artificial compressibility parameter (or artificial wave speed). The problem is completed by specifying appropriate initial and boundary conditions for u_i , p , and extra stresses. The nondimensional form of the governing equations can be obtained by employing the following scales:

$$\begin{aligned} u_i^* &= \frac{u_i}{u_\infty}, & \rho^* &= \frac{\rho}{\rho_\infty}, & x_i^* &= \frac{x_i}{L} \\ t^* &= \frac{tu_\infty}{L}, & p^* &= \frac{pL}{\mu u_\infty}, & \tau_{ij}^{2*} &= \frac{\tau_{ij}^v L}{\mu u_\infty} \end{aligned} \quad (5.23)$$

where u_∞ is the free stream velocity, ρ_∞ is the free stream density, and L is any characteristic length. The nondimensional forms of the equations are:

Continuity equation

$$\frac{\partial \rho^*}{\partial t^*} + \frac{\partial U_i^*}{\partial x_i^*} = 0 \quad (5.24)$$

Momentum equation

$$\frac{\partial U_i^*}{\partial t^*} + \frac{\partial}{\partial x_j^*} \left(u_j^* U_i^* \right) = -\frac{1}{Re} \frac{\partial p^*}{\partial x_i^*} + \frac{1}{Re} \left(\alpha \frac{\partial \tau_{ij}^{n*}}{\partial x_j^*} + \frac{\partial \tau_{ij}^{v*}}{\partial x_j^*} \right) \quad (5.25)$$

Constitutive equation

$$\begin{aligned} \tau_{ij}^{v*} + De \left(\frac{\partial \tau_{ij}^{v*}}{\partial t^*} + \frac{\partial}{\partial x_k^*} (u_k^* \tau_{ij}^{v*}) \right) &= De \left(\tau_{ik}^{v*} \frac{\partial u_j^*}{\partial x_k^*} + \tau_{jk}^{v*} \frac{\partial u_i^*}{\partial x_k^*} \right) \\ &\quad + (1 - \alpha) \left(\frac{\partial u_i^*}{\partial x_j^*} + \frac{\partial u_j^*}{\partial x_i^*} \right) \end{aligned} \quad (5.26)$$

In the above nondimensional equations

$$\tau_{ij}^{n*} = \left(\frac{\partial u_i^*}{\partial x_j^*} + \frac{\partial u_j^*}{\partial x_i^*} \right) \quad (5.27)$$

Re is the Reynolds number and De is the Deborah number defined as

$$Re = \frac{\rho_\infty u_\infty L}{\mu}, \quad De = \frac{\lambda u_\infty}{L} \quad (5.28)$$

Here $\alpha = \mu_2/\mu$. With $\alpha = 0$ we recover the upper-convected Maxwell (UCM) model and $\alpha \neq 0$ gives the Oldroyd-B model. For incompressible viscoelastic flows the density term in Eq. (5.24) disappears.

The equations discussed above along with appropriate boundary conditions will form the governing equation system for solving viscoelastic flow problems. The solution procedure adopted here is the CBS scheme explained in Chapter 3 [77, 80, 81]. The basic three steps are the same as for Newtonian incompressible flows. However, an additional fourth step is necessary to get solutions to the constitutive equations. The simple explicit characteristic-Galerkin approach is adopted here to solve the constitutive equations. Additional dissipation is necessary at higher Deborah numbers to smooth overshoots in the solution if a fully explicit scheme is used. The artificial dissipation methods are discussed in Chapter 7. The method used in the examples of the next section is a second-order method with a pressure switch [77].

Example 5.4. Viscoelastic flow past a circular cylinder

The problem definition is shown in Fig. 5.11. A circular cylinder of radius R is placed between two solid walls of a channel. The distances to inlet and exit from the center of the cylinder are $12R$ and $16R$ respectively. The top and bottom walls are assumed to be at a distance of $2R$ from the center of the cylinder. The Deborah number De is defined based on the radius R of the cylinder as

$$De = \frac{\lambda u_\infty}{R} \quad (5.29)$$

The following nondimensional forms of boundary conditions are employed in the flow calculations [88]. At inlet and exit $u_2 = 0$,

$$u_1 = 1.5(1 - \frac{1}{4}x_2^2) \quad (5.30a)$$

$$\tau_{11}^v = \frac{9}{8}(De)x_2^2 \quad (5.30b)$$

$$\tau_{12}^v = -\frac{3}{4}x_2 \quad (5.30c)$$

and $\tau_{22}^v = 0$. On solid walls (both channel walls and cylinder surface), no-slip conditions ($u_1 = 0$ and $u_2 = 0$) are assumed. The stress boundary conditions on the solid channel walls are given as

$$\tau_{11}^v = 2\alpha De \left(\frac{\partial u_1}{\partial x_2} \right)^2 \quad (5.31a)$$

$$\tau_{12}^v = \alpha \frac{\partial u_1}{\partial x_2} \quad (5.31b)$$

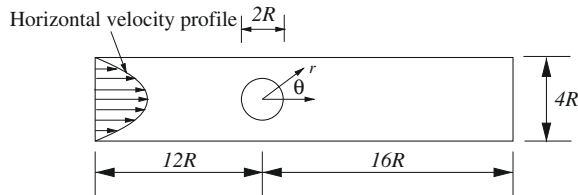


FIGURE 5.11

Viscoelastic flow past a circular cylinder. Geometry and boundary conditions.

and $\tau_{22} = 0$. On the cylinder wall the stress boundary conditions are similar to those above but in cylindrical coordinates. Thus the stress boundary conditions on the cylinder surface are

$$\tau_{\theta\theta} = 2\alpha De \left(\frac{\partial u_\theta}{\partial r} \right)^2 \quad (5.32a)$$

$$\tau_{r\theta} = \alpha \frac{\partial u_\theta}{\partial r} \quad (5.32b)$$

and $\tau_{rr} = 0$. Note that a transformation of quantities from cylindrical coordinate to Cartesian coordinates is essential in order to apply boundary conditions on the cylinder surface. To compare the present results with those available in the literature [88,89], the Reynolds number is assumed to be equal to zero and $\alpha = 0.41$ for this problem. The axial drag force on the cylinder per unit length is calculated in nondimensional form as

$$F_x = \int_0^{2\pi} [(-p + \tau_{11}^n + \tau_{11}^v) \cos \theta + (\tau_{12}^n + \tau_{12}^v) \sin \theta] R d\theta \quad (5.33)$$

The details for meshes are given in [Table 5.2](#) (for a full cylinder).

[Figure 5.12](#) shows Mesh4, which is used in all the calculations. Note that due to symmetry [88,89], only one half of the domain is used in the calculations. The closeup of the mesh in the vicinity of the cylinder is shown in [Fig. 5.12b](#). As seen the mesh is very fine close to the cylinder surface.

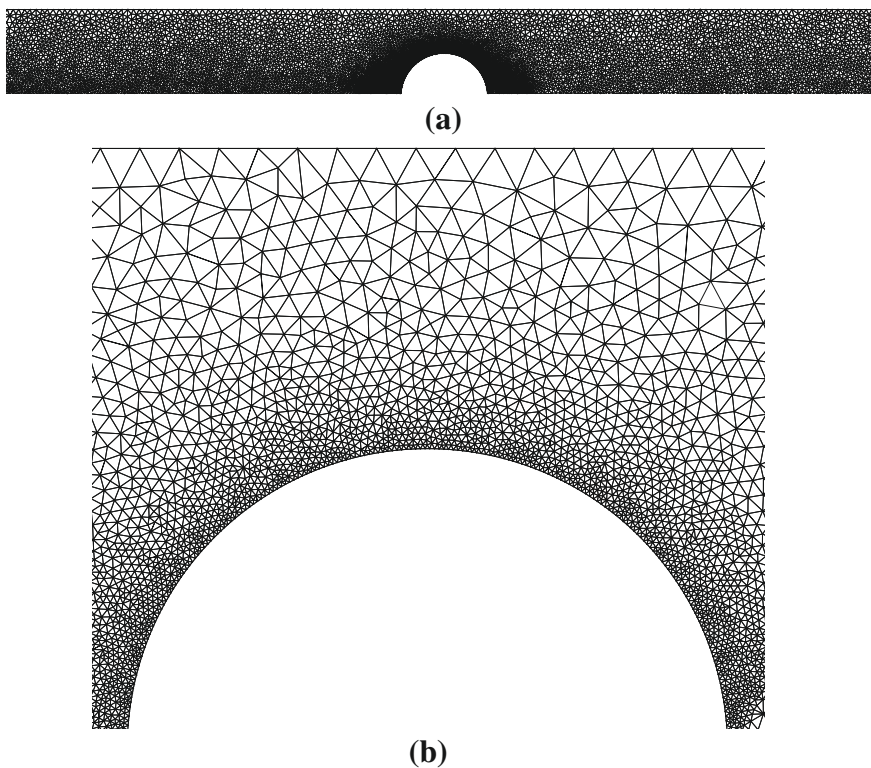
[Figure 5.13](#) shows the contours of velocity and pressure for Newtonian flow at $Re = 0$. These patterns are in excellent agreement with the results reported in the literature [90]. The drag force calculated for this Newtonian case on Mesh4 is compared with reported fine mesh results in [Table 5.3](#).

[Figure 5.14](#) gives the contours of nondimensional velocity components, pressure, and extra stress components for a Deborah number of 0.5. All variable distributions are generally smooth without exhibiting any appreciable oscillatory behavior. These images show the existence of a strong stress gradient on the cylinder surface and on the solid side wall in the vicinity of the cylinder, which is an indication of the converging-diverging effect between the cylinder and the wall.

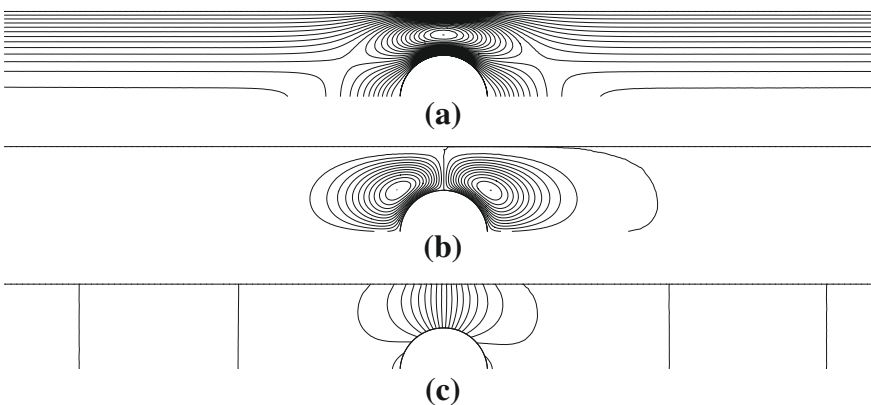
[Figure 5.15](#) shows the comparison of drag forces calculated by different authors. The difference in the drag force values of different methods is small up to a Deborah number value of 0.4. However at higher De differences do exist between the methods. The results of Sun et al. [89] and Liu et al. [92] are produced on structured meshes.

Table 5.2 Details of Unstructured Meshes Employed

Mesh	Nodes	Elements	Typical Element Size on the Cylinder Surface
Mesh1	3151	5980	0.1
Mesh2	5848	11,272	0.051
Mesh3	12,217	23,832	0.022
Mesh4	21,238	40,768	0.016

**FIGURE 5.12**

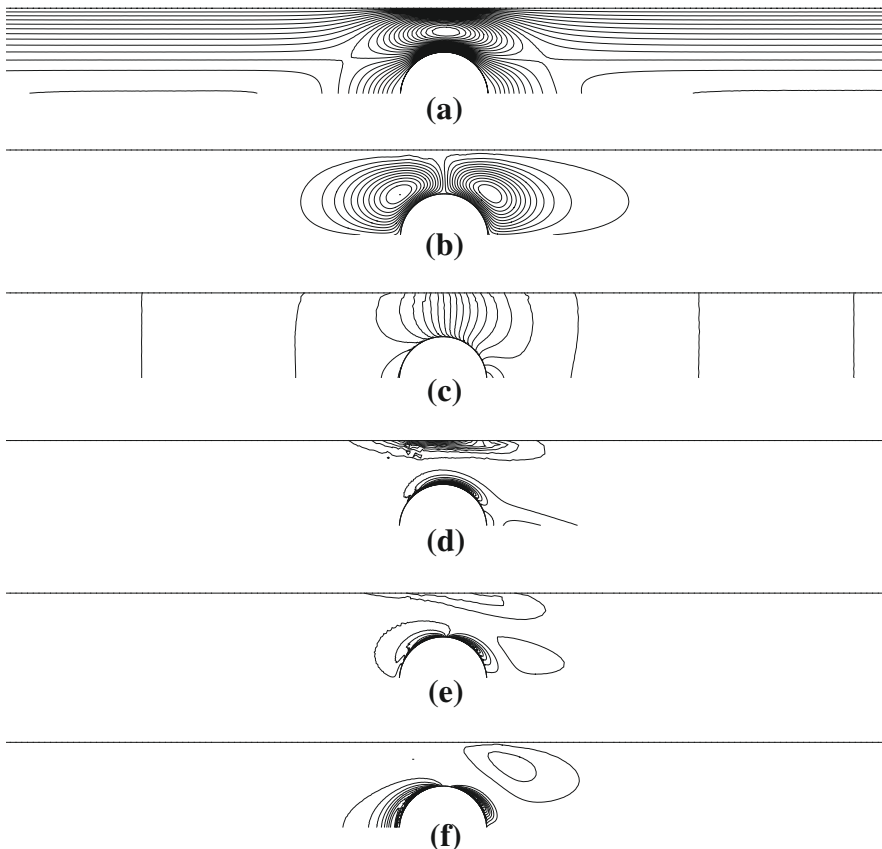
Viscoelastic flow past a circular cylinder. Unstructured mesh (nodes: 10,619; elements: 20,384): (a) mesh; (b) mesh in the vicinity of the cylinder.

**FIGURE 5.13**

Stokes flow past a circular cylinder. $Re = 0$, $De = 0.0$. Contours of velocity components and pressure: (a) u_1 velocity contours, $u_{1\min} = 0$, $u_{1\max} = 2.94$; (b) u_2 velocity contours, $u_{2\min} = -0.895$, $u_{2\max} = 0.893$; (c) pressure contours, $p_{\min} = -29.28$, $p_{\max} = 36.04$.

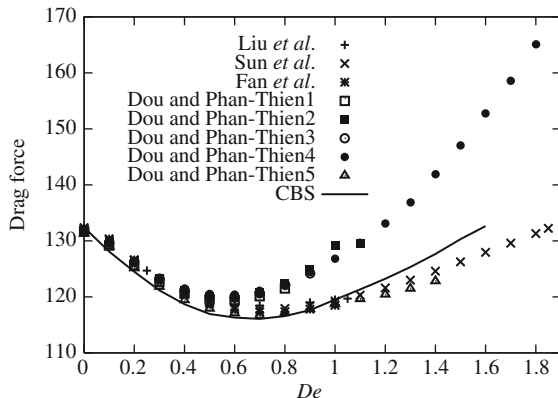
Table 5.3 Comparison of Drag Force for the Newtonian Case

[88]	[91]	[89]	[90]	[92]	CBS
131.74	132.29	132.28	132.34	132.34	132.39

**FIGURE 5.14**

Viscoelastic flow past a circular cylinder. $Re = 0$, $De = 0.5$. Contours of velocity, pressure, and elastic stresses: (a) u_1 velocity contours, $u_{1\min} = 0$, $u_{1\max} = 2.99$; (b) u_2 velocity contours, $u_{2\min} = -0.929$, $u_{2\max} = 0.884$; (c) pressure contours, $p_{\min} = -28.35$, $p_{\max} = 34.97$; (d) τ_{11}^v contours, $\tau_{11\min}^v = -0.979$, $\tau_{11\max}^v = 76.45$; (e) τ_{12}^v contours, $\tau_{12\min}^v = -18.59$, $\tau_{12\max}^v = 22.92$; (f) τ_{22}^v contours, $\tau_{22\min}^v = -0.463$, $\tau_{22\max}^v = 16.82$.

Understandably they are more accurate compared to other reported results. It is also noticed that the extrapolated drag force for a zero mesh size given by Dou and Phan-Thian [88] matches excellently with the results of Liu et al. [92] and Sun et al.

**FIGURE 5.15**

Viscoelastic flow past a circular cylinder. Comparison of drag force distribution with other available numerical data. Dou and Phan-Thian1 = Plain Oldroyd-B formulation without stress splitting; Dou and Phan-Thian2 = EVSS; Dou and Phan-Thian3 = DEVSS- ω ; Dou and Phan-Thian4 = DAVSS- ω ; Dou and Phan-Thian5 = Extrapolated results for zero mesh size.

[89] and to some extent agrees with the results of CBS. It should be noted the present CBS results are produced on a high-resolution unstructured mesh with a typical minimum size on the cylinder surface of around 0.01. However, the minimum size used by Dou and Phan-Thian [88] is 0.0402.

5.4 Direct displacement approach to transient metal forming

Explicit dynamic codes using quadrilateral or hexahedral elements have achieved considerable success in modeling short-duration impact phenomena with plastic deformation. The prototypes of finite element codes of this type are DYNA2d and DYNA3d, developed at Lawrence Livermore National Laboratory [93, 94]. For problems of relatively slow metal forming, such codes present some difficulties as in general the time step is governed by the elastic compressibility of the metal and a vast number of time steps would be necessary to cover a realistic metal forming problem. Nevertheless much use has been made of such codes in slow metal forming processes by the simple expedient of increasing the density of the material by many orders of magnitude. This is one of the drawbacks of using such codes whose description rightly belongs to the matter discussed in Ref. [1]. However, a further drawback is the lack of triangular or tetrahedral elements of a linear kind which could compete with linear quadrilaterals or hexahedra currently used and permit an easier introduction of adaptive refinement. It is well known that linear triangles or tetrahedra in a pure displacement (velocity) formulation will lock for incompressible

or nearly incompressible materials. However, we have already found that the CBS algorithm will avoid such locking even if the same (linear) interpolation is used for both velocities and pressure [95].

It is therefore possible to proceed in each step by solving a simple Stokes problem to evaluate the Lagrangian velocity increment. We have described the use of such velocity formulation in the previous chapter. The update of the displacement allows new stresses to be evaluated by an appropriate plasticity law and the method can be used without difficulty as shown by Zienkiewicz et al. [95].

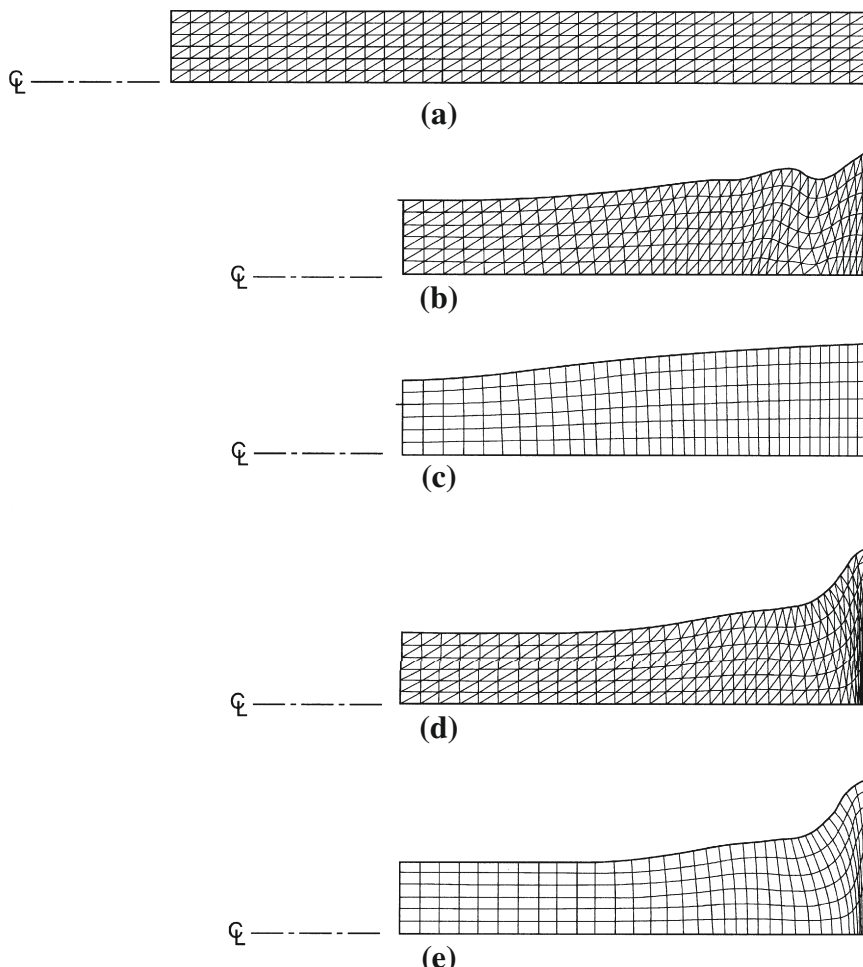
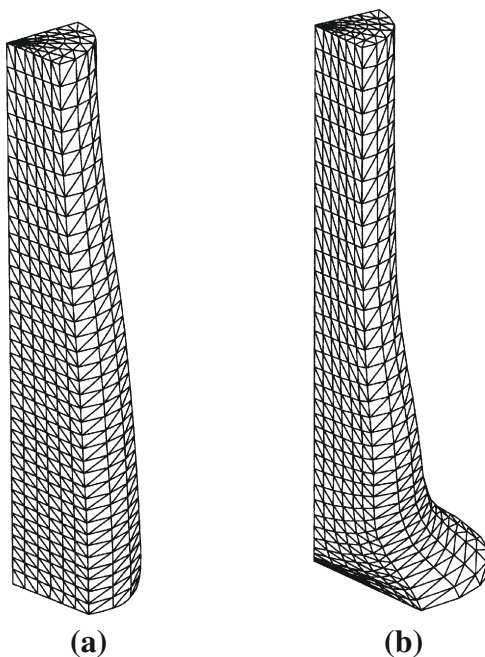


FIGURE 5.16

Axisymmetric solutions to the bar impact problem: (a) initial shape; (b) linear triangles—displacement algorithm; (c) bilinear quadrilaterals—displacement algorithm; (d) linear triangles—CBS algorithm; (e) bilinear quadrilaterals—CBS algorithm.

**FIGURE 5.17**

Three-dimensional solution: (a) tetrahedral elements—standard displacement algorithm; (b) tetrahedral elements—CBS algorithm.

Example 5.5. Impact of a circular bar

In Fig. 5.16, we show a comparison between various methods of solving the impact of a circular bar made of an elastoplastic metal using an axisymmetric formulation. In this figure we show the results of a linear triangle displacement (Fig. 5.16b) form with a single integrating point for each element and a similar study again using displacement linear quadrilaterals (Fig. 5.16c) also with a single integration point. This figure also shows the same triangles and quadrilaterals solved using the CBS algorithm and now giving very accurate final results (Fig. 5.16d and e).

In Fig. 5.17 we show similar results obtained with a full three-dimensional analysis. Similar methods for this problem have been presented by Bonet and Burton [96].

5.5 Concluding remarks

The range of examples for which an incompressible formulation applies is very large as we have shown in this chapter. Indeed many other examples could have been included but for lack of space we proceed directly to Chapter 6 where the incompressible formulation is used for problems in which free surface or buoyancy occurs, with gravity forces being the most important factor.

References

- [1] O.C. Zienkiewicz, R.L. Taylor, D.D. Fox, *The Finite Element Method for Solids and Structural Mechanics*, seventh ed., Elsevier, Oxford, 2013.
- [2] K. Palit, R.T. Fenner, Finite element analysis of two dimensional slow non-Newtonian flows, *AIChE J.* 18 (1972) 1163–1169.
- [3] B. Atkinson, C.C.M. Card, B.M. Irons, Application of the finite element method to creeping flow problems, *Trans. Inst. Chem. Eng.* 48 (1970) 276–284.
- [4] O.C. Zienkiewicz, P.N. Godbole, A penalty function approach to problems of plastic flow of metals with large surface deformation, *J. Strain Anal.* 10 (1975) 180–183.
- [5] G.C. Cornfield, R.H. Johnson, Theoretical prediction of plastic flow in hot rolling including the effect of various temperature distributions, *J. Iron Steel Inst.* 211 (1973) 567–573.
- [6] C.H. Lee, S. Kobayashi, New solutions to rigid plastic deformation problems using a matrix method, *Trans. ASME J. Eng. Ind.* 95 (1973) 865–873.
- [7] J.T. Oden, D.R. Bhandari, G. Yagewa, T.J. Chung, A new approach to the finite element formulation and solution of a class of problems in coupled thermoelastoviscoplasticity of solids, *Nucl. Eng. Des.* 24 (1973) 420.
- [8] R.E. Nickell, R.I. Tanner, B. Caswell, The solution of viscous incompressible jet and free surface flows using finite elements, *J. Fluid Mech.* 65 (1974) 189–206.
- [9] R.I. Tanner, R.E. Nickell, R.W. Bilger, Finite element method for the solution of some incompressible non-Newtonian fluids mechanics problems with free surface, *Comput. Methods Appl. Mech. Eng.* 6 (1975) 155–174.
- [10] J.M. Alexander, J.W.H. Price, Finite element analysis of hot metal forming, in: *Proceedings of 18th MTDR Conference*, 1977, pp. 267–274.
- [11] O.C. Zienkiewicz, P.C. Jain, E. Oñate, Flow of solids during forming and extrusion: some aspects of numerical solutions, *Int. J. Solids Struct.* 14 (1978) 15–38.
- [12] P.R. Dawson, E.G. Thompson, Finite element analysis of steady state elastoviscoplastic flow by the initial stress rate method, *Int. J. Numer. Methods Eng.* 12 (1978) 47–57.
- [13] O.C. Zienkiewicz, E. Oñate, J.C. Heinrich, Plastic flow in metal forming, in: *Proceedings of the Winter Annual Meeting of ASME*, San Francisco, December 1978, pp. 107–120.
- [14] N. Rebelo, S. Kobayashi, A coupled analysis of viscoplastic deformation and heat transfer: I. Theoretical consideration, *Int. J. Mech. Sci.* 22 (1980) 699–705.
- [15] O.C. Zienkiewicz, E. Oñate, J.C. Heinrich, A general formulation for coupled thermal flow of metals using finite elements, *Int. J. Numer. Methods Eng.* 17 (1980) 1497–1514.
- [16] Y. Shimizaki, E.G. Thompson, Elasto-visco-plastic flow with special attention to boundary conditions, *Int. J. Numer. Meth. Eng.* 17 (1981) 97–112.
- [17] S. Nakazawa, J.F. Pittman, O.C. Zienkiewicz, Numerical solution of flow and heat transfer in polymer melts, in: R.H. Gallagher et al. (Eds.), *Finite Elements in Fluids*, vol. 4, John Wiley & Sons, Chichester, 1982, pp. 251–283 (Chapter 13).

- [18] S. Nakazawa, J.F.T. Pittman, O.C. Zienkiewicz, A penalty finite element method for thermally coupled non-Newtonian flow with particular reference to balancing dissipation and the treatment of history dependent flows, in: International Symposium of Refined Modelling of Flows, Ecole Nationale des Ponts et Chaussees, Paris, September 1982, pp. 7–10.
- [19] S.I. Oh, G.D. Lahoti, A.T. Altan, Application of finite element method to industrial metal forming processes, in: Proceedings of Conference on Industrial Forming Processes, Pineridge Press, Swansea, 1982, pp. 146–153.
- [20] J.F.T. Pittman, O.C. Zienkiewicz, R.D. Wood, J.M. Alexander (Eds.), Numerical Analysis of Forming Processes, John Wiley & Sons, Chichester, 1984.
- [21] O.C. Zienkiewicz, Flow formulation for numerical solutions of forming problems, in: J.F.T. Pittman et al. (Eds.), Numerical Analysis of Forming Processes, John Wiley & Sons, Chichester, 1984, pp. 1–44 (Chapter 1).
- [22] S. Kobayashi, Thermoviscoplastic analysis of metal forming problems by the finite element method, in: J.F.T. Pittman et al. (Eds.), Numerical Analysis of Forming Processes, John Wiley & Sons, Chichester, 1984, pp. 45–70 (Chapter 2).
- [23] J.L. Chenot, F. Bay, L. Fourment, Finite element simulation of metal powder forming, *Int. J. Numer. Meth. Eng.* 30 (1990) 1649–1674.
- [24] P.A. Balaji, T. Sundararajan, G.K. Lal, Viscoplastic deformation analysis and extrusion die design by FEM, *J. Appl. Mech. Trans. ASME* 58 (1991) 644–650.
- [25] K.H. Raj, J.L. Chenot, L. Fourment, Finite element modelling of hot metal forming, *Indian J. Eng. Mat. Sci.* 3 (1996) 234–238.
- [26] J.L. Chenot, Recent contributions to the finite element modelling of metal forming processes, *J. Mater. Process. Technol.* 34 (1992) 9–18.
- [27] J. Bonet, P. Bhargava, R.D. Wood, The incremental flow formulation for the finite element analysis of 3-dimensional superplastic forming processes, *J. Mater. Process. Technol.* 45 (1994) 243–248.
- [28] R.D. Wood, J. Bonet, A review of the numerical analysis of super-plastic forming, *J. Mater. Process. Technol.* 60 (1996) 45–53.
- [29] J.L. Chenot, Y. Chastel, Mechanical, thermal and physical coupling methods in FE analysis of metal forming processes, *J. Mater. Process. Technol.* 60 (1996) 11–18.
- [30] D. Brokken, W.A.M. Brekelmans, F.P.T. Baaijens, Numerical modelling of the metal blanking process, *J. Mater. Process. Technol.* 83 (1–3) (1998) 192–199.
- [31] J. Rojek, E. Oñate, E. Postek, Application of explicit FE codes to simulation of sheet and bulk metal forming processes, *J. Mater. Process. Technol.* 80 (1998) 620–627.
- [32] S.W. Hsiao, N. Kikuchi, Numerical analysis and optimal design of composite thermoforming process, *Comput. Methods Appl. Mech. Eng.* 177 (1–2) (1999) 1–34.
- [33] J. Bonet, A.J. Gil, Finite element modelling of thin metal sheet forming, in: G. Giuliano (Ed.), Superplastic Forming of Advanced Metallic Materials: Methods and Applications, Woodhead Publishing in Materials, 2011, pp. 136–153.

- [34] J.-L. Chenot, R.D. Wood, O.C. Zienkiewic (Eds.), Numerical Methods in Industrial Forming Processes: NUMIFORM 92, Valbonne, France, 14–19, A.A. Balkema, Rotterdam, September 1992.
- [35] J. Huetink, F.P.T. Baaijens (Eds.), Simulation of Materials Processing: Theory, Methods and Applications: NUMIFORM 98, Enschede, Netherlands, A.A. Balkema, Rotterdam, 22–25 june 1998.
- [36] S. Ghosh, J.M. Castro, J.K. Lee (Eds.), Materials Processing and Design: Theory, Methods and Applications, NUMIFORM 2004, American Institute of Physics, 2004.
- [37] Jose M.A. Cesar de Sa, Abel D. Santos (Eds.), Materials Processing and Design: Modeling, Simulation and Applications, NUMIFORM 2007: Proceedings of the 9th International Conference on Numerical Methods in Industrial Forming Processes. AIP Conference Proceedings 908, 2007.
- [38] F. Barlat, Y.H. Moon, M.G. Lee (Eds.), NUMIFORM 2010: Proceedings of the 10th International Conference on Numerical Methods in Industrial Forming Processes Dedicated to Professor O.C. Zienkiewicz (1921–2009), AIP Conference Proceedings, vol. 1252, 2010.
- [39] W. Johnson, P.B. Mellor, Engineering Plasticity, Van Nostrand-Reinhold, London, 1973.
- [40] O.C. Zienkiewicz, Y.C. Liu, G.C. Huang, Error estimates and convergence rates for various incompressible elements, *Int. J. Numer. Methods Eng.* 28 (1989) 2191–2202.
- [41] G.C. Huang, Error estimates and adaptive remeshing in finite element analysis of forming processes, Ph.D Thesis, Department of Civil Engineering, University of Wales, Swansea, 1989.
- [42] G.C. Huang, Y.C. Liu, O.C. Zienkiewicz, Error control, mesh updating schemes and automatic adaptive remeshing for finite element analysis of unsteady extrusion processes, in: J.L. Chenot, E. Oñate (Eds.), Modelling of Metal Forming Processes, Kluwer Academic, Dordrecht, 1988, pp. 75–83.
- [43] O.C. Zienkiewicz, Y.C. Liu, G.C. Huang, An error estimate and adaptive refinement method for extrusion and other forming problems, *Int. J. Numer. Methods Eng.* 25 (1988) 23–42.
- [44] O.C. Zienkiewicz, Y.C. Liu, J.Z. Zhu, S. Toyoshima, Flow formulation for numerical solution of forming processes. II—Some new directions, in: K. Mattiasson, A. Samuelsson, R.D. Wood, O.C. Zienkiewicz (Eds.), Proceedings of 2nd International Conference on Numerical Methods in Industrial Forming Processes, NUMIFORM 86, A.A. Balkema, Rotterdam, 1986.
- [45] T. Belytschko, D.P. Flanagan, J.M. Kennedy, Finite element methods with user controlled mesh for fluid structure interaction, *Comput. Methods Appl. Mech. Eng.* 33 (1982) 669–688.
- [46] J. Donea, S. Giuliani, H. Laval, L. Quartapelle, Finite element solution of unsteady Navier-Stokes equations by a fractional step method, *Comput. Methods Appl. Mech. Eng.* 33 (1982) 53–73.

- [47] P.J.G. Schreurs, F.E. Veldpaus, W.A.M. Brakalmans, An Eulerian and Lagrangian finite element model for the simulation of geometrical non-linear hyper-elastic and elasto-plastic deformation processes, in: Proceedings of Conference on Industrial Forming Processes, Pineridge Press, Swansea, 1983, pp. 491–500.
- [48] J. Donea, Arbitrary Lagrangian-Eulerian finite element methods, in: T. Belytschko, T.J.R. Hughes (Eds.), Computation Methods for Transient Analysis, Elsevier, Amsterdam, 1983, pp. 474–516 (Chapter 10).
- [49] J. van der Lught, J. Huetnik, Thermo-mechanically coupled finite element analysis in metal forming processes, *Comput. Methods. Appl. Mech. Eng.* 54 (1986) 145–160.
- [50] E. Oñate, O.C. Zienkiewicz, A viscous sheet formulation for the analysis of thin sheet metal forming, *Int. J. Mech. Sci.* 25 (1983) 305–335.
- [51] N.M. Wang, B. Budiansky, Analysis of sheet metal stamping by a finite element method, *J. Appl. Mech. ASME* 45 (1976) 73.
- [52] A.S. WiFi, An incremented complete solution of the stretch forming and deep drawing of a circular blank using a hemispherical punch, *Int. J. Mech. Sci.* 18 (1976) 23–31.
- [53] J. Bonet, R.D. Wood, O.C. Zienkiewicz, Time stepping schemes for the numerical analysis of superplastic forming of thin sheets, in: J.L. Chenot, E. Oñate (Eds.), Modelling of Metal Forming Processes, Kluwer Academic, Dordrecht, 1988, pp. 179–186.
- [54] E. Massoni, M. Bellet, J.L. Chenot, Thin sheet forming numerical analysis with membrane approach, in: J.L. Chenot, E. Oñate (Eds.), Modelling of Metal Forming Processes, Kluwer Academic, Dordrecht, 1988.
- [55] J. Bonet, R.D. Wood, O.C. Zienkiewicz, Finite element modelling of the superplastic forming of a thin sheet, in: C.H. Hamilton, N.E. Paton (Eds.), Proceedings Conference on Superquality and Superplastic Forming, The Minerals, Metals and Materials Society, USA, 1988.
- [56] R.D. Wood, J. Bonet, A.H.S. Wargedipura, Simulation of the superplastic forming of thin sheet components using the finite element method, in: Proceedings of NUMIFORM 89, A.A. Balkema, Rotterdam, 1989, pp. 85–94.
- [57] E. Oñate, C.A. Desaracibar, Finite element analysis of sheet metal forming problems using a selective bending membrane formulation, *Int. J. Numer. Meth. Eng.* 30 (1990) 1577–1593.
- [58] W. Sosnowski, E. Oñate, C.A. Desaracibar, Comparative study of sheet metal forming processes by numerical modelling and experiment, *J. Mater. Process. Technol.* 34 (1992) 109–116.
- [59] J. Bonet, R.D. Wood, Incremental flow procedures for the finite element analysis of thin sheet superplastic forming processes, *J. Mater. Process. Technol.* 42 (1994) 147–165.
- [60] W. Sosnowski, M. Kleiber, A study on the influence of friction evolution on thickness changes in sheet metal forming, *J. Mat. Proc. Tech.* 60 (1996) 469–474.

- [61] M. Kawka, T. Kakita, A. Makinouchi, Simulation of multi-step sheet metal forming processes by a static explicit FEM code, *J. Mat. Proc. Tech.* 80 (1998) 54–59.
- [62] S.K. Esche, G.K. Kinzel, J.K. Lee, An axisymmetric membrane element with bending stiffness for static implicit sheet metal forming simulation, *J. Appl. Mech. ASME* 66 (1999) 153–164.
- [63] M.J. Crochet, R. Keunings, Finite element analysis of die swell of highly elastic fluid, *J. Non-Newtonian Fluid Mech.* 10 (1982) 339–356.
- [64] M.J. Crochet, A.R. Davies, K. Walters, Numerical simulation of non-Newtonian flow, *Rheology Series*, vol. 1, Elsevier, Amsterdam, 1984.
- [65] R. Keunings, M.J. Crochet, Numerical simulation of the flow of a viscoelastic fluid through an abrupt contraction, *J. Non-Newtonian Fluid Mech.* 14 (1984) 279–299.
- [66] S. Dupont, J.M. Marchal, M.J. Crochet, Finite element simulation of viscoelastic fluids of the integral type, *J. Non-Newtonian Fluid Mech.* 17 (1985) 157–183.
- [67] J.M. Marchal, M.J. Crochet, A new mixed finite element for calculating visco elastic flow, *J. Non-Newtonian Fluid Mech.* 26 (1987) 77–114.
- [68] M.J. Crochet, V. Legat, The consistent streamline upwind Petrov-Galerkin method for viscoelastic flow revisited, *J. Non-Newtonian Fluid Mech.* 42 (1992) 283–299.
- [69] H.R. Tamaddonjahromi, D. Ding, M.F. Webster, P. Townsend, A Taylor-Galerkin finite element method for non-Newtonian flows, *Int. J. Numer. Methods Eng.* 34 (1992) 741–757.
- [70] E.O.A. Carew, P. Townsend, M.F. Webster, A Taylor-Galerkin algorithm for viscoelastic flow, *J. Non-Newtonian Fluid Mech.* 50 (1993) 253–287.
- [71] D. Ding, P. Townsend, M.F. Webster, Finite element simulation of an injection moulding process, *Int. J. Num. Methods Heat Fluid Flow* 7 (1997) 751–766.
- [72] H. Matallah, P. Townsend, M.F. Webster, Recovery and stress-splitting schemes for viscoelastic flows, *J. Non-Newtonian Fluid Mech.* 75 (1998) 139–166.
- [73] F.P.T. Baaijens, Mixed finite element methods for viscoelastic flow analysis: a review, *J. Non-Newtonian Fluid Mech.* 79 (2–3) (1998) 361–385.
- [74] M.D. Smith, R.C. Armstrong, R.A. Brown, R. Sureshkumar, Finite element analysis of stability of two-dimensional viscoelastic flows to three-dimensional perturbations, *J. Non-Newtonian Fluid Mech.* 93 (2–3) (2000) 203–244.
- [75] J. Petera, A new finite element scheme using the Lagrangian framework for simulation of viscoelastic fluid flows, *J. Non-Newtonian Fluid Mech.* 103 (2002) 1–43.
- [76] A.G. Lee, E.S.G. Shaqfeh, B. Khomami, A study of viscoelastic free surface flows by the finite element method: Hele-Shaw and slot coating flows, *J. Non-Newtonian Fluid Mech.* 108 (1–3) (2002) 327–362.
- [77] P. Nithiarasu, A fully explicit characteristic based split (CBS) scheme for viscoelastic flow calculations, *Int. J. Numer. Methods Eng.* 60 (5) (2004) 949–978.

- [78] J.M. Kim, C. Kim, J.H. Kim, C. Chung, K.H. Ahn, S.J. Lee, High-resolution finite element simulation of 4:1 planar contraction flow of viscoelastic fluid, *J. Non-Newtonian Fluid Mech.* 129 (1) (2005) 23–37.
- [79] P. Yue, C. Zhou, J.J. Feng, C.F. Ollivier-Gooch, H.H. Hu, Phase-field simulations of interfacial dynamics in viscoelastic fluids using finite elements with adaptive meshing, *J. Comput. Phys.* 219 (2006) 47–67.
- [80] C.-B. Liu, P. Nithiarasu, The characteristic-based split (CBS) scheme for viscoelastic flow past a circular cylinder, *Int. J. Numer. Methods Fluids* 57 (2008) 157–176.
- [81] C.-B. Liu, P. Nithiarasu, An artificial-dissipation-based fractional step scheme for upper-convedted Maxwell (UCM) fluid flow past a circular cylinder, *Int. J. Numer. Methods Fluids* 57 (2008) 1171–1187.
- [82] Z. Cai, C.R. Westphal, An adaptive mixed least-squares finite element method for viscoelastic fluids of Oldroyd type, *J. Non-Newtonian Fluid Mech.* 159 (1–3) (2009) 72–80.
- [83] X. Li, H. Xianhong, W. Xuanping, Numerical modeling of viscoelastic flows using equal low-order finite elements, *Comput. Methods Appl. Mech. Eng.* 199 (9–12) (2010) 570–581.
- [84] Y.-J. Lee, J. Xu, C.-S. Zhang, Stable finite element discretizations for viscoelastic flow models, in: R. Glowinski, J. Xu (Eds.), Special Volume: Numerical Methods for Non-Newtonian Fluids, *Handbook of Numerical Analysis*, vol. 16, Elsevier, 2011, pp. 371–432.
- [85] W.R. Hwang, M.A. Walkley, O.G. Harlen, A fast and efficient iterative scheme for viscoelastic flow simulations with the DEVSS finite element method, *J. Non-Newtonian Fluid Mech.* 166 (7–8) (2011) 354–362.
- [86] Y.J. Choi, M.A. Hulsen, H.E.H. Meijer, Simulation of the flow of a viscoelastic fluid around a stationary cylinder using an extended finite element method, *Comput. Fluids* 57 (2012) 183–194.
- [87] N. Phan-Thien, *Understanding Viscoelasticity. Basics of Rheology*, Springer Verlag, Berlin, 2002.
- [88] H.S. Dou, N. Phan-Thien, The flow of an Oldroyd-B fluid past a cylinder in a channel: adaptive viscosity vorticity (DAVSS-omega) formulation, *J. Non-Newtonian Fluid Mech.* 87 (1) (1999) 47–73.
- [89] J. Sun, M.D. Smith, R.C. Armstrong, R.A. Brown, Finite element method for viscoelastic flows based on the discrete adaptive viscoelastic stress splitting and the discontinuous Galerkin method: DAVSS-G/DG, *J. Non-Newtonian Fluid Mech.* 86 (3) (1999) 281–307.
- [90] E. Mitsoulis, Numerical simulation of confined flow of polyethylene melts around a cylinder in a planar channel, *J. Non-Newtonian Fluid Mech.* 76 (1–3) (1998) 327–350.
- [91] Y.R. Fan, R.I. Tanner, N. Phan-Thien, Galerkin/least-square finite-element methods for steady viscoelastic flows, *J. Non-Newtonian Fluid Mech.* 84 (2–3) (1999) 233–256.

- [92] A.W. Liu, D.E. Bornside, R.C. Armstrong, R.A. Brown, Viscoelastic flow of polymer solutions around a periodic, linear array of cylinders: comparisons of predictions for microstructure and flow fields, *J. Non-Newtonian Fluid Mech.* 77 (3) (1998) 153–190.
- [93] G.L. Goudreau, J.O. Hallquist, Recent developments in large scale Lagrangian hydrocodes, *Comput. Methods Appl. Mech. Eng.* 33 (1982) 725–757.
- [94] J.O. Hallquist, G.L. Goudreau, D.J. Benson, Sliding interfaces with contact-impact in large scale Lagrangian computations, *Comput. Methods Appl. Mech. Eng.* 51 (1985) 107–137.
- [95] O.C. Zienkiewicz, J. Rojek, R.L. Taylor, M. Pastor, Triangles and tetrahedra in explicit dynamics codes for solids, *Int. J. Numer. Methods Eng.* 43 (1998) 565–583.
- [96] J. Bonet, A.J. Burton, A simple average nodal pressure tetrahedral element for incompressible and nearly incompressible dynamic explicit applications, *Commun. Numer. Methods Eng.* 14 (1998) 437–449.

Free Surface and Buoyancy Driven Flows

6

6.1 Introduction

In [Chapter 4](#) we introduced the reader to the solution of incompressible flow problems and illustrated these with many examples of Newtonian ([Chapter 4](#)) and non-Newtonian flows ([Chapter 5](#)). In the present chapter, we shall address two separate topics of incompressible flow, which were not dealt with in the previous chapters. This chapter is thus divided into two parts. The common theme is that of the action of the body force due to gravity. We start with a section addressed to problems of free surfaces and continue with the second section, which deals with buoyancy effects caused by temperature differences in various parts of the domain.

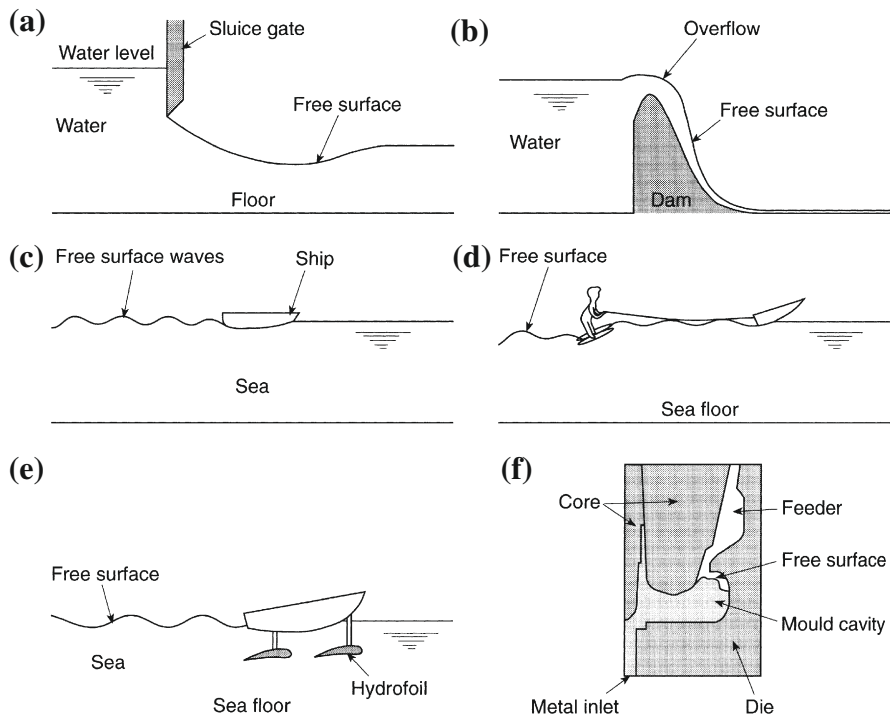
The first part of this chapter, [Section 6.2](#), deals with problems in which a free surface of flow occurs when gravity forces are acting throughout the domain. Typical examples here would be for instance given by the disturbance of the free surface of water and the creation of waves by moving ships or submarines. Of course other problems of similar kinds arise in practice. Indeed in [Chapter 10](#), where we deal with shallow water flows, a free surface is an essential condition but other assumptions and simplifications have to be introduced. In the present chapter, we shall deal with the full incompressible flow equations without any further physical assumptions. There are other topics of free surfaces which occur in practice. One of these for instance is that of mold filling, which is frequently encountered in manufacturing where a particular fluid or polymer is poured into a mold and solidified.

In [Section 6.3](#), we invoke problems of buoyancy and here we can deal with natural convection when the only force causing the flow is that of the difference between uniform density and density which has been perturbed by a given temperature field. In such examples it is a fairly simple matter to modify the equations so as to deal only with the perturbation forces, but on occasion forced convection is coupled with such naturally occurring convection.

6.2 Free surface flows

6.2.1 General remarks

In many problems of practical importance a free surface will occur in the fluid (always liquid). In general the position of such a free surface is not known and the main problem

**FIGURE 6.1**

Typical problems with a free surface.

is that of determining it. In Fig. 6.1, we show a set of typical problems of free surfaces; these range from flow over and under water control structures and flow around ships, to industrial processes such as filling of molds. All these situations deal with a fluid which is incompressible and in which the viscous effects either can be important or on the other hand may be neglected. The only difference from solving the type of problem which we have discussed in the previous two chapters is the fact that the position of the free surface is not known *a priori* and has to be determined during the computation.

There are several ways of dealing with such free surface flows. We broadly classify them into three categories. They are (1) pure Lagrangian methods, (2) Eulerian methods, and (3) arbitrary Lagrangian-Eulerian (ALE) methods.

6.2.1.1 *Lagrangian methods*

In this method we write the equations for the fluid particles whose position is changing continuously in time. Such Lagrangian methods almost always are used in the study of solid mechanics but are relatively seldom applied in fluid dynamics due to the fact that deformation is extremely large in fluids. There is an immediate advantage of Lagrangian formulation in the fact that convective acceleration is nonexistent and

the problem is immediately self-adjoint. Further, for problems in which free surface occurs it allows the free surface to be continuously updated and maintained during the fluid motion [1–9].

6.2.1.2 Eulerian methods

In Eulerian methods for which we have established the equation in Chapter 1 the boundaries of the fluid motion are fixed in position and so indeed are any computational meshes. For free surface problems an immediate difficulty arises as the position of the free surface is not known *a priori*. The numerical method will therefore have to include an additional algorithm to trace the free surface positions [10–24].

6.2.1.3 Arbitrary Langrangian-Eulerian (ALE) methods

With both Lagrangian and Eulerian methods certain difficulties and advantages occur and on occasion it is possible to provide an alternative which attempts to secure the best features of both the Lagrangian and Eulerian descriptions by combining these. Such methods are known as ALE methods. These methods are generally complex to implement and we shall give further description of these methods later [25–43].

6.2.2 Lagrangian method

As mentioned before the mesh moves with the flow in the Lagrangian methods. Thus after completion of the CBS steps involved it is necessary to determine the new positions of the mesh. The fluid dynamics equations solved are the same as the ones presented in Chapter 4 except that the convective terms are absent. The governing equations for isothermal Lagrangian fluid dynamics can be written as

$$\frac{\partial \mathbf{V}}{\partial t} + \frac{\partial \mathbf{G}_i}{\partial x_i} + \mathbf{Q} = 0 \quad (6.1)$$

with

$$\mathbf{V}^T = (\rho, \rho u_j) j = 1, N_{\text{dim}} \quad (6.2)$$

being the independent variable vector, and

$$\mathbf{G}_i^T = (0, -\tau_{ij}) j = 1, N_{\text{dim}} \quad (6.3)$$

where N_{dim} is the number of spatial dimensions. The source term \mathbf{Q} represents the body force due to gravity.

In the above, the deviatoric stress components τ_{ij} are related to velocity as

$$\tau_{ij} = \mu \left(\frac{\partial u_i}{\partial x_j} + \frac{\partial u_j}{\partial x_i} \right) \quad (6.4)$$

In the above equations, u_i are the velocity components, ρ is the density, p is the pressure, and μ is the dynamic viscosity.

The continuity and dynamic momentum equations are repeated in a detailed individual form as

Continuity

$$\frac{\partial \rho}{\partial t} + \frac{\partial}{\partial x_i} (U_i) = 0 \quad (6.5)$$

Momentum

$$\frac{\partial U_i}{\partial t} = -\frac{\partial p}{\partial x_i} + \frac{\partial \tau_{ij}}{\partial x_j} + \rho g_i \quad (6.6)$$

where $U_i = \rho u_i$ and g_i is the gravity force. It should be noted that the transient density term in the continuity equation can be replaced by the following relation:

$$\frac{\partial \rho}{\partial t} = \frac{1}{\beta^2} \frac{\partial p}{\partial t} \quad (6.7)$$

where β is an artificial wave speed (Chapter 3). The problem is completed by specifying appropriate initial conditions for u_i and p together with boundary conditions.

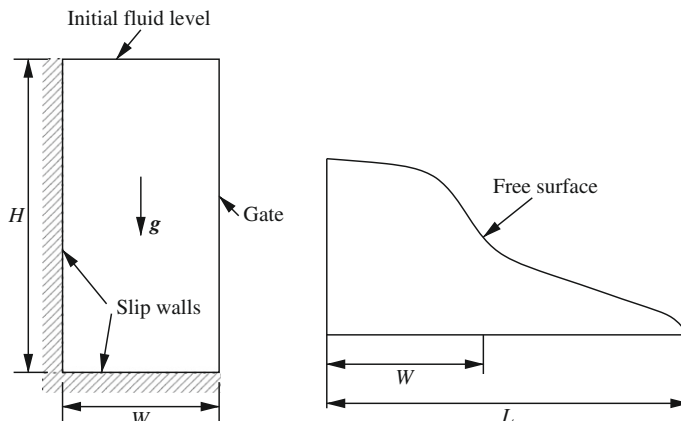
The solution procedure follows one of the time discretizations discussed in Chapter 3. For using semi-implicit schemes the transient term is omitted in Eq. (6.5). For fully explicit schemes, this term is retained along with the artificial compressible wave speed [Eq. (6.7)]. However, dual time stepping is necessary when the artificial compressibility method is employed (Chapter 3). The coordinates of the nodes are moved using the following relation after every real time step [3]:

$$x_i^{n+1} = x_i^n + \frac{1}{2} \Delta t (u_i^{n+1} + u_i^n) \quad (6.8)$$

Here Δt is the real time step.

Example 6.1. Lagrangian free surface method for a model broken dam problem

An example problem of a somewhat idealized dam failure as shown in Fig. 6.2 is solved using the semi-implicit form of CBS [44]. Although not realistic, this problem is frequently used as a benchmark for validating Lagrangian algorithms. The experimental data are indeed available and will be used here for comparison. As seen from

**FIGURE 6.2**

Broken dam problem. Problem definition and schematic of the free surface.

[Fig. 6.2](#) the problem consists of two slip walls on which slip boundary conditions are applied (normal velocity zero or tangential traction zero). The initial fluid position is as shown in [Fig. 6.2](#) (left) with velocities at all nodes equal to zero. The dimensions of the dam are $H = 7$ and $W = 3.5$. The gravity was assumed to act with a magnitude equal to unity (nondimensional). The viscosity was assumed to be 0.01 (nondimensional quantity). At $t = 0$, the gate was opened and the fluid from the dam was assumed to flow freely. The quantity of interest is the extreme horizontal free surface position L as shown in [Fig. 6.2](#) (right). The unstructured mesh used consists of 339 nodes and 604 elements.

[Figures 6.3 and 6.4](#) give the distorted mesh and contours at various time levels. As seen the results are generally smooth all over the domain. The pressure contours are perfect and free of oscillation, which shows the effect of the good pressure stabilization properties of the CBS scheme.

[Figure 6.5](#) shows the comparison of the extreme horizontal position reached by the free surface with the experimental data [45]. As seen the numerical results are in good agreement with the experimental data. The nondimensional time in the horizontal coordinate is calculated as $t\sqrt{2g/W}$.

[Figures 6.3 and 6.4](#) show how a reasonably regular mesh at $t = 0$ becomes distorted after a certain number of time steps. While the results show a good agreement with

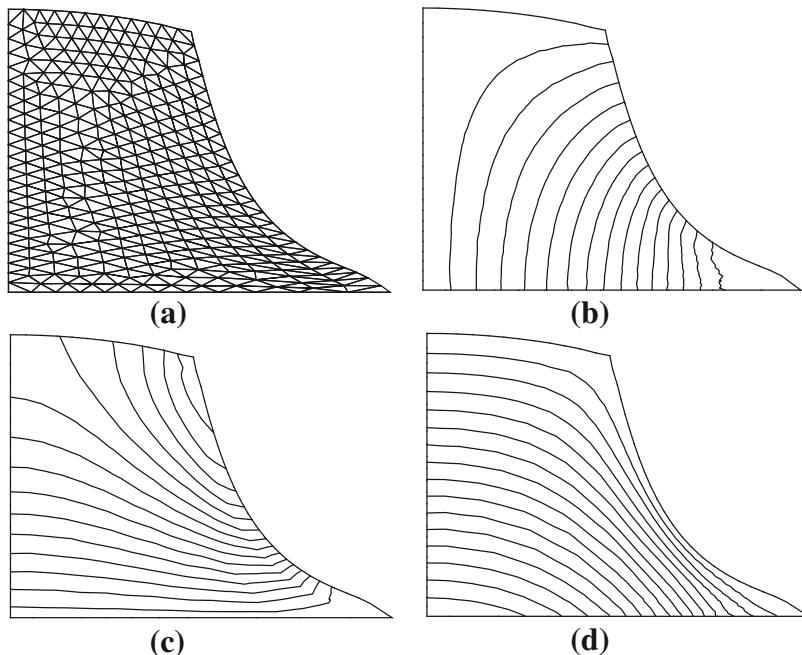
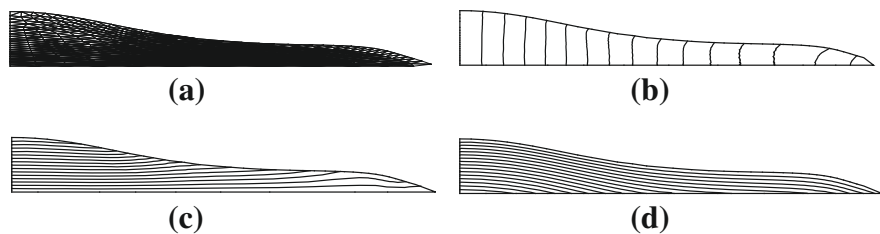
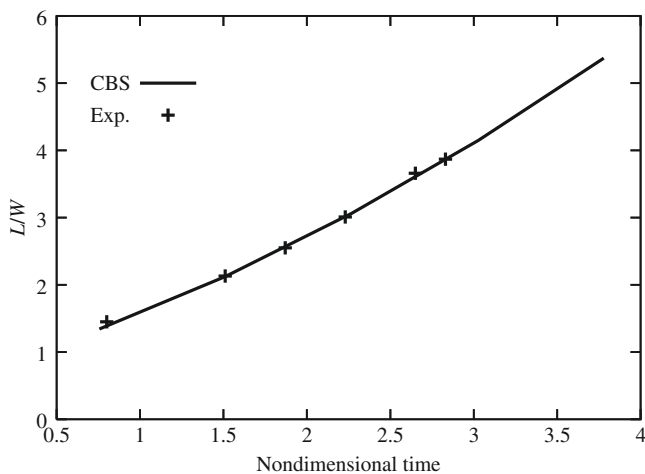


FIGURE 6.3

Broken dam problem. Mesh and contours after $t = 2.0$: (a) mesh; (b) u_1 velocity contours; (c) u_2 velocity contours; (d) pressure contours.

**FIGURE 6.4**

Broken dam problem. Mesh and contours after $t = 5.0$: (a) mesh; (b) u_1 velocity contours; (c) u_2 velocity contours; (d) pressure contours.

**FIGURE 6.5**

Broken dam problem. Comparison of numerical results with experimental data [45].

In the experimental data the irregularity of the mesh can cause errors and indeed in complicated problems this irregularity may cause element overlapping and *unphysical* results. Here lies one of the serious disadvantages of Lagrangian updating and care has to be taken to avoid extreme errors. Indeed it may be necessary to remesh from time to time the whole problem to avoid element *inversion*. An interesting procedure showing continuous remeshing with a rather novel approach is discussed by Idelshon et al. [46]. We shall not give the details of the procedure here but interested readers should consult appropriate Refs. [47] and [48].

6.2.3 Eulerian methods

As mentioned before the flow domain in Eulerian methods is fixed and the fluid is allowed to pass through the domain. Thus an additional procedure is necessary to track the free surface when Eulerian methods are employed.

In order to correctly track the free surface, we need both dynamic and kinematic conditions to be satisfied on the free surface. Thus, on the free surface we have at all times to ensure that (1) the pressure (which approximates the normal traction) is known (dynamic condition) and (2) that the material particles of the fluid belonging to the free surface remain on this at all times (kinematic condition). These conditions are expressed as

$$\begin{aligned} p &= \bar{p} \\ u_n &= \mathbf{n}^T \mathbf{u} = 0 \end{aligned} \quad (6.9)$$

on the free surface Γ_f . In the above equation u_n is the velocity component in the normal direction to the free surface and \bar{p} is the known pressure. For a non-breaking free surface the kinematic condition (material surface) can be restated for $x_3 = \eta(t, x_1, x_2)$ as

$$\frac{D\eta}{Dt} = u_3 \quad (6.10)$$

or

$$\frac{\partial \eta}{\partial t} + u_1 \frac{\partial \eta}{\partial x_1} + u_2 \frac{\partial \eta}{\partial x_2} - u_3 = 0 \quad (6.11)$$

where u_1 , u_2 , and u_3 are the velocity components in the x_1 , x_2 , and x_3 directions shown in Fig. 6.6. At this point it is important to remark that two independent Eulerian approaches in solving free surface flow problems exist. In the first method the free surface is determined by solving Eq. (6.10) along with the dynamic conditions.

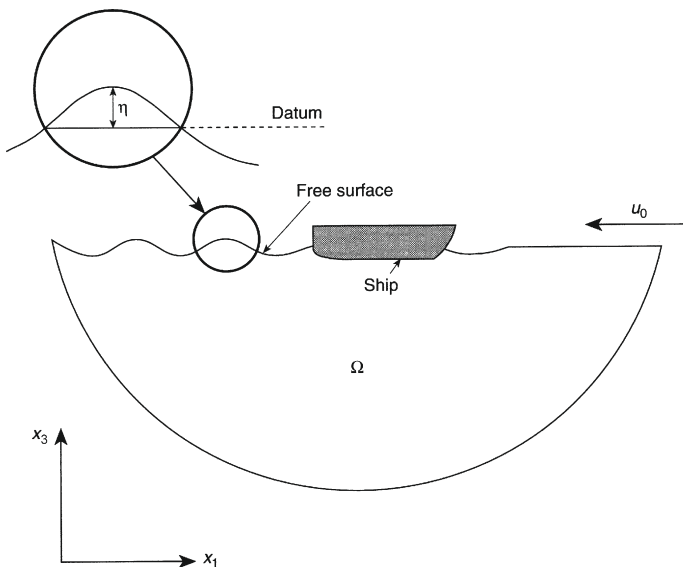


FIGURE 6.6

A typical problem of ship motion.

Once the free surface position η is determined remeshing follows either once at the end of the solution procedure or frequently within the time-stepping iterations. This process of mesh updating is well suited for solving problems of steady-state nature. If this method is employed for the solution of transient problems, some details of the Lagrangian approach need to be included close to the free surface.

In the second Eulerian method the mesh is often fixed throughout the calculation but the free surface is tracked to satisfy the kinematic condition. Once the free surface is tracked the dynamic boundary conditions are applied to satisfy the pressure/traction conditions. The standard procedure used in tracking the free surface is the so-called volume of fluid (VOF) method or one of its variants [10, 18, 49–52]. The major drawback of this method is that a rough idea about the external free surface is necessary *a priori* in order to generate a mesh which contains the free surface all the time. The VOF-based Eulerian methods are more suitable for internal flows than large-scale external flows.

6.2.3.1 Mesh updating or regeneration methods

Figure 6.6 shows a typical problem of ship motion together with the boundaries limiting the domain of analysis. This is an example of an external free surface flow problem. In the interior of the domain we can use either the full Navier-Stokes equations or, neglecting viscosity effects, a pure potential or Euler approximation. Both assumptions have been discussed in previous chapters but it is interesting to remark here that the resistance caused by the waves may be four or five times greater than that due to viscous drag. Clearly surface effects are of great importance for ship design.

Historically many solutions that ignore viscosity totally have been used in the ship industry with good effect by involving so-called boundary solution procedures or panel methods [53–63]. Early finite element studies on the field of ship hydrodynamics have also used potential flow equations [64]. A full description of these is given in many papers. However complete solutions with viscous effects and full nonlinearity are difficult to deal with. In the procedures that we present in this section, the door is opened to obtain a full solution without any extraneous assumptions and indeed such solutions could include turbulence effects, etc. The nondimensional form of the incompressible flow equations can be written as

$$\frac{\partial u_i}{\partial x_i} = 0 \quad (6.12)$$

and

$$\frac{\partial u_i}{\partial t} + \frac{\partial(u_i u_j)}{\partial x_j} = -\frac{\partial p}{\partial x_i} + \frac{1}{Re} \frac{\partial^2 u_i}{\partial x_i^2} - \frac{x_3}{Fr^2} \quad (6.13)$$

The viscous term in the above equation is simplified using the conservation of mass Eq. (6.12). In the above equations Re is the Reynolds number defined in Chapters 3 and 4 and Fr is the Froude number given as

$$Fr = \frac{u_\infty}{\sqrt{gL}} \quad (6.14)$$

where u_∞ is a reference velocity and L is a reference length.

Further details of the equations can be found in [Section 4.1 of Chapter 4](#) and indeed the same CBS procedure can be used in the solution. However, considerable difficulties arise on the free surface, despite the fact that on such a surface normal traction is known. The difficulties are caused by the fact that at all times we need to ensure that this surface is a material one and contains the particles of the fluid.

Equation [\(6.11\)](#) for free surface height η is a pure convection equation (see [Chapter 2](#)) in terms of the variables t, u_1, u_2 , and u_3 in which u_3 is a source term. At this stage it is worthwhile remarking that this surface equation has been known for a very long time and was dealt with previously by upwind differences, in particular those introduced on a regular grid by Dawson [\[54\]](#). However in [Chapter 2](#), we have already discussed other perfectly stable, finite element methods, any of which can be used for dealing with this equation. In particular the characteristic-Galerkin procedure can be applied most effectively.

On occasion additional artificial dissipation is added to stabilize the convection equation [\(6.11\)](#) in its discrete form at the inlet and exit of the domain [\[16\]](#).

It is important to observe that when the steady state is reached we simply have

$$u_3 = u_1 \frac{\partial \eta}{\partial x_1} + u_2 \frac{\partial \eta}{\partial x_2} \quad (6.15)$$

which ensures that the velocity vector is tangential to the free surface. The solution method for the whole problem can now be fully discussed.

The first of these solutions is that involving *mesh updating*, where we proceed as follows. Assuming a known reference surface, say the original horizontal surface of the water, we specify that the pressure on this surface is zero and solve the resulting fluid mechanics problem by the methods of the previous chapter. Using the CBS algorithm we start with known values of the velocities and find the necessary increment obtaining \mathbf{u}^{n+1} and p^{n+1} from initial values. Immediately following this step we compute the increment of η using the newly calculated values of the velocities. We note here that this last equation is solved only in two dimensions on a mesh corresponding to the projected coordinates of x_1 and x_2 ([Figure 6.6](#)).

At this stage the surface can be immediately updated to a new position which now becomes the new reference surface and the procedure can then be repeated to steady state.

6.2.3.2 Hydrostatic adjustment

Obviously the method of repeated mesh updating can be extremely costly and in general we follow the process described as *hydrostatic adjustment*. In this process we note that once the incremental η has been established, we can adjust the surface pressure at the reference surface by

$$p_{ref} = \bar{p} + \Delta \eta^n \rho g \quad (6.16)$$

After each time step the above pressure value is forced on the free surface without altering the mesh. Of course this introduces an approximation but this approximation can be quite satisfactorily used for starting the following step.

If we proceed in this manner until the solution of the basic flow problem is well advanced and the steady state has nearly been reached we have a solution which is reasonably accurate for small waves but which can now be used as a starting point of the mesh adjustment if so desired.

In all practical calculations it is recommended that many steps of the *hydrostatic adjustment* be used before repeating the *mesh updating*, which is quite expensive. In many ship problems it has been shown that with a single mesh quite good results can be obtained without the necessity of proceeding with mesh adjustment. We shall refer to such examples later.

The methodologies suggested here follow the work of Hino et al. [65–67], Idelsohn et al., Löhner et al., and Onâte et al. [17, 13, 16, 21]. The methods which we discussed in the context of ships here provide a basis on which other free surface problems can be started at all times and are obviously an improvement on a very primitive adjustment of the surface by trial and error.

6.2.3.3 Numerical examples using mesh regeneration methods

Example 6.2. A submerged hydrofoil

We start with the two-dimensional problem shown in Fig. 6.7, where a NACA0012 aerofoil profile is used in submerged form as a hydrofoil, which could in the

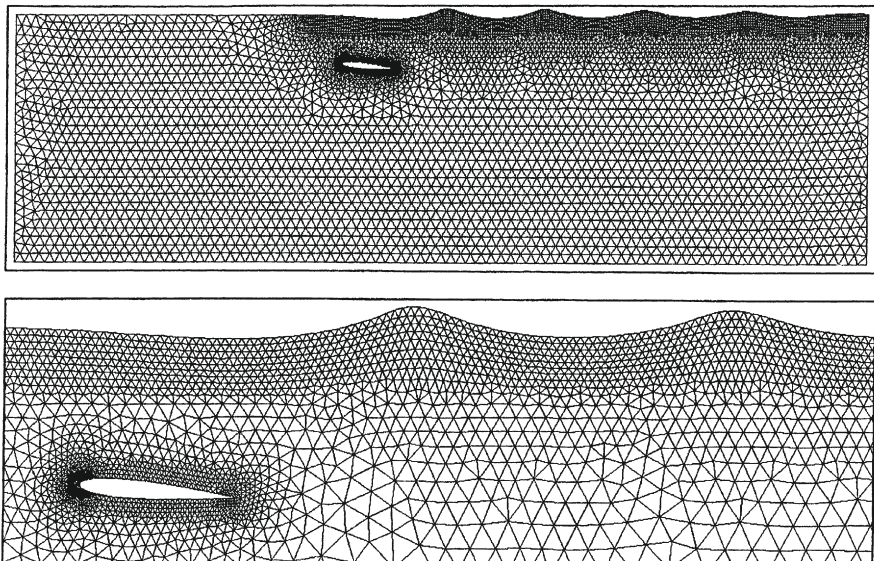
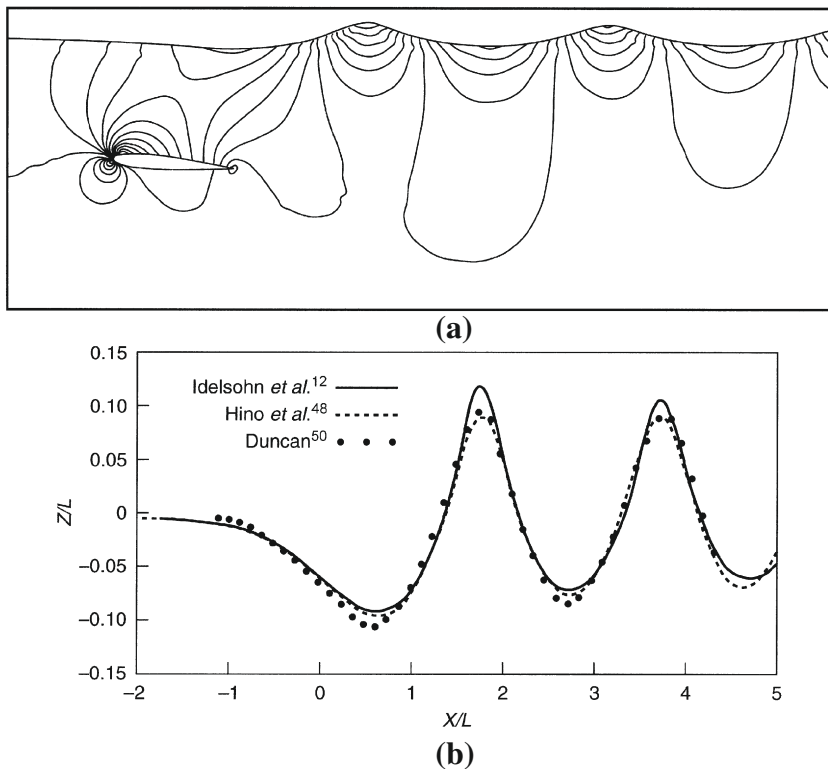


FIGURE 6.7

A submerged hydrofoil. Mesh updating procedure. Euler flow. Mesh after 1900 iterations.

**FIGURE 6.8**

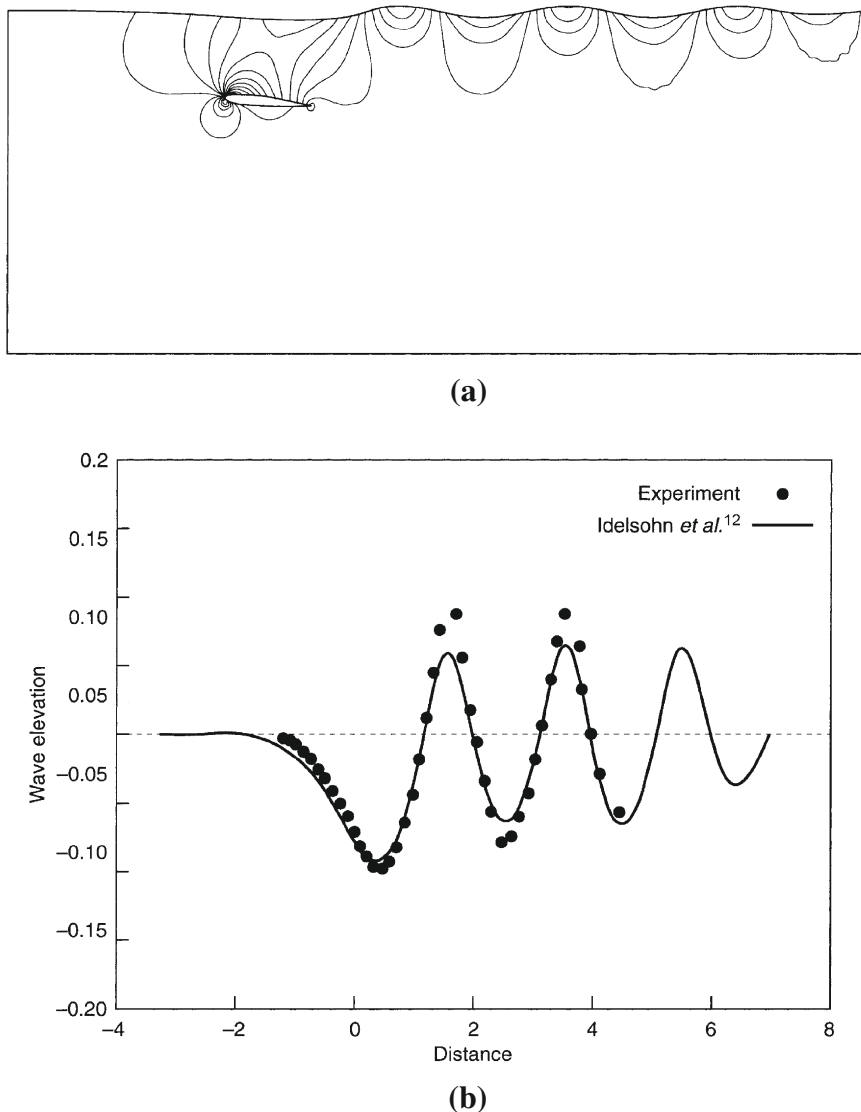
A submerged hydrofoil. Mesh updating procedure. Euler flow: (a) pressure distribution; (b) comparison with experiment.

imagination of the reader be attached to a ship. This is a model problem, as many two-dimensional situations are not realistic. Here the angle of attack of the flow is 5° and the Froude number is 0.5672.

In Fig. 6.8 we show the pressure distribution throughout the domain and the comparison of the computed wave profiles with the experimental [68] and other numerical solutions [66]. In Figs. 6.7 and 6.8, the mesh is moved after a certain number of iterations using an advancing front technique [69].

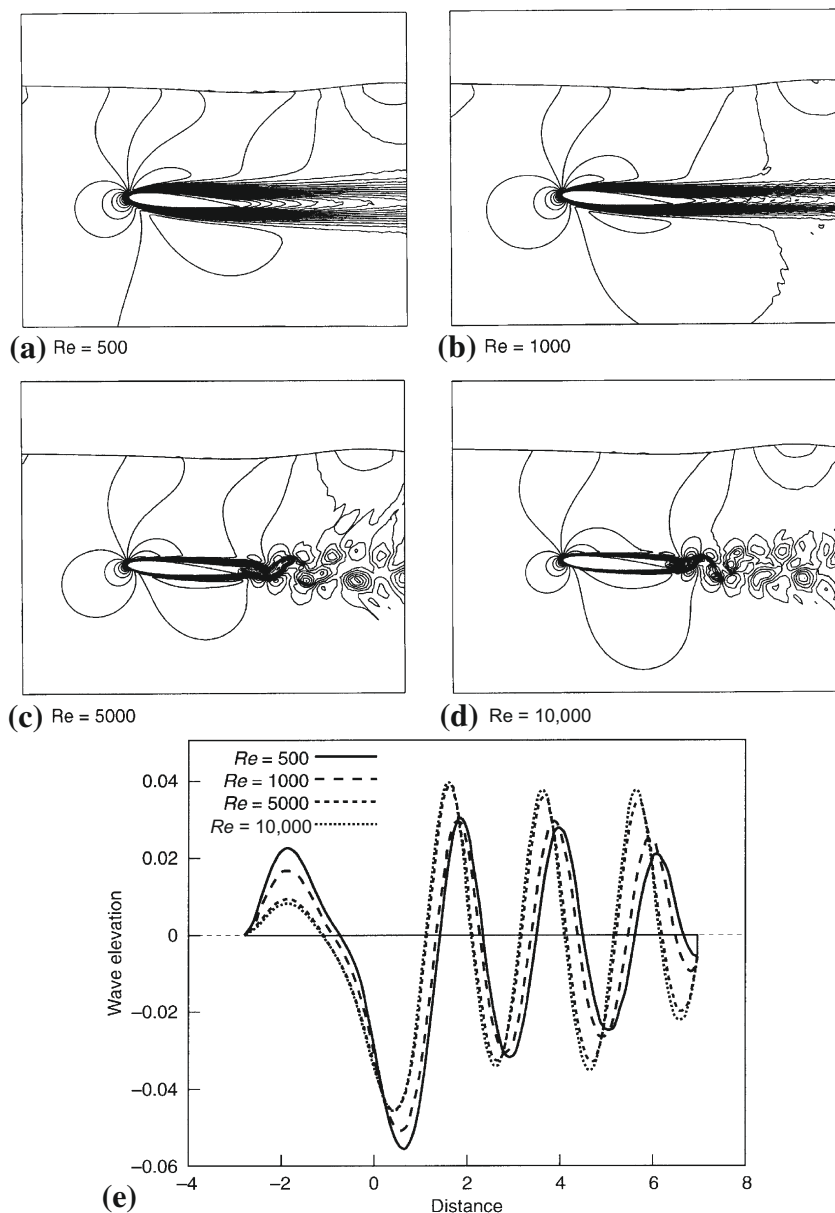
Figure 6.9 shows the same hydrofoil problem solved now using hydrostatic adjustment without moving the mesh. For the same conditions, the wave profile is somewhat underpredicted by the hydrostatic adjustment (Fig. 6.9b) while the mesh movement overpredicts the peaks (Fig. 6.8b).

In Fig. 6.10, the results for the same hydrofoil in the presence of viscosity are presented for different Reynolds numbers. As expected the wake is now strong as seen from the velocity magnitude contours (Fig. 6.10a–d). Also at higher Reynolds

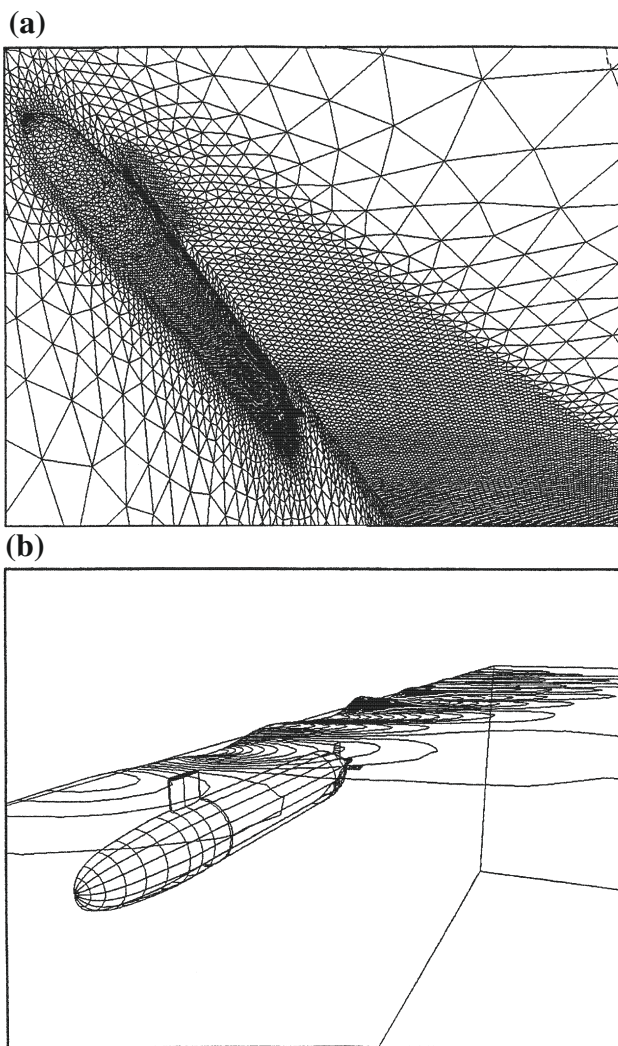
**FIGURE 6.9**

A submerged hydrofoil. Hydrostatic adjustment. Euler flow: (a) pressure contours and surface wave pattern; (b) comparison with experiment [68].

numbers (5000 and above), the solution is not stable behind the aerofoil and here an unstable vortex street is predicted as shown in Fig. 6.10c and 6.10d. Figure 6.10e shows the comparison of wave profiles for different Reynolds numbers.

**FIGURE 6.10**

A submerged hydrofoil. Hydrostatic adjustment. Navier-Stokes flow: (a)–(d) magnitude of total velocity contours for different Reynolds numbers; (e) wave profiles for different Reynolds numbers.

**FIGURE 6.11**

Submerged DARPA submarine model: (a) surface mesh; (b) wave pattern.

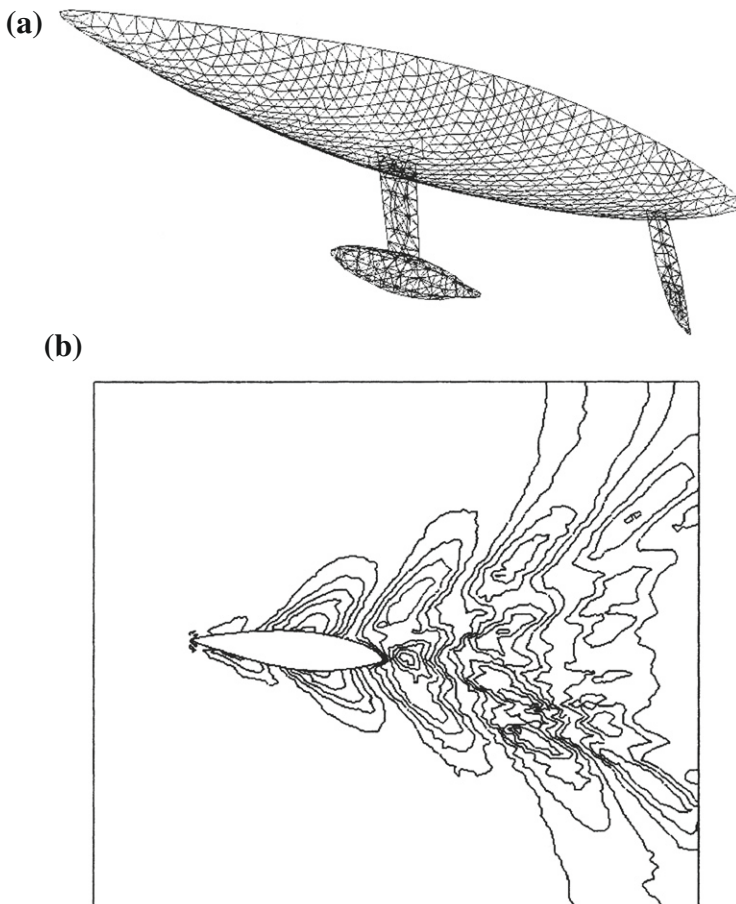
Example 6.3. Submarine

In Fig. 6.11, we show the mesh and wave pattern contours for a submerged DARPA submarine model. Here the Froude number is 0.25. The converged solution is obtained by about 1500 time steps using a parallel computing environment. The mesh consists of approximately 321,000 tetrahedral elements.

Example 6.4. Sailing boat

The last example presented here is that of a sailing yacht. In this case the yacht has a 25° heel angle and a drift angle of 4° . Here it is essential to use either the Euler or Navier-Stokes equations to satisfy the Kutta-Joukoski condition as the potential form has difficulty in satisfying these conditions on the trailing edge of the keel and rudder.

Here we used the Euler equations to solve this problem. [Figure 6.12a](#) shows a surface mesh of hull, keel, bulb, and rudder. A total of 104,577 linear tetrahedral elements were used in the computation. [Figure 6.12b](#) shows the wave profile contours corresponding to a sailing speed of 10 knots.

**FIGURE 6.12**

A sailing boat: (a) surface mesh of hull, keel, bulb, and rudder; (b) wave profile.

6.2.4 Arbitrary Langrangian-Eulerian (ALE) method

As mentioned before ALE methods have some features of both Lagrangian and Eulerian methods. First, let us deal with the basics of the ALE description of flow (for an alternative description see Ref. [39]). Assume a scalar convection-diffusion equation of the form

$$\frac{D\phi}{Dt} = \frac{\partial}{\partial x_i} \left(k \frac{\partial \phi}{\partial x_i} \right) \quad (6.17)$$

where D/Dt is the total time derivative.

Let ϕ be transported to a new position P_f in a time increment of Δt with a velocity of \mathbf{u} as shown in Fig. 6.13 [31]. The ALE method allows independent movement of grid points, i.e., the grid point is moved to a new position P_r in the time increment Δt with a velocity of \mathbf{u}_g . The scalar variable ϕ at $t + \Delta t$ at position P_f may be expressed using Taylor series expansion (in both space and time) as

$$\phi_{P_f} = \phi^{n+1} = \phi_P + \Delta t \frac{\partial \phi}{\partial t} + u_i \Delta t \frac{\partial \phi}{\partial x_i} + \dots \quad (6.18)$$

where u_i are the convective velocity components. In a similar fashion ϕ at position P_r at time t may be expanded (only in space) as

$$\phi_{P_r} = \phi^n = \phi_P + u_{gi} \Delta t \frac{\partial \phi}{\partial x_i} + \dots \quad (6.19)$$

Here u_{gi} are the grid velocity components. The relative value of the scalar variable ϕ with respect to the reference point P_r may be written as

$$\Delta\phi = \phi^{n+1} - \phi^n = \Delta t \frac{\partial \phi}{\partial t} + (u_i - u_{gi}) \Delta t \frac{\partial \phi}{\partial x_i} \quad (6.20)$$

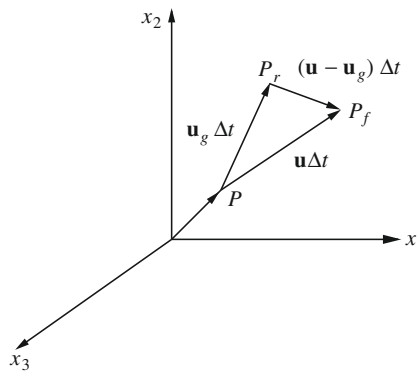


FIGURE 6.13

ALE description in Cartesian coordinates.

The above equation may be rewritten as $\Delta t \rightarrow 0$ as

$$\frac{D\phi}{Dt} = \frac{\partial\phi}{\partial t} + (u_i - u_{gi}) \frac{\partial\phi}{\partial x_i} \quad (6.21)$$

Substituting Eq. (6.21) into Eq. (6.17) gives the following equation in an ALE framework:

$$\frac{\partial\phi}{\partial t} + (u_i - u_{gi}) \frac{\partial\phi}{\partial x_i} - \frac{\partial}{\partial x_i} \left(k \frac{\partial\phi}{\partial x_i} \right) = 0 \quad (6.22)$$

Similarly the incompressible fluid dynamics equations in terms of total derivatives can be written as (for simplicity it is written in terms of primitive variables)

Continuity

$$\frac{D\rho}{Dt} + \rho \frac{\partial u_i}{\partial x_i} = 0 \quad (6.23)$$

Momentum

$$\frac{Du_i}{Dt} = -\frac{1}{\rho} \frac{\partial p}{\partial x_i} + \frac{1}{\rho} \frac{\partial \tau_{ij}}{\partial x_j} - g_i \quad (6.24)$$

The ALE settings for the incompressible flows can be written as

Continuity

$$\frac{\partial\rho}{\partial t} + (u_i - u_{gi}) \frac{\partial\rho}{\partial x_i} + \rho \frac{\partial u_i}{\partial x_i} = 0 \quad (6.25)$$

Momentum

$$\frac{\partial u_i}{\partial t} + (u_i - u_{gi}) \frac{\partial u_i}{\partial x_i} = -\frac{1}{\rho} \frac{\partial p}{\partial x_i} + \frac{1}{\rho} \frac{\partial \tau_{ij}}{\partial x_j} + g_i \quad (6.26)$$

For constant density flows the continuity equation becomes

$$\frac{\partial u_i}{\partial x_i} = 0 \quad (6.27)$$

It is easy to observe that Eq. (6.26) becomes a Lagrangian equation if grid velocity u_{gi} is equal to fluid velocity u_i and it becomes an Eulerian equation if $u_{gi} = 0$. Thus using an ALE method it is possible to shift between the Lagrangian and Eulerian frameworks if necessary.

6.2.4.1 ALE implementation

As mentioned before implementation of the ALE method is difficult and varies depending on the problem to be solved. However, many have used this method to solve free surface problems with relatively small free surface displacement [25–27, 29, 31, 33–40, 44]. The most difficult problem in an ALE algorithm is allocating an appropriate mesh velocity u_{gi} . There is no universal method of determining the mesh velocity. Most of the time mesh velocity is problem dependent. It is standard practice

in ALE algorithms to split the scheme into three phases. They are (1) Lagrangian solution, (2) mesh rezoning action, and (3) Eulerian calculation. However, these phases are seldom discriminated in a computer code.

The ALE procedure starts with a Lagrangian step as discussed in [Section 6.2.2](#). If the mesh is expected to undergo too much distortion then a mesh rezoning procedure should be employed. There are various ways of rezoning available, including remeshing. Once the rezoning is carried out a mesh velocity can be calculated from the nodal displacements to use it in the calculation of the convection velocity in [Eq. \(6.26\)](#).

There are several mesh rezoning procedures available for triangular and tetrahedral elements. One such procedure was introduced by Giuliani [70] in which a function is constructed from measures of distortion and squeeze and minimized. This procedure works well for domains with fixed boundaries. Several improvements have been later carried out by many authors [71]. A variable smoothing method based on a combination of Laplacian smoothing and Winslow's method was introduced by Hermansson and Hansbo [72] which preserves the element stretching. It is also possible to use simple smoothing procedures widely employed in mesh generation, for instance a smoothing procedure in which coordinates of a node are recalculated as an average of the coordinates of the surrounding nodes. Depending on the requirements this smoothing procedure can be employed several times within a single time step.

Apart from the simple mesh moving procedures mentioned above, more robust methods can also be employed for complex situations. Some of the methods based on differential equations are described in detail in [Chapter 13](#).

Example 6.5. Solitary wave propagation

We now consider a simple example of a solitary wave propagation between two walls. [Figure 6.14](#) shows the problem definition. It consists of a liquid with free surface constrained within three wall (two vertical walls and one bottom horizontal wall). The total horizontal length of the domain is 16 and $d = 1$. The gravity direction is downward vertical with $g = 9.81$. The viscosity of the fluid is assumed to be 0.01. The time step employed is 0.025.

The walls are assumed to be slip walls and initial conditions are calculated based on the work presented by Laitone [73] for an infinite domain. The relationships for

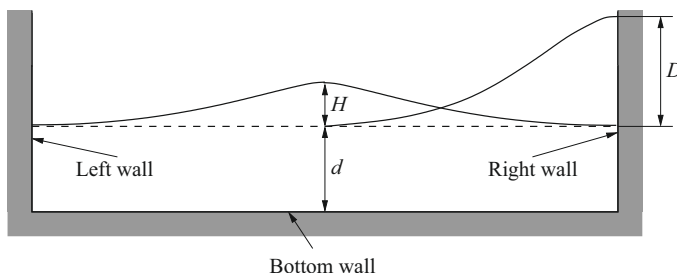


FIGURE 6.14

Solitary wave propagation. Problem definition.

total wave height, velocity components, and pressure are given as

$$h = d + H \operatorname{sech}^2 \left[\sqrt{\frac{3H}{4d^3}} (x_1 - ct) \right] \quad (6.28a)$$

$$u_1 = \sqrt{gd} \frac{H}{d} \operatorname{sech}^2 \left[\sqrt{\frac{3H}{4d^3}} (x_1 - ct) \right] \quad (6.28b)$$

$$u_2 = \sqrt{3gd} \left(\frac{h}{d} \right)^{3/2} \left(\frac{x_2}{d} \right) \operatorname{sech}^2 \left[\sqrt{\frac{3H}{4d^3}} (x_1 - ct) \right] \tanh \left[\sqrt{\frac{3H}{4d^3}} (x_1 - ct) \right] \quad (6.28c)$$

and

$$p = \rho g (h - x_2) \quad (6.28d)$$

In the above equation c is given as

$$\frac{c}{\sqrt{gd}} = 1 + \frac{1}{2} \frac{H}{d} - \frac{3}{20} \left(\frac{H}{d} \right)^2 + O \left(\frac{H}{d} \right)^3 \quad (6.29)$$

The initial solution and mesh are generated by substituting $t = 0$ into Eqs. (6.28a)–(6.28c).

In Figs. 6.15 and 6.16 we show the meshes and the velocity vectors at various time levels for $H/d = 0.3$. The total number of elements and nodes is unchanged

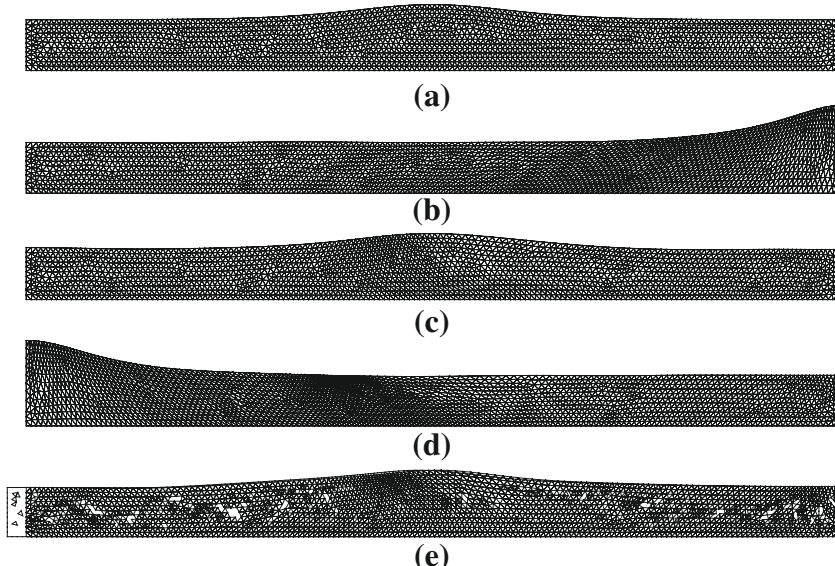
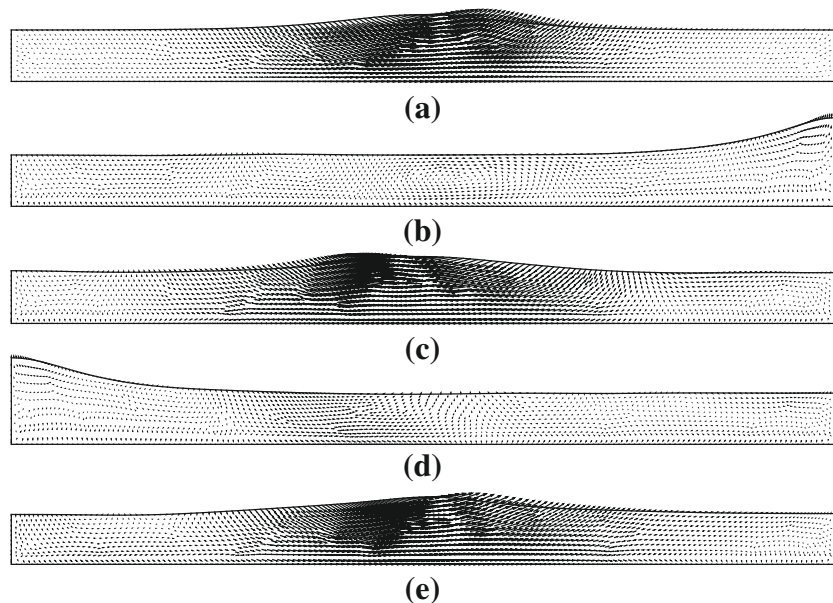


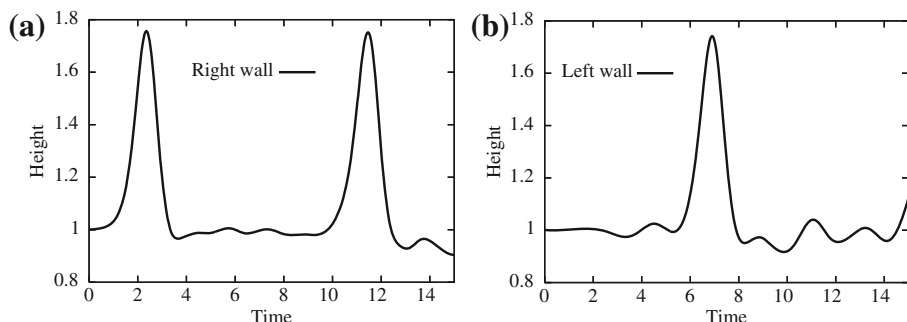
FIGURE 6.15

Solitary wave propagation. Meshes at various time levels: (a) $t = 0.0$; (b) $t = 2.28$; (c) $t = 4.58$; (d) $t = 6.84$; (e) $t = 9.12$.

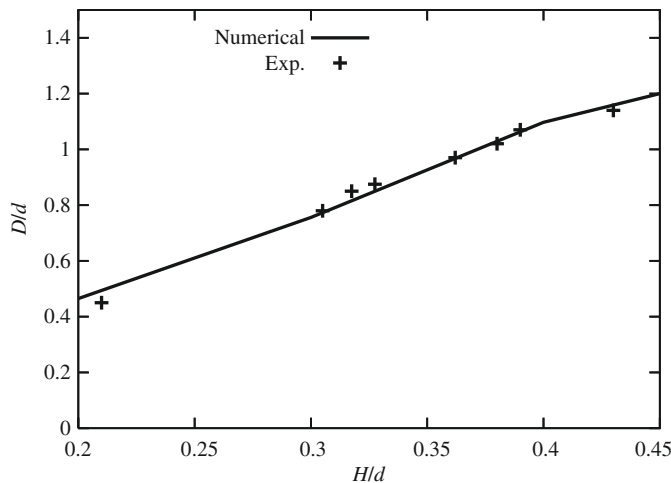
**FIGURE 6.16**

Solitary wave propagation. Velocity vector distribution at various time levels: (a) $t = 0.0$; (b) $t = 2.28$; (c) $t = 4.58$; (d) $t = 6.84$; (e) $t = 9.12$.

during the calculation; they are 3838 and 2092, respectively. The semi-implicit form of the CBS scheme was used in the calculations. The small portion close to the bottom wall was assumed to be Eulerian all the time. After every time step the Lagrangian portion of the mesh is moved with the fluid and followed by mesh smoothing. The convection term is a part of the ALE scheme. However, during the Lagrangian phase the convection velocity is automatically calculated as equal to zero. However, after

**FIGURE 6.17**

Wave heights with respect to time on the right and left side walls: (a) right wall; (b) left wall.

**FIGURE 6.18**

Solitary wave propagation. Comparison of wave heights with experimental data [74].

the mesh smoothing phase the convection velocity will have a value due to the mesh movement. Note that after mesh smoothing ($u_i - u_{ig}$) will be nonzero on the nodes, which moved relative to the fluid motion.

Figure 6.17 shows the fluid height at the right and left walls with time. As seen the first peak at the right wall is reached around a time of 2.28 and at the left wall the peak is reached at 6.9. Fig. 6.18 shows the comparison of maximum height reached D against the experimental data of Maxworthy [74].

6.3 Buoyancy driven flows

In some problems of incompressible flow the heat transport equation and the equations of motion are weakly coupled. If the temperature distribution is known at any time, the density changes caused by this temperature variation can be evaluated. These may on occasion be the only driving force of the problem. In this situation it is convenient to note that the body force with constant density can be considered as balanced by an initial hydrostatic pressure and thus the driving force which causes the motion is in fact the body force caused by the difference of local density values. We can thus write the body force at any point in the equations of motion as

$$\rho_\infty \left[\frac{\partial u_i}{\partial t} + \frac{\partial}{\partial x_j} (u_j u_i) \right] = - \frac{\partial p}{\partial x_i} + \frac{\partial \tau_{ij}}{\partial x_j} + g_i (\rho - \rho_\infty) \quad (6.30)$$

where ρ is the actual density applicable locally and ρ_∞ is the undisturbed constant density. The actual density entirely depends on the coefficient of thermal expansion of the fluid as compressibility is by definition excluded. Denoting the coefficient of

thermal expansion as γ_T , we can write

$$\gamma_T = \frac{1}{\rho_\infty} \left(\frac{\partial \rho}{\partial T} \right) \quad (6.31)$$

where T is the absolute temperature. The above equation can be approximated to

$$\gamma_T \approx \frac{1}{\rho_\infty} \left(\frac{\rho - \rho_\infty}{T - T_\infty} \right) \quad (6.32)$$

Replacing the body force term in the momentum equation by the above relation we can write

$$\rho_\infty \left[\frac{\partial u_i}{\partial t} + \frac{\partial}{\partial x_j} (u_j u_i) \right] = - \frac{\partial p}{\partial x_i} + \frac{\partial \tau_{ij}}{\partial x_j} + \gamma_T g_i \rho_\infty (T - T_\infty) \quad (6.33)$$

The various governing nondimensional numbers used in the buoyancy flow calculations are the Rayleigh number (for a detailed nondimensionalization procedure see Refs. [75–78])

$$Ra = \frac{g \gamma_T (T - T_\infty) L^3}{\nu \alpha} \quad (6.34)$$

and the Prandtl number

$$Pr = \frac{\nu}{\alpha} \quad (6.35)$$

where L is a reference dimension, and ν and α are the kinematic viscosity and thermal diffusivity respectively and are defined as

$$\nu = \frac{\mu}{\rho}, \quad \alpha = \frac{k}{\rho c_p} \quad (6.36)$$

where μ is the dynamic viscosity, k is the thermal conductivity, and c_p is the specific heat at constant pressure.

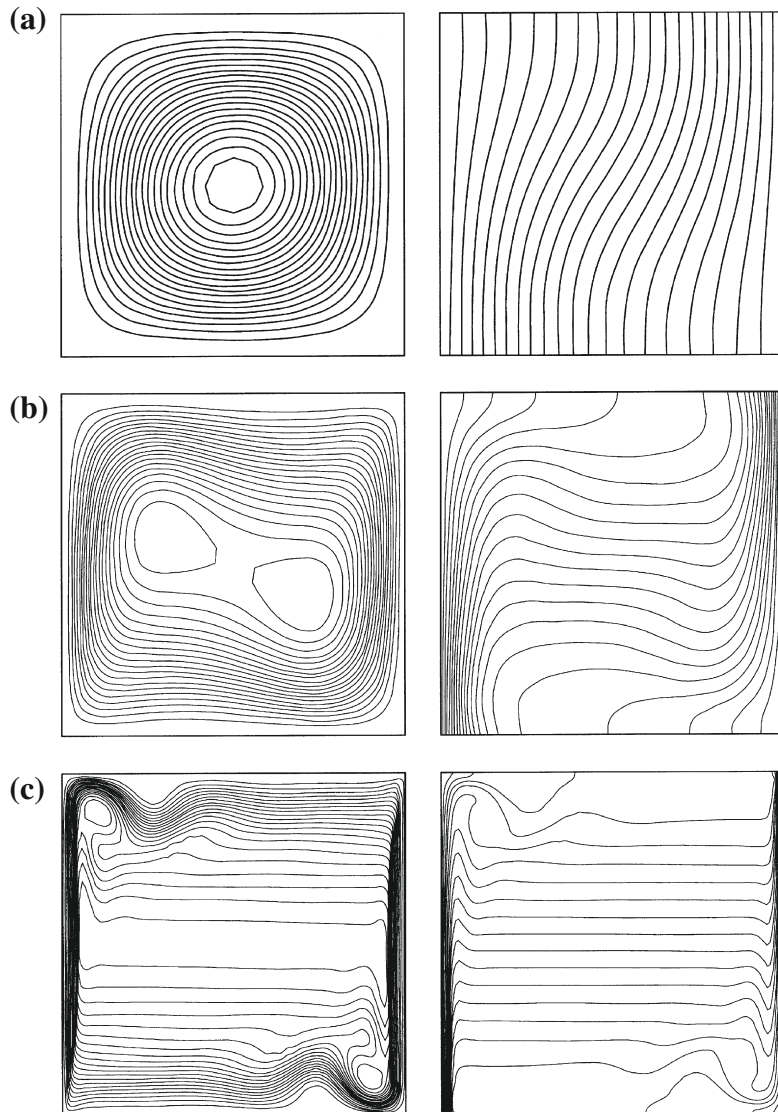
The resulting momentum equation in nondimensional form is

$$\left[\frac{\partial u_i}{\partial t} + \frac{\partial}{\partial x_j} (u_j u_i) \right] = - \frac{\partial p}{\partial x_i} + \frac{\partial \tau_{ij}}{\partial x_j} + n_i Ra Pr T \quad (6.37)$$

Note that n_i in the above equation is a unit vector in the gravity direction. In many practical situations, both buoyancy and forced flows are equally strong and such cases are often called mixed convective flows. Here in addition to the above-mentioned nondimensional numbers, the Reynolds number also plays a role. The reader can refer to several available basic heat transfer books and other publications to get further details [75, 78–95].

Example 6.6. Buoyancy driven flow in an enclosure

Fundamental buoyancy flow analysis in closed cavities can be classified into two categories. The first one is flow in closed cavities heated from the vertical sides and the second is bottom-heated cavities (Rayleigh-Benard convection). In the former, the CBS algorithm can be applied directly. However, the latter needs some perturbation to start the convective flow as they represent essentially an unstable problem.

**FIGURE 6.19**

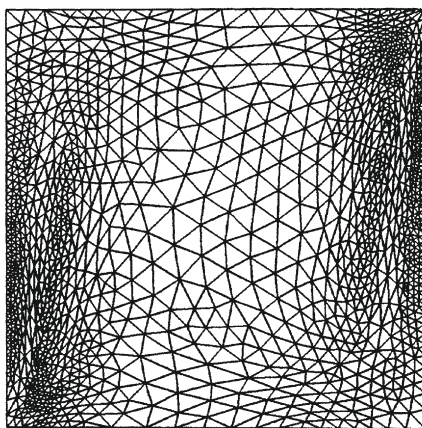
Natural convection in a square enclosure. Streamlines and isotherms for different Rayleigh numbers. (a) $Ra = 10^4$; (b) $Ra = 10^5$; (c) $Ra = 10^7$.

Figure 6.19 shows the results obtained for a closed square cavity heated at a vertical side and cooled at the other [76]. Both the horizontal sides are assumed to be adiabatic. At all surfaces both of the velocity components are zero (no-slip conditions). The mesh used here was a nonuniform structured mesh of size 51×51 .

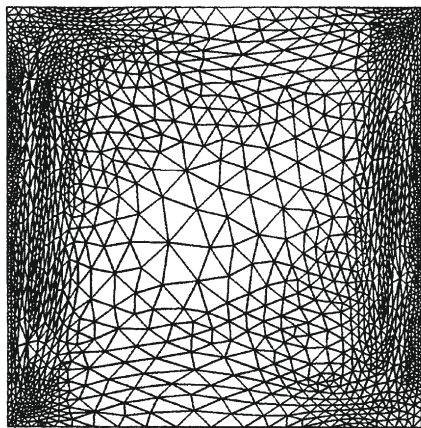
Table 6.1 Natural Convection in a Square Enclosure. Comparison with Available Numerical Solutions [76]. References Are Shown in Square Brackets

Ra	v			ψ_{\max}			v_{\max}		
	[90]	[91]	CBS	[90]	[91]	CBS	[90]	[91]	CBS
10^3	1.116	1.118	1.117	1.174	1.175	1.167	3.696	3.697	3.692
10^4	2.243	2.245	2.243	5.081	5.074	5.075	19.64	19.63	19.63
10^5	4.517	4.522	4.521	9.121	9.619	9.153	68.68	68.64	68.85
10^6	8.797	8.825	8.806	16.41	16.81	16.49	221.3	220.6	221.6
10^7	–	16.52	16.40	–	30.17	30.33	–	699.3	702.3
4×10^7	–	23.78	23.64	–	–	43.12	–	–	1417

(a)



(b)

**FIGURE 6.20**

Natural convection in a square enclosure. Adapted meshes for (a) $Ra = 10^5$ and (b) $Ra = 10^6$.

As the reader can see, the essential features of a buoyancy driven flow are captured using the CBS algorithm. The quantitative results are shown in Table 6.1 [76].

The adapted meshes for two different Rayleigh numbers are shown in Fig. 6.20. The adaptive methods are discussed in Chapter 4 for incompressible flows.

6.4 Concluding remarks

We have summarized all major methods for dealing with free surface flow analysis in this chapter. The numerical formulation of the free surface problems was only briefly discussed. Although brief, we believe that we have provided the readers with some essential technique to start their research on free surface flows. The section on the

buoyancy driven flows is kept purposely brief. Interested readers should consult the quoted references.

References

- [1] P. Bach, O. Hassager, An algorithm for the use of the Lagrangian specification in Newtonian fluid mechanics and applications to free-surface flow, *J. Fluid Mech.* 152 (1985) 173–190.
- [2] B. Ramaswamy, M. Kawahara, T. Nakayama, Lagrangian finite element method for the analysis of two dimensional sloshing problems, *Int. J. Numer. Methods Fluids* 6 (1986) 659–670.
- [3] B. Ramaswamy, M. Kawahara, Lagrangian finite element analysis applied to viscous free surface fluid flow, *Int. J. Numer. Methods Fluids* 7 (9) (1987) 953–984.
- [4] M. Hayashi, K. Hatanaka, M. Kawahara, Lagrangian finite element method for free surface Navier-Stokes flow using fractional step methods, *Int. J. Numer. Methods Fluids* 13 (7) (1991) 805–840.
- [5] F. Muttin, T. Coupez, M. Bellet, J.L. Chenot, Lagrangian finite element analysis of time dependent viscous free surface flow using automatic remeshing technique—application to metal casting flow, *Int. J. Numer. Methods Engineering* 36 (12) (1993) 2001–2015.
- [6] Y.T. Feng, D. Peric, A time-adaptive space-time finite element method for incompressible Lagrangian flows with free surfaces: computational issues, *Comput. Methods. Appl. Mech. Eng.* 190 (5–7) (2000) 499–518.
- [7] R. Aubry, S.R. Idelsohn, E. Oñate, Fractional step like schemes for free surface problems with thermal coupling using the Lagrangian PFEM, *Comput. Mech.* 38 (4–5) (2006) 294–309, 13th Conference on Finite Elements for Flow Problems, Swansea, Wales, APR 04–06 2005.
- [8] F. Del Pin, S.R. Idelsohn, E. Oñate, R. Aubry, The ALE/Lagrangian particle finite element method: a new approach to computation of free-surface flows and fluid-object interactions, *Comput. Fluids* 36 (1) (2007) 27–38.
- [9] D. Gonzalez, E. Cueto, F. Chinesta, M. Doblaré, A natural element updated Lagrangian strategy for free-surface fluid dynamics, *J. Comput. Phys.* 223 (1) (2007) 127–150.
- [10] C.W. Hirt, B.D. Nichols, Volume of fluid (VOF) method for the dynamics of free surface boundaries, *J. Comput. Phys.* 39 (1981) 210–225.
- [11] J. Farmer, L. Martinelli, A. Jameson, Fast multigrid method for solving incompressible hydrodynamic problems with free surfaces, *AIAA J.* 32 (1994) 1175–1182.
- [12] M. Beddhu, L.K. Taylor, D.L. Whitfield, A time accurate calculation procedure for flows with a free surface using a modified artificial compressibility formulation, *Appl. Math. Comput.* 65 (1994) 33–48.
- [13] R. Löhner, C. Yang, E. Onate, I.R. Idelsohn, An unstructured grid based, parallel free surface solver, *AIAA* 97–1830 (1997).

- [14] G.D. Tzabiras, A numerical investigation of 2D, steady free surface flows, *Int. J. Numer. Methods Fluids* 25 (1997) 567–598.
- [15] J.H. Jeong, D.Y. Yang, Finite element analysis of transient fluid flow with free surface using VOF (volume-of-fluid) method and adaptive grid, *Int. J. Numer. Methods Fluids* 26 (10) (1998) 1127–1154.
- [16] R. Löhner, C. Yang, E. Oñate, Free surface hydrodynamics using unstructured grids, in: 4th ECCOMAS CFD Conference, Athens, September 7–11, 1998.
- [17] S.R. Idelsohn, E. Oñate, C. Sacco, Finite element solution of free surface ship wave problems, *Int. J. Numer. Methods Eng.* 45 (1999) 503–528.
- [18] S. Shin, W.I. Lee, Finite element analysis of incompressible viscous flow with moving free surface by selective volume of fluid method, *Int. J. Heat Fluid Flow* 21 (2000) 197–206.
- [19] E.H. van Brummelen, H.C. Raven, B. Koren, Efficient numerical solution of steady free-surface Navier-Stokes flow, *J. Comput. Phys.* 174 (2001) 120–137.
- [20] M.S. Kim, J.S. Park, W.I. Lee, A new VOF-based numerical scheme for the simulation of fluid flow with free surface. Part II: Application to the cavity filling and sloshing problems, *Int. J. Numer. Methods Fluids* 42 (7) (2003) 791–812.
- [21] E. Oñate, J. García, S.R. Idelsohn, Ship hydrodynamics, *Encyclopedic Comput. Mech.* (2004).
- [22] C.L. Lin, H. Lee, T. Lee, L.J. Weber, A level set characteristic Galerkin finite element method for free surface flows, *Int. J. Numer. Methods Fluids* 49 (5) (2005) 521–547.
- [23] C.E. Kees, I. Akkerman, M.W. Farthing, Y. Bazilevs, A conservative level set method suitable for variable-order approximations and unstructured meshes, *J. Comput. Phys.* 230 (12) (2011) 4536–4558.
- [24] R. Rossi, A. Larese, P. Dadvand, E. Onate, An efficient edge-based level set finite element method for free surface flow problems, *Int. J. Numer. Methods Fluids* 71 (6) (2013) 687–716.
- [25] C.W. Hirt, A.A. Amsden, J.L. Cook, An arbitrary Lagrangian-Eulerian computing method for all flow speeds, *J. Comput. Phys.* 14 (1974) 227–253.
- [26] B. Ramaswamy, M. Kawahara, Arbitrary Lagrangian Eulerian finite element method for unsteady, convective incompressible viscous free surface fluid flow, *Int. J. Numer. Methods Fluids* 7 (1987) 1053–1075.
- [27] S.E. Navti, K. Ravindran, C. Taylor, R.W. Lewis, Finite element modelling of surface tension effects using a Lagrangian-Eulerian kinematic description, *Comput. Methods Appl. Mech. Eng.* 147 (1997) 41–60.
- [28] T. Okamoto, M. Kawahara, 3-D sloshing analysis by an arbitrary Lagrangian-Eulerian finite element method, *Int. J. Comput. Fluid Dyn.* 8 (2) (1997) 129–146.
- [29] S. Ushijima, Three dimensional arbitrary Lagrangian Eulerian numerical prediction method for non-linear free surface oscillation, *Int. J. Numer. Methods Fluids* 26 (1998) 605–623.
- [30] A. Soulaimani, Y. Saad, An arbitrary Lagrangian-Eulerian finite element method for solving three-dimensional free surface flows, *Comput. Methods Appl. Mech. Eng.* 162 (1–4) (1998) 79–106.

- [31] J.G. Zhou, P.K. Stansby, An arbitrary Lagrangian-Eulerian σ (ALES) model with non-hydrostatic pressure for shallow water flows, *Comput. Methods Appl. Mech. Eng.* 178 (1999) 199–214.
- [32] L. Gaston, A. Kamara, M. Bellet, An arbitrary Lagrangian-Eulerian finite element approach to non-steady state turbulent fluid flow with application to mould filling in casting, *Int. J. Numer. Methods Fluids* 34 (4) (2000) 341–369.
- [33] H. Braess, P. Wriggers, Arbitrary Lagrangian Eulerian finite element analysis of free surface flow, *Comput. Methods Appl. Mech. Eng.* 190 (2000) 95–109.
- [34] M. Iida, Numerical analysis of self-induced free surface flow oscillation by fluid dynamics computer code SPLASH-ALE, *Nucl. Eng. Des.* 200 (2000) 127–138.
- [35] J. Sung, H.G. Choi, J.Y. Yoo, Time accurate computation of unsteady free surface flows using an ALE-segregated equal order FEM, *Comput. Methods Appl. Mech. Eng.* 190 (2000) 1425–1440.
- [36] M. Souli, J.P. Zolesio, Arbitrary Lagrangian-Eulerian and free surface methods in fluid mechanics, *Comput. Methods Appl. Eng.* 191 (2001) 451–466.
- [37] M.-H. Hsu, C.-H. Chen, W.-H. Teng, An arbitrary Lagrangian-Eulerian finite difference method for computations of free surface flows, *J. Hydraul. Res.* 39 (2002) 1–11.
- [38] S. Rabier, M. Medale, Computation of free surface flows with a projection FEM in a moving framework, *Comput. Methods Appl. Mech. Eng.* 192 (2003) 4703–4721.
- [39] J. Donea, A. Huerta, *Finite Element Methods for Flow Problems*, John Wiley & Sons, Chichester, 2003.
- [40] DC Lo, DL Young, Arbitrary Lagrangian-Eulerian finite element analysis of free surface flow using a velocity-vorticity formulation, *J. Comput. Phys.* 195 (1) (2004) 175–201.
- [41] F. Duarte, R. Gormaz, S. Natesan, Arbitrary Lagrangian-Eulerian method for Navier-Stokes equations with moving boundaries, *Comput. Methods Appl. Mech. Eng.* 193 (45–47) (2004) 4819–4836.
- [42] X. Li, Q. Duan, X. Han, D.C. Sheng, Adaptive coupled arbitrary Lagrangian-Eulerian finite element and meshfree method for injection molding process, *Int. J. Numer. Methods Eng.* 73 (8) (2008) 1153–1180.
- [43] S. Ganesan, L. Tobiska, A coupled arbitrary Lagrangian-Eulerian and Lagrangian method for computation of free surface flows with insoluble surfactants, *J. Comput. Phys.* 228 (8) (2009) 2859–2873.
- [44] P. Nithiarasu, An arbitrary Lagrangian Eulerian (ALE) formulation for free surface flows using the characteristic-based split (CBS) scheme, *Int. J. Numer. Methods Fluids* 48 (2005) 1415–1428.
- [45] J.C. Martin, W.J. Moyce, An experimental study of the collapse of liquid columns on a rigid horizaontal plane, *Philos. Trans. R. Soc. Lond. Ser. A* 244 (1952) 312–324.
- [46] S.R. Idelsohn, N. Calvo, E. Oñate, Polyhedrization of an arbitrary 3D point set, *Comput. Methods Appl. Mech. Eng.* 192 (2003) 2649–2667.

- [47] S.R. Idelsohn, E. Oñate, F. Del Pin, A Lagrangian meshless finite element method applied to fluid-structure interaction problems, *Comput. Struct.* 81 (2003) 655–671.
- [48] S.R. Idelsohn, N. Calvo, E. Oñate, F. Del Pin, The meshless finite element method, *Int. J. Numer. Methods Eng.* 58 (2003) 893–912.
- [49] W.E. Johnson, Development and application of computer programs related to hypervelocity impact, *Systems Science and Software, Report 3SR-353*, 1970.
- [50] R. Codina, U. Schäfer, E. Oñate, Mould filling simulation using finite elements, *Int. J. Numer. Methods Heat Fluid Flow* 4 (1994) 291–310.
- [51] K. Ravindran, R.W. Lewis, Finite element modelling of solidification effects in mould filling, *Finite Elem. Anal. Des.* 31 (1998) 99–116.
- [52] R.W. Lewis, K. Ravindran, Finite element simulation of metal casting, *Int. J. Numer. Methods Eng.* 47 (2000).
- [53] J.V. Wehausen, The wave resistance of ships, *Adv. Appl. Mech.* (1970).
- [54] C.W. Dawson, A practical computer method for solving ship wave problems, in: *Proceedings of the Second International Conference on Numerical Ship Hydrodynamics*, USA, 1977.
- [55] K.J. Bai, J.H. McCarthy (Eds.), *Proceedings of the Second DTNSRDC Workshop on Ship Wave Resistance Computations*, Bethesda, MD, USA, 1979.
- [56] F. Noblesse, J.H. McCarthy (Eds.), *Proceedings of the Second DTNSRDC Workshop on Ship Wave Resistance Computations*. Bethesda, MD, USA, 1983.
- [57] G. Jenson, H. Soding, Ship wave resistance computation, in *Notes on Numerical Fluid Mechanics*, Vol. 25, Vieweg, Braunschweig, 1989.
- [58] Y.H. Kim, T. Lucas, Non-linear ship waves, in: *Proceedings of the 18th Symposium on Naval Hydrodynamics*, MI, USA, 1990.
- [59] D.E. Nakos, P. Sclavounos, On the steady and unsteady ship wave patterns, *J. Fluid Mech.* 215 (1990) 256–288.
- [60] H. Raven, A practical non-linear method for calculating ship wave making and wave resistance, in: *Proceedings of the 19th Symposium on Ship Hydrodynamics*, Seoul, Korea, 1992.
- [61] R.F. Beck, Y. Cao, T.H. Lee, Fully non-linear water wave computations using the desingularized method, in: *Proceedings of the 6th Symposium on Numerical Ship Hydrodynamics*, Iowa City, Iowa, USA, 1993.
- [62] H. Soding, Advances in panel methods, in: *Proceedings of the 21st Symposium on Naval Hydrodynamics*, Trondheim, Norway, 1996.
- [63] C. Janson, L. Larsson, A method for the optimization of ship hulls from a resistance point of view, in: *Proceedings of the 21st Symposium on Naval Hydrodynamics*, Trondheim, Norway, 1996.
- [64] C.C. Mei, H.S. Chen, A hybrid element method for steady linearized free surface flows, *Int. J. Numer. Methods Eng.* 10 (1976) 1153–1175.
- [65] T. Hino, Computation of free surface flow around an advancing ship by Navier-Stokes equations, in: *Proceedings of the 5th International Conference on Numerical Ship Hydrodynamics*, Hiroshima, Japan, 1989, pp. 103–117.

- [66] T. Hino, L. Martinelli, A. Jameson, A finite volume method with unstructured grid for free surface flow, in: Proceedings of the 6th International Conference on Numerical Ship Hydrodynamics, Iowa City, IA, 1993, pp. 173–194.
- [67] T. Hino, An unstructured grid method for incompressible viscous flows with free surface, AIAA-97-0862, 1997.
- [68] J.H. Duncan, The breaking and non-breaking wave resistance of a two dimensional hydrofoil, *J. Fluid Mech.* 126 (1983) 507–516.
- [69] O.C. Zienkiewicz, R.L. Taylor, J.Z. Zhu, *The Finite Element Method: Its Basis and Fundamentals*, seventh ed., Elsevier, Oxford, 2013.
- [70] S. Giuliani, An algorithm for continuous rezoning of the hydrodynamic grid in arbitrary Lagrangian-Eulerian computer codes, *Nucl. Eng. Des.* 72 (1982) 205–212.
- [71] J. Sarrate, A. Huerta, An improved algorithm to smooth graded quadrilateral meshes preserving the prescribed element size, *Commun. Numer. Methods Eng.* 17 (2001) 89–99.
- [72] J. Hermansson, P. Hansbo, A variable diffusion method for mesh smoothing, *Commun. Numer. Methods Eng.* 19 (2003) 897–908.
- [73] E.V. Laitone, The second approximation to cnoidal and solitary waves, *J. Fluid Mech.* 9 (1960) 430–444.
- [74] T. Maxworthy, Experiments on collisions between solitary waves, *J. Fluid Mech.* 76 (1976) 177–186.
- [75] N. Massarotti, P. Nithiarasu, O.C. Zienkiewicz, Characteristic-based-split algorithm, Part II: Incompressible flow problems with heat transfer, in: K.D. Papailiou et al. (Eds.), *Proceedings of the ECCOMAS CFD 1998*, vol. 2, Athens, Greece, 1998, pp. 17–21.
- [76] N. Massarotti, P. Nithiarasu, O.C. Zienkiewicz, Characteristic-based-split (CBS) algorithm for incompressible flow problems with heat transfer, *Int. J. Numer. Methods Heat Fluid Flow* 8 (1998) 969–990.
- [77] P. Nithiarasu, T. Sundararajan, K.N. Seetharamu, Finite element analysis of transient natural convection in an odd-shaped enclosure, *Int. J. Numer. Methods Heat Fluid Flow* 8 (1998) 199–220.
- [78] R.W. Lewis, P. Nithiarasu, K.N. Seetharamu, *Fundamentals of the finite element method for heat and fluid flow*, John Wiley and Sons, 2004.
- [79] F.P. Incropera, D.P. Dewitt, *Fundamentals of Heat and Mass Transfer*, third ed., John Wiley, New York, 1990.
- [80] A. Bejan, *Heat Transfer*, John Wiley, New York, 1993.
- [81] Y. Jaluria, *Natural Convection Heat Transfer*, Springer-Verlag, New York, 1980.
- [82] O.C. Zienkiewicz, R.H. Gallagher, P. Hood, Newtonian and non-Newtonian viscous incompressible flow, in: J. Whiteman (Ed.), *Mathematics of Finite Elements and Applications*, vol. II, Academic Press, London, 1976, pp. 235–267.
- [83] J.C. Heinrich, R.S. Marshall, O.C. Zienkiewicz, Penalty function solution of coupled convective and conductive heat transfer, in: C. Taylor, K. Morgan, C.A.

- Brebbia (Eds.), Numerical Methods in Laminar and Turbulent Flows, Pentech Press, 1978, pp. 435–447.
- [84] J.C. Heinrich, C.C. Yu, Finite element simulation of buoyancy driven flow with emphasis on natural convection in horizontal circular cylinder, *Comput. Methods Appl. Mech. Eng.* 69 (1988) 1–27.
 - [85] B. Ramaswamy, Finite element solution for advection and natural convection flows, *Comput. Fluids* 16 (1988) 349–388.
 - [86] B.V.K. Sai, K.N. Seetharamu, P.A.A. Narayana, Finite element analysis of the effect of radius ratio on natural convection in an annular cavity, *Int. J. Numer. Methods Heat Fluid Flow* 3 (1993) 305–318.
 - [87] C. Nonino, S. Del Giudice, Finite element analysis of laminar mixed convection in the entrance region of horizontal annular ducts, *Numer. Heat Trans., Part A: Appl.* 29 (1996) 313–330.
 - [88] S.C. Lee, C.K. Chen, Finite element solutions of laminar and turbulent mixed convection in a driven cavity, *Int. J. Numer. Methods Fluids* 23 (1996) 47–64.
 - [89] Y.T.K. Gowda, P.A.A. Narayana, K.N. Seetharamu, Finite element analysis of mixed convection over in-line tube bundles, *Int. J. Heat Mass Trans.* 41 (1998) 1613–1619.
 - [90] G. De Vahl Davis, Natural convection of air in a square cavity: a benchmark numerical solution, *Int. J. Numer. Methods Fluids* 3 (1983) 249–264.
 - [91] P. Le Quere, T.A. De Roquefort, Computation of natural convection in two dimensional cavity with Chebyshev polynomials, *J. Comput. Phys.* 57 (1985) 210–228.
 - [92] P. Nithiarasu, N. Massarotti, J.S. Mathur, Forced convection heat transfer from solder balls on a printed circuit board using the characteristic based split (CBS) scheme, *Int. J. Numer. Methods Heat Fluid Flow* 15 (1) (2005) 73–95.
 - [93] N. Massarotti, F. Arpino, R.W. Lewis, P. Nithiarasu, Explicit and semi-implicit CBS procedures for incompressible viscous flows, *Int. J. Numer. Methods Eng.* 66 (10) (2006) 1618–1640.
 - [94] A. Mauro, P. Nithiarasu, N. Massarotti, F. Arpino, The finite element method: discretization and application to heat convection problems, in: R.S. Amano, B. Sundén (Eds.), Computational Fluid Dynamics and Heat Transfer: Emerging Topics, International Series on Developments in Heat Transfer, WIT Press, Billerica, MA, 2011, pp. 129–170.
 - [95] F. Arpino, N. Massarotti, A. Mauro, P. Nithiarasu, Artificial compressibility based CBS solutions for double diffusive natural convection in cavities, *Int. J. Numer. Methods Heat Fluid Flow* 23 (2013) 205–225.

Compressible High-Speed Gas Flow

7

7.1 Introduction

Problems posed by high-speed gas flow are of obvious practical importance. Applications range from the *exterior flows* associated with flight to *interior flows* typical of turbomachinery. As the cost of physical experiments is high, the possibilities of computations were explored early and the development concentrated on the use of finite difference and associated finite volume methods. It was only in the 1980s that the potential offered by the finite element forms was realized and the field is expanding rapidly.

One of the main advantages in the use of the finite element approximation here is its capability of fitting complex forms and permitting local refinement where required. However, the improved approximation is also of substantial importance as practical problems will often involve three-dimensional discretization with the number of degrees of freedom much larger than those encountered in typical structural problems.

For such large problems direct solution methods are obviously not practicable and iterative methods based generally on transient computation forms are invariably used. Here of course we follow and accept much that has been established by the finite difference applications but generally will lose some computational efficiency associated with *structured meshes*. However, the reduction of the problem size which, as we shall see, can be obtained by local refinement and adaptivity will more than compensate for this loss (though of course structured meshes are included in the finite element forms).

In [Chapters 1](#) and [3](#) we introduced the basic equations governing the flow of compressible gases as well as of incompressible fluids. Indeed in the latter, as in [Chapter 4](#), we can introduce small amounts of compressibility into the procedures developed there specifically for incompressible flow. In this chapter we shall deal with high-speed flows. Such flows will usually involve the formation of shocks with characteristic discontinuities. For this reason we shall concentrate on the use of low-order elements and explicit methods, such as those introduced in [Chapters 2](#) and [3](#).

Here the pioneering work of the author's colleagues Morgan, Löhner, Peraire, Hassan, and Weatherill must be acknowledged [[1–48](#)]. It was this work that opened the doors to practical finite element analysis in the field of aeronautics. We shall refer to their work frequently.

In the first practical applications the Taylor-Galerkin process outlined in [Appendix D](#) for vector-valued variables was used almost exclusively. Here we recommend however the CBS algorithm discussed in [Chapter 3](#) as it presents a better approximation and has the advantage of dealing directly with incompressibility, which invariably occurs in small parts of the domain, even at high Mach numbers (e.g., in stagnation regions).

7.2 The governing equations

The Navier-Stokes governing equations for compressible flow were derived in [Chapter 1](#). We shall repeat only the simplified form of [Eq. \(1.25\)](#) here again using indicial notation. We thus write, for $i = 1, 2, 3$,

$$\frac{\partial \Phi}{\partial t} + \frac{\partial \mathbf{F}_i}{\partial x_i} + \frac{\partial \mathbf{G}_i}{\partial x_i} + \mathbf{Q} = \mathbf{0} \quad (7.1)$$

with

$$\Phi = [\rho, \rho u_1, \rho u_2, \rho u_3, \rho E]^T \quad (7.2a)$$

$$\mathbf{F}_i = [\rho u_i, \rho u_1 u_i + p \delta_{1i}, \rho u_2 u_i + p \delta_{2i}, \rho u_3 u_i + p \delta_{3i}, \rho H u_i]^T \quad (7.2b)$$

$$\mathbf{G}_i = \left[0, -\tau_{1i}, -\tau_{2i}, -\tau_{3i}, -\frac{\partial}{\partial x_i}(\tau_{ij} u_j) - k \left(\frac{\partial T}{\partial x_i} \right) \right]^T \quad (7.2c)$$

and

$$\mathbf{Q} = [0, -\rho f_1, -\rho f_2, -\rho f_3, -\rho f_i u_i - q_H]^T \quad (7.2d)$$

In the above

$$\tau_{ij} = \mu \left[\left(\frac{\partial u_i}{\partial x_j} + \frac{\partial u_j}{\partial x_i} \right) - \delta_{ij} \frac{2}{3} \frac{\partial u_k}{\partial x_k} \right] \quad (7.2e)$$

The above equations need to be “closed” by addition of the constitutive law relating the pressure, density, and energy (see [Chapter 1](#)). For many flows the ideal gas law [[49](#)] suffices and this is

$$\rho = \frac{p}{RT} \quad (7.3)$$

where R is the universal gas constant. In terms of specific heats

$$R = (c_p - c_v) = (\gamma - 1)c_v \quad (7.4)$$

where

$$\gamma = \frac{c_p}{c_v}$$

is the ratio of the constant pressure and constant volume-specific heats.

The internal energy e and total specific energy E are given as

$$\begin{aligned} e &= c_v T = \left(\frac{1}{\gamma - 1} \right) \frac{p}{\rho} \\ E &= e + \frac{1}{2} u_i u_i \end{aligned} \quad (7.5)$$

and hence

$$\rho E = \left(\frac{1}{\gamma - 1} \right) p + \rho \frac{u_i u_i}{2} \quad (7.6a)$$

$$\rho H = \rho E + p = \left(\frac{\gamma}{\gamma - 1} \right) p + \rho \frac{u_i u_i}{2} \quad (7.6b)$$

The variables for which we shall solve are usually taken as the set of Eq. (7.2a), i.e.

$$\rho, \rho u_i, \text{ and } \rho E$$

but of course other sets could be used, though then the conservative form of Eq. (7.1) could be lost.

In many of the problems discussed in this chapter inviscid behavior will be assumed, with

$$\mathbf{G}_i = \mathbf{0}$$

and we shall then deal with the *Euler equations*.

In many problems the Euler solution will provide information about the main features of the flow and will suffice for many purposes, especially if augmented by separate boundary layer calculations (see Section 7.13). However, in principle it is possible to include the viscous effects without much apparent complication. Here in general steady-state conditions will never arise as the high speed of the flow will be associated with turbulence and this will usually be of a small scale capable of resolution with very small-sized elements only. If a “finite” size of element mesh is used then such turbulence will often be suppressed and steady-state answers will be obtained. We shall in some examples include such full Navier-Stokes solutions using a viscosity dependent on the temperature according to Sutherland’s law [49]. In the SI system of units for air this gives

$$\mu = \frac{1.45 T^{3/2}}{T + 110} \times 10^{-6} \quad (7.7)$$

where T is in Kelvin. Further turbulence modeling can be done by using the Reynolds-averaged equations and solving additional transport equations for some additional parameters in the manner discussed in Chapter 8.

7.3 Boundary conditions: Subsonic and supersonic flow

The question of boundary conditions which can be prescribed for Euler and Navier-Stokes equations in compressible flow is by no means trivial and has been addressed in

a general sense by Demkowicz et al. [50], determining their influence on the existence and uniqueness of solutions. In the following we shall discuss the case of the inviscid Euler form and of the full Navier-Stokes problem.

We have already discussed the general question of boundary conditions in Chapter 3 dealing with numerical approximations. Some of these matters have to be repeated in view of the special behavior of high-speed flow problems.

7.3.1 Euler equation

Here only first-order derivatives occur and the number of boundary conditions is less than that for the full Navier-Stokes problem.

For a *solid wall boundary*, Γ_u , only the normal component of velocity u_n needs to be specified (zero if the wall is stationary). Further, with lack of conductivity the energy flux across the boundary is zero and hence ρE (and ρ) remain unspecified.

In general the analysis domain will be limited by some arbitrarily chosen *external boundaries*, Γ_s , for exterior or internal flows, as shown in Fig. 7.1 (see also Section 3.9, Chapter 3).

Here, it will in general be necessary to perform a linearized Riemann analysis in the direction of the outward normal to the boundary \mathbf{n} to determine the speeds of wave propagation of the equations. For this linearization of the Euler equations three propagation speed values (characteristics) can be found in one dimension (eigenvalues of the Jacobian matrix) [49, 51]:

$$\begin{aligned} c_o &= u_n \\ c_+ &= u_n + c \\ c_- &= u_n - c \end{aligned} \quad (7.8)$$

where u_n is the normal velocity component and c is the compressible wave celerity (speed of sound) given by

$$c = \sqrt{\frac{\gamma p}{\rho}} \quad (7.9)$$

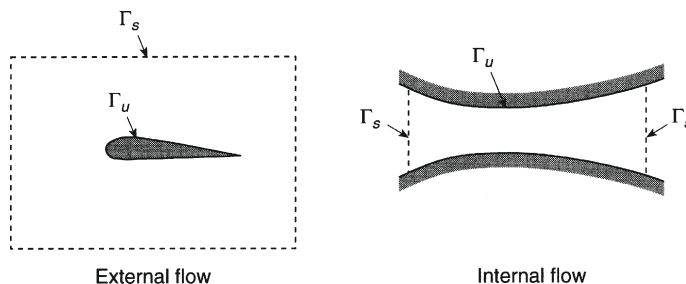


FIGURE 7.1

Boundaries of a computation domain. Γ_u , wall boundary; Γ_s , fictitious boundary.

As of course no disturbances can propagate at velocities greater than those of Eq. (7.8) in the case of supersonic flow, i.e., when the local Mach number is

$$M = \frac{|u_n|}{c} \geq 1 \quad (7.10)$$

we shall have to distinguish two possibilities:

- (a) *Supersonic inflow boundary* where

$$u_n > c$$

and the analysis domain cannot influence the upstream position (all characteristics are directed into the domain at the inlet); for such boundaries all components of the vector Φ must be specified.

- (b) *Supersonic outflow boundaries* where

$$u_n > c$$

and here by the same reasoning no components of Φ are prescribed (all characteristics are directed out of the domain).

For subsonic boundaries the situation is more complex and here the values of Φ that can be specified are the components of the incoming Riemann variables. However, this may frequently present difficulties as the incoming wave may not be known and the usual compromises may be necessary as in the treatment of elliptic problems possessing infinite boundaries (see Chapter 3, Section 3.9).

It is often convenient to prescribe boundary conditions for a subsonic flow by once again considering the direction of characteristics from Eq. (7.8). Since $u_n < c$ in subsonic flows, one characteristic at the inlet will be directed outwards and two will be directed inwards. At the exit one characteristic is directed inward and two outwards as shown in Figure 7.2. Thus, it is necessary to prescribe two boundary conditions at the inlet and one at the exit for the subsonic condition shown in Figure 7.2. However, this procedure is not easy to follow in multidimensional problems.

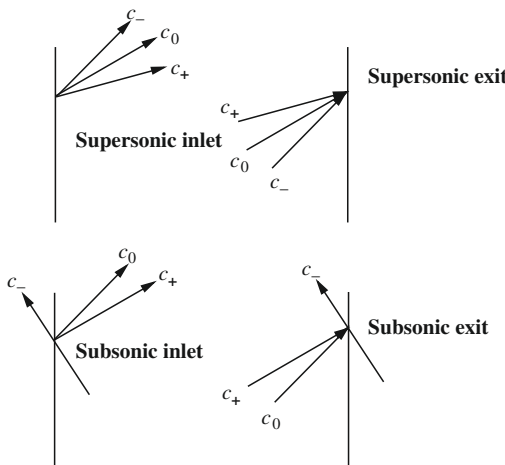
7.3.2 Navier-Stokes equations

Here, due to the presence of second derivatives, additional boundary conditions are required.

For the *solid wall boundary*, Γ_u , all the velocity components are prescribed assuming, as in the previous chapter for incompressible flow, that the fluid is attached to the wall. Thus for a stationary boundary we put

$$u_i = 0$$

Further, if conductivity is not negligible, boundary temperatures or heat fluxes will generally be given in the usual manner.

**FIGURE 7.2**

Characteristic directions at inlet and exit for supersonic and subsonic flows.

For exterior boundaries Γ_s of the supersonic inflow kind, the treatment is identical to that used for Euler equations. However, for outflow boundaries a further approximation must be made, either specifying tractions as zero or making their gradient zero in the manner described in [Section 3.9, Chapter 3](#).

7.4 Numerical approximations and the CBS algorithm

Various forms of finite element approximation and of solution have been used for compressible flow problems. The first successfully used algorithm here was, as we have already mentioned, the Taylor-Galerkin procedure either in its single-step or two-step form. We have outlined both of these algorithms in [Appendix D](#). However, the most generally applicable and advantageous form is that of the CBS algorithm which we have presented in detail in [Chapter 3](#). In all compressible flows in certain parts of the domain where the velocities are small, the flow is nearly incompressible and without additional damping the direct use of the Taylor-Galerkin method may result in oscillations there. We indeed mentioned an example of such oscillations in [Chapter 3](#) where they are pronounced near the leading edge of an aerofoil even at quite high Mach numbers ([Fig 3.4](#)). With the use of the CBS algorithm such oscillations disappear and the solution is perfectly stable and accurate.

In the same example we also discussed the single-step and two-step forms of the CBS algorithm. We recommend the two-step procedure, which is only slightly more expensive than the single-step version but more stable.

As we have already remarked if the algorithm is used for steady-state problems it is always convenient to use a localized time step rather than proceed with the same

time step globally. The full description of the local time step procedure is given in [Section 3.4.4](#) of [Chapter 3](#) and this was invariably used in the examples of this chapter when only the steady state was considered. We now summarize the explicit solution procedure below:

```

do i = 1,number of time steps
    step1: calculation of intermediate momentum
    step2: calculation of density
    step3: correction of momentum
    step4: energy equation
    step5: pressure calculation from energy and density
  enddo !i

```

For further details on the algorithm, readers are referred to [Chapter 3](#). If shock capturing or any other form of smoothing is found necessary this is integrated into the first step of the above solution procedure.

One of the additional problems that we need to discuss further for compressible flows is that of the treatment of shocks, which is the subject of the next section.

7.5 Shock capture

Clearly with the finite element approximation in which all the variables are interpolated using C_0 continuity the exact reproduction of shocks is not possible. In all finite element solutions we therefore represent the shocks simply as regions of very high gradient. The ideal situation will be if the rapid variations of variables are confined to a few elements surrounding the shock. Unfortunately it will generally be found that such an approximation of a discontinuity introduces local oscillations and these may persist throughout quite a large area of the domain. For this reason, we shall usually introduce into the finite element analysis additional viscosities which will help us in damping out any oscillations caused by shocks and, yet, deriving as sharp a solution as possible.

Such procedures using artificial viscosities are known as shock capture methods. It must be mentioned that some investigators have tried to allow the shock discontinuity to occur explicitly and thus allowed a discontinuous variation of an analytically defined kind. This presents very large computational difficulties and it can be said that to date such trials have only been limited to one-dimensional problems and have not really been used to any extent in two or three dimensions. For this reason we shall not discuss such *shock fitting* methods further [[52,53](#)].

The concept of adding additional viscosity or diffusion to capture shocks was first suggested by von Neumann and Richtmyer [[54](#)] as early as 1950. They recommended that stabilization can be achieved by adding a suitable artificial dissipation term that mimics the action of viscosity in the neighborhood of shocks. Significant developments in this area are those of Lapidus [[55](#)], Steger [[56](#)], MacCormack and Baldwin [[57](#)], and Jameson and Schmidt [[58](#)]. At Swansea, a modified form of the method based on the second derivative of pressure has been developed by Peraire et al. [[14](#)]

and Morgan et al. [59] for finite element computations. This modified form of viscosity with a pressure switch calculated from the nodal pressure values is used subsequently in compressible flow calculations. Lately an anisotropic viscosity for shock capturing [60] has been introduced to add diffusion in a more rational way.

The implementation of artificial diffusion is very much simpler than shock fitting and we proceed as follows. In this we first calculate the approximate quantities of the solution vector by using the direct explicit method. Now we modify each scalar component of these quantities by adding a correction which smoothes the result. Thus for instance if we consider a typical scalar component quantity ϕ and have determined the values of ϕ^{n+1} , we establish the new values as below:

$$\phi_s^{n+1} = \phi^{n+1} + \Delta t \mu_a \frac{\partial}{\partial x_i} \left(\frac{\partial \phi}{\partial x_i} \right) \quad (7.11)$$

where μ_a is an appropriate artificial diffusion coefficient. It is important that whatever the method used, the calculation of μ_a should be limited to the domain which is close to the shock as we do not wish to distort the results throughout the problem. For this reason many procedures add a *switch* usually activated by such quantities as gradients of pressure. In all of the procedures used we can write the quantity μ_a as a function of one or more of the dependent variables calculated at time n . Below we only quote two of the possibilities.

7.5.1 Second derivative-based methods

In these it is generally assumed that the coefficient μ_a must be the same for each of the equations dealt with and only one of the dependent variables Φ is important. It has usually been assumed that the most typical variable here is the pressure and that we should write [57]

$$\mu_a = C_e h^3 \frac{|\mathbf{u}| + c}{\bar{p}} \left| \frac{\partial^2 p}{\partial x_i \partial x_i} \right|_e \quad (7.12)$$

where C_e is a nondimensional coefficient, \mathbf{u} is the velocity vector, c is the speed of sound, \bar{p} is the average pressure, and the subscript e indicates an element. In the above equation, the second derivative of pressure over an element can be established either by averaging the smoothed nodal pressure gradients or using any of the methods described in Chapter 4, Section 4.3.3.

A particular variant of the above method evaluates approximately the value of the second derivative of any scalar variable ϕ (e.g., p) as [59, 61]

$$h^2 \overline{\frac{\partial^2 \phi}{\partial x^2}} \approx (\mathbf{M} - \mathbf{M}_L) \tilde{\phi} \quad (7.13)$$

where \mathbf{M} and \mathbf{M}_L are consistent and lumped mass matrices respectively and the tilde indicates a nodal value. Though the derivation of the above expression is not obvious, the reader can verify that in the one-dimensional finite difference approximation

it gives the correct result. The heuristic extension to multidimensional problem therefore seems reasonable. Now μ_a for this approximate method can be rewritten in any space dimensions as [Eq. (7.12)]

$$\tilde{\mu}_a = C_e h \frac{|\mathbf{u}| + c}{\bar{p}} (\mathbf{M} - \mathbf{M}_L) \tilde{\mathbf{p}} \quad (7.14)$$

Note now that $\tilde{\mu}_a$ is a nodal quantity. However a further approximation can give the following form of μ_a over elements:

$$\mu_{ae} = C_e h (|\mathbf{u}| + c) S_e \quad (7.15)$$

where S_e is the element pressure switch which is a mean of nodal switches S_i calculated as [59, 61]

$$S_i = \frac{|\Sigma_e(p_i - p_k)|}{\Sigma_e|p_i - p_k|} \quad (7.16)$$

It can be verified that $S_i = 1$ when the pressure has a local extremum at node i and $S_i = 0$ when the pressure at node i is the average of the values for all nodes adjacent to node i (e.g., if p varies linearly). The user-specified coefficient C_e normally varies between 0.0 and 2.0.

The smoothed variables can now be rewritten with the Galerkin finite element approximations [from Eqs. (7.11) and (7.15)] as

$$\tilde{\phi}_s^{n+1} = \tilde{\phi}^{n+1} + \Delta t \mathbf{M}_L^{-1} \frac{C_e S_e}{\Delta t_e} (\mathbf{M} - \mathbf{M}_L) \tilde{\phi}^n \quad (7.17)$$

Note that, in Eq. (7.15), $(|\mathbf{u}| + c)$ is replaced by $h/\Delta t_e$ to obtain the above equation. This method has been widely used and is very efficient. The cutoff localizing the effect of added diffusion is quite sharp. A direct use of second derivatives can however be employed without the above-mentioned modifications. In such a procedure, we have the following form of smoothing [from Eqs. (7.11) and (7.12)]:

$$\tilde{\phi}_s^{n+1} = \tilde{\phi}^{n+1} - \Delta t \mathbf{M}_L^{-1} C_e h^3 \frac{|\mathbf{u}| + c}{\bar{p}} \left| \frac{\partial^2 p}{\partial x_i^2} \right|_e \left(\int_{\Omega} \frac{\partial \mathbf{N}^T}{\partial x_i} \frac{\partial \mathbf{N}}{\partial x_i} \tilde{\phi}^n d\Omega \right) \tilde{\phi}^n \quad (7.18)$$

This method was successful in many viscous problems. Another alternative is to use residual-based methods.

7.5.2 Residual-based methods

In these methods $\mu_{ai} = \mu(R_i)$, where R_i is the residual of the i th equation. Such methods were first introduced in 1986 by Hughes and Malett [62] and later used by many others [63–66].

A variant of this was suggested by Codina [60]. We sometimes refer to this as anisotropic shock capturing. In this procedure the artificial viscosity coefficient is

adjusted by subtracting the diffusion introduced by the characteristic-Galerkin method along the streamlines. We do not know whether there is any advantage gained in this but we have used the anisotropic shock capturing algorithm with considerable success. The full residual-based coefficient is given by

$$\mu_{a_i} = C_e \frac{|R_i|}{|\nabla \phi_i|} \quad (7.19)$$

We shall not discuss here a direct comparison between the results obtained by different shock capturing diffusivities, and the reader is referred to various papers already published [61, 67]. Another smoothing procedure occasionally used in low Mach number flows is referred to as “variable smoothing” and this method is discussed in the following section.

7.6 Variable smoothing

At low Mach numbers, we found it often necessary to include a variable smoothing procedure if the coupling between the energy and other variables exists. Of course isothermal approximations are possible to get a smooth solution. However, to solve a compressible flow problem at low Mach numbers (< 0.8) without removing energy coupling we recommend a variable smoothing approach [68]. In the proposed variable smoothing approach the conservation variables, $\{\Phi\}$, at a node are smoothed by applying the following redistribution:

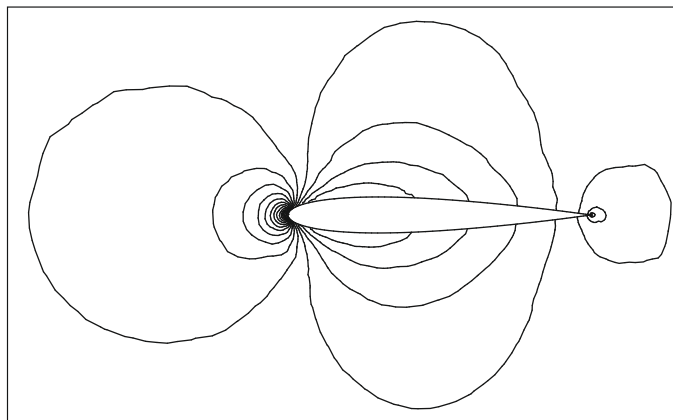
$$\{\Phi\} = \left[\frac{1}{1 + 0.5\alpha} \{\Phi\} + \frac{\alpha}{1 + 0.5\alpha} \mathbf{M}_L^{-1} (\mathbf{M} - \mathbf{M}_D) \{\Phi\} \right] \quad (7.20)$$

where α is a variable smoothing parameter which varies between 0 and 0.05, \mathbf{M} is the consistent mass matrix, \mathbf{M}_D is the consistent mass matrix without nondiagonal terms, and \mathbf{M}_L is the lumped mass matrix. By increasing α the weighting on the node in question is decreased while the influence of the surrounding nodes is increased. In [Figure 7.3](#) we show the smoothed density contours of subsonic flow past a NACA0012 airfoil at a Mach number of 0.25. The results without smoothing give a very oscillatory solution as shown in [Figure 7.4](#) in which the pressure coefficients from smoothed and unsmoothed solutions are compared.

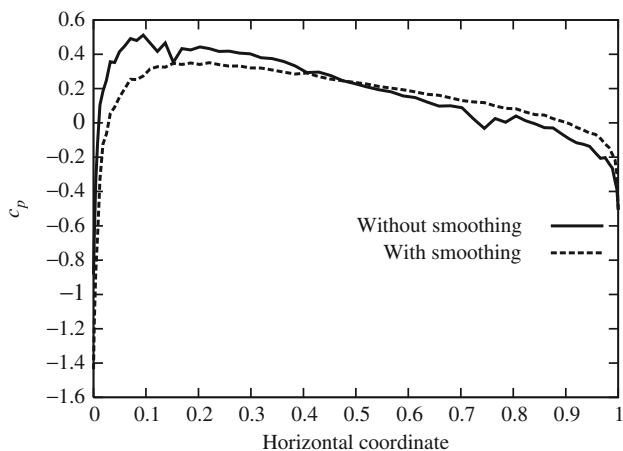
At transonic and supersonic speeds, an additional shock capturing dissipation ([Section 7.5](#)) is necessary to capture and to smooth local oscillations in the vicinity of shocks.

7.7 Some preliminary examples for the Euler equation

The computation procedures outlined can be applied with success to many transient and steady-state problems. In this section we illustrate its performance on a few relatively simple examples.

**FIGURE 7.3**

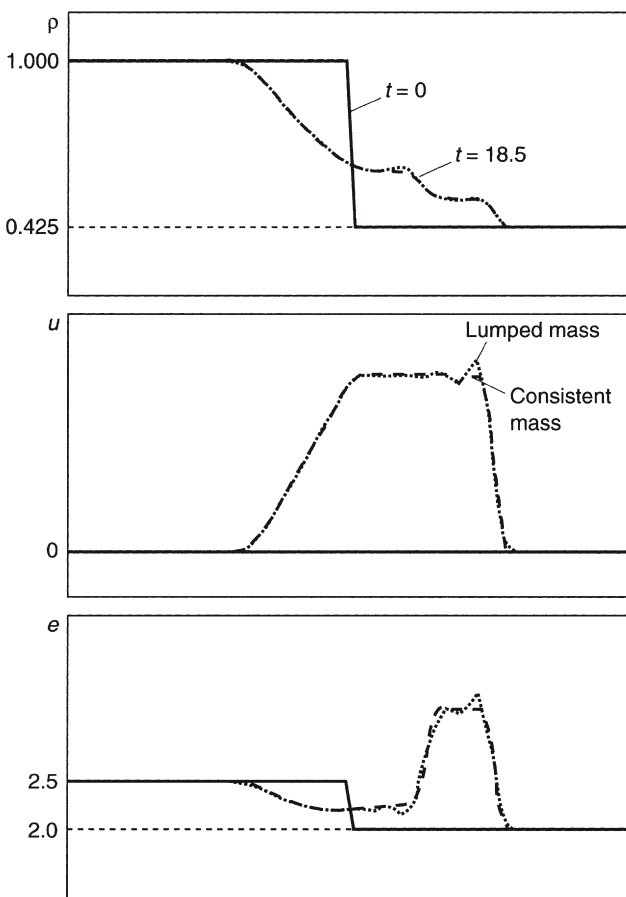
Subsonic inviscid flow past a NACA0012 airfoil at Mach number of 0.25 and zero angle of attack. Smoothed density contours [68].

**FIGURE 7.4**

Subsonic inviscid flow past a NACA0012 airfoil at Mach number of 0.25 and zero angle of attack. Comparison between smoothed and unsmoothed pressure coefficients [68].

Example 7.1. Riemann shock tube: A transient problem in one dimension

This is treated as a one-dimensional problem. Here an initial pressure difference between two sections of the tube is maintained by a diaphragm which is destroyed at $t = 0$. Figure 7.5 shows the pressure, velocity, and energy contours at the 70th time increment, and the effect of including consistent and lumped mass matrices is illustrated. The problem has an analytical, exact, solution presented by Sod [69] and the numerical solution is from Ref. [1].

**FIGURE 7.5**

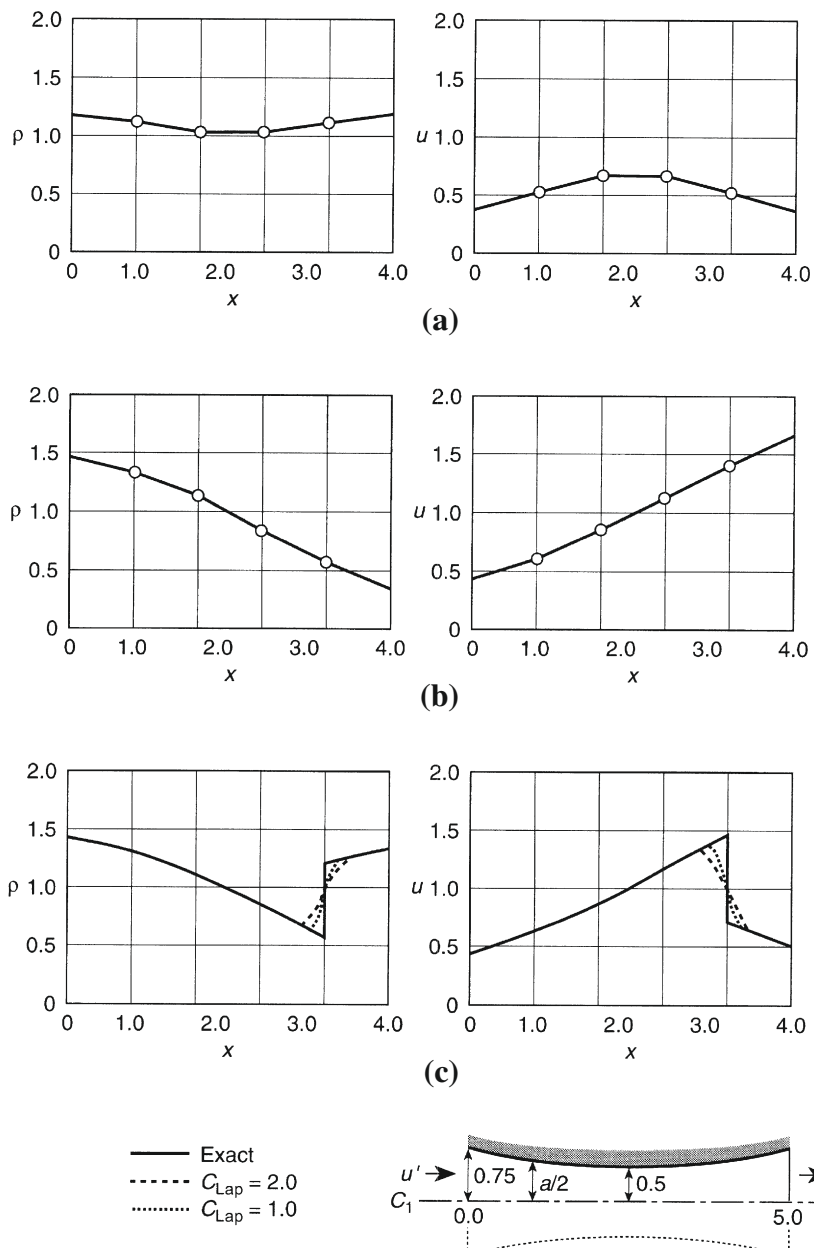
The Riemann shock tube problem [1, 69]. The total length is divided into 100 elements. Profile illustrated corresponds to 70 time steps ($\Delta t = 0.25$). Lapidus constant $C_{\text{Lap}} = 1.0$.

Example 7.2. Isothermal flow through a nozzle in one dimension

Here a variant of the Euler equation is used in which isothermal conditions are assumed and in which the density is replaced by ρa where a is the cross-sectional area [1] assumed to vary as [70]

$$a = 1.0 + \frac{(x - 2.5)^2}{12.5} \quad \text{for } 0 \leq x \leq 5 \quad (7.21)$$

The speed of sound is constant as the flow is isothermal and various conditions at inflow and outflow limits were imposed as shown in Fig. 7.6. In all problems steady

**FIGURE 7.6**

Isothermal flow through a nozzle [1]. Forty elements of equal size used: (a) subsonic inflow and outflow; (b) supersonic inflow and outflow; (c) supersonic inflow–subsonic outflow with shock.

state was reached after some 500 time steps. For the case with supersonic inflow and subsonic outflow, a shock forms and Lapidus-type artificial diffusion was used to deal with it, showing in Fig. 7.6c the increasing amount of “smearing” as the coefficient C_{Lap} is increased.

Example 7.3. Two-dimensional transient supersonic flow over a step

This final example concerns the transient initiation of supersonic flow in a wind tunnel containing a step. The problem was first studied by Woodward and Colella [71] and the results of Ref. [5] presented here are essentially similar.

In this problem a uniform mesh of linear triangles, shown in Fig. 7.7, was used and no difficulties of computation were encountered although a Lapidus constant $C_{\text{Lap}} = 2.0$ had to be used due to the presence of shocks.

Example 7.4. Inviscid flow past a NACA0012 aerofoil

This is one of the widely studied problems in aerodynamics that has a large number of benchmark steady-state data. Here we have solved this problem over a range of Mach numbers within subsonic, transonic, and supersonic flow regimes at zero angle of attack. The problem domain and mesh used are shown in Figure 7.8. The diameter of the circular domain is equal to 25 times the chord length of the aerofoil. The leading edge of the aerofoil is assumed to be at the center of the domain. All the inlet quantities are prescribed and no variable is prescribed at the exit at supersonic and transonic speeds. At subsonic speeds however, one of the primitive variables is prescribed at the exit. The Mach number is varied between 0.25 and 1.2 to capture all different flow regimes.

Figure 7.9 shows the steady-state convergence histories at different Mach numbers. As expected convergence to steady state at supersonic and transonic Mach numbers is rapid but the subsonic cases took longer to reach steady state. The pressure coefficients are calculated as $-2(p_a - p_{\text{ref}})$. Here p_{ref} is the reference pressure at inlet.

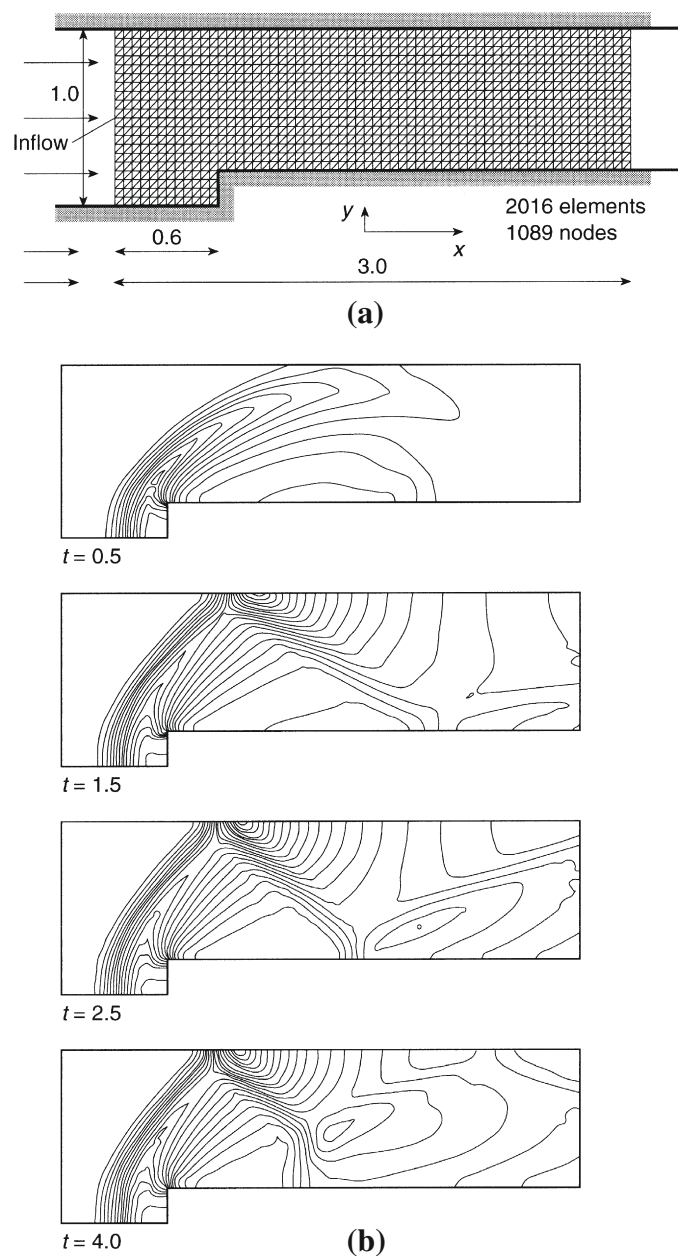
Figures 7.10 and 7.11 show the pressure contours and surface pressure coefficient distribution at subsonic Mach numbers. At both subsonic Mach numbers, we invoke the variable smoothing in the place of shock capturing viscosities. A detailed comparison of stagnation quantities with an analytical solution at subsonic Mach numbers is presented in Ref. [68].

Figures 7.12 and 7.13 show the pressure contours and surface pressure coefficient distribution at transonic and supersonic Mach numbers. In Figure 7.13 pressure coefficient results at two Mach numbers are compared with the AGARD results [72].

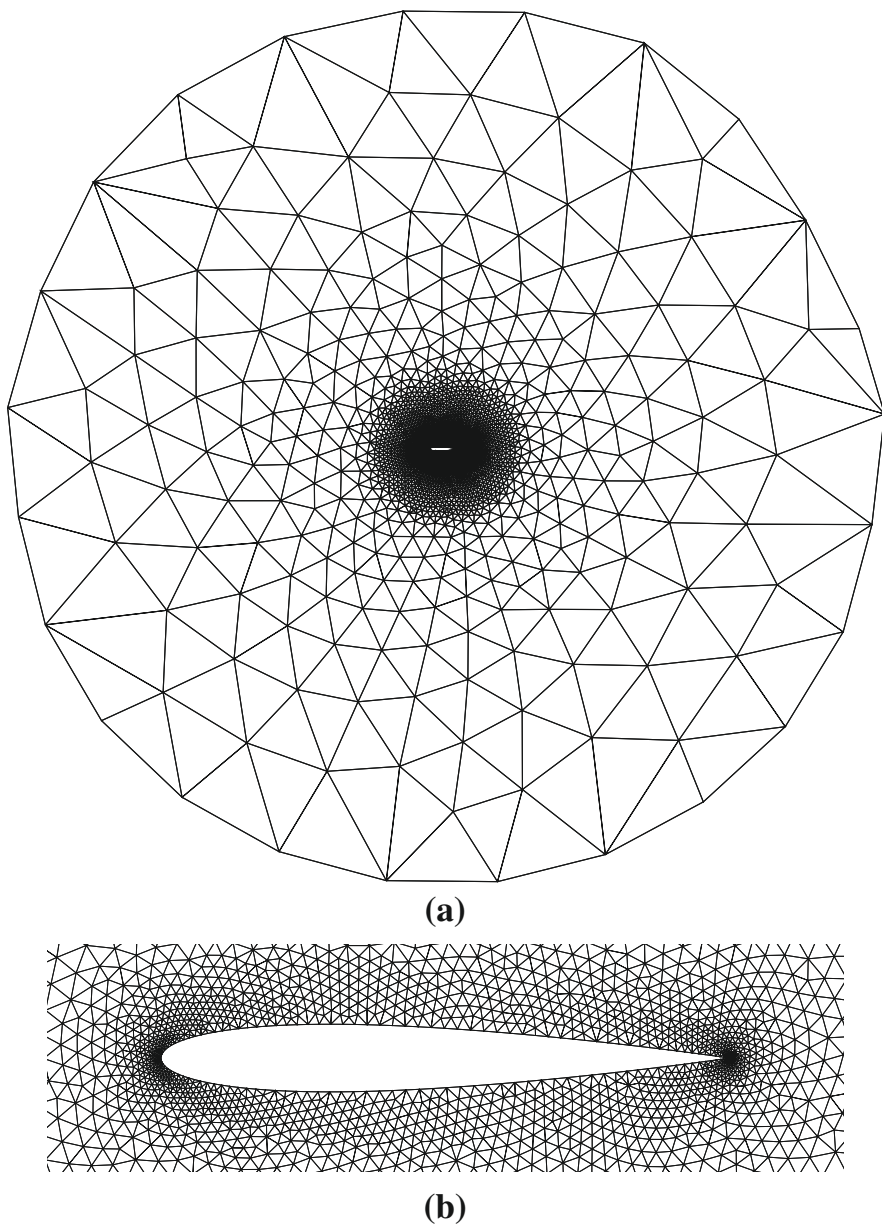
7.8 Adaptive refinement and shock capture in Euler problems

7.8.1 General

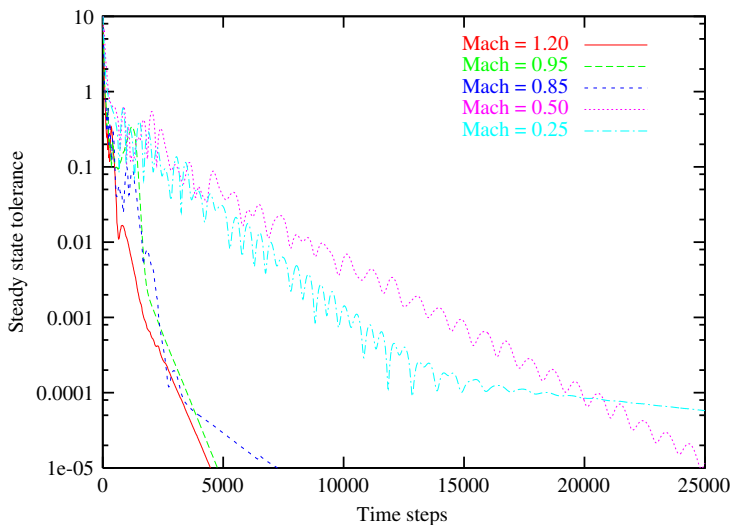
The examples of the previous section have indicated the formation of shocks both in transient and steady-state problems of high-speed flow. Clearly the resolution of

**FIGURE 7.7**

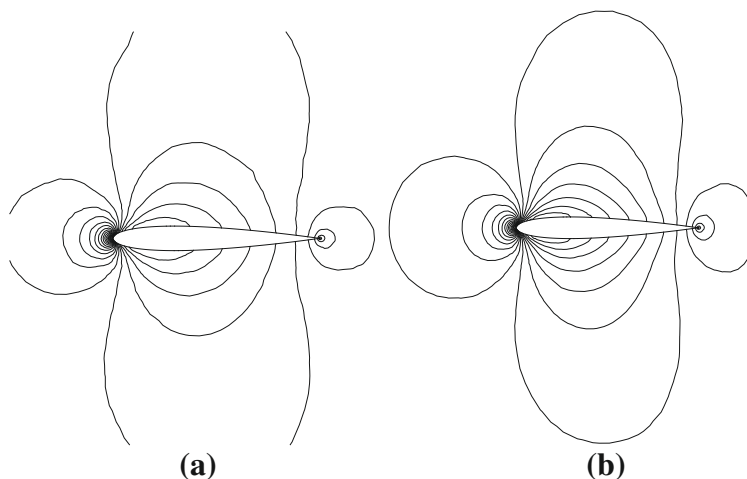
Transient supersonic flow over a step in a wind tunnel [5] (problem of Woodward and Colella [71]). Inflow Mach 3 uniform flow: (a) structured uniform mesh; (b) solution – contours of pressure at various times.

**FIGURE 7.8**

Inviscid flow past a NACA0012 aerofoil. Unstructured mesh. Number of nodes: 3753; number of elements: 7351. (a) Finite element mesh and domain; (b) mesh distribution in the vicinity of the aerofoil.

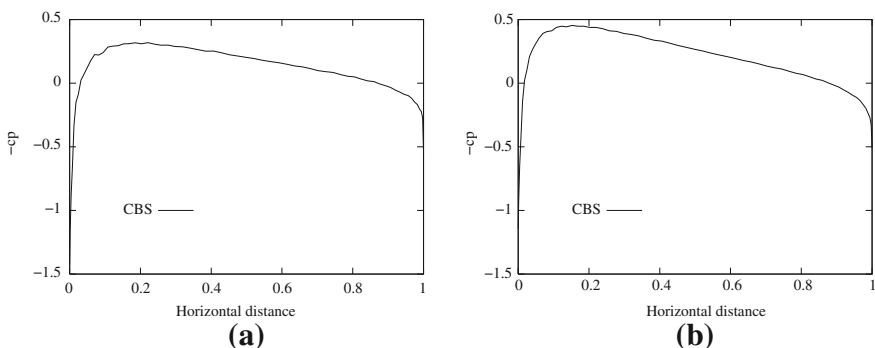
**FIGURE 7.9**

Inviscid flow past a NACA0012 aerofoil. Convergence histories to steady state.

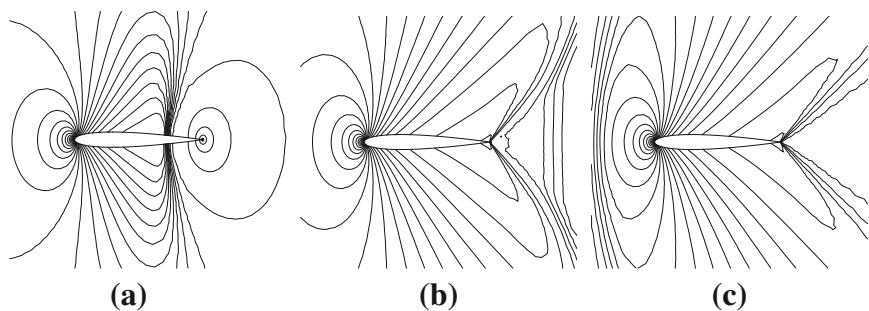
**FIGURE 7.10**

Inviscid subsonic flow past a NACA0012 aerofoil. Pressure contours: (a) Mach number = 0.25; (b) Mach number = 0.5.

such discontinuities or near discontinuities requires a very fine mesh. Here the use of “engineering judgement,” which is often used in solid mechanics by designing *a priori* mesh refining near singularities posed by corners in the boundary, etc., can no

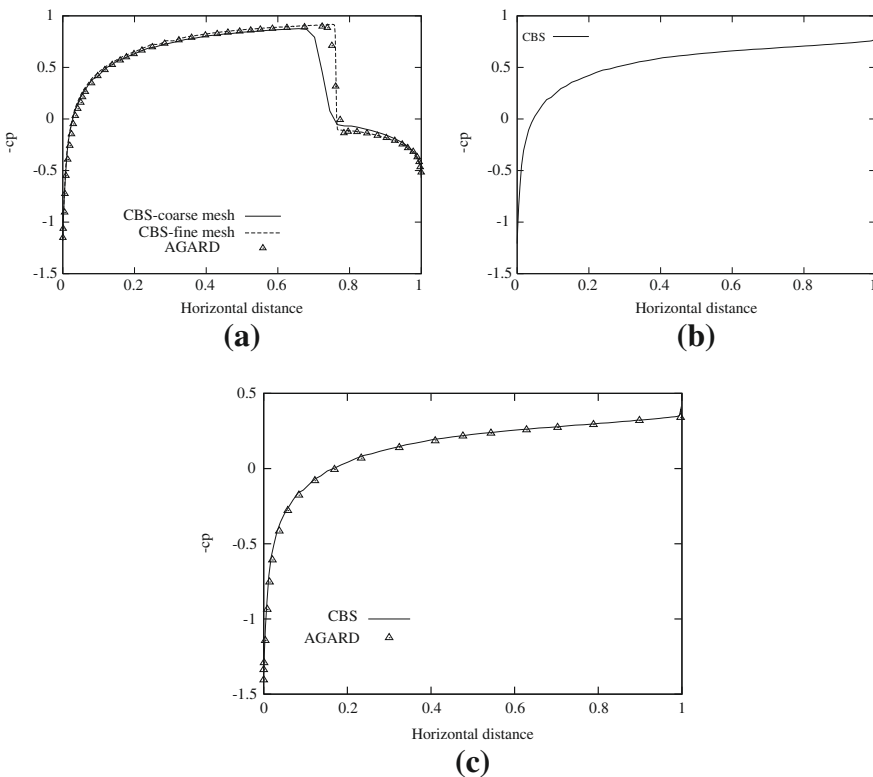
**FIGURE 7.11**

Inviscid subsonic flow past a NACA0012 aerofoil. Pressure coefficient distribution:
(a) Mach number = 0.25; (b) Mach number = 0.5.

**FIGURE 7.12**

Inviscid transonic and supersonic flow past a NACA0012 aerofoil. Pressure contours:
(a) Mach number = 0.85; (b) Mach number = 0.95; (c) Mach number = 1.2.

longer be used. In problems of compressible flow the position of shocks, where the refinement is most needed, is not known in advance. For this and other reasons, the use of adaptive mesh refinement based on error indicators is essential for obtaining good accuracy and “capturing” the location of shocks. It is therefore not surprising that the science of adaptive refinement has progressed rapidly in this area and indeed, as we shall see later, has been extended to deal with Navier-Stokes equations where a higher degree of refinement is also required in boundary layers. We have discussed the history of such adaptive development and procedures for its use in [Section 4.3](#), [Chapter 4](#).

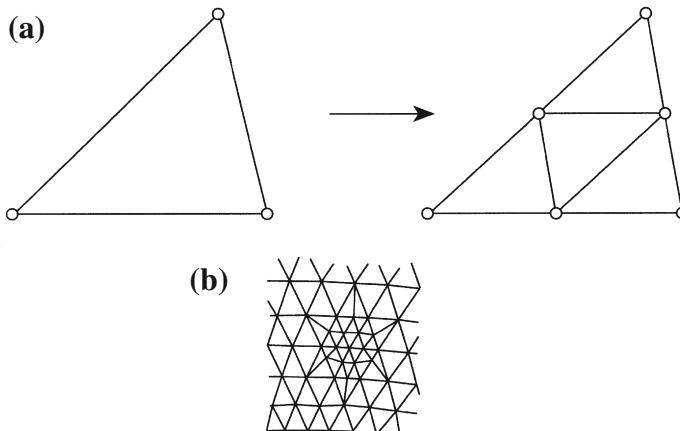
**FIGURE 7.13**

Inviscid transonic and supersonic flow past a NACA0012 aerofoil. Pressure coefficient distribution: (a) Mach number = 0.85; (b) Mach number = 0.95; (c) Mach number = 1.2.

7.8.2 The *h*-refinement process and mesh enrichment

Once an approximate solution has been achieved on a given mesh, the local errors can be evaluated and new element sizes (and elongation directions if used) can be determined for each element. For some purposes it is again convenient to transfer such values to the nodes so that they can be interpolated continuously. The procedure here is of course identical to that of smoothing the derivatives discussed in [Section 4.3, Chapter 4](#).

To achieve the desired accuracy various procedures can be used. The most obvious is the process of *mesh enrichment* in which the existing mesh is locally subdivided into smaller elements still retaining the “old” mesh in the configuration. [Figure 7.14a](#) shows how triangles can be readily subdivided in this way. With such enrichment an obvious connectivity difficulty appears. This concerns the manner in which the subdivided elements are connected to ones not so refined. A simple process is illustrated showing

**FIGURE 7.14**

Mesh enrichment. (a) Triangle subdivision. (b) Restoration of connectivity.

element halving in the manner of Fig. 7.14b. Here of course it is fairly obvious that this process, first described in Ref. [73], can only be applied in a gradual manner to achieve the predicted subdivisions. However, element elongation is not possible with such mesh enrichment.

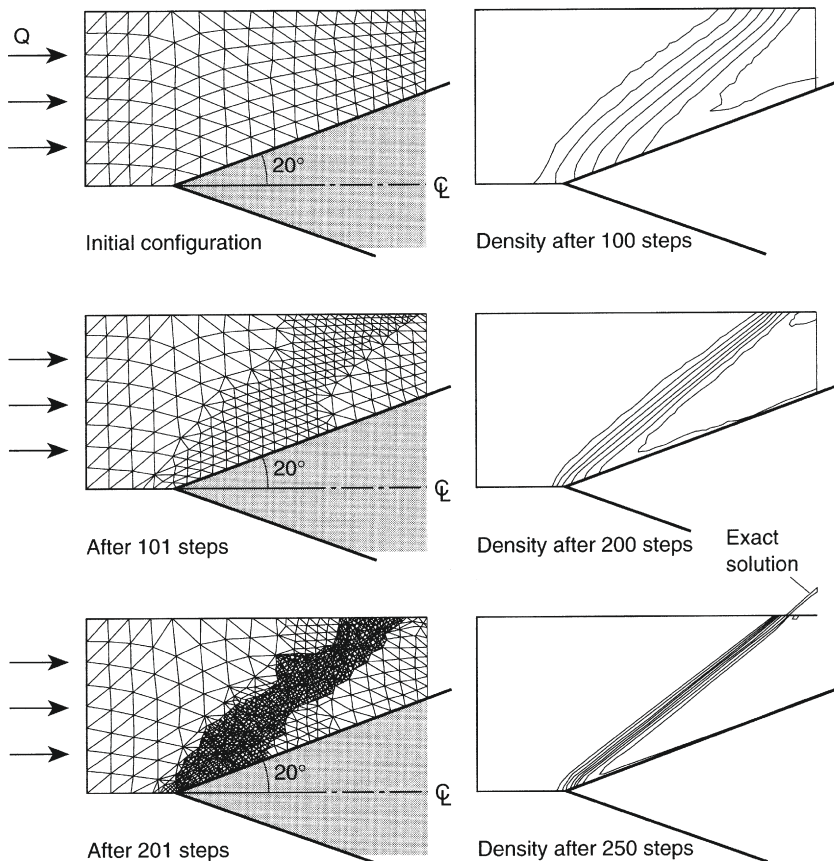
Despite such drawbacks the procedure is very effective in localizing (or capturing) shocks, as we illustrate in Fig. 7.15.

In Fig. 7.15, the theoretical solution is simply one of a line discontinuity shock in which a jump of all the components of Φ occurs. The original analysis carried out on a fairly uniform mesh shows a very considerable “blurring” of the shock. In Fig. 7.15 we also show the refinement being carried out at two stages and we see how the shock is progressively reduced in width.

In the above example, the mesh enrichment preserved the original, nearly equilateral, element form with no elongation possible.

Whenever a sharp discontinuity is present, local refinement will proceed indefinitely as curvatures increase without limit. Precisely the same difficulty indeed arises in mesh refinement near singularities for elliptic problems [74] if local refinement is the only guide. In such problems, however, the limits are generally set by the overall energy norm error consideration and the refinement ceases automatically. In the present case, the limit of refinement needs to be set and we generally achieve this limit by specifying the *smallest element size* in the mesh.

The h -refinement of the type proposed can of course be applied in a similar manner to quadrilaterals. Here clever use of data storage allows the necessary refinement to be achieved in a few steps by ensuring proper transitions [75].

**FIGURE 7.15**

Supersonic, Mach 3, flow past a wedge. Exact solution forms a stationary shock. Successive mesh enrichment and density contours.

7.8.3 *h*-refinement and remeshing in steady-state two-dimensional problems

Many difficulties mentioned above can be resolved by *automatic generation of meshes of a specified density*. Such automatic generation has been the subject of much research in many applications of finite element analysis. We have discussed this subject in [Section 4.3, Chapter 4](#). The closest achievement of a prescribed element size and directionality can be obtained for triangles and tetrahedra. Here the procedures developed by Peraire et al. [11, 14] are most direct and efficient, allowing element stretching in prescribed directions (though of course the amount of such stretching is sometimes restricted by practical considerations).

We refer the reader for details of such mesh generation to the original publications. In the examples that follow we shall exclusively use this type of mesh adaptivity.

Example 7.5. Inviscid flow with shock reflection from a solid wall

In Fig. 7.16 we show a simple example [11] of shock wave reflection from a solid wall. Here only a typical “cutout” is analyzed with appropriate inlet and outlet conditions imposed. The elongation of the mesh along the discontinuity is clearly shown. The solution was remeshed after the iterations nearly reached a steady state.

Example 7.6. Hypersonic inviscid flow past a blunt body

In Fig. 7.17 a somewhat more complex example of *hypersonic flow* around a blunt, two-dimensional obstacle is shown. Here it is of interest to note that:

1. A detached shock forms in front of the body.
2. A very coarse mesh suffices in front of such a shock where simple free stream flow continues and the mesh is made “finite” by a maximum element size prescription.
3. For the same minimum element size a reduction of degrees of freedom is achieved by refinement which shows much improved accuracy.

For such hypersonic problems, it is often claimed that special methodologies of solution need to be used. References [24, 76, 26] present quite sophisticated methods for dealing with such high-speed flows.

Example 7.7. Supersonic inviscid flow past a full circular cylinder

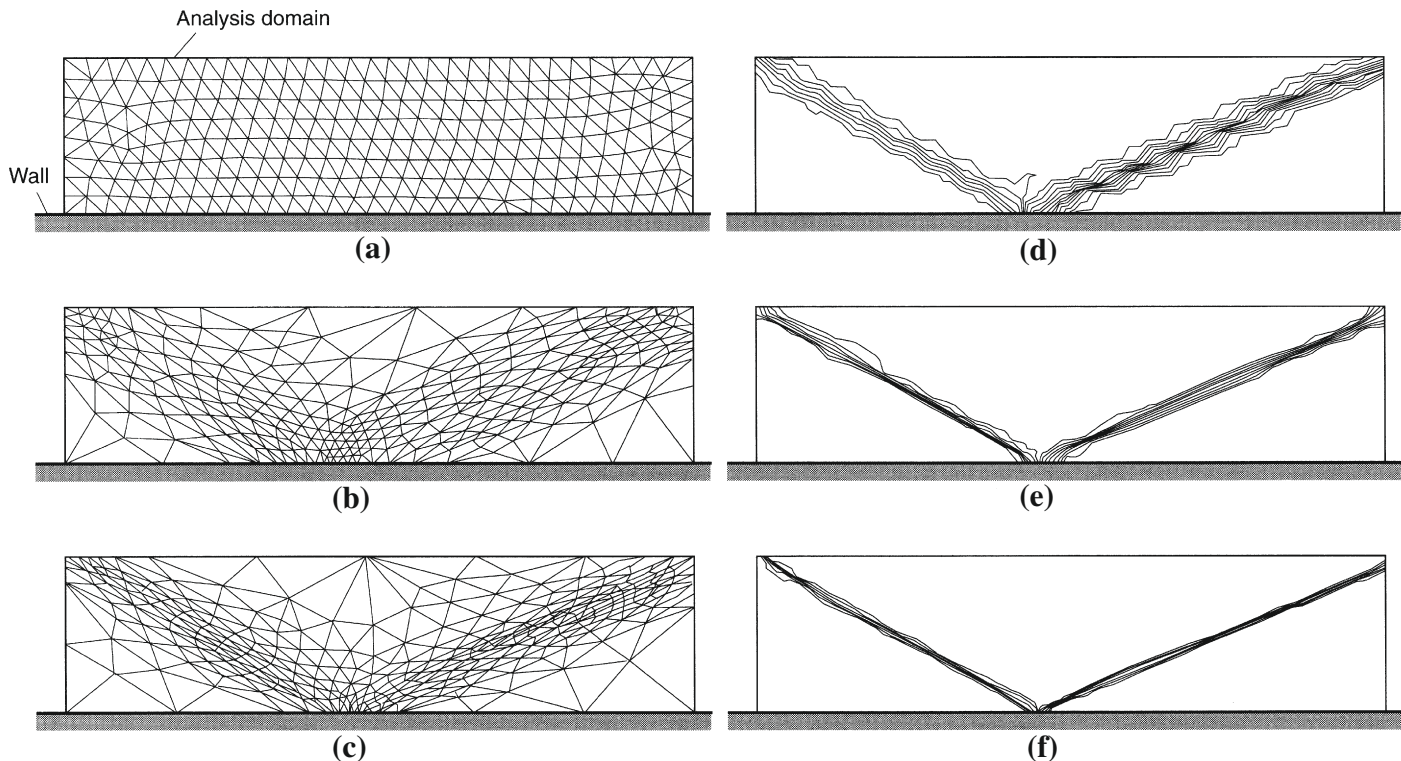
In Figs. 7.18 and 7.19, we show the results of supersonic Mach 3 flow past a full cylinder [61]. The mesh (Fig. 7.18b) is adapted along the shock front to get a good resolution of the shock. The mesh behind the cylinder is very fine to capture the complex motion. In Figs. 7.18c and d, the Mach contours are obtained using the CBS algorithm using the second derivative-based shock capture and residual-based shock capture respectively. In Fig. 7.19, the coefficient of pressure values and Mach number distribution along the mid-height through the surface of the cylinder are presented. Here the results generated by the MUSCL [24] scheme are also plotted for the sake of comparison.

Example 7.8. Inviscid shock interaction

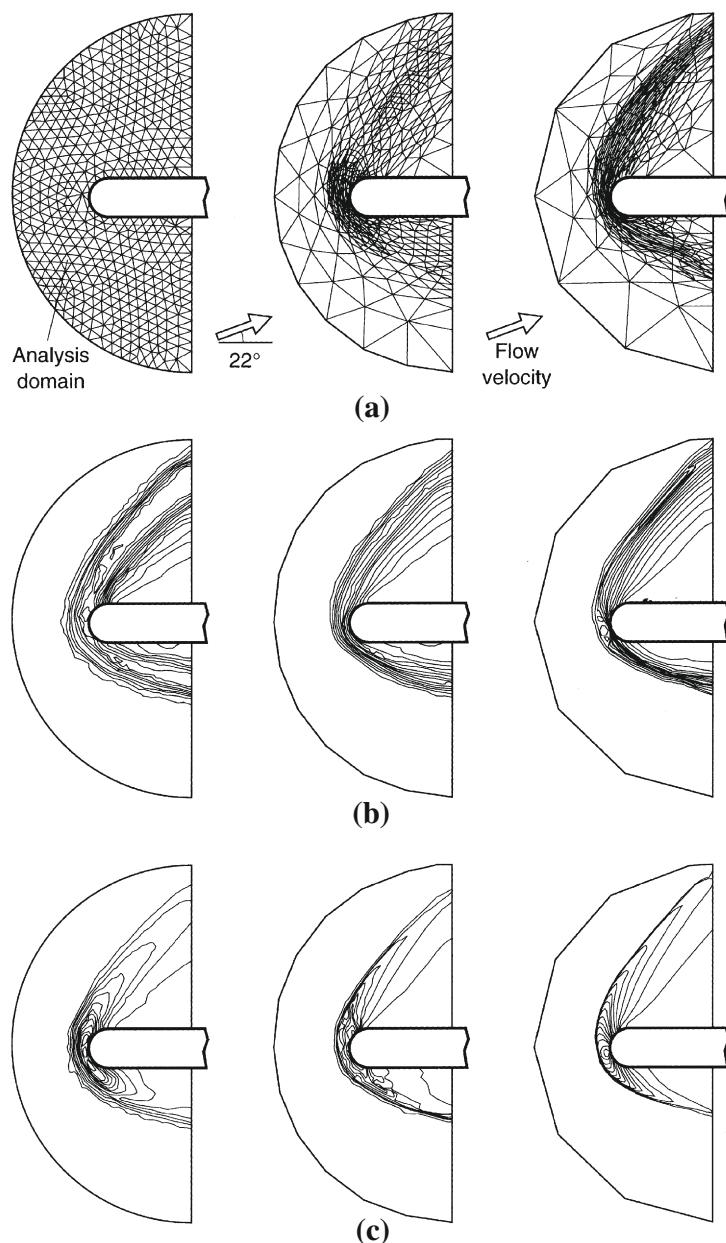
Figure 7.20 shows a yet more sophisticated example in which an impinging shock interacts with a bow shock [77].

7.9 Three-dimensional inviscid examples in steady state

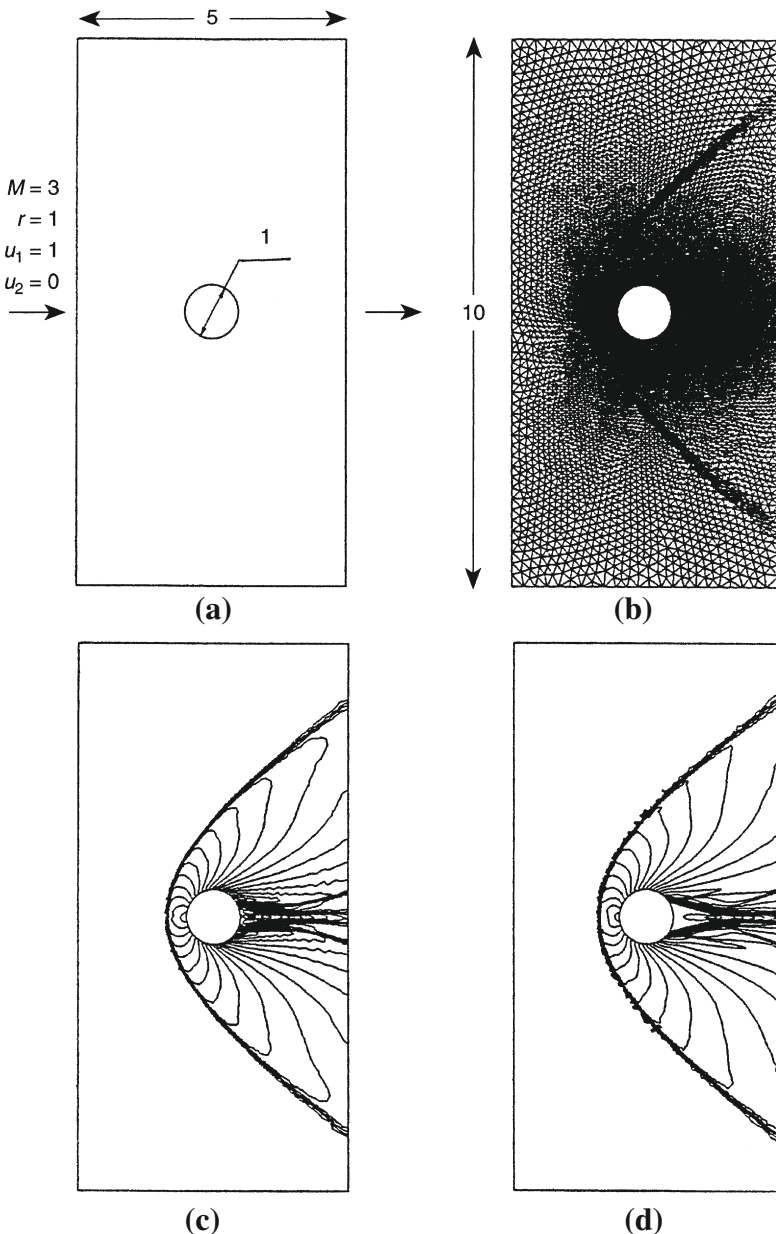
Two-dimensional problems in fluid mechanics are much rarer than two-dimensional problems in solid mechanics and invariably they represent a very crude approximation to reality. Even the problem of an aerofoil cross-section, which we have discussed previously, hardly exists as a two-dimensional problem as it applies only to infinitely long wings. For this reason attention has largely been focused, and much creative

**FIGURE 7.16**

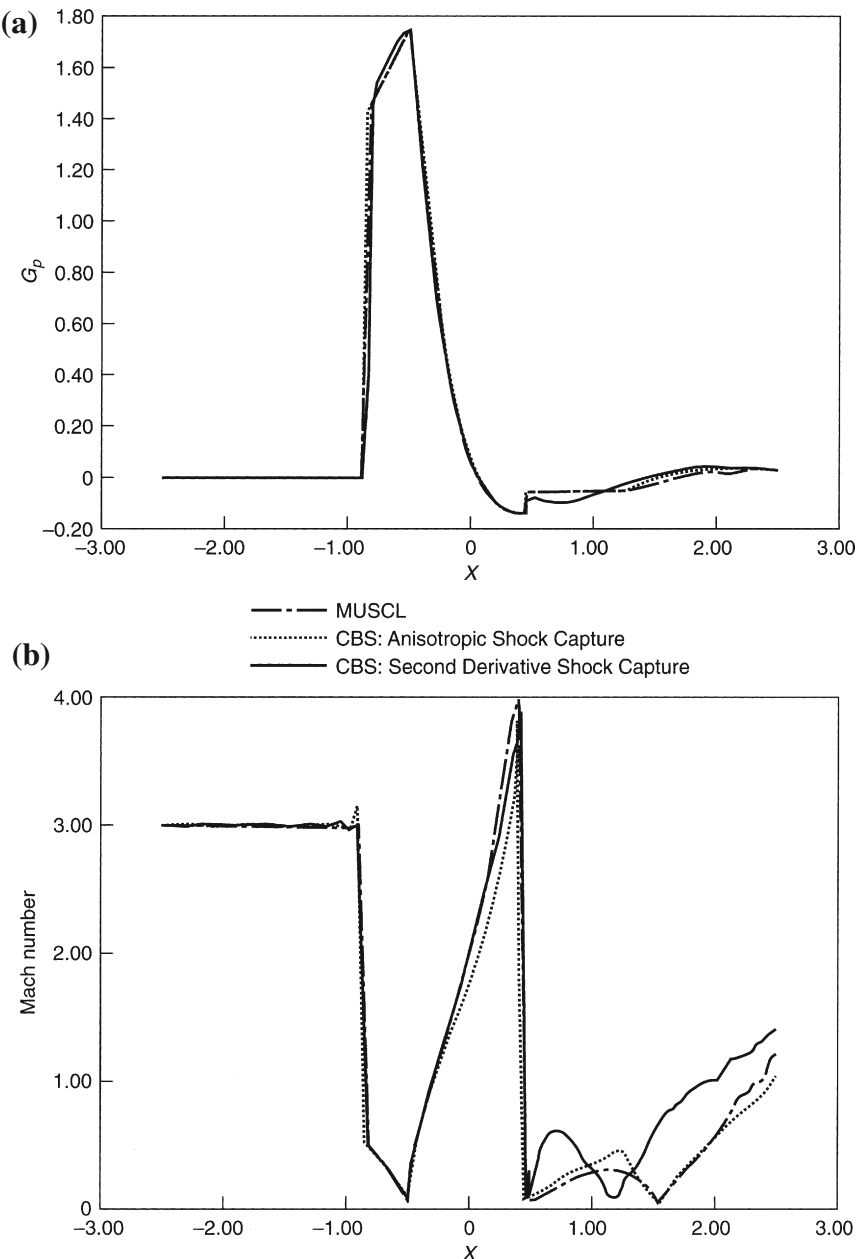
Reflection of a shock wave at a wall [11]: Euler equations. A sequence of meshes: (a) nodes: 279, elements: 478; (b) nodes: 265, elements: 479; (c) nodes: 285, elements: 528; and corresponding pressure contours, (d) to (f).

**FIGURE 7.17**

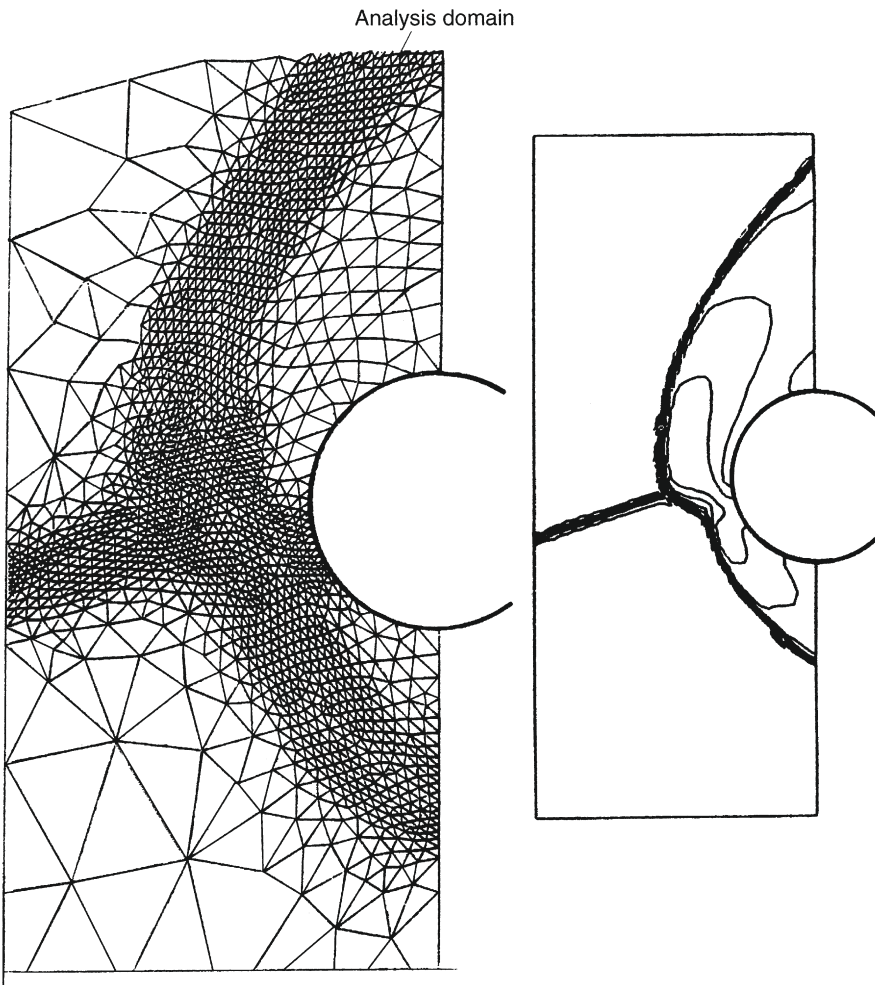
Hypersonic flow past a blunt body [11] at Mach 25, 22° angle of attack. (a) Sequence of meshes deployed; (b) the corresponding density; (c) the corresponding pressure contours. Initial mesh, nodes: 547, elements: 978; first mesh, nodes: 383, elements: 696; final mesh, nodes: 821, elements: 1574.

**FIGURE 7.18**

Supersonic flow past a full cylinder [61]. $M = 3$: (a) geometry and boundary conditions; (b) adapted mesh, nodes: 12651, elements: 24,979; (c) Mach contours using second derivative shock capture; (d) Mach contours using anisotropic shock capture.

**FIGURE 7.19**

Supersonic flow past a full cylinder [61]. $M = 3$: comparison of (a) coefficient of pressure, (b) Mach number distribution along the mid-height and cylinder surface.

**FIGURE 7.20**

Interaction of an impinging and bow shock wave [77]. Adapted mesh and pressure contours.

research done, in developing three-dimensional codes for solving realistic problems. In this section we shall consider some examples derived by the use of such three-dimensional codes and in all these the basic element used will be the tetrahedron, which now replaces the triangle of two dimensions. Although the solution procedure and indeed the whole formulation in three dimensions is almost identical to that described for two dimensions, it is clear that the number of unknowns will increase very rapidly when realistic problems are dealt with. It is common when using linear

elements to encounter several million variables as unknowns and for this reason here, more than anywhere else, iterative processes are necessary.

Indeed much effort has gone into the development of special procedures of solution which will accelerate the iterative convergence and which will reduce the total computational time. In this context we should mention three approaches which are of help.

The recasting of element formulation in an edge form

Here a considerable reduction of storage can be achieved by this procedure and some economies in computational time achieved. We have not discussed this matter in detail but refer the reader to Ref. [30] where the method is fully described and for completeness we summarize the essential features of edge formulation in [Appendix F](#).

Multigrid approaches

In the standard iteration we proceed in a time frame by calculating point by point the changes in various quantities and we do this on the finest mesh. As we have seen this may become very fine if adaptivity is used locally. In the multigrid solution, as initially introduced into the finite element field, the solution starts on a coarse mesh, the results of which are used subsequently for generating the first approximation to the fine mesh. Several iterative steps are then carried out on the fine mesh. In general a return to the coarse mesh is then made to calculate the changes of residuals there and the process is repeated on several meshes done subsequently. This procedure can be used on several meshes and the iterative process is much accelerated. We discuss this process in [Appendix H](#) in a little more detail. However, we quote here several references [78–83] in which such multigrid procedures have been used and these are of considerable value.

Multigrid methods are obviously designed for meshes which are “nested,” i.e., in which coarser and finer mesh nodes coincide. This need not be the case generally. In many applications completely different meshes of varying density are used at various stages.

Parallel computation

The third procedure for reducing the solution time is to use parallelization. We do not discuss it here in detail as the matter is potentially coupled with the computational aspects of the problem. Here the reader should consult the current literature on the subject [31,37].

In what follows we shall illustrate three-dimensional applications on a few inviscid examples as this section deals with Euler problems. However in [Section 7.12](#) we shall return to a formulation using viscous Navier-Stokes equations.

7.9.1 Solution of the flow pattern around a complete aircraft

In the early days of numerical analysis applied to computational fluid dynamics which used finite differences, no complete aircraft was analyzed as in general only structured meshes were admissible. The analysis thus had to be carried out on isolated components of the aircraft as shown in [Figure 7.21](#). Later construction of distorted and partly structured meshes increased the possibility of analysis. Nevertheless the first complete aircraft analyses were done only in the mid-1980s. In all of these, finite elements using unstructured meshes were used (though we include here the finite volume formulation which was almost identical to finite elements and was used by Jameson et al. [85]). The very first aircraft was the one dealt with using potential theory in the Dassault establishment. The results were published later by Periaux and coworkers [86]. Very shortly after that a complete supersonic aircraft was analyzed by Peraire et al. [84] in Swansea in 1987.

Example 7.9. Inviscid flow past full aircraft

[Figure 7.22](#) shows the aircraft analyzed in Swansea [84], which is a supersonic fighter of generic type at Mach 2. The analysis was made slightly adaptive though adaptivity was not carried very far (due to cost). Nevertheless the refinement localized the shocks which formed.

In the analysis some 125,000 elements were used with approximately 70,000 nodes and therefore some 350,000 variables. This of course is not a precise analysis and many more variables would be used currently to get a more accurate representation of flow and pressure variables.

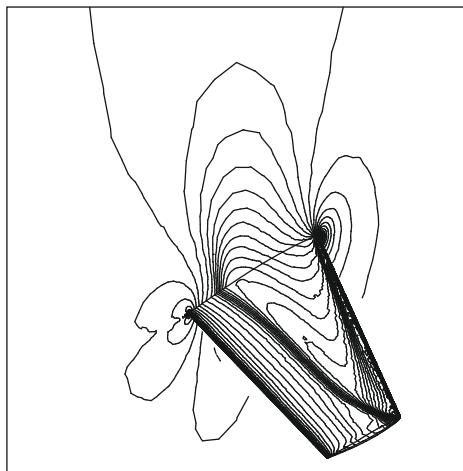
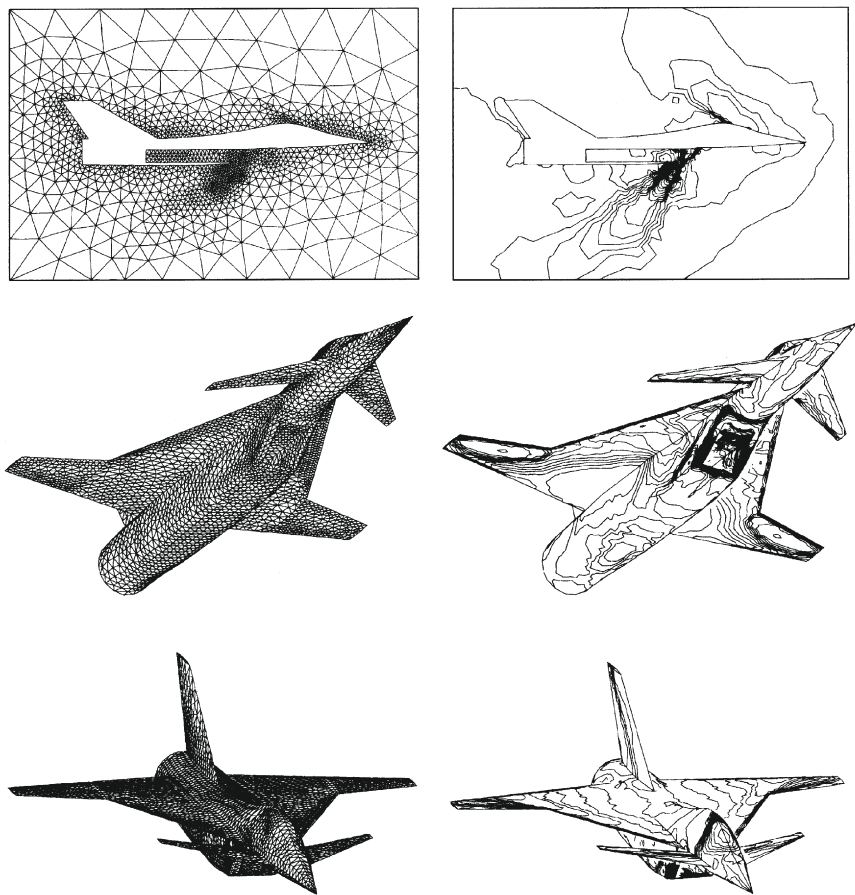


FIGURE 7.21

Inviscid flow past an ONERA M6 wing. Density contours. Mach number = 0.78, angle of attack to horizontal = 2.8° .

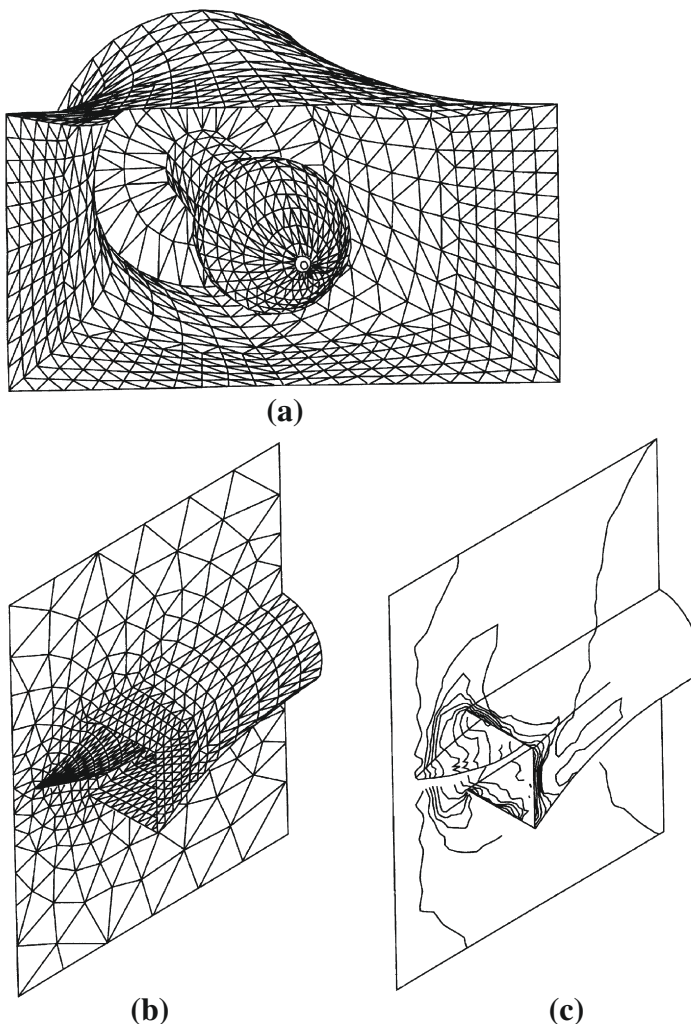
**FIGURE 7.22**

Adaptive three-dimensional solution of compressible inviscid flow around a high-speed (Mach 2) aircraft [84]. Nodes: 70,000, elements: 125,000.

A more sophisticated analysis is given in Ref. [26]. Here a civil aircraft in subsonic flow is modeled and this illustrates the use of multigrid methods. In this particular multigrid applications three meshes of different refinement were used and the iteration is fully described in Ref. [26]. In this example the total number of unknown quantities was 1,616,000 in the finest mesh.

Example 7.10. Inviscid engine intake

There are many other three-dimensional examples which could at this stage be quoted but we only show here a three-dimensional analysis of an engine intake [84] at Mach 2. This is given in Fig. 7.23.

**FIGURE 7.23**

Three-dimensional analysis of an engine intake [84] at Mach 2 (14,000 elements): (a) mesh on analysis surface; (b) mesh on analysis surface; (c) pressure contours.

7.9.2 THRUST: The supersonic car

A very similar problem to that posed by the analysis of the whole aircraft was given by the team led by Professor Morgan. This was the analysis of a car which was attempting to create the world speed record by establishing this in the supersonic range [35,36,87]. This attempt was indeed successfully made on October 15, 1997.

Unlike in the problem of the aircraft, the alternative of wind tunnel tests was not available. While in aircraft design, wind tunnels which are supersonic and subsonic

are well used in practice (though at a cost which is considerably more than that of a numerical analysis) the possibility of doing such a test on a motor car was virtually nonexistent. The reason for this is the fact that the speed of the air flow past the body of the car and the speed of the ground relative to the car are identical. Any test would therefore require the bed of the wind tunnel to move at a speed in excess of 750+ miles an hour. For this reason calculations were therefore preferable.

The moving ground will of course create a very important boundary layer such as that which we will discuss in later sections. However the simple omission of viscosity permitted the inviscid solution by a standard Euler-type program to be used. It is well known that the Euler solution is perfectly capable of simulating all shocks very adequately and indeed results in very well-defined pressure distributions over the bodies whether it is over an aircraft or a car. The object of the analysis was indeed that of determining such pressure distributions and the lift caused by these pressures. It was essential that the car should remain on the ground, indeed this is one of the conditions of the ground speed record and any design which would result in substantial lift overcoming the gravity on the car would be disastrous for obvious reasons.

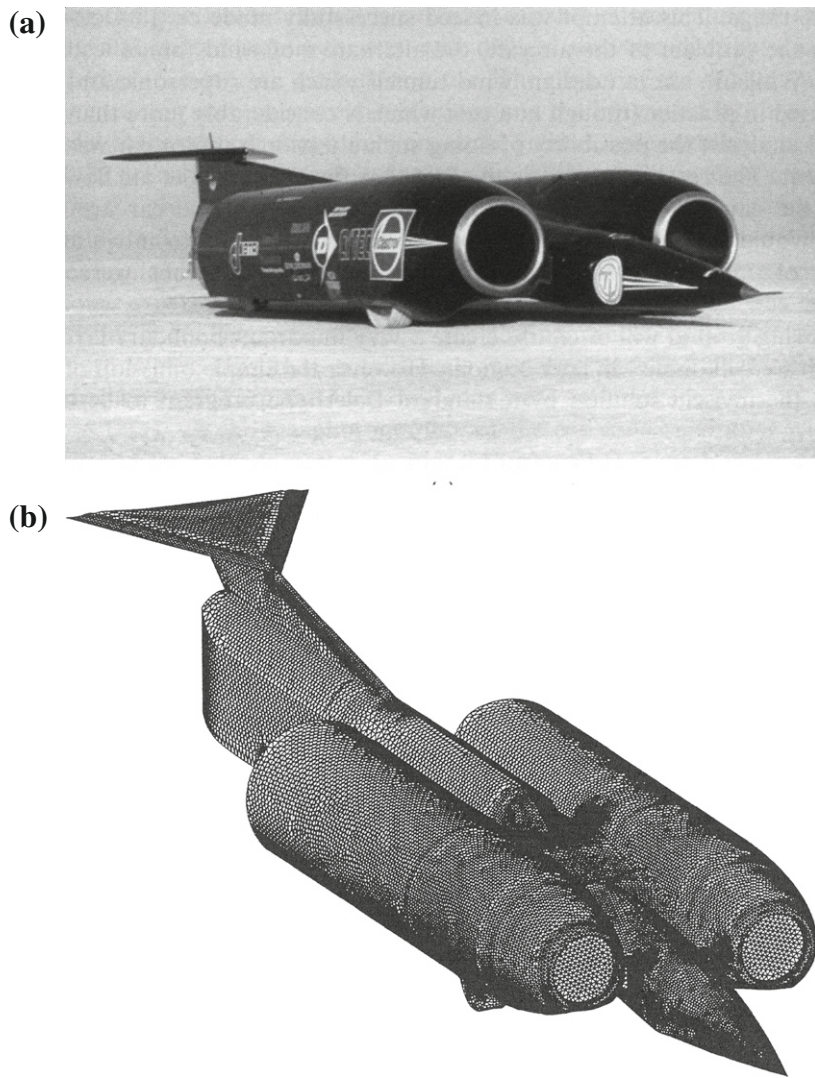
The complete design of the supersonic car was thus made with several alternative geometries until the computer results were satisfactory. Here it is interesting however to have some experimental data and the preliminary configuration was tested by a rocket driven sled. This was available for testing rocket projectiles at Pendine Sands, South Wales, UK. Here a 1:25 scale model of the car was attached to such a rocket and 13 supersonic and transonic runs were undertaken.

In Fig. 7.24a, we show a photograph [35] of the car concerned after winning the speed record in the Nevada desert. In Fig. 7.24b a surface mesh is presented from which the full three-dimensional mesh at the surrounding atmosphere was generated (surface mesh, nodes: 39,528, elements: 79,060; volume mesh, nodes: 134,272, elements: 887,634).

In Fig. 7.25, pressure contours [35] on the surface of the car body are given. In Fig. 7.26, a detailed comparison of CFD results [35] with experiments is shown. The results of this analysis show a remarkable correlation with experiments. The data points which do not appear close to the straight line are the result of the sampling point being close to, but the wrong side of, a shock wave. If conventional correlation techniques for inviscid flow (viscous correction) are applied, these data points also lie on the straight line. In total, nine pressure points were used situated on the upper and lower surfaces of the car. The plot shows the comparison of pressures at specific positions on the car for Mach numbers of 0.71, 0.96, 1.05, and 1.08.

7.10 Transient two- and three-dimensional problems

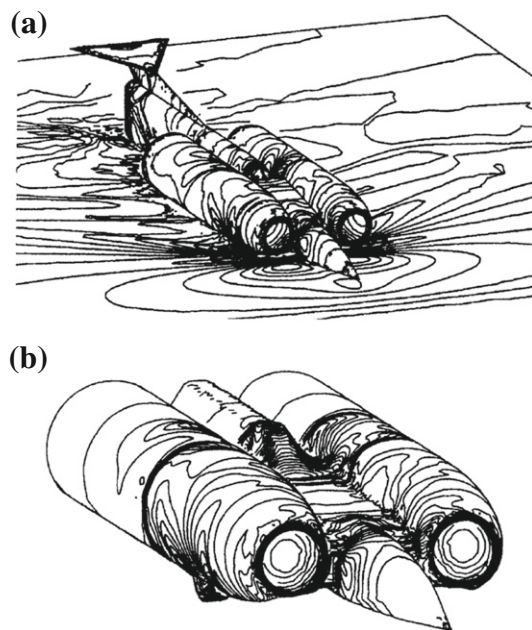
In all of the previous problems the time stepping was used simply as an iterative device for reaching the steady-state solutions. However this can be used in real time and the transient situation can be studied effectively. Many such transient problems have been dealt with from time to time and here we illustrate the process on three examples.

**FIGURE 7.24**

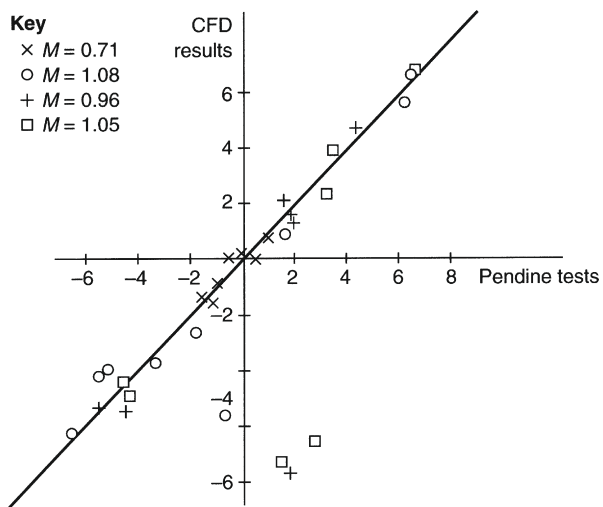
Supersonic car, THRUST SSC [35]. (a) Car and (b) finite element surface mesh. (*Image used in (a) courtesy of SSC Programme Ltd. Photographer Jeremy C.R. Davey.*)

Example 7.11. Exploding pressure vessel

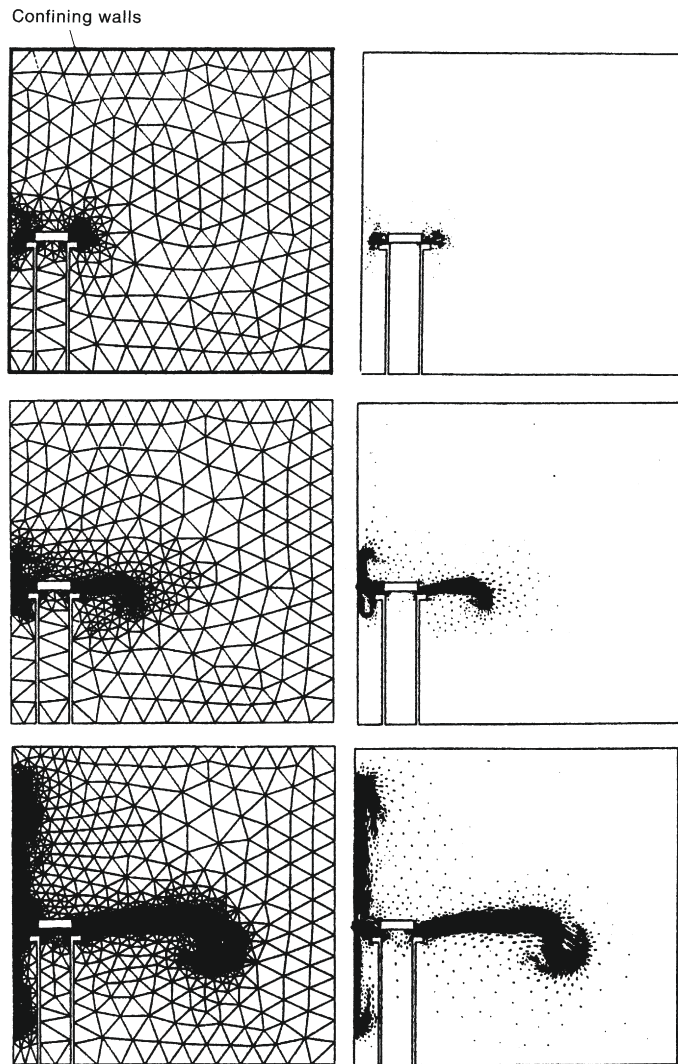
The first one concerns an exploding pressure vessel [71] as a two-dimensional model as shown in Fig. 7.27. Here of course adaptivity had to be used and the mesh is regenerated every few steps to reproduce the transient motion of the shock front.

**FIGURE 7.25**

Supersonic car, THRUST SSC [35] pressure contours: (a) full configuration; (b) front portion.

**FIGURE 7.26**

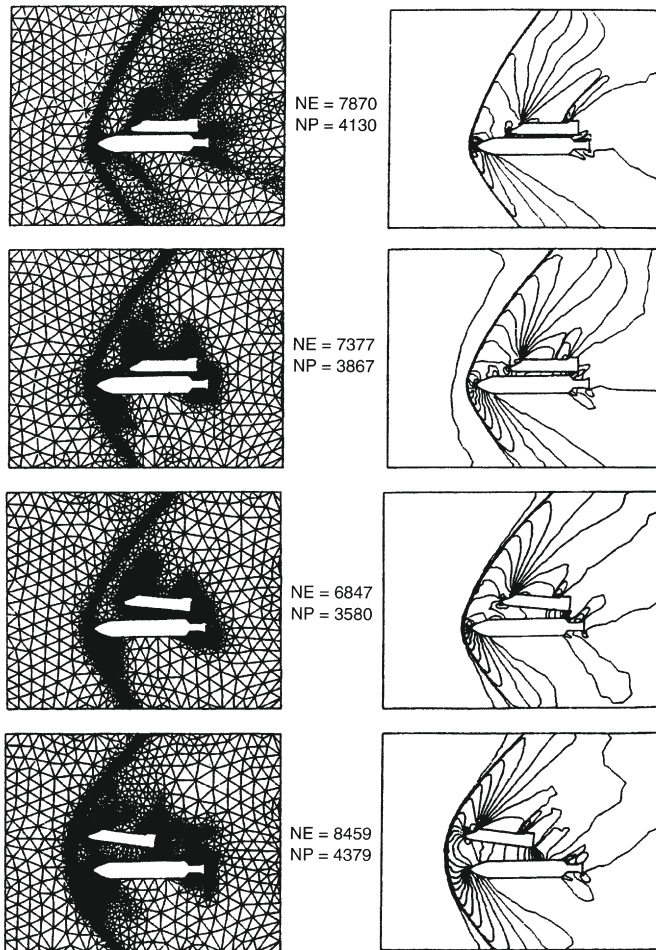
Supersonic car, THRUST SSC [35] comparison of finite element and experimental results.

**FIGURE 7.27**

A transient problem with adaptive remeshing [88]. Simulation of a sudden failure of a pressure vessel. Progression of refinement and velocity patterns shown. Initial mesh 518 nodes.

Example 7.12. Shuttle launch

A similar computation is shown in Fig. 7.28 where a diagrammatic form of a shuttle launch is modeled again as a two-dimensional problem [88]. Of course this two-dimensional model is purely imaginary but it is useful for showing the general configuration. In Fig. 7.29 however, we show a three-dimensional shuttle

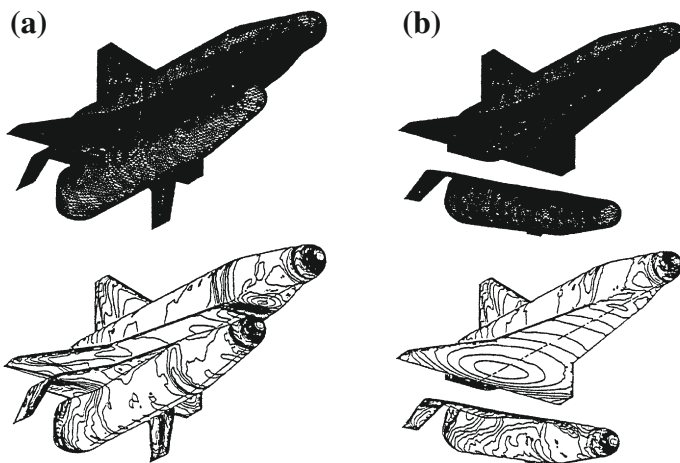
**FIGURE 7.28**

A transient problem with adaptive remeshing [88]. Model of the separation of shuttle and rocket. Mach 2, angle of attack -4° , initial mesh 4130 nodes.

approximating closely to reality [32]. The picture shows the initial configuration and the separation from the rocket.

7.11 Viscous problems in two dimensions

Clearly the same procedures which we have discussed previously could be used for the full Navier-Stokes equations by the introduction of viscous and other heat diffusion

**FIGURE 7.29**

Separation of a generic shuttle vehicle and rocket booster [32]. (a) Initial surface mesh and surface pressure; (b) final surface mesh and surface pressure.

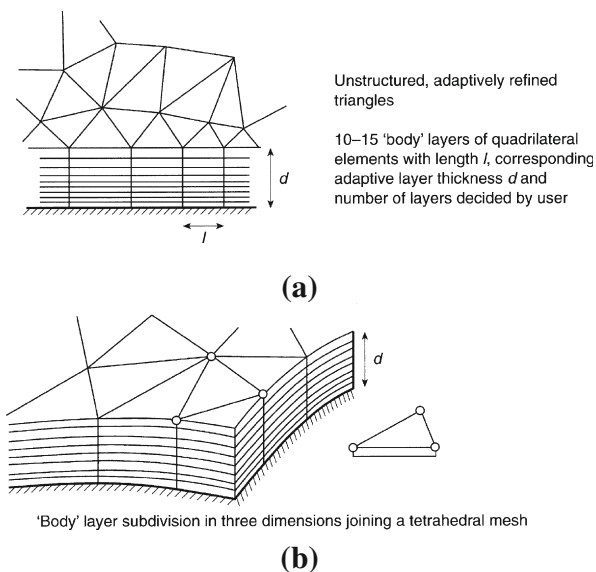
terms. Although this is possible we will note immediately that very rapid gradients of velocity will develop in the boundary layers (we have remarked on this already in Chapter 4) and thus special refinement will be needed there. In the first example we illustrate a viscous solution by using meshes designed *a priori* with fine subdivision near the boundary. However, in general the refinement must be done adaptively and here various methodologies of doing so exist. The simplest of course is the direct use of mesh refinement with elongated elements which we have also discussed in Chapter 4. This will be dealt with by a few examples in Section 7.11.1. However in Section 7.11.2 we shall address the question of much finer refinement with very elongated elements in the boundary layer. Generally we shall do such a refinement with a structured grid near the solid surfaces merging into the general unstructured meshing outside. In that section we shall introduce methods which can automatically separate structured and unstructured regions both in the boundary layer and in the shock regions.

The methodology is of course particularly important in problems of three dimensions.

The special refinement which we mentioned above is well illustrated in Fig. 7.30. In this we show the possibility of using a structured mesh with quadrilaterals in the boundary layer domain (for two-dimensional problems) and a three-dimensional equivalent of such a structured mesh using prismatic elements. Indeed such elements have been used as a general tool by some investigators [89–91].

Example 7.13. Viscous flow past a plate

The example given here is that in which both shock and boundary layer development occur simultaneously in high-speed flow over a flat plate [92]. This problem

**FIGURE 7.30**

Refinement in the boundary layer: (a) a two-dimensional sublayer of structured quadrilaterals; (b) a three-dimensional sublayer of prismatic elements.

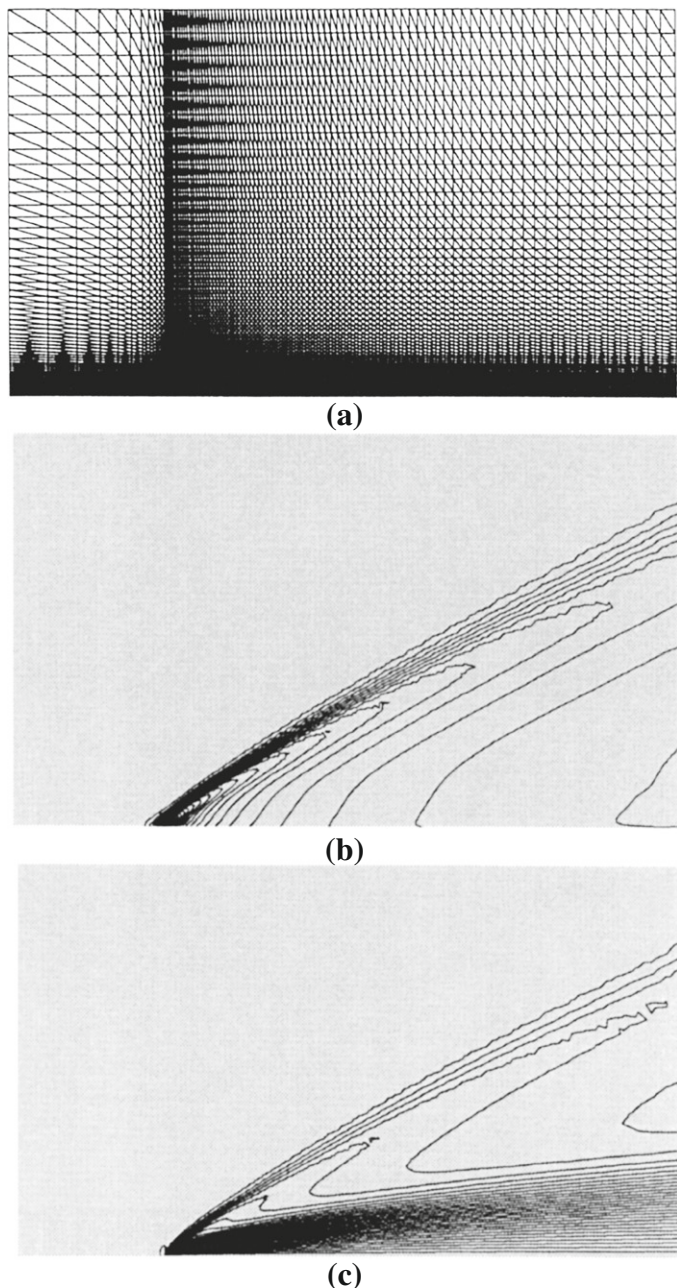
was studied extensively by Carter [93]. His finite difference solution is often used for comparison purposes although some oscillations can be seen.

A fixed mesh which is graded from a rather fine subdivision near the boundary to a coarser one elsewhere is shown in Fig. 7.31. We obtained the solution using the CBS algorithm. In Fig. 7.32, comparisons with Carter's [93] solution are presented and it will be noted that the CBS solution appears to be more consistent, avoiding oscillations near the leading edge.

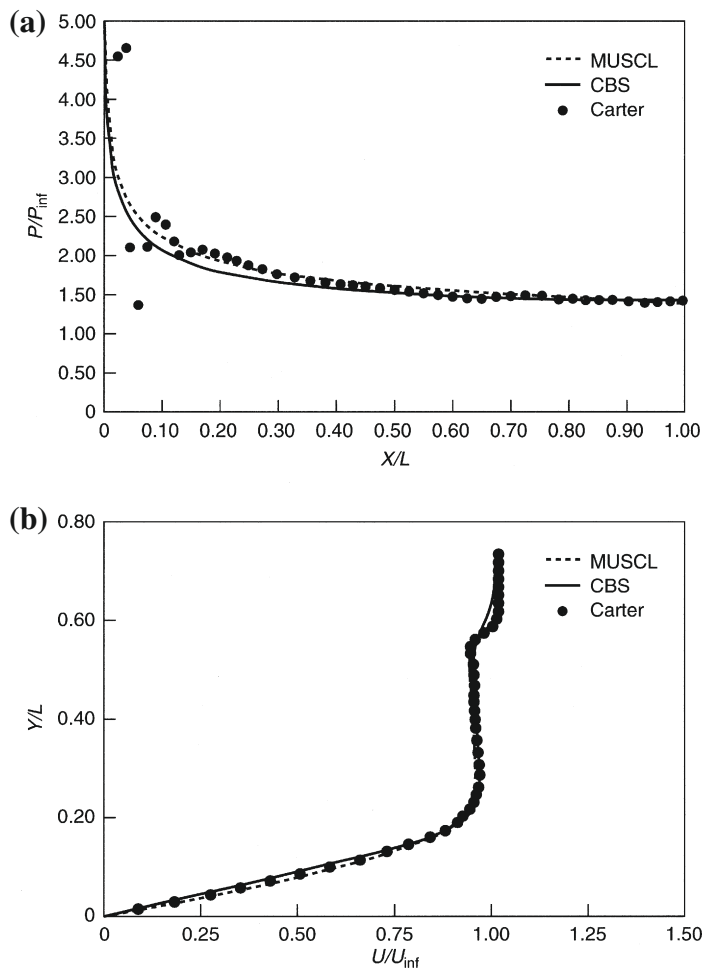
7.11.1 Adaptive refinement in both shock and boundary layer

In this section we shall pursue mesh generation and adaptivity in precisely the same manner as we have done in Chapter 4 and previously in this chapter, i.e., using elongated finite elements in the zones where rapid variation of curvature occurs. An example of this application is given in Fig. 7.33. Here now a problem of the interaction of a boundary layer generated by a flat plate and externally impinging shock is presented [94]. In this problem, some structured layers are used near the wall in addition to the direct approach of Chapter 4. The reader will note the progressive refinement in the critical area.

In such a problem it would be simpler to refine near the boundary or indeed at the shock using structured meshes and the idea of introducing such refinement is explored in the next section.

**FIGURE 7.31**

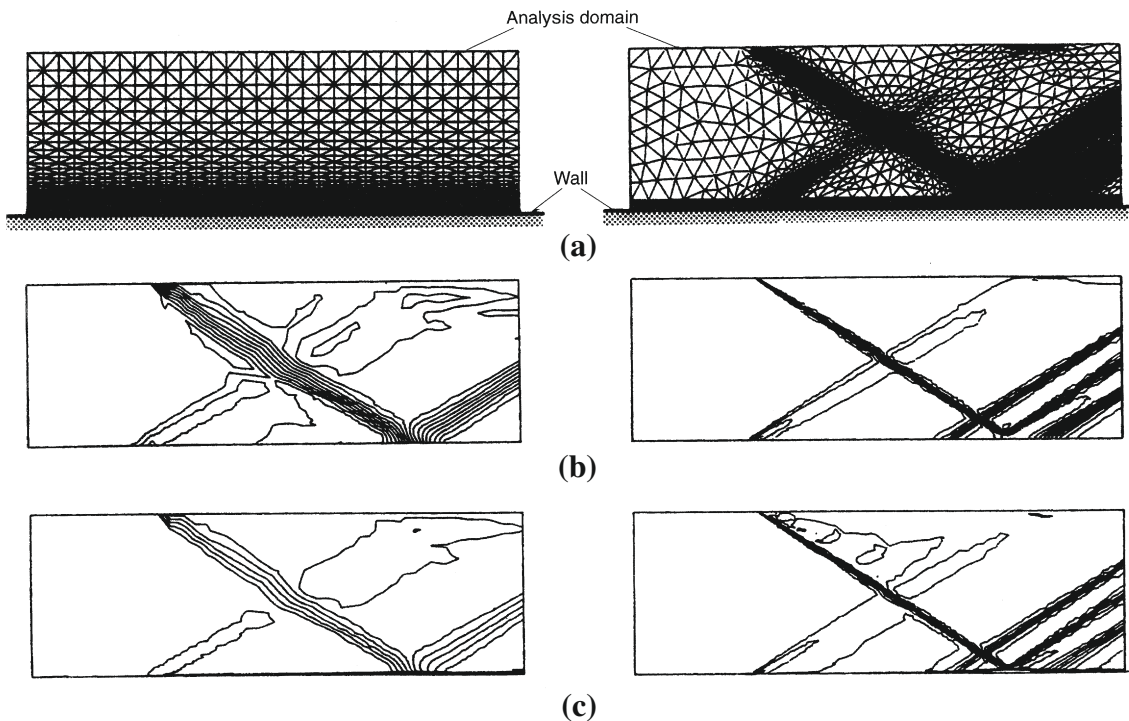
Viscous flow past a flat plate (Carter problem) [92]. Mach 3, $Re = 1000$. (a) Mesh, nodes: 6750, elements: 13,172. Contours of (b) pressure and (c) Mach number.

**FIGURE 7.32**

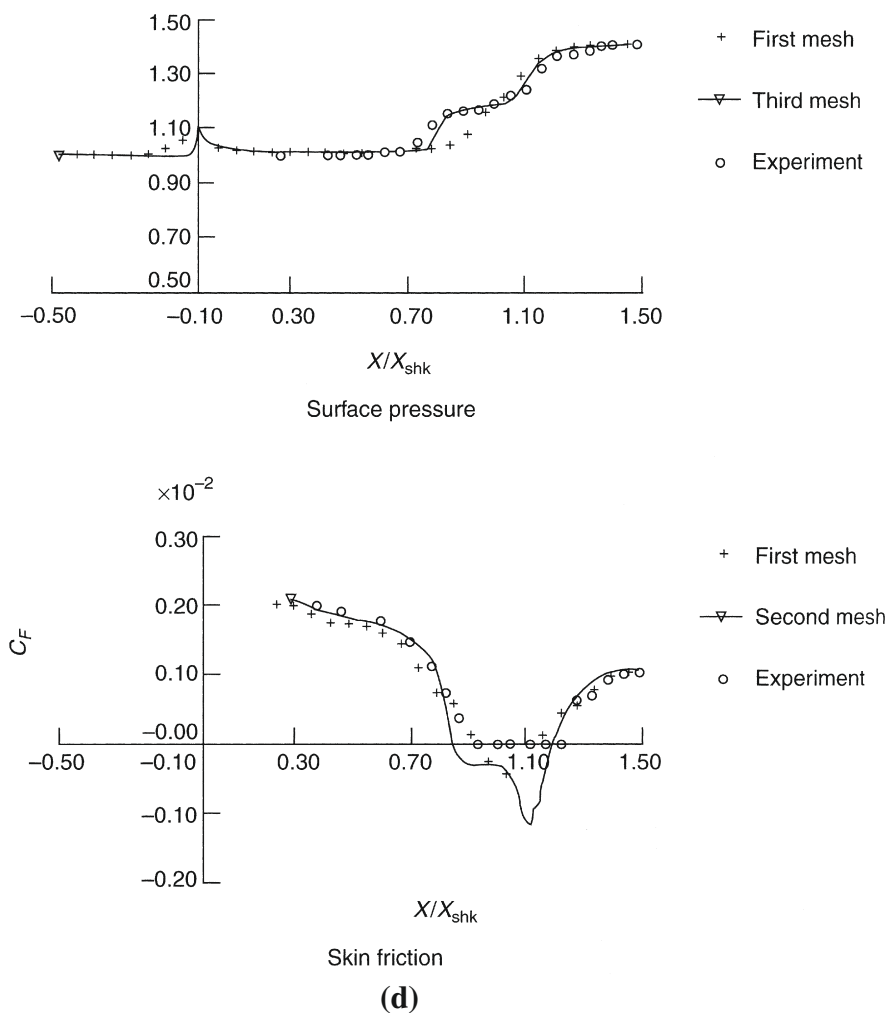
Viscous flow past a flat plate (Carter problem) [92]. Mach 3, $Re = 1000$. (a) Pressure distribution along the plate surface, (b) exit velocity profile.

7.11.2 Special adaptive refinement for boundary layers and shocks

As with the direct iterative approach, it is difficult to arrive at large elongations during mesh generation, and the procedures just described tend to be inaccurate. For this reason it is useful to introduce a structured layer within the vicinity of solid boundaries to model the boundary layers and indeed it is possible to do the same in the shocks

**FIGURE 7.33**

Shock and boundary layer interaction [94]. Final mesh, nodes: 4198. (a) Initial and final (second) adapted mesh; (b) initial and final (second) pressure contours; (c) initial and final (second) Mach number contours; (d) surface pressure and skin tension.

**FIGURE 7.33**

(Continued).

once these are defined. Within the boundary layer this can be done readily as shown in Fig. 7.30 using a layer of structured triangles or indeed quadrilaterals. On many occasions triangles have been used here to avoid the use of two kinds of elements in the same code. However if possible it is better to use directly quadrilaterals. The same problem can of course be done three dimensionally and we shall in Section 7.12 discuss application of such layers. Again in the structured layer we can use either prismatic

elements or simply tetrahedra though if the latter are used many more elements are necessary for the same accuracy. It is clear that unless the structured meshes near the boundary are specified *a priori*, an adaptive procedure will be somewhat complicated and on several occasions fixed boundary meshes have been used. However alternatives exist and here two possibilities should be mentioned. The first possibility, and that which has not yet been fully exploited, is that of refinement in which structured meshes are used in both shocks and boundary layers and the width of the domains is determined after some iterations. The procedure is somewhat involved and has been used with success in many trial problems as shown by Zienkiewicz and Wu [95]. We shall not describe the method in detail here but essentially structured meshes again composed of triangles or at least quadrilaterals divided into two triangles were used near the boundary and in the shock regions. In the second method we could imagine that normals are created on the boundaries, and a boundary layer thickness is predicted using some form of boundary layer analytical computation [25, 33, 96]. Within this layer structured meshes are adopted using a geometrical progression of thickness. The structured boundary layer meshing can of course be terminated where its need is less apparent and unstructured meshes continued outside.

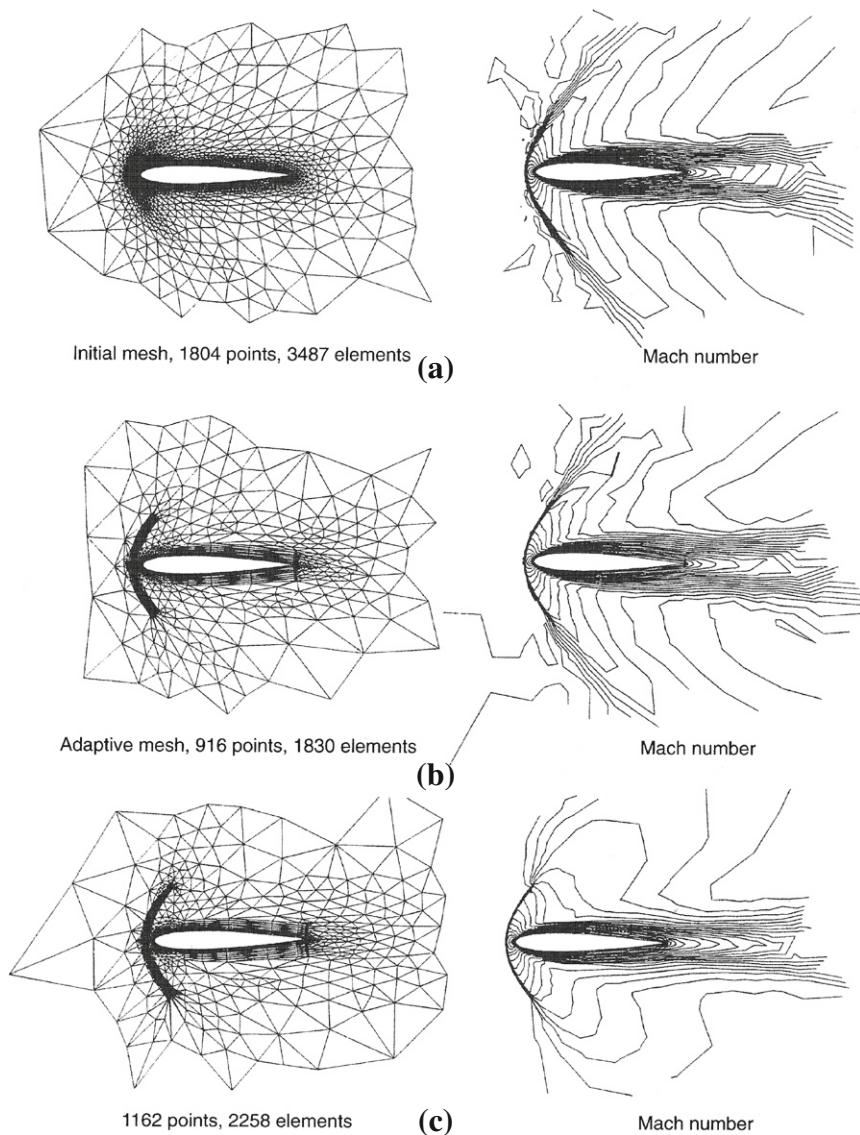
Figure 7.34 illustrates supersonic flow around an NACA0012 aerofoil using the automatic generation of structured and unstructured domains taken from Ref. [95]. The second method, in which normals are grown from the solid surface to create a structured layer, is illustrated in Fig. 7.35 on a two-component aerofoil.

Example 7.14. Transonic viscous flow past a NACA0012 aerofoil

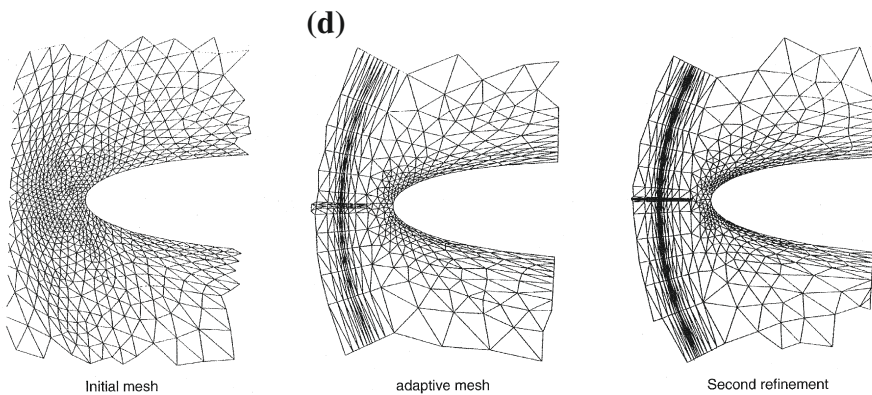
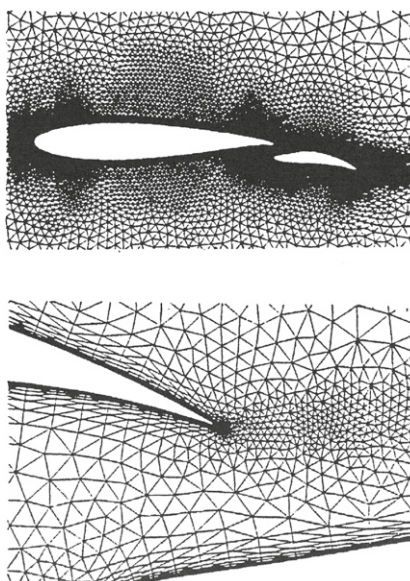
The external flow past a NACA0012 aerofoil is one of the popular benchmark problems of compressible fluid dynamics [97–99]. The transonic viscous flow is especially difficult to handle with many numerical schemes. The explicit schemes are generally difficult to use without additional acceleration procedures such as multigrid methods. Here, however we provide a solution using the explicit scheme without any additional acceleration technique. The problem consists of a NACA0012 aerofoil placed at the center of a circular domain of diameter 20 times the chord length. The inlet Mach number was assumed to be 0.85 and the Reynolds number was 2000. On the solid wall the no-slip conditions were assumed. The angle of attack in this problem was assumed to be zero. All the inlet conditions were assumed to be known.

In Figure 7.36 we show the mesh used for the calculations. As shown the mesh close to the solid wall is generated by constructing structured layers. Away from the wall the mesh is purely unstructured. This way we will be able to capture the strong boundary layer effects close to the walls. A total of 16,496 elements and 8425 nodes were employed in the calculation.

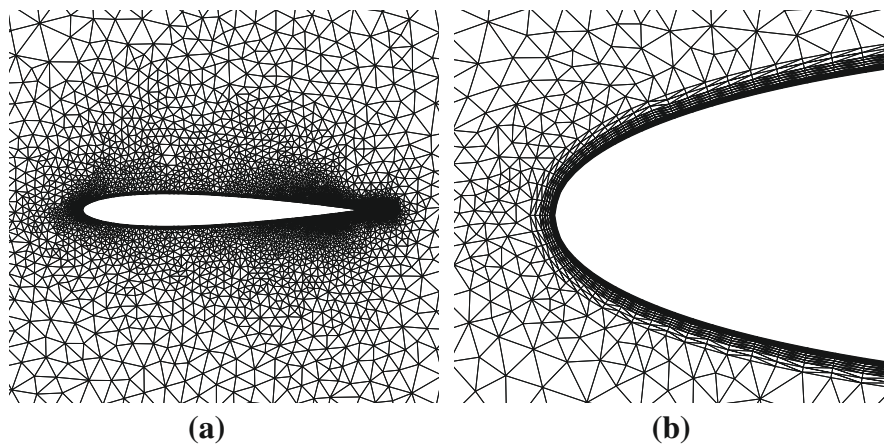
Figure 7.37 shows the Mach contours. In Figure 7.38 we show the surface quantity distribution. The quantity distribution in general is in excellent agreement with the fully structured mesh solutions [97–99].

**FIGURE 7.34**

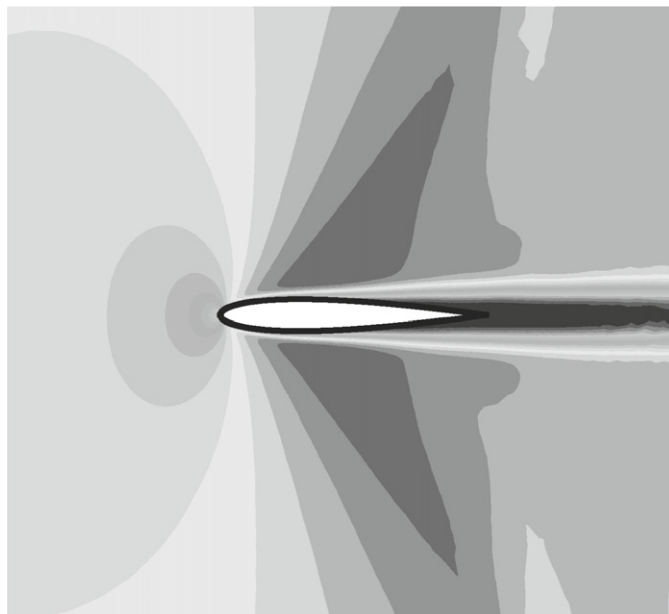
Hybrid mesh for supersonic viscous flow past a NACA0012 aerofoil [95], Mach 2, and contours of Mach number: (a) initial mesh; (b) first adapted mesh; (c) final mesh; (d) mesh near stagnation point (shown opposite).

**FIGURE 7.34***(Continued).***FIGURE 7.35**

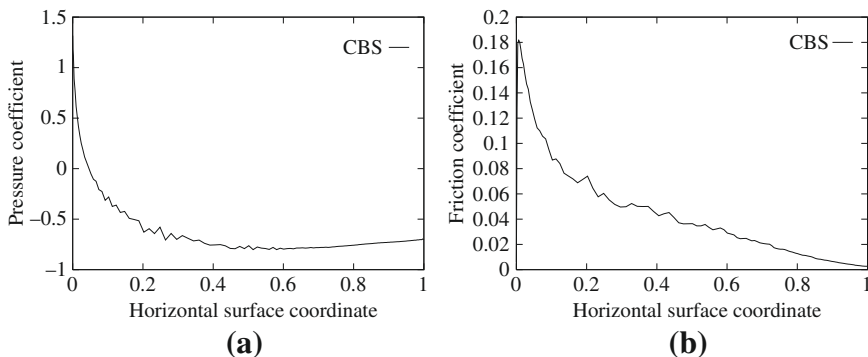
Structured grid in boundary layer for a two-component aerofoil [25]. Advancing boundary normals.

**FIGURE 7.36**

Transonic viscous flow past a NACA0012 aerofoil. Mach number 0.85, Reynolds number = 2000. (a) Finite element mesh; (b) structured layers close to the wall.

**FIGURE 7.37**

Transonic viscous flow past a NACA0012 aerofoil. Mach number 0.85, Reynolds number = 2000. Mach contours.

**FIGURE 7.38**

Transonic viscous flow past a NACA0012 aerofoil. Mach number 0.85, Reynolds number = 2000. (a) Surface pressure and (b) friction coefficients distribution.

7.12 Three-dimensional viscous problems

The same procedures which we have described in the previous section can of course be used in three dimensions. Quite realistic high Reynolds number boundary layers were so modeled. Figure 7.39 shows the mesh employed to solve viscous flow at a very high Reynolds number around a fore body of a double ellipsoid [25]. In this example a structured boundary layer is assumed *a priori*. The density contours are shown in Fig. 7.40.

7.13 Boundary layer: Inviscid Euler solution coupling

It is well known that high-speed flows which exist without substantial flow separation develop a fairly thin boundary layer to which all the viscous effects are confined. The flow outside this boundary layer is purely inviscid. Such problems have for some years been solved approximately by using pure Euler solutions from which the pressure distribution is obtained. Coupling these solutions with a boundary layer approximation written for a very small thickness near the solid body provides the complete solution. The theory by which the separation between inviscid and viscous domains is predicted is that based on the work of Prandtl and for which much development has taken place since his original work. Clearly various methods of solving boundary layer problems can be used and many different techniques of inviscid solution can be implemented.

In the boundary layer full Navier-Stokes equations are used and generally these equations are specialized by introducing the assumptions of a boundary layer in which no pressure variation across the thickness occurs.

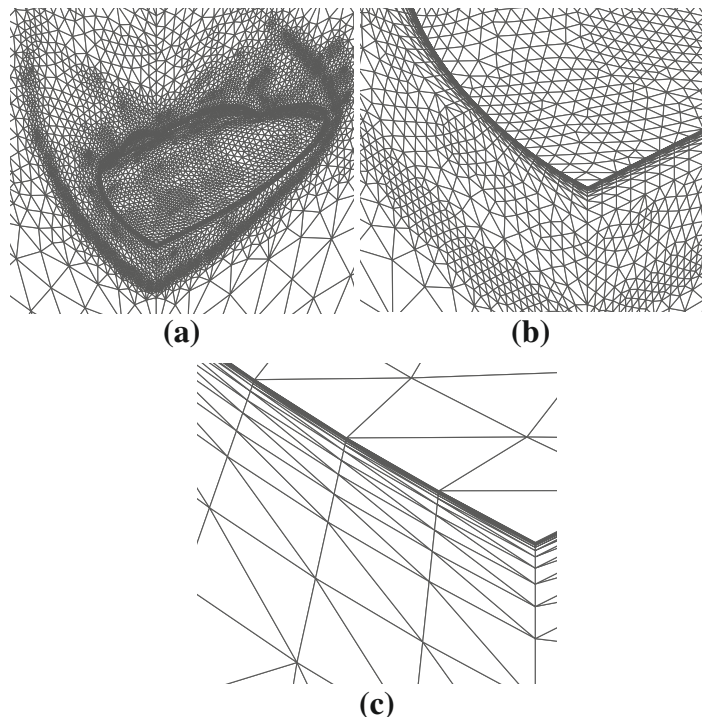


FIGURE 7.39

Hypersonic viscous flow past a double ellipsoid. Unstructured mesh with structured mesh layers close to the walls: (a) adapted mesh; (b) structured layers close to the wall; (c) close-up of structured layers.

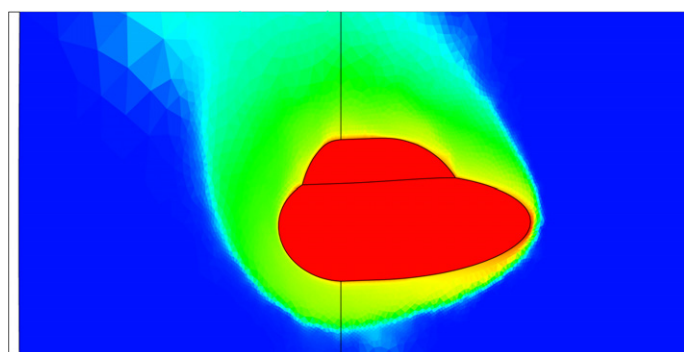


FIGURE 7.40

Hypersonic viscous flow past a double ellipsoid. Density contours.

An alternative to solving the equations in the whole boundary layer is the integral approach in which the boundary layer equations need to be solved only close to the solid surface. Here the “transpiration velocity model” for laminar flows [100] and the “lag-entrainment” method [101] for turbulent flows are notable approaches. Further extensions of these procedures can be found in many available research articles [102–106].

Many studies illustrate further developments and implementation procedures of viscous-inviscid coupling [107–109]. Although the use of such viscous-inviscid coupling is not directly applicable in problems where boundary layer separation occurs, many studies are available to deal with separated flows [110–112].

7.14 Concluding remarks

This chapter describes the most important and far-reaching possibilities of finite element application in the design of aircraft and other high-speed vehicles. The solution techniques described and examples presented illustrate that the possibility of realistic results exists. However, we do admit that there are still many unsolved problems. Most of these refer to either the techniques used for solving the equations or to modeling satisfactorily viscous and turbulence effects. The paths taken for simplifying and more efficient calculations have been outlined previously and we have mentioned possibilities such as multigrid methods, edge formulation, etc., designed to achieve faster convergence of numerical solutions. However full modeling of boundary layer effects is much more difficult, especially for high-speed flows. Use of boundary layer theory and turbulence models is of course only an approximation and here it must be stated that much “engineering art” has been used to achieve acceptable results. This inside knowledge is acquired from the use of data available from experiments and becomes necessary whether the turbulence models of any type are used or whether boundary layer theories are applied directly. In either case the freedom of choice is given to the user who will decide which model is satisfactory and which is not. For this reason the subject departs from being a precise mathematical science. The only possibility for such a science exists in direct turbulence modeling. Here of course only the Navier-Stokes equations which we have previously described are solved in a transient state when steady-state solutions do not exist. Doing this may involve billions of elements and at the moment is out of reach. We anticipate however that within the near future both computers and the methods of solution will be developed to such an extent that such direct approaches will become a standard procedure. At that time this chapter will serve purely as an introduction to the essential formulation possibilities. One aspect which can be visualized is that realistic three-dimensional turbulent computations will only be used in regions where these effects are important, leaving the rest to simpler Eulerian flow modeling. However the computational procedure which we are all striving for must be automatic and the formulation must be such that all choices made in the computation are predictable rather than imposed.

References

- [1] R. Löhner, K. Morgan, O.C. Zienkiewicz, The solution of non-linear hyperbolic equation systems by the finite element method, *Int. J. Numer. Methods Fluids* 4 (1984) 1043–1063.
- [2] R. Löhner, K. Morgan, O.C. Zienkiewicz, The use of domain splitting with an explicit hyperbolic solver, *Comput. Methods Appl. Mech. Eng.* 45 (1984) 313–329.
- [3] O.C. Zienkiewicz, K. Morgan, J. Peraire, M. Vahdati, R. Löhner, Finite elements for compressible gas flow and similar systems, in: *Seventh International Conference in Computational Methods in Applied Sciences and Engineering*, Versailles, December, 1985.
- [4] O.C. Zienkiewicz, R. Löhner, K. Morgan, J. Peraire, High speed compressible flow and other advection dominated problems of fluid mechanics, in: R.H. Gallagher, G.F. Carey, J.T. Oden, O.C. Zienkiewicz (Eds.), *Finite Elements in Fluids*, vol. 6, John Wiley, Chichester, 1985, pp. 41–88.
- [5] R. Löhner, K. Morgan, O.C. Zienkiewicz, An adaptive finite element procedure for compressible high speed flows, *Comput. Methods Appl. Mech. Eng.* 51 (1985) 441–465.
- [6] R. Löhner, K. Morgan, J. Peraire, O.C. Zienkiewicz, Finite element methods for high speed flows, AIAA paper 85–1531-CP, 1985.
- [7] J. Peraire, A finite method for convection dominated flows, Ph.D. Thesis, University of Wales, Swansea, Swansea, 1986.
- [8] R. Löhner, K. Morgan, J. Peraire, O.C. Zienkiewicz, L. Kong, Finite element methods for compressible flow, in: K.W. Morton, M.J. Baines (Eds.), *Numerical Methods in Fluid Dynamics*, vol. II, Clarendon Press, Oxford, 1986, pp. 27–52.
- [9] R. Löhner, K. Morgan, O.C. Zienkiewicz, Adaptive grid refinement for the Euler and compressible Navier-Stokes equations, in: I. Babuška, O.C. Zienkiewicz, J. Gago, E.R. de A. Oliveira (Eds.), *Accuracy Estimates and Adaptive Refinement in Finite Element Computations*, John Wiley & Sons, New York, 1986, pp. 281–298, (Chapter 15).
- [10] R. Löhner, K. Morgan, J. Peraire, M. Vahdati, Finite element, flux corrected transport (FEM–FCT) for the Euler and Navier–Stokes equations, *Int. J. Numer. Methods Fluids* 7 (1987) 1093–1109.
- [11] J. Peraire, M. Vahdati, K. Morgan, O.C. Zienkiewicz, Adaptive remeshing for compressible flow computations, *J. Comput. Phys.* 72 (1987) 449–466.
- [12] J. Peraire, K. Morgan, O.C. Zienkiewicz, Convection dominated problems, *Numerical Methods for Compressible Flows – Finite Difference, Element and Volume Techniques*, vol. AMD 78, ASME, New York, 1987, pp. 129–147.
- [13] R. Löhner, The efficient simulation of strongly unsteady flows by the finite element method, in: *25th Aerospace Science Meeting*, Reno, Nevada, 1987, AIAA Paper 87–0555.

- [14] J. Peraire, K. Morgan, J. Peiro, O.C. Zienkiewicz, An adaptive finite element method for high speed flows, in: AIAA 26th Aerospace Sciences Meeting, Reno, NV, 1987, Paper AIAA-87-0558.
- [15] O.C. Zienkiewicz, J.Z. Zhu, Y.C. Liu, K. Morgan, J. Peraire, Error estimates and adaptivity. From elasticity to high speed compressible flow, in: J. Whiteman (Ed.), *The Mathematics of Finite Elements and Applications*, vol. VII, Academic Press, London, 1988, pp. 483–512.
- [16] L. Formaggia, J. Peraire, K. Morgan, Simulation of state separation using the finite element method, *Appl. Math. Modelling* 12 (1988) 175–181.
- [17] O.C. Zienkiewicz, K. Morgan, J. Peraire, J. Peiro, L. Formaggia, Finite elements in fluid mechanics: compressible flow, shallow water equations and transport, ASME Conference on Recent Developments in Fluid Dynamics, vol. AMD 95, ASME, New York, December 1988.
- [18] J. Peraire, J. Peiro, L. Formaggio, K. Morgan, O.C. Zienkiewicz, Finite element Euler computations in three dimensions, *Int. J. Numer. Methods Eng.* 26 (1988) 2135–2159.
- [19] R.R. Thareja, J.R. Stewart, O. Hassan, K. Morgan, J. Peraire, A point implicit unstructured grid solver for the Euler and Navier–Stokes equation, *Int. J. Num. Meth. Fluids* 9 (1989) 405–425.
- [20] R. Löhner, Adaptive remeshing for transient problems, *Comput. Methods Appl. Mech. Eng.* 75 (1989) 195–214.
- [21] O. Hassan, K. Morgan, J. Peraire, An implicit–explicit scheme for compressible viscous high speed flows, *Comp. Meth. Appl. Mech. Eng.* 76 (1989) 245–258.
- [22] E.J. Probert, O. Hassan, K. Morgan, J. Peraire, An adaptive finite element method for transient compressible flows with moving boundaries, *Int. J. Numer. Methods Eng.* 32 (1991) 751–765.
- [23] E.J. Probert, O. Hassan, K. Morgan, J. Peraire, Adaptive explicit and implicit finite element methods for transient thermal analysis, *Int. J. Numer. Methods Eng.* 35 (1992) 655–670.
- [24] M.T. Manzari, P.R.M. Lyra, K. Morgan, J. Peraire, An unstructured grid FEM/MUSCL algorithm for the compressible Euler equations, in: Proceedings of the Eighth International Conference on Finite Elements in Fluids. New Trends and Applications, Pineridge Press, Swansea, 1993, pp. 379–388.
- [25] O. Hassan, E.J. Probert, K. Morgan, J. Peraire, Mesh generation and adaptivity for the solution of compressible viscous high speed flows, *Int. J. Numer. Methods Eng.* 38 (1995) 1123–1148.
- [26] P.R.M. Lyra, M.T. Manzari, K. Morgan, O. Hassan, J. Peraire, Upwind side based unstructured grid algorithms for compressible viscous flow computations, *Int. J. Eng. Anal. Des.* 2 (1995) 197–211.
- [27] O. Hassan, K. Morgan, E.J. Probert, J. Peraire, Unstructured tetrahedral mesh generation for three dimensional viscous flows, *Int. J. Numer. Methods Eng.* 39 (1996) 549–567.

- [28] M.T. Manzari, O. Hassan, K. Morgan, N.P. Weatherill, Turbulent flow computations on 3D unstructured grids, *Finite Elements Anal. Des.* 30 (1998) 353–363.
- [29] J.R. Stewart, T.J.R. Hughes, A tutorial in elementary finite element error analysis: A systematic presentation of a *priori* and a *posteriori* error estimates, *Comput. Methods Appl. Mech. Eng.* 158 (1–2) (1998) 1–22.
- [30] K. Morgan, J. Peraire, Unstructured grid finite element methods for fluid mechanics, *Rep. Prog. Phys.* 61 (1998) 569–638.
- [31] K. Morgan, P.J. Brookes, O. Hassan, N.P. Weatherill, Parallel processing for the simulation of problems involving scattering of electromagnetic waves, *Comput. Methods Appl. Mech. Eng.* 152 (1998) 157–174.
- [32] O. Hassan, L.B. Bayne, K. Morgan, N.P. Weatherill, An adaptive unstructured mesh method for transient flows involving moving boundaries, *ECCOMAS '98*, Wiley, New York, 1998.
- [33] O. Hassan, E.J. Probert, K. Morgan, Unstructured mesh procedures for the simulation of three dimensional transient compressible inviscid flows with moving boundary components, *Int. J. Num. Meth. Fluids* 27 (1998) 41–55.
- [34] N.P. Weatherill, E.A. Turner-Smith, J. Jones, K. Morgan, O. Hassan, An integrated software environment for multi-disciplinary computational engineering, *Eng. Comput.* 16 (1999) 913–933.
- [35] R. Ayers, O. Hassan, K. Morgan, N.P. Weatherill, The role of computational fluid dynamics in the design of the thrust supersonic car, *Design Optim. Int. J. Prod. & Proc. Improvement* 1 (1999) 79–99.
- [36] K. Morgan, O. Hassan, N.P. Weatherill, Why didn't the supersonic car fly? *Mathematics Today. Bull. Inst. Math. Appl.* 35 (Aug 1999) 110–114.
- [37] K. Morgan, N.P. Weatherill, O. Hassan, P.J. Brookes, R. Said, J. Jones, A parallel framework for multidisciplinary aerospace engineering simulations using unstructured meshes, *Int. J. Num. Meth. Fluids* 31 (1999) 159–173.
- [38] R. Said, N.P. Weatherill, K. Morgan, N.A. Verhoeven, Distributed parallel Delaunay mesh generation, *Comp. Meth. Appl. Mech. Eng.* 177 (1999) 109–125.
- [39] P.M.R. Lyra, K. Morgan, A review and comparative study of upwind biased schemes for compressible flow computation. Part I: 1-D first-order schemes, *Arch. Comp. Meth. Eng.* 7 (2000) 19–55.
- [40] K.A. Sorensen, O. Hassan, K. Morgan, N.P. Weatherill, Agglomerated multigrid on hybrid unstructured meshes for compressible flow, *Int. J. Numer. Methods Fluids* 40 (2002) 593–603.
- [41] K.A. Sorensen, O. Hassan, K. Morgan, N.P. Weatherill, A multigrid accelerated time-accurate inviscid compressible fluid flow solution algorithm employing mesh movement and local remeshing, *Int. J. Numer. Methods Fluids* 43 (2003) 517–536.
- [42] K.A. Sorensen, O. Hassan, K. Morgan, N.P. Weatherill, A multigrid accelerated hybrid unstructured mesh method for 3D compressible turbulent flow, *Comput. Mech.* 31 (2003) 101–114.

- [43] O. Hassan, K.A. Sorensen, K. Morgan, N.P. Weatherill, A method for time accurate turbulent compressible fluid flow simulation with moving boundary components employing local remeshing, *Int. J. Numer. Methods Fluids* 53 (8) (March 20 2007) 1243–1266, 13th International Conference on Finite Elements for Flow Problems, Swansea, Wales, 04–06 April 2005.
- [44] R. Löhner, H. Luo, J.D. Baum, D. Rice, Improvements in speed for explicit, transient compressible flow solvers, *Int. J. Numer. Methods Fluids* 56 (12) (2008) 2229–2244, APR 30.
- [45] O. Hassan, K. Morgan, N.P. Weatherill, Unstructured mesh methods for the solution of the unsteady compressible flow equations with moving boundary components, *Philos. Trans. Roy. Soc. A - Math. Phys. Eng. Sci.* 365 (1859) (2007) 2531–2552, October 15.
- [46] O. Hassan, K. Morgan, Fully parallel environment, for the simulation of unsteady flow with moving boundary components, in: B.H.V. Topping, P. Ivanyi (Eds.), *Parallel, Distributed and Grid Computing for Engineering, Computational Science Engineering and Technology Series*, vol. 21, Univ Pecs, Pollack Mihaly Fac Engn, Pecs, Hungary, 2009, pp. 1–20, First International Conference on Parallel, Distributed and Grid Computing for Engineering, 06–08 April 2009.
- [47] B.J. Evans, O. Hassan, J.W. Jones, K. Morgan, L. Remaki, Computational fluid dynamics applied to the aerodynamic design of a land-based supersonic vehicle, *Numer. Methods Part. D. E.* 27 (1, SI) (JAN 2011) 141–159, Conference on Mathematics of Finite Elements and Applications, London, England, 09–12 June 2009.
- [48] R. Sevilla, O. Hassan, K. Morgan, An analysis of the performance of a high-order stabilised finite element method for simulating compressible flows, *Comput. Methods Appl. Mech. Eng.* 253 (2013) 15–27.
- [49] C. Hirsch, *Numerical computation of internal and external flows, Fundamentals of Numerical Discretization*, vol. I, John Wiley & Sons, Chichester, 1988.
- [50] L. Demkowicz, J.T. Oden, W. Rachowicz, A new finite element method for solving compressible Navier-Stokes equations based on an operator splitting method and $h\text{-}p$ adaptivity, *Comput. Methods Appl. Mech. Eng.* 84 (1990) 275–326.
- [51] C. Hirsch, *Numerical computation of internal and external flows: II Computational method for inviscid and viscous flows*, in: *Wiley Series in Numerical Methods in Engineering*, John Wiley and Sons, Chichester, UK, 1990.
- [52] J. Vadyak, J.D. Hoffman, A.R. Bishop, Flow computations in inlets at incidence using a shock fitting bicharacteristic method, *AIAA J.* 18 (1980) 1495–1502.
- [53] K.W. Morton, M.F. Paisley, A finite volume scheme with shock fitting for steady Euler equations, *J. Comput. Phys.* 80 (1989) 168–203.
- [54] J. von Neumann, R.D. Richtmyer, A method for the numerical calculations of hydrodynamical shocks, *J. Math. Phys.* 21 (1950) 232–237.
- [55] A. Lapidus, A detached shock calculation by second order finite differences, *J. Comp. Phys.* 2 (1967) 154–177.

- [56] J.L. Steger, Implicit finite difference simulation of flow about two dimensional geometries, *AIAA J.* 16 (1978) 679–686.
- [57] R.W. MacCormack, B.S. Baldwin, A numerical method for solving the Navier–Stokes equations with application to shock boundary layer interaction, Paper AIAA-75-1, 1975.
- [58] A. Jameson, W. Schmidt, Some recent developments in numerical methods in transonic flows, *Comp. Meth. Appl. Mech. Eng.* 51 (1985) 467–493.
- [59] K. Morgan, J. Peraire, J. Peiro, O.C. Zienkiewicz, Adaptive remeshing applied to the solution of a shock interaction problem on a cylindrical leading edge, in: P. Stow (Ed.), *Computational Methods in Aeronautical Fluid Dynamics*, Clarendon Press, Oxford, 1990, pp. 327–344.
- [60] R. Codina, A discontinuity capturing crosswind-dissipation for the finite element solution of convection diffusion equation, *Comput. Methods Appl. Mech. Eng.* 110 (1993) 325–342.
- [61] P. Nithiarasu, O.C. Zienkiewicz, B.V.K.S. Sai, K. Morgan, R. Codina, M. Vázquez, Shock capturing viscosities for the general fluid mechanics algorithm, *Int. J. Num. Meth. Fluids* 28 (1998) 1325–1353.
- [62] T.J.R. Hughes, M. Malett, A new finite element formulation for fluid dynamics. Part IV: A discontinuity capturing operator for multidimensional advective–diffusive problems, *Comp. Mech. Appl. Mech. Eng.* 58 (1986) 329–336.
- [63] C. Johnson, A. Szepessy, On convergence of a finite element method for a nonlinear hyperbolic conservation law, *Math. Comput.* 49 (1987) 427–444.
- [64] A.C. Galeão, E.G. Dutra Do Carmo, A consistent approximate upwind Petrov–Galerkin method for convection dominated problems, *Comp. Meth. Appl. Mech. Eng.* 68 (1988) 83–95.
- [65] P. Hansbo, C. Johnson, Adaptive streamline diffusion methods for compressible flow using conservation variables, *Comp. Meth. Appl. Mech. Eng.* 87 (1991) 267–280.
- [66] F. Shakib, T.R.J. Hughes, Z. Johan, A new finite element formulation for computational fluid dynamics: Part X. The compressible Euler and Navier–Stokes equations, *Comput. Methods Appl. Mech. Eng.* 89 (1991) 141–219.
- [67] P. Nithiarasu, O.C. Zienkiewicz, B.V.K.S. Sai, K. Morgan, R. Codina, M. Vázquez, Shock capturing viscosities for the general algorithm, in: M. Hafez, J.C. Heinrich (Eds.), *Tenth International Conference on Finite Elements in Fluids*, 5–8 January, Tucson, Arizona, USA, 1998, pp. 350–356.
- [68] C.G. Thomas, P. Nithiarasu, Influences of element size and variable smoothing on inviscid compressible flow solution, *Int. J. Numer. Methods Heat Fluid Flow* 15 (5–6) (2005) 420–428.
- [69] G. Sod, A survey of several finite difference methods for systems of non-linear hyperbolic conservation laws, *J. Comput. Phys.* 27 (1978) 1–31.

- [70] T.E. Tezduyar, T.J.R. Hughes, Finite element methods for first order hyperbolic systems with particular emphasis on the compressible Euler equation, *Comput. Methods Appl. Mech. Eng.* 45 (1984) 217–284.
- [71] P. Woodward, P. Colella, The numerical simulation of two dimensional flow with strong shocks, *J. Comput. Phys.* 54 (1984) 115–1173.
- [72] T.H. Pulliam, J.T. Barton, Euler computations of AGARD Working Group 07 airfoil test cases, in: AIAA-85-0018, AIAA 23rd Aerospace Sciences Meeting, 1985, 14–17 January.
- [73] O.C. Zienkiewicz, K. Morgan, J. Peraire, M. Vahdati, R. Löhner, Finite elements for compressible gas flow and similar systems, in: Seventh International Conference in Computational Methods in Applied Sciences and Engineering, Versailles, December 1985.
- [74] O.C. Zienkiewicz, J.Z. Zhu, A simple error estimator and adaptive procedure for practical engineering analysis, *Int. J. Numer. Methods Eng.* 24 (1987) 337–357.
- [75] J.T. Oden, L. Demkowicz, Advance in adaptive improvements: A survey of adaptive methods in computational fluid mechanics, in: A.K. Noor, J.T. Oden (Eds.), *State of the Art Survey in Computational Fluid Mechanics*, American Society of Mechanical Engineers, 1988.
- [76] P.R.M. Lyra, K. Morgan, J. Peraire, J. Peiro, TVD algorithms for the solution of compressible Euler equations on unstructured meshes, *Int. J. Num. Meth. Fluids* 19 (1994) 827–847.
- [77] J.R. Stewart, R.R. Thareja, A.R. Wieting, K. Morgan, Application of finite elements and remeshing techniques to shock interference on a cylindrical leading edge, Paper AIAA-88-0368, 1988.
- [78] R.A. Nicolaides, On finite element multigrid algorithms and their use, in: J.R. Whiteman (Ed.), *MAFELAP 1978, The Mathematics of Finite Elements and Applications III*, Academic Press, London, 1979, pp. 459–466.
- [79] W. Hackbusch, U. Trottenberg (Eds.), *Multigrid Methods*, Springer-Verlag, Berlin, 1982.
- [80] R. Löhner, K. Morgan, An unstructured multigrid method for elliptic problems, *Int. J. Numer. Methods Eng.* 24 (1987) 101–115.
- [81] M.C. Rivara, Local modification of meshes for adaptive and or multigrid finite element methods, *J. Comp. Appl. Math.* 36 (1991) 79–89.
- [82] S. Lopez, R. Casciaro, Algorithmic aspects of adaptive multigrid finite element analysis, *Int. J. Num. Meth. Eng.* 40 (1997) 919–936.
- [83] P. Wessling, *An Introduction to Multigrid Methods*, R.T. Edwards Inc., 2004.
- [84] J. Peraire, J. Peiro, L. Formaggia, K. Morgan, O.C. Zienkiewicz, Finite element Euler computations in 3-dimensions, *Int. J. Numer. Methods Eng.* 26 (1989) 2135–2159.
- [85] A. Jameson, T.J. Baker, N.P. Weatherill, Calculation of inviscid transonic flow over a complete aircraft, in: AIAA 24th Aerospace Science Meeting, Reno, Nevada, 1986, Paper AIAA-86-0103.

- [86] V. Billey, J. Periaux, P. Perrier, B. Stoufflet, 2D and 3D Euler computations with finite element methods in aerodynamics, *Lect. Notes Math.* 1270 (1987) 64–81.
- [87] R. Noble, *THRUST, The Remarkable Story of One Man's Quest for Speed*, Bantam, London, 1998.
- [88] E.J. Probert, Finite element method for convection dominated flows, Ph.D. Thesis, University of Wales, Swansea, 1986.
- [89] Y. Kallinderis, S. Ward, Prismatic grid generation for 3-dimensional complex geometries, *AIAA J.* 31 (1993) 1850–1856.
- [90] Y. Kallinderis, Adaptive hybrid prismatic tetrahedral grids, *Int. J. Num. Meth. Fluids* 20 (1995) 1023–1037.
- [91] A.J. Chen, Y. Kallinderis, Adaptive hybrid (prismatic-tetrahedral) grids for incompressible flows, *Int. J. Num. Meth. Fluids* 26 (1998) 1085–1105.
- [92] O.C. Zienkiewicz, P. Nithiarasu, R. Codina, M. Vazquez, P. Ortiz, The characteristic-based-split (CBS) procedure: An efficient and accurate algorithm for fluid problems, *Int. J. Numer. Methods Fluids* 31 (1999) 359–392.
- [93] J.E. Carter, Numerical solutions of the Navier–Stokes equations for the supersonic laminar flow over a two-dimensional compression corner, *NASA TR-R-385*, 1972.
- [94] O. Hassan, Finite element computations of high speed viscous compressible flows, Ph.D. Thesis, University of Wales, Swansea, 1990.
- [95] O.C. Zienkiewicz, J. Wu, Automatic directional refinement in adaptive analysis of compressible flows, *Int. J. Numer. Methods Eng.* 37 (1994) 2189–2219.
- [96] M.J. Castro-Diaz, H. Borouchaki, P.L. George, F. Hecht, B. Mohammadi, Anisotropic adaptive mesh generation in two dimensions for CFD, in: *Computational Fluid Dynamics '96*, 1996, pp. 181–186.
- [97] L. Cambier, Computation of viscous transonic flows using an unsteady type method and a zonal grid refinement technique, in: M.O. Bristrau, R. Glowinski, J. Periaux, H. Viviand (Eds.), *Numerical Simulation of Compressible Navier–Stokes Flows*, Notes of Numerical Fluid Mechanics, vol. 18, Vieweg, Wiesbaden, 1987.
- [98] N. Satofuka, K. Morinishi, Y. Nishida, Numerical simulation of two-dimensional compressible Navier–Stokes equations using rational Runge–Kutta method, in: M. OBristrau, R. Glowinski, J. Periaux, H. Viviand (Eds.), *Numerical Simulation of Compressible Navier–Stokes Flows*, Notes of Numerical Fluid Mechanics, vol. 18, Vieweg, Wiesbaden, 1987.
- [99] S. Mittal, Finite element computation of unsteady viscous compressible flows, *Comput. Methods Appl. Mech. Eng.* 157 (1998) 151–175.
- [100] M.J. Lighthill, On displacement thickness, *J. Fluid Mech.* 4 (1958) 383.
- [101] J.E. Green, D.J. Weeks, J.W.F. Brooman, Prediction of turbulent boundary layers and wakes in compressible flow by a lag-entrainment method, *Aeronautical Research Council Report and Memo Report No. 3791*, 1973.

- [102] P. Bradshaw, The analogy between streamline curvature and buoyancy in turbulent shear flow, *J. Fluid Mech.* 36 (1969) 177–191.
- [103] J.E. Green, The prediction of turbulent boundary layer development in compressible flow, *J. Fluid Mech.* 31 (1969) 753–778.
- [104] H.B. Squire, A.D. Young, The calculation of the profile drag of aerofoils, Aeronautical Research Council Repo. and Memo 1838, 1937.
- [105] R.E. Melnok, R.R. Chow, H.R. Mead, Theory of viscous transonic flow over airfoils at high Reynolds number, Paper AIAA-77-680, 1977.
- [106] J.C. Le Balleur, Calcul par copulage fort des écoulements visqueux transsoniques incluant sillages et décollemants. La Recherche Aerospatiale, Profils d'aile portant, May–June 1981.
- [107] J. Szmelter, A. Pagano, Viscous flow modelling using unstructured meshes for aeronautical applications, in: S.M. Deshpande et al. (Eds.), *Lecture Notes in Physics*, vol. 453, Springer-Verlag, Berlin, 1994.
- [108] J. Szmelter, Viscous coupling techniques using unstructured and multiblock meshes, ICAS Paper ICAS-96-1.7.5, Sorrento, 1996.
- [109] J. Szmelter, Aerodynamic wing optimisation. Paper AIAA-99-0550, 1999.
- [110] J.C. Le Balleur, Viscous–inviscid calculation of high lift separated compressible flows over airfoils and wings, in: Proceedings AGARD/FDP High Lift Aerodynamics, AGARD-CP515, Banff, Canada, 1992.
- [111] J.C. Le Balleur, Calculation of fully three-dimensional separated flows with an unsteady viscous–inviscid interaction method, in: Fifth International Symposium on Numerical and Physical Aspects of Aerodynamic Flows, Long Beach CA (USA), 1992.
- [112] J.C. Le Balleur, P. Girodroux-Lavigne, Calculation of dynamic stall by viscous–inviscid interaction over airfoils and helicopter-blade sections, in: AHS 51st Annual Forum and Technology Display, Fort Worth, TX USA, 1995.

Turbulent Flows

8

8.1 Introduction

Turbulent flow is defined as a flow with random variation of various flow quantities such as velocity, pressure, and density. Turbulence is a property of the flow, not the property of a fluid. Despite serious progress on the topic of turbulence modeling over the last century, one has to admit that turbulence is still an unresolved problem and will remain so for a foreseeable future. In this chapter we will provide a brief overview on the numerical solution of turbulent fluid dynamics equations, based upon existing turbulence models and the characteristic-based split (CBS) scheme. We also make reference to various other works on turbulent flows and numerical modeling. Before going into such details we have summarized some important fundamental properties of turbulence in the following paragraphs. At this point it is worth noting that a turbulent flow is three-dimensional and occurs at relatively high Reynolds numbers. The turbulent flow is marked with random variation of quantities as shown in Fig. 8.1.

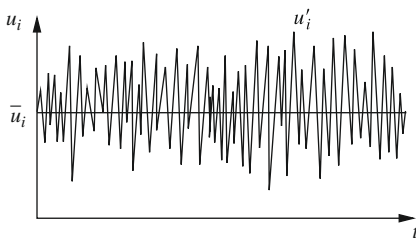
The Navier-Stokes equations are sufficient to resolve all turbulent scales if adequate mesh resolution is used. However, this requires extremely large computer resources. With present-day computers this is possible only for low Reynolds numbers. Until sufficiently fast computing power is available it is essential to employ Reynolds decomposition and turbulence models.

In a real turbulent flow the kinetic energy is transferred from larger scales to smaller scales. At the smallest scale the kinetic energy is transformed into internal energy; this process is called dissipation and the process of energy transfer between the scales is called “the cascade process.” The smallest turbulent length scale is determined by the molecular viscosity and the rate of kinetic energy dissipation. Such a length scale is often referred to as *Kolmogorov length scale*, η [1], and given as

$$\left(\frac{\nu^3}{\varepsilon}\right)^{1/4} \quad (8.1)$$

where ν is the kinematic viscosity and ε is the average rate of dissipation of turbulent kinetic energy. Similarly Kolmogorov velocity and time scales are denoted by

$$v = (\nu\varepsilon)^{1/4} \quad (8.2)$$

**FIGURE 8.1**

Random variation of velocity in a turbulent flow with respect to time.

and

$$\tau = \left(\frac{\nu}{\varepsilon} \right)^{1/2} \quad (8.3)$$

The turbulent kinetic energy dissipation rate occurring at small scales can be linked to the energy of large eddies as

$$\varepsilon = \frac{U^3}{l} \quad (8.4)$$

where U is the large eddy velocity scale and l is the large eddy length scale.

The above relations are given here to make the readers aware that the length scales and dissipation rate are closely related. The turbulence modeling procedures are developed based on these relationships.

8.1.1 Time averaging

As mentioned previously extremely high mesh resolution is required to solve down to the smallest turbulence scales. This is very expensive and presently not possible for high Reynolds number flows. It is, therefore, obvious that other alternatives are necessary to get an approximate solution. The standard procedure is to employ time-averaged Navier-Stokes equations along with a turbulence modeling approach to determine the essential time-averaged quantities, which reduces the excessive grid resolution otherwise needed. With reference to Fig. 8.1 any turbulence quantity of interest may be expressed as

$$\phi = \bar{\phi} + \phi' \quad (8.5)$$

The time-averaged quantity may be defined as

$$\bar{\phi} = \frac{1}{2T} \int_{-T}^T \phi(t) dt \quad (8.6)$$

To demonstrate time averaging we consider a one-dimensional steady state incompressible momentum equation:

$$\frac{d}{dx}(u^2) + \frac{1}{\rho} \frac{dp}{dx} - \frac{d}{dx} \left(\nu \frac{du}{dx} \right) = 0 \quad (8.7)$$

Substituting a variation of the form of Eq. (8.5) for velocity u and pressure p into Eq. (8.7) and time averaging, we have

$$\frac{d}{dx} \left[\overline{(u+u')(u+u')} \right] + \frac{1}{\rho} \frac{d}{dx} \overline{(p+p')} - \frac{d}{dx} \left[\nu \frac{d}{dx} \overline{(u+u')} \right] = 0 \quad (8.8)$$

In the above equation the average of fluctuating components, $\overline{u'}$ and $\overline{p'}$, is equal to zero. Hence, a simplified form of the above equation may be written as

$$\frac{d}{dx} \left[(\overline{u}^2 + \overline{u'}^2) \right] + \frac{1}{\rho} \frac{d\overline{p}}{dx} - \frac{d}{dx} \left[\nu \frac{d}{dx} \overline{(u)} \right] = 0 \quad (8.9)$$

Rearranging and rewriting the above momentum equation in multidimensions and including the time term, we have

$$\rho \left(\frac{\partial \bar{u}_i}{\partial t} + \frac{\partial}{\partial x_j} (\bar{u}_j \bar{u}_i) \right) = -\frac{\partial \bar{p}}{\partial x_i} + \frac{\partial \bar{\tau}_{ij}}{\partial x_j} - \frac{\partial}{\partial x_j} (\rho \overline{u'_i u'_i}) \quad (8.10)$$

where

$$\bar{\tau}_{ij} = \mu \left(\frac{\partial \bar{u}_i}{\partial x_j} + \frac{\partial \bar{u}_j}{\partial x_i} \right) \quad (8.11)$$

is the time-averaged deviatoric stress and $\rho \overline{u'_i u'_i}$ is a new unknown referred to as *Reynolds stress*. A fundamental property of the Reynolds stress is the turbulent kinetic energy of a flow, κ , which is defined as

$$\kappa = \frac{1}{2} \overline{u'_i u'_i} \quad (8.12)$$

The *Boussinesq assumption* gives the Reynolds stress as

$$\bar{\tau}_{ij}^R = -\rho \overline{u'_i u'_i} = \mu_T \left(\frac{\partial \bar{u}_i}{\partial x_j} + \frac{\partial \bar{u}_j}{\partial x_i} \right) - \frac{2}{3} \rho \kappa \delta_{ij} \quad (8.13)$$

From Eq. (8.13) it is clear that the unknown quantity to be modeled is the turbulent dynamic viscosity $\mu_T = \rho v_T$. Often the last term in the above equation is dropped for simplicity.

8.1.2 Relation between κ , ε , and ν_T

The turbulent kinematic viscosity or turbulent eddy viscosity ν_T has the same dimensions as the laminar kinematic viscosity. Thus, we can express the turbulent eddy viscosity in terms of velocity and length scales of a large eddy, i.e.,

$$\nu_T = CUL \quad (8.14)$$

where C is a constant. The definitions of U and l are discussed in [Section 8.1](#). In the above equation U may be replaced with $\sqrt{\kappa}$. With such a substitution the turbulent eddy viscosity may be determined by solving a scalar transport equation for κ and assuming an appropriate turbulent length scale l ($\kappa - l$ or one-equation models). However, a better expression for turbulent eddy viscosity may be obtained by substituting [Eq. \(8.4\)](#) into [Eq. \(8.14\)](#) as

$$\nu_T = c_\mu \frac{\kappa^2}{\varepsilon} \quad (8.15)$$

where c_μ is a constant. To employ the above equation, we need to solve two transport equations, one for κ and another for ε ($\kappa - \varepsilon$ or two-equation model). Details of many one- and two-equation models are provided in the following sections.

In the sections that follow we treat the incompressible and compressible flows separately and identify the differences. In addition to discussions on the Reynolds-averaged Navier-Stokes (RANS) models, we also provide brief summary of large eddy simulation (LES) and topics such as detached eddy simulation (DES) and monotonically integrated LES (MILES) approaches. Many useful examples are also provided to demonstrate the presented turbulent flow modeling approaches. For further details on turbulence and turbulence modeling the readers are referred to standard textbooks on this topic [[2–4](#)].

8.2 Treatment of incompressible turbulent flows

8.2.1 Reynolds-averaged Navier-Stokes

For turbulent flow computations, Reynolds-averaged Navier-Stokes equations of motion are written in conservation form as follows:

Mean-continuity

$$\frac{1}{\beta^2} \frac{\partial \bar{p}}{\partial t} + \frac{\partial(\rho \bar{u}_i)}{\partial x_i} = 0 \quad (8.16)$$

Mean-momentum

$$\rho \left(\frac{\partial \bar{u}_i}{\partial t} + \frac{\partial}{\partial x_j} (\bar{u}_j \bar{u}_i) \right) = - \frac{\partial \bar{p}}{\partial x_i} + \frac{\partial \bar{\tau}_{ij}}{\partial x_j} + \frac{\partial \bar{\tau}_{ij}^R}{\partial x_j} \quad (8.17)$$

where β is an artificial compressibility parameter, \bar{u}_i are the mean velocity components, p is the pressure, ρ is the density, $\bar{\tau}_{ij}$ is the laminar shear stress tensor given by [Eq. \(8.11\)](#), and the Reynolds stress tensor $\bar{\tau}_{ij}^R$ is given in [Eq. \(8.13\)](#).

8.2.2 One-equation models

8.2.2.1 Wolfstein $\kappa - l$ model [5]

In this model the turbulent eddy viscosity is determined from a mixing length and turbulent kinetic energy as

$$\nu_T = c_\mu^{1/4} \kappa^{1/2} l_m \quad (8.18)$$

where c_μ is a constant equal to 0.09, κ is the turbulent kinetic energy, and l_m is a mixing length. The mixing length l_m is related to the length scale of turbulence L as

$$l_m = \left(\frac{c'_\mu^3}{C_D} \right)^{1/4} L \quad (8.19)$$

where C_D and c'_μ are constants.

The transport equation for turbulent kinetic energy κ is

$$\frac{\partial \kappa}{\partial t} + \frac{\partial}{\partial x_i} (\bar{u}_i \kappa) = \frac{\partial}{\partial x_i} \left(\nu + \frac{\nu_T}{\sigma_\kappa} \right) \frac{\partial \kappa}{\partial x_i} + \frac{\tilde{\tau}_{ij}^R}{\rho} \frac{\partial \bar{u}_i}{\partial x_j} - \varepsilon \quad (8.20)$$

where σ_κ is the diffusion Prandtl number for turbulent kinetic energy. The dissipation, ε , is modeled as

$$\varepsilon = C_D \frac{\kappa^{3/2}}{L} \quad (8.21)$$

Near solid walls, the Reynolds number tends to zero and the highest mean velocity gradient occurs at the solid boundary. Thus, the one-equation model has to be used in conjunction with empirical wall functions, i.e., ν_T is multiplied by damping function $f_\mu = 1 - e^{-0.160R_\kappa}$ and ε is divided by $f_b = 1 - e^{-0.263R_\kappa}$, where $R_\kappa = \sqrt{\kappa}y/\nu$. Here y is the shortest distance to a nearest wall. The constants are $\sigma_\kappa = 1$ and $C_D = 1.0$.

8.2.2.2 Spalart-Allmaras (SA) model [6]

The Spalart-Allmaras (SA) model was first introduced for aerospace applications and then adopted for incompressible flow calculations. This is another one-equation model that employs a single scalar equation and several constants to model turbulence. The scalar transport equation used by this model is

$$\frac{\partial \hat{v}}{\partial t} + \frac{\partial (u_j \hat{v})}{\partial x_j} = c_{b1} \hat{S} \hat{v} + \frac{1}{\sigma} \left[\frac{\partial}{\partial x_i} (\nu + \hat{v}) \frac{\partial \hat{v}}{\partial x_i} + c_{b2} \left(\frac{\partial \hat{v}}{\partial x_i} \right)^2 \right] - c_{w1} f_w \left[\frac{\hat{v}}{y} \right]^2 \quad (8.22)$$

where

$$\hat{S} = S + (\hat{v}/k^2 y^2) f_{v2} \quad (8.23)$$

$$f_{v2} = 1 - X/(1 + X f_{v1}) \quad (8.24)$$

In Eq. (8.23), S is the magnitude of vorticity and y is the shortest distance from a node to the nearest solid wall. The eddy viscosity is calculated as

$$\nu_T = \hat{v} f_{v1} \quad (8.25)$$

where

$$f_{v1} = X^3 / (X^3 + c_{v1}^3) \quad (8.26)$$

and

$$X = \hat{v}/\nu \quad (8.27)$$

The parameter f_w is given as

$$f_w = g \left[\frac{1 + c_{w3}^6}{g^6 + c_{w3}^3} \right]^{1/6} \quad (8.28)$$

where

$$g = r + c_{w2}(r^6 - r) \quad (8.29)$$

and

$$r = \frac{\hat{v}}{\hat{S}k^2y^2} \quad (8.30)$$

The constants are $c_{b1} = 0.1355$, $\sigma = 2/3$, $c_{b2} = 0.622$, $k = 0.41$, $c_{w1} = c_{b1}/k^2 + (1 + c_{b2})/\sigma$, $c_{w2} = 0.3$, $c_{w3} = 2$, and $c_{v1} = 7.1$.

8.2.3 Two-equation models

8.2.3.1 The standard $\kappa - \varepsilon$ model

In this model, the transport equation for κ is the same as that in the one-equation model of Section 8.2.2.1. The second transport equation for calculating the turbulence energy dissipation rate ε is

$$\frac{\partial \varepsilon}{\partial t} + \frac{\partial}{\partial x_i} (\bar{u}_i \varepsilon) = \frac{\partial}{\partial x_i} \left(\nu + \frac{\nu_T}{\sigma_\varepsilon} \right) \frac{\partial \varepsilon}{\partial x_i} + C_{\varepsilon 1} \frac{\varepsilon}{\kappa} \frac{\bar{\tau}_{ij}^R}{\rho} \frac{\partial \bar{u}_i}{\partial x_j} - C_{\varepsilon 2} \frac{\varepsilon^2}{\kappa} \quad (8.31)$$

where $C_{\varepsilon 1} = 1.44$, $C_{\varepsilon 2} = 1.92$, and σ_ε is the diffusion Prandtl number for isotropic turbulence energy dissipation rate and equal to 1.3. These constants are proposed by Jones and Launder [7].

In addition, ν_T is evaluated by

$$\nu_T = C_\mu \frac{\kappa^2}{\varepsilon} \quad (8.32)$$

For near-wall treatments, modifications to the source terms of ε equation are needed in the near-wall region. Multiplying the coefficients c_μ , $C_{\varepsilon 1}$, and $C_{\varepsilon 2}$ by the

turbulence damping functions f_μ , $f_{\varepsilon 1}$, and $f_{\varepsilon 2}$, appropriate low Reynolds number status near the walls is achieved. Numerous wall damping functions have been proposed. The ones suggested by Lam and Bremhorst [8] for steady flows are

$$f_\mu = (1 - e^{-0.0165R_\kappa})^2 \left(1 + \frac{20.5}{R_t}\right) \quad (8.33a)$$

$$f_{\varepsilon 1} = 1 + \left(\frac{0.05}{f_\mu}\right)^3 \quad (8.33b)$$

and

$$f_{\varepsilon 2} = 1 - e^{-R_t^2} \quad (8.33c)$$

where $R_t = \kappa^2/\nu\varepsilon$. The damping functions of Fan et al. [9] are

$$f_\mu = 0.4 \frac{f_w}{\sqrt{R_t}} \left(1 - 0.4 \frac{f_w}{\sqrt{R_t}}\right) \left[1 - \exp\left(-\frac{R_y}{42.63}\right)\right]^3 \quad (8.34)$$

where

$$\begin{aligned} f_w &= 1 - \exp\left\{-\frac{\sqrt{R_y}}{2.30} + \left(\frac{\sqrt{R_y}}{2.30} - \frac{R_y}{8.89}\right) \left[1 - \exp\left(-\frac{R_y}{20}\right)\right]^3\right\} \\ f_{\varepsilon 2} &= \left\{1 - \frac{0.4}{0.8} \exp\left[-\left(\frac{R_t}{6}\right)^2\right]\right\} f_w^2 \end{aligned} \quad (8.35)$$

and $f_{\varepsilon 1} = 1$. The constants are $c_\mu = 0.09$, $\sigma_k = 1.0$, $\sigma_\varepsilon = 1.3$, $C_{\varepsilon 1} = 1.4$, and $C_{\varepsilon 2} = 1.8$.

8.2.4 Nondimensional form of the governing equations

The turbulent flow solution is obtained by solving Eqs. (8.16) and (8.17) with appropriate boundary conditions along with one of the turbulence models. The following nondimensional scales may be used in the calculations:

$$\begin{aligned} \bar{u}_i^* &= \frac{\bar{u}_i}{u_\infty}, \quad x_i^* = \frac{x_i}{D}, \quad \bar{p}^* = \frac{\bar{p}}{\rho_\infty u_\infty^2}, \quad t^* = \frac{tu_\infty}{D} \\ \kappa^* &= \frac{\kappa}{u_\infty^2}, \quad \varepsilon^* = \frac{\varepsilon D}{u_\infty^3}, \quad v_T^* = \frac{v_T}{v_\infty}, \quad \hat{v}^* = \frac{\hat{v}}{v_\infty} \end{aligned} \quad (8.36)$$

where D is a characteristic length and the subscript ∞ indicates a reference value. Substituting the nondimensional scales into Eqs. (8.16) and (8.17), and dropping asterisks leads to

$$\frac{1}{\beta^2} \frac{\partial(\bar{p})}{\partial t} + \frac{\partial(\rho \bar{u}_i)}{\partial x_i} = 0 \quad (8.37a)$$

$$\frac{\partial \bar{u}_i}{\partial t} + \frac{\partial}{\partial x_j} (\bar{u}_j \bar{u}_i) = -\frac{\partial \bar{p}}{\partial x_i} + \frac{\partial (\bar{\tau}_{ij} + \bar{\tau}_{ij}^R)}{\partial x_j} \quad (8.37b)$$

and

$$\bar{\tau}_{ij} + \bar{\tau}_{ij}^R = \frac{(1.0 + \nu_T)}{Re} \left(\frac{\partial \bar{u}_i}{\partial x_j} + \frac{\partial \bar{u}_j}{\partial x_i} \right) \quad (8.37c)$$

The Reynolds number, Re , in the above equation is defined as

$$Re = \frac{\bar{u}_\infty D}{\nu_\infty} \quad (8.38)$$

The viscosity, ν , is assumed to be constant and equal to ν_∞ in the above equations. Note that the turbulent kinetic energy term is dropped from Eq. (8.13) to arrive at Eq. (8.37c). The nondimensional form of the turbulence transport equations are given below

8.2.4.1 $\kappa - l$ model

The nondimensional form of the κ equation is

$$\frac{\partial \kappa}{\partial t} + \frac{\partial}{\partial x_i} (\bar{u}_i \kappa) = \frac{1}{Re} \frac{\partial}{\partial x_i} \left(1 + \frac{\nu_T}{\sigma_\kappa} \right) \frac{\partial \kappa}{\partial x_i} + \bar{\tau}_{ij}^R \frac{\partial \bar{u}_i}{\partial x_j} - \varepsilon \quad (8.39)$$

The mixing length and the turbulence length scales are normalized using the characteristic length D . In this study we assume $L = D$. The nondimensional form of R_k is $\sqrt{\kappa} y Re$.

8.2.4.2 Spalart-Allmaras model

The nondimensional form of the transport equation is

$$\frac{\partial \hat{v}}{\partial t} + \frac{\partial (\bar{u}_j \hat{v})}{\partial x_j} = c_{b1} \hat{S} \hat{v} + \frac{1}{Re \sigma} \left[\frac{\partial}{\partial x_i} \left(1 + \hat{v} \right) \frac{\partial \hat{v}}{\partial x_i} + c_{b2} \left(\frac{\partial \hat{v}}{\partial x_i} \right)^2 \right] - \frac{c_{w1} f_w}{Re} \left[\frac{\hat{v}}{y} \right]^2 \quad (8.40)$$

where

$$\hat{S} = S + \frac{1}{Re} \left(\hat{v} / k^2 y^2 \right) f_{v2} \quad (8.41)$$

and

$$r = \frac{1}{Re} \frac{\hat{v}}{\hat{S} k^2 y^2} \quad (8.42)$$

The structures of all the remaining parameters are unchanged.

8.2.4.3 $\kappa - \varepsilon$ model

The κ equation is identical to that of the one-equation model and the dissipation equation is given as

$$\frac{\partial \varepsilon}{\partial t} + \frac{\partial}{\partial x_i} (\bar{u}_i \varepsilon) = \frac{1}{Re} \frac{\partial}{\partial x_i} \left(1 + \frac{v_T}{\sigma_\varepsilon} \right) \frac{\partial \varepsilon}{\partial x_i} + C_{\varepsilon 1} \frac{\varepsilon}{\kappa} \bar{\tau}_{ij}^R \frac{\partial \bar{u}_i}{\partial x_j} - C_{\varepsilon 2} \frac{\varepsilon^2}{\kappa} \quad (8.43)$$

The parameter R_t in its nondimensional form is $\kappa^2 Re / \varepsilon$.

8.2.5 Shortest distance to a solid wall

In all the turbulence models described above, distance from a node to the nearest wall is essential. For meshes with a small number of nodes it is a matter of checking the number of solid wall nodes against the total number of nodes in a mesh. However, such a procedure will consume a significant part of the computational time if the number of nodes is in the hundreds of thousands. Nowadays, it is common to solve flow equations over several million number of nodes. Hence, we need to have a faster and reliable wall distance calculation procedure in place.

The wall distance calculation may be accelerated by creating linelets emanating from solid wall nodes as discussed in Refs. [10,11]. This method works by allocating all nonwall nodes to a linelet and then finding a short distance to the wall. This method was proved to reduce computing time to calculate wall distance. In time-dependent flow problems which involve moving solid walls, the standard procedures of calculating the wall distances will again be expensive. In recent years, differential equation-based wall distance calculation procedures have been developed to reduce the cost of repeated wall distance computation [12–14]. One of the simplest models used to calculate shortest distance is the one based on the numerical solution of the Eikonal equation:

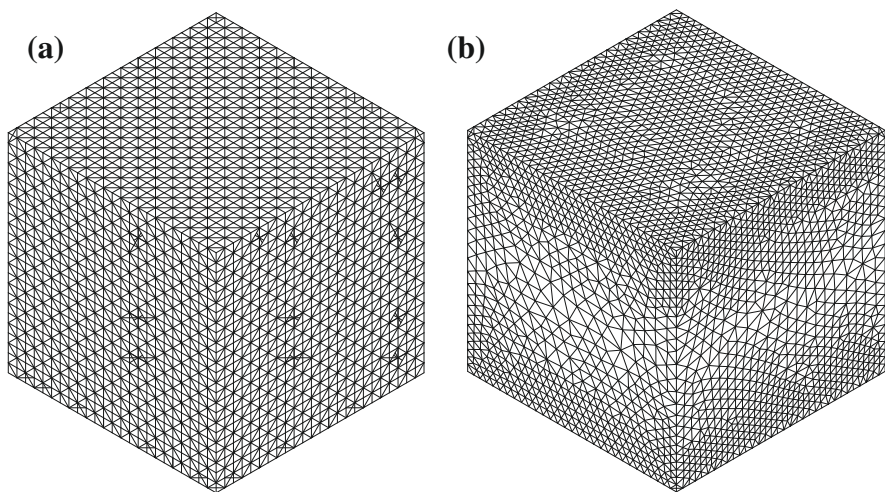
$$\frac{\partial \phi}{\partial t} + \left(\frac{\partial \phi}{\partial x_i} \right)^2 = 1 \quad (8.44)$$

This is a convection equation and any of the stable methods discussed in Chapter 2 may be used to solve for shortest distance to a solid wall ϕ as shown in the following example.

Example 8.1. Shortest distance to walls inside a cube

The structured and unstructured meshes of a cube of unit size are shown in Fig. 8.2. All the six surfaces of the cube are assumed to be solid walls. The exact solution is obtained using a standard search procedure of looping over the number of tetrahedron elements and surface faces. For the structured mesh, a node is placed exactly at the center of the domain to give the shortest distance to the wall of 0.5. Since a nodal position at the center is not guaranteed in an unstructured mesh, the maximum shortest distance to the nearest wall may not be 0.5.

Figure 8.3 compares the solutions obtained by the standard search procedure and the numerical solution to the Eikonal equation using both the meshes of Fig. 8.2. As seen the analytical and numerical results obtained are almost identical [14].

**FIGURE 8.2**

(a) Structured mesh S1 (nodes: 15,625; elements: 69,120); (b) unstructured mesh U1 (nodes: 23,597; elements: 127,692).

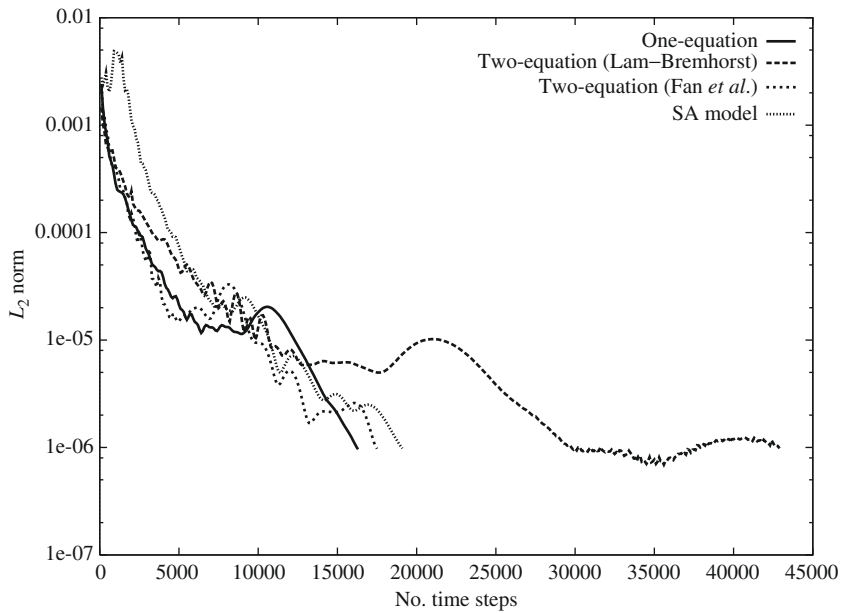
8.2.6 Solution procedure for turbulent flow equations

It is evident from the RANS equations discussed above that the governing turbulent flow equations take the form of standard fluid dynamics equations discussed in the previous chapters. However, we have additional scalar transport equation(s) that need to be solved in conjunction with the RANS equations. We therefore recommend the CBS scheme along with any valid procedure for solving the convection-diffusion equation from [Chapter 2](#) for the solution of scalar turbulence transport equations.

The transient solutions may be obtained via an artificial compressibility scheme using a dual time-stepping algorithm [15]. Alternatively a semi- or quasi-implicit form of the scheme may be employed to obtain unsteady state solutions. Unsteady state RANS solutions are often referred to as URANS solutions [15–20].

Example 8.2. Turbulent flow in a rectangular channel

Often structured meshes are preferred for turbulent flow calculations. Since structured meshes give the best solution, we recommend structured meshes or meshes with structured layers close to the wall wherever possible. However, if unstructured meshes are employed it may be important to assess their applicability. In order to estimate the applicability of unstructured meshes we provide a comparison between the structured and unstructured mesh results for flow through a rectangular channel at a moderate Reynolds number of 12,300. [Figures 8.4](#) and [8.5](#) show the results. The first node of the structured mesh was placed at a distance of 0.005 and the unstructured mesh was placed roughly around 0.01. As seen the logarithmic representation of time-averaged velocity variation is close to the experimental data of Laufer [21]. The small difference between the structured and unstructured meshes is attributed to the slightly larger

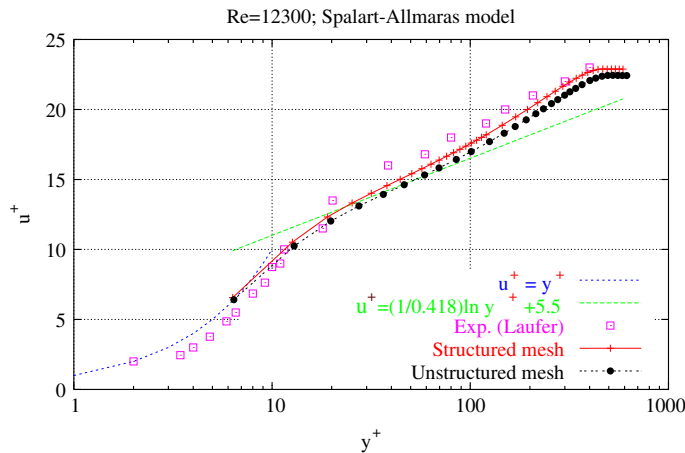
**FIGURE 8.3**

Wall distance contours at a central section in the x_1 direction (uniformly structured mesh S1). Comparison between search procedure and implicit GMRES scheme. (a) Simple search procedure (structured mesh): $\phi_{min} = 0.0$, $\phi_{max} = 0.5000$; (b) Eikonal equation (structured mesh): $\phi_{min} = 0.0$, $\phi_{max} = 0.5000$; (c) simple search procedure (unstructured mesh): $\phi_{min} = 0.0$, $\phi_{max} = 0.4923$; (d) Eikonal equation (unstructured mesh): $\phi_{min} = 0.0$, $\phi_{max} = 0.4887$.

elements of the unstructured mesh used close to the wall. The point we are trying to prove here is that the turbulence model and the artificial compressibility-based CBS schemes together can predict the time-averaged turbulence quantities satisfactorily. In several ways these results allow us to present the unstructured mesh results with confidence. We also show the comparison of fully developed velocity profiles with the experimental data of Laufer [21] in Fig. 8.5a. As seen the agreement between the numerical and experimental data is excellent. Figure 8.5b shows the convergence histories of structured and unstructured meshes to steady state. As seen the convergence is rapid and it took only about 5000 time steps to reach an L_2 norm velocity residual of 10^{-5} . We use local time steps to accelerate the solution to steady state.

Example 8.3. Turbulent flow past a backward facing step

A standard test case commonly employed for testing turbulent incompressible flow models at a moderate Reynolds number is the recirculating flow past a backward facing step. Unlike the channel flow, here the model has to handle the recirculation region immediately downstream of the step. The nonequilibrium turbulent flow conditions in the recirculation region make most of the one-equation turbulence models inadequate.

**FIGURE 8.4**

Turbulent incompressible flow through a rectangular channel using the Spalart-Allmaras model at $Re = 12,300$. Logarithmic representation of time-averaged velocity profile. (Note: $u^+ = u/u_\tau$ with $u_\tau = \sqrt{\tau_w/\rho}$ being the friction velocity; $y^+ = yu_\tau/v$ with y being the shortest distance to the wall.)

The definition of the problem is shown in Fig. 8.6. The characteristic dimension of the problem is the step height (L). All other dimensions are defined with respect to this. The inlet is located at a distance of four times the step height upstream of the step. The inlet channel height is $2L$. The total length of the channel is $40L$.

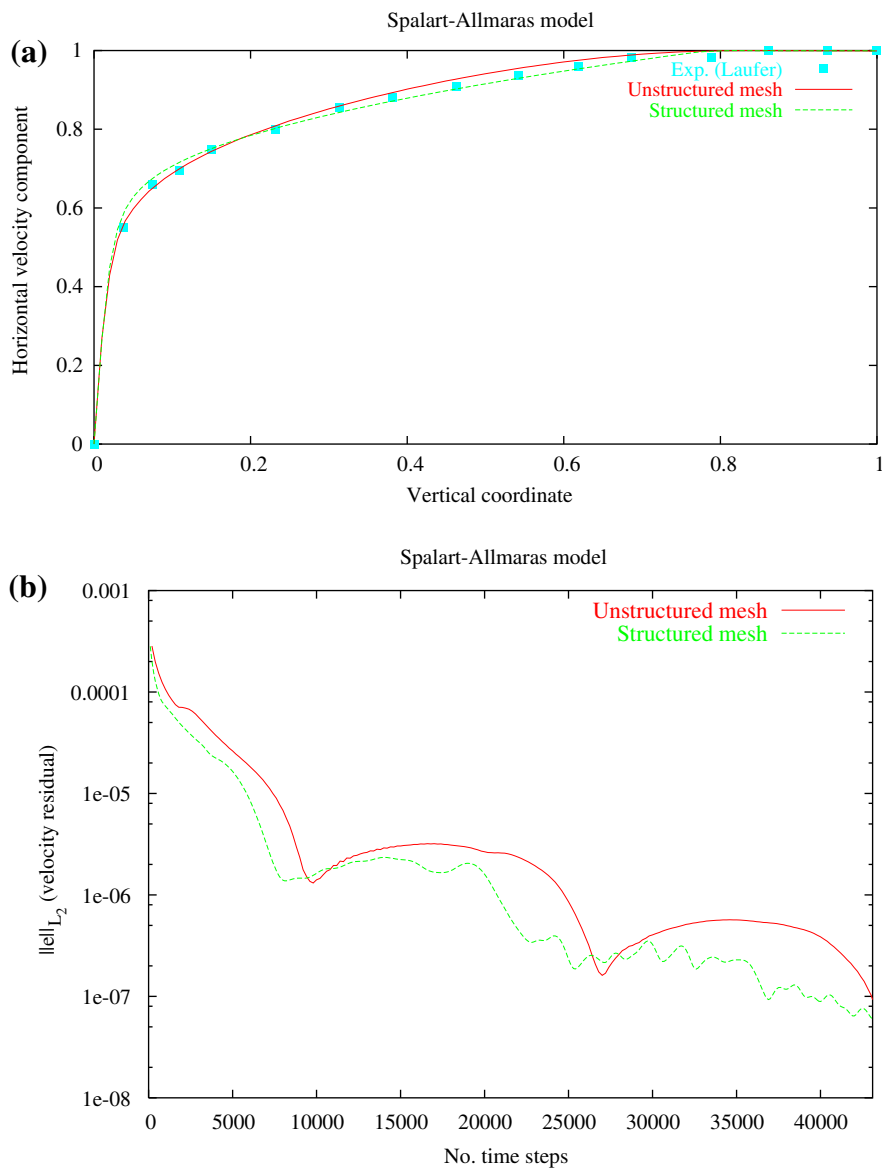
The inlet velocity profile is obtained from measurements reported by Denham et al. [22]. No-slip conditions apply on the solid walls. For the one-equation and two-equation models the inlet κ and ε profiles were obtained by solving a channel flow problem. For the SA model, a fixed value of 0.05 for the turbulent scalar variable at the inlet was prescribed. On the walls κ was assumed to be equal to zero. The wall conditions for ε are

$$\varepsilon = \frac{2}{Re} \left(\frac{d\kappa^{1/2}}{dy} \right)^2 \quad (8.45)$$

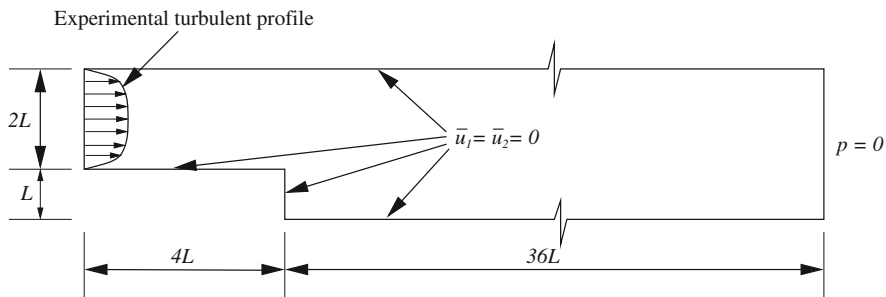
as discussed in Ref. [23]. The scalar variable of the SA model was also assumed to be zero on the walls.

Figure 8.7 shows the comparison of velocity profiles against the experimental data of Denham et al. [22]. It is obvious that the one-equation model failed to predict the recirculation region accurately. The SA model and the two-equation models on the other hand predict the recirculation better than the one-equation model. Among the SA and two-equation models, the former seems to predict the recirculation more accurately.

Both structured and unstructured meshes were employed in the calculation. Figures 8.8 and 8.9 show the SA model solutions on structured and unstructured

**FIGURE 8.5**

Turbulent incompressible flow in a rectangular channel using the Spalart-Allmaras model at $Re = 12,300$. (a) Comparison of fully developed velocity profiles; (b) convergence to the steady state.

**FIGURE 8.6**

Turbulent flow past a two-dimensional backward facing step. Problem definition.

meshes respectively. The qualitative difference between the two results is almost nil. The quantitative difference between the two solutions was also found to be negligibly small.

Example 8.4. Unsteady turbulent flow past a circular cylinder

The example considered is the standard test case of transient turbulent incompressible flow past a circular cylinder at a Reynolds number of 10,000.

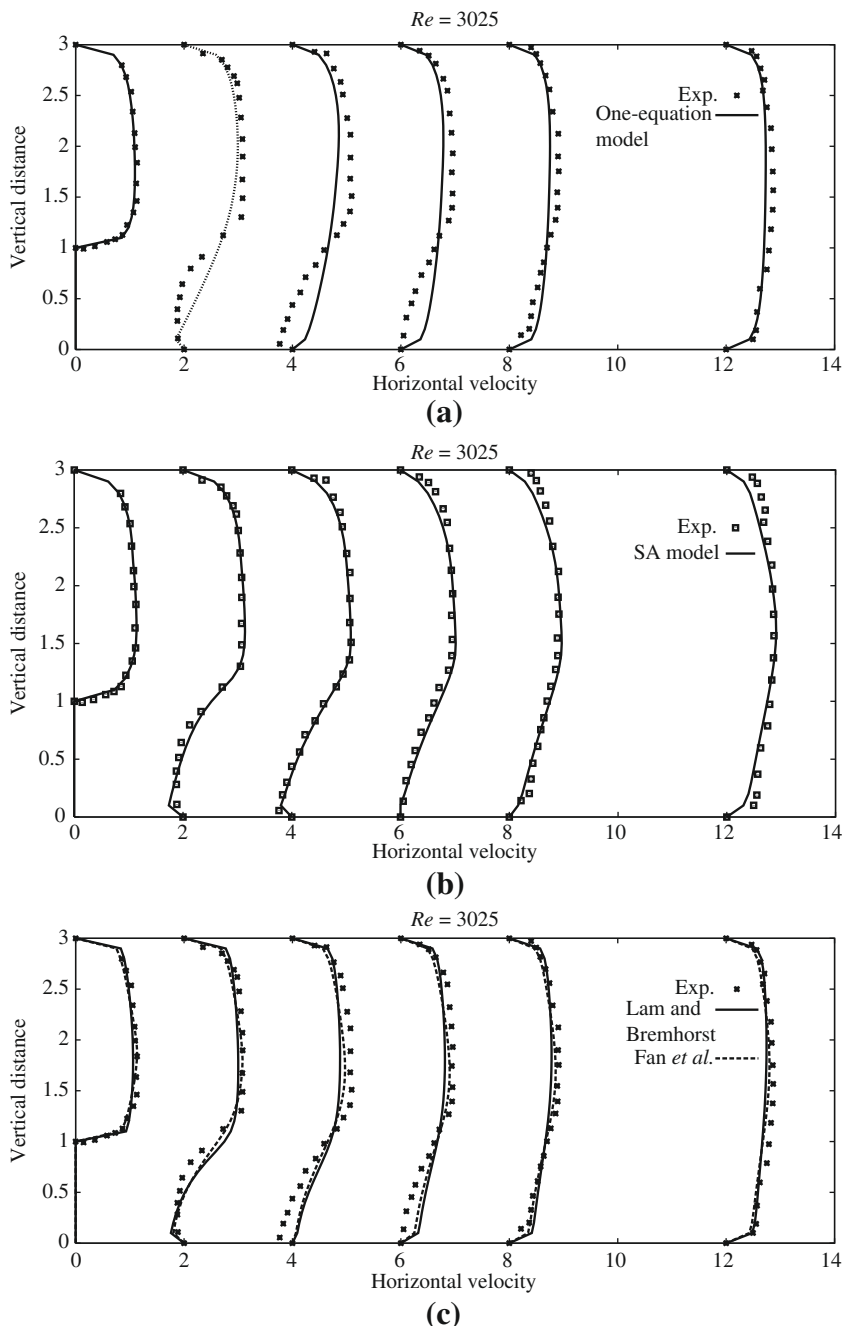
The domain consists of a circular cylinder placed at a distance of $4D$ from the inlet, where D is the diameter of the cylinder. The distance from the center of the cylinder to the top and bottom sides is equal to $4D$. The exit of the domain is placed at a distance of $12D$ from the center of the cylinder (Fig. 8.10). The finite element mesh used is shown in Fig. 8.10. The mesh in the vicinity of the cylinder and along the wake region is refined with structured layers in the vicinity of the cylinder surface to capture the transient feature of the problem.

Uniform velocity conditions were assumed at the inlet. The turbulent scalar variable was assumed to be equal to 0.05 at the inlet for the SA model. On the top and bottom sides slip conditions were assumed and no turbulence quantity was prescribed. On the cylinder walls no-slip conditions are assumed and the turbulent scalar variable of the SA model was assumed to be zero.

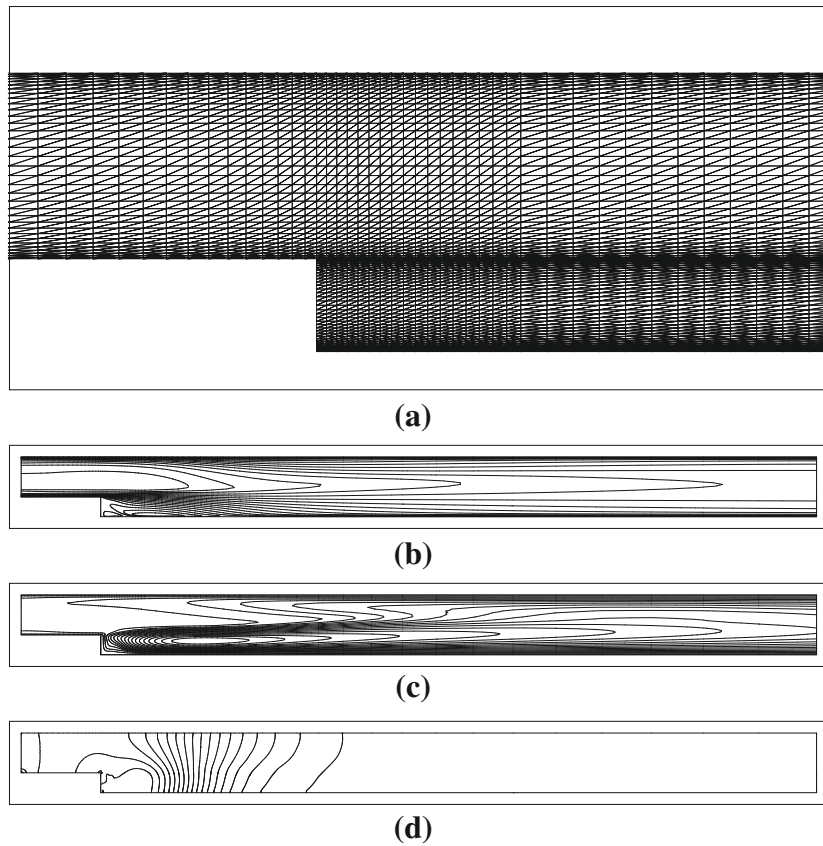
Dual time stepping was employed in this problem. A true transient term was added to both Step 3 of the scheme as discussed in Chapter 3 and to the turbulence transport equations. The pseudo time step used within each real time step is local and varies between the nodes depending on the local flow field and mesh size. The L_2 norm of velocity residual was reduced to less than 10^{-6} within every real time step in order to make sure that local steady state is achieved within each real time step.

Snapshots of different variables are shown in Fig. 8.11. These figures show that the vortex shedding is present (SA model).

Figure 8.12 shows temporal drag and lift coefficients when using the SA model. Periodic flow and vortex shedding are clearly evident from the graphs. The average experimental value of drag coefficient is around 1.12 and the Strouhal number is

**FIGURE 8.7**

Incompressible turbulent flow past a backward facing step. Velocity profiles at various downstream sections at $Re = 3025$: (a) one-equation model; (b) SA model; (c) two-equation model.

**FIGURE 8.8**

Incompressible turbulent flow past a backward facing step (a) Structured mesh (elements: 8092, nodes: 4183), (b) velocity contours, (c) \hat{v} contours, and (d) pressure contours at $Re = 3015$ using the SA model.

around 0.2 [24]. The time-averaged coefficient of pressure distribution is shown in Fig. 8.13.

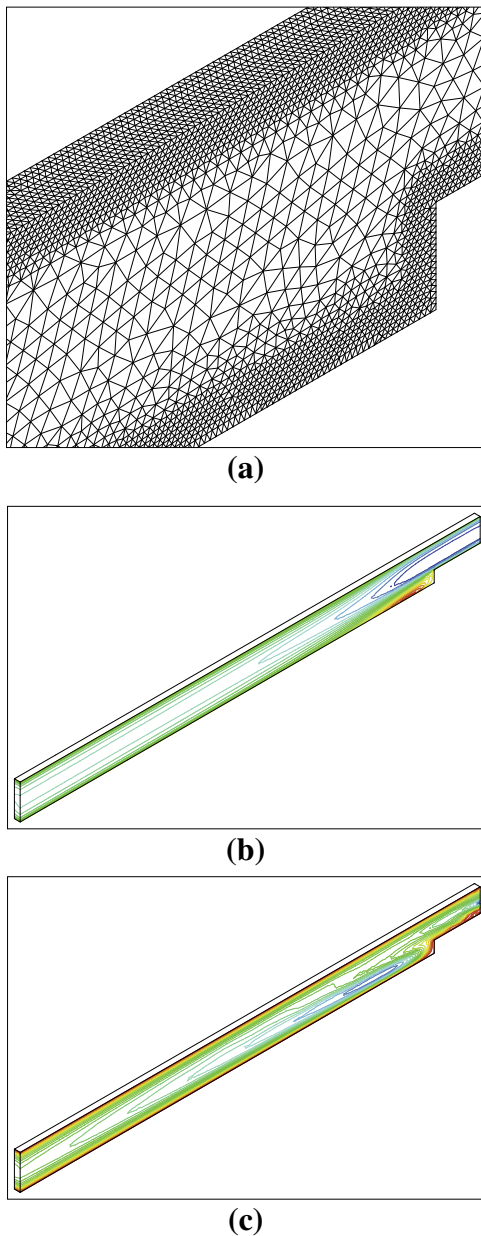
8.3 Treatment of compressible flows

The conservation equations for compressible flows may be rewritten from Chapters 1 and 2.

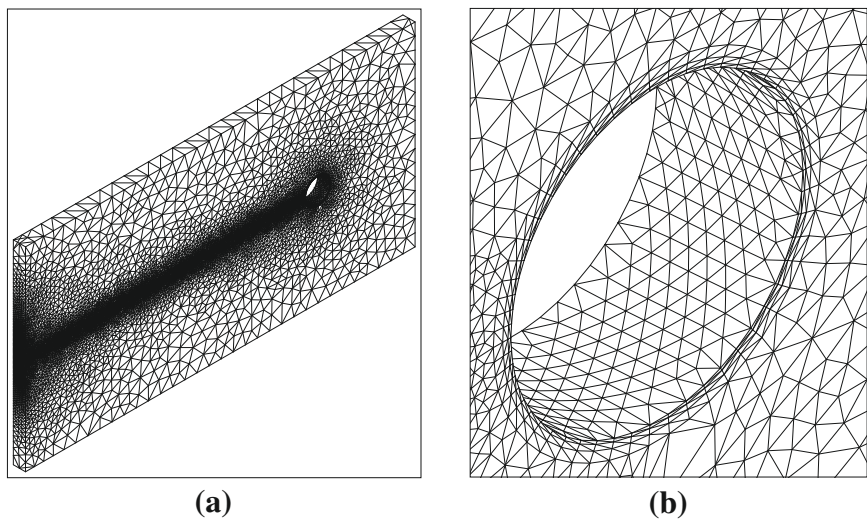
Mass conservation

$$\frac{\partial \rho}{\partial t} + \frac{1}{c^2} \frac{\partial p}{\partial t} = - \frac{\partial U_i}{\partial x_i} \quad (8.46)$$

where c is the speed of sound and depends on E , p , and ρ .

**FIGURE 8.9**

Incompressible turbulent flow past a backward facing step (a) Unstructured mesh (elements: 47,359, nodes: 24,336), (b) velocity contours, and (c) \hat{v} contours at $Re = 3025$ using the SA model.

**FIGURE 8.10**

Incompressible turbulent flow past a circular cylinder. Finite element mesh: (a) overall mesh; (b) close-up of the cylinder.

Momentum conservation

$$\frac{\partial U_i}{\partial t} = -\frac{\partial}{\partial x_j}(u_j U_i) + \frac{\partial \tau_{ij}}{\partial x_j} - \frac{\partial p}{\partial x_i} + \rho g_i \quad (8.47)$$

Energy conservation

$$\frac{\partial(\rho E)}{\partial t} = -\frac{\partial}{\partial x_i}(u_i \rho E) + \frac{\partial}{\partial x_i}\left(k \frac{\partial T}{\partial x_i}\right) - \frac{\partial}{\partial x_i}(u_i p) + \frac{\partial}{\partial x_i}(\tau_{ij} u_j) + \rho g_i u_i \quad (8.48)$$

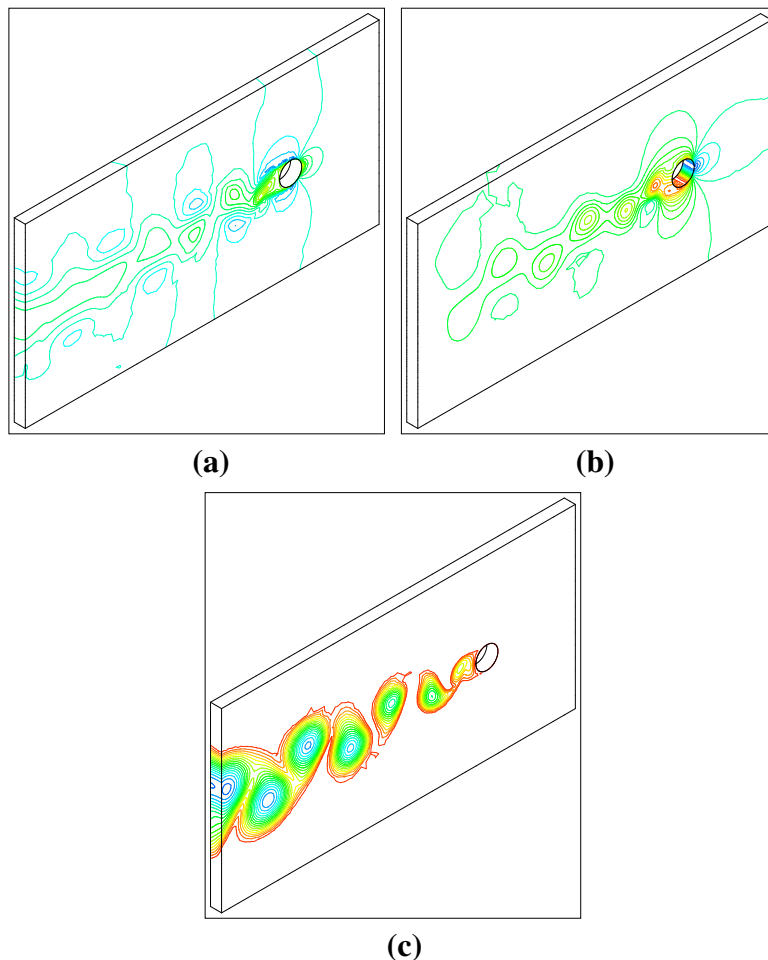
In all of the above u_i are the velocity components, ρ is the density, E is the specific energy, p is the pressure, T is the absolute temperature, ρg_i represents body forces and other source terms, k is the thermal conductivity, and τ_{ij} are the deviatoric stress components given by [Eq. (1.11b)]

$$\tau_{ij} = \mu \left(\frac{\partial u_i}{\partial x_j} + \frac{\partial u_j}{\partial x_i} - \frac{2}{3} \delta_{ij} \frac{\partial u_k}{\partial x_k} \right) \quad (8.49)$$

In general, the dynamic viscosity μ in the above equation is a function of temperature, $\mu(T)$, and appropriate relations will be used if necessary (see Chapter 7).

8.3.1 Mass-weighted (Favre) time averaging

Conventional time averaging discussed in Section 8.1.1 introduces additional terms in compressible flows and needs additional equations to close the system. Thus, in compressible flow calculations it is often useful to introduce mass-weighted averaging.

**FIGURE 8.11**

Incompressible turbulent flow past a circular cylinder. Snapshots of variables at $Re = 10,000$ using the SA model: (a) u_1 contours; (b) p contours; (c) v_T contours.

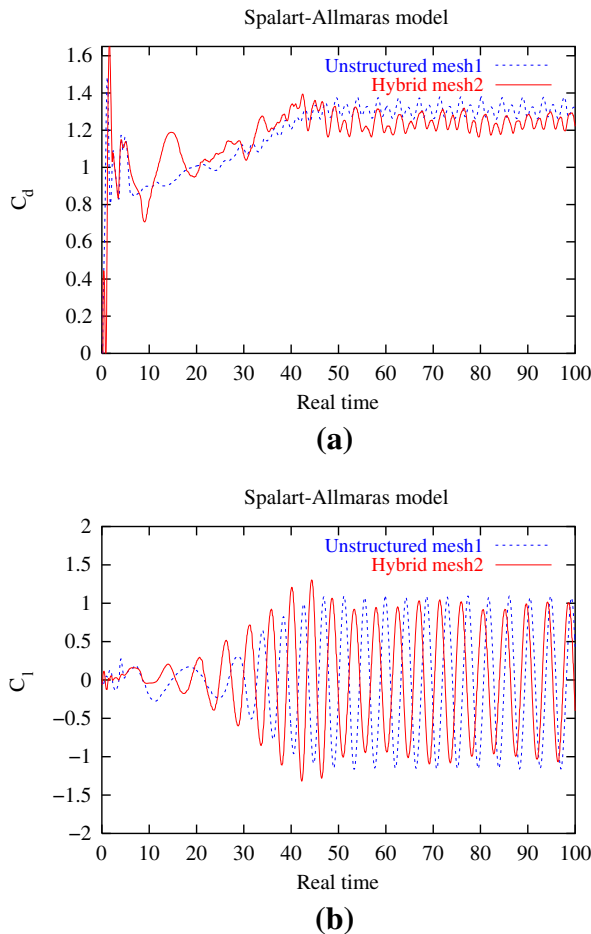
In such a procedure, a mass-weighted average velocity is given as

$$\tilde{u}_i = \frac{\overline{\rho u_i}}{\overline{\rho}} \quad (8.50)$$

where the overline in the above equation indicates a standard time-averaged quantity. Here, the time-dependent velocity may be written as

$$u_i = \tilde{u}_i + u''_i \quad (8.51)$$

The above equation has a similar form as standard time averaging relation (8.5). However, in the above equation the mass-weighted averaging term \tilde{u}_i replaces the

**FIGURE 8.12**

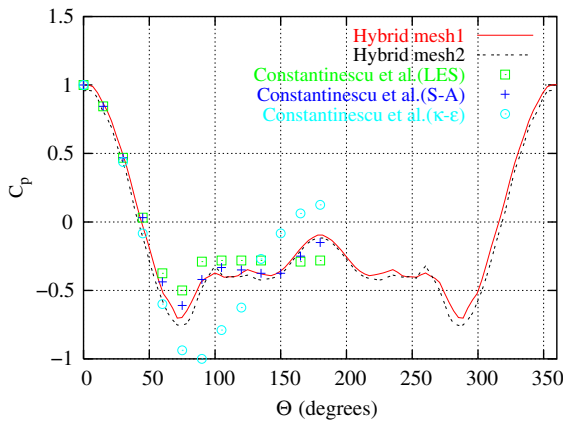
Incompressible turbulent flow past a circular cylinder. (a) Drag and (b) lift coefficient distributions with respect to real time at $Re = 10,000$ using the SA model.

conventional time averaging term \bar{u}_i . Now employing the mass-weighted velocity and standard time averaging for ρ and p we get the conservation of mass and momentum equations as

$$\frac{\partial \bar{\rho}}{\partial t} + \frac{\partial}{\partial x_i} (\bar{\rho} \bar{u}_i) = 0 \quad (8.52)$$

and

$$\frac{\partial}{\partial t} (\bar{\rho} \bar{u}_i) + \frac{\partial}{\partial x_j} (\bar{\rho} \bar{u}_i \bar{u}_j) = -\frac{\partial \bar{p}}{\partial x_i} + \frac{\partial}{\partial x_j} (\bar{\tau}_{ij} - \overline{\rho u''_i u''_j}) \quad (8.53)$$

**FIGURE 8.13**

Incompressible turbulent flow past a circular cylinder. Time-averaged coefficient of pressure at $Re = 10,000$ using the SA model. Data for comparison from Ref. [20].

It should be noted here that in standard mass averaging $\bar{u}'_i = 0$ and $\bar{\rho}u'_i \neq 0$ and in mass-weighted averaging $\bar{u}''_i \neq 0$ and $\bar{\rho}u''_i = 0$. In Eq. (8.53) $\bar{\rho}u''_i u''_j$ are the Reynolds stresses. In a similar fashion the mass-weighted averaging for energy gives

$$\frac{\partial(\bar{\rho}\tilde{E})}{\partial t} = -\frac{\partial}{\partial x_i}(\bar{\rho}\tilde{u}_i \tilde{E}) + \frac{\partial}{\partial x_i}\left(k \frac{\partial \bar{T}}{\partial x_i} - \bar{\rho}E''u''_i\right) - \frac{\partial}{\partial x_i}(\tilde{u}_i \bar{p}) + \overline{\frac{\partial}{\partial x_i}(\tau_{ij}u_j)} + \rho g_i \tilde{u}_i \quad (8.54)$$

The extra terms in Eqs. (8.53) and (8.54) are modeled to solve the compressible turbulent flow equations. The mass-weighted averaged turbulence transport equations for compressible flows are discussed in Appendix I.

8.4 Large eddy simulation (LES)

The idea of LES is developed based on splitting large-scale motions from small scales using a filtering operation such as

$$\bar{\phi}(x) = \int_{\Omega} f(x') G(x, x') dx' \quad (8.55)$$

If the variables of the incompressible Newtonian equations are subjected to the above filtering operation, we get

$$\frac{\partial \bar{u}_i}{\partial x_i} = 0 \quad (8.56)$$

and

$$\frac{\partial \bar{u}_i}{\partial t} + \frac{\partial}{\partial x_j}(\bar{u}_i \bar{u}_j) = -\frac{1}{\rho} \frac{\partial \bar{p}}{\partial x_i} + \frac{\partial \tau_{ij}}{\partial x_j} + \frac{\partial \tau_{ij}}{\partial x_j}^{SGS} \quad (8.57)$$

where

$$\tau_{ij}^{SGS} = \bar{u}_i \bar{u}_j - \bar{u}_i \bar{u}_j \quad (8.58)$$

τ^{SGS} in the above equation is generally modeled using various subgrid scale (SGS) models. The standard SGS models [25], dynamic models [26], and nonlinear models are a few to mention. It is a vast area of research and difficult to cover all the theory behind these models in a chapter. For the sake of completeness, we provide the standard SGS model below. The SGS stress of Eq. (8.58) is represented exactly as Eq. (8.13). However, the eddy viscosity is modeled differently here.

8.4.1.1 Standard SGS model

The eddy viscosity here is defined as

$$\nu_T = (C \Delta)^2 \bar{\omega} \quad (8.59)$$

The most widely used eddy-viscosity model was proposed by the meteorologist Smagorinsky [25]. Smagorinsky was simulating a two-layer quasi-geostrophic model in order to represent large (synoptic) scale atmospheric motions. He introduced an eddy viscosity that was supposed to model three-dimensional turbulence in the subgrid scales.

In Smagorinsky's model, a mixing-length assumption is made, in which the eddy viscosity is assumed to be proportional to the subgrid scale characteristic length Δ and to a characteristic turbulent velocity based on the second invariant of the filtered field deformation tensor (i.e., strain-rate tensor). In other words, the well-known Smagorinsky's model, where the SGS time scaling, $\bar{\omega}$, in Eq. (8.59) is set as the magnitude of the local resolved strain-rate tensor, namely

$$\bar{\omega} = |\bar{S}| = (2\bar{S}_{ij}\bar{S}_{ij})^{1/2} \quad (8.60)$$

and

$$C = C_s \quad (8.61)$$

If one assumes that the cutoff wave number in Fourier space, $k_c = \pi/\Delta$, lies within a $k^{-5/3}$ Kolmogorov cascade $E(k) = C_K \varepsilon^{2/3} k^{-5/3}$ (where C_K is the Kolmogorov constant), one can adjust the constant C_s so that the ensemble-averaged subgrid kinetic energy dissipation is identical to ε . An approximate value for the constant is

$$C_s \approx \frac{1}{\pi} \left(\frac{3C_K}{2} \right)^{-3/4} \quad (8.62)$$

For a Kolmogorov constant of 1.4, which is obtained by measurements in the atmosphere, this yields, $C_s \approx 0.18$. Most workers prefer $C_s = 0.1$ —a value for which Smagorinsky's model behaves reasonably well for free-shear flows and for channel flow. However, the Smagorinsky constant C_s is required to have a sensible value to avoid excessive damping of resolved structures and the grid size Δ , as an indication of characteristic length scale, separates large- and small-scale eddies from each other

and is considered to be an average cell size. It is calculated for three-dimensional elements as follows:

$$\Delta = f(\Delta x_1 \Delta x_2, \Delta x_3)^{1/2} \quad (8.63)$$

Note that the above definition of mesh size can be changed to the usual finite element mesh size as discussed in [Chapter 4](#).

Despite increasing interest in developing more advanced subgrid scale stress models, Smagorinsky's model is still successfully used.

8.5 Detached eddy simulation (DES) and monotonically integrated LES (MILES)

The large eddy simulation (LES), despite less use of empirical relations, needs a very high computational overhead compared to RANS models. This is due to the fact that LES needs a very fine grid in the flow direction to capture flow-aligned streak-like structures occurring in the boundary layers. Motivated by this Spalart et al. [27] suggested an approach that attempts to combine the best features of RANS and LES. This approach is referred to as the detached eddy simulation (DES). This hybrid method reduces to RANS near solid boundaries and LES away from the wall. A minor modification to the SA model presented previously does the trick. Such a model will take advantage of RANS in the thin shear layers close to the walls where RANS models are calibrated. Away from the wall in the separated regions large eddies are resolved.

The model used will be the same as the one in [Section 8.2.2](#) except that the shortest distance to the wall, y , is modified in such a way that the model calculates a RANS eddy viscosity close to the walls and SGS eddy viscosity away from the wall. The modification is simple and given as

$$\tilde{y} = \min(y, C_{DES}\Delta) \quad (8.64)$$

Δ has the same meaning as discussed in the previous section. The constant C_{DES} was calibrated for homogeneous turbulence as 0.65. It is now possible to see that close to the walls Δ is larger and the model becomes a RANS model. However, away from the wall the model becomes one for calculating the SGS eddy viscosity [20]. Obviously the difficulty of where and how to fix the grid interface between the RANS and LES zones arises. Two possibilities exist to define this interface. The interface location for the differing models is either explicitly specified, or, based on length scale compatibility, allowed to naturally locate. With the latter approach the location is strongly grid controlled. When explicitly specified (based on turbulence physics grounds), length scale smoothing is necessary to enhance results [28].

The MILES approach [29–31] is similar to LES but instead of using the eddy viscosity, numerical diffusion is used to drain turbulence.

8.6 Direct numerical simulation (DNS)

The direct numerical simulation method can be used to solve all turbulence length scales including the *Kolmogorov* length scale given by Eq. (8.1). The standard Navier-Stokes equation without any modeling is adequate to compute all turbulence scales. The difficulty here is the prohibitively expensive computing cost required to carry out a calculation even at a very small Reynolds number. The enhanced computational overhead is mainly due to the extremely fine mesh necessary to carry out the calculation and the need for higher-order accurate numerical schemes. The number of nodes necessary to resolve all scales in a three-dimensional flow problem may be written in terms of the Reynolds number as (derived based on the assumption that the Kolmogorov length scales are solved)

$$\text{No. Nodes} = Re^{9/4} \quad (8.65)$$

Similarly the time step in a calculation is limited by the Kolmogorov time scale in Eq. (8.3). The time step size calculated from the time scale is [32]

$$\Delta t = \frac{0.003H}{u_T \sqrt{(Re_T)}} \quad (8.66)$$

where u_T is the shear velocity and $Re_T = u_T H / 2\nu$ is the turbulence Reynolds number [32].

Although DNS can resolve all turbulence length scales, the currently available computing facilities allow only very small Reynolds number turbulent flow calculations. The turbulence modeling approaches discussed in the previous sections (predominantly RANS) will not be replaced for the foreseeable future.

8.7 Concluding remarks

This chapter was intended to give a brief summary of different turbulence solution techniques. We hope we have summarized all the essential information necessary for a fluid dynamist. The turbulence modeling field is so vast, it may require several books to cover the full details. We recommend the interested reader to refer to the turbulence modeling books listed at the end of this chapter for further details.

References

- [1] A.N. Kolmogorov, Local structure of turbulence in incompressible viscous fluid for very large Reynolds number, *Doklady Akad. Nauk SSR* 30 (1941) 299–303.
- [2] B.E. Launder, B. Spalding, *Mathematical Models of Turbulence*, Academic Press, New York, 1972.

- [3] T. Cebeci, A.M.O. Smith, *Analysis of Turbulent Boundary Layers*, Academic Press, New York, 1974.
- [4] D.C. Wilcox, *Turbulence Modelling for CFD*, DCW Industries Inc., La Canada, CA, 1992.
- [5] M. Wolfstein, Some solutions of plane turbulent impinging jets, *Trans. ASME J. Basic Eng.* 92 (1970) 915–922.
- [6] P.R. Spalart, S.R. Allmaras, A one-equation turbulence model for aerodynamic flows, *AIAA Paper 92-0439*, AIAA 30th Aerospace Sciences Meeting, 1992.
- [7] W.P. Jones, B.E. Launder, The prediction of laminarization with a two-equation model of turbulence, *Int. J. Heat Mass Transfer* 15 (1972) 301–314.
- [8] C.K.G. Lam, K. Bremhorst, A modified form of the $\kappa - \varepsilon$ model for predicting wall turbulence, *Trans. ASME J. Fluids Eng.* 103 (1981) 456–460.
- [9] S. Fan, B. Lakshminarayana, M. Barnett, Low-Reynolds-number $\kappa - \varepsilon$ model for unsteady turbulent boundary layer flows, *AIAA J.* 31 (1993) 1777–1784.
- [10] O. Hassan, K. Morgan, J. Peraire, An implicit finite element method for high speed flows, *Int. J. Numer. Methods Eng.* 32 (1991) 183–205.
- [11] K.A. Sorensen, A Multigrid Accelerated Procedure for the Solution of Compressible Fluid Flows on Unstructured Hybrid Meshes, Ph.D. thesis, School of Engineering, University of Wales Swansea, UK, 2001.
- [12] E. Fares, W. Schröder, A differential equation for approximate wall distance, *Int. J. Numer. Methods Fluids* 39 (2002) 743–762.
- [13] P.G. Tucker, Differential equation based wall distance computation for DES and RANS, *J. Comput. Phys.* 190 (2003) 229–248.
- [14] C.-B. Liu, P. Nithiarasu, P.G. Tucker, Wall distance calculation using the Eikonal/Hamilton-Jacobi equations on unstructured meshes: A finite element approach, *Eng. Comput.* 27 (5–6) (2010) 645–657.
- [15] P. Nithiarasu, C.-B. Liu, An artificial compressibility based characteristic based split (CBS) scheme for steady and unsteady turbulent incompressible flows, *Comput. Methods Appl. Mech. Eng.* 195 (2006) 2961–2982.
- [16] S.H. Johansson, L. Davidson, E. Olsson, Numerical simulation of vortex shedding past triangular cylinders at high Reynolds number using a $\kappa - \varepsilon$ model, *Int. J. Numer. Methods Fluids* 16 (1993) 859–878.
- [17] P.A. Durbin, Separated flow computations using the $\kappa - \varepsilon - v^2$ model, *AIAA J.* 33 (1995) 659–664.
- [18] G. Bosch, W. Rodi, Simulation of vortex shedding past a square cylinder, *Int. J. Numer. Methods Fluids* 28 (1998) 601–616.
- [19] M. Tutar, A.E. Holdo, Computational modelling of flow around a circular cylinder in sub-critical flow regime with various turbulence models, *Int. J. Numer. Methods Fluids* 35 (2001) 763–784.
- [20] G. Constantinescu, C. Matthieu, K. Squires, Turbulence modelling applied to flow over a sphere, *AIAA J.* 41 (2003) 1733–1742.
- [21] J. Laufer, Investigation of turbulent flow in a two-dimensional channel, *NACA Rep.* 1053 (1951) 1247–1266.

- [22] M.K. Denham, P. Briard, M.A. Patrick, A directionally-sensitive laser anemometer for velocity measurements in highly turbulent flows, *J. Phys. E: Sci. Instrum.* 8 (1975) 681–683.
- [23] Z. Yang, T.H. Shih, New time scale based $\kappa - \varepsilon$ model for near-wall turbulence, *AIAA J.* 31 (1993) 1191–1198.
- [24] H. Schlichting, *Boundary Layer Theory*, Pergamon Press, London, 1955.
- [25] J. Smagorinsky, General circulation experiments with the primitive equations. I. The basic experiment, *Mon. Weather Rev.* 91 (1963) 99.
- [26] M. Germano, Turbulence: the filtering approach, *J. Fluid Mech.* 238 (1992) 325.
- [27] P.R. Spalart, W.H. Jou, M. Strelets, S.R. Allmaras, Comments on the feasibility of LES for wings, and on a hybrid RANS/LES approach, in: C. Liu, Z. Liu (Eds.), *Advances in DNS/LES: First AFOSR International Conference on DNS/LES*, Greyden, Columbus, OH, 1997.
- [28] P.G. Tucker, L. Davidson, Zonal k-1 based large eddy simulations, *Comput. Fluids* 33 (2004) 267–287.
- [29] J.P. Boris, F.F. Grinstein, E.S. Oran, R.L. Kolbe, New insights into large eddy simulation, *Fluid Dyn. Res.* 10 (1992) 199–228.
- [30] P.G. Tucker, Novel MILES computations for jet flows and noise, *Int. J. Heat Fluid Flow* 25 (2004) 625–635.
- [31] W.J. Rider, Effective subgrid modeling from the ILES simulation of compressible turbulence, *J. Fluids Eng.* 129 (2007) 1493–1496.
- [32] J. Kim, P. Moin, R. Moser, Turbulence statistics in fully developed channel flow at low Reynolds numbers, *J. Fluid Mech.* 177 (1987) 133–166.

Generalized Flow and Heat Transfer in Porous Media

9

9.1 Introduction

Flow through porous media has been recognized as a fluid dynamics topic which has applications in a variety of engineering fields including seepage through soil, concrete, insulating media, and packed beds; flows in heat exchangers and alloy solidification; and cooling of electronic components. Several books on porous media flow and heat transfer have been published covering both analytical and numerical solution methodologies [1–4].

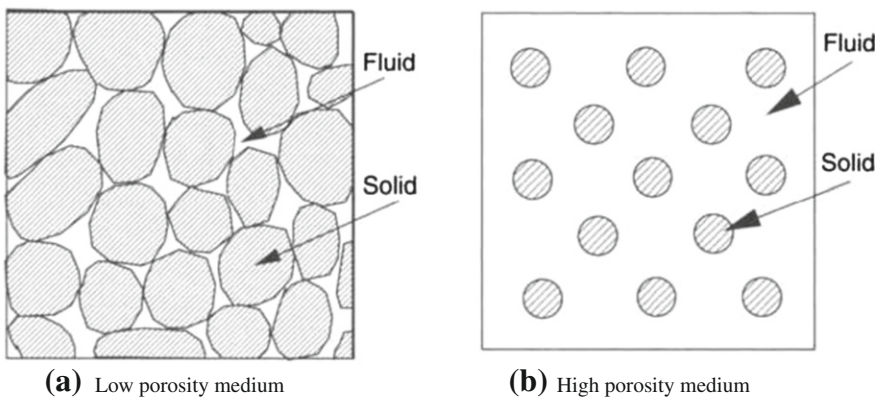
It appears that the usage of porous media flow models is divided into two parts. In the first of these we generally consider materials of low porosity (Fig. 9.1a) and relate *a priori* by physical law the quantity of flow passing through all the pores in the appropriate coordinate directions. Here we find that at low velocities, as generally occur here, the relationship is linear and the quantity of flow is related linearly to the pressure gradient. Thus, we generally write that (Darcy's law [5])

$$u_i = -\frac{\kappa}{\mu} \left(\frac{\partial p}{\partial x_i} - \rho g_i \right) \quad (9.1)$$

where u_i are the seepage velocity components, μ is the dynamic viscosity of the fluid, and κ is permeability of the medium expressed in m^2 . The permeability may be directional and in such situations, κ will be a tensor [1]. We now concentrate on the balance of total quantities and consider a unit volume of porous medium to which we apply the mass conservation (incompressible flow) $\partial u_i / \partial x_i = 0$. Using directly the linear relationship [Eq. (9.1)] we immediately find that the following equation is obtained (ignoring the gravity effects):

$$\frac{\partial}{\partial x_i} \left(-\frac{\kappa}{\mu} \frac{\partial p}{\partial x_i} \right) = 0 \quad (9.2)$$

The problem now becomes simply a solution to a potential equation if either the pressure or its gradients are known at the boundaries and we have discussed such solutions using the finite element method in Ref. [1] and in Chapter 1 of this book. However, more recent and alternative application of porous media has been used at high porosities. We refer to this second category as a high-porosity model in which the porosity is large, often approaching unity. Such a model is extremely useful for some problems. For instance, a network of conduits distributed throughout the fluid

**FIGURE 9.1**

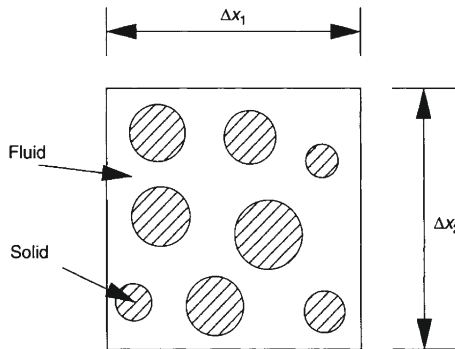
Typical examples of porous media.

and kept rigidly in space by external means is an example (Fig. 9.1b). This collection of obstructions will exact a force on the fluid in a complex manner. Now the relation between the force and the velocity is no longer linear as in the first model but can be determined by suitable experiments. Such models are generally useful for examples such as cooling of electronic components, flow past heat exchanger pipes, etc. At very high porosity we generally consider the equations to be almost those of Navier-Stokes to which an experimental addition of measured force values caused by the solid is carried out [6–10]. Various quadratic equations relating this force per unit volume to the velocity field and to the solid matrix geometry are available in the literature.

Clearly such models are generally valid if the volume of the obstructions is fairly small compared to the total volume [11, 12] or if an interface is shared between a saturated porous medium and flow with no obstructions [13–15]. However, in principle this model can be used at low porosities but it will be very expensive. Thus, the low- and high-porosity models can be considered as two models dealing with different phenomena. A number of examples with the first type of model are included in Ref. [1] and we shall not consider this further again. However, we shall show how the problems can be dealt with using the generalized high-porosity models. In the following sections we derive the high-porosity model and present some examples.

9.2 A generalized porous medium flow approach

In this section, a generalized model for solving porous medium flows will be presented. Let us consider the balance of mass, momentum, and energy for two-dimensional flow in a fluid-saturated porous medium of variable porosity. We shall assume the medium to be isotropic with constant physical properties, except for the medium porosity. Let a^f be the fraction of area (nondimensional) available for flow per unit cross-sectional area (Fig. 9.2), at a location in a given direction. In fact, a^f is an averaged

**FIGURE 9.2**

Fluid-saturated porous medium. Infinitesimal control volume.

quantity, the average being taken over the length scale of the voids (or the length scale of the particles, if the porous bed is made up of particles) in the flow direction. For an isotropic porous bed, a^f will be identical in all directions and can also be equal to the local bed porosity, ε . In spite of averaging over the void length scale, the fractional area a^f may vary from location to location on the macro-length scale “L” of the physical problem, due to the variation of the bed porosity.

The porosity, ε , of the medium is defined as

$$\varepsilon = \frac{\text{void volume}}{\text{total volume}} = \frac{a^f \Delta x_1 \Delta x_2}{\Delta x_1 \Delta x_2} = a^f \quad (9.3)$$

Now, the mass balance of an arbitrary control volume, as shown in Fig. 9.2, gives [9]

$$\frac{\partial \rho^f}{\partial t} + \frac{\partial (\rho^f u_i^f)}{\partial x_i} = 0 \quad (9.4)$$

where the superscript “ f ” stands for fluid, ρ is the density, and u_i are the velocity components in the x_i directions, respectively. The volume-averaged velocity components may be defined as [4]

$$u_i = \varepsilon u_i^f \quad (9.5)$$

Equation (9.4) can be simplified for an incompressible flow (constant density) as follows:

$$\frac{\partial u_i}{\partial x_i} = 0 \quad (9.6)$$

Similarly, the equation for momentum balance can be derived as

$$\frac{\rho^f}{\varepsilon} \left[\frac{\partial u_i}{\partial t} + \frac{\partial}{\partial x_j} \left(\frac{u_i u_j}{\varepsilon} \right) \right] = -\frac{1}{\varepsilon} \frac{\partial}{\partial x_i} (p^f \varepsilon) + \frac{\mu_e}{\varepsilon} \frac{\partial^2 u_i}{\partial x_i^2} - D_{x_i} + \rho^f g_i \quad (9.7)$$

where μ_e is the equivalent viscosity, p^f is the fluid pressure; g_i is the acceleration due to gravity, and D_{x_i} is the matrix drag per unit volume of the porous medium. [Equation \(9.7\)](#) may be written in conservation form as (not essential for solving incompressible flow problems)

$$\frac{1}{\varepsilon} \left[\frac{\partial U_i}{\partial t} + \frac{\partial}{\partial x_j} \left(\frac{U_i u_j}{\varepsilon} \right) \right] = -\frac{1}{\varepsilon} \frac{\partial}{\partial x_i} (p^f \varepsilon) + \frac{1}{\varepsilon} \frac{\partial \tau_{ij}}{\partial x_j} - D_{x_i} + \rho^f g_i \quad (9.8)$$

where $U_i = \rho^f u_i$ and

$$\tau_{ij} = \mu_e \left(\frac{\partial u_i}{\partial x_j} + \frac{\partial u_j}{\partial x_i} \right) \quad (9.9)$$

Several experimental correlations are available for the matrix drag, D_{x_i} , and one of them is the experimental data reported by Ergun [16]. The Ergun correlation is written as

$$D_{x_i} = \frac{\mu^f u_i}{\kappa} + \frac{1.75}{\sqrt{150}} \frac{\rho^f}{\sqrt{\kappa}} \frac{|\mathbf{u}|}{\varepsilon^{3/2}} u_i \quad (9.10)$$

where \mathbf{u} is the velocity vector in the field. The final form of the governing equations for incompressible flow through a porous medium in dimensional form may be written as

Continuity

$$\frac{\partial u_i}{\partial x_i} = 0 \quad (9.11)$$

Momentum

$$\begin{aligned} \frac{\rho^f}{\varepsilon} \left[\frac{\partial u_i}{\partial t} + \frac{\partial}{\partial x_j} \left(\frac{u_i u_j}{\varepsilon} \right) \right] &= -\frac{1}{\varepsilon} \frac{\partial}{\partial x_i} (p^f \varepsilon) + \frac{\mu_e}{\varepsilon} \frac{\partial^2 u_i}{\partial x_i^2} \\ &- \frac{\mu^f u_i}{\kappa} - \frac{1.75}{\sqrt{150}} \frac{\rho^f}{\sqrt{\kappa}} \frac{|\mathbf{u}|}{\varepsilon^{3/2}} u_i + \rho^f g_i \end{aligned} \quad (9.12)$$

If the porosity of the medium is small ($\varepsilon \rightarrow 0$) the velocity values will be small and the nonlinear term in [Eq. \(9.12\)](#) will also be small compared to the linear drag term. Thus, if the porosity approaches zero, the linear drag term (Darcy term) becomes prominent and all other terms will be negligibly small, leading to an approximation of [Eq. \(9.1\)](#). On the other hand if the porosity approaches unity ($\varepsilon \rightarrow 1$), the incompressible fluid equations are recovered. It is therefore possible to solve problems in which both single phase fluid and porous medium are part of the same domain [13]. Thus applications such as alloy solidification, which involves solid, liquid, and porous mushy regions, can be tackled easily using the proposed approach [17]. The energy conservation equation is also derived in a similar manner. The final form of the energy equation is

Energy

$$\left[\varepsilon(\rho c_p)^f + (1 - \varepsilon)(\rho c_p)^s \right] \frac{\partial T}{\partial t} + (\rho c_p)^f u_i \frac{\partial T}{\partial x_i} = k \left(\frac{\partial^2 T}{\partial x_i^2} \right) \quad (9.13)$$

In the above equation, c_p is the specific heat, T is the temperature, and k is the equivalent thermal conductivity. The superscripts f and s stand for the fluid and solid phases, respectively.

It should be noted that the permeability and thermal conductivity values can be directional, in which case they are tensors.

9.2.1 Nondimensional scales

The following final form of the nondimensional equations may be obtained by suitable scaling. The nondimensional scales used here are taken based on the assumption that the energy and momentum equations are weakly coupled via local density variation (see [Chapter 6](#)).

Continuity equation

$$\frac{\partial u_i^*}{\partial x_i^*} = 0 \quad (9.14)$$

Momentum equations

$$\begin{aligned} \frac{1}{\varepsilon} \frac{\partial u_i^*}{\partial t^*} + \frac{1}{\varepsilon} u_j^* \frac{\partial}{\partial x_j^*} \left(\frac{u_i^*}{\varepsilon} \right) &= -\frac{1}{\varepsilon} \frac{\partial}{\partial x_i^*} (\varepsilon p_f^*) - \frac{u_i^*}{Re Da} \\ &- \frac{1.75}{\sqrt{150}} \frac{|\mathbf{u}^*|}{\sqrt{Da}} \frac{u_i^*}{\varepsilon^{3/2}} + \frac{J}{Re \varepsilon} \left(\frac{\partial^2 u_i^*}{\partial x_i^{*2}} \right) + \gamma_i \frac{Gr}{Re^2} T^* \end{aligned} \quad (9.15)$$

Energy equation

$$\sigma \frac{\partial T^*}{\partial t^*} + u_i^* \frac{\partial T^*}{\partial x_i^*} = \frac{k^*}{Re Pr} \left(\frac{\partial^2 T^*}{\partial x_i^{*2}} \right) \quad (9.16)$$

In the above equations, the parameters governing the flow and heat transfer are the Darcy number (Da), Reynolds number (Re), Prandtl number (Pr), Grashoff number (Gr), ratio of heat capacities (σ), porosity of the medium (ε), conductivity ratio (k^*), and viscosity ratio (J), and γ_i is the unit vector in the buoyancy direction. The definitions for the scales and nondimensional parameters are

$$\begin{aligned} x_i^* &= \frac{x_i}{L}, \quad u_i^* = \frac{u_i}{u_a}, \quad t^* = \frac{tu_a}{L}, \quad p_f^* = \frac{p_f}{\rho_f u_a^2}, \quad T^* = \frac{T - T_a}{T_w - T_a}, \quad J = \frac{\mu_e}{\mu_f} \\ \sigma &= \frac{\varepsilon(\rho c_p)_f + (1 - \varepsilon)(\rho c_p)_s}{(\rho c_p)_f}, \quad k^* = \frac{k}{k_f}, \quad Re = \frac{\rho_f u_a L}{\mu_f} \\ Pr &= \frac{\nu_f}{\alpha_f}, \quad Da = \frac{\kappa}{L^2}, \quad Gr = \frac{g \beta \Delta T L^3}{\nu_f^2} \end{aligned} \quad (9.17)$$

where subscripts a and f respectively refer to a free stream quantity and fluid and the subscript w indicates a wall. The above scales are suitable for most forced and mixed convection problems. However, for buoyancy driven flows, it is convenient to handle the equations using the following definition of the Rayleigh number (Ra), i.e.,

$$Ra = \frac{g\beta\Delta TL^3}{\nu\alpha} \quad (9.18)$$

where the following different scales need to be employed in solving natural convection problems:

$$u_i^* = \frac{u_i L}{\alpha_f}, \quad t^* = \frac{t \alpha_f}{L^2}, \quad p^* = \frac{p L^2}{\rho_f \alpha_f^2} \quad (9.19)$$

The nondimensional governing equations for natural convection are

Continuity equation

$$\frac{\partial u_i^*}{\partial x_i^*} = 0 \quad (9.20)$$

Momentum equations

$$\begin{aligned} \frac{1}{\varepsilon} \frac{\partial u_i^*}{\partial t^*} + \frac{1}{\varepsilon} u_j^* \frac{\partial}{\partial x_j^*} \left(\frac{u_i^*}{\varepsilon} \right) &= -\frac{1}{\varepsilon} \frac{\partial}{\partial x_i^*} (\varepsilon p_f^*) - \frac{Pr u_i^*}{Da} \\ -\frac{1.75}{\sqrt{150}} \frac{|\mathbf{u}^*|}{\sqrt{Da}} \frac{u_i^*}{\varepsilon^{3/2}} + \frac{J Pr}{\varepsilon} \left(\frac{\partial^2 u_i^*}{\partial x_i^{*2}} \right) &+ \gamma_i Ra Pr T^* \end{aligned} \quad (9.21)$$

Energy equation

$$\sigma \frac{\partial T^*}{\partial t^*} + u_i^* \frac{\partial T^*}{\partial x_i^*} = k^* \left(\frac{\partial^2 T^*}{\partial x_i^{*2}} \right) \quad (9.22)$$

Other alternative scales are possible and the appropriate references should be consulted to learn more about scaling. In the above formulation, the buoyancy effects are incorporated by invoking the Boussinesq approximation as discussed in [Chapter 6](#). The kinematic viscosity ν , used in the above scales, is defined as

$$\nu = \frac{\mu}{\rho} \quad (9.23)$$

and α is the thermal diffusivity, given as

$$\alpha_f = \frac{k_f}{(\rho c_p)_f} \quad (9.24)$$

It may be observed that the scales and nondimensional parameters are defined by using the fluid properties. Often, a quantity called the Darcy-Rayleigh number is used in the literature as a governing nondimensional parameter for Darcy flow. This is the product of the Darcy (Da) and fluid Rayleigh (Ra) numbers defined previously. For isothermal flow problems, the energy equation is not solved.

9.3 Discretization procedure

The CBS scheme will be employed to solve the porous medium flow equations. In this context the same four steps, with minor modifications, will be utilized as discussed in [Chapter 3](#).

The momentum equation is subjected to the CBS procedure and finite element discretization, as discussed in [Chapter 3](#). Following Eq. (3.51), we may write the first step of the CBS algorithm for porous medium equations as (assuming constant ε)

$$\begin{aligned} \frac{\rho^f}{\varepsilon} \Delta \tilde{\mathbf{u}}^* = & -\mathbf{M}_u^{-1} \Delta t \left[\left(\frac{\rho^f}{\varepsilon^2} \mathbf{C}_u \tilde{\mathbf{u}}^n + \frac{1}{\varepsilon} \mathbf{K}_\tau \tilde{\mathbf{u}}^{n+\theta_3} + \mathbf{M}_d \tilde{\mathbf{u}}^{n+\theta_4} - \mathbf{f}^n \right) \right. \\ & \left. - \Delta t \left(\frac{\rho^f}{\varepsilon^2} \mathbf{K}_u \tilde{\mathbf{u}} + \mathbf{C}_s \tilde{\mathbf{u}} + \mathbf{f}_s \right)^n \right] \end{aligned} \quad (9.25)$$

All the matrices except \mathbf{M}_d and \mathbf{C}_s are defined and described in [Chapter 3](#). The undefined matrices are

$$\mathbf{M}_d = D_p \mathbf{M}_u \quad \text{and} \quad \mathbf{C}_s = -\frac{1}{2} \int_{\Omega} [\nabla^T(\mathbf{u} \mathbf{N}_u)]^T D_p (\mathbf{u} \mathbf{N}_u) d\Omega \quad (9.26)$$

where

$$D_p = \left[\frac{\mu^f}{\kappa} + \frac{1.75}{\sqrt{150}} \frac{\rho^f}{\sqrt{\kappa}} \frac{|\mathbf{u}|^n}{\varepsilon^{3/2}} \right] \quad (9.27)$$

For a smooth solution, the parameter θ_4 should be nonzero and equal to or below unity. $\theta_3 = 0$ gives a semi-implicit scheme and $\theta_3 = 1$ gives a quasi-implicit scheme. The superscript θ should be interpreted as

$$f^{n+\theta} = \theta f^{n+1} + (1 - \theta) f^n \quad (9.28)$$

where the superscript n indicates the n th time iteration. Following the CBS algorithm in [Chapter 3](#), semi- and quasi-implicit forms of the method are discussed in the next subsection.

9.3.1 Semi- and quasi-implicit forms

Single phase incompressible fluid flow problems can be solved in a fully explicit form, which is quite popular in fluid dynamics calculations [18]. However, a solution to the generalized porous medium equations using a fully explicit form has been less successful although some recent attempts have been made [19]. This is mainly due to the large values of the solid matrix drag terms, especially at smaller Darcy numbers. In order to eliminate some of the time step restrictions imposed by these terms, schemes other than the fully explicit forms are discussed below.

In the semi-implicit (SI) form [20], the porous medium source terms are treated implicitly. In other words, $\theta_1 = \theta_2 = \theta_4 = 1$ [see Eqs. (3.56) and (9.25)] and $\theta_3 = 0$, i.e.,

$$\begin{aligned}\tilde{\mathbf{u}}^* = & \left[\frac{\rho_f}{\varepsilon} + \Delta t D_p \right]^{-1} \left\{ \frac{\rho_f}{\varepsilon} \mathbf{u}^n - \mathbf{M}_u^{-1} \Delta t \left[\left(\frac{\rho}{\varepsilon^2} \mathbf{C}_u \tilde{\mathbf{u}}^n + \frac{1}{\varepsilon} \mathbf{K}_\tau \tilde{\mathbf{u}}^n - \mathbf{f}^n \right) \right. \right. \\ & \left. \left. - \Delta t \left(\frac{\rho_f}{\varepsilon^2} \mathbf{K}_u \tilde{\mathbf{u}} + \mathbf{C}_s \tilde{\mathbf{u}} + \mathbf{f}_s \right)^n \right] \right\} \end{aligned} \quad (9.29)$$

The Step 2 pressure calculation becomes [see Eq. (3.56)]

$$\Delta t \mathbf{H} \tilde{\mathbf{p}}^{n+1} = \left[\frac{\rho_f}{\varepsilon} + \Delta t D_p \right] \mathbf{G} \tilde{\mathbf{u}}^* \quad (9.30)$$

Step 3 is given as

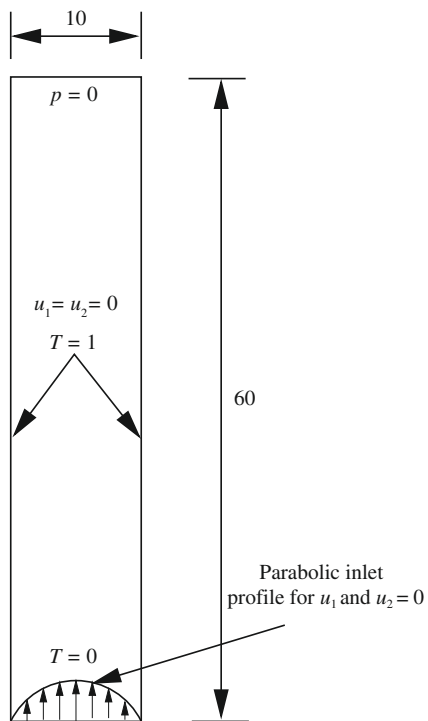
$$\Delta \tilde{\mathbf{u}}^{**} = \Delta \tilde{\mathbf{u}} - \Delta \tilde{\mathbf{u}}^* = -\Delta t \left[\frac{\rho_f}{\varepsilon} + \Delta t D_p \right]^{-1} \mathbf{G} \tilde{\mathbf{p}}^{n+1} \quad (9.31)$$

As seen the semi-implicit form described at Step 1 avoids simultaneous solution of the algebraic equations [20]. A suitable Poisson equation solver is required at Step 2. The quasi-implicit (QI) [21] form is very similar to that of the above scheme but now the viscous, second-order terms are also treated implicitly ($\theta_3 = 1$) [9]. The important difference, however, is that the quasi-implicit scheme does not benefit from mass lumping when solving for the intermediate velocity values. A simultaneous solution of the LHS matrices is essential here. It has been proven that both the QI and SI schemes generally perform well as shown elsewhere [22].

For nonisothermal flows, Eq. (9.13) is also solved along with the three steps of isothermal flows discussed above. To solve this convection-diffusion equation, any of the methods discussed in Chapter 2 may be employed. For forced convective heat transfer problems, the flow field may be established first before solving for the temperature field. However, in buoyancy driven flows a weak, simultaneous coupling between temperature and flow field exists and thus the flow and temperature equations should be solved simultaneously.

9.4 Forced convection

Flow through packed beds is important in many chemical engineering applications. Generally, the grain size in the packed beds will vary depending on the application. As the particle size increases, the packing close to the walls will become nonuniform thereby creating a channelling effect close to the solid walls. In such cases, the porosity value can be close to unity near the walls but will decrease to a free stream value away from the walls.

**FIGURE 9.3**

Forced convection in a channel filled with a variable porosity medium. Geometry and boundary conditions.

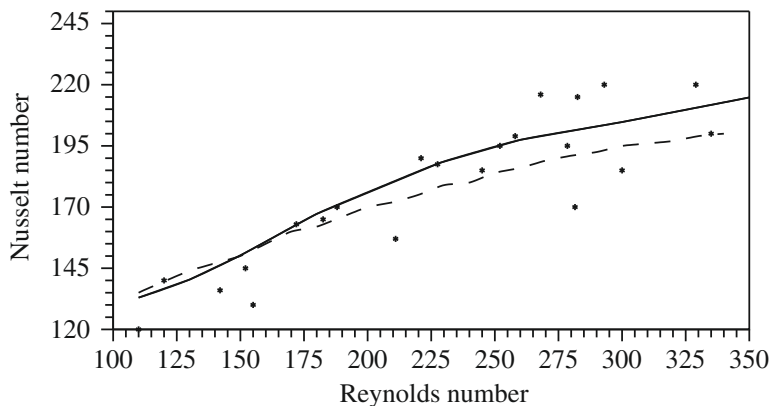
In such situations, the ability to vary the porosity within the domain itself is essential in order to obtain a correct solution. Although the theoretical determination of the near-wall porosity variation is difficult, there are some experimental correlations available to tackle this issue. One such widely employed correlation, given by Berenati and Brosilow [23], will be used here, i.e.,

$$\varepsilon = \varepsilon_e \left[1 + \exp \left(-\frac{cl}{d_p} \right) \right] \quad (9.32)$$

where ε_e is the free stream bed porosity taken to be equal to 0.39, c is an empirical constant ($c = 2$ for $d_p = 5$ mm), and l is the shortest distance to the wall. In general, the problem in this case is formulated based on the particle size d_p , i.e., the Reynolds number is based on the particle size.

Example 9.1. Forced convection heat transfer in a packed channel

Figure 9.3 shows the problem definition of forced flow through a packed bed. The inlet channel width is 10 times the size of the grain. The length of the channel is 10 times that of the inlet width. Zero pressure conditions are assumed at the exit.

**FIGURE 9.4**

Forced convection in a channel. Comparison of Nusselt number with experimental data for different particle Reynolds numbers. Points—experimental [24]; dashed line—numerical [24]; solid line—CBS.

The inlet velocity profile is parabolic and no-slip boundary conditions apply on the solid side walls. Both the walls are assumed to be at a higher, uniform temperature than the inlet fluid temperature. The analysis is carried out for different particle Reynolds numbers ranging from 150 to 350. The *quasi-implicit* (QI) scheme with $\theta_3 = \theta_4 = 1$ has been employed to solve this problem. A nonuniform mesh with triangular elements was also used in the analysis. The mesh is fine close to the walls and coarse toward the center. The total number of nodes and elements used in the calculation is 3003 and 5776, respectively.

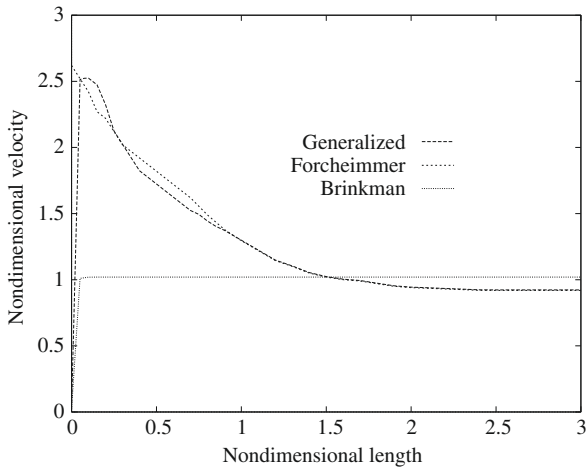
Figure 9.4 shows a comparison of the calculated steady-state average Nusselt number distribution on a hot wall with the available experimental and numerical data. The Nusselt number is calculated as

$$Nu = \frac{hL}{k} = \int_0^L \frac{\partial T}{\partial x_1} dl \quad (9.33)$$

Figure 9.5 shows the difference between the generalized model and the Brinkman [25] and Forcheimme [26] extensions for the velocity profiles close to the wall in a variable porosity medium at steady state. As may be seen the Forcheimme and Brinkman extensions fail to predict the channelling effect close to the wall. While the Brinkman extension is insensitive to porosity values, the Forcheimme model does not predict the viscous effect close to the channel walls.

9.5 Natural convection

The fluid flow in a variable porosity medium within an enclosed cavity under the influence of buoyancy is another interesting and difficult problem to analyze. In order

**FIGURE 9.5**

Forced convection in a channel. Comparison between the generalized model and the Forcheimmer and Brinkman extensions to Darcy's law.

to study such a problem, an enclosure packed with a fluid-saturated porous medium is considered as in the following example.

Example 9.2. Buoyancy driven convection in a packed enclosure

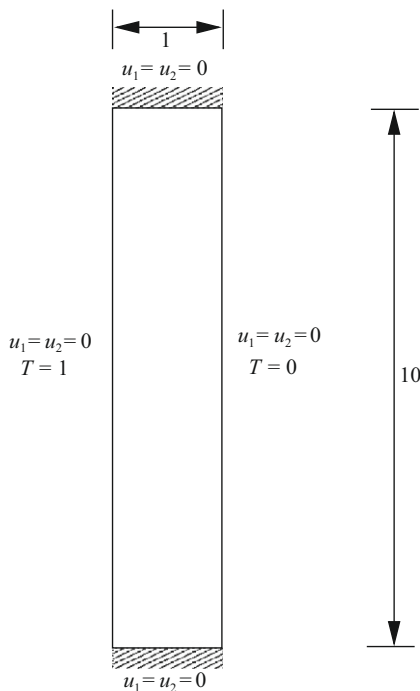
The aspect ratio of the enclosure is 10 (ratio between height and width). All the enclosure walls are subjected to “no-slip” boundary conditions. The left vertical wall is assumed to be at a higher, uniform temperature than the right side wall. Both the horizontal walls are assumed to be insulated (Fig. 9.6). The properties of the saturating fluid are assumed to be constant other than that of the density. The density variation is invoked by the Boussinesq approximation.

Table 9.1 shows the steady-state quantitative results and a comparison with the available numerical and experimental data. These data were obtained on a nonuniform structured 61x61 mesh. The accuracy of the prediction can be improved by further refinement of the mesh. An extremely fine mesh is essential near the cavity walls in order to predict the channelling effect in this region. In Table 9.1, experimental data is obtained from Ref. [27] and the numerical data for comparison is obtained from Ref. [28]. The following Nusselt number relation was used for this problem:

$$Nu = \frac{1}{L} \int_0^L \frac{\partial T}{\partial x} dx \quad (9.34)$$

9.5.1 Constant-porosity medium

Problems where the variation in porosity is of less significance normally occur in porous media that have small solid particle sizes. For instance, thermal insulation is one such example where the variation in porosity near the solid walls is not important

**FIGURE 9.6**

Natural convection in a fluid-saturated variable-porosity medium. Problem boundary conditions.

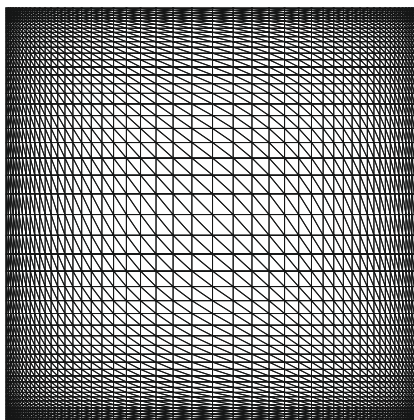
Table 9.1 Average Hot Wall Nusselt Number Distribution for Natural Convection in a Variable Porosity Medium, Aspect Ratio = 10

Fluid	d_p	ϵ_e	Pr	k^*	Ra	Experimental	Numerical	CBS
Water	5.7	0.39	7.1	1.929	1.830×10^7	2.595	2.405	2.684
					3.519×10^7	3.707	3.496	3.892
Ethyl alcohol	5.7	0.39	2.335	15.4	2.270×10^8	12.56	13.08	12.17
					3.121×10^8	15.13	15.57	14.28

but the uniform free stream porosity value can be very high. In order to investigate such media, a benchmark problem involving buoyancy driven convection in a square cavity has been solved.

Example 9.3. Buoyancy driven flow in a cavity filled with fluid-saturated constant-porosity medium

The problem definition is similar to the one shown in Fig. 9.6, the difference being that the aspect ratio is unity. The square enclosure is filled with a fluid-saturated

**FIGURE 9.7**

Buoyancy driven flow in a fluid-saturated porous medium. Finite element mesh (nodes: 2601, elements: 5000).

porous medium with constant and uniform properties except for the density, which is again incorporated via the Boussinesq approximation. A 51×51 nonuniform mesh (Fig. 9.7) is employed for this problem.

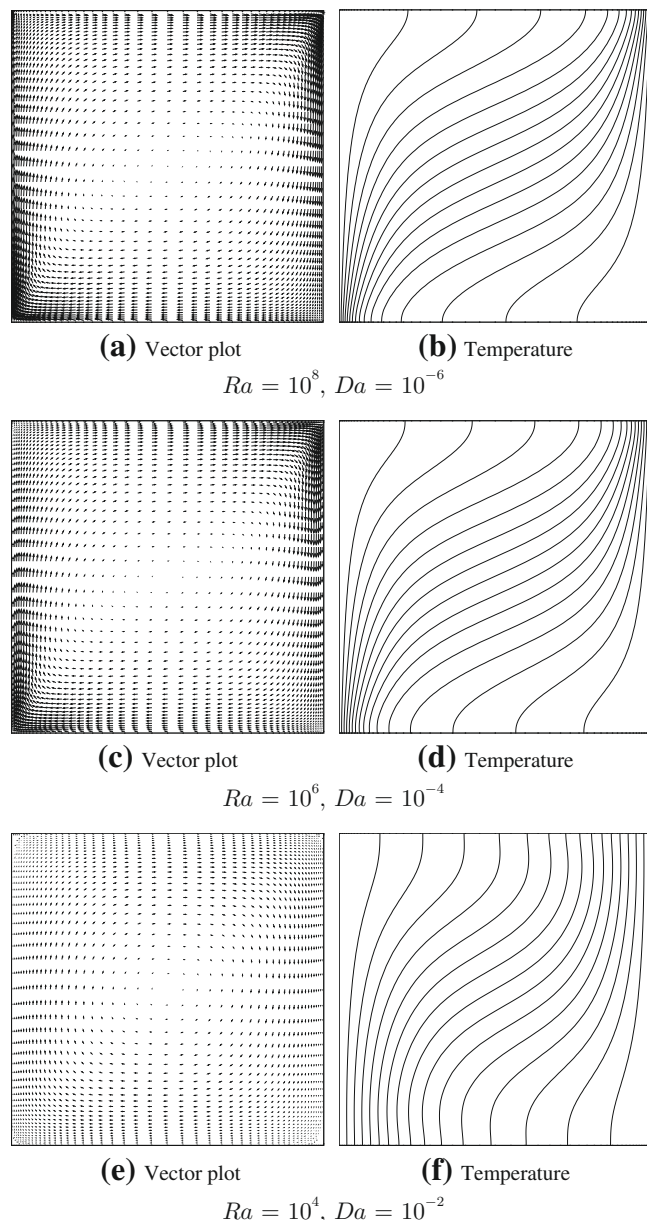
In Fig. 9.8, we show the velocity and temperature distribution at different Darcy and Rayleigh numbers. In this case the product of the Darcy and Rayleigh numbers is kept at a constant value in order to amplify the non-Darcy effects. It is clearly obvious that the maximum velocity in the Darcy flow regime, at a Darcy number of 10^{-6} , is located very close to the solid walls. The non-Darcy velocity profile, at a Darcy number of 10^{-2} , on the other hand looks very similar to that of a single phase fluid and the maximum velocity is located away from the solid walls. At a Darcy number of 10^{-4} the flow undergoes a transition from a Darcy flow regime to a non-Darcy flow regime. The temperature contours also undergo noticeable changes as the Darcy number increases from 10^{-6} to 10^{-2} .

Both the scheme and the model implementation have been designed in such a way that as the Darcy number increases, the flow approaches a single phase fluid flow, which is evident from Fig. 9.8.

In Table 9.2, the quantitative results obtained from the above analysis (only for the Darcy flow regime, $Da < 10^{-5}$) are compared with other available analytical and numerical results. In Table 9.2, the analytical solution has been obtained from Refs. [29], and “Numerical 1” and “Numerical 2” have been obtained from Refs. [30,31] respectively.

Example 9.4. Buoyancy driven convection in an axisymmetric enclosure filled with fluid-saturated constant-porosity medium

In order to compare the present numerical results with experimental data, an axisymmetric model was developed and a buoyancy driven flow problem was studied. The boundary and initial conditions are the same as for the previous problem,

**FIGURE 9.8**

Natural convection in a fluid-saturated porous, square enclosure. Vector plots and temperature contours for different Rayleigh and Darcy numbers, $Pr = 0.71$.

Table 9.2 Average Nusselt Number Comparison with Analytical and Numerical Results

$Ra^* = RaDa$	Nu			
	Analytical	Numerical 1	Numerical 2	CBS
10	—	1.07	—	1.08
50	1.98	—	2.02	1.96
100	3.09	3.09	3.27	3.02
500	8.40	—	—	8.38
1000	12.49	13.41	18.38	12.52

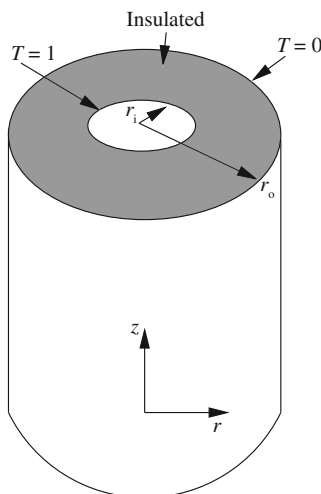


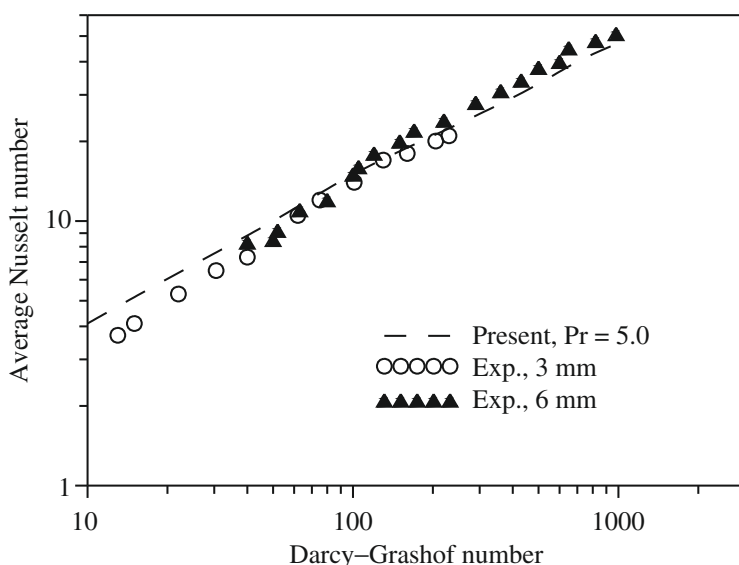
FIGURE 9.9

Natural convection in a fluid-saturated constant-porosity medium. Problem definition.

the main difference being in the definition of the geometry. In this case, the geometry is an annulus with a radius ratio (ratio between outer and inner radii) of 5.338 (see Fig. 9.9). The fluid used to saturate the medium is water with a Prandtl number of 5. The results are generated for different Grashof numbers (Ra/Pr) and compared with the experimental Nusselt number predictions as shown in Fig. 9.10. In general the agreement is excellent for the range of Grashof numbers considered.

9.6 Concluding remarks

In this chapter a brief summary of flow through porous media has been discussed. It is important to fully understand the concepts given in Chapter 3 before carrying out the porous medium flow calculations. The brief overview given in this chapter

**FIGURE 9.10**

Natural convection in a fluid-saturated constant-porosity medium within an annular enclosure. Comparison of hot wall steady-state Nusselt number with the experimental and numerical data [32].

provides the reader with essential knowledge on how the CBS scheme is extended to a nonstandard fluid dynamics problem.

References

- [1] O.C. Zienkiewicz, A.H.C. Chan, M. Pastor, B.A. Schrefler, T. Shiomi, Computational Geomechanics with Special Reference to Earthquake Engineering, John Wiley & Sons, Chichester, 1999.
- [2] R.W. Lewis, B.A. Schrefler, The Finite Element Method in the Deformation and Consolidation of Porous Media, John Wiley & Sons, Chichester, 1998.
- [3] M. Kaviany, Principles of Heat Transfer in Porous Media, Springer-Verlag, New York, 1991.
- [4] D.A. Nield, A. Bejan, Convection in Porous Media, Springer Verlag, New York, 1992.
- [5] H. Darcy, in: Victor Dalmont (Ed.), Les fontaines publiques de la ville de Dijon, Paris, 1856.
- [6] S. Whitaker, Diffusion and dispersion in porous media, Am. Inst. Chem. Eng. J. 13 (1961) 420–427.
- [7] K. Vafai, C.L. Tien, Boundary and inertia effects on flow and heat transfer in porous media, Int. J. Heat Mass Transfer 24 (1981) 195–203.

- [8] C.T. Hsu, P. Cheng, Thermal dispersion in a porous medium, *Int. J. Heat Mass Transfer* 33 (1990) 1587–1597.
- [9] P. Nithiarasu, K.N. Seetharamu, T. Sundararajan, Natural convective heat transfer in an enclosure filled with fluid saturated variable porosity medium, *Int. J. Heat Mass Transfer* 40 (1997) 3955–3967.
- [10] P. Nithiarasu, K.N. Seetharamu, T. Sundararajan, Finite element modelling of flow, heat and mass transfer in fluid saturated porous media, *Arch. Comput. Methods Eng., State of the Art Reviews* 9 (2002) 3–42.
- [11] K.I. Salas, A.M. Waas, Convective heat transfer in open cell metal foams, *J. Heat Transfer-Trans. ASME* 129 (9) (2007) 1217–1229.
- [12] G. Laschet, Forchheimer law derived by homogenization of gas flow in turbomachines, *J. Comput. Appl. Math.* 215 (2) (2008) 467–476.
- [13] N. Massarotti, P. Nithiarasu, O.C. Zienkiewicz, Porous medium - fluid interface problems. The finite element analysis by using the CBS procedure, *Int. J. Numer. Methods Heat Fluid Flow* 11 (2001) 473–490.
- [14] F. Arpino, A. Carotenuto, N. Massarotti, P. Nithiarasu, A robust model and numerical approach for solving solid oxide fuel cell (SOFC) problems, *Int. J. Numer. Methods Heat Fluid Flow* 18 (7–8) (2008) 811–834.
- [15] F. Arpino, A. Carotenuto, N. Massarotti, A. Mauro, New solutions for axial flow convection in porous and partly porous cylindrical domains, *Int. J. Heat Mass Transfer* 57 (1) (2013) 155–170.
- [16] S. Ergun, Fluid flow through packed column, *Chem. Eng. Prog.* 48 (1952) 89–94.
- [17] S.K. Sinha, T. Sundararajan, V.K. Garg, A variable property analysis of alloy solidification using the anisotropic porous medium approach, *Int. J. Heat Mass Transfer* 35 (1992) 2865–2877.
- [18] P. Nithiarasu, An efficient artificial compressibility (AC) scheme based on the characteristic based split (CBS) method for incompressible flows, *Int. J. Numer. Methods Eng.* 56 (2003) 1815–1845.
- [19] F. Arpino, N. Massarotti, A. Mauro, P. Nithiarasu, Artificial compressibility-based CBS scheme for the solution of the generalized porous medium model, *Numer. Heat Transfer B—Fundam.* 55 (3) (2009) 196–218.
- [20] P. Nithiarasu, K. Ravindran, A new semi-implicit time stepping procedure for buoyancy driven flow in a fluid saturated porous medium, *Comput. Methods Appl. Mech. Eng.* 165 (1998) 147–154.
- [21] P. Nithiarasu, K.N. Seetharamu, T. Sundararajan, Double-diffusive natural convection in an enclosure filled with fluid-saturated porous medium: A generalized non-Darcy approach, *Numer. Heat Transfer A—Appl.* 30 (1996) 413–426.
- [22] P. Nithiarasu, A comparative study on the performance of two time stepping schemes for convection in a fluid saturated porous medium, *Int. J. Numer. Methods Heat Fluid Flow* 11 (2001) 308–328.

- [23] R.F. Berenati, C.B. Brosilow, Void fraction distribution in packed beds, *AIChE J.* 8 (1962) 359–361.
- [24] K. Vafai, R.L. Alkire, C.L. Tien, An experimental investigation of heat transfer in variable porosity media, *ASME J. Heat Transfer* 107 (1984) 642–647.
- [25] H.C. Brinkman, A calculation of viscous force exerted by a flowing fluid on a dense swarm of particles, *Appl. Sci. Res.* 1 (1947) 27–34.
- [26] P. Forchheimer, Wasserbewegung durch bodem, *Z. Ver. Deutsch. Ing.* 45 (1901) 1782.
- [27] H. Inaba, N. Seki, An experimental study of transient heat transfer characteristics in a porous layer enclosed between two opposing vertical surfaces with different temperatures, *Int. J. Heat Mass Transfer* 24 (1981) 1854–1857.
- [28] E. David, G. Lauriat, P. Cheng, A numerical solution of variable porosity effects on natural convection in a packed sphere cavity, *ASME J. Heat Transfer* 113 (1991) 391–399.
- [29] K.L. Walker, G.M. Homsy, Convection in a porous cavity, *J. Fluid Mech.* 87 (1978) 449–474.
- [30] G. Lauriat, V. Prasad, Non-Darcian effects on natural convection in a vertical porous enclosure, *Int. J. Heat Mass Transfer* 32 (1989) 2135–2148.
- [31] O.V. Trevisan, A. Bejan, Natural convection with combined heat and mass transfer buoyancy effects in porous medium, *Int. J. Heat Mass Transfer* 28 (1985) 1597–1611.
- [32] V. Prasad, F.A. Kulacki, M. Keyhani, Natural convection in porous media, *J. Fluid Mech.* 150 (1985) 80.

Shallow-Water Problems[★]

10

10.1 Introduction

The flow of water in shallow layers such as the ones that occur in coastal estuaries, oceans, rivers, etc., is of obvious practical importance. The prediction of tidal currents and elevations is vital for navigation and for the determination of pollutant dispersal which, unfortunately, is still frequently deposited there. The transport of sediments associated with such flows and algal growth and transport are other fields of interest.

If the free surface flow is confined to relatively thin layers the horizontal velocities are of primary importance and the problem can be reasonably approximated in two dimensions. Here we find that the resulting equations, which include in addition to the horizontal velocities the free surface elevation, can once again be written in the same conservation form as the Euler equations studied in previous chapters.

Indeed, the detailed form of these equations bears a striking similarity to that of compressible gas flow—despite the fact that now a purely incompressible fluid (water) is considered. It follows therefore that:

1. The methods developed in the previous chapters are in general applicable.
2. The type of phenomena (e.g., shocks, etc.) which we have encountered in compressible gas flows can occur again.

It will of course be found that practical interest focuses on different aspects. The objective of this chapter is therefore to introduce the basis of the derivation of the equation and to illustrate the numerical approximation techniques by a series of examples.

The approximations made in the formulation of the flow in shallow-water bodies are similar in essence to those describing the flow of air in the earth's environment and hence are widely used in meteorology. Here the vital subject of weather prediction involves their daily solution and a very large amount of computation. The interested reader will find much of the background in standard texts dealing with the subject, e.g., [Refs. \[1\]](#) and [\[2\]](#).

A particular area of interest occurs in the linearized version of the shallow-water equations which, in periodic response, are similar to those describing acoustic

*Contributed partly by P. Ortiz, Professor, University of Granada, Spain.

phenomena. In the next chapter we shall therefore discuss some of these periodic phenomena involved in the action and forces due to waves [3].

10.2 The basis of the shallow-water equations

In previous chapters we have introduced the essential Navier-Stokes equations and presented their incompressible, isothermal form, which we repeat below assuming full incompressibility. We now have the equation of mass conservation

$$\frac{\partial u_i}{\partial x_i} = 0 \quad (10.1a)$$

and the equation of momentum conservation

$$\frac{\partial u_j}{\partial t} + \frac{\partial}{\partial x_i} (u_i u_j) + \frac{1}{\rho} \frac{\partial p}{\partial x_j} - \frac{1}{\rho} \frac{\partial}{\partial x_i} \tau_{ij} - g_j = 0 \quad (10.1b)$$

with i, j being 1, 2, 3.

In the case of shallow-water flow, which we illustrate in Fig. 10.1 and where the direction x_3 is vertical, the vertical velocity u_3 is small, and the corresponding accelerations are negligible. The momentum equation in the vertical direction can

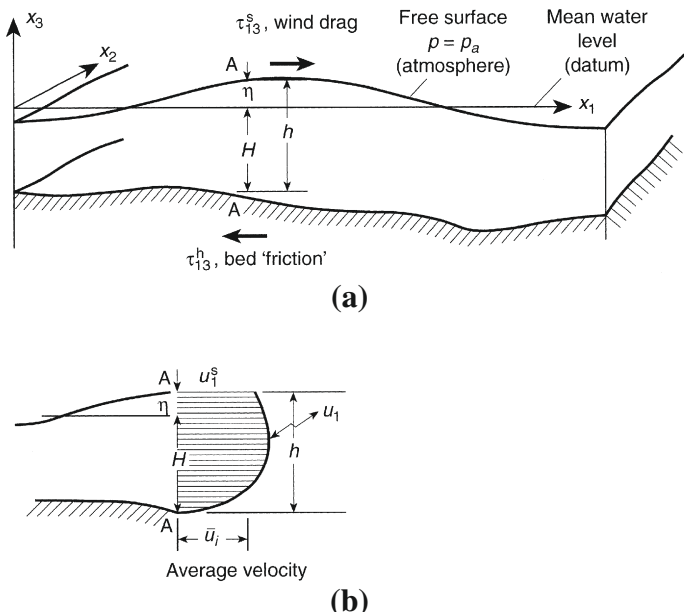


FIGURE 10.1

The shallow-water problem. Notation: (a) coordinates; (b) velocity distribution.

therefore be reduced to

$$\frac{1}{\rho} \frac{\partial p}{\partial x_3} + g = 0 \quad (10.2)$$

where $g_3 = -g$ is the gravity acceleration. After integration this yields

$$p = \rho g(\eta - x_3) + p_a \quad (10.3)$$

as, when $x_3 = \eta$, the pressure is atmospheric (p_a) (which may on occasion not be constant over the body of the water and can thus influence its motion).

On the free surface the vertical velocity u_3 can of course be related to the total time derivative of the surface elevation as discussed in [Chapter 6](#).

With reference to [Fig. 10.1](#) we can directly derive the depth-averaged conservation of mass equation by considering an infinitesimal control volume in the horizontal plane as

$$\frac{\partial h}{\partial t} + \frac{\partial(h\bar{u}_i)}{\partial x_i} = 0 \quad (10.4)$$

where \bar{u}_i is the averaged velocity field. We can immediately see the similarity with the conservation of mass equation for compressible gas flows with h replacing density ρ here. It should be noted that [Eq. \(10.4\)](#) can also be derived by integrating [Eq. \(10.1a\)](#) between $-H$ and η (see [Fig. 10.1](#)) [4].

Now we shall perform depth integration on the momentum equations in the horizontal directions, which results in depth-averaged momentum equations. We integrate [Eq. \(10.6\)](#) between the top and bottom surfaces, i.e.,

$$\int_{-H}^{\eta} \left[\frac{\partial u_i}{\partial t} + \frac{\partial}{\partial x_j}(u_i u_j) + \frac{1}{\rho} \frac{\partial p}{\partial x_i} - \frac{1}{\rho} \frac{\partial \tau_{ij}}{\partial x_i} - f_i \right] dx_3 = 0 \quad (10.5)$$

with $i = 1, 2$ and where f_i in the above equations are Coriolis accelerations. In order to integrate the above equation, we need to use the following integration formula:

$$\int_a^b \frac{\partial}{\partial s} F(r, s) dr = \frac{\partial}{\partial s} \int_a^b F(r, s) dr - F(b, s) \frac{\partial b}{\partial s} + F(a, s) \frac{\partial a}{\partial s} \quad (10.6)$$

A simple example of using the above formula is

$$\int_{-H}^{\eta} \frac{1}{\rho} \frac{\partial p}{\partial x_i} dx_3 = \frac{\partial}{\partial x_i} \int_{-H}^{\eta} \frac{p}{\rho} dx_3 - \left[\frac{p}{\rho} \right]_{\eta} \left(\frac{\partial \eta}{\partial x_i} \right) + \left[\frac{p}{\rho} \right]_{-H} \left(-\frac{\partial H}{\partial x_i} \right) \quad (10.7)$$

After integration the depth-averaged momentum [Eq. \(10.5\)](#) becomes (substituting [Eq. 10.3](#))

$$\frac{\partial h\bar{u}_i}{\partial t} + \frac{\partial h\bar{u}_i \bar{u}_j}{\partial x_j} = -gh \frac{\partial \eta}{\partial x_i} + \frac{1}{\rho} (\tau_{3i}^s - \tau_{3i}^b) + h f_i - \frac{h}{\rho} \frac{\partial p_a}{\partial x_i} + \frac{1}{\rho} \frac{\partial}{\partial x_j} \int_{-H}^{\eta} \tau_{ij} dx_3 \quad (10.8)$$

where superscripts s and b respectively indicate top and bottom (seafloor) surfaces. In [Eq. \(10.8\)](#) the shear stresses on the surface can be prescribed externally, given,

say, the wind drag. The bottom shear is frequently expressed by suitable hydraulic resistance formulae, e.g., the Chézy expression, giving

$$\tau_{3i}^b = \frac{\rho g |\bar{\mathbf{u}}| \bar{u}_i}{Ch^2} \quad (10.9)$$

where

$$|\bar{\mathbf{u}}| = \sqrt{\bar{u}_i \bar{u}_i}, \quad i = 1, 2$$

and C is the Chézy coefficient. The Coriolis accelerations, f_i , in Eq. (10.8) are important in large-scale problems and defined as

$$f_1 = \hat{f} \bar{u}_2 \quad f_2 = -\hat{f} \bar{u}_1 \quad (10.10)$$

where \hat{f} is the Coriolis parameter. At this stage we omit the stresses acting within the fluid and simply consider the surface and base drag, which can be evaluated independently. The addition of shear stresses on vertical faces of the slice can be included but are neglected in this book. Thus, the simplified momentum equation without the fluid stress terms is

$$\frac{\partial h \bar{u}_i}{\partial t} + \frac{\partial h \bar{u}_i \bar{u}_j}{\partial x_j} = -gh \frac{\partial \eta}{\partial x_i} + \frac{1}{\rho} (\tau_{3i}^s - \tau_{3i}^b) + hf_i - \frac{h}{\rho} \frac{\partial p_a}{\partial x_i} \quad (10.11)$$

If we compare the above equation with the Euler equations for compressible gas flows we find the equivalent pressure term in Eq. (10.11) appears in its non-conservation form. Also, an additional variable η is introduced. In order to write the above equation in conservation form and to eliminate the additional variable η , let us consider the following alternative form of the equivalent pressure term with $\eta = h - H$:

$$-gh \frac{\partial \eta}{\partial x_i} = -\frac{\partial}{\partial x_i} \left(g \frac{h^2 - H^2}{2} \right) + g(h - H) \frac{\partial H}{\partial x_i} \quad (10.12)$$

Substituting the above alternative form into Eq. (10.11) gives

$$\begin{aligned} \frac{\partial(h \bar{u}_i)}{\partial t} + \frac{\partial}{\partial x_j} (h \bar{u}_i \bar{u}_j) &= -\frac{\partial}{\partial x_i} \left[\frac{1}{2} g(h^2 - H^2) \right] + \frac{1}{\rho} (\tau_{3i}^s - \tau_{3i}^b) \\ &\quad + hf_i + g(h - H) \frac{\partial H}{\partial x_i} - \frac{h}{\rho} \frac{\partial p_a}{\partial x_i} \end{aligned} \quad (10.13)$$

Now the above equation is in a form identical to that of inviscid compressible momentum equations with h replacing ρ . The first three terms in the above equations represent transient, convection, and equivalent pressure terms. All the remaining four terms can be assumed to be source terms.

Equations (10.4) and (10.13) form the shallow-water problem. These equations may be rewritten in a compact form as

$$\frac{\partial \Phi}{\partial t} + \frac{\partial \mathbf{F}_i}{\partial x_i} + \mathbf{Q} = 0 \quad (10.14)$$

where

$$\Phi = \begin{Bmatrix} h \\ h\bar{u}_1 \\ h\bar{u}_2 \end{Bmatrix} \quad (10.15a)$$

$$\mathbf{F}_i = \begin{Bmatrix} h\bar{u}_i \\ h\bar{u}_1\bar{u}_i + \delta_{1i}\frac{1}{2}g(h^2 - H^2) \\ h\bar{u}_2\bar{u}_i + \delta_{2i}\frac{1}{2}g(h^2 - H^2) \end{Bmatrix} \quad (10.15b)$$

and

$$\mathbf{Q} = \begin{Bmatrix} 0 \\ -h\hat{f}\bar{u}_2 - g(h - H)\frac{\partial H}{\partial x_1} + \frac{h}{\rho}\frac{\partial p_a}{\partial x_1} - \frac{1}{\rho}\tau_{31}^s + \frac{g\bar{u}_1|\bar{\mathbf{u}}|}{Ch^2} \\ h\hat{f}\bar{u}_1 - g(h - H)\frac{\partial H}{\partial x_2} + \frac{h}{\rho}\frac{\partial p_a}{\partial x_2} - \frac{1}{\rho}\tau_{32}^s + \frac{g\bar{u}_2|\bar{\mathbf{u}}|}{Ch^2} \end{Bmatrix} \quad (10.15c)$$

with $i = 1, 2$.

The above, conservative, form of shallow-water equations was first presented in Refs. [4] and [5] and is generally applicable. However, many variants of the general shallow-water equations exist in the literature, introducing various approximations.

In the following sections of this chapter we shall discuss time-stepping solutions of the full set of the above equations in transient situations and in corresponding steady-state applications.

If we deal with the linearized form of Eqs. (10.4) and (10.13), we see immediately that on omission of all nonlinear terms, bottom drag, etc., and taking $h \sim H$, we can write these equations as

$$\frac{\partial h}{\partial t} + \frac{\partial}{\partial x_i}(H\bar{u}_i) = 0 \quad (10.16a)$$

$$\frac{\partial(H\bar{u}_i)}{\partial t} + gH\frac{\partial}{\partial x_i}(h - H) = 0 \quad (10.16b)$$

Noting that

$$\eta = h - H \quad \text{and} \quad \frac{\partial h}{\partial t} = \frac{\partial \eta}{\partial t}$$

the above becomes

$$\frac{\partial \eta}{\partial t} + \frac{\partial}{\partial x_i}(H\bar{u}_i) = 0 \quad (10.17a)$$

$$\frac{\partial(H\bar{u}_i)}{\partial t} + gH\frac{\partial \eta}{\partial x_i} = 0 \quad (10.17b)$$

Elimination of $H\bar{u}_i$ immediately yields

$$\frac{\partial^2 \eta}{\partial t^2} - \frac{\partial}{\partial x_i}\left(gH\frac{\partial \eta}{\partial x_i}\right) = 0 \quad (10.18)$$

or the standard Helmholtz wave equation. For this, many special solutions are analyzed in the next chapter.

The shallow-water equations derived in this section consider only the depth-averaged flows and hence cannot reproduce certain phenomena that occur in nature and in which some velocity variation with depth has to be allowed for. In many such problems the basic assumption of a vertically hydrostatic pressure distribution is still valid and a form of shallow-water behavior can be assumed.

The extension of the formulation can be achieved by an *a priori* division of the flow into strata in each of which different velocities occur. The final set of discretized equations consists then of several, coupled, two-dimensional approximations. Alternatively, the same effect can be introduced by using several different velocity “trial functions” for the vertical distribution, as was suggested by Zienkiewicz and Heinrich [6]. Such generalizations are useful but outside the scope of the present text.

10.3 Numerical approximation

Both finite difference and finite element procedures have for many years been used widely in solving the shallow-water equations. The latter approximation has been applied in the 1980s and Kawahara [7] and Navon [8] survey the early applications to coastal and oceanographic engineering. In most of these the standard procedures of spatial discretization followed by suitable time-stepping schemes are adopted [9–16]. In meteorology the first application of the finite element method dates back to 1972, as reported in the survey given in Ref. [17], and the range of applications has been increasing steadily [4,5,18–57].

At this stage the reader may well observe that with the exception of source terms, the isothermal compressible flow equations can be transformed into the depth integrated shallow-water equations with the variables being changed as follows:

$$\begin{aligned}\rho \text{ (density)} &\rightarrow h \text{ (depth)} \\ u_i \text{ (velocity)} &\rightarrow \bar{u}_i \text{ (mean velocity)} \\ p \text{ (velocity)} &\rightarrow \frac{1}{2}g(h^2 - H^2)\end{aligned}$$

These similarities suggest that the characteristic-based-split (CBS) algorithm adopted in the previous chapters for compressible flows be used for the shallow-water equations [58].

By using the Cartesian system and notation of the Fig. 10.1 the shallow-water equations can now be rewritten in a convenient form for the general CBS formulation developed in Chapter 3, as

$$\begin{aligned}\frac{\partial h}{\partial t} + \frac{\partial U_i}{\partial x_i} &= 0 \\ \frac{\partial U_i}{\partial t} + \frac{\partial(\bar{u}_j U_i)}{\partial x_j} + \frac{\partial}{\partial x_i} \left[\frac{1}{2}g(h^2 - H^2) \right] + Q_i &= 0\end{aligned}$$

where $U_i = h\bar{u}_i$. The rest of the variables are the same as described before. The extension of effective finite element solutions of high-speed flows to shallow-water problems has already been successful in the case of the Taylor-Galerkin method [4,5,48]. However, the semi-implicit form of the general CBS formulation provides a critical time step dependent only on the current velocity of the flow \mathbf{U} (for pure convection),

$$\Delta t \leq \frac{d}{|\mathbf{U}|} \quad (10.19)$$

where d is the element size, instead of a critical time step in terms of the wave celerity $c = \sqrt{gh}$,

$$\Delta t \leq \frac{d}{c + |\mathbf{U}|} \quad (10.20)$$

which places a severe constraint on fully explicit methods such as the Taylor-Galerkin approximation and others [4,5,32] particularly for the analysis of long-wave propagation in shallow waters and in general for low Froude number problems.

Important savings in computation can be reached in these situations obtaining for some practical cases up to 20 times the critical (explicit) time step, without seriously affecting the accuracy of the results. When nearly critical to supercritical flows must be studied, the fully explicit form is recovered, and the results observed for these cases are also excellent [59,60]. The three essential steps of the CBS scheme may be written in its semi-discrete form as

Step 1:

$$\Delta U_i^* = \Delta t \left[-\frac{\partial}{\partial x_j} (u_j U_i) - Q_i + \frac{\Delta t}{2} u_k \frac{\partial}{\partial x_k} \left(\frac{\partial}{\partial x_j} (u_j U_i) + Q_i \right) \right]^n \quad (10.21)$$

Step 2:

$$\Delta h = -\Delta t \left[\frac{\partial U_i^n}{\partial x_i} + \theta_1 \frac{\partial \Delta U_i^*}{\partial x_i} - \Delta t \theta_1 \left(\frac{\partial^2 p^n}{\partial x_i \partial x_i} + \theta_2 \frac{\partial^2 \Delta p}{\partial x_i \partial x_i} \right) \right] \quad (10.22)$$

Step 3:

$$\Delta U_i = U_i^{n+1} - U_i^n = \Delta U_i^* - \Delta t \frac{\partial p^{n+\theta_2}}{\partial x_i} + \frac{\Delta t^2}{2} u_k \frac{\partial^2 p^n}{\partial x_k \partial x_i} \quad (10.23)$$

with $p = g(h^2 - H^2)/2$. In the above equations, $0.5 \geq \theta_1 \geq 1.0$ and $\theta_2 = 0$ for explicit scheme and $0.5 \geq \theta_1 \geq 1.0$ and $0.5 \geq \theta_2 \geq 1.0$ for semi-implicit scheme. For further details on the time and spatial discretizations, the readers are referred to Chapter 3.

In the examples that follow we shall illustrate several problems solved by the CBS procedure, and with the Taylor-Galerkin method.

10.4 Examples of application

10.4.1 Transient one-dimensional problems: A performance assessment

In this section we present some relatively simple examples in one space dimension to illustrate the applicability of the algorithms.

Example 10.1. Solitary wave

The first, illustrated in Fig. 10.2, shows the progress of a solitary wave [61] onto a shelving beach. This frequently studied situation [62,63] shows well the progressive steepening of the wave often obscured by schemes that are very dissipative.

Example 10.2. Dam break

The second example, illustrated in Fig. 10.3, illustrates the so-called “dam break” problem diagrammatically. Here a dam separating two stationary water levels is suddenly removed and the almost vertical waves progress into the two domains. This problem, somewhat similar to those of a shock tube in compressible flow, has been solved quite successfully even without artificial diffusivity.

Example 10.3. Bore

The final example of this section, Fig. 10.4, shows the formation of an idealized “bore” or a steep wave progressing into a channel carrying water at a uniform speed caused by a gradual increase of the downstream water level. Despite the fact that the flow speed is “subcritical” (i.e., velocity $< \sqrt{gh}$), a progressively steepening, traveling shock clearly develops.

10.4.2 Two-dimensional periodic tidal motions

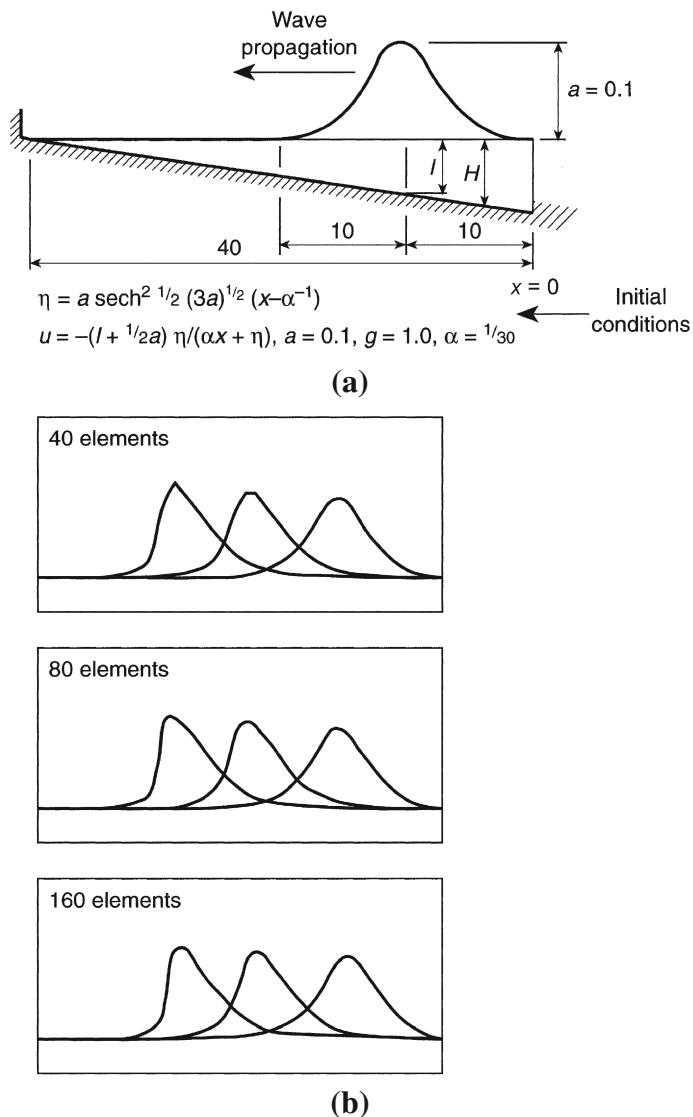
The extension of the computation into two space dimensions follows the same pattern as that described in compressible formulations. Again linear triangles are used to interpolate the values of h , hu_1 , and hu_2 . The main difference in the solutions is that of emphasis.

Example 10.4. Periodic wave

The first example of Fig. 10.5 is presented merely as a test problem. Here the frictional resistance is linearized and an exact solution known for a periodic response [64] is used for comparison. This periodic response is obtained numerically by performing five cycles with the input boundary conditions. Although the problem is essentially one-dimensional, a two-dimensional uniform mesh was used and the agreement with analytical results is found to be quite remarkable.

Example 10.5. Bristol channel

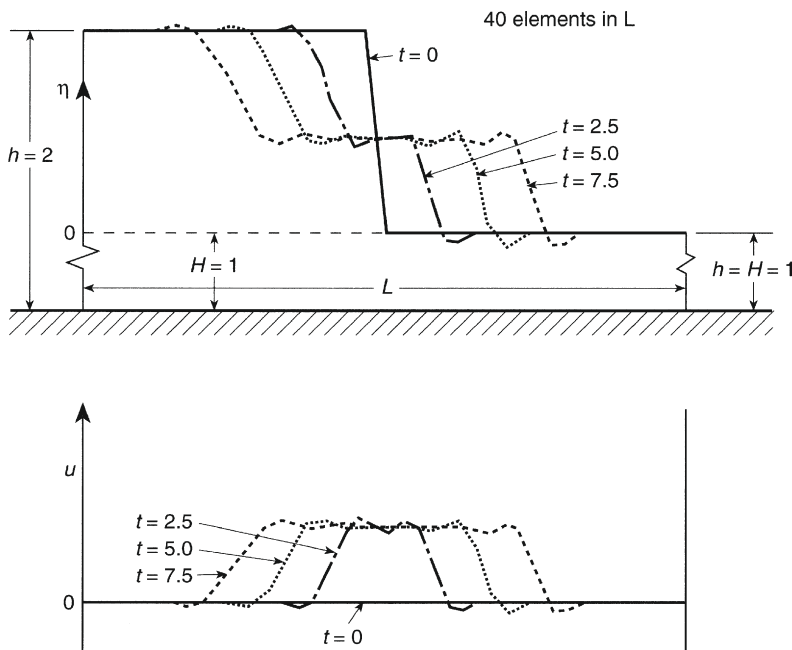
In the second example we enter the domain of more realistic applications [4,5,58–60,65]. Here the “test bed” is provided by the Bristol Channel and the Severn Estuary,

**FIGURE 10.2**

Shoaling of a wave: (a) problem statement; (b) solution, for 40, 80, and 160 elements at various times.

known for some of the highest tidal motions in the world. Figure 10.6 shows the location and the scale of the problem.

The objective is here to determine tidal elevations and currents currently existing (as a possible preliminary to a subsequent study of the influence of a barrage which

**FIGURE 10.3**

Propagation of waves due to dam break ($C_{\text{Lap}} = 0$). Forty elements in analysis domain. $C = \sqrt{gH} = 1$, $\Delta t = 0.25$.

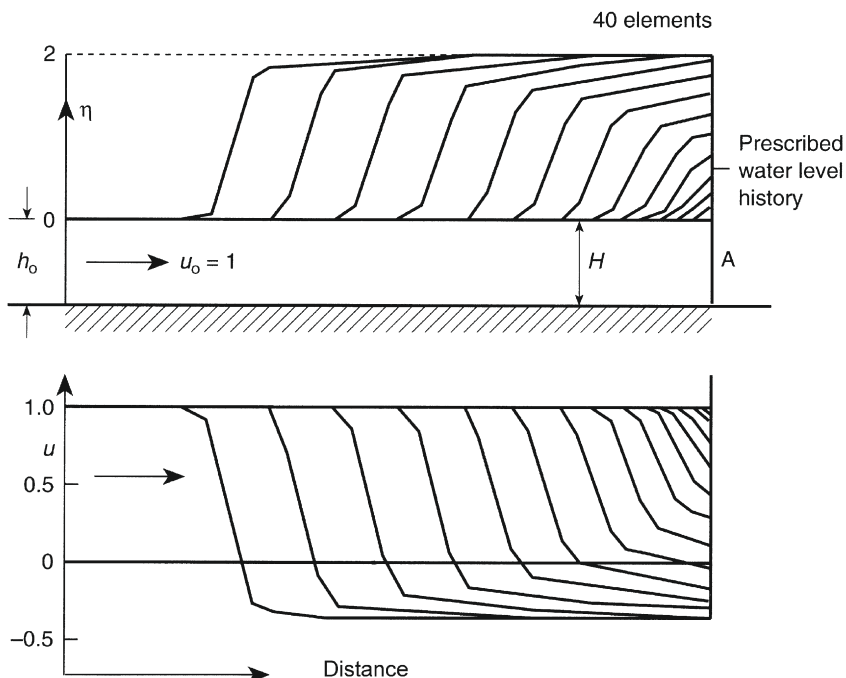
some day may be built to harness the tidal energy). Before commencement of the analysis the extent of the analysis domain must be determined by an arbitrary, seaward, boundary. On this the measured tidal heights will be imposed.

This height-prescribed boundary condition is not globally conservative and can produce undesired reflections. These effects sometimes lead to considerable errors in the calculations, particularly if long-term computations are to be carried out (like, for instance, in some pollutant dispersion analysis). For these cases, more general open boundary conditions can be applied, as, for example, those described in Refs. [35] and [36].

The analysis was carried out on four meshes of linear triangles shown in Fig. 10.7. These meshes encompass two positions of the external boundary and it was found that the differences in the results obtained by four separate analyses were insignificant.

The mesh sizes ranged from 2 to 5 km in minimum size for the fine and coarse subdivisions. The average depth is approximately 50 m but of course full bathymetry information was used with depths assigned to each nodal point.

The numerical study of the Bristol Channel was completed by a comparison of performance between the explicit and semi-explicit algorithms [59]. The results for the coarse mesh were compared with measurements obtained by the Institute of Oceanographic Science (IOS) for the M_2 tide [65], with time steps corresponding to the critical

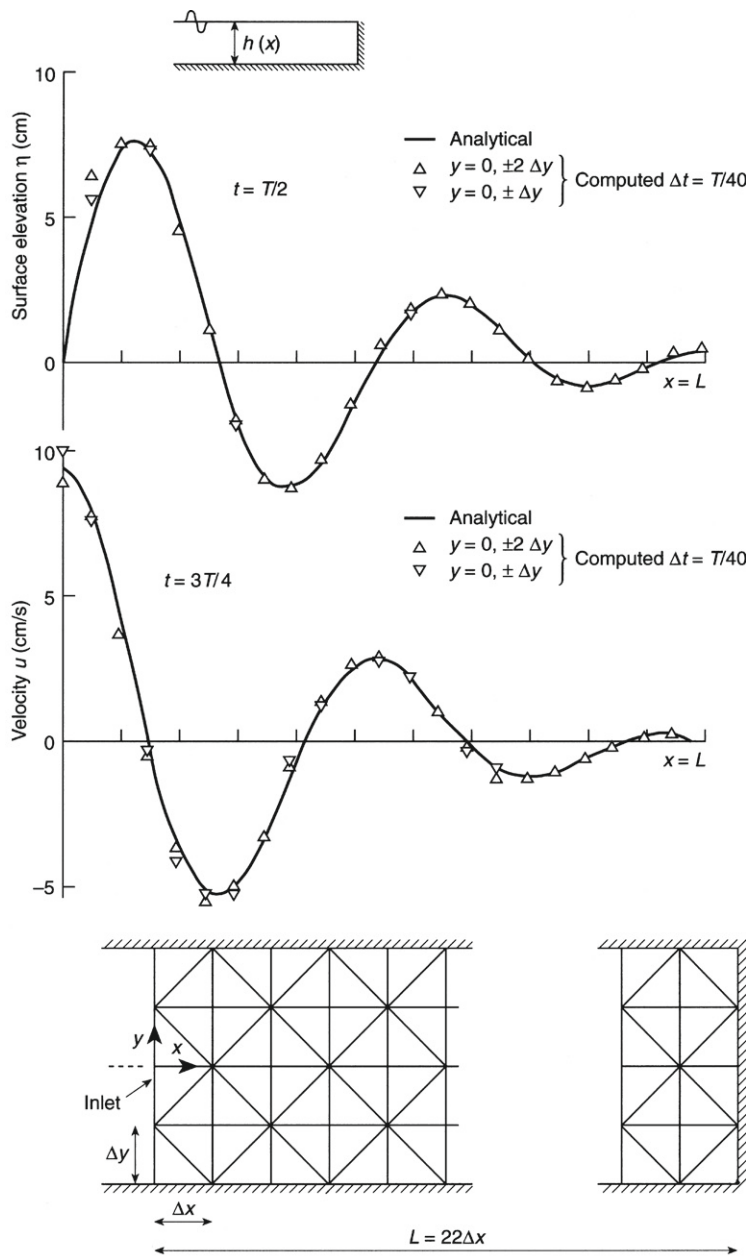
**FIGURE 10.4**

A “bore” created in a stream due to water level rise downstream (A). Level at A, $\eta = 1 - \cos \pi t / 30$ ($0 \leq t \leq 30$), 2 ($30 \leq t$). Levels and velocities at intervals of 5 time units, $\Delta t = 0.5$.

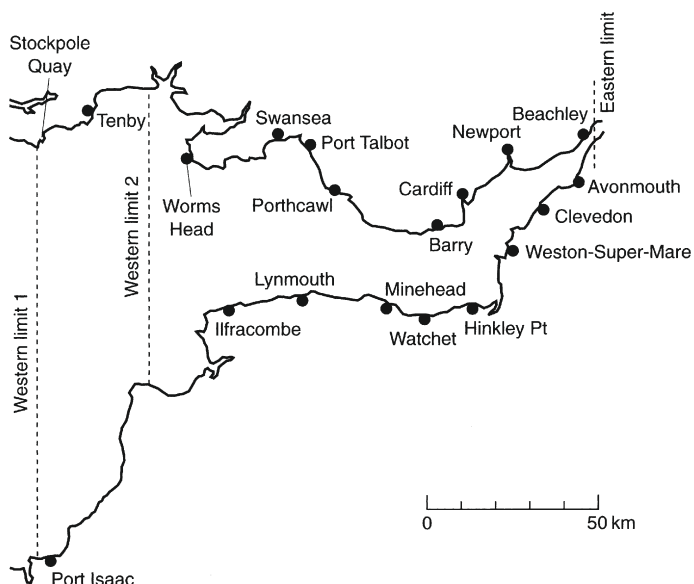
(explicit) time step (50 s), and four times (200 s) and eight times (400 s) the critical time step. A constant real friction coefficient (Manning) of 0.038 was adopted for all of the estuary. Coriolis forces were included. The analysis proved that the Coriolis effect was very important in terms of phase errors. Table 10.1 represents a comparison between observations and computations in terms of amplitudes and phases for seven different points which are represented in the location map (Fig. 10.6), for the three different time steps described above. The maximum error in amplitude only increases by 1.4% when the time step of 400 s is used with respect to the time step of 50 s, while the absolute error in phases (-13°) is two degrees more than the case of 50 s (-11°). These bounds show a remarkable accuracy for the semi-explicit model. In Fig. 10.8 the distribution of velocities at different times of the tide is illustrated (explicit model).

Example 10.6. River Severn bore

In the analysis presented we have omitted details of the River Severn upstream of the eastern limit (see Figs. 10.6 and 10.9a), where a “bore” moving up the river can be observed. An approach to this phenomenon is made by a simplified straight

**FIGURE 10.5**

Steady-state oscillation in a rectangular channel due to periodic forcing of surface elevation at an inlet. Linear frictional dissipation [32].

**FIGURE 10.6**

Location map. Bristol Channel and Severn Estuary.

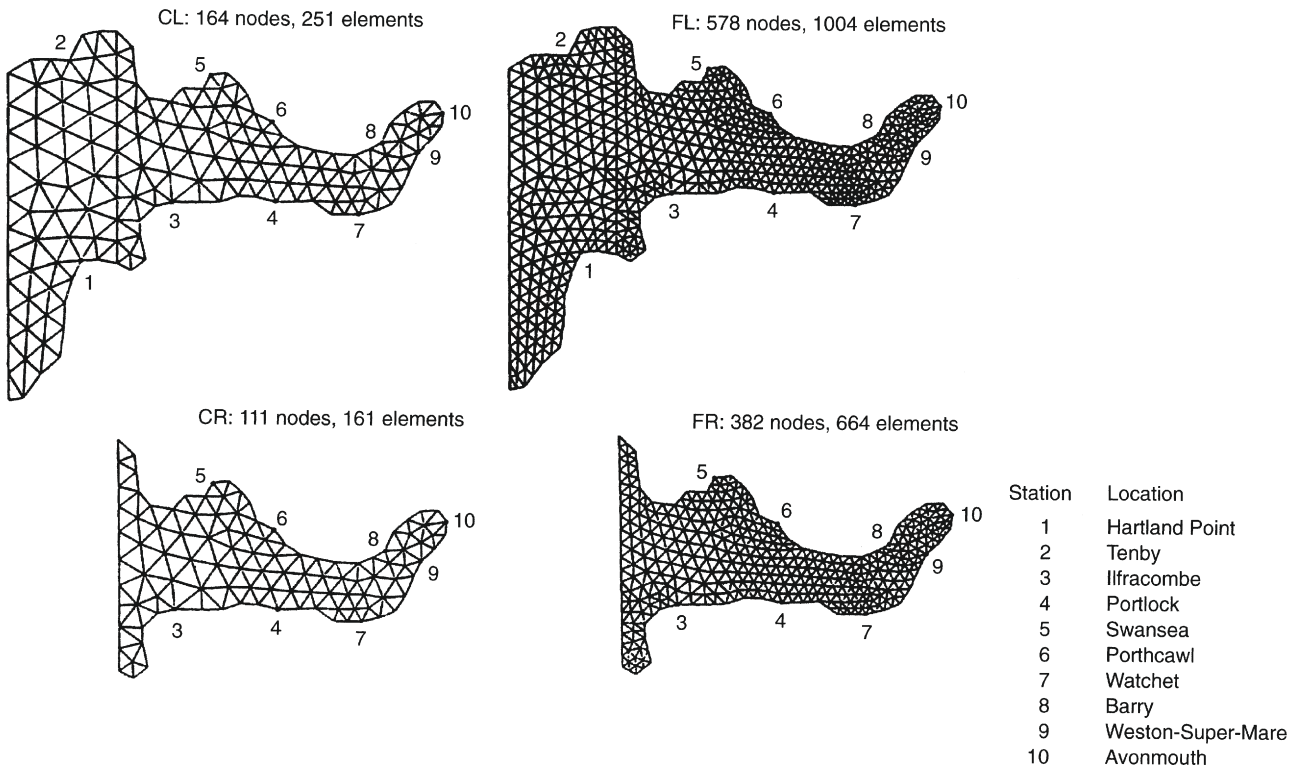
extension of the mesh used previously, preserving an approximate variation of the bottom and width until the point G (Gloucester) (77.5 km from Avonmouth), but obviously neglecting the dissipation and inertia effects of the bends. Measurement points are located at B and E, and the results (elevations) are presented in Fig. 10.9d for the points A, B, and E in time, along with a steady river flow. A typical shape for a tidal bore can be observed for the point E, with fast flooding and a smooth ebbing of water. (The flooding takes place from the minimum to maximum level in less than 25 min.)

10.4.3 Tsunami waves

A problem of some considerable interest in earthquake zones is that of so-called tidal waves or tsunamis. These are caused by sudden movements in the earth's crust and can on occasion be extremely destructive. The analysis of such waves presents no difficulties in the general procedure demonstrated and indeed is computationally cheaper as only relatively short periods of time need be considered. To illustrate a typical possible tsunami wave we have created one in the Severn Estuary just analyzed (to save problems of mesh generation, etc., for another more likely configuration).

Example 10.7. Tsunami wave in Severn Estuary

Here the tsunami is forced by an instantaneous raising of an element situated near the center of the estuary by some 6 m and the previously designed mesh was used

**FIGURE 10.7**

Finite element meshes. Bristol Channel and Severn Estuary.

Table 10.1 Bristol Channel and Severn Estuary—Observed Results and FEM Computation (FL Mesh) of Tidal Half-Amplitude ($m \times 10^2$)

Location	Observed	FEM
Tenby	262	260 (-1%)
Swansea	315	305 (-3%)
Cardiff	409	411 (0%)
Porthcawl	317	327 (+3%)
Barry	382	394 (+3%)
Port Talbot	316	316 (-1%)
Newport	413	420 (+2%)
Ilfracombe	308	288 (-6%)
Minehead	358	362 (+1%)

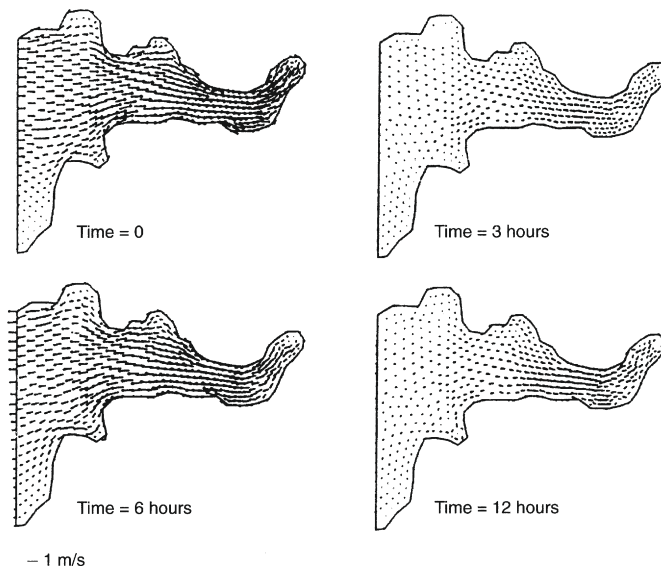


FIGURE 10.8

Velocity vector plots (FL mesh).

(FL). The progress of the wave is illustrated in Fig. 10.10. The tsunami wave was superimposed on the tide at its highest level—though of course the tidal motion was allowed for. This example was included in Ref. [5].

One particular point only needs to be mentioned in this calculation. This is the boundary condition on the seaward, arbitrary, limit. Here the Riemann decomposition of the type discussed earlier has to be made if tidal motion is to be incorporated and

note taken of the fact that the tsunami forms only an outgoing wave. This, in the absence of tides, results simply in application of the free boundary condition there.

The clean way in which the tsunami is seen to leave the domain in Fig. 10.10 testifies to the effectiveness of this process.

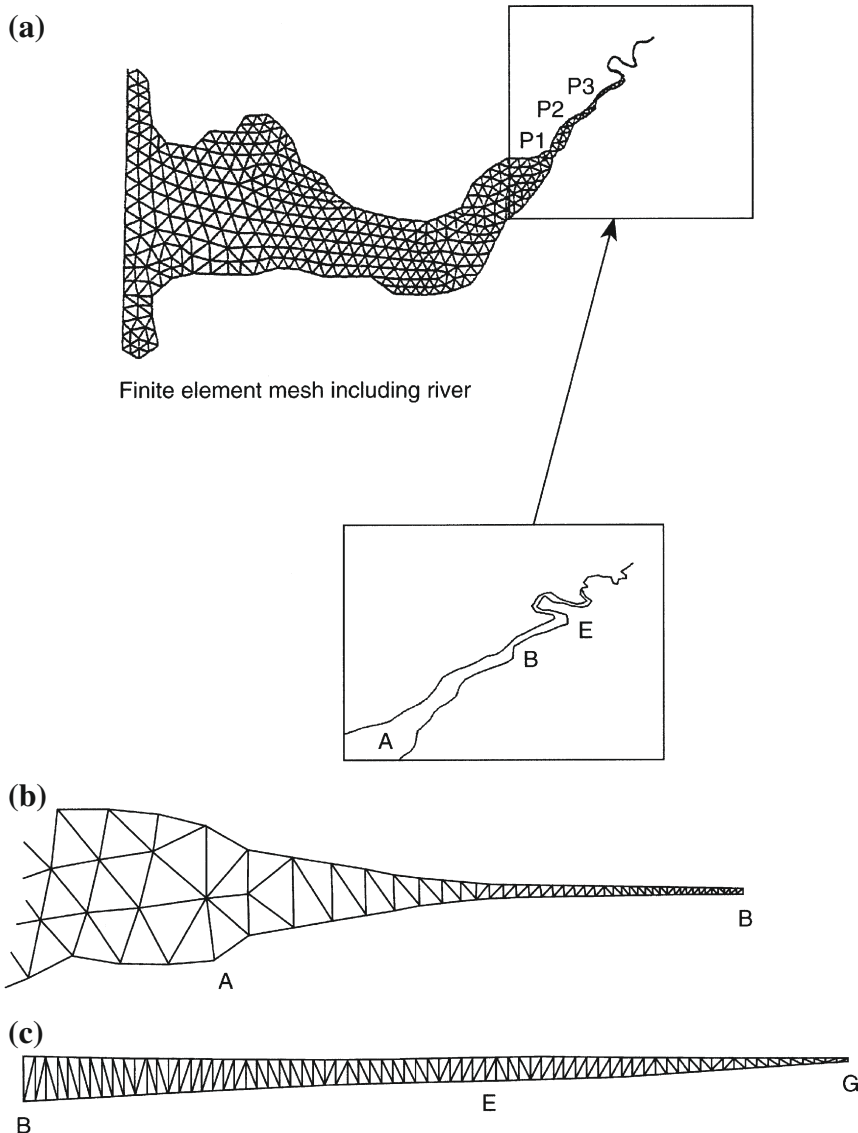
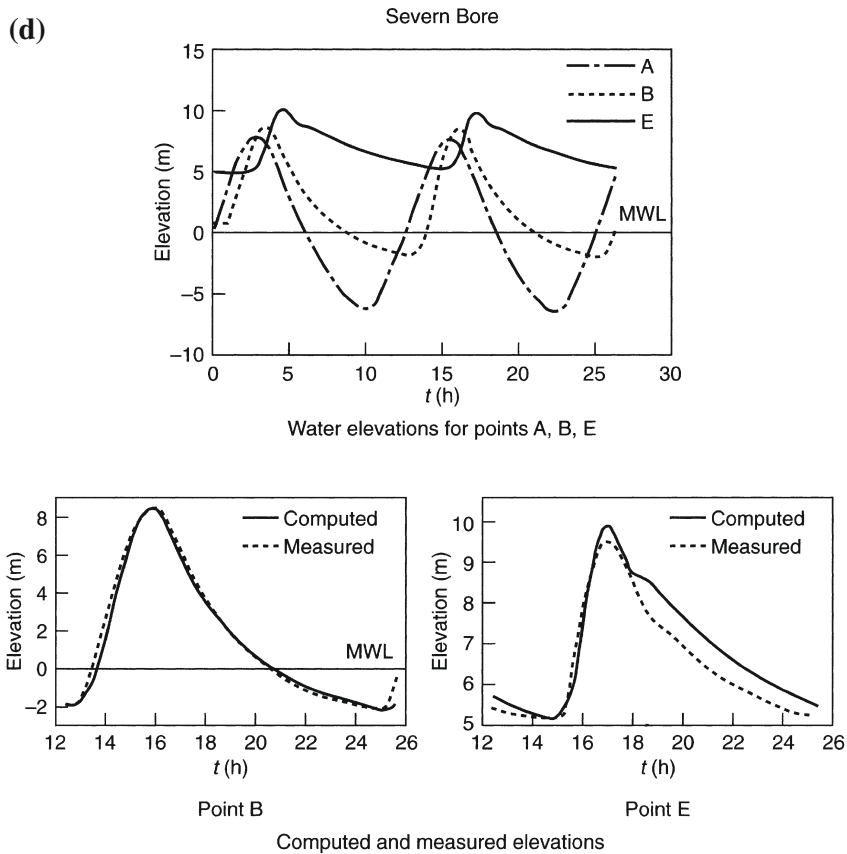


FIGURE 10.9

Finite element mesh used in the Severn bore calculations (a) Full domain (b) Part of the domain between points A and B (c) Part of the domain beyond point B.

**FIGURE 10.9**

(Continued).

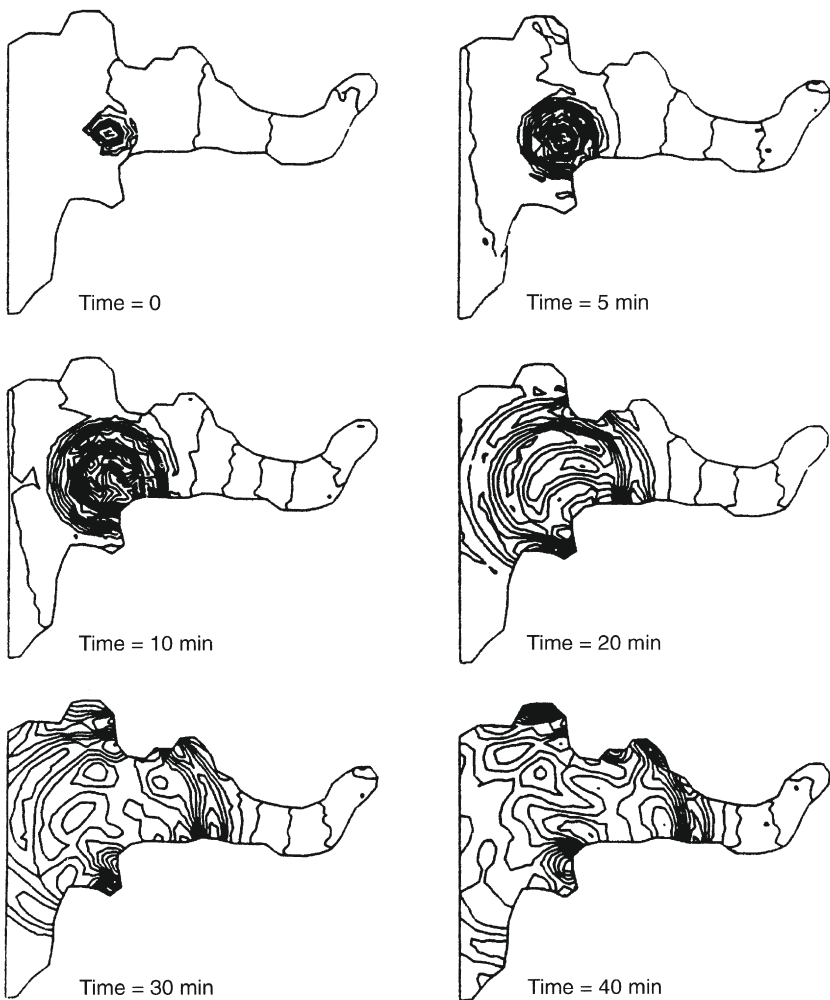
10.4.4 Steady-state solutions

On occasion steady-state currents such as the ones caused by persistent wind motion or other influences have to be considered. Here once again the transient form of explicit computation proves very effective and convergence is generally more rapid than in compressible flow as the bed friction plays a greater role. The interested reader will find many such steady-state solutions in the literature.

Example 10.8. Steady-state solution

In Fig. 10.11 we show a typical example. Here the currents are induced by the breaking of waves which occurs when these reach small depths creating so-called radiation stresses [6,30,66]. The “forces” due to breaking are the cause of longshore currents and rip currents in general. The figure illustrates this effect on a harbor.

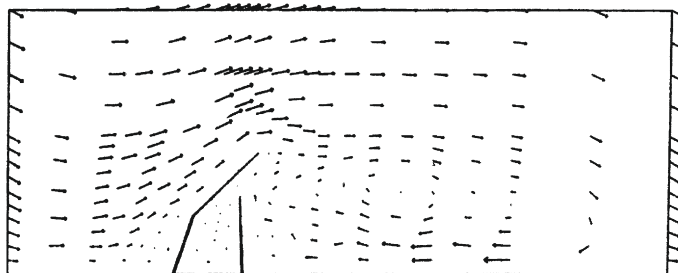
It is of interest to remark that in the problem discussed, the side boundaries have been “repeated” to model an infinite harbor series [66].

**FIGURE 10.10**

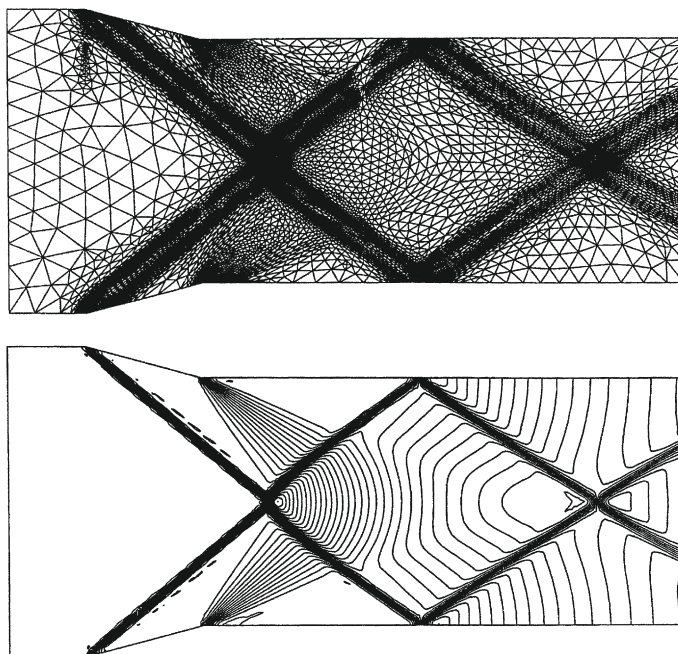
Severn tsunami. Generation during high tide. Water height contours (times after generation).

Example 10.9. Supercritical flow

Another type of interesting steady-state (and transient) problem concerns supercritical flows over hydraulic structures, with shock formation similar to those present in high-speed compressible flows. To illustrate this range of flows, the problem of a symmetric channel of variable width with a supercritical inflow is shown here. For a supercritical flow in a rectangular channel with a symmetric transition on both sides, a combination of a “positive” jump and “negative” waves, causing a decrease in depth, appears. The profile of the negative wave is gradual and an approximate solution

**FIGURE 10.11**

Wave-induced steady-state flow past a harbor [30].

**FIGURE 10.12**

Supercritical flow and formation of shock waves in symmetric channel of variable width contours of h . Inflow Froude number = 2.5. Constriction: 15° .

can be obtained by assuming no energy losses and that the flow near the wall turns without separation. The constriction and enlargement analyzed here was 15° , and the final mesh used was of only 6979 nodes, after two remeshings. The supercritical flow had an inflow Froude number of 2.5 and the boundary conditions were as follows: heights and velocities prescribed in inflow (left boundary of Fig. 10.12), slip boundary on walls (upper and lower boundaries in Fig. 10.12), and free variables on the outflow boundary (right side of Fig. 10.12). The explicit version with local time

step was adopted. Figure 10.12 represents contours of heights, where “cross” waves and “negative” waves are contained. One can observe the “gradual” change in the behavior of the negative wave created at the origin of the wall enlargement.

10.5 Drying areas

A special problem encountered in transient, tidal, computations is that of boundary change due to changes of water elevation. This has been ignored in the calculation presented for the Bristol Channel-Severn Estuary as the movements of the boundary are reasonably small in the scale analyzed. However, in that example these may be of the order of 1 km and in tidal motions near Mont St. Michel, France, can reach 12 km. Clearly on some occasions such movements need to be considered in the analysis and many different procedures for dealing with the problem have been suggested. In Fig. 10.13 we show the simplest of these which is effective if the total movement can be confined to one element size. Here the boundary nodes are repositioned along the normal direction as required by elevation changes $\Delta\eta$.

If the variations are larger than those that can be absorbed in a single element some alternatives can be adopted, such as partial remeshing over layers surrounding the distorted elements or a general smooth displacement of the mesh.

10.6 Shallow-water transport

Shallow-water currents are frequently the carrier for some quantities which may disperse or decay in the process. Typical here is the transport of hot water when discharged from power stations, or of the sediment load or pollutants. The mechanism

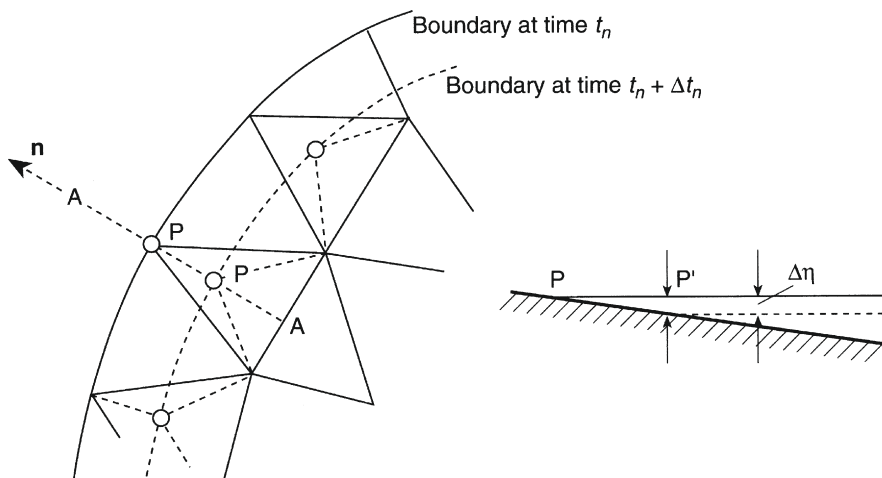


FIGURE 10.13

Adjustment of boundary due to tidal variation.

of sediment transport is quite complex [67] but in principle follows similar rules to that of the other equations. In all cases it is possible to write *depth-averaged transport equations* in which the average velocities \bar{u}_i have been determined independently.

A typical averaged equation can be written—using a scalar variable (e.g., temperature (T)) as the transported quantity—as

$$\frac{\partial(hT)}{\partial t} + \frac{\partial(h\bar{u}_iT)}{\partial x_i} - \frac{\partial}{\partial x_i}\left(hk\frac{\partial T}{\partial x_i}\right) + R = 0 \quad \text{for } i = 1, 2 \quad (10.24)$$

where h and \bar{u}_i are the previously defined and computed quantities, k is an appropriate diffusion coefficient, and R is a source term.

A quasi-implicit form of the general CBS algorithm can be obtained when diffusion terms are included. In this situation practical horizontal viscosity ranges (and diffusivity in the case of transport equations) can produce limiting time steps much lower than the convection limit. To circumvent this restraint, a quasi-implicit computation, requiring an implicit computation of the viscous terms, is recommended.

The application of the CBS method for any scalar transport equation is straightforward, because of the absence of the pressure gradient term. Then, the second and third steps of the method are not necessary. The computation of the scalar hT is analogous to the intermediate momentum computation, but now a new time integration parameter θ_3 is introduced for the diffusion term such that $0 \leq \theta_3 \leq 1$.

The application of the characteristic-Galerkin procedure gives the following final matrix form (neglecting terms higher than second order):

$$(\mathbf{M} + \theta_3 \Delta t \mathbf{D}) \Delta \mathbf{T} = -\Delta t [\mathbf{C}\mathbf{T}^n + \mathbf{M}\mathbf{R}^n] - \frac{\Delta t^2}{2} [\mathbf{K}_u \mathbf{T}^n + \mathbf{f}_R] - \Delta t \mathbf{D}\mathbf{T}^n + \mathbf{f}_b \quad (10.25)$$

where now \mathbf{T} is the vector of nodal hT values and we have

$$\begin{aligned} \mathbf{M} &= \int_{\Omega} \mathbf{N}^T \mathbf{N} d\Omega \\ \mathbf{C} &= \int_{\Omega} \mathbf{N}^T \bar{u}_i \frac{\partial \mathbf{N}}{\partial x_j} d\Omega \\ \mathbf{K}_u &= \int_{\Omega} \frac{\partial}{\partial x_k} (\mathbf{N}^T \bar{u}_k) \frac{\partial}{\partial x_j} (\mathbf{N} \bar{u}_j) d\Omega \\ \mathbf{D} &= \int_{\Omega} \frac{\partial \mathbf{N}^T}{\partial x_i} k \frac{\partial \mathbf{N}}{\partial x_i} d\Omega \\ \mathbf{f}_R &= \int_{\Omega} \frac{\partial}{\partial x_k} (\mathbf{N}^T) \mathbf{N} \mathbf{R} d\Omega \end{aligned}$$

and

$$\mathbf{f}_b = \Delta t \int_{\Gamma} \mathbf{N} k \frac{\partial T}{\partial x_i} \cdot \mathbf{n}_i d\Gamma$$

As an illustration of a real implementation, the parameters involved in the study of transport of salinity in an industrial application for a river area are considered here. The region studied was approximately 55 km long and the mean value of the eddy

diffusivity was $k = 40 \text{ ms}^{-1}$. The limiting time step for convection (considering eight components of tides) was 3.9 s. This limit was severely reduced to 0.1 s if the diffusion term was active and solved explicitly. The convective limit was recovered assuming an implicit solution with $\theta_3 = 0.5$. The comparisons of diffusion error between computations with 0.1 s and 3.9 s had a maximum diffusion error of 3.2% for the 3.9 s calculation, showing enough accuracy for engineering purposes, taking into account that the time stepping was increased 40 times, reducing dramatically the cost of computation. This reduction is fundamental when, in practical applications, the behavior of the transported quantity must be computed for long-term periods, as was this problem, where the evolution of the salinity needed to be calculated for more than 60 periods of equivalent M_2 tides and for very different initial conditions. The boundary conditions are the same as for tidal problems: a partially closed region with an open boundary condition where the tide components are imposed. For this case a radiation condition based on Riemann invariants has been used. The reader can find a detailed description in Ref. [35]. For the salinity transport equation, the open boundary condition also can be derived on the basis of Riemann invariants in a similar way as for the rest of the equations.

In Fig. 10.14 we show by way of an example the dispersion of a *continuous* hot water discharge in an area of the Severn Estuary. Here we note not only the convection movement but also the diffusion of the temperature contours.

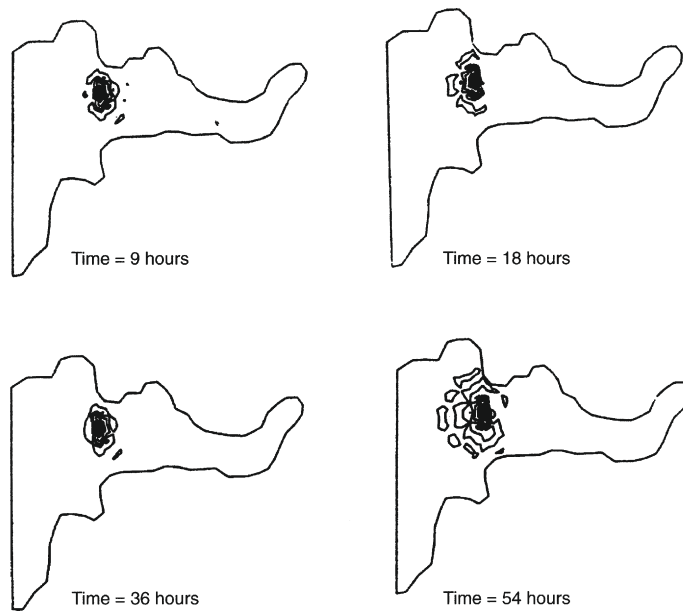


FIGURE 10.14

Heat convection and diffusion in tidal currents. Temperature contours at several times after discharge of hot fluid.

10.7 Concluding remarks

In this chapter we summarized another important form of incompressible fluid dynamics equations to solve shallow-water flows. The important features of various numerical solution procedures are also mentioned here. Turbulent fluid dynamics and accurate estimation of free surface in estuaries are a growing area of research but much more complicated approaches are necessary to tackle such problems. However, the procedure explained in this chapter, though it has limitations, is easy to follow and very effective in getting a quick solution to shallow-water problems.

References

- [1] M.B. Abbott, Computational Hydraulics. Elements of the Theory of Free Surface Flows, Pitman, London, 1979.
- [2] G.J. Haltiner, R.T. Williams, Numerical Prediction and Dynamic Meteorology, Wiley, New York, 1980.
- [3] O.C. Zienkiewicz, R.W. Lewis, K.G. Stagg, Numerical Methods in Offshore Engineering, Wiley, Chichester, 1978.
- [4] J. Peraire, A finite method for convection dominated flows, Ph.D. Thesis, University of Wales, Swansea, 1986.
- [5] J. Peraire, O.C. Zienkiewicz, K. Morgan, Shallow water problems: a general explicit formulation, *Int. J. Numer. Methods Eng.* 22 (1986) 547–574.
- [6] O.C. Zienkiewicz, J.C. Heinrich, A unified treatment of steady state shallow water and two dimensional Navier-Stokes equations, *Comput. Methods Appl. Mech. Eng.* 17/18 (1979) 673–689, Finite element penalty function approach
- [7] M. Kawahara, On finite-element methods in shallow-water long-wave flow analysis, in: J.T. Oden (Ed.), Computational Methods in Nonlinear Mechanics, NorthHolland, Amsterdam, 1980, pp. 261–287.
- [8] I.M. Navon, A review of finite element methods for solving the shallow water equations, *Computer Modelling in Ocean Engineering*, Balkema, Rotterdam, 1988, pp. 273–278.
- [9] J.J. Connor, C.A. Brebbia, Finite-Element Techniques for Fluid Flow, Newnes-Butterworth, London and Boston, 1976.
- [10] J.J. O'Brien, H.E. Hulbert, A numerical model of coastal upwelling, *J. Phys. Oceanogr.* 2 (1972) 14–26.
- [11] M. Crepon, M.C. Richez, M. Chartier, Effects of coastline geometry on upwellings, *J. Phys. Oceanogr.* 14 (1984) 365–382.
- [12] M.G.G. Foreman, An analysis of two-step time-discretisations in the solution of the linearized shallow-water equations, *J. Comput. Phys.* 51 (1983) 454–483.
- [13] W.R. Gray, D.R. Lynch, Finite-element simulation of shallow-water equations with moving boundaries, in: A. Brebbia et al. (Eds.), *Proceedings of 2nd Conference on Finite-Elements in Water Resources*, 1978, pp. 23–42.

- [14] T.D. Malone, J.T. Kuo, Semi-implicit finite-element methods applied to the solution of the shallow-water equations, *J. Geophys. Res.* 86 (1981) 4029–4040.
- [15] G.J. Fix, Finite-element models for ocean-circulation problems, *SIAM J. Appl. Math.* 29 (1975) 371–387.
- [16] C. Taylor, J. Davis, Tidal and long-wave propagation, a finite-element approach, *Comput. Fluids* 3 (1975) 125–148.
- [17] M.J.P. Cullen, A simple finite element method for meteorological problems, *J. Inst. Math. Appl.* 11 (1973) 15–31.
- [18] H.H. Wang, P. Halpern, J. Douglas Jr., I. Dupont, Numerical solutions of the one-dimensional primitive equations using Galerkin approximations with localised basis functions, *Mon. Weekly Rev.* 100 (1972) 738–746.
- [19] I.M. Navon, Finite-element simulation of the shallow-water equations model on a limited area domain, *Appl. Math. Modell.* 3 (1979) 337–348.
- [20] M.J.P. Cullen, The finite element method, in: *Numerical Methods Used in Atmosphere Models*, WMO/GARP Publication Series, vol. 7, World Meteorological Organisation, Geneva, Switzerland, 1979, pp. 330–338.
- [21] M.J.P. Cullen, C.D. Hall, Forecasting and general circulation results from finite-element models, *Q. J. Roy. Met. Soc.* 102 (1979) 571–592.
- [22] D.E. Hinsman, R.T. Williams, E. Woodward, Recent advances in the Galerkin finite-element method as applied to the meteorological equations on variable resolution grids, in: T. Kawai (Ed.), *Finite-Element Flow-Analysis*, University of Tokyo Press, Tokyo, 1982.
- [23] I.M. Navon, A Numerov-Galerkin technique applied to a finite-element shallow-water equations model with enforced conservation of integral invariants and selective lumping, *J. Comput. Phys.* 52 (1983) 313–339.
- [24] I.M. Navon, R. de Villiers, Gustaf, a quasi-Newton nonlinear ADI FORTRAN IV program for solving the shallow-water equations with augmented lagrangians, *Comput. Geosci.* 12 (1986) 151–173.
- [25] A.N. Staniforth, A review of the application of the finite-element method to meteorological flows, in: T. Kawai (Ed.), *Finite-Element Flow-Analysis*, University of Tokyo Press, Tokyo, 1982, pp. 835–842.
- [26] A.N. Staniforth, The application of the finite element methods to meteorological simulations—a review, *Int. J. Numer. Methods Fluids* 4 (1984) 1–22.
- [27] R.T. Williams, O.C. Zienkiewicz, Improved finite element forms for shallow-water wave equations, *Int. J. Numer. Methods Fluids* 1 (1981) 91–97.
- [28] M.G.G. Foreman, A two-dimensional dispersion analysis of selected methods for solving the linearised shallow-water equations, *J. Comput. Phys.* 56 (1984) 287–323.
- [29] I.M. Navon, FEUDX: A two-stage, high-accuracy, finite-element FORTRAN program for solving shallow-water equations, *Comput. Geosci.* 13 (1987) 225–285.
- [30] P. Bettess, C.A. Fleming, J.C. Heinrich, O.C. Zienkiewicz, D.I. Austin, A numerical model of longshore patterns due to a surf zone barrier, in: *A Numerical Model of Longshore Patterns Due to a Surf Zone Barrier*, Hamburg, Germany, 1978.

- [31] N. Takeuchi, M. Kawahara, T. Yoshida, Two step explicit finite element method for tsunami wave propagation analysis, *Int. J. Numer. Methods Eng.* 12 (1978) 331–351.
- [32] J.H.S. Lee, J. Peraire, O.C. Zienkiewicz, The characteristic Galerkin method for advection dominated problems—an assessment, *Comput. Methods Appl. Mech. Eng.* 61 (1987) 359–369.
- [33] D.R. Lynch, W. Gray, A wave equation model for finite element tidal computations, *Comput. Fluids* 7 (1979) 207–228.
- [34] O. Daubert, J. Hervouet, A. Jami, Description on some numerical tools for solving incompressible turbulent and free surface flows, *Int. J. Numer. Methods Eng.* 27 (1989) 3–20.
- [35] G. Labadie, S. Dalsecco, B. Latteaux, Resolution des équations de Saint-Venant par une méthode d'éléments finis, *Electricité de France, Report HE/41*, 1982.
- [36] T. Kodama, T. Kawasaki, M. Kawahara, Finite element method for shallow water equation including open boundary condition, *Int. J. Numer. Methods Fluids* 13 (1991) 939–953.
- [37] S. Bova, G. Carey, An entropy variable formulation and applications for the two dimensional shallow water equations, *Int. J. Numer. Methods Fluids* 23 (1996) 29–46.
- [38] K. Kashiyama, H. Ito, M. Behr, T. Tezduyar, Three-step explicit finite element computation of shallow water flows on a massively parallel computer, *Int. J. Numer. Methods Fluids* 21 (1995) 885–900.
- [39] S. Chippada, C. Dawson, M. Martinez, M.F. Wheeler, Finite element approximations to the system of shallow water equations, *SIAM J. Numer. Analysis* 35 (1998) 692–711, Part I. Continuous time a priori error estimates. TICAM Report, Univ. of Texas at Austin
- [40] S. Chippada, C. Dawson, M. Martinez, M.F. Wheeler, Finite element approximations to the system of shallow water equations, *SIAM J. Numer. Analysis* 36 (1998) 226–250, Part II. Discrete time a priori error estimates. TICAM Report, Univ. of Texas at Austin
- [41] O.C. Zienkiewicz, J. Wu, J. Peraire, A new semi-implicit or explicit algorithm for shallow water equations, *Math. Mod. Sci. Comput.* 1 (1993) 31–49.
- [42] M.M. Cecchi, L. Salasnich, Shallow water theory and its application to the Venice lagoon, *Comput. Methods Appl. Mech. Eng.* 151 (1998) 63–74.
- [43] M.M. Cecchi, A. Pica, E. Secco, A projection method for shallow water equations, *Int. J. Numer. Methods Fluids* 27 (1998) 81–95.
- [44] F.X. Giraldo, The Lagrange-Galerkin method for the two-dimensional shallow water equations on adaptive grids, *Int. J. Numer. Methods Fluids* 33 (2000) 789–832.
- [45] C.N. Dawson, M.L. Martinez-Canales, A characteristic-Galerkin approximation to a system of shallow water equations, *Numer. Math.* 86 (2000) 239–256.
- [46] V. Aizinger, C. Dawson, A discontinuous Galerkin method for two-dimensional flow and transport in shallow water, *Adv. Water Resour.* 25 (2002) 67–84.

- [47] C. Dawson, J. Proft, Discontinuous and coupled continuous/discontinuous Galerkin methods for the shallow water equations, *Comput. Methods Appl. Mech. Eng.* 191 (2002) 4721–4746.
- [48] M. Quecedo, M. Pastor, A reappraisal of Taylor-Galerkin algorithm for drying-wetting areas in shallow water computations, *Int. J. Numer. Methods Eng.* 38 (2002) 515–532.
- [49] F.X. Giraldo, Strong and weak Lagrange-Galerkin spectral methods for the shallow water equations, *Comput. Math. Appl.* 45 (2003) 97–121.
- [50] C. Dawson, J. Proft, Discontinuous/continuous Galerkin methods for coupling the primitive and wave continuity equations of shallow water, *Comput. Methods Appl. Mech. Eng.* 192 (2003) 5123–5145.
- [51] C. Dawson, J. Proft, Coupled discontinuous and continuous Galerkin finite element methods for the depth integrated shallow water equations, *Comput. Methods Appl. Mech. Eng.* 193 (2004) 289–318.
- [52] M. Morandi-Cecchi, M. Venturin, Characteristic-based split (CBS) algorithm finite element modelling for shallow waters in the Venice lagoon, *Int. J. Numer. Methods Eng.* 66 (2006) 1641–1657.
- [53] V. Rostand, D.Y. Le Roux, Raviart-Thomas and Brezzi-Douglas-Marini finite-element approximations of the shallow-water equations, *Int. J. Numer. Methods Fluids* 57 (8) (2008) 951–976.
- [54] D.Y. Le Roux, E. Hanert, V. Rostand, B. Pouliot, Impact of mass lumping on gravity and Rossby waves in 2D finite-element shallow-water models, *Int. J. Numer. Methods Fluids* 59 (7) (2009) 767–790.
- [55] R. Combлен, J. Lambrechts, J.-F. Remacle, V. Legat, Practical evaluation of five partly discontinuous finite element pairs for the non-conservative shallow water equations, *Int. J. Numer. Methods Fluids* 63 (6) (2010) 701–724.
- [56] D.Y. Le Roux, R. Walters, E. Hanert, J. Pietrzak, A comparison of the GWCE and mixed P-P1 formulations in finite-element linearized shallow-water models, *Int. J. Numer. Methods Fluids* 68 (12) (2012) 1497–1523.
- [57] C.J. Trahan, C. Dawson, Local time-stepping in Runge-Kutta discontinuous Galerkin finite element methods applied to the shallow-water equations, *Comput. Methods Appl. Mech. Eng.* 217 (2012) 139–152.
- [58] O.C. Zienkiewicz, P. Ortiz, A split characteristic based finite element model for shallow water equations, *Int. J. Numer. Methods Fluids* 20 (1995) 1061–1080.
- [59] O.C. Zienkiewicz, P. Ortiz, The CBS (characteristic-based-split) algorithm in hydraulic and shallow water flow, in: Second International Symposium River Sedimentation and Environment Hydraulics, University of Hong Kong, December 1998, pp. 3–12.
- [60] O.C. Zienkiewicz, R. Codina, A general algorithm for compressible and incompressible flow—Part I: The split, characteristic-based scheme, *Int. J. Numer. Methods Fluids* 20 (1995) 869–885.
- [61] R. Löhner, K. Morgan, O.C. Zienkiewicz, The solution of non-linear hyperbolic equation systems by the finite element method, *Int. J. Numer. Methods Fluids* 4 (1984) 1043–1063.

- [62] S. Nakazawa, D.W. Kelly, O.C. Zienkiewicz, I. Christie, M. Kawahara, An analysis of explicit finite element approximations for the shallow water wave equations, in: Proceedings of the 3rd International Conference on Finite Elements in Flow Problems, Banff, vol. 2, 1980, pp. 1–7.
- [63] M. Kawahara, H. Hirano, K. Tsubota, K. Inagaki, Selective lumping finite element method for shallow water flow, *Int. J. Numer. Methods Fluids* 2 (1982) 89–112.
- [64] D.R. Lynch, W.G. Gray, Analytic solutions for computer flow model testing, *Trans. ASCE* 104 (1978) 1409–1428, *J. Hydr. Div.* (10)
- [65] Hydraulic Research Station, Severn tidal power, Report EX985, 1981.
- [66] D.I. Austin, P. Bettess, Longshore boundary conditions for numerical wave model, *Int. J. Numer. Mech. Fluids* 2 (1982) 263–276.
- [67] C.K. Ziegler, W. Lick, The transport of fine grained sediments in shallow water, *Environ. Geol. Water Sci.* 11 (1988) 123–132.

Long and Medium Waves[★] 11

11.1 Introduction and equations

The main developments in this chapter relate to linearized surface waves in water, but acoustic and electromagnetic waves will also be mentioned. We start from the wave equation, [Eq. \(10.18\)](#), which was developed from the equations of momentum balance and mass conservation in shallow water. The wave elevation, η , is small in comparison with the water depth, H . If the problem is periodic, we can write the wave elevation, η , quite generally as

$$\eta(x, y, t) = \bar{\eta}(x, y) \exp(i\omega t) \quad (11.1)$$

where ω is the angular frequency and $\bar{\eta}$ may be complex. [Equation \(10.18\)](#) now becomes

$$\nabla^T (H \nabla \bar{\eta}) + \frac{\omega^2}{g} \bar{\eta} = 0 \quad \text{or} \quad \frac{\partial}{\partial x_i} \left(H \frac{\partial \bar{\eta}}{\partial x_i} \right) + \frac{\omega^2}{g} \bar{\eta} = 0 \quad (11.2)$$

or, for constant depth, H ,

$$\nabla^2 \bar{\eta} + k^2 \bar{\eta} = 0 \quad \text{or} \quad \frac{\partial^2 \bar{\eta}}{\partial x_i \partial x_i} + k^2 \bar{\eta} = 0 \quad (11.3)$$

where the wavenumber $k = \omega/\sqrt{gH}$ is related to the wavelength, λ , by $k = 2\pi/\lambda$. The wave speed is $c = \omega/k$. [Equation \(11.3\)](#) is the Helmholtz equation [which was also derived in [Chapter 10](#), in a slightly different form, as [Eq. \(10.18\)](#)] which models very many wave problems. This is only one form of the equation of surface waves, for which there is a very extensive literature [[1–4](#)]. From now on all problems will be taken to be periodic, and the overbar on η will be dropped. The Helmholtz [equation \(11.3\)](#) also describes periodic acoustic waves. The wavenumber k is now given by ω/c , whereas in surface waves ω is the angular frequency and c is the wave speed. This is given by $c = \sqrt{K/\rho}$, where ρ is the density of the fluid and K is the bulk modulus. Boundary conditions need to be applied to deal with radiation and absorption of acoustic waves. The first application of finite elements to acoustics was by Gladwell [[5](#)]. This was followed in 1969 by the solution of acoustic equations by Zienkiewicz and Newton [[6](#)], and further finite element models by Craggs [[7](#)].

[★]Contributed by Peter Bettess, Formerly Professor, School of Engineering, University of Durham, UK.

A more comprehensive survey of the development of the method is given by Astley [8]. Provided that the dielectric constant, ε , and the permeability, μ , are constant, then Maxwell's equations for electromagnetics can be reduced to the form

$$\nabla^2\phi - \frac{\varepsilon\mu}{c^2} \frac{\partial^2\phi}{\partial t^2} = -\frac{4\pi\rho}{\varepsilon} \quad \text{and} \quad \nabla^2\mathbf{A} - \frac{\varepsilon\mu}{c^2} \frac{\partial^2\mathbf{A}}{\partial t^2} = -\frac{4\pi\mu\mathbf{J}}{c} \quad (11.4)$$

where ρ is the charge density, \mathbf{J} is the current, and ϕ and \mathbf{A} are scalar and vector potentials, respectively. When ρ and \mathbf{J} are zero, which is a frequent case, and the time dependence is harmonic, Eqs. (11.4) reduce to the Helmholtz equations. More details are given by Morse and Feshbach [9].

For surface waves on water when the wavelength, $\lambda = 2\pi/k$, is small relative to the depth, H , the velocities and the velocity potential vary vertically as $\cosh kz$ [1, 2, 10, 11]. The full equation can now be written as

$$\nabla^T(cc_g\nabla\eta) + \frac{\omega^2}{g}\eta = 0 \quad \text{or} \quad \frac{\partial}{\partial x_i} \left(cc_g \frac{\partial\eta}{\partial x_i} \right) + \frac{\omega^2}{g}\eta = 0 \quad (11.5)$$

where the group velocity, $c_g = nc$, $n = (1 + (2kH/\sinh 2kH))/2$, and the *dispersion relation*

$$\omega^2 = gk \tanh kH \quad (11.6)$$

links the angular frequency, ω , and the water depth, H , to the wavenumber, k .

11.2 Waves in closed domains: Finite element models

We now consider a closed domain of any shape. For waves on water this could be a closed basin, for acoustic or electromagnetic waves it could be a resonant cavity. In the case of surface waves we consider a two-dimensional basin, with varying depth. In plan it can be divided into two-dimensional elements, of any of the types discussed in Ref. [12]. The wave elevation, η , at any point (ξ, η) within the element, can be expressed in terms of nodal values, using the element shape function \mathbf{N} , as follows:

$$\eta \approx \hat{\eta} = \mathbf{N}\tilde{\eta} \quad (11.7)$$

Next Eq. (11.2) is weighted with the shape function, and integrated by parts in the usual way, to give

$$\int_{\Omega} \left(\frac{\partial \mathbf{N}^T}{\partial x_i} H \frac{\partial \mathbf{N}}{\partial x_i} - \mathbf{N}^T \frac{\omega^2}{g} \mathbf{N} \right) d\Omega \tilde{\eta} = 0 \quad (11.8)$$

The integral is taken over all the elements of the domain, and $\tilde{\eta}$ represents all the nodal values of η .

The natural boundary condition which arises is $\partial\eta/\partial n = 0$, where n is the normal to the boundary, corresponding to zero flow normal to the boundary. Physically this

corresponds to a vertical, perfectly reflecting wall. Equation (11.8) can be recast in the familiar form

$$(\mathbf{K} - \omega^2 \mathbf{M}) \tilde{\eta} = \mathbf{0} \quad (11.9)$$

where

$$\mathbf{M} = \int_{\Omega} \mathbf{N}^T \frac{1}{g} \mathbf{N} d\Omega \quad \mathbf{K} = \int_{\Omega} \mathbf{B}^T \mathbf{D} \mathbf{B} d\Omega \quad (11.10)$$

and the \mathbf{D} matrix is constructed from the depths, H . H can vary with position:

$$\mathbf{D} = \begin{bmatrix} H & 0 \\ 0 & H \end{bmatrix}$$

It is thus an *eigenvalue* problem as discussed in Chapter 12 of Ref. [12]. The \mathbf{K} and \mathbf{M} matrices are analogous to structure stiffness and mass matrices. The *eigenvalues* will give the natural frequencies of oscillation of the water in the basin and the *eigenvectors* give the mode shapes of the water surface. Such an analysis was first carried out using finite elements by Taylor et al. [13] and the results are shown as Fig. 12.5 of Ref. [12]. There are analytical solutions for harbors of regular shape and constant depth [1,3]. The reader should find it easy to modify the standard element routine contained in the computer program available from the website given in Chapter 18 of Ref. [12] to generate the wave equation “stiffness” and “mass” matrices. In the corresponding acoustic problems, the eigenvalues give the natural resonant frequencies and the eigenvectors give the modes of vibration. The model described above will give good results for harbor and basin resonance problems, and other problems governed by the Helmholtz equation. In modeling the Helmholtz equation, it is necessary to retain a mesh which is sufficiently fine to ensure an accurate solution. A “rule of thumb,” which has been used for some time, is that there should be 10 nodes per wavelength. This has been accepted as giving results of acceptable engineering accuracy for many wave problems. However, recently more accurate error analysis of the Helmholtz equation has been carried out [14,15]. In wave problems it is not sufficient to use a fine mesh only in zones of interest. The entire domain must be discretized to a suitable element density. There are essentially two types of errors:

- The wave shape may not be a good representation of the true wave, that is the local elevations or pressures may be wrong.
- The wavelength may be in error.

This second case causes a poor representation of the wave in one part of the problem to cause errors in another part of the problem. This effect, where errors build up across the model, is called a *pollution error*. It has been implicitly understood since the early days of modeling of the Helmholtz equation, as can be seen from the uniform size of finite element used in meshes.

Babuška et al. [14,15] show some results for various finite element models, using different element types, and the error is calculated as a function of element size, h , and wavenumber, k . The sharper error results show that the simple rule of thumb given above is not always adequate. Since the wavenumber, k , and the wavelength, λ ,

are related by $k = 2\pi/\lambda$, the condition of 10 nodes per wavelength can be written as $kh \approx 0.6$. But keeping to this limit is not sufficient. The pollution error grows as k^3h^2 . Babuška et al. propose *a posteriori* error indicators to assess the pollution error. See the cited references and Chapter 15, Ref. [12], for further discussion of these matters.

11.3 Difficulties in modeling surface waves

The main defects of the simple surface-wave model described above are the following:

1. Inaccuracy when the wave height becomes large. The equations are no longer valid when η becomes large, and for very large η , the waves will break, which introduces energy loss.
2. Lack of modeling of bed friction. This will be discussed below.
3. Lack of modeling of separation at re-entrant corners. At re-entrant corners there is a singularity in the velocity of the form $1/\sqrt{r}$, where r is the distance from the corner. The velocities become large, and physically the viscous effects, neglected above, become important. They cause retardation, flow separation, and eddies. This effect can only be modeled in an approximate way.

Now the response can be determined for a given excitation frequency, as discussed in Chapter 12 of Ref. [12].

11.4 Bed friction and other effects

The engineering approach to the energy loss in the boundary layer close to the sea bed is to introduce a friction force proportional to the water velocity. This is called the Chézy bed friction. Since the force is nonlinear in the velocity if it is included in its original form, it makes the equations difficult to solve. The usual procedure is to assume that its main effect is to damp the system, by absorbing energy, and to introduce a linear term, which in one period absorbs the same amount of energy as the Chézy term. The linearized bed friction version of Eq. (11.2) is

$$\nabla^T (H \nabla \eta) + \frac{\omega^2}{g} \eta - i\omega M \eta = 0 \quad \text{or} \quad \frac{\partial}{\partial x_i} \left(H \frac{\partial \eta}{\partial x_i} \right) + \frac{\omega^2}{g} \eta - i\omega M \eta = 0 \quad (11.11)$$

where M is a linearized bed friction coefficient, which can be written as $M = 8u_{\max}/3\pi C^2 H$, C is the Chézy constant, and u_{\max} is the maximum velocity at the bed at that point. In general the results for η will now be complex, and iteration has to be used, since M depends upon the unknown u_{\max} . From the finite element point of view, there is no longer any need to separate the “stiffness” and “mass” matrices. Instead, Eq. (11.11) is weighted using the element shape function and the entire complex element matrix is formed. The matrix right-hand side arises from whatever exciting forces are present. The re-entrant corner effect and wave-absorbing walls

and permeable breakwaters can also be modeled in a similar way, as both of these introduce a damping effect, due to viscous dissipation. The method is explained in Ref. [16], where an example showing flow through a perforated wall in an offshore structure is solved.

11.5 The short-wave problem

Short-wave diffraction problems are those in which the wavelength is much smaller than any of the dimensions of the problem. Such problems arise in surface waves on water, acoustic and pressure waves, electromagnetic waves, and elastic waves. The methods described in this chapter will solve the problems, but the requirement of 10 nodes or thereabouts per wavelength makes the necessary finite element meshes prohibitively fine. To take one example, radar waves of wavelength 1 mm might impinge on an aircraft of 10 m wingspan. It is easy to see that the computing requirements are truly astronomical. This topic is considered in more detail in Chapter 12.

11.6 Waves in unbounded domains (exterior surface wave problems)

Problems in this category include the diffraction and refraction of waves close to fixed and floating structures, the determination of wave forces and wave response for offshore structures and vessels, and the determination of wave patterns adjacent to coastlines, open harbors, and breakwaters. In electromagnetics there are scattering problems of the type already described, and in acoustics we have various noise problems. In the interior or finite part of the domain, finite elements, exactly as described in Section 11.2, can be used, but special procedures must be adopted for the part of the domain extending to infinity. The main difficulty is that the problem has no outer boundary. This necessitates the use of a *radiation condition*. Such a condition was introduced in Chapter 18 of Ref. [17] as Eq. (18.18) for the case of a one-dimensional wave, or a normally incident plane wave in two or more dimensions. Work by Bayliss et al. [18,19] has developed a suitable radiation condition, in the form of an infinite series of operators. The starting point is the representation of the outgoing wave in the form of an infinite series. Each term in the series is then annihilated by using a boundary operator. The sequence of boundary operators thus constitutes the radiation condition. In addition there is a classical form of the boundary condition for periodic problems, given by Sommerfeld [20,21]. A summary of some of the available radiation conditions is given in Table 11.1.

11.6.1 Background to wave problems

The simplest type of exterior, or unbounded wave problem is that of some exciting device which sends out waves which do not return. This is termed the *radiation problem*. The next type of exterior wave problem is where we have a known incoming wave which encounters an object, is modified, and then again radiates away to infinity.

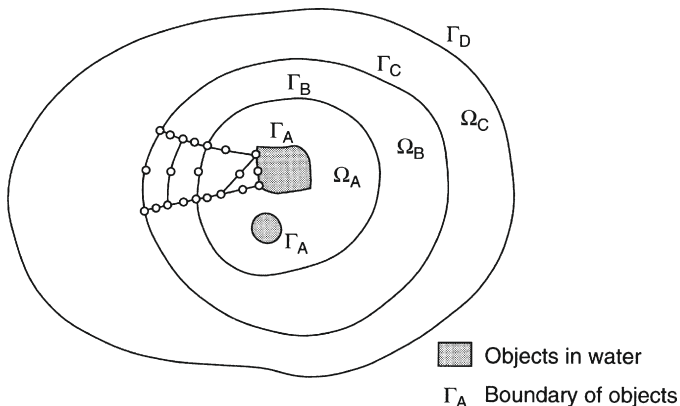
Table 11.1 Radiation Conditions for Exterior Wave Problems

Dimensions		
1	2	3
General boundary conditions		
<i>Transient</i>		
$\frac{\partial \phi}{\partial x} + \frac{1}{c} \frac{\partial \phi}{\partial t} = 0$	$B_m \phi = 0, m \rightarrow \infty$	$B_m \phi = 0, m \rightarrow \infty$
	$B_m = \prod_{j=1}^m \left(\frac{\partial}{\partial r} + \frac{\partial}{\partial t} + \frac{2j - (3/2)}{r} \right)$	$B_m = \prod_{j=1}^m \left(\frac{\partial}{\partial r} + \frac{\partial}{\partial t} + \frac{2j - 1}{r} \right)$
<i>Periodic</i>		
$\frac{\partial \phi}{\partial x} + ik\phi = 0$	$\lim_{r \rightarrow \infty} \sqrt{r} \left(\frac{\partial \phi}{\partial r} + ik\phi \right) = 0$	$\lim_{r \rightarrow \infty} r \left(\frac{\partial \phi}{\partial r} + ik\phi \right) = 0$
or		or
$B_m \phi = 0, m \rightarrow \infty$		$B_m \phi = 0, m \rightarrow \infty$
	$B_m = \prod_{j=1}^m \left(\frac{\partial}{\partial r} + ik + \frac{2j - (3/2)}{\gamma} \right)$	$B_m = \prod_{j=1}^m \left(\frac{\partial}{\partial r} + ik + \frac{2j - 1}{r} \right)$
Symmetric boundary conditions		
<i>Transient</i>		
$\frac{\partial \phi}{\partial r} + \frac{1}{c} \frac{\partial \phi}{\partial t} = 0$	$\frac{\partial \phi}{\partial r} + \frac{\phi}{2r} + \frac{1}{c} \frac{\partial \phi}{\partial t} = 0$	$\frac{\partial \phi}{\partial r} + \frac{\phi}{r} + \frac{1}{c} \frac{\partial \phi}{\partial t} = 0$
Axisymmetric		Spherically symmetric
<i>Periodic</i>		
$\frac{\partial \phi}{\partial r} + ik\phi = 0$	$\frac{\partial \phi}{\partial r} + \left(\frac{1}{2r} + ik \right) \phi = 0$	$\frac{\partial \phi}{\partial r} + \left(\frac{1}{r} + ik \right) \phi = 0$
Axisymmetric		Spherically symmetric

This case is known as the *scattering* problem, and is more complicated, inasmuch as we have to deal with both incident and radiated waves. Even when both waves are linear, this can lead to complications. Both the above cases can be complicated by wave refraction, where the wave speeds change, because of changes in the medium, for example changes in water depth. Usually this phenomenon leads to changes in the wave direction. Waves can also reflect from boundaries, both physical and computational.

11.6.2 Wave diffraction

We now consider the problem of an incident wave diffracted by an object. The problem consists of an object in some medium, which diffracts the incident waves. We divide

**FIGURE 11.1**

General wave domains.

the medium as shown in Fig. 11.1, into two regions, with boundaries Γ_A , Γ_B , Γ_C , and Γ_D . These boundaries have the following meanings. Γ_A is the boundary of the body which is diffracting the waves. Γ_B is the boundary between the two computational domains, that in which the total wave elevation (or other field variable) is used, and that in which the elevation of the radiated wave is used. Γ_C is the outer boundary of the computational model, and Γ_D is the boundary at infinity. Some of these boundaries may be merged.

A variational treatment will now be used, as described in Chapters 3 and 4 of Ref. [12]. A weighted residual treatment is also possible. The elevation of the total wave, η_T , is split into those for incident and radiated waves, η_I and η_R . Hence $\eta_T = \eta_I + \eta_R$. The incident wave elevation, η_I , is assumed to be known. For the surface wave problem, the functional for the exterior can be written as

$$\Pi = \iint_{\Omega_B} \frac{1}{2} \left[cc_g (\nabla \eta)^T \nabla \eta - \frac{\omega^2 c_g}{c} \eta^2 \right] dx dy \quad (11.12)$$

where making Π stationary with respect to variations in η corresponds to satisfying the shallow-water wave equation (11.5), with natural boundary condition $\partial \eta / \partial n = 0$, or zero velocity normal to the boundary. The functional is rewritten in terms of the incident and radiated elevations, and then Green's theorem in the plane (Ref. [12], Appendix F) is applied on the domain exterior to Γ_B . But the radiation condition discussed above should be included. In order to do this the variational statement must be changed so that variations in η yield the correct boundary condition. Details are given by many authors, see for example Bettess and Bettess [22]. After some manipulation the final functional for the exterior is

$$\begin{aligned}\Pi = & \iint_{\Omega_b} \frac{1}{2} \left[cc_g (\nabla \eta^s)^T \nabla \eta^s - \frac{\omega^2 cc_g}{c} (\eta^s)^2 \right] dx dy \\ & + \int_{\Gamma_b} cc_g \left[\frac{\partial \eta^i}{\partial x} \eta^s dy - \frac{\partial \eta^i}{\partial y} \eta^s dx \right] + \frac{1}{2} \int_{\Gamma_d} ikcc_g (\eta^s)^2 d\Gamma \quad (11.13)\end{aligned}$$

The influence of the incident wave is thus to generate a “forcing term” on the boundary Γ_B . For two of the most popular methods for dealing with exterior problems, linking to boundary integrals and infinite elements, the “damping” term in Eq. (11.13), corresponding to the radiation condition, is actually irrelevant, because both methods use functions which automatically satisfy the radiation condition at infinity.

11.6.3 Incident waves, domain integrals, and nodal values

It is possible to choose any known solution of the wave equation as the incident wave. Usually this is a plane monochromatic wave, for which the elevation is given by $\eta_I = a_0 \exp[ikr \cos(\theta - \gamma)]$, where γ is the angle that the incident wave makes to the positive x -axis, r and θ are the polar coordinates, and a_0 is the incident wave amplitude. On the boundary Γ_B , we have two types of variables, the total elevation, η_T , on the interior, and η_R , the radiation elevation, in the exterior. Clearly the nodal values of η in the finite element model must be unique, and on this boundary, as well as the line integral, of Eq. (11.13), we must transform the nodal values, either to η_T or to η_R . This can be done simply by enforcing the change of variable, which leads to a contribution to the “right-hand side” or “forcing” term [22].

11.7 Unbounded problems

There are several methods of dealing with exterior problems using finite elements in combination with other methods. Some of these methods are also applicable to finite differences. The literature in this field has grown enormously in the past few years, and this section cannot begin to pretend to be comprehensive. A book could be written on each of the subheadings below. The monograph by Givoli [23] is devoted exclusively to this field and gives much more detail on the competing algorithms. It is a very useful source and gives many more algorithms than can be covered here. The book edited by Geers [24], from an IUTAM symposium, gives a very useful and up-to-date overview of the field. Methods for exterior Helmholtz problems are also discussed by Ihlenburg in his monograph [25].

Four of the main methods are listed below. The first three are usually local in their effect. The last is always global, linking together all the nodes on the exterior of the finite element mesh.

- Local nonreflecting boundary conditions (NRBCs)
- *Sponge layers*, perfectly matched layers (PMLs)
- Infinite elements

- Linking to exterior solutions, both series and boundary integrals [also called Dirichlet to Neumann mapping (DtN)].

11.8 Local nonreflecting boundary conditions (NRBCs)

The term comes from the mathematical literature. These conditions are also called boundary dampers by engineers because of the obvious physical analogy. As was seen in Chapter 12 of Ref. [12], we can simply apply the plane damper at the boundary of the mesh. This was first done in fluid problems by Zienkiewicz and Newton [6]. However the low-order versions of the more sophisticated NRBCs or dampers proposed by Bayliss et al. [18, 19] can be used at little extra computational cost and a big increase in accuracy. The NRBCs are developed from the series given in Table 11.1. Details for low-order cases are given in Ref. [26]. For the case of two-dimensional waves the line integral which should be applied on the circular boundary of radius r is

$$A = \int_{\Gamma} \left[\frac{\alpha}{2} \eta^2 + \frac{\beta}{2} \left(\frac{\partial \eta}{\partial s} \right)^2 \right] ds \quad (11.14)$$

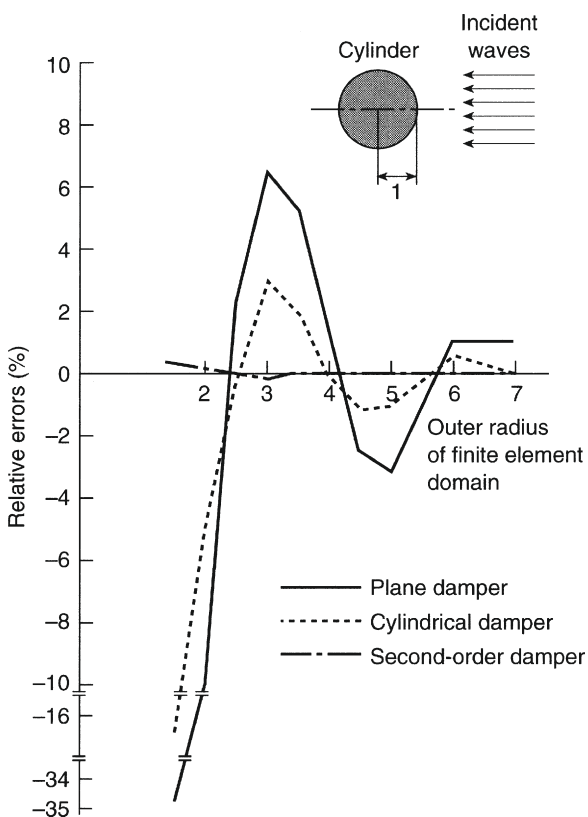
where ds is an element of distance along the boundary and

$$\alpha = \frac{3/4r^2 - 2k^2 + 3ik/r}{2/r + 2ik} \quad \text{and} \quad \beta = \frac{1}{2/r + 2ik} \quad (11.15)$$

For the plane damper, $\beta = 0$ and $\alpha = ik$. For the cylindrical damper $\beta = 0$ and $\alpha = ik - 1/2r$. The corresponding expressions for three-dimensional waves are different. Noncircular boundaries can be handled but the expressions become much more complicated. This is because as the higher-order terms are included in the boundary condition, then higher-order derivatives in the normal direction are required. These can be transformed into derivatives in the circumferential direction by using the governing wave equation. However, even derivatives in the circumferential direction pose difficulties. So NRBCs based on the Bayliss expressions have, in practice, been limited to the lowest few terms. Some results are given by Bando et al. [26]. Figure 11.2 shows the waves diffracted by a cylinder problem for which there is a solution, due to Havelock [27]. In this case the second-order damper is the highest order modeled. The higher-order dampers are clearly a big improvement over the plane and cylindrical dampers, for little or no extra computational cost. Other researchers, of whom we mention only Engquist and Majda [28, 29], Higdon [30, 31], and Hagstrom et al. [32, 33], have also proposed NRBCs. Although the derivations vary considerably the effect is similar, in that a hierarchy of boundary operators is defined, but the resulting terms are different to those of Bayliss et al.

For the Helmholtz equation the general form of these NRBCs can be written as

$$\prod_{j=1}^N \left(\frac{\partial}{\partial t} + C_j \frac{\partial}{\partial n} \right) \phi = 0 \quad (11.16)$$

**FIGURE 11.2**

Damper solutions for waves diffracted by circular cylinder. Comparison of relative errors for various outer radii ($ka = 1$). Relative error = $(\text{abs}(\eta_n) - \text{abs}(\eta_a)) / \text{abs}(\eta_a)$.

where ϕ is the field variable, n is the normal to the boundary, and C_j is the j term in the boundary condition. The expressions for C_j vary, depending upon whose theory is used. One approach is simply to use a range of waves with different angles of incidence. (Obviously the plane damper case arises when $N = 1$ and C_1 is the wave speed.) All these sets of NRBCs have in common the problem of the escalating order of derivatives, arising from expansion of the products of the operator terms in Eq. (11.16). This has been a problem but Givoli [34, 35] has recently demonstrated how the high-order derivative difficulty can be sidestepped through the use of auxiliary variables. The most straightforward way of using auxiliary variables leads to an unsymmetric matrix for the boundary condition terms. But Givoli [35] proves that this unsymmetric matrix can always be transformed into a symmetric form and gives the necessary construction. The method results in the addition of auxiliary variables on the boundary of the mesh, but no other difficulties. Givoli expands Eq. (11.16), using auxiliary

variables so that it becomes

$$\left(\frac{\partial}{\partial t} + C_j \frac{\partial}{\partial n} \right) \phi = u_1 \quad (11.17)$$

$$\left(\frac{\partial}{\partial t} + C_j \frac{\partial}{\partial n} \right) u_1 = u_2 \quad (11.18)$$

⋮

$$\left(\frac{\partial}{\partial t} + C_j \frac{\partial}{\partial n} \right) u_{N-1} = u_N \quad (11.19)$$

where u_j are the auxiliary variables. The resulting matrix (which in general is unsymmetric), representing the effect of these auxiliary variables on the boundary, is then transformed according to Givoli's procedure into a symmetrical matrix. The procedure works for both transient and harmonic problems.

The literature on these boundary conditions has grown remarkably in recent years and this section has only been able to give an outline of the possibilities available. For further information the reader is referred to the book by Givoli [23] and the volume edited by Geers [24], which gives access to recent developments. The papers in the Geers volume by Bielak, Givoli, Hagstrom, Hariharan, Higdon, Pinsky, and Kallivokas should be consulted.

11.8.1 Sponge layers or perfectly matched layers (PMLs)

As was seen earlier, nonreflecting boundary conditions (NRBCs) attempt to absorb the outgoing wave on the boundary of the computational domain. An obvious extension of this idea is to absorb the wave over an artificial domain, external to the domain of interest. It is intuitively obvious that if the domain is made large enough and the correct damping is inserted, then the wave energy reflected back into the domain of interest must become very small. In surface waves the physical analogy is to the energy absorbers, often made of horse hair, at the ends of wave tanks. The theoretical developments in this field go under two names, *sponge layer* which tends to be used in hydraulic computations and meteorology and *perfectly matched layers* (PMLs), in electromagnetics, or Maxwell's equations, and related fields such as acoustics, quantum mechanics, and elastodynamics. Some authors do use both terms. The first paper on the method appears to be that of Larsen and Dancy [36] in 1983. The PML was first applied to Maxwell's equations by Bérenger [37,38], in 1994. In this method a damping factor is introduced in each equation in those places where a normal spatial derivative appears. That is the governing equations are modified so that in the sponge layer or PML region a damping term is introduced. The damping factor is selected in a semi-empirical way and typically varies in space. More details are given in Refs. [39,40] and in the papers by Monk and Collino, Hayder, and Driscoll in Ref. [24].

11.9 Infinite elements

Infinite elements are described in the book by Bettess [41], which although out-of-date, can be used as an introduction to the topic. More recent reviews are by Astley [42] and Gerdes [43]. The methods described Chapter 7 of Ref. [12], can be developed to include periodic effects. This was first done by Bettess and Zienkiewicz, using so-called “decay function” procedures and they were very effective [11,44]. Comparison results with Chen and Mei [45,46] for the artificial island problem are shown in Fig. 12.6 of Ref. [12]. Later “mapped” infinite elements were developed for wave problems, and as these are more accurate than those using exponentials, they will be described here.

11.9.1 Mapped periodic (unconjugated) infinite elements

The theory developed in Chapter 7 of Ref. [12] for static infinite elements will not be repeated here. Details are given in Refs. [11,22,41–44,47–51]. Finite element polynomials of the form

$$P = \alpha_0 + \alpha_1 \xi + \alpha_2 \xi^2 + \dots \quad \text{become} \quad P = \beta_0 + \frac{\beta_1}{r} + \frac{\beta_2}{r^2} + \dots \quad (11.20)$$

in which β_i can be determined from the α 's and a . If the polynomial is zero at infinity then $\beta_0 = 0$.

Many exterior wave problems have solutions in which the wave amplitude decays radially like $1/r$ (and higher-order terms) and an advantage of this mapping is that such a decay can be represented exactly. In some cases, however, the amplitude decays approximately as $1/\sqrt{r}$, and this case needs a slightly different treatment. Accuracy can be increased by adding extra terms to the series (11.20).

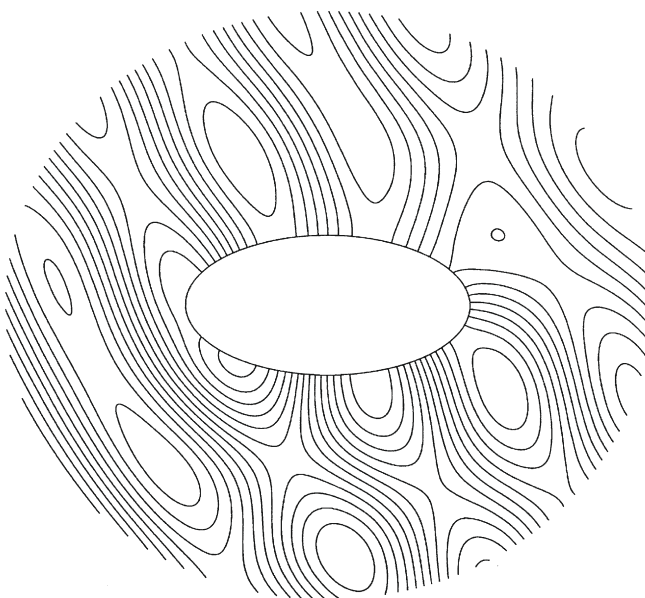
11.9.1.1 Introducing the wave component

In two-dimensional exterior domains the solution to the Helmholtz equation can be described by a series of combined Hankel and trigonometric functions, the simplest solution to the Helmholtz equation being $H_0(kr)$. For large r the zeroth-order Hankel function oscillates roughly like $\cos(kr) + i \sin(kr)$, while decaying in magnitude as $r^{-1/2}$. A series of terms $1/r, 1/r^2$, etc., generated by the mapping, multiplied by $r^{1/2}$ and the periodic component $\exp(ikr)$ will be used to model the $r^{-1/2}$ decay. The shape function is thus

$$N(\xi, \eta) = M(\xi, \eta) r^{1/2} \exp(ikr) \quad (11.21)$$

where $r = A/(1 - \xi)$. The shape function in Eq. (11.21) will now be, for compatibility with the finite elements,

$$N(\xi, \eta) = M(\xi, \eta) \left(\frac{2}{A} \right)^{1/2} \left(\frac{A}{1 - \xi} \right)^{1/2} \exp \left(\frac{ikA}{2} \right) \exp \left(\frac{ikA}{1 - \xi} \right) \quad (11.22)$$

**FIGURE 11.3**

Real part of elevations of plane wave diffracted by an ellipse, of aspect ratio 2, Bettess [22].

In the improved version of this element [22], the constant, A , varies within the element. A is now determined on each radial line from the positions of the nodes. It is interpolated between these values. The original mapped infinite element did not include the possibility of varying the mapping, so that the infinite elements had to be placed exterior to a cylinder or sphere. There was also an uncertainty about the integrations in the infinite radial direction, which was resolved by Astley et al. [51]. This arose because the boundary terms at infinity were incompletely stated, although the element, as presented in Refs. [49, 50], is correct. Following the introduction of a shape function of the form given in Eq. (11.22), the standard finite element methodology is used. That is to say the weighted residual or variational expression is formed and integrated over the infinite domain. The only novelties are the oscillatory nature of the shape function, and the infinite extent of the domain. Mapped wave envelope infinite elements were later developed, using the same methodology, but with a complex conjugate weighting (see Section 11.9.2). Later still Astley et al. [52], Cremers, and Fyfe and Coyette [53, 54] generalized the mapping of these wave envelope infinite elements, so that it was no longer necessary to place them exterior to a sphere or cylinder. After this work Bettess and Bettess [22] generalized the original mapped wave infinite elements. Figure 11.3 shows some results from the diffraction of waves by an ellipse, for which there is an analytical solution.

11.9.2 Ellipsoidal type infinite elements of Burnett and Holford

Burnett with Holford [55–57] proposed a completely new type of infinite element for exterior acoustics problems. This uses prolate or oblate spheroidal coordinates, and separates the radial and angular coordinates. Burnett also further clarified the variational statement of the problem and explained in more detail the terms at the infinite boundary. It is known that a scattered wave exterior to a sphere can be written in spherical polar coordinates as

$$p = \frac{e^{-kr}}{r} \sum_{n=0}^{\infty} \frac{G_n(\theta, \phi, k)}{r^n} \quad (11.23)$$

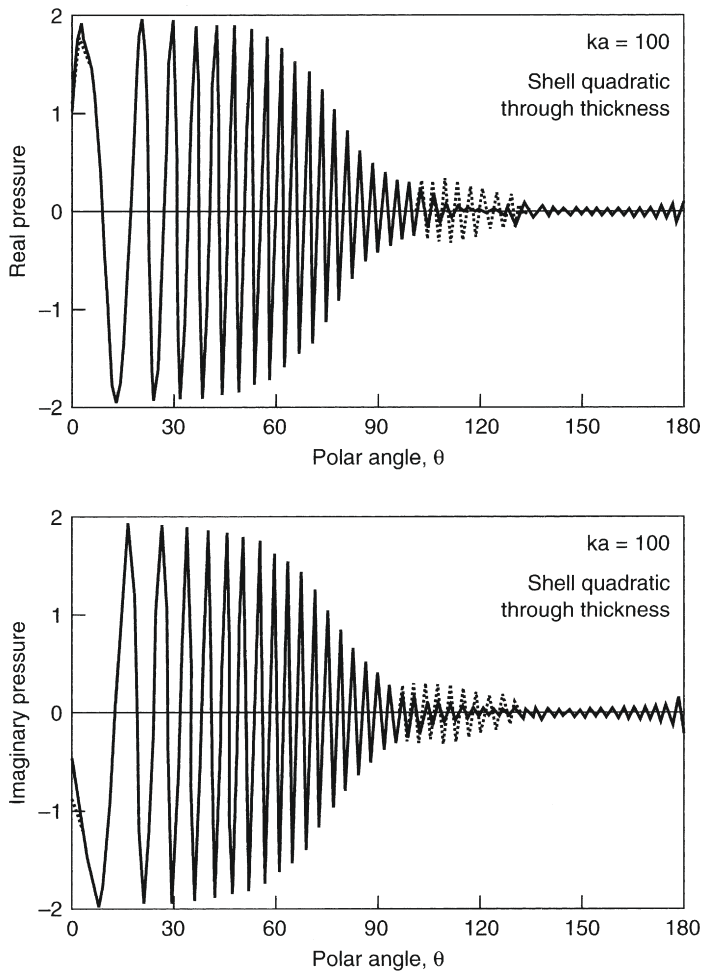
This proof was generalized to the case when the coordinates θ, ϕ, r are not simply spherical, but prolate or oblate spheroidal or ellipsoidal. There are several benefits to using such coordinate systems:

- The volume integrals separate into radial and angular parts which can be carried out independently. This leads to economies in computation.
- The radial integration is identical for every such infinite element, so that the only integration which needs to be carried out for every infinite element is along the finite element interface.
- The radial integration is the only part containing the wavenumber.
- The ellipsoidal coordinates can be used to enclose a large variety of different geometries in the finite element interior, while still retaining a guarantee of convergence in 3D.

The angular shape functions are written in the conventional polynomial form. The radial shape functions take the form

$$N_i = e^{-ikr} \sum_{j=1}^m \frac{h_{ij}}{(kr)^j} \quad (11.24)$$

The coefficients h_{ij} are given from the condition of circumferential compatibility between adjacent infinite elements. There is effectively no difference between this radial behavior and that originally proposed in the mapped infinite wave elements by Bettess et al. [49,50]. The difference in the infinite element methodology lies in the fact that the radial variable, r , is now in ellipsoidal coordinates. Burnett and Holford [55–57] give the necessary detailed information for the element integrations and the programming of these infinite elements, together with some results. The analytical expressions are too long to include here. The elements have been used on submarine fluid-structure interaction problems, and substantial efficiencies over the use of boundary integral models for the scattered waves have been claimed. In one case Burnett states that the finite and infinite element model ran for 7 h on a workstation. His projected time for the corresponding boundary element model was about 3000 h, the infinite elements giving a dramatic improvement!

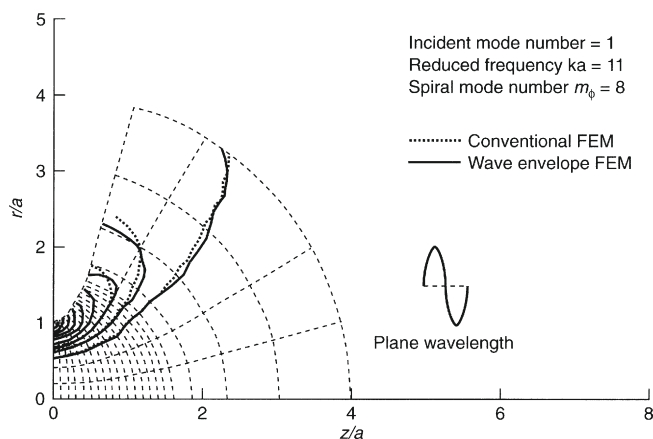
**FIGURE 11.4**

Waves scattered by an elastic sphere for $ka = 100$, Burnett and Halford [57].

The Burnett elements have been tested up to very short-wave cases, up to $ka = 100$ for an elastic sphere diffraction problem, which is shown in Fig. 11.4.

11.9.3 Wave envelope (or conjugated) infinite elements

Astley introduced a new type of finite element, in which the weighting function is the complex conjugate of the shape function [58,59]. The great simplification which this introduces is that the oscillatory function $\exp(ikr)$ cancels after being multiplied by $\exp(-ikr)$, and the remaining terms are all polynomials, which can be integrated using standard techniques, like Gauss-Legendre integration (see Chapters 3 and 6 of Ref.

**FIGURE 11.5**

Computed acoustical pressure contours for a hyperbolic duct ($\theta_0 = 70^\circ$, $ka = 11$, $m_\phi = 8$). Conventional and wave envelope element solutions, Astley [59].

[12]). This type of element was originally large (i.e., many wavelengths in extent), but not infinite. Figure 11.5 shows an example from acoustics, that of acoustical pressure in a hyperbolic duct. Good results were obtained despite using a relatively coarse mesh. Astley's shape function was of the form

$$N_i(r, \theta) \frac{r_i}{r} e^{-ik(r-r_i)} \quad (11.25)$$

where N_i is the standard shape function. The weighting function is thus

$$N_i(r, \theta) \frac{r_i}{r} e^{ik(r-r_i)} \quad (11.26)$$

Bettess [60] showed that for a one-dimensional synthetic wave-type equation the infinite wave envelope element recovers the exact solution. The element matrix is now hermitian rather than symmetric (though still complex), which necessitates a small alteration to the equation solver. (There are not usually any problems in changing standard profile or front solvers to deal with complex systems of equations.) Unfortunately the problem tackled by Bettess did not include the essential feature of physical waves, in two and three dimensions. Later workers applied the wave envelope concept to true wave problems. In this case it can be shown that if the weighting function is simply the complex conjugate of the shape function, terms arise on the boundary at infinity.¹ This is discussed by Bettess [41]. The terms can be evaluated, but they are not symmetrical (or hermitian), and therefore impose a change of solution technique. An alternative, which eliminates the terms at infinity, was proposed by

¹Some writers, particularly mathematicians, prefer to call the usual wave infinite elements unconjugated infinite elements, and the Astle-type wave envelope infinite elements conjugated infinite elements.

Astley et al. [52]. In this a “geometrical factor” is included in the weighting function, which then takes the form

$$N_i(r, \theta) \left(\frac{r_i}{r}\right)^3 e^{ik(r-r_i)} \quad (11.27)$$

It has been shown that this form of weighting functions gives very good results. Such wave envelope infinite elements have been further developed by Coyette, Cremers and Fyfe [53,54]. These elements have incorporated a more general mapping than that in the original Zienkiewicz et al. mapped infinite wave element. Cremers and Fyfe allow the mapping to vary in the local ξ and η directions.

11.9.4 Accuracy of infinite elements

The use of a complex conjugate weighting in the wave envelope infinite elements means that the original variational statement, Eq. (11.12), must be changed to allow the use of the different weighting function. This gives rise to a number of issues relating to the nature of the weighted residual statement and the existence of various terms. These issues were touched upon by Bettess [41], but have been subsequently subjected to more detailed study. Gerdes and Demkowitz [61,62] analyzed the wave envelope elements, and subsequently the wave infinite elements [63]. Some of this work is restricted to spherical scatterers. Other analysis is carried out by Shirron and Babuška [64,65], who reveal a somewhat paradoxical result. The original (unconjugated) infinite elements give better results in the finite element mesh, but worse results in the infinite elements themselves. But the wave envelope (conjugated) elements give worse results in the finite elements, and better results in the far field. This result, which is ascribed to ill-conditioning, does seem to be counterintuitive. Astley [42] and Gerdes [43] have also surveyed current formulations and accuracies. Infinite elements have traditionally been used with relatively small numbers of radial terms. Recent investigations have addressed the problems of ill-conditioning and accuracy of infinite elements when the number of terms in the radial direction is increased [42,66–68]. In general it is found that the more radial terms that are retained, the worse the conditioning of the infinite element. This is similar to the effect noted in plane wave basis finite elements, which are discussed in Chapter 12. It has been suggested by Dreyer and von Estorff [68] that the ill-conditioning effect can be reduced by the use of Jacobi polynomials in the radial direction.

11.9.5 Other applications

Infinite elements have been applied to a large range of applications, and it is impossible to survey the field in the scope of this chapter. The reader is directed to Refs. [41–43]. An interesting application of infinite elements to Maxwell’s equations by Demkowitz and Pal [69] is worthy of mention.

11.9.6 Trefftz-type infinite elements

Harari, with various coworkers [70–73], has developed infinite elements for the Helmholtz equation in two and three dimensions. The elements are sectors, bounded by radial lines defined by θ_s and θ_{s+1} , and the arc $r = R$. Then $\Delta\theta_s = \theta_{s+1} - \theta_s$. Hankel functions are used to describe the radial behavior and the circumferential behavior is modeled using linear polynomials in θ . For a two-noded element the shape functions can be written

$$N_1 = \frac{H_0(kr)}{H_0(kR)} \frac{\theta_{s+1} - \theta}{\Delta\theta_s} \quad \text{and} \quad N_2 = \frac{H_0(kr)}{H_0(kR)} \frac{\theta - \theta_s}{\Delta\theta_s} \quad (11.28)$$

The advantage of this formulation is that because the Hankel functions are solutions of the Helmholtz equation the integrations over the infinite elements can be eliminated. Continuity between the finite element domain and the infinite element domain is enforced weakly, as is the continuity between adjacent infinite elements. Harari shows that the matrices which arise for the case of linear infinite elements, with an orientation as specified, are

$$kR \frac{H'_0(kR)}{H_0(kR)} \frac{\Delta\theta_s}{6} \begin{bmatrix} 2 & 1 \\ 1 & 2 \end{bmatrix} \quad (11.29)$$

for the finite/infinite element interface and

$$kR \frac{\alpha_{00}}{\Delta\theta_s} \begin{bmatrix} 1 & -1 \\ -1 & 1 \end{bmatrix} \quad (11.30)$$

where

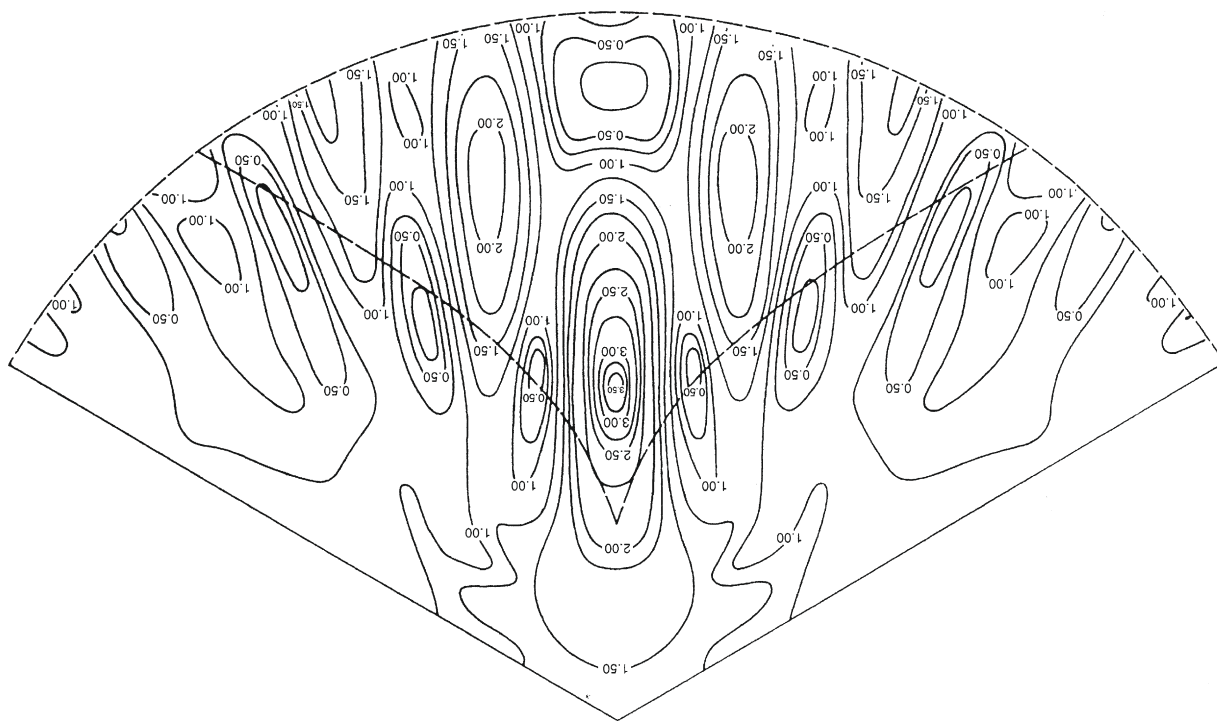
$$\alpha_{00} = \int_0^\infty \frac{H_0(kr)H_0(kr)}{H_0(kR)H_0(kR)} \frac{dr}{r} \quad (11.31)$$

for the boundaries between the infinite element radial boundaries. He also goes on to develop higher-order infinite elements of similar type. He gives results for some academic type problems.

11.10 Convection and wave refraction

Conventional wave finite elements will deal satisfactorily with wave refraction caused by local changes in wave speed. This is seen in the example of [Figure 11.6](#), where changes in water depth lead to local changes in wave speed. In exterior domains infinite elements have difficulties if the problem has a wave speed which is a function of position. There are also difficulties with linking to exterior solutions, or DtN methods, if an analytical solution or Green's function is used, since these almost invariably assume constant wave speed, in which case the Helmholtz equation is homogeneous.

However acoustic waves in inhomogeneous media have been solved using finite elements in conjunction with large (but finite) wave envelope elements by Astley

**FIGURE 11.6**

Refraction-diffraction solution: lines of equal wave height, lines every 0.25 unit [10].

and Eversman [74]. In this case the governing equation is the inhomogeneous wave equation

$$\rho \nabla \cdot \left(\frac{1}{\rho} \nabla p^* \right) - \left(1/c^2 \right) \frac{\partial^2 p^*}{\partial t^2} = 0 \quad (11.32)$$

where ρ is the density, c is the wave speed, and p^* is the acoustical pressure.

Wave refraction can also occur because the waves are superposed upon a underlying flow field. Important applications are surface waves on water currents and sound waves on air flows, for example in aircraft noise. This case is more difficult and the general equations become complicated. See for example, Lighthill [4]. For the case of sound waves superposed on a flow field Astley [75] has applied wave envelope finite elements to problems in which a substantial amount of convection is present. In this case the governing equation is no longer the Helmholtz equation. A detailed discussion is beyond the scope of this chapter.

11.11 Transient problems

Astley [76–78] has extended his wave envelope infinite elements using the prolate and oblate spheroidal coordinates adopted by Burnett and Holford [55–57], and has shown that they give accurate solutions to a range of transient wave problems. With the geometric factor of Astley, which reduces the weighting function and eliminates the surface integrals at infinity, the stiffness, \mathbf{K} , damping, \mathbf{C} , and mass, \mathbf{M} , matrices of the wave envelope infinite element become well defined and *frequency independent*, although unsymmetric. This makes it possible to apply such elements to unbounded transient wave problems. Figure 11.7 shows the transient response of a dipole.

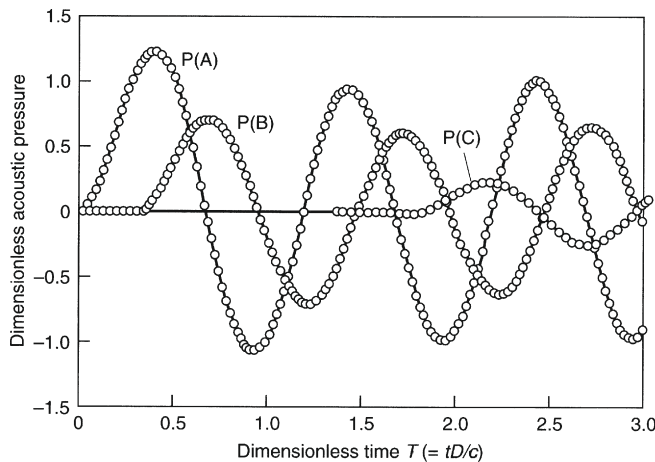


FIGURE 11.7

Transient response of a dipole, Astley [66].

More results from the application of infinite elements to transient problems are given by Cipolla and Butler [79], who created a transient version of the Burnett infinite element. There appear to be more difficulties with such elements than with the wave envelope elements, and a consensus that the latter are better for transient problems seems to be emerging. Dampers and boundary integrals can also be used for transient problems. Space is not available to survey these fields, but the reader is directed, again, to Givoli [23] and Geers [24]. One set of interesting results was obtained using transient dampers by Thompson and Pinsky [80].

11.12 Linking to exterior solutions (or DtN mapping)

A general methodology for linking finite elements to exterior solutions was proposed by Zienkiewicz et al. [81, 82], following various *ad hoc* developments, and this is also discussed in Ref. [12], particularly in Chapter 11. The linking of interior and exterior solutions is also sometimes called *Dirichlet to Neumann* or DtN mapping. Under this title it is discussed by many authors, including Givoli [23]. The exterior solution can take any form, and those chiefly used are (a) exterior series solutions and (b) exterior boundary integrals, although others are possible. The two main innovators in these cases were Berkhoff [10, 83], for coupling to boundary integrals, and Chen and Mei [45, 46], for coupling to exterior series solutions (although there are earlier papers on the linking of finite elements and exterior solutions). Astley [84] demonstrates for the wave equation that the Chen and Mei methods are effectively the same as what has been more recently termed DtN mapping. Although the methods which have been proposed for linking finite elements to exterior series solutions and boundary integrals are quite different in detail, it is useful to cast them in the same general form. More details of this procedure are given in Ref. [81]. Basically the energy functional given in Eq. (11.13) is again used. If the functions used in the exterior automatically satisfy the wave equation, then the contribution on the boundary reduces to a line integral of the form

$$\Pi = \frac{1}{2} \int_{\Gamma} \eta \frac{\partial \eta}{\partial n} d\Gamma \quad (11.33)$$

It can be shown [16, 81, 82] that if the free parameters in the interior and exterior are **b** and **a**, respectively, the coupled equations can be written as

$$\begin{bmatrix} \mathbf{K} & \bar{\mathbf{K}}^T \\ \bar{\mathbf{K}} & \bar{\mathbf{K}} \end{bmatrix} \begin{Bmatrix} \mathbf{a} \\ \mathbf{b} \end{Bmatrix} + \begin{Bmatrix} \mathbf{f} \\ \mathbf{0} \end{Bmatrix} = \begin{Bmatrix} \mathbf{0} \\ \mathbf{0} \end{Bmatrix} \quad (11.34)$$

where

$$\check{K}_{ji} = \frac{1}{2} \int_{\Gamma} [(PN_j)N_i + N_j(PN_i)] d\Gamma \quad \text{and} \quad \bar{K}_{ji} = \int_{\Gamma} [(PN_j)(\bar{N}_i)] d\Gamma \quad (11.35)$$

In the above P is an operator giving the normal derivative, i.e., $P \equiv \partial/\partial n$, $\bar{\mathbf{N}}$ is the finite element shape function, \mathbf{N} is the exterior shape function, and \mathbf{K} corresponds

to the normal finite element matrix. The approach described above can be used with any suitable form of exterior solution, as we will see. All the nodes on the boundary become coupled.

11.12.1 Linking to boundary integrals

Berkhoff [10,83] adopted the simple expedient of identifying the nodal values of velocity potential obtained using the boundary integral, with the finite element nodal values. This leads to a rather clumsy set of equations, part symmetrical, real and banded, and part unsymmetrical, complex and dense. The direct boundary integral method for the Helmholtz equation in the exterior leads to a matrix set of equations

$$\mathbf{A}\tilde{\eta} = \mathbf{B}\frac{\partial\tilde{\eta}}{\partial n} \quad (11.36)$$

(The indirect boundary integral method can also be used.) The values of η and $\partial\eta/\partial n$ on the boundary are next expressed in terms of shape functions, so that

$$\eta \approx \hat{\eta} = \mathbf{N}\tilde{\eta} \quad \text{and} \quad \frac{\partial\eta}{\partial n} \approx \frac{\partial\hat{\eta}}{\partial n} = \mathbf{M} \left\{ \frac{\partial\tilde{\eta}}{\partial n} \right\} \quad (11.37)$$

\mathbf{N} and \mathbf{M} are equivalent to \mathbf{N} in the previous section. Using this relation, the integral for the outer domain can be written as

$$\Pi = \frac{1}{2} \int_{\Gamma} \frac{\partial\tilde{\eta}}{\partial n} \mathbf{M}^T \mathbf{N} \tilde{\eta} d\Gamma \quad (11.38)$$

where Γ is the boundary between the finite elements and the boundary integrals. The normal derivatives can now be eliminated, using the relation (11.36), and η can be identified with the finite element nodal values, η , to give

$$\Pi = \frac{1}{2} \mathbf{b}^T (\mathbf{B}^{-1} \mathbf{A})^T \int_{\Gamma} \mathbf{M}^T \mathbf{N} d\Gamma \mathbf{b} \quad (11.39)$$

Variations of this functional with respect to \mathbf{b} can be set to zero, to give

$$\frac{\partial\Pi}{\partial\mathbf{b}} = \frac{1}{2} \left\{ (\mathbf{B}^{-1} \mathbf{A}) \int_{\Gamma} \mathbf{M}^T \mathbf{N} d\Gamma + \left[(\mathbf{B}^{-1} \mathbf{A}) \int_{\Gamma} \mathbf{M}^T \mathbf{N} d\Gamma \right]^T \right\} \mathbf{b} = \check{\mathbf{K}}\mathbf{b} \quad (11.40)$$

where $\check{\mathbf{K}}$ is a “stiffness” matrix for the exterior region. It is symmetric and can be created and assembled like any other element matrix. The integrations involved must be carried out with care, as they involve singularities. Results obtained for the problem of waves refracted by a parabolic shoal are shown in Fig. 5.6 of Ref. [82].

11.12.2 Linking to series solutions

Chen and Mei [45,46] took the series solution for waves in the exterior, and worked out explicit expressions for the exterior and coupling matrices, $\bar{\mathbf{K}}$ and $\hat{\mathbf{K}}$, for piecewise

linear shape functions, $\tilde{\mathbf{N}}$, in the finite elements. The series used in the exterior consists of Hankel and trigonometric functions which automatically satisfy the Helmholtz equation and the radiation condition:

$$\eta = \sum_{j=0}^m H_j(kr)(\alpha_j \cos j\theta + \beta_j \sin j\theta) \quad (11.41)$$

The method described above leads to the following matrices:

$$\tilde{\mathbf{K}}^T = \frac{-knL_c}{2} \begin{bmatrix} 2H'_0 & \cdots & H'_n(\cos n\theta_p + \cos n\theta_1) & H'_n(\sin n\theta_p + \sin n\theta_1) & \cdots \\ 2H'_0 & \cdots & H'_n(\cos n\theta_1 + \cos n\theta_2) & H'_n(\sin n\theta_1 + \sin n\theta_2) & \cdots \\ 2H'_0 & \cdots & H'_n(\cos n\theta_2 + \cos n\theta_3) & H'_n(\sin n\theta_2 + \sin n\theta_3) & \cdots \\ \vdots & \cdots & \vdots & \vdots & \ddots \\ 2H'_0 & \cdots & H'_n(\cos n\theta_{p-1} + \cos n\theta_p) & H'_n(\sin n\theta_{p-1} + \sin n\theta_p) & \cdots \end{bmatrix} \quad (11.42)$$

$$\hat{\mathbf{K}} = \pi rkh \left\{ \text{diag}[2H_0 H'_0 \ H'_1 H_1 \ H'_1 H_1 \ \cdots \ H'_s H_s \ H'_s H_s] \right\} \quad (11.43)$$

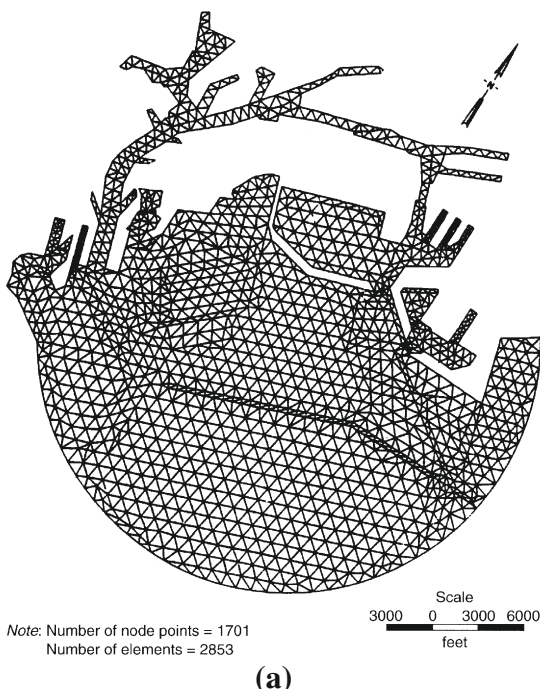
where m is the number of terms in the Hankel function series, r is the radius of the boundary, L_c is the distance between the equidistant nodes on Γ_C , p is the number of nodes, and H_n and H'_n are Hankel functions and derivatives evaluated with argument (kr) .

Other authors have worked out the explicit forms of the above matrices for linear shape functions, and it is possible to work them out for any type of shape function, using, if necessary, numerical integration. It will be noticed that the matrix $\hat{\mathbf{K}}$ is diagonal. This is because the boundary Γ_B is circular and the Hankel functions are orthogonal. If a noncircular domain is used, $\hat{\mathbf{K}}$ will become dense. Chen and Mei [45] applied the method very successfully to a range of problems, most notably that of resonance effects in an artificial offshore harbor, the results for which are shown in Chapter 12, Fig. 12.6 of Ref. [12].

The method was also utilized by Houston [85], who applied it to a number of real problems, including resonance in Long Beach harbor, shown in Fig. 11.8.

11.13 Three-dimensional effects in surface waves

As has already been described, when the water is deep in comparison with the wavelength, the shallow-water theory is no longer adequate. For constant or slowly varying depth, Berkhoff's theory is applicable. Also the geometry of the problem may necessitate another approach. The flow in the body of water is completely determined by the conservation of mass, which in the case of incompressible flow reduces to Laplace's equation. The free surface condition is zero pressure. On using Bernoulli's equation and the kinematic condition, the free surface condition can be expressed, in terms of

**FIGURE 11.8**

Finite element mesh and wave height magnification for Long Beach Harbor, Houston [85]: (a) finite element grid, grid 3; (b) contours of wave height amplification, grid 3, 232 s wave period.

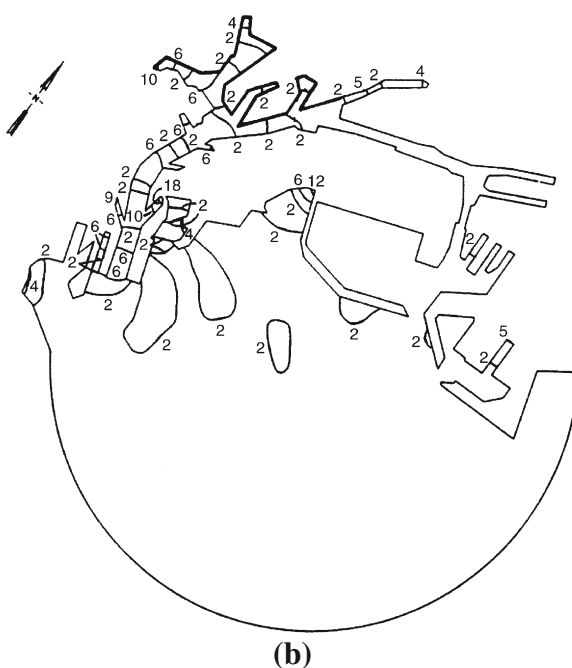
the velocity potential, ϕ , as

$$\frac{\partial^2 \phi}{\partial t^2} + g \frac{\partial \phi}{\partial t} + 2(\nabla \phi)^T \left[\nabla \left(\frac{\partial \phi}{\partial t} \right) \right] + \frac{1}{2} (\nabla \phi)^T \nabla [(\nabla \phi)^T \nabla \phi] = 0 \quad (11.44)$$

where the velocities are $u_i = \partial \phi / \partial x_i$. This condition is applied on the free surface, whose position is unknown *a priori*. If only linear terms are retained, Eq. (11.44) becomes, for transient and periodic problems

$$\frac{\partial^2 \phi}{\partial t^2} + g \frac{\partial \phi}{\partial z} = 0 \quad \text{or} \quad \frac{\partial \phi}{\partial z} = \frac{\omega^2}{g} \phi \quad (11.45)$$

which is known as the *Cauchy-Poisson* free surface condition. It was derived in terms of pressure as Eq. (18.13) of Chapter 18 of Ref. [17]. Three-dimensional finite elements can be used to solve such problems. The actual three-dimensional element is very simple, being a potential element of the type described in Chapter 7 of Ref. [17] or Chapter 5 of Ref. [12]. The natural boundary condition is $\partial \phi / \partial n = 0$, where n is the outward normal, so to apply the free surface condition it is only necessary to add

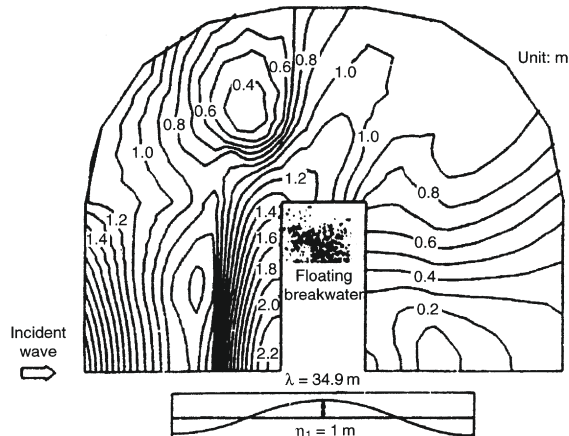
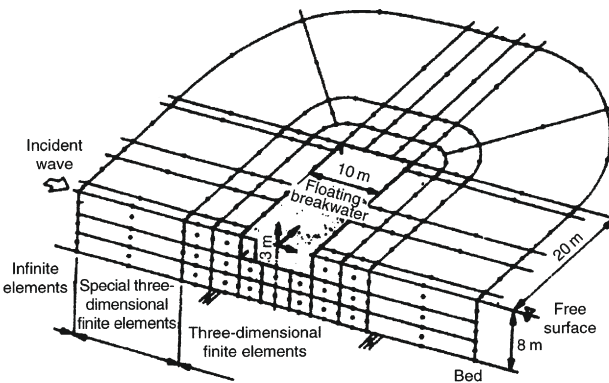
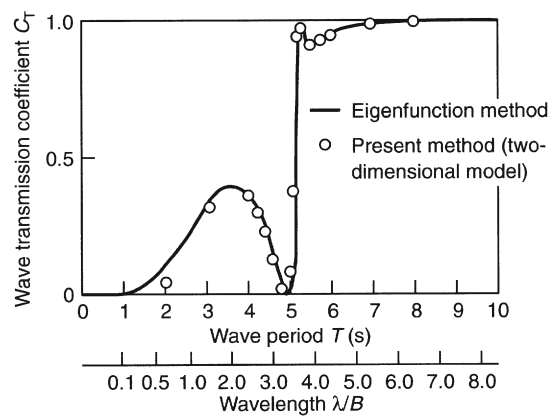
**FIGURE 11.8**

(Continued)

a surface integral to generate the ω^2/g term from the Cauchy-Poisson condition (see Eq. (18.13) of Ref. [17]). Two-dimensional elements in the far field can be linked to three-dimensional elements in the near field around the object of interest. Such models will predict velocity potentials, pressures throughout the fluid, and wave elevations. They can also be used to predict fluid-structure interaction. All the necessary equations are given in Chapter 18 of Ref. [17]. More details of fluid-structure interactions of this type are given by Zienkiewicz and Bettess [86]. Essentially the fluid equations must be solved for incident waves, and for motion of the floating body in each of its degrees of freedom (usually six). The resulting fluid forces, masses, stiffnesses, and damping are used in the equations of motion of the structure to determine its response. Figure 11.9 shows some results obtained by Hara et al. [87] for a floating breakwater. They obtained good agreement between the infinite elements and the methods of Section 11.12.

11.13.1 Large-amplitude water waves

There is no complete wave theory which deals with the case when η is not small in comparison with the other dimensions of the problem. Various special theories are invoked for different circumstances. We consider two of these, namely, large wave

**FIGURE 11.9**

Element mesh, contours of wave elevation, and wave transmission coefficients for floating breakwater, Hara [87].

elevations in shallow water and large wave elevations in intermediate to deep water. We discussed a similar problem in [Chapter 10](#).

11.13.2 Cnoidal and solitary waves

The equations modeled in [Chapter 10](#) can deal with large-amplitude waves in shallow water. These are called cnoidal waves when periodic, and solitary waves when the period is infinite. For more details, see [Refs. \[1–4\]](#). The finite element methodology of [Chapter 10](#) can be used to model the propagation of such waves. It is also possible to reduce the equations of momentum balance and mass conservation to corresponding wave equations in one variable, of which there are several different forms. One famous equation is the Korteweg–de Vries equation, which in physical variables is

$$\frac{\partial \eta}{\partial t} + \sqrt{gH} \left(1 + \frac{3\eta}{2h} \right) \frac{\partial \eta}{\partial x} + \frac{h^2}{6} \sqrt{gH} \frac{\partial^3 \eta}{\partial x^3} = 0 \quad (11.46)$$

This equation has been given a great deal of attention by mathematicians. It can be solved directly using finite element methods, and a general introduction to this field is given by Mitchell and Schoombie [\[88\]](#).

11.13.3 Stokes waves

When the water is deep, a different asymptotic expansion can be used in which the velocity potential, ϕ , and the surface elevation, η , are expanded in terms of a small parameter, ε , which can be identified with the slope of the water surface. When these expressions are substituted into the free surface condition, and terms with the same order in ε are collected, a series of free surface conditions is obtained. The equations were solved by Stokes initially, and then by other workers, to very high orders, to give solutions for large-amplitude progressive waves in deep water. There is an extensive literature on these solutions, and they are used in the offshore industry for calculating loads on offshore structures. In recent years, attempts have been made to model the second-order wave diffraction problem, using finite elements, and similar techniques. The first-order diffraction problem is as described in [Section 11.8.1](#). In the second-order problem, the free surface condition now involves the first-order potential.

First order

$$\frac{\partial \phi^{(1)}}{\partial z} - \frac{\omega^2}{g} \phi^{(1)} = 0 \quad (11.47)$$

Second order

$$\frac{\partial \phi^{(2)}}{\partial z} - \frac{\omega^2}{g} \phi^{(2)} = \alpha_D^{(2)} \quad (11.48)$$

$$\alpha_D^{(2)} = \alpha_{DI}^{(2)} + \alpha_{DD}^{(2)} \quad \text{and} \quad v = \frac{\omega^2}{g} \quad (11.49)$$

$$\begin{aligned}\alpha_{DI}^{(2)} = & -i \frac{\omega}{2g} \phi_D^{(1)} \left(\frac{\partial^2 \phi_I^{(1)}}{\partial z^2} - v \frac{\partial \phi_I^{(1)}}{\partial z} \right) - i \frac{\omega}{2g} \phi_I^{(1)} \left(\frac{\partial^2 \phi_D^{(1)}}{\partial z^2} - v \frac{\partial \phi_D^{(1)}}{\partial z} \right) \\ & + i \frac{2\omega}{g} \nabla \phi_I^{(1)} \nabla \phi_D^{(1)}\end{aligned}\quad (11.50)$$

$$\alpha_{DD}^{(2)} = -i \frac{\omega}{2g} \phi_D^{(1)} \left(\frac{\partial^2 \phi_D^{(1)}}{\partial z^2} - v \frac{\partial \phi_D^{(1)}}{\partial z} \right) + i \frac{2\omega}{g} (\nabla \phi_D^{(1)})^2 \quad (11.51)$$

The second-order boundary condition can be thought of as identical to the first-order problem, but with a specified pressure applied over the entire free surface, of value α . Now there is no *a priori* reason why such a pressure distribution should give rise to outgoing waves as in the first-order problem, and so the usual radiation condition is not applicable. The conventional procedure is to split the second-order wave into two parts, one the “locked” wave, in phase with the first-order wave, and the other the “free” wave, which is like the first-order wave but at twice the frequency, and with an appropriate wavenumber obtained from the dispersion relation. For further details of the theory, see Clark et al. [89]. Figure 11.10 shows results for the second-order wave elevation around a circular cylinder, obtained by Clark et al. Although not shown, good agreement has been obtained with predictions made by bound-

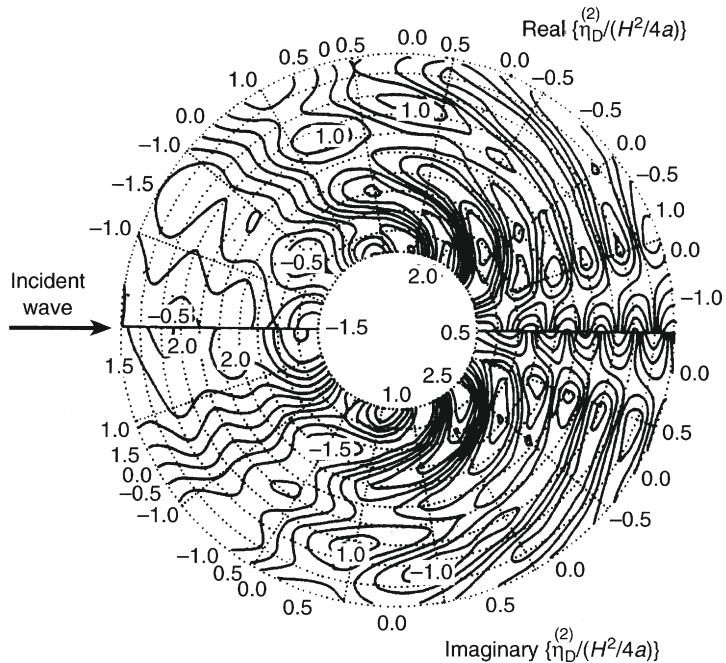


FIGURE 11.10

Second-order wave elevations around cylinder—real and imaginary parts, Clark et al. [89].

ary integrals. Preliminary results, for wave forces only, have also been produced by Lau et al. [90]. A much finer finite element mesh is needed to resolve the details of the waves at second order. The second-order wave forces can be very significant for realistic values of the wave parameters (those encountered in the North Sea for example). The first-order problem is solved first and the first-order potential is used to generate the forcing terms in Eqs. (11.50) and (11.51). These values have to be very accurate. In principle the method could be extended to third and higher orders, but in practice the difficulties multiply, and in particular the dispersion relation changes and the waves become unstable [4].

11.14 Concluding remarks

For waves which are linear and of medium or large length, compared with the size of the problem, in closed and unbounded domains, finite elements are in a fairly mature state. Improvements in element efficiency, such as spectral methods, which are discussed in Chapter 12, are not so critically important if there are few wavelengths in the problem. Incremental improvements in methods for dealing with the exterior domain continue to be made. As well as higher accuracy from the exterior models, a better mathematical understanding is being obtained. The position is not so well developed in the case of elastic waves, which have not been covered in this chapter, for lack of space. The multiple wave speeds in elasticity make some of the exterior domain methods (discussed in Sections 11.6–11.12) either impossible, or highly complicated in practice. There are some results on error indicators for wave problems, which we could not cover due to lack of space. In general, error indicators do not give such a great payoff as they do in static and potential problems, because usually the waves extend throughout the problem and making the mesh coarse anywhere may have the result of polluting the solution in other regions. See the earlier discussion and that in Chapter 12. Error bounds for the exterior methods are thinner on the ground. Nonlinear waves, such as surface waves of large elevation which have been discussed in Section 11.13, remain a significant challenge. Anyone who has seen a wave break on a shoreline must be aware of how difficult it is to model that process on a computer. But apart from surface waves there are not really that many nonlinear waves of great importance. Effects like shocks arising from bores on water, or shock waves and sonic booms in compressible flow, have been dealt with in other chapters.

References

- [1] H. Lamb, *Hydrodynamics*, sixth ed., Cambridge University Press, Cambridge, 1932.
- [2] G.B. Whitham, *Linear and Nonlinear Waves*, John Wiley, New York, 1974.
- [3] C.C. Mei, *The Applied Dynamics of Ocean Surface Waves*, Wiley, New York, 1983.

- [4] M.J. Lighthill, Waves in Fluids, Cambridge University Press, 1978.
- [5] G.M.L. Gladwell, A variational model of damped acousto-structural vibration, *J. Sound Vib.* 4 (1965) 172–186.
- [6] O.C. Zienkiewicz, R.E. Newton, Coupled vibrations of a structure submerged in a compressible fluid, in: Proceedings of the International Symposium on Finite Element Techniques, Stuttgart, 1–15 May 1969, pp. 360–378.
- [7] A. Craggs, The transient response of a coupled plate acoustic system using plate and acoustic finite elements, *J. Sound Vib.* 15 (1971) 509–528.
- [8] R.J. Astley, Finite elements in acoustics, in: Proceedings of Inter-noise 98: Sound and Silence: Setting the Balance, Christchurch, New Zealand, vol. 1, 16–18 November 1998, pp. 3–17.
- [9] P.M. Morse, H. Feshbach, Methods of Theoretical Physics, McGraw-Hill, New York, 1953.
- [10] J.C.W. Berkhoff, Linear wave propagation problems and the finite element method, in: R.H. Gallagher et al. (Eds.), Finite Elements in Fluids, vol. 1, Wiley, Chichester, 1975, pp. 251–280.
- [11] O.C. Zienkiewicz, P. Bettess, Infinite elements in the study of fluid structure interaction problems, in: J. Ehlers et al. (Eds.), Proceedings of the Second International Symposium on Computing Methods in Applied Science and Engineering, Versailles, Springer-Verlag, Berlin, 1975 (also published in J. Ehlers et al., Lecture Notes in Physics, vol. 58, Springer-Verlag, Berlin).
- [12] O.C. Zienkiewicz, R.L. Taylor, J.Z. Zhu, The Finite Element Method: Its Basis and Fundamentals, seventh ed., Elsevier, Oxford, 2013.
- [13] C. Taylor, B.S. Patil, O.C. Zienkiewicz, Harbour oscillation: a numerical treatment for undamped natural modes, *Proc. Inst. Civ. Eng.* 43 (1969) 141–156.
- [14] I. Babuška, F. Ihlenburg, T. Stroubolis, S.K. Gangaraj, A posteriori error estimation for finite element solutions of Helmholtz' equations. Part I: The quality of local indicators and estimators, *Int. J. Numer. Methods Eng.* 40 (1997) 3443–3462.
- [15] I. Babuška, F. Ihlenburg, T. Stroubolis, S.K. Gangaraj, A posteriori error estimation for finite element solutions of Helmholtz' equations. Part II, *Int. J. Numer. Methods Eng.* 40 (1997) 3883–3900.
- [16] O.C. Zienkiewicz, P. Bettess, D.W. Kelly, The finite element method for determining fluid loadings on rigid structures: two- and three-dimensional formulations, in: O.C. Zienkiewicz, R.W. Lewis, K.G. Stagg (Eds.), Numerical Methods in Offshore Engineering, John Wiley, 1978 (Chapter 4).
- [17] O.C. Zienkiewicz, R.L. Taylor, J.Z. Zhu, The Finite Element Method: Its Basis and Fundamentals, sixth ed., Elsevier, Oxford, 2005.
- [18] A. Bayliss, M. Gunzberger, E. Turkel, Boundary conditions for the numerical solution of elliptic equations in exterior regions, ICASE, Report No. 80–1, 1980.
- [19] A. Bayliss, M. Gunzberger, E. Turkel, Boundary conditions for the numerical solution of elliptic equations in exterior regions, *SIAM J. Appl. Math.* 42 (1982) 430–451.

- [20] A. Sommerfeld, Theorie mathematique de la diffraction, *Math. Ann.* 47 (1896) 317–374.
- [21] A. Sommerfeld, *Partial Differential Equations in Physics*, Academic Press, New York, 1949.
- [22] J.A. Bettess, P. Bettess, A new mapped infinite wave element for general wave diffraction problems and its validation on the ellipse diffraction problem, *Comput. Methods Appl. Mech. Eng.* 164 (1998) 17–48.
- [23] D. Givoli, *Numerical Methods for Problems in Infinite Domains*, Elsevier, Amsterdam, 1992.
- [24] T.L. Geers (Ed.), *Computational Methods for Unbounded Domains*, Kluwer Academic Publishers, Dordrecht, 1998.
- [25] F. Ihlenburg, *Finite Element Analysis of Acoustic Scattering*, Springer, New York, 1998.
- [26] K. Bando, P. Bettess, C. Emson, The effectiveness of dampers for the analysis of exterior wave diffraction by cylinders and ellipsoids, *Int. J. Numer. Methods Fluids* 4 (1984) 599–617.
- [27] T.H. Havelock, The pressure of water waves on a fixed obstacle, *Proc. Roy. Soc. Lond. A* 175 (1950) 409–421.
- [28] B. Engquist, A. Majda, Absorbing boundary conditions for the numerical simulation of waves, *Math. Comput.* 31 (1977) 629–652.
- [29] B. Engquist, A. Majda, Radiation boundary conditions for acoustic and elastic wave calculations, *Commun. Pure Appl. Math.* 32 (1979) 313–357.
- [30] R.L. Higdon, Absorbing boundary conditions for difference approximations to the multi-dimensional wave equation, *Math. Comput.* 47 (176) (1986) 437–459.
- [31] R.L. Higdon, Radiation boundary conditions for dispersive waves, *SIAM J. Numer. Anal.* 31 (1994) 64–100.
- [32] T. Hagstrom, T. Warburton, High-order radiation boundary conditions for time-domain electromagnetics using an unstructured discontinuous Galerkin method, in: K. Bathe (Ed.), *Computational Fluid and Solid Mechanics*, Elsevier, 2003, pp. 1358–1363.
- [33] T. Hagstrom, S.I. Hariharan, A formulation of asymptotic and exact boundary conditions using local operators, *Appl. Numer. Math.* 27 (1998) 403.
- [34] D. Givoli, High-order nonreflecting boundary conditions without high-order derivatives, *J. Comput. Phys.* 170 (2001) 849–870.
- [35] D. Givoli, B. Neta, High-order non-reflecting boundary scheme for time-dependent waves, *J. Comput. Phys.* 186 (2003) 24–46.
- [36] J. Larsen, H. Dancy, Open boundaries in short wave simulations – a new approach, *Coast. Eng.* 7 (1983) 285–297.
- [37] J.P. Bérenger, A perfectly matched layer for the absorption of electromagnetic waves, *J. Comput. Phys.* 114 (1994) 185–200.
- [38] J.P. Bérenger, Perfectly matched layer for the FDTD solution of wave-structure interaction problems, *IEEE Trans. Antenn. Propag.* 44 (1996) 110–117.

- [39] T.G. Shepherd, K. Semeniuk, J.N. Koshyk, Sponge layer feedbacks in middle-atmosphere models, *J. Geophys. Res.* 101 (1996) 23447–23464.
- [40] S. Abarbanel, D. Gottlieb, J.S. Hesthaven, Well-posed perfectly matched layers for advective acoustics, *J. Comput. Phys.* 154 (1999) 266–283.
- [41] P. Bettess, *Infinite Elements*, Penshaw Press, Cleadon, U.K., 1992.
- [42] R.J. Astley, Infinite elements for wave problems: a review of current formulations and an assessment of accuracy, *Int. J. Numer. Methods Eng.* 49 (2000) 951–976.
- [43] K. Gerdes, Infinite elements for wave problems, *J. Comput. Acoust.* 8 (2000) 43–62.
- [44] P. Bettess, O.C. Zienkiewicz, Diffraction and refraction of surface waves using finite and infinite elements, *Int. J. Numer. Methods Eng.* 11 (1977) 1271–1290.
- [45] H.S. Chen, C.C. Mei, Oscillations and water forces in an offshore harbour, Technical Report 190, Ralph M. Parsons Laboratory for Water Resources and Hydrodynamics, Massachusetts Institute of Technology, Cambridge, MA, 1974.
- [46] H.S. Chen, C.C. Mei, Oscillations and wave forces in a man-made harbor in the open sea, in: Proceedings of the 10th Symposium on Naval Hydrodynamics Office of Naval Research, 1974, pp. 573–594.
- [47] O.C. Zienkiewicz, C. Emson, P. Bettess, A novel boundary infinite element, *Int. J. Numer. Methods Eng.* 19 (1983) 393–404.
- [48] O.C. Zienkiewicz, P. Bettess, T.C. Chiam, C. Emson, Numerical methods for unbounded field problems and a new infinite element formulation, in: ASME AMD, vol. 46, New York, 1981, pp. 115–148.
- [49] P. Bettess, C. Emson, T.C. Chiam, A new mapped infinite element for exterior wave problems, in: P. Bettess, R.W. Lewis, E. Hinton (Eds.), *Numerical Methods in Coupled Systems*, John Wiley, Chichester, 1984 (Chapter 17).
- [50] O.C. Zienkiewicz, K. Bando, P. Bettess, C. Emson, T.C. Chiam, Mapped infinite elements for exterior wave problems, *Int. J. Numer. Methods Eng.* 21 (1985) 1229–1251.
- [51] R.J. Astley, P. Bettess, P.J. Clark, Letter to the editor concerning ref, *Int. J. Numer. Methods Eng.* 32 (1991) 207–209.
- [52] R.J. Astley, G.J. Macaulay, J.P. Coyette, Mapped wave envelope elements for acoustical radiation and scattering, *J. Sound Vib.* 170 (1994) 97–118.
- [53] L. Cremers, K.R. Fyfe, J.P. Coyette, A variable order infinite acoustic wave envelope element, *J. Sound Vib.* 171 (1994) 483–508.
- [54] L. Cremers, K.R. Fyfe, On the use of variable order infinite wave envelope elements for acoustic radiation and scattering, *J. Acoust. Soc. Am.* 97 (1995) 2028–2040.
- [55] D.S. Burnett, A three-dimensional acoustic infinite element based on a prolate spheroidal multipole expansion, *J. Acoust. Soc. Am.* 95 (1994) 2798–2816.
- [56] D.S. Burnett, R.L. Holford, Prolate and oblate spheroidal acoustic infinite elements, *Comput. Methods Appl. Mech. Eng.* 158 (1998) 117–141.
- [57] D.S. Burnett, R.L. Holford, An ellipsoidal acoustic infinite element, *Comput. Methods Appl. Mech. Eng.* 164 (1998) 49–76.

- [58] R.J. Astley, W. Eversman, A note on the utility of a wave envelope approach in finite element duct transmission studies, *J. Sound Vib.* 76 (1981) 595–601.
- [59] R.J. Astley, Wave envelope and infinite elements for acoustical radiation, *Int. J. Numer. Methods Fluids* 3 (1983) 507–526.
- [60] P. Bettess, A simple wave envelope element example, *Commun. Appl. Numer. Methods* 3 (1987) 77–80.
- [61] K. Gerdes, L. Demkowitz, Solution of 3D Laplace and Helmholtz equation in exterior domains of arbitrary shape, using hp-finite-infinite elements, *Comput. Methods Appl. Mech. Eng.* 137 (1996) 239–273.
- [62] L. Demkowitz, K. Gerdes, Convergence of the infinite element methods for the Helmholtz equation in separable domains, *Numer. Math.* 79 (1998) 11–42.
- [63] L. Demkowitz, K. Gerdes, The conjugated versus the unconjugated infinite element method for the Helmholtz equation in exterior domains, *Comput. Methods Appl. Mech. Eng.* 152 (1998) 125–145.
- [64] J.J. Shirron, Solution of Exterior Helmholtz Problems Using Finite and Infinite Elements, Ph.D. Thesis, University of Maryland, 1995.
- [65] J.J. Shirron, I. Babuška, A comparison of approximate boundary conditions and infinite element methods for exterior Helmholtz problems, *Comput. Methods Appl. Mech. Eng.* 164 (1998) 121–139.
- [66] R.J. Astley, Mapped spheroidal wave-envelope elements for unbounded wave problems, *Int. J. Numer. Methods Eng.* 41 (1998) 1235–1254.
- [67] R.J. Astley, J.-P. Coyette, Conditioning of infinite element schemes for wave problems, *Int. J. Numer. Methods Eng.* 17 (2001) 31–41.
- [68] D. Dreyer, O. van Estorff, Improved conditioning of infinite elements for exterior acoustics, *Int. J. Numer. Methods Eng.* 58 (2003) 933–953.
- [69] L. Demkowitz, M. Pal, An infinite element for Maxwell's equations, *Comput. Methods Appl. Mech. Eng.* 164 (1998) 77–94.
- [70] I. Harari, P. Barai, P.E. Barbone, Higher-order boundary infinite elements, *Comput. Methods Appl. Mech. Eng.* 164 (1998) 107–119.
- [71] I. Harari, A unified variational approach to domain based computation of exterior problems of time-harmonic acoustics, *Appl. Numer. Math.* 27 (1998) 417–441.
- [72] I. Harari, P. Barai, P.E. Barbone, Numerical and spectral investigations of Trefftz infinite elements, *Int. J. Numer. Methods Eng.* 46 (1999) 553–577.
- [73] I. Harari, P. Barai, P.E. Barbone, M. Slavutin, Three-dimensional infinite elements based on a Trefftz formulation, *Comput. Acoust.* 9 (2000) 381–394.
- [74] R.J. Astley, W. Eversman, Wave envelope elements for acoustical radiation in inhomogeneous media, *Comput. Struct.* 30 (1988) 951–976.
- [75] R.J. Astley, A finite element, wave envelope formulation for acoustical radiation in moving flows, *J. Sound Vib.* 103 (1985) 471–485.
- [76] R.J. Astley, Transient wave envelope elements for wave problems, *J. Sound Vib.* 192 (1996) 245–261.
- [77] R.J. Astley, G.J. Macaulay, J.P. Coyette, L. Cremers, Three dimensional wave-envelope elements of variable order for acoustic radiation and scattering.

- Part 1. Formulation in the frequency domain, *J. Acoust. Soc. Am.* 103 (1998) 49–63.
- [78] R.J. Astley, G.J. Macaulay, J.P. Coyette, L. Cremers, Three dimensional wave-envelope elements of variable order for acoustic radiation and scattering. Part 2. Formulation in the time domain, *J. Acoust. Soc. Am.* 103 (1998) 64–72.
 - [79] J.L. Cipolla, M.J. Butler, Infinite elements in the time domain using a prolate spheroidal multipole expansion, *Int. J. Numer. Methods Eng.* 43 (1998) 889–908.
 - [80] L.L. Thompson, P.M. Pinsky, A space-time finite element method for the exterior structural acoustics problem: time dependent radiation boundary conditions in two space dimensions, *Int. J. Numer. Methods Eng.* 39 (1996) 1635–1657.
 - [81] O.C. Zienkiewicz, D.W. Kelly, P. Bettess, The coupling of the finite element method and boundary solution procedures, *Int. J. Numer. Methods Eng.* 11 (1977) 355–375.
 - [82] O.C. Zienkiewicz, D.W. Kelly, P. Bettess, Marriage à la mode – the best of both worlds (finite elements and boundary integrals), in: *Energy Methods in Finite Element Analysis*, Wiley, 1978 (Chapter 5).
 - [83] J.C.W. Berkhoff, Computation of combined refraction–diffraction, in: *Proceedings of the 13th International Conference on Coastal Engineering*, Vancouver, 1972, pp. 10–14.
 - [84] R.J. Astley, Fe mode matching schemes for the exterior Helmholtz problems and their relationship to the FE-DtN approach, *Commun. Numer. Methods Eng.* 12 (1996) 257–267.
 - [85] J.R. Houston, Long Beach Harbor: Numerical Analysis of Harbor Oscillations, Vicksburg, MS. Report 1, Misc. Paper h-, US Army Engineering Waterways Experimental Station, 1976.
 - [86] O.C. Zienkiewicz, P. Bettess, Fluid–structure interaction and wave forces an introduction to numerical treatment, *Int. J. Numer. Methods Eng.* 13 (1978) 1–16.
 - [87] H. Hara, K. Kanehiro, H. Ashida, T. Sugawara, T. Yoshimura, Numerical simulation system for wave diffraction and response of offshore structures, Technical Bulletin, TB, October, Mitsui Engineering and Shipbuilding Co., 1983.
 - [88] A.R. Mitchell, S.W. Schoombie, Finite element studies of solitons, in: P. Bettess, R.W. Lewis, E. Hinton (Eds.), *Numerical Methods in Coupled Systems*, John Wiley, Chichester, 1984, pp. 465–488 (Chapter 16).
 - [89] P.J. Clark, P. Bettess, M.J. Downie, G.E. Hearn, Second order wave diffraction and wave forces on offshore structures, using finite elements, *Int. J. Numer. Methods Fluids* 12 (1991) 343–367.
 - [90] L. Lau, K.K. Wong, Z. Tam, Nonlinear wave loads on large body by time-space finite element method, in: *Proceedings of the International Conference on Computers in Engineering*, ASME, New York, 1987, pp. 331–337.

Short Waves[★]

12

12.1 Introduction

As was seen in the previous chapter, classical finite element methods can deal relatively easily with linear waves in two and three dimensions, when there are few wavelengths in the problem domain. But many problems of practical importance contain many wavelengths. The computational demands of conventional numerical methods for an accurate solution cannot be met. So in recent years, attention has turned to new types of finite elements for such problems. Similar special variations have also been developed for other numerical methods, such as boundary elements. Surveys of these methods are available [1,2]. A variety of new finite elements have been developed, and they will be surveyed briefly in this chapter. A common feature is that most incorporate more of our knowledge of waves and wave behavior into the algorithm. The problem of short waves in a large domain is part of the general class of multiscale problems [3,4]. That is, the problem is of large scale, but the overall behavior is significantly influenced by small-scale behavior. Other important examples are the behavior of structures composed of materials with microstructure, for example composites or concrete, and turbulent flows. In the latter the details of the flow, with very small length scales, strongly influence the behavior of the entire system.

12.2 Background

A prime example of a short-wave problem is that of radar waves incident upon an aircraft. The wavelength of the radio wave may be of the order of several mm, whereas the size of the aircraft is of the order of tens of meters. Since about 10 degrees of freedom are needed per wavelength in conventional numerical models this gives a scale factor of over 1000. Classical finite element methods generate large systems of equations with literally astronomical numbers of unknowns for the solution of such problems. This makes them virtually intractable. If we imagine a computational domain around

*Contributed by Peter Bettess, Formerly Professor School of Engineering, University of Durham, UK.

an aircraft of a cube of 20 m per side and a wavelength of the incident wave of 2 cm, it is possible to compute the size of the computational problem. The above model requires $n = 10^{12}$ nodal variables, all complex. The semi-bandwidth of a finite element model would be $b = 10^8$ degrees of freedom, leading to a storage requirement for a classical direct solver of $nb = 10^{20}$ complex words, or 1.6×10^{21} bytes. The number of complex arithmetic operations would be $nb^2/2 = 0.5 \times 10^{27}$. Twenty meters is not large for a model size and 2 cm is not small for a radar wavelength. It corresponds to a frequency of about 15 GHz, and radar can operate at higher frequencies. So it can be seen that conventional methods, even on supercomputers, struggle to make an impact on such problems. But the solutions are of great practical interest.

For most short-wave problems the frequency domain solutions are of the most interest. Even in radar applications, where the radar beam is transient, it still endures for many wave cycles so the problem is really in the frequency domain. There are important short-wave transient problems, but these are in the minority. There are essentially two approaches to frequency domain problems. The first is to iterate a general transient solution to a steady state. The second is to factor the frequency out of the problem and to operate on the resulting complex equations.

- 1. Time domain solutions.** These methods imply some kind of stepping forward in time, usually based on a finite difference in time scheme. Many different schemes have been proposed. The advantage of this approach is that any transient problem can be solved. If an explicit scheme is used, together with a diagonal mass matrix, then the computation involved in a time step is very small, and the storage requirements are very small. Such methods are explained in detail in Ref. [5] and in Chapter 3 of the present book.
- 2. Frequency domain solutions.** These methods solve the response for a given frequency. All terms in the problem are factored by $\exp(i\omega t)$, as explained in the previous chapter. The advantage is that a single solution of a complex system matrix gives a complete solution at all times. The disadvantage is that they cannot directly solve transient problems, although Fourier transforms can be used to move from a set of frequency domain solutions to a transient solution, for linear problems. The complex system matrix to be solved, though sparse for finite elements, is very large and direct solutions are very computationally expensive. Such problems have been described in Ref. [5].

In recent years the problem described above, that of the limitation in the short waves, has been subjected to attack from a number of different directions, which have shown considerable promise. It is fair to say that in the last 10 years, the wavelengths in the scattering problems which can be solved have decreased dramatically. As a consequence the frequencies have increased.

The historical trend is toward tailoring the numerical algorithms to the known nature of the wave problem, and to use the best possible algorithms, for example in integrating the various matrices which arise.

12.3 Errors in wave modeling

It was earlier stated that about 10 degrees of freedom are needed to model each wavelength. However that is an oversimplification. There are two sorts of errors which arise from wave modeling using polynomials. These are *local* errors and *pollution* errors. Error estimates for these errors have been given by several authors [6–9]. Ihlenburg and Babuška [6] give expressions for the error, e , in the H^1 -seminorm, in a domain of *unit length*, as

$$e \leq C_1(p) \left(\frac{hk}{2p} \right)^m + C_2(p)k \left(\frac{hk}{2p} \right)^{m+1} \quad (12.1)$$

where p is the order of the finite element polynomial, h is the element size, and m is the minimum of l and p , where $l + 1$ is the regularity of the exact solution. C_1 and C_2 are constants depending only upon p . The first term in Eq. (12.1) is the *local* error and the second term is the *pollution* error, which increases with k , even for (hk) fixed. If the domain is large the second term will come to dominate. It is evident from Eq. (12.1) that, other things being equal, it is desirable to have the highest possible order of polynomial in the finite element, if we seek to minimize the error for a given discretization. The pollution error can be thought of as an error in the numerical value for the wavelength. Obviously, the larger the number of wavelengths in a problem then the more the errors from this source will accumulate.

12.4 Recent developments in short-wave modeling

There have been several important developments in recent years, which have enabled the finite element method to be applied to wave scattering problems with much smaller wavelengths, or at much higher frequencies. The approaches can be outlined as follows:

1. Conventional finite element polynomials, with a transient solution scheme, possibly with characteristic-based algorithms
2. Finite elements which incorporate the wave shape
 - (a) Shape functions using *products* of waves and polynomials
 - (b) Shape functions using *sums* of waves and polynomials
 - (c) Ultra weak formulations
 - (d) Trefftz-type finite elements which incorporate wave shapes
3. Spectral schemes
4. Discontinuous Galerkin methods in transient schemes

There have been similar developments within the boundary element field, which are too extensive to discuss here. Other surveys are available [1,2].

12.5 Transient solution of electromagnetic scattering problems

The penalty in using a fine mesh of conventional finite elements in solving wave problems, referred to above, is the storage and solution of the system matrix. The approach of Morgan et al. [10, 11] is to not assemble and solve the system matrix, and to treat the problem as transient. The Maxwell equations are

$$\varepsilon_0 \frac{\partial \mathbf{E}}{\partial t} = \operatorname{curl} \mathbf{H} \quad \text{and} \quad \mu_0 \frac{\partial \mathbf{H}}{\partial t} = -\operatorname{curl} \mathbf{E} \quad (12.2)$$

where \mathbf{E} and \mathbf{H} are the electric and magnetic field intensity vectors respectively. The equations are combined and expressed in the conservation form

$$\frac{\partial \mathbf{U}}{\partial t} = \sum_{j=1}^3 \frac{\partial \mathbf{F}^j}{\partial x_j} = \mathbf{0} \quad \text{where} \quad \mathbf{U} = \begin{bmatrix} \mathbf{E} \\ \mathbf{H} \end{bmatrix} \quad (12.3)$$

and the flux vectors, \mathbf{F} , are derived from the curl operators. That is

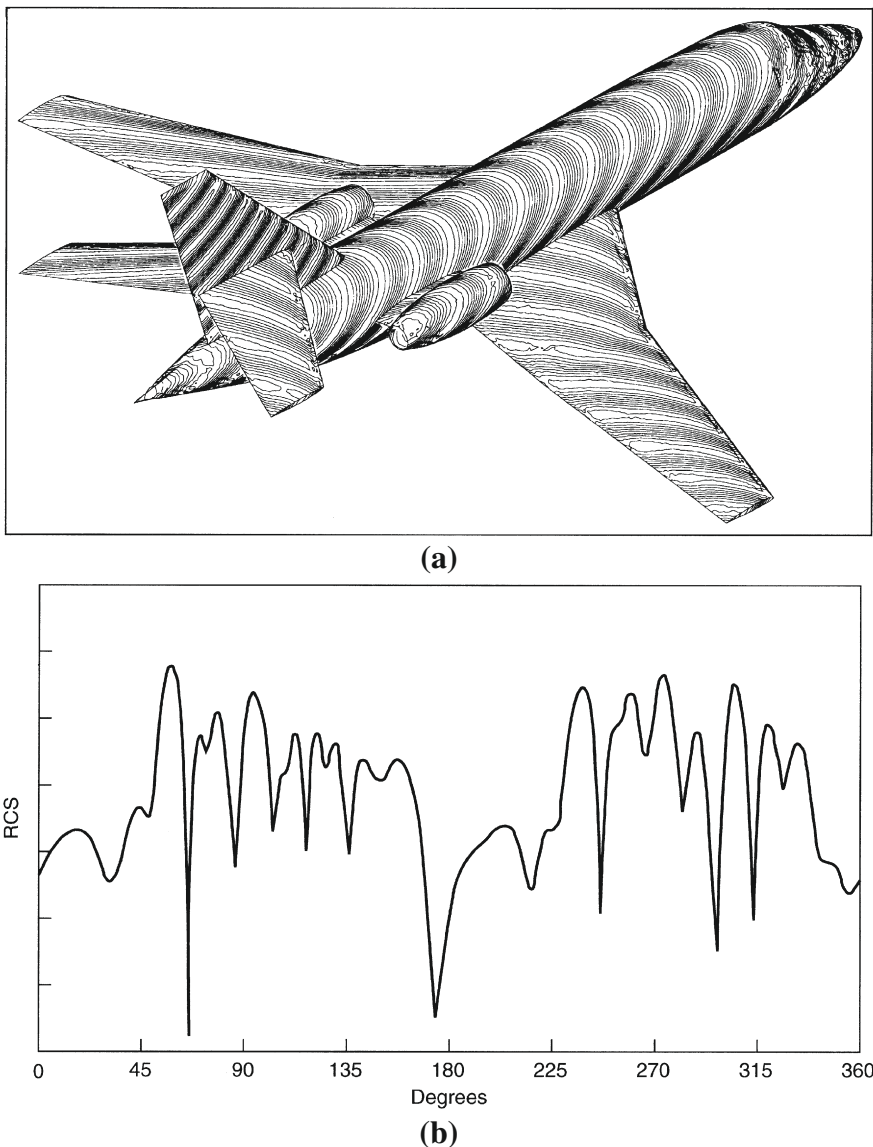
$$\begin{aligned} \mathbf{F}^1 &= [0, H_3, -H_2, 0, -E_3, E_2]^T \\ \mathbf{F}^2 &= [-H_3, 0, H_1, E_3, 0, -E_1]^T \\ \mathbf{F}^3 &= [H_2, -H_1, 0, -E_2, E_1, 0]^T \end{aligned} \quad (12.4)$$

The algorithm used is the characteristic-Galerkin (or Lax-Wendroff) method as described in [Chapter 2](#). Details of the algorithm as applied to the electromagnetic problem are given by Morgan et al. Improved CPU efficiency and reduced storage requirements are obtained by the use of a representation in which each edge of the tetrahedral mesh is numbered and the data structure employed provides the numbers of the two nodes which are associated with each edge. Because of the massive computations needed for problems of scattering by short waves, parallel processing has also been used. The problem of radar scattering by an aircraft is shown in [Fig. 12.1a](#) and [12.1b](#) shows the radar cross-section obtained for the aircraft.

Morgan et al. present results for electromagnetic waves scattered by an aircraft of length 18 m, for a wavelength of 1 m. The model was run on a CRAY parallel computer and had about 1,500,000 elements.

12.6 Finite elements incorporating wave shapes

In these elements the usual polynomial shape functions are extended with functions which enhance the solution space used in the element. The first attempt to do this was the infinite elements of Bettess and Zienkiewicz [12, 13]. The first attempt on *finite* elements was that of Astley [14, 15], using his wave envelope, or complex conjugate weighting method. For more details, see [Chapter 11, Section 11.12](#). Following

**FIGURE 12.1**

Scattering of a plane wavelength 2 m by a perfectly conducting aircraft of length 18 m: (a) waves impacting aircraft, (b) computed distribution of radar cross-section (RCS), Morgan [10].

Astley's wave envelope technique, Chadwick et al. [16] attempted to develop wave envelope finite elements in which the wave direction was unknown, *a priori*, and to iterate for the correct wave direction, using some type of residual. In the above

methods single waves were included in the elements either in a radial or some predefined direction.

Chadwick's approach had some success but has difficulties. The next step was the method proposed by Melenk and Babuška [17, 18] in which *multiple* plane waves are used. This is categorized as a form of the partition of unity finite element method (see Chapter 3 of Ref. [5]). Melenk and Babuška demonstrated that if such shape functions are used the method works for a plane wave propagated through a square mesh of square finite elements, even when the direction of the wave was not included in the nodal directions. The set of plane waves is complete [19], so the choice is rational. Other wave functions have been suggested such as cylindrical waves, or a series of Hankel functions. Melenk and Babuška [17, 18] and Huttunen et al. [20, 21] consider various choices for the wave functions. Mayer and Mandel [22] have also used shape functions which incorporate the wave shape.

Similar ideas were also developed in the boundary integral method by de La Bourdonnaye, under the title of *microlocal discretization* [23, 24]. All the methods mentioned above use trial functions, or shape functions, formed from the product of the usual polynomial shape functions and plane (or almost plane) waves. One of the problems with this approach is that the integrations over the element domain may become computationally intensive. It is also possible to *add* the wave solutions to the polynomial element shape functions or to use different methods which sidestep the integration difficulties (see Section 12.6.3.).

12.6.1 Shape functions using products of polynomials and waves

Laghrouche and Bettess applied the method originated by Melenk and Babuška [17, 18] to a range of wave problems, and enjoyed some success [25, 26]. The starting point is the standard Galerkin weighted residual form of the Helmholtz equation, which leads to

$$\int_{\Omega} (-\nabla^T W(\nabla \phi + k^2 W \phi)) d\Omega + \int_{\Gamma} W(\nabla \phi)^T \mathbf{n} d\Gamma = 0 \quad (12.5)$$

The element approximation is now taken as

$$\phi = \sum_{a=1}^n \sum_{l=1}^m N_a \psi_l A_a^l \quad (12.6)$$

where N_j are the normal polynomial element shape functions,

$$\psi_l = e^{ik(x \cos \theta_l + y \sin \theta_l)} \quad (12.7)$$

n is the number of nodes in the element, and m is the number of directions considered at each node. The shape function consists of a set of plane waves traveling in different directions, the nodal degrees of freedom corresponding to the amplitudes of the different waves, and the normal polynomial element shape functions allowing a variation in the amplitude of each wave component within the finite element. The derivatives of the shape and weighting functions can be obtained in the normal way,

but these now also include derivatives of the wave shapes. The new shape function, P_l , gives

$$\begin{Bmatrix} \frac{\partial P_{(a-1)m+l}}{\partial x} \\ \frac{\partial P_{(a-1)m+l}}{\partial y} \end{Bmatrix} = \left[\begin{Bmatrix} \frac{\partial N_a}{\partial x} \\ \frac{\partial N_a}{\partial y} \end{Bmatrix} + ik N_a \begin{Bmatrix} \cos \theta_l \\ \sin \theta_l \end{Bmatrix} \right] \psi_l \quad (12.8)$$

The global derivatives are obtained in the usual way from the local derivatives, using the inverse of the Jacobian matrix. The element stiffness and mass matrices are

$$K_{rs} = \int_{\Omega} (\nabla W_r)^T \nabla P_s d\Omega \quad M_{rs} = \int_{\Omega} W_r P_s d\Omega \quad (12.9)$$

where r and s are integers which vary over the range of $1, 2, \dots, (n \times m)$. When calculating the element matrices, the integrals encountered are of the form (for a quadrilateral element)

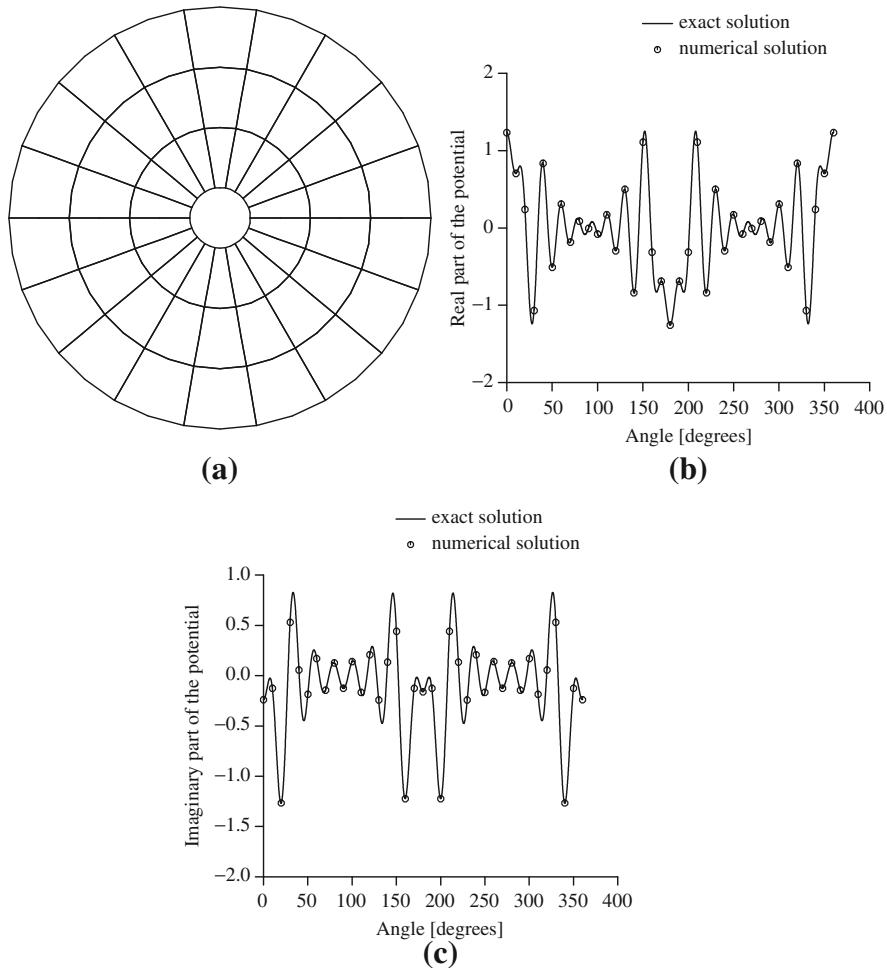
$$I_{al} = \int_{-1}^1 \int_{-1}^1 f(\xi, \eta) e^{ik(x \cos \theta_a + y \sin \theta_a)} e^{ik(x \cos \theta_l + y \sin \theta_l)} d\xi d\eta \quad (12.10)$$

This integral has often been performed numerically. But when the waves are short, many Gauss-Legendre integration points are needed. Typically about 10 integration points per wavelength are needed. Laghrouche and Bettess solve a range of wave diffraction problems, including that of plane waves diffracted by a cylinder. The mesh and the results are shown in Fig. 12.2. As can be seen the results are in good agreement with the analytical series solution. In this problem $ka = 8\pi$, $\lambda = 0.25a$, radius of cylinder, $a = 1$, and the mesh extends to $r = 7a$. For a conventional radial finite element mesh, the requirement of 10 nodes per wavelength would lead to a mesh with 424,160 degrees of freedom. But in the results shown, with 36 directions per node and 252 nodes there are only 9072 degrees of freedom. The dramatic reduction in the number of variables has prompted investigation and development of the method. The method still has a number of uncertainties regarding the conditioning of the system matrix and the stability of the technique. Various approaches have been suggested to reduce the cost of integrating the element matrix.

For the choice of a plane wave basis, any term in the element matrix can be written as the product of two plane waves, and a polynomial term. The general integral which arises, in two dimensions, is of the form

$$\int_{\Omega} f(\xi, \eta) e^{ig(\xi, \eta)} d\Omega \quad (12.11)$$

where ξ and η are the local coordinates, $f(\xi, \eta)$ is a rational function which reduces to a polynomial if the Jacobian is constant, $g(\xi, \eta)$ is some function related to the element mapping, and Ω is the element domain. If the Jacobian is constant, then $g(\xi, \eta) = \alpha\xi + \beta\eta$ (α and β being constants), which greatly simplifies the integrations. Such integrals are highly oscillatory and difficult to evaluate. The first analyses using such elements used large numbers of Gauss-Legendre integration points [17, 18, 25, 26]. The approach of Ortiz and Sanchez [27] is to combine the two plane waves traveling in

**FIGURE 12.2**

Short waves diffracted by a cylinder, modeled using special finite elements [26]; (a) cylinder mesh; (b) real potential; (c) imaginary potential. *Reprinted from Ref. [26], with permission from Journal of Computational Acoustics.*

directions θ_1 and θ_2 to the x -axis, to give a single wave traveling in the mean direction, $\theta = (\theta_1 + \theta_2)/2$ with a local wavenumber, k' given by $k' = 2k \cos(\theta_1 - \theta_2)/2$. The integral then takes the simpler form

$$\int_{\Omega} f(\xi, \eta) e^{i\gamma\xi} d\Omega \quad (12.12)$$

where in Eq. (12.12), ξ is oriented in the mean wave direction, η is perpendicular, and γ depends on the local wavenumber and element geometry. Ortiz and Sanchez used this result to develop a special integration scheme in the direction of the wave

resultant, ξ , which contains all the oscillatory effects, in combination with classical integration in the orthogonal η direction, where the variation is of a polynomial form. This has the advantage that the integration of the oscillatory function has been reduced by one dimension. The price that has to be paid is that a new local coordinate system must be set up for each pair of wave directions, and the limits of integration are no longer simple. To date their approach has only been applied to linear triangular elements. Whether the limits of integration will be easy to manipulate with higher-order elements, and in three dimensions, has not yet been investigated. Ortiz has extended his approach to refraction problems and this is described below in [Section 12.7](#).

Another approach to the integral of [Eq. \(12.10\)](#) was suggested by Bettess et al. [28]. In Bettess et al.'s method the constant Jacobian for simpler finite elements is exploited to transform the integrations into the local coordinates. This integral takes the following specific form for the linear triangular finite element:

$$\int_0^1 \int_0^{1-\xi} f(\xi, \eta) e^{i\alpha\xi} e^{i\beta\eta} d\eta d\xi \quad (12.13)$$

In the above ξ and η are the local coordinates, and $f(\xi, \eta)$ is a polynomial. Unfortunately the resulting expressions, though straightforward, become complicated and it is almost essential to use computer algebra [28]. Nevertheless an integration scheme can be developed. Both the Ortiz and Bettess et al. approaches have been demonstrated to give large reductions in computer time, when the waves become short. Bettess et al. have also demonstrated that the integrations over rectangular and cuboid finite elements can be greatly simplified. Their method has also been applied to tetrahedral element integrations (unpublished work). The other feature of these approaches is that although the integration of each finite element matrix is computationally intensive, the calculations are highly parallelizable. There is no difficulty in obtaining an n times speed-up on a computer with n processors. Any repetition in the element geometries can also be exploited.

A feature of these partition of unity finite elements (PUFE) is that the system matrix is often ill-conditioned. This has concerned some authors [18, 22]. Strouboulis et al. [4] suggest that in this general class of methods the equations may be ill-conditioned, but that this is not necessarily a bad thing. The final results may be acceptable, even if the coefficients of the wave components are not unique. Astley [29] has analyzed the conditioning of the element matrices, for some simple cases, and has evolved a semi-empirical rule relating condition number, number of wave directions, and wavenumber. Babuška et al. [17, 18] also consider *a posteriori* error estimation for such elements. Mayer and Mandel [22] also discuss strategies for selecting wave directions. The method can be extended to three dimensions [29, 30] and can be linked to conventional infinite elements [31].

12.6.2 Shape functions using sums of polynomials and waves

The complications arising from the integration of products of shape functions and wave functions can be eliminated by introducing the waves in a different form, for

example by adding the set of waves to the conventional shape function polynomials. Two of these approaches will now be considered. These are

1. The discontinuous enrichment method of Farhat [32–34]
2. The ultra weak variational formulation of Després and Cessenat [35,36], and Huttunen and Monk [20,21]

12.6.3 The discontinuous enrichment method

The Farhat et al. [32–34] approach uses the original polynomial shape function and adds to it the set of plane waves. (This is in contrast to the Babuška and Melenk approach, described above in Section 12.3, in which the plane waves are multiplied by the polynomials.) Continuity with adjacent elements is enforced weakly by using Lagrange multipliers. The integrations relating to the plane waves, which Farhat terms *enrichment functions*, can be reduced to integrations along element boundaries. Moreover, these terms can be eliminated from the element matrix, by the use of static condensation. There are three sets of variables in the finite elements:

1. ϕ^P , the usual nodal variables for the finite element polynomial which is used.
2. ϕ^E , the variables relating to the solutions of the Helmholtz equation used for “enrichment.” These may be coefficients of plane waves, Hankel sources, or other wave solutions.
3. \mathbf{p} , the Lagrange variables which are defined along the edges of the element.

The boundary value problem is put in variational form. The Lagrange multipliers which enforce compatibility are defined as the trace, or outward normal, of vectors \mathbf{p} . The contribution to the functional for an element is then

$$\Pi(u, \mathbf{p}) = \frac{1}{2} \int_{\Omega^e} (\nabla^T \phi \cdot \nabla \phi - k^2 \phi^T \phi) d\Omega - \int_{\Gamma^e} \mathbf{p} \cdot \mathbf{n} \phi d\Gamma \quad (12.14)$$

The potential ϕ is split into the polynomial and enrichment functions as described above. That is, $\phi = \phi^P + \phi^E$. The resulting element matrix is similar, but not identical to those shown in Chapter 11 of Ref. [5]. It takes the form

$$\begin{bmatrix} \mathbf{K}^{PP} & \mathbf{K}^{PE} & \mathbf{K}^{PC} \\ \mathbf{K}^{EP} & \mathbf{K}^{EE} & \mathbf{K}^{EC} \\ \mathbf{K}^{CP} & \mathbf{K}^{CE} & \mathbf{0} \end{bmatrix} \begin{Bmatrix} \phi^P \\ \phi^E \\ \mathbf{p}^C \end{Bmatrix} \quad (12.15)$$

where the various matrices \mathbf{K}^{ij} arise from the variational statement of the Helmholtz equation. Because the “enrichment” variables ϕ^E are only defined internally to each element, they can be eliminated at the element level using static condensation. This leads to a final element matrix with only polynomial ϕ^P and Lagrange multipliers \mathbf{p} as variables. The element matrix then takes the form

$$\tilde{\mathbf{k}}^e = \begin{bmatrix} \tilde{\mathbf{k}}^{PP} & \tilde{\mathbf{k}}^{PC} \\ \tilde{\mathbf{k}}^{CP} & \tilde{\mathbf{k}}^{CC} \end{bmatrix} \quad (12.16)$$

where

$$\tilde{\mathbf{k}}^{PP} = \tilde{\mathbf{k}}^{PP} - \tilde{\mathbf{k}}^{PE} \left(\tilde{\mathbf{k}}^{EE} \right)^{-1} \tilde{\mathbf{k}}^{EP}, \quad \tilde{\mathbf{k}}^{PC} = \tilde{\mathbf{k}}^{PC} - \tilde{\mathbf{k}}^{PE} \left(\tilde{\mathbf{k}}^{EE} \right)^{-1} \tilde{\mathbf{k}}^{EC} \quad (12.17)$$

$$\tilde{\mathbf{k}}^{CP} = \tilde{\mathbf{k}}^{CP} - \tilde{\mathbf{k}}^{CE} \left(\tilde{\mathbf{k}}^{EE} \right)^{-1} \tilde{\mathbf{k}}^{EP}, \quad \tilde{\mathbf{k}}^{CC} = -\tilde{\mathbf{k}}^{CE} \left(\tilde{\mathbf{k}}^{PP} \right)^{-1} \tilde{\mathbf{k}}^{EC} \quad (12.18)$$

The vectors \mathbf{p} used to generate the Lagrange multiplier must be chosen correctly. For a triangle element Farhat gives

$$\mathbf{p}(x, y) = s \begin{Bmatrix} c_1 + c_3x \\ c_2 + c_3y \end{Bmatrix} \quad (12.19)$$

where c_i are constants. This gives a constant Lagrange multiplier along the element edge. Farhat points out that because the enrichment functions satisfy the homogeneous Helmholtz equation, the integrals over the domain can be reduced to integrals over the boundaries of the elements. The Lagrange multiplier terms can also be scaled to improve matrix conditioning. These are all very attractive features of the method. Farhat also reports better conditioning of the system matrix with this approach. The results given in his report are all quite academic, being mostly concerned with the propagation of plane waves through square meshes of square elements. Some studies of errors are given. Errors are very low when the plane wave is traveling in one of the directions used for the plane wave basis, or a direction close to it. For other directions, although the errors are larger, they are much smaller than in conventional Galerkin finite elements.

12.6.4 Ultra weak formulation

Another promising approach is termed the ultra weak formulation. Among the leading innovators here have been Després [35], Cessenat and Després [36], and Huttunen et al. [20,21]. To quote Huttunen, “In this approach integration by parts is used to derive a variational formulation that weakly enforces appropriate continuity conditions between elements via impedance boundary conditions.” The significant advantage of this approach is that the integrations over each element can be obtained in closed form. This is because the variational principle used relies on a test function which satisfies the Helmholtz equation. As a result all the integrals over the element domain vanish, leaving only integrals along element boundaries, which enforce compatibility between elements. This contrasts with the integration of classical plane wave basis (or other wave basis) element matrices which can be very computer intensive. As in the PUFE method described above, ill conditioning of the system matrix may be a problem. Cessenat and Després [36] developed the mathematics of the procedure and applied it to the scattering of electromagnetic waves by a NACA 0012 aerofoil, at 1500 MHz. Huttunen et al. [20] considered an inhomogeneous version of the Helmholtz equation, which looks similar to the shallow-water wave equation, Eq. (11.2):

$$\nabla \cdot \left(\frac{1}{\rho} \nabla u \right) + \frac{k^2}{\rho} u = 0 \quad \text{in } \Omega \quad (12.20)$$

$$\left(\frac{1}{\rho} \frac{\partial u}{\partial v} - i\sigma u \right) = Q \left(-\frac{1}{\rho} \frac{\partial u}{\partial v} - i\sigma u \right) + g \quad \text{on } \Gamma \quad (12.21)$$

where Ω is the domain and Γ is the smooth boundary. Both $\rho(x_1, x_2)$, and $k(x_1, x_2)$ are functions of position. Q is a parameter defined on the boundary, Γ , $Q \leq 1$. Although this formulation allows for spatial variation in ρ and k , in practice the treatment in the paper takes them to be piecewise constant in each element. The method is applied to problems in which different zones have different wave speeds. Richardson [27] and stabilized bi-conjugate gradient iterative methods were used for solving the system matrix. Huttunen et al. [21] have also applied the method to elastic wave problems.

Cessenat and Després [36] present results for the scattering of an electromagnetic wave of frequency 1500 MHz by a NACA 0012 aerofoil. The mesh was laid down in three layers around the aerofoil. A total of 2976 elements with 1615 nodes were used. Figure 12.3 shows the radar cross-section of the aerofoil.

Huttunen et al. solved a number of example problems [20], using the ultra weak variational method, including that shown in Figs. 12.4–12.6. This is an inner domain of radius 5 cm, with a wave speed of 3000 m s^{-1} and a computational domain of radius 10 cm, with a wave speed of 1500 m s^{-1} . A cylindrical wave source, of the

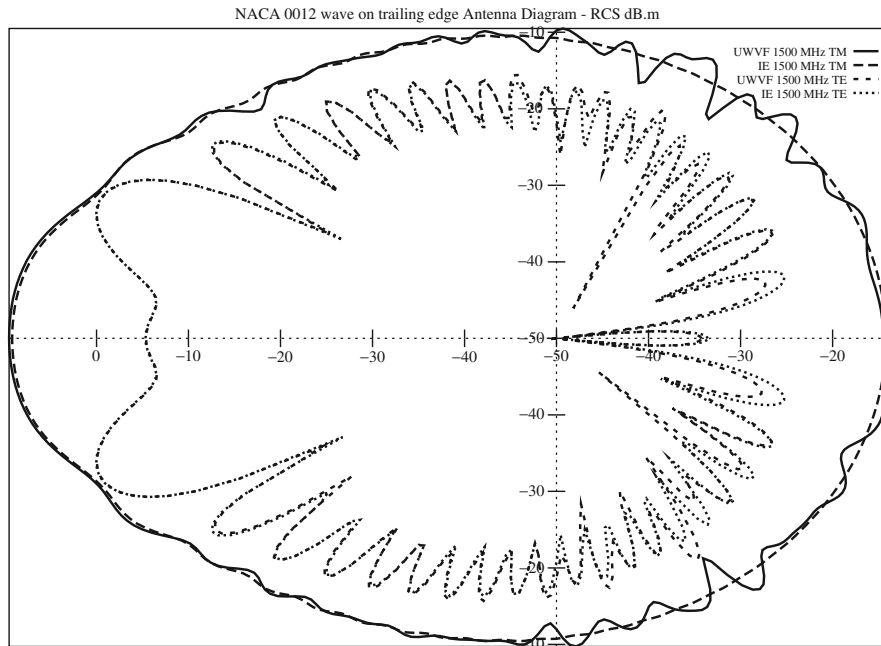
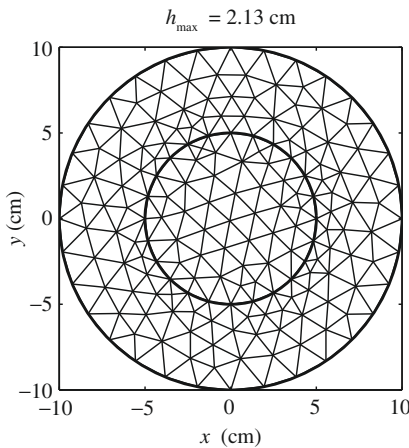


FIGURE 12.3

Radar cross-section for NACA 0012 on trailing edge at 1500 MHz [36]. Comparisons of UWVF and boundary integral results for frequency 1500 MHz, and TM and TE polarizations. Figure reprinted from Ref. [36], with permission from SIAM.

**FIGURE 12.4**

Ultra weak variational element mesh, Huttunen et al. [20]. Reprinted from Ref. [20], with permission from Elsevier.

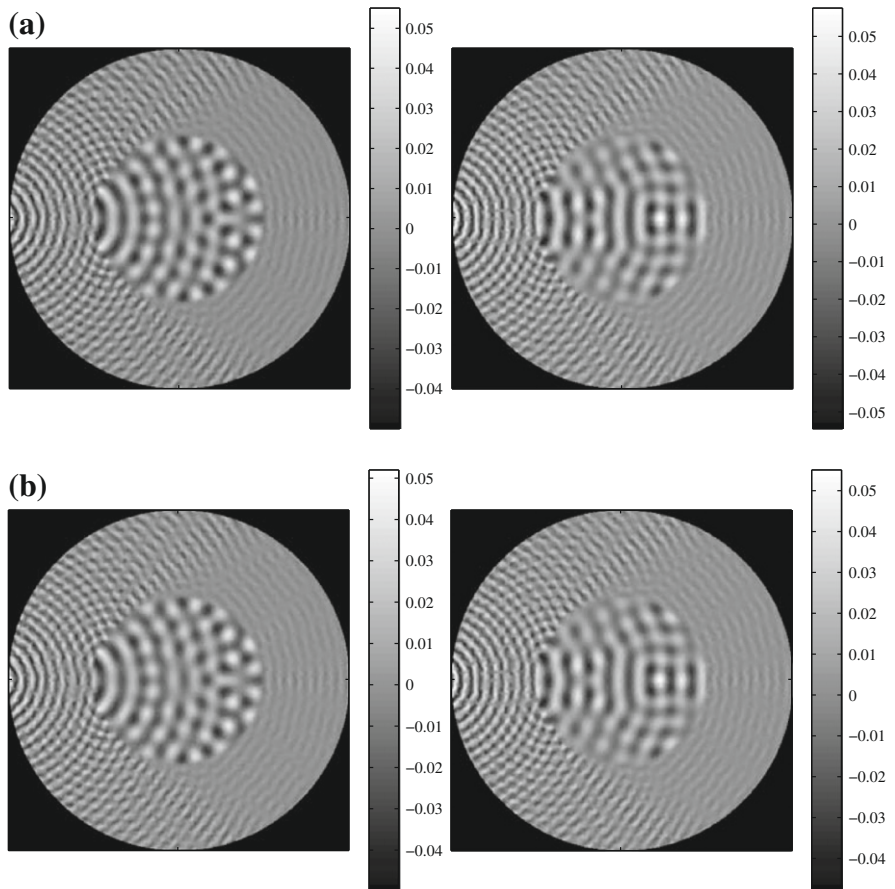
form

$$u^{in} = \frac{i}{4} H_0^{(1)}(k_2 r) \quad (12.22)$$

has an origin, for the radius, r , located at $x = -11$ cm, $y = 0$ cm. The maximum element size is $h_{max} = 2.13$ cm. Figure 12.5 shows the analytical solution compared with the solution obtained using the ultra weak variational formulation (UWVF), for $f = 250$ kHz. Huttunen et al. report good results for frequencies up to 450 kHz, corresponding to about six wavelengths per element. Two strategies were used, one of uniform number of bases for each element and the other in which the number of bases was dictated by the condition number. The details of the strategy are too complicated to report here. However better results were obtained by using the varying number of basis functions. The relative errors at different frequencies and the condition number are shown in Fig. 12.6.

12.6.5 Trefftz-type finite elements for waves

There is now a considerable literature on the Trefftz-type finite (or T-element) methods. Two of the key workers in this field are Jirousek and Herrera. Survey papers are available [37,38]. It is assumed that the scattering form of the Helmholtz equation is to be solved. The theory has been developed by Jirousek and Stojek [39,40]. Background theory on suitable functions for the Trefftz method and T-completeness is given by Herrera [41]. The method has also been applied by Cheung et al. [42] to wave scattering and wave force problems. The theory here follows Stojek [40]. The problem domain Ω is divided into n computational subdomains, Ω_k , each with their own local coordinate system, (r_k, θ_k) . In each subdomain, Ω_k , the total wave potential is written as ϕ_k . It is assumed to be an approximate solution which satisfies the

**FIGURE 12.5**

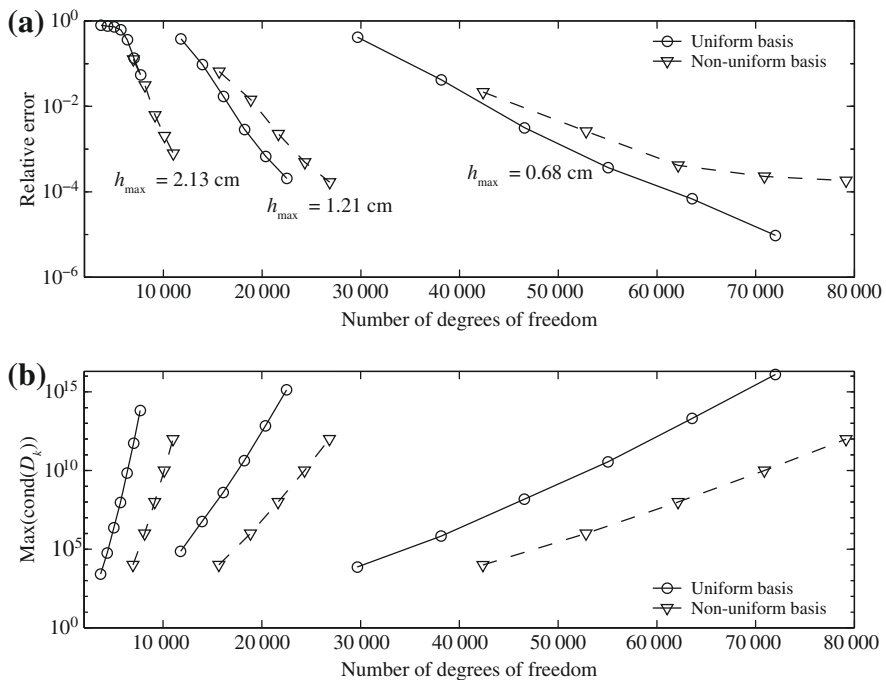
Cylindrical wave scattered by a circular region of different wave speeds [20]. Top figure (a) shows the analytical solution of the problem with $f = 250$ kHz. Bottom figure (b) shows the UWVF solution of the problem using a uniform basis of 21 wave directions per node. *Reprinted from Ref. [20], with permission from Elsevier.*

governing differential equation exactly. The total potential of the wave, ϕ , is expressed as the sum of the incident potential ϕ^i and the scattered potential, ϕ^s .

$$\phi_k = \phi^i + \phi_k^s = \phi^i + \sum_{j=1}^m N_{kj} c_{kj} = \phi^i + \mathbf{N}_k \mathbf{c}_k \quad (12.23)$$

or

$$\phi_k = \sum_{j=1}^m N_{kj} c_{kj} = \mathbf{N}_k \mathbf{c}_k \quad (12.24)$$

**FIGURE 12.6**

Relative discrete L_2 errors and condition numbers for three different frequencies against the number of degrees of freedom [20]. Top figure (a) shows the relative discrete L_2 error for three different frequencies against the number of degrees of freedom. Bottom figure (b) shows the condition number. *Reprinted from Ref. [20], with permission from Elsevier.*

where \mathbf{N}_k is a truncated complete set of local solutions to the Helmholtz equation, and \mathbf{c}_k is a set of unknown complex valued coefficients, so that

$$\nabla^2 \mathbf{N}_k + k^2 \mathbf{N}_k = 0 \quad \text{in } \Omega_k \quad (12.25)$$

The corresponding outward normal velocity $v_k = \nabla \phi_k \cdot \mathbf{n}$ on $\partial \Omega_k$ is given by

$$v_k = v^i + \mathbf{T}_k \mathbf{c}_k \quad \text{or} \quad v_k = \mathbf{T}_k \mathbf{c}_k \quad (12.26)$$

The functional to be minimized enforces in a least-squares sense the Neumann boundary conditions on Γ_B and the continuity in potential ϕ and normal derivative v on all the subdomain interfaces, Γ_I . It is given by

$$I(\phi) = I(\mathbf{c}) = w^2 \int_{\Gamma_B} |v|^2 d\Gamma + \int_{\Gamma_I} |\phi_I^+ - \phi_I^-|^2 d\Gamma + w^2 \int_{\Gamma_I} |v_I^+ + v_I^-|^2 d\Gamma \quad (12.27)$$

where the subscripts $+$, $-$ in integrals along Γ_i indicate solutions from the two respective neighboring Trefftz fields and w is some positive weight. It is assumed that for unbounded domains the selected functions automatically satisfy the Sommerfeld

radiation condition. Setting the first variation of the functional $I(\phi)$ with respect to ϕ equal to zero gives a set of linear equations to solve. Stojek [40] has applied this method to wave scattering problems involving numbers of circular and rectangular cylinders.

12.6.5.1 T-complete systems

The functions used in the various domains of the problem must be complete. They are chosen as follows:

1. Bounded subdomain, Bessel and trigonometric functions:

$$\{J_0(kr), J_n(kr) \cos n\theta, J_n(kr) \sin n\theta\} \quad (12.28)$$

2. Unbounded subdomain, Hankel and trigonometric functions:

$$\left\{H_0^{(1)}(kr), H_n^{(1)}(kr) \cos n\theta, H_n^{(1)}(kr) \sin n\theta\right\} \quad (12.29)$$

3. Special-purpose functions for a bounded subdomain with a circular hole, which are linear combinations of the solutions above, satisfying the boundary conditions on the hole of radius b :

$$\left\{\left(J_0(kr) - \frac{J'_0(kb)}{H'_0(kb)} H_0(kr)\right), \left(J_n(kr) - \frac{J'_n(kb)}{H'_n(kb)} H_n(kr)\right) \cos n\theta, \left(J_n(kr) - \frac{J'_n(kb)}{H'_n(kb)} H_n(kr)\right) \sin n\theta\right\} \quad (12.30)$$

4. Special-purpose functions for the bounded angular corner subdomain:

$$\left\{J_0(kr), J_{n/\alpha}(kr) \cos \left[\frac{n}{\alpha}(\theta - \theta_1)\right]\right\} \quad (12.31)$$

where θ_1 is the angle between the straight boundary and the x -axis, and α is the total angle subtended by the angular corner.

12.7 Refraction

As was discussed in [Chapter 11](#), waves can be refracted in two ways:

1. By changes in the local wave speed
2. By movements of the medium through which the waves pass

Examples of the former include transmission of acoustic waves through material with changing density and transmission of surface waves on water of changing depth. Examples of the latter include acoustic waves transmitted through a flow field, like the noise from jet engines and surface waves on ocean, or nearshore currents.

The wave equations take a different form in these two cases. In general the former problem is much simpler than the latter. Conventional finite elements can deal in a straightforward way with refraction caused by changes in the local wave speed,

and no special procedures are needed. The governing equation is simply the inhomogeneous Helmholtz equation and finite elements can solve this just as easily as the homogeneous Helmholtz equation. But for waves refracted by flows, the equation is much more complicated and depends upon the particular application.

12.7.1 Wave speed refraction

The ultra weak variational formulation of [Section 12.6.4](#) above has been applied by Huttunen et al. [20,21] to cases where the wave speed changes between regions of the problem. This is shown in [Figs. 12.4–12.6](#).

Ortiz [43] has extended his method to deal with refracted waves on the surface of water. Ortiz considers an inhomogeneous form of the Helmholtz equation which was developed by Berkhoff [44] for waves on water of gradually changing depth:

$$\nabla(A(x, y)\nabla\phi) + B(x, y)\phi = 0 \quad (12.32)$$

where

$$\begin{aligned} A(x, y) &= cc_g = \frac{\omega^2}{k^2} \frac{1}{2} \left(1 + \frac{2kh}{\sinh 2kh} \right) \\ B(x, y) &= \omega^2 \frac{c_g}{c} = \omega^2 \frac{1}{2} \left(1 + \frac{2kh}{\sinh 2kh} \right) \end{aligned} \quad (12.33)$$

In this case, strictly speaking, the plane wave basis is no longer valid, since the plane waves are not solutions to the inhomogeneous Helmholtz equation. Ortiz assumes that in each element the plane wave functions still form a valid solution space, since the wave speed does not vary greatly over any element. He modifies the earlier integration scheme [27] to deal with the Berkhoff mild slope wave equation. Again for each pair of wave directions in the element he generates a local coordinate system based on the averaged wave direction. He then integrates analytically in that direction, which contains the most oscillatory variations, and uses conventional integration in the orthogonal direction. His elements are all linear triangles. He uses a Higdon boundary condition to absorb the outgoing waves (see [Chapter 11](#)). He presents numerical results for waves scattered by a parabolic shoal and compares them with those of other researchers [43].

The above wave finite elements are strictly only effective for the Helmholtz equation, or other equations with a constant wave speed. The Ortiz formulation is a kind of halfway house, in which the depth is allowed to vary in the governing partial differential equation, but a set of plane waves is still used in the solution space.

Bettess [45] has suggested methods for dealing with refraction. In his proposed method, the wave speed is supposed to vary linearly within triangular elements. It is well known that for a linear variation in the wave speed, waves which are initially plane will follow circular arcs. This effect is used in ray tracing techniques. He therefore proposes to replace the usual set of plane waves with waves following circular arcs. The arc trajectories are relatively straightforward to calculate. Apart from this innovation, the plane wave basis element theory goes over unchanged.

Another possibility which can occur is to have a step change in wave speed. This occurs for example in shallow-water waves where the waves pass over a step, and in elastic waves when there is a discontinuity in the density or stiffness of the elastic material. This is the case modeled by Huttunen et al. [20,21]. The plane wave basis finite elements have recently been extended to deal with this case by Lagrouche et al. [46]. Lagrange multipliers were used to link together the regions with the different wave speeds. The method is as explained by Zienkiewicz et al. [47] Consider a problem in which for simplicity there are only two domains with different wavenumbers, k_1 and k_2 . The starting point is the Helmholtz equation

$$(\nabla^2 + k_1^2)\phi_1 = 0 \quad \text{in } \Omega_1 \quad (12.34)$$

We now consider a problem with subdomains with a different constant wave speed in each subdomain. It is sufficient to consider the two-subdomain problem. We begin by considering the solution of the Helmholtz equation expressed in terms of the scalar potential ϕ_1 in the subdomain Ω_1 bounded by $\Gamma_1 \cup \Gamma_{\text{int}}$, where ∇^2 denotes the Laplacian operator and k_1 is the wavenumber in the subdomain Ω_1 . Robin boundary conditions are specified on the boundary Γ_1 . These are

$$\nabla\phi_1 \cdot \mathbf{n}_1 + ik_1\phi_1 = g_1 \quad \text{on } \Gamma_1 \quad (12.35)$$

where g_1 is the boundary condition, ∇ is the gradient vector operator, and \mathbf{n}_1 is the outward normal to the line boundary $\Gamma_1 \cup \Gamma_{\text{int}}$.

12.7.1.1 Weighted residual scheme

The differential equation (12.34) is multiplied by an arbitrary weight function W_1 and then integrated by parts to give the weak form

$$B(W_1, \phi_1) = L(W_1) \quad (12.36)$$

where B stands for the bilinear form

$$\begin{aligned} B(W_1, \phi_1) &= \int_{\Omega_1} \left(\nabla W_1 \cdot \nabla\phi_1 - k_1^2 W_1 \phi_1 \right) d\Omega \\ &\quad + ik_1 \int_{\Gamma_1} W_1 \phi_1 d\Gamma - \int_{\Gamma_{\text{int}}} W_1 \nabla\phi_1 \cdot \mathbf{n}_1 d\Gamma \end{aligned} \quad (12.37)$$

and

$$L(W_1) = \int_{\Gamma_1} W_1 g_1 d\Gamma \quad (12.38)$$

Following the same procedure, we obtain for the subdomain Ω_2 bounded by $\Gamma_2 \cup \Gamma_{\text{int}}$ the weak form

$$B(W_2, \Phi_2) = L(W_2) \quad (12.39)$$

where all functions and parameters are defined in a similar way as for the weak form (12.36) replacing the subscript 1 by 2.

12.7.1.2 Plane wave basis finite elements

The two subdomains are divided into n -noded finite elements. In each finite element, the potential is first written as a polynomial interpolation of the nodal values of the potential. Then each nodal potential is approximated by a discrete sum of plane waves propagating in different directions in the plane. In our case, a number m_j of plane waves are used in the approximating system at the node j which is similar to that of Eqs. (12.5) and (12.6). Equation (12.5) is retained, but Eq. (12.6) now has different wavenumbers in the two adjacent elements:

$$\psi_1 = e^{ik_1(x \cos \theta_l + y \sin \theta_l)} \quad \psi_2 = e^{ik_2(x \cos \theta_l + y \sin \theta_l)} \quad (12.40)$$

The continuity of potential and the gradient condition are written as follows:

$$\phi_1 = \phi_2 \quad (12.41)$$

and

$$\frac{1}{k_1^2} \nabla \phi_1 \cdot \mathbf{n}_1 + \frac{1}{k_2^2} \nabla \phi_2 \cdot \mathbf{n}_2 = 0 \quad (12.42)$$

Lagrange multipliers are then introduced to enforce this condition between the two domains, so that

$$\lambda = \frac{1}{k_1^2} \nabla \phi_1 \cdot \mathbf{n}_1 = -\frac{1}{k_2^2} \nabla \phi_2 \cdot \mathbf{n}_2 \quad (12.43)$$

where $k = \max(k_1, k_2)$ and λ_{jl} are the Lagrange multipliers at node j with respect to direction ξ_l . We put $Q_{jl} = N_j \exp(ik[x \cos \theta_l + y \sin \theta_l])$ and then $\lambda = Q\lambda$. A Galerkin scheme is used so that the weighting functions are chosen to be the same as the interpolating oscillatory functions. The Galerkin equations for the two domains may be written in a matricial form:

$$\begin{aligned} H_1 \mathbf{A}_1 - C_1 \boldsymbol{\lambda} &= \mathbf{f}_1 \\ H_2 \mathbf{A}_2 + C_2 \boldsymbol{\lambda} &= \mathbf{f}_2 \end{aligned} \quad (12.44)$$

where

$$H_1 = \int_{\Omega_1} \left(\nabla \mathbf{P}_1^T \nabla \mathbf{P}_1 - k_1^2 \mathbf{P}_1^T \mathbf{P}_1 \right) d\Omega + ik_1 \int_{\Gamma_1} \mathbf{P}_1^T \mathbf{P}_1 d\Gamma \quad (12.45)$$

$$C_1 = k_1^2 \int_{\Gamma_{\text{int}}} \mathbf{P}_1^T \mathbf{Q} d\Gamma \quad (12.46)$$

and

$$\mathbf{f}_1 = \int_{\Gamma_1} \mathbf{P}_1^T g_1 d\Gamma \quad (12.47)$$

For the second set of equations in the system (12.44), the matrices are obtained in the same way by replacing subscript 1 by 2. At this stage, there are more unknowns than equations. Therefore, we add the continuity condition as

$$\int_{\Gamma_{\text{int}}} \mathbf{Q}^T [\Phi_2 - \Phi_1] d\Gamma = 0 \quad (12.48)$$

Substituting the approximations for the fields, then writing compactly the above steps gives the following system to solve:

$$\begin{bmatrix} H_1 & 0 & -C_1 \\ 0 & H_2 & C_2 \\ -C_1^T & C_2^T & 0 \end{bmatrix} \begin{Bmatrix} A_1 \\ A_2 \\ \lambda \end{Bmatrix} = \begin{Bmatrix} f_1 \\ f_2 \\ 0 \end{Bmatrix} \quad (12.49)$$

12.7.1.3 Example problems

A study of the accuracy of the elements was carried out. When waves pass from a region of slow wave speed to a region of high wave speed, with a large angle between

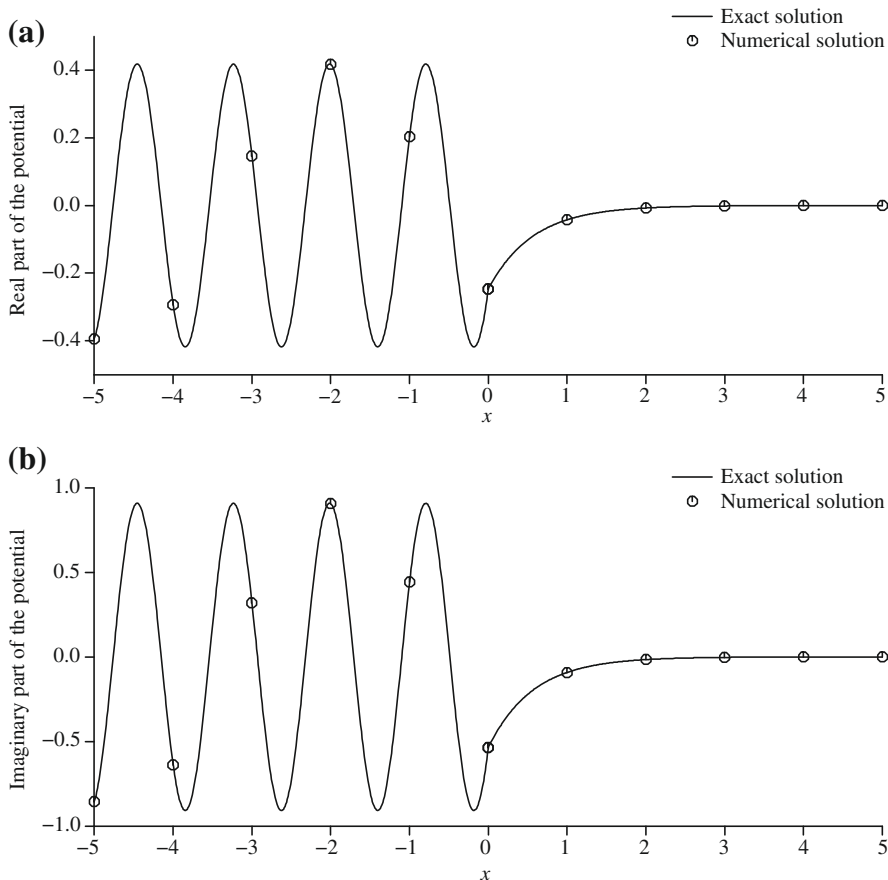


FIGURE 12.7

Evanescence modes, two-subdomain varying wave speed example [46]. Rectangular problem $-5 \leq x \leq 5, -5 \leq x \leq 5$. $k_1, -5 \leq x \leq 0; k_2, -5 \leq x \leq 0$. Robin boundary conditions, angle of incidence 45° , critical angle 30° . k_1 and k_2 chosen to give evanescent transmitted wave potential plotted on $y = 0$. Reproduced by permission of Elsevier.

the normal to the interface and the direction of wave propagation, edge waves, or evanescent waves, can appear. It is perhaps not obvious that a solution space of plane waves in the plane wave basis elements should be able to accurately represent such evanescent waves, although the proof of completeness would indicate that they should work. [Figure 12.7](#) shows some results where the angle of incidence was chosen to be such that only evanescent waves would arise in the second medium. The element mesh which is not shown is rectangular and appropriate Robin boundary conditions were applied. The plane wave direction set included the incident and reflected wave directions. The results demonstrate that the evanescent effects are properly captured by these elements.

12.7.1.4 Plane scattered by stepped cylinder

This example deals with the diffraction of a plane wave by a rigid circular cylinder, of radius r_1 , which is assumed to be vertical, and the plane wave is incident horizontally on the surface of water. Around the cylinder, the water is of depth h_1 up to a circular region of radius r_2 . Then for $r \geq r_2$, the depth is h_2 . In [Fig. 12.8](#), the outer region is deeper than the one around the cylinder ($h_1 < h_2$). However, the theory remains the same if $h_1 > h_2$. The physical domain of this problem is infinite in extent. This means that it must be truncated at a finite distance from the scatterer to enable a numerical simulation. An analytical solution for the problem in terms of Bessel and Hankel functions was developed in [46]. The problem was analyzed for a range of different k values. The errors are summarized in [Table 12.1](#). ε_2 is the error in the L^2 norm. The parameter τ is the number of degrees of freedom per wavelength.

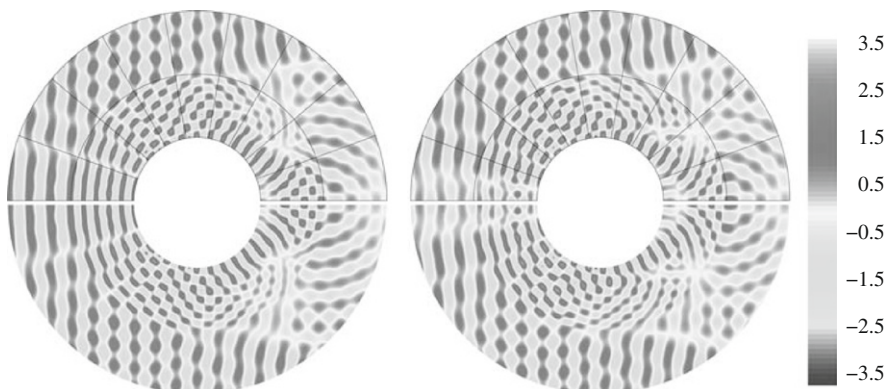


FIGURE 12.8

Waves scattered by stepped cylinder, two-subdomain varying wave speed example [46]. Inner domain: $1 \geq r \geq 2$, $k_1 = 10\pi$, Robin boundary conditions applied and plane wave incident along x -axis. Outer domain: $2 \geq r \geq 3$, $k_2 = 6\pi$. Upper half shows the solution using plane wave basis finite elements and lower half presents plane analytical solution. A total of 3.4 degrees of freedom per wavelength used. L_2 error is 0.4%. Reproduced by permission of Elsevier.

Table 12.1 Plane Wave Scattering by a Rigid Circular Cylinder, $k_1 = 2k_2$

k_1	2π	4π	6π	8π	10π	12π	14π	16π	18π	20π
τ	25.9	12.9	8.6	6.5	5.2	4.3	3.7	3.2	2.8	2.6
$\varepsilon_2(\%)$	0.002	0.007	0.02	0.1	0.5	2.5	0.9	0.4	0.6	1.1

Figure 12.8 shows contours of the real and imaginary components of the wave potential around the cylinder for $k_1 = 10\pi$ and $k_2 = 6\pi$. The results are similar to those of Huttunen et al. obtained using the ultra weak variational formulation.

12.7.2 Refraction caused by flows

The problem of waves refracted by flows is more difficult than the case of refraction due to changing wave speed. The topic is dealt with briefly in Chapter 11. Recently Astley and Gamallo [48,49] have applied plane wave basis type methods to wave refraction in the presence of a known flow field in one and two dimensions. In the one-dimensional case the flow is along a duct with changing cross-sectional area. So the flow speed varies with position along the duct. x is the distance along the duct and $A(x)$ is the corresponding cross-sectional area of the duct. The sound speed, $c_0(x)$, the density, $\rho_0(x)$, and the velocity $u_0(x)$ along the duct have been previously found using the one-dimensional nozzle equation. The velocity is given as $u(x) = d\phi/dx$, where ϕ is the *acoustic velocity potential*. The governing equation for small acoustic perturbations, derived from the linearized momentum and continuity equations, is then the *convected wave equation*

$$\frac{1}{A\rho_0} \frac{d}{dx} \left(\rho_0 A \frac{d\phi}{dx} \right) + \frac{\omega^2}{c_0^2} \phi = i\omega u_0 \left(\frac{1}{c_0^2} \frac{d}{dx} \left(\frac{\phi}{c_0^2} \right) \right) + u_0 \frac{d}{dx} \left(\frac{u_0}{c_0^2} \frac{d\phi}{dx} \right) \quad (12.50)$$

In the two-dimensional scheme the wavenumber varies in accordance with the prevailing flow. In this case uniform flow in the x -direction, with Mach number M , was considered in a duct, extending from $x = 0$ to $x = L$ and of width a . The resulting convected wave equation in nondimensionalized form is

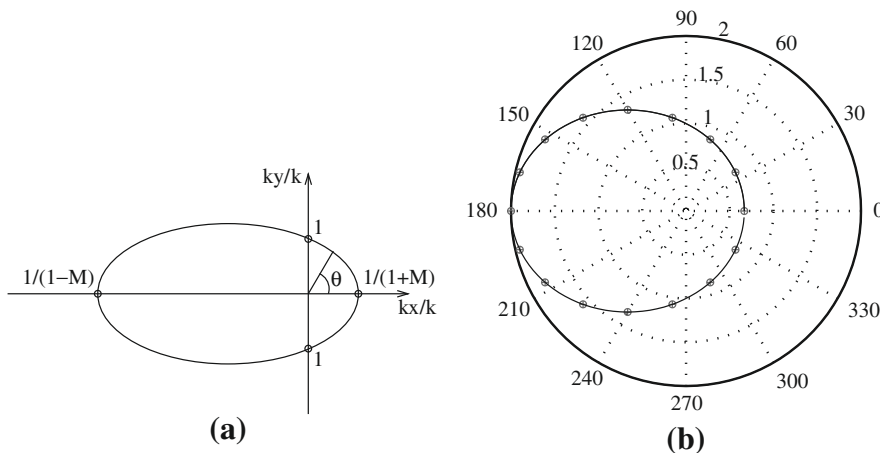
$$\frac{\partial^2 \phi}{\partial y^2} + (1 - M^2) \frac{\partial^2 \phi}{\partial x^2} - 2ikM \frac{\partial \phi}{\partial x} + k^2 \phi = 0 \quad (12.51)$$

The specific boundary conditions considered are as follows:

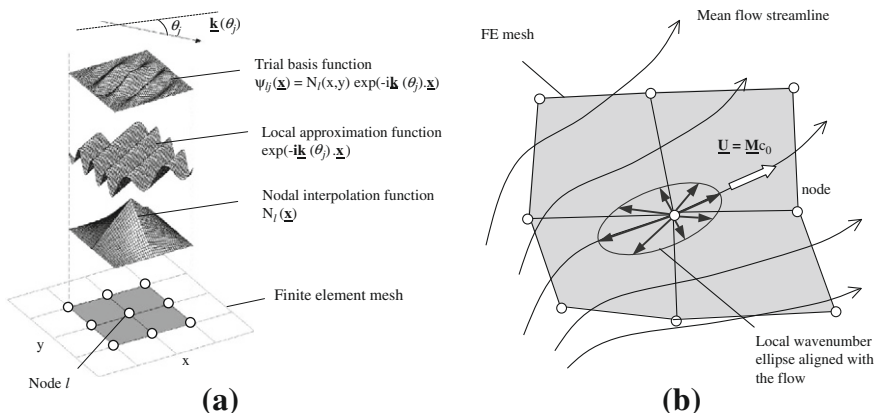
$$(1 - M^2) \frac{\partial \phi}{\partial x} - ikM \phi = -\cos(m\pi y) \quad \text{on } x = 0 \quad (12.52)$$

$$(1 - M^2) \frac{\partial \phi}{\partial x} - ikM \phi = -ik\phi \quad \text{on } x = L/a \quad (12.53)$$

$$\frac{\partial \phi}{\partial y} = 0 \quad \text{on } y = 0, 1 \quad (12.54)$$

**FIGURE 12.9**

Wavenumber ellipse for the convective wave equation [49]: (a) the continuous set of wavenumber vectors; (b) a finite set of wavenumber vectors uniformly distributed. Reproduced by permission from Ref. [49], copyright John Wiley and Sons Ltd.

**FIGURE 12.10**

PUFEM basis [49]: (a) construction of the PUFEM trial basis; (b) the local wavenumber ellipse. Reproduced by permission from Ref. [49], copyright John Wiley and Sons Ltd.

A polar plot of the wavenumber as a function of direction at any point takes the form of an ellipse. This is illustrated in Fig. 12.9. The local plane wave basis is also shown in Fig. 12.10. Astley and Gamallo report on the accuracy of the partition of unity elements. In summary they state that “Clearly *all* of the PUM models offer a huge improvement over conventional low order FEM.” Astley and Gamallo report the same general experiences as in the zero flow case for such types of element, namely

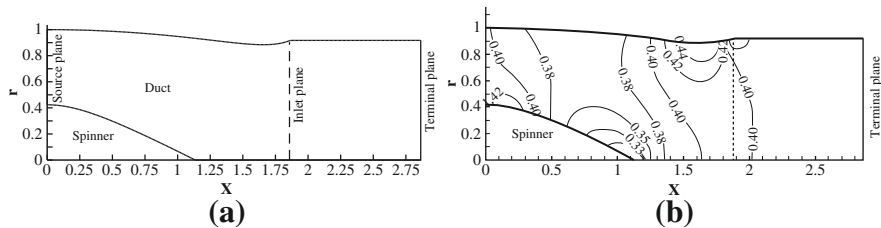


FIGURE 12.11

Nonuniform axisymmetric duct [49]: (a) computational domain; (b) mean flow Mach numbers. Reproduced by permission from Ref. [49], copyright John Wiley and Sons Ltd.

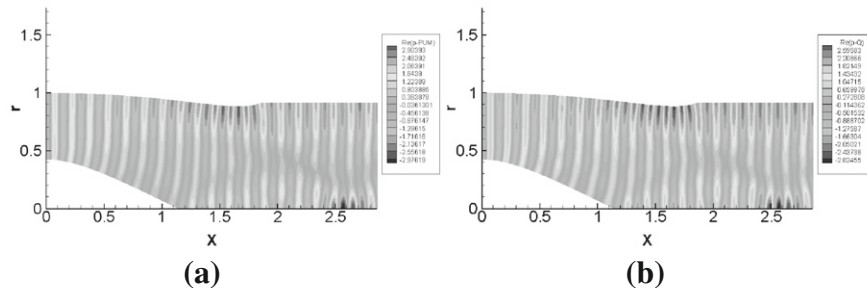


FIGURE 12.12

Nonuniform axisymmetric duct, acoustic pressure field (real part) for $\omega = 25$ [49]: (a) PUFEM, 12,000 degrees of freedom (1500 points and 8 directions); (b) Q-FEM, 100,000 degrees of freedom. Reproduced by permission from Ref. [49], copyright John Wiley and Sons Ltd.

reduction in the number of degrees of freedom compared with conventional elements and large condition numbers. The problem of completely general flow fields is more difficult. The plane waves are no longer solutions to the wave pattern in the presence of a general flow field. However they are still a legitimate solution space, though with no guarantee of completeness. The refracted plane wave solutions can still be used on the assumption that they are a good approximation if the flow is not varying rapidly, and is fairly constant locally. Gamallo and Astley [49] have applied the same elements to a general flow field through a nonuniform axisymmetric duct. Figure 12.11 shows the geometry, and Fig. 12.12 shows results obtained using the PUFEM and Q-FEM (quadratic finite elements). They report that accurate solutions are obtained using 12,000 degrees of freedom with PUFEM, whereas 100,000 degrees of freedom are needed for the quadratic conventional finite elements. If the conventional finite element mesh was made any coarser, pollution errors were encountered.

12.8 Spectral finite elements for waves

Spectral finite elements are elements which exploit choices in the selection of the finite element node locations and integration schemes. Conventional consistent mass

matrices lead to a large, though sparse system mass matrix. This is expensive in time-stepping schemes, since even if the time-stepping scheme is explicit the mass matrix has to be factorized and a back substitution carried out at each time step. If the mass matrix is lumped, the formulation is no longer strictly consistent and the results may be unreliable. If it were possible to integrate exactly the mass matrix by sampling only at the nodes within an element, then the mass matrix though theoretically consistent, would be diagonal and explicit time-stepping schemes would be much more economical. If a linear finite element is considered, then the general terms in the mass matrix are quadratic. If a Newton-Cotes formula is used to integrate the mass matrix exactly, then three sampling points are needed in one dimension. As there are only two nodes in a linear element, the number of nodes is inconsistent with an exact integration using a Newton-Cotes integration scheme. If Gauss-Legendre integration is used, then two sampling points are needed to exactly integrate the mass matrix. But these are not at the ends of the element and so the element cannot enforce continuity. However the N point Gauss-Lobatto scheme integrates over the range -1 to $+1$, and samples at the two end points of the range and $N - 2$ internal points. The scheme integrates exactly powers of x up to $1 + 2(N - 2) - 1 = 2N - 3$, for N sampling points. The scheme comes close to integrating the mass matrix exactly. For example in a one-dimensional quintic finite element with six nodes, the highest power of x in the mass matrix would be 10. The corresponding Gauss-Lobatto scheme would integrate exactly powers of x up to 9. Such integration formulas appear to have been first adopted by Fried and Malkus [50]. They achieved orders of integration, using Gauss-Lobatto schemes which were sufficiently accurate to integrate the stiffness matrix exactly, though not the mass matrix.

The Gauss-Chebyshev scheme also is close to integrating the mass matrix exactly. In both these types of elements the internal nodes of an element are not equally spaced, but are located at the positions dictated by the integration formulas. The Gauss-Legendre-Lobatto scheme is given by

$$\int_{-1}^{+1} f(x) dx \approx \frac{2}{n(n-1)} [f(1) + f(-1)] + \sum_{j=2}^{n-1} w_j f(x_j) \quad (12.55)$$

where x_j is the $(j - 1)$ th zero of $P'_{n-1}(x)$, where $P(x)$ is a Legendre polynomial and the weights, w_j , are given by

$$w_j = \frac{2}{n(n-1) [P_{n-1}(x_j)]^2} \quad (12.56)$$

The corresponding Gauss-Chebyshev-Lobatto points are given by [50–52]

$$- \cos \frac{\pi i}{N} \quad (12.57)$$

where N is the number of integration points.

The Gauss-Legendre-Lobatto elements have been investigated by Mulder and others [53–55] and the Gauss-Chebyshev-Lobatto elements by Dauksher, Gottlieb,

Hesthaven, and others [51, 52, 56–62]. There are numerous references to these methods and the above citations are only given as examples of recent work. They are not meant to be exhaustive. In general the numerical investigations demonstrate that spectral elements outperform conventional finite elements in transient wave problems. They have lower dispersion and better phase properties. The Gauss-Chebyshev formulation has also been used for direct collocation approaches to wave problems. This will not be discussed here but references are available [56–62].

In their basic form the spectral elements are not applicable to problems meshed with triangles or tetrahedra. In order to do this, it is necessary to generalize the Gauss-Lobatto and Gauss-Chebyshev-Lobatto schemes to triangles. It is notoriously difficult to generalize integration schemes from straight line segments, squares, and cubes, to triangles and tetrahedra. Although there are proofs that efficient symmetrical integration schemes for triangles and tetrahedral exist there are no general (open-ended) formulas for them, but only special results for certain numbers of points [63, 64]. Considerable effort has gone into generalizing the Gauss-Lobatto schemes for triangles and tetrahedra. The corresponding points are called *Fekete* points. The Fekete points are defined as the points which maximize the determinant of the Vandermonde matrix relating the coordinates of the sampling points to the polynomial coefficients. For large numbers of points the interpolating polynomials may become oscillatory and the Vandermonde matrix can become ill-conditioned. The Fekete points are closely related to the Lebesgue points, but are easier to determine [65]. Karniadakis and Sherwin [66] give a very comprehensive treatment of spectral finite elements applied to CFD.

12.9 Discontinuous Galerkin finite elements (DGFE)

This method is frequently used in the time domain, although it can be applied to virtually any finite element problem and not just the Helmholtz wave equation. In the discontinuous Galerkin method, elements are linked together by constraints, which approximately satisfy continuity of various quantities between elements. The jumps between elements are of the same magnitude as the truncation error. The most natural way of applying the constraints is probably the method of Lagrange multipliers. However, this has two disadvantages: the introduction of additional equations to solve, and the indefiniteness of the resulting matrix. In practice the constraints are applied using the element variables themselves. This can be done using some kind of penalty formulation. The mathematical details of the method are explained in Ref. [5]. A comprehensive set of papers on the method edited by Cockburn et al. [67] are available. The paper by Zienkiewicz et al. [47] gives an approachable introduction to the method. The method has been applied to a large range of problems, including waves [68]. Important applications to electromagnetic wave scattering problems are given by Hesthaven and Warburton [69, 70]. They explain in considerable detail the techniques needed to extract the full potential of the method. Some of the points are explained below.

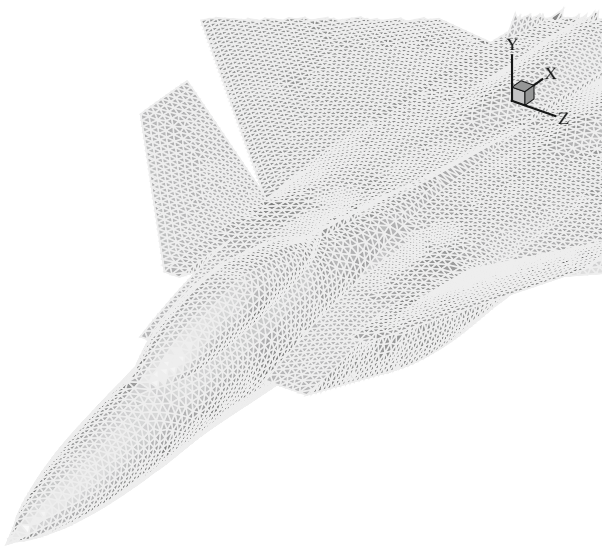
A significant property of the discontinuous Galerkin finite element method is that the associated mass matrix is local to each element. Furthermore, the affine nature of straight-sided triangles and tetrahedra implies that their mass matrices differ only by a multiplicative constant. In practical computations, the relatively small reference triangle (or tetrahedron) mass matrix can be inverted in preprocessing, leading to an extremely efficient method. In the conventional finite element method, the assembled stiffness and mass matrices are large sparse matrices, linking together all adjacent degrees of freedom. In the DGFE method the system stiffness matrix need not be formed, and only its product with the vector of field variables from the previous iteration need be retained. This greatly reduces the storage requirement of the method, which becomes $O(N)$, where N is the number of variables in the problem. The other features of the method, as developed by Hesthaven and Warburton and others, are that high-order finite elements are used. They show a 56-node tetrahedron, for example, and use tetrahedra with up to 286 nodes. The node locations are selected using special procedures, and the shape functions are formed using Lagrange polynomial interpolation. Error-bound results, Eq. (12.1), show that for a given number of degrees of freedom in a wave problem, it is better to use higher-order polynomials. The use of higher-order elements involves the use of dense, local, reference element operator matrices. However, in the case of straight-sided triangle meshes only one set of reference operator matrices is required. For a given operation, say differentiation, the reference element matrix is only loaded into cache once and the field data in all elements can be differentiated with this one matrix and then physical derivatives are computed using the chain rule. Coupling this approach with standard, optimized linear algebra mathematics libraries leads to extremely efficient codes.

Exact analytic integration is used where necessary. The authors analyze their scheme for consistency and accuracy. They present a number of results including the scattering of a plane wave by a sphere of radius a at $ka = 10$. Warburton [69] also gives results for the scattering of electromagnetic waves by a F15 fighter aircraft. Results are shown in Figures 12.13 and 12.14.

Eskilsson and Sherwin [68] discuss the modeling of the shallow-water equations using the discontinuous Galerkin method. They consider as an example the modeling of the Port of Visby, on the Baltic Sea. Figure 12.15 shows the mesh of elements which was used and the water depths, and Fig. 12.16 shows a snapshot of the surface elevations after 500 s.

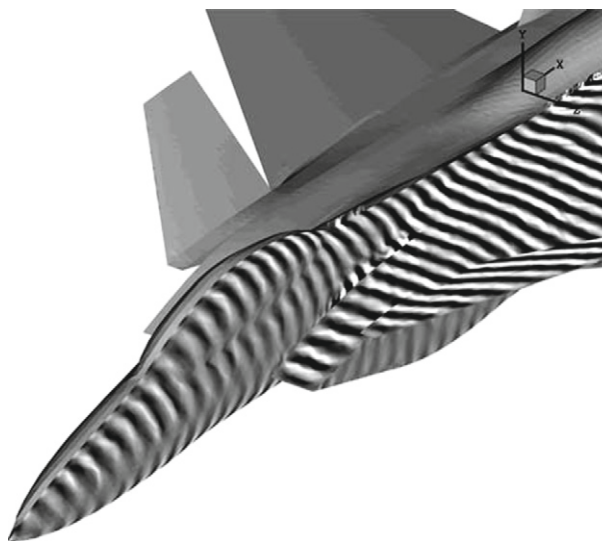
12.10 Concluding remarks

The field of short-wave modeling is currently the focus of intense research activity, not only using finite element, but also boundary integral and other domain and boundary-based methods. At the moment there are a number of promising algorithms, some of which have been described above. The most powerful finite element-based method appears to be the discontinuous Galerkin method. Certainly this has achieved the solution of problems containing the largest number of wavelengths. The other finite element-based algorithms do not seem to be quite so powerful. However given the

**FIGURE 12.13**

Electromagnetic waves scattered by fighter aircraft. Projection of finite element mesh onto surface of aircraft. Results due to Hesthaven and Warburton and published in Ref. [61].

Results reproduced with permission from Elsevier.

**FIGURE 12.14**

Electromagnetic waves scattered by fighter aircraft. Contours of electrical field on the surface of aircraft. Results due to Hesthaven and Warburton and published in Ref. [61].

Results reproduced with permission from the publishers.

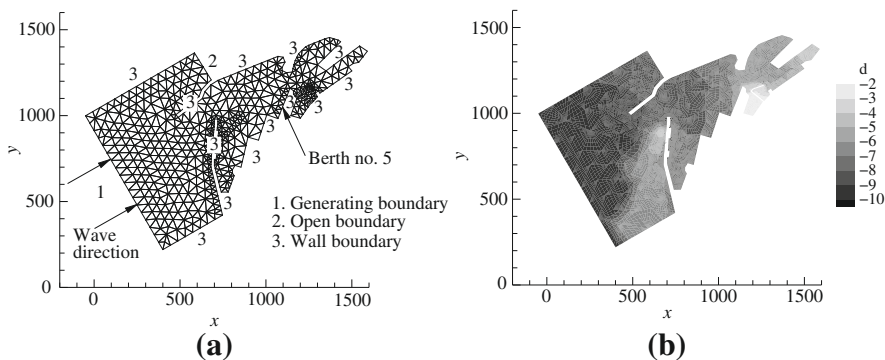


FIGURE 12.15

Harbor layout, Eskilsson and Sherwin [68]: (a) mesh and boundary conditions; (b) depth.
Reproduced by permission from Ref. [68], copyright John Wiley and Sons Ltd.

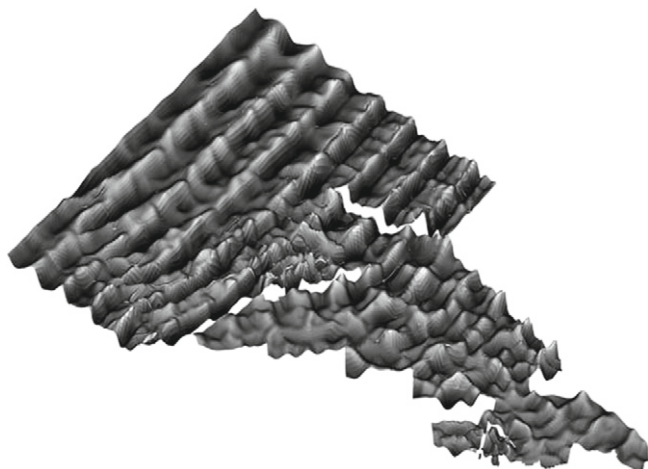


FIGURE 12.16

Snapshot of surface elevation after 500 s [68]. Reproduced by permission from Ref. [68], copyright John Wiley and Sons Ltd.

high level of research activity, this may change. The chief competing boundary-based method seems to be the fast multipole method, based on a more efficient formulation of the boundary integral method.

References

- [1] P. Bettess, O. Laghrouche, E. Perrey-Debain, Short-wave scattering, Philos. Trans. R. Soc. Ser. A 362 (2004) (Theme Issue).

- [2] M. Ainsworth, P. Davies, D. Duncan, P. Martin, B. Rynne, Topics in computational wave propagation, Lecture Notes in Computational Science and Engineering, vol. 51, Springer, Berlin, 2003.
- [3] T.J.R. Hughes, Multiscale phenomena: Green's functions, the Dirichlet to Neumann formulation, subgrid scale models, bubbles and the origins of stabilized methods, *Comput. Methods Appl. Mech. Eng.* 127 (1995) 387–401.
- [4] T. Strouboulis, I. Babuška, K. Copps, The design and analysis of the generalised finite element method, *Comput. Methods Appl. Mech. Eng.* 181 (2000) 43–69.
- [5] O.C. Zienkiewicz, R.L. Taylor, J.Z. Zhu, *The Finite Element Method: Its Basis and Fundamentals*, seventh ed., Elsevier, Oxford, 2013.
- [6] F. Ihlenburg, I. Babuška, Dispersion analysis and error estimation of Galerkin finite element methods for the Helmholtz equation, *Int. J. Numer. Methods Eng.* 38 (1995) 3745–3774.
- [7] I. Babuška, F. Ihlenburg, T. Stroubolis, S.K. Gangaraj, A posteriori error estimation for finite element solutions of Helmholtz' equations. Part II: the quality of local indicators and estimators, *Int. J. Numer. Methods Eng.* 40 (1997) 3443–3462.
- [8] I. Babuška, F. Ihlenburg, T. Stroubolis, S.K. Gangaraj, A posteriori error estimation for finite element solutions of Helmholtz' equations. Part II, *Int. J. Numer. Methods Eng.* 40 (1997) 3883–3900.
- [9] M. Ainsworth, Discrete dispersion relation for hp-finite element approximation at high wave number, *SIAM J. Numer. Anal.* 42 (2004) 553–575.
- [10] K. Morgan, O. Hassan, J. Peraire, A time domain unstructured grid approach to the simulation of electromagnetic scattering in piecewise homogeneous media, *Comp. Methods Appl. Mech. Eng.* 152 (1996) 157–174.
- [11] K. Morgan, P.J. Brookes, O. Hassan, N.P. Weatherill, Parallel processing for the simulation of problems involving scattering of electromagnetic waves, *Comput. Methods Appl. Mech. Eng.* 152 (1998) 157–174.
- [12] O.C. Zienkiewicz, P. Bettess, Infinite elements in the study of fluid structure interaction problems, in: Proceedings of the 2nd International Symposium on Computational Methods in Applied Science, Versailles, 1975, in: J. Ehlers et al. (Eds.), *Lecture Notes in Physics*, vol. 58, Springer-Verlag, Berlin, 1976.
- [13] P. Bettess, O.C. Zienkiewicz, Diffraction and refraction of surface waves using finite and infinite elements, *Int. J. Num. Methods Eng.* 11 (1977) 1271–1290.
- [14] R.J. Astley, W. Eversman, A note on the utility of a wave envelope approach in finite element duct transmission studies, *J. Sound Vibr.* 76 (1981) 595–601.
- [15] R.J. Astley, Wave envelope and infinite elements for acoustical radiation, *Int. J. Num. Methods Fluids* 3 (1983) 507–526.
- [16] E. Chadwick, P. Bettess, O. Lagrouche, Diffraction of short waves modelled using new mapped wave envelope finite and infinite elements, *Int. J. Numer. Methods Eng.* 45 (1999) 335–354.
- [17] J.M. Melenk, I. Babuška, The partition of unity finite element method: basic theory and applications, *Comput. Methods Appl. Mech. Eng.* 139 (1996) 289–314.

- [18] J.M. Melenk, I. Babuška, The partition of unity finite element method, *Int. J. Numer. Methods Eng.* 40 (1997) 727–758.
- [19] P.M. Morse, H. Feshbach, *Methods of Theoretical Physics*, McGraw-Hill, New York, 1953.
- [20] T. Huttunen, P. Monk, J.P. Kaipio, Computational aspects of the ultra weak variational formulation, *J. Comput. Phys.* 182 (2002) 27–46.
- [21] T. Huttunen, P. Monk, F. Collino, J.P. Kaipio, Computation aspects of the ultra weak variational formulation, *SIAM J. Sci. Comput.* 25 (2004) 1717–1742.
- [22] P. Mayer, J. Mandel, The finite ray element method for the Helmholtz equation of scattering: first numerical experiments, Technical report, Report Number CU-CAS-00-20, College of Engineering, University of Colorado, Boulder, Colorado, USA. UCD/CCM Report 111, 1997. URL: <http://www-math.cudenver.edu/ccm/reports.html>.
- [23] A. de La Bourdonnaye, High frequency approximation of integral equations modelizing scattering phenomena, *Mod. Math. Anal. Numer.* 28 (1994) 223–241.
- [24] A. de La Bourdonnaye, Convergence of the approximation of wave functions by oscillatory functions in the high frequency limit, *C. R. Acad. Paris Sér. I* 318 (1994) 765–768.
- [25] O. Lagrouche, P. Bettess, Short wave modelling using special finite elements - towards an adaptive approach, in: J.R. Whiteman (Ed.), *The Mathematics Finite Elements and Applications X*, Elsevier, 2000, pp. 181–194.
- [26] O. Lagrouche, P. Bettess, Short wave modelling using special finite elements, *J. Comput. Acoust.* 8 (2000) 189–210.
- [27] P. Ortiz, E. Sanchez, An improved partition of unity finite element model for diffraction problems, *Int. J. Numer. Methods Eng.* 50 (2001) 2727–2740.
- [28] P. Bettess, J. Shirron, O. Lagrouche, B. Peseux, R. Sugimoto, J. Trevelyan, A numerical integration scheme for special finite elements for the Helmholtz equation, *Int. J. Numer. Methods Eng.* 56 (2002) 531–552.
- [29] O. Lagrouche, P. Bettess, E. Perrey-Debain, J. Trevelyan, Plane wave basis for wave scattering in three dimensions, *Commun. Numer. Methods Eng.* 19 (2003) 715–723.
- [30] E. Perrey-Debain, O. Lagrouche, P. Bettess, J. Trevelyan, Plane wave basis finite elements and boundary elements for three dimensions, *Philos. Trans. R. Soc.* 362 (2004) 561–578, (Theme Issue)
- [31] R. Sugimoto, P. Bettess, Coupling of mapped wave infinite elements and plane wave basis finite elements for the Helmholtz equation in exterior domains, *Commun. Numer. Methods Eng.* 19 (2003) 761–777.
- [32] C. Farhat, I. Harari, L. Franca, The discontinuous enrichment method, Report CU-CAS-00-20, Center for Aerospace Structures, University of Colorado, 2000.
- [33] C. Farhat, I. Harari, L. Franca, A discontinuous finite element method for the Helmholtz equation, in: Proceedings of the European Congress on Computational Methods in Applied Sciences and Engineering, 2000, ECCOMAS Barcelona, Spain, 11-14 2000, pp. 1–15.

- [34] C. Farhat, I. Harari, L. Franca, The discontinuous enrichment method, *Comput. Methods Appl. Mech. Eng.* 190 (2001) 645–679.
- [35] B. Després, Sur une formulation variationnelle de type ultra-faible, *Comptes Rendus de l'Académie des Sciences-Series I* (318) (1994) 939–944.
- [36] O. Cessenat, B. Després, Application of an ultra weak variational formulation of elliptic PDEs to the two dimensional Helmholtz problem, *SIAM J. Numer. Anal.* 35 (1998) 255–299.
- [37] J. Jirousek, A. Wróblewski, T-elements: state of the art and future trends, *Arch. Comput. Methods Eng.* 3 (4) (1996).
- [38] I. Herrera, Trefftz method: a general theory, *Numer. Methods Partial Differential Equations* 16 (2000) 561–580.
- [39] J. Jirousek, Basis for development of large finite elements locally satisfying all field equations, *Comput. Methods Appl. Mech. Eng.* 14 (1978) 65–92.
- [40] M. Stojek, Least-squares Trefftz-type elements for the Helmholtz equation, *Int. J. Numer. Methods Eng.* 41 (1998) 831–849.
- [41] I. Herrera, *Boundary Methods: An Algebraic Theory*, Pitman, London, 1984.
- [42] Y.K. Cheung, W.G. Jin, O.C. Zienkiewicz, Solution of Helmholtz equation by the Trefftz method, *Int. J. Numer. Methods Eng.* 32 (1991) 63–78.
- [43] P. Ortiz, Finite elements using plane wave basis, *Philos. Trans. R. Soc.* 362 (2004) 525–540.
- [44] J.C.W. Berkhoff, Refraction and diffraction of waver waves: derivation and method of solution of the two-dimensional refraction-diffraction equation. Report and mathematical investigation, w154, Delft Hydraulics Laboratory, 1973.
- [45] P. Bettess, Special wave basis finite elements for very short wave refraction and scattering problems, *Commun. Numer. Methods Eng.* 20 (2004) 291–298.
- [46] O. Lagrouche, P. Bettess, E. Perrey-Debain, J. Trevelyan, Wave interpolation finite elements for Helmholtz problems with jumps in the wave speed, *Comput. Methods Appl. Mech. Eng.* 194 (2004) 367–381.
- [47] O.C. Zienkiewicz, R.L. Taylor, S.J. Sherwin, J. Peiró, On discontinuous Galerkin methods, *Int. J. Numer. Methods Eng.* 58 (2003) 1119–1148.
- [48] R.J. Astley, P. Gamallo, Special short wave elements for flow acoustics, *Comput. Methods Appl. Mech. Eng.* 194 (2005) 341–353.
- [49] P. Gamallo, R.J. Astley, The partition of unity finite element method for short wave acoustic propagation on nonuniform potential flows, *Int. J. Numer. Methods Eng.* 65 (2006) 425–444.
- [50] I. Fried, D.S. Malkus, Finite element mass matrix lumping by numerical integration without convergence rate loss, *Int. J. Solids Struct.* 11 (1976) 461–466.
- [51] W. Dauksher, A.F. Emery, Accuracy in modeling the acoustic wave equation with Chebyshev spectral finite elements, *Finite Elem. Anal. Des.* 26 (1997) 115–128.
- [52] W. Dauksher, A.F. Emery, An evaluation of the cost effectiveness of Chebyshev spectral and p -finite element solutions to the scalar wave equation, *Int. J. Numer. Methods Eng.* 45 (1999) 1099–1114.

- [53] W.A. Mulder, Spurious modes in finite-element discretizations of the wave equation may not be all that bad, *Appl. Numer. Math.* 30 (1999) 425–445.
- [54] W.A. Mulder, Higher-order mass-lumped finite elements for the wave equation, *J. Comput. Acoust.* 9 (2001) 671–680.
- [55] M.J.S. Chin-Joe-Kong, W.A. Mulder, M. Van Veldhuizen, Higher-order triangular and tetrahedral finite elements with mass lumping for solving the wave equation, *J. Eng. Math.* 35 (1999) 405–426.
- [56] J.S. Hesthaven, P.G. Dinesen, J.P. Lynov, Spectral collocation time-domain modeling of diffractive optical elements, *J. Comput. Phys.* 155 (1999) 287–306.
- [57] J.S. Hesthaven, Spectral penalty methods, *Appl. Numer. Math.* 33 (2000) 23–41.
- [58] J.S. Hesthaven, C.H. Teng, Stable spectral methods on tetrahedral elements, *SIAM J. Sci. Comput.* 21 (2000) 2352–2380.
- [59] B. Yang, D. Gottlieb, J.S. Hesthaven, Spectral simulations of electromagnetic waves scattering, *J. Comput. Phys.* 134 (1997) 216–230.
- [60] J.S. Hesthaven, D. Gottlieb, Stable spectral methods for conservation laws on triangles with unstructured grids, *Comput. Methods Appl. Mech. Eng.* 175 (1999) 361–381.
- [61] D. Gottlieb, J.S. Hesthaven, Spectral methods for hyperbolic problems, *J. Comput. Appl. Math* 128 (2001) 83–131.
- [62] J.S. Hesthaven, From electrostatics to almost optimal nodal sets for polynomial interpolation in a simplex, *SIAM J. Numer. Anal.* 35 (1998) 655–676.
- [63] R. Cools, P. Rabinowitz, Monomial cubature rules since ‘stroud’: a compilation, *J. Comput. Appl. Math* 48 (1993) 309–326.
- [64] R. Cools, Monomial cubature rules since ‘Stroud’: A compilation–part 2, *J. Comput. Appl. Math.* 112 (1999) 21–27.
- [65] M.A. Taylor, B.A. Wingate, R.E. Vincent, An algorithm for computing Fekete points in the triangle, *SIAM J. Numer. Anal.* 38 (2000) 1707–1720.
- [66] G.E. Karniadakis, S.J. Sherwin, *Spectral hp Element Methods for CFD*, Oxford University Press, Oxford, 1999.
- [67] B. Cockburn, G.E. Karniadakis, C.-W. Shu, *Discontinuous Galerkin Methods*, Springer, Berlin, 2000.
- [68] C. Eskilsson, S.J. Sherwin, A triangular spectral/hp discontinuous Galerkin method for modelling 2D shallow water equations, *Int. J. Numer. Methods Fluids* 45 (2004) 605–624.
- [69] T. Warburton, Application of the discontinuous Galerkin method to Maxwell’s equations using unstructured polymorphic hp-finite elements, in: B. Cockburn, G.E. Karniadakis, C.-W. Shu (Eds.), *Discontinuous Galerkin Methods*, Springer, 2000, pp. 451–458.
- [70] J.S. Hesthaven, T. Warburton, Nodal high-order methods on unstructured grids—I. Time domain solution of Maxwell’s equations, *J. Comput. Phys.* 181 (2002) 186–221.

Fluid–Structure Interaction 13

13.1 Introduction

Fluid-structure interaction is an interdisciplinary subject of interest to many researchers in the field of fluid dynamics. The finite element method has been at the forefront of research in this important area. Fluid-structure interaction exists in its various forms in both natural systems and man-made objects. The interaction between a tree and wind and groundwater interaction with the soil are typical examples of fluid-structure interaction in nature. Fluid-structure interaction for engineered systems occurs in modeling behavior of offshore platforms with the ocean, flight characteristics of aircraft, and dams with reservoirs. Although the nature and the interaction between the solid and fluid in these problems are different, all these problems come under the category of fluid-structure interaction. It is also important to note that the degree of severity in interaction between the solid and fluid varies between different problems. While many problems involve solid deformation as an integral part, there are many man-made problems in which the solid may be considered to move as a rigid body. It is also possible to have one-directional coupling between the fluid and solid in certain problems. For the sake of completeness and clarity, we classify the subject below.

The subject may be divided into two categories based on the flow physics as (a) gas and (b) liquid interaction with solids. While incompressible flow assumption is always made for liquid-solid interaction, both compressible and incompressible flow assumptions are made when a gas interacts with a solid. When the Mach number of flow is under 0.3, an incompressible flow assumption is justified for gas-solid interaction. The main application of air-solid interaction is in the determination of aerodynamic forces on structures such as aircraft wings. Such study is often referred to as aeroelasticity. Static aeroelasticity involves the study of the interaction between aerodynamic and elastic forces, while dynamic aeroelasticity is the topic that normally investigates the interaction between aerodynamic, elastic, and inertial forces. Aerodynamic flutter is one of the severe consequences of dynamic aerodynamic forces and responsible for destructive effects in aircrafts and other structures. The infamous example of the Tacoma bridge collapse is historical evidence for the destructive nature of flutter and a constant reminder of the importance of fluid-structure interaction.

The subject may also be classified based on the nature of the structure interacting with a fluid as (a) rigid body and (b) deforming body interaction with the fluid. Examples where rigid body interaction may often be used include internal combustion engines, gas and water turbines, ships, and offshore platforms. Although the rigid body–fluid interaction problem is simpler to some extent, the dynamics of rigid body motion requires a solution that reflects the fluid forces. Examples of deforming body–fluid interaction include aeroelasticity, a majority of biomedical applications, and poroelasticity. Both the rigid body and deforming body interaction with a fluid is often strongly coupled, influencing both fluid and solid forces. Within the deformable body–fluid interaction, the nature of the deforming body may vary from very simple linear elastic models in small strain to highly complex nonlinear deformations of inelastic materials. The material may also be compressible or nearly incompressible in nature.

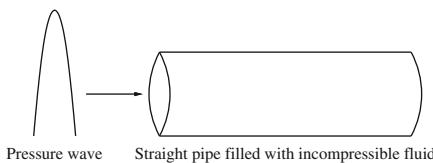
In addition to the classification based on the physical nature of the problems, the fluid–structure interaction may also be classified based on the solution procedure employed. These classifications include (a) a monolithic approach in which both fluid and solid are treated as one unified system and (b) a partitioned approach in which the fluid and solid are treated as two different systems coupled through the interface. A partitioned approach is often preferred in practical engineering applications as this method allows the use of independently developed and tested solvers for fluids and solids. Within the partitioned approach the coupling between the fluid and solid may be carried out using a strongly or weakly coupled approach. Although the weakly coupled approach is used in aerodynamic applications, it is seldom used in other areas due to instability issues. Thus, a strongly coupled approach is the one that is preferred by most researchers. This obviously leads to various issues of coupling procedures at the interface between the fluid and solid.

Due to the emergence of immersed boundary methods in the last two decades, a further classification based on immersed boundary methods or nonconforming mesh methods may also be used. In an immersed boundary method the structure is assumed to be immersed into the fluid and the forces are transferred between fluid and solid boundaries. Since only interface forces require transferring, the need for conforming meshes is eliminated in such methods. These methods are useful in complex problems of fluid–structure interaction in which complex mesh regeneration may be difficult to carry out.

13.2 One-dimensional fluid–structure interaction

13.2.1 Equations

Fluid–structure interaction in its simplest form occurs in flexible pipes or pipe networks. In addition to normal engineering applications, a network of flexible pipes can be used to approximate blood circulation within an arterial vessel system. Since the one-dimensional fluid–structure interaction is simple to understand and implement, this is studied here first before investigating multidimensional fluid–structure

**FIGURE 13.1**

Flow through a flexible pipe.

interaction problems. To introduce the formulation, consider a simple problem of a flexible straight pipe as shown in Fig. 13.1. With a pressure wave passing through the flexible pipe, the surface is expected to stretch radially. By assuming only one-dimensional incompressible fluid flow and radial stretch of the flexible wall, the equations governing the cross-sectional area and velocity may be derived by reducing the continuity and momentum equations to

$$\frac{\partial A}{\partial t} + \frac{\partial(Au)}{\partial x} = 0 \quad (13.1)$$

and

$$\frac{\partial u}{\partial t} + u \frac{\partial u}{\partial x} + \frac{1}{\rho} \frac{\partial p}{\partial x} - \frac{1}{\rho} \frac{\partial \tau}{\partial r} = 0 \quad (13.2)$$

where A is cross-sectional area, t is time, u is velocity, x is axis direction, ρ is density of the fluid, p is pressure, τ is shear stress, and r is radial direction. Shear stress for a fully developed flow may be given as $\tau = \mu(\frac{\partial u}{\partial r})|_R$. Using Poiseuille flow assumptions, the shear stress may be expressed as

$$\frac{d\tau}{dr} = -\frac{8\pi\mu u}{A} \quad (13.3)$$

This is a reasonable approximation for laminar and Newtonian flows. Substituting the approximation for the shear stress, Eq. (13.2) may now be written as

$$\frac{\partial u}{\partial t} + u \frac{\partial u}{\partial x} + \frac{1}{\rho} \frac{\partial p}{\partial x} + \frac{8\pi\mu u}{\rho A} = 0 \quad (13.4)$$

The system of conservation of mass and momentum equations may now be written as

$$\frac{\partial \Phi}{\partial t} + \frac{\partial \mathbf{F}}{\partial x} + \mathbf{Q} = \mathbf{0} \quad (13.5)$$

where $\Phi = \begin{Bmatrix} A \\ u \end{Bmatrix}$, $\mathbf{F} = \begin{Bmatrix} uA \\ \frac{u^2}{2} + \frac{p}{\rho} \end{Bmatrix}$, and $\mathbf{Q} = \begin{Bmatrix} 0 \\ \frac{8\pi\mu}{\rho} \frac{u}{A} \end{Bmatrix}$.

Since there are three variables (A , u , and p), a third equation is required to close the system. This may be achieved through a constitutive equation that describes how pipe (or vessel) area varies with pressure and thus deals with the fluid–structure interaction

of the problem. In arterial vessel systems many different relationships are available and may be categorized as linear elastic models [1,2], where pressure is linearly related to area; nonlinear elastic models [3–17] where this relation is nonlinear; collapsible tube models [18–20], where special effort is made to accommodate tubes that can collapse as well as distend; and viscoelastic models [5,21,22], which account for the viscoelasticity of the vessel wall. While the viscoelastic models are the most complete, they are also the most complicated. Since the effects of wall viscosity are generally small, a nonlinear elastic relation is often sufficient.

The most common elastic relation used in studies of this type is that used by Formaggia et al. [23], Olufsen [12], and others and is written here (following [8,23]) as

$$p = p_{ext} + \beta \left(\sqrt{A} - \sqrt{A_0} \right) \quad (13.6)$$

where p_{ext} is external pressure, A_0 is area at zero transmural pressure (i.e., $p = p_{ext}$ or $A = A_0$), and β accounts for material properties of the elastic vessel:

$$\beta = \frac{\sqrt{\pi} h E}{A_0 (1 - \sigma^2)} \quad (13.7)$$

where h is vessel wall thickness, E is Young's modulus of the material, and σ is Poisson's ratio. All of these parameters are assumed to be independent of transmural pressure. Note that Eq. (13.6) may be rewritten in terms of wave speed as follows:

$$p = p_{ext} + 2\rho c^2 \left(1 - \sqrt{\frac{A_0}{A}} \right) \quad (13.8)$$

The intrinsic wave speed of the pipe is related to β via

$$c_0 = \sqrt{\frac{\beta \sqrt{A_0}}{2\rho}} = \sqrt{\frac{h E}{2\rho R_0 (1 - \sigma^2)}} \quad (13.9)$$

where the second expression is called the Moens-Korteweg equation (with $A_0 = \pi R_0^2$ where R_0 is the vessel radius) and relates the material properties of the vessel to its intrinsic longitudinal wave speed, that is, the speed at which an infinitesimally small pulse would propagate in an *initially unstressed* (i.e., $A(x, 0) = A_0$) pipe. Infinitesimally small pulses in *initially stressed* (i.e., $A(x, 0) = A$) pipes propagate at a slightly different speed,

$$c = \sqrt{\frac{\beta \sqrt{A}}{2\rho}} \quad (13.10)$$

Note that finite amplitude pulses do not propagate at a speed c , but at $|u + c|$, as will be discussed in Section 13.2.2. As a consequence, the peak of a pressure wave propagates faster than its foot which would inevitably lead to shock formation in a long enough tube.

13.2.2 Characteristic analysis

The system of Eq. (13.5) is nonlinear and highly coupled, making direct analytical solutions difficult. Thus, a numerical solution is required. However when implementing a numerical solution procedure, it is useful to have a linearized decoupled form of the equations which can be used when applying boundary conditions. Following the work of Formaggia et al. [4] and Sherwin et al. [8], the system is first written in quasi-linear form, which is then used to derive the characteristic system. By taking the spatial derivative of Eq. (13.8),

$$\frac{\partial p}{\partial x} = \frac{\partial p_{ext}}{\partial x} + \frac{\beta}{2\sqrt{A}} \frac{\partial A}{\partial x} - \frac{\beta}{2\sqrt{A_0}} \frac{\partial A_0}{\partial x} + (\sqrt{A} - \sqrt{A_0}) \frac{\partial \beta}{\partial x} \quad (13.11)$$

the number of independent variables in the momentum equation can be reduced by replacing $\frac{\partial p}{\partial x}$ with Eq. (13.11). Substituting into Eq. (13.5) and rearranging, the quasi-linear form becomes

$$\frac{\partial \Phi}{\partial t} + \mathbf{A} \frac{\partial \Phi}{\partial x} = \mathbf{S} \quad (13.12)$$

where

$$\begin{aligned} \Phi &= \begin{bmatrix} A \\ u \end{bmatrix}, \quad \mathbf{A} = \begin{bmatrix} u & A \\ \frac{\beta}{2\rho\sqrt{A}} & u \end{bmatrix} \\ \mathbf{S} &= -\frac{1}{\rho} \left[8\pi\mu \frac{u}{A} + \frac{\partial p_{ext}}{\partial x} - \frac{\beta}{2\sqrt{A_0}} \frac{\partial A_0}{\partial x} + (\sqrt{A} - \sqrt{A_0}) \frac{\partial \beta}{\partial x} \right] \end{aligned}$$

The eigenvalues (Λ) of Eq. (13.12) are given by $|\Lambda I - \mathbf{A}| = 0$ [24]. For incompressible flows, $u < c$, so there are two real eigenvalues and the system is hyperbolic [8,25]:

$$\Lambda = \begin{bmatrix} \lambda_f \\ \lambda_b \end{bmatrix} = u \pm \sqrt{\frac{\beta\sqrt{A}}{2\rho}} = \begin{bmatrix} u + c \\ u - c \end{bmatrix} \quad (13.13)$$

where c is the wave speed given in Eq. (13.10) and subscripts f and b represent respectively the forward and backward pointing characteristics.

Example 13.1. Derivation of characteristic variables

The characteristic speeds given in Eq. (13.13) may now be used to derive the characteristic variables. The characteristic variables and the primitive variables u and A are related via the eigenmatrix, i.e.,

$$\frac{\partial \mathbf{W}}{\partial \Phi} = \mathbf{L} \quad \text{with} \quad \mathbf{W} = \begin{bmatrix} w_f \\ w_b \end{bmatrix} \quad (13.14)$$

where subscripts f and b , respectively, indicate the forward- and backward-moving characteristic variables. Equation (13.12) may now be transformed by multiplying Eq. (13.14) as

$$\mathbf{L} \frac{\partial \Phi}{\partial t} + \mathbf{L}\mathbf{A} \frac{\partial \Phi}{\partial x} = \mathbf{L}\mathbf{S} \quad (13.15)$$

or

$$\frac{\partial \mathbf{W}}{\partial t} + \mathbf{L} \mathbf{A} \mathbf{L}^{-1} \frac{\partial \mathbf{W}}{\partial x} = \mathbf{L} \mathbf{S} \quad (13.16)$$

Since characteristic variables travel along the characteristic lines λ_1 and λ_2 of the system, the eigenvalues of Eq. (13.13) may also be expressed as $\mathbf{L} \mathbf{A} \mathbf{L}^{-1} = \Lambda$. From this relationship, a set of left eigenvectors may be derived using $\mathbf{l}_i \mathbf{A} = \lambda_i \mathbf{l}_i$, which leads to the left eigenmatrix. Substituting the first eigenvalue into this relationship gives

$$\begin{bmatrix} l_1 & l_2 \end{bmatrix} \begin{bmatrix} u & A \\ \frac{c^2}{A} & u \end{bmatrix} = \begin{bmatrix} l_1 & l_2 \end{bmatrix} (u + c) \quad (13.17)$$

From the above system we can write $l_1 = (c/A)l_2$. Using $l_2 = 1$ and $l_1 = (c/A)$ satisfies both equations of the system. Similarly, the left eigenvector for the second characteristic variable $(u - c)$ may be calculated as $l_1 = -(c/A)$ and $l_2 = 1$. The eigenmatrix \mathbf{L} may thus be written as

$$\mathbf{L} = \begin{bmatrix} \mathbf{l}_1^T \\ \mathbf{l}_2^T \end{bmatrix} = \begin{bmatrix} \frac{c}{A} & 1 \\ -\frac{c}{A} & 1 \end{bmatrix} \quad (13.18)$$

Using Eq. (13.14), we have

$$d\mathbf{W} = \mathbf{L} d\Phi \quad (13.19)$$

or

$$d \begin{Bmatrix} w_f \\ w_b \end{Bmatrix} = \begin{bmatrix} \frac{c}{A} & 1 \\ -\frac{c}{A} & 1 \end{bmatrix} d \begin{Bmatrix} A \\ u \end{Bmatrix} \quad (13.20)$$

Substituting Eq. (13.10) and integrating between initial (subscript 0) and instantaneous values gives

$$\begin{Bmatrix} w_f \\ w_b \end{Bmatrix} = \begin{Bmatrix} u - u_o + 4(c - c_0) \\ u - u_o - 4(c - c_0) \end{Bmatrix} = \begin{Bmatrix} w_f^* - w_f^0 \\ w_b^* - w_b^0 \end{Bmatrix} \quad (13.21)$$

where $w_{f,b}^* = u \pm 4c$ and $w_{f,b}^0 = u_o \pm 4c_0$. Since \mathbf{S} in Eq. (13.16) is approximately equal to zero near the boundaries, the characteristic variables of Eq. (13.21) satisfy

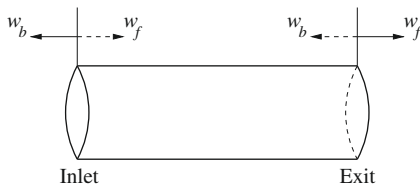
$$\frac{\partial w_{f,b}}{\partial t} + \lambda_{f,b} \frac{\partial w_{f,b}}{\partial x} = 0 \quad (13.22)$$

The primitive variables can be calculated from the characteristic variables by adding or subtracting the two equations in Eq. (13.21), giving

$$A = \left[\frac{(w_f - w_b)}{8} + c_0 \right]^4 \left(\frac{2\rho}{\beta} \right)^2 \quad (13.23)$$

$$u = u_0 + \frac{1}{2} (w_f + w_b) \quad (13.24)$$

Figure 13.2 schematically represents the forward- and backward-running characteristic variables. The figure also shows the direction of incoming wavefronts using dashed arrows and outgoing wavefronts using solid arrows.

**FIGURE 13.2**

Nonreflecting boundary conditions in a one-dimensional domain. Solid arrow lines represent the outgoing characteristic and dashed arrow lines represent the incoming characteristic.

13.2.3 Boundary conditions

From the characteristic system discussed previously, it is obvious that the pressure and velocity *wavefronts* propagate forwards at a speed of $u + c$ [see Eq. (13.13)] and backwards at $u - c$. A “wavefront” strictly refers to an infinitesimal change in one of the characteristic variables, w_f or w_b (see Fig. 13.2). Forward-running wavefronts are initially generated by a disturbance at the inlet. These wavefronts, which compose the forward-running pressure wave, then propagate throughout the domain. To obtain a nonreflective condition at the boundaries, Eqs. (13.23) and (13.24) should be satisfied. Thus, both the forward- and backward-running wavefronts (w_f and w_b) should be computed at every time step using any prescribed condition.

Since $u < c$, $\lambda_f > 0$ and $\lambda_b < 0$ (i.e., the system is subsonic), and so one boundary condition must be specified at both the inlet and outlet. In both cases, the outgoing characteristic may be calculated via linear extrapolation in the x - t plane, where for the next time step $n + 1$,

$$w_b^{n+1} \Big|_{x=x_0} = w_b^n \Big|_{x=x_0 - \lambda_b^n \Delta t} \quad (13.25)$$

and

$$w_f^{n+1} \Big|_{x=x_L} = w_f^n \Big|_{x=x_L - \lambda_f^n \Delta t} \quad (13.26)$$

at the inlet and outlet, respectively, where x_0 and x_L are the coordinates of the inlet and outlet. Since the governing equations (13.12) are written only in terms of cross-sectional area and velocity, one of these values or pressures should be prescribed at a boundary. All the remaining unknowns at the boundary should be computed using the wavefronts and Eqs. (13.23) and (13.24).

13.2.3.1 Prescribed forward area, pressure, and velocity

Prescribing the *forward* component of a variable can be achieved by prescribing the incoming characteristic (w_1) [4]. The actual values assigned to both A_{in} and u_{in} are determined at runtime based on the prescribed incoming characteristic and the current value of the outgoing characteristic [from Eq. (13.25)] which is not known *a priori*. Thus, the outgoing characteristic variable is often retained at the initial value when

applying boundary conditions. To prescribe the forward area, rearrange (13.23) to give at the inlet

$$w_f^{*n+1} = w_b^{*0} + 8 \left(\bar{A}^{n+1} \right)^{1/4} \sqrt{\frac{\beta}{2\rho}} \quad (13.27)$$

Note that $w_{f,b}^*$ are defined in Eq. (13.21). Similarly, to prescribe the forward pressure, substitute (13.6) into (13.27):

$$w_f^{*n+1} = w_b^{*0} + 4 \sqrt{\frac{2}{\rho}} \sqrt{(\bar{p}^{n+1} - p_{ext}) + \beta \sqrt{A_0}} \quad (13.28)$$

Finally, the forward velocity may be prescribed by rearranging (13.24):

$$w_f^{*n+1} = 2\bar{u}^{n+1} - w_b^{*0} \quad (13.29)$$

In these equations, w_b^{*0} is the initial value of w_b^* and is also equal to the value of w_b^* at any time if no backward-running waves reach the inlet. If not given, the values of A_{in}^{n+1} and u_{in}^{n+1} may be calculated from Eqs. (13.25), (13.26), (13.23), and (13.24). Since prescribing the forward component of a variable using a forward-moving characteristic variable is more physically intuitive, this approach will be adopted in this section unless otherwise stated. Prescribing *backward* components of the variables at the outlet could also be achieved in a similar manner.

13.2.4 Solution method: Taylor-Galerkin method

Standard Galerkin discretization of Eq. (13.5) leads to spatial instability in the presence of the dominant convective term. One possible way of achieving better spatial stability is by including the Taylor-Galerkin stabilization. In this method, Eq. (13.5) is used to obtain a semi-discrete form using the Taylor expansion. We rewrite the governing equation as

$$\frac{\partial \Phi}{\partial t} = -\mathbf{Q} - \frac{\partial \mathbf{F}}{\partial x} \quad (13.30)$$

where Φ , \mathbf{F} , and \mathbf{Q} are vectors of primitive variables, fluxes, and source terms, respectively. Differentiating Eq. (13.30) with respect to time and applying the chain rule,

$$\frac{\partial^2 \Phi}{\partial t^2} = -\mathbf{S} \frac{\partial \Phi}{\partial t} - \frac{\partial}{\partial x} \left(\mathbf{A} \frac{\partial \Phi}{\partial t} \right) \quad (13.31)$$

where $\mathbf{A} = \frac{\partial \mathbf{F}}{\partial \Phi}$ and $\mathbf{S} = \frac{\partial \mathbf{Q}}{\partial \Phi}$. Substituting Eq. (13.30) into Eq. (13.31) removes the time derivatives from the right-hand side, i.e.,

$$\frac{\partial^2 \Phi}{\partial t^2} = \mathbf{S} \left(\mathbf{Q} + \frac{\partial \mathbf{F}}{\partial x} \right) + \frac{\partial (\mathbf{A} \mathbf{Q})}{\partial x} + \frac{\partial}{\partial x} \left(\mathbf{A} \frac{\partial \mathbf{F}}{\partial x} \right) \quad (13.32)$$

The Taylor series expansion of Φ^{n+1} in time is

$$\Phi^{n+1} = \Phi^n + \Delta t \frac{\partial \Phi^n}{\partial t} + \frac{1}{2} \Delta t^2 \frac{\partial^2 \Phi^n}{\partial t^2} + O(\Delta t^3) \quad (13.33)$$

where Δt is the time step and n refers to the current time step. Ignoring third- and higher-order terms, and substituting Eqs. (13.30) and (13.31) into Eq. (13.33) yields the final explicit semi-discrete form as

$$\frac{\Phi^{n+1} - \Phi^n}{\Delta t} = -\mathbf{Q}^n - \frac{\partial \mathbf{F}^n}{\partial x} + \frac{1}{2} \Delta t \left[\frac{\partial}{\partial x} \left(\mathbf{A}^n \mathbf{Q}^n + \mathbf{A}^n \frac{\partial \mathbf{F}^n}{\partial x} \right) + \mathbf{S}^n \frac{\partial \mathbf{F}^n}{\partial x} + \mathbf{S}^n \mathbf{Q}^n \right] \quad (13.34)$$

Note that the second bracketed term is the Taylor-Galerkin stabilization term. Now, application of standard Galerkin weighting along with the application of conditional stability on the time step provides a stable solution.

The standard spatial discretization for the finite element method is performed over the global domain Ω which has boundaries denoted by Γ . The Galerkin weighting \mathbf{N}^T along with a linear spatial discretization provides a residual equation which converges to the exact solution when the element size approaches zero, that is,

$$\int_{\Omega} \left(\mathbf{N}^T \frac{\Delta \hat{\Phi}^n}{\Delta t} - \mathbf{N}^T \hat{\mathbf{R}}^n \right) d\Omega = 0 \quad (13.35)$$

where $\hat{\mathbf{R}}$ is the right-hand side of Eq. (13.34). The hat signifies that these variables are approximated by the finite element method, where for any variable Φ , for example, $\hat{\Phi} = N_a \tilde{\Phi}_a + N_b \tilde{\Phi}_b = \mathbf{N} \tilde{\Phi}$ means that the value of $\hat{\Phi}$ anywhere in a given one-dimensional element is interpolated between two discrete nodes (a, b) with nodal values $\tilde{\Phi}_a$ and $\tilde{\Phi}_b$ using the linear interpolation functions $N_a = (x_b - x)/(x_b - x_a)$ and $N_b = (x - x_a)/(x_b - x_a)$. Evaluation of Eq. (13.35) results in the following equation in compact matrix form:

$$\mathbf{M} \Delta \Phi = \Delta t (\mathbf{K} \mathbf{F}^n - \mathbf{L} \mathbf{Q}^n + \mathbf{f}^n) \quad (13.36)$$

where \mathbf{M} is called the mass matrix and \mathbf{K} and \mathbf{L} are coefficient matrices for convection, Taylor-Galerkin, and source terms; each of these are $N_{nodes} \times N_{nodes}$ matrices, where N_{nodes} is the number of nodes in Ω . Also, $\Delta \Phi = \Phi^{n+1} - \Phi^n$ and \mathbf{f} contains boundary fluxes and boundary conditions. The element matrices for a linear element inside the domain are given below.

The element mass matrix is

$$\mathbf{M}_e = \frac{l_e}{6} \begin{bmatrix} 2 & 1 \\ 1 & 2 \end{bmatrix} \quad (13.37)$$

where l_e is the element length. The lumped mass matrix

$$\mathbf{M}_e^L = \frac{l_e}{2} \begin{bmatrix} 1 & 0 \\ 0 & 1 \end{bmatrix} \quad (13.38)$$

may also be used.

The convection term is integrated by parts over an element as

$$-\int_{\Omega_e} \mathbf{N}^T \frac{\partial \hat{\mathbf{F}}^n}{\partial x} d\Omega_e = \int_{\Omega_e} \frac{\partial \mathbf{N}^T}{\partial x} \hat{\mathbf{F}}^n d\Omega_e - \int_{\Gamma_e} \mathbf{N}^T \hat{\mathbf{F}}^n \mathbf{n} d\Gamma_e \quad (13.39)$$

The last term in the above equation is active only for elements at the boundaries. Similarly the Taylor-Galerkin term is integrated by parts, giving

$$\int_{\Omega_e} \mathbf{N}^T \frac{\partial}{\partial x} \left(\mathbf{A}^n \frac{\partial \hat{\mathbf{F}}^n}{\partial x} \right) d\Omega_e = - \int_{\Omega_e} \frac{\partial \mathbf{N}^T}{\partial x} \mathbf{A}^n \frac{\partial \hat{\mathbf{F}}^n}{\partial x} d\Omega_e + \int_{\Gamma_e} \mathbf{N}^T \bar{\mathbf{A}}^n \frac{\partial \hat{\mathbf{F}}^n}{\partial x} d\Gamma_e \quad (13.40)$$

Evaluation of Eqs. (13.39) and (13.40) provides the coefficient matrix \mathbf{K}_e for the inviscid case. If a source term is also included, the full matrix is found to be

$$\mathbf{K}_e = \left(\frac{1}{2} - \frac{\Delta t}{4} \bar{\mathbf{S}}^n \right) \begin{bmatrix} -1 & -1 \\ 1 & 1 \end{bmatrix} - \frac{\Delta t}{2l_e} \bar{\mathbf{A}}^n \begin{bmatrix} 1 & -1 \\ -1 & 1 \end{bmatrix} \quad (13.41)$$

where $\bar{\mathbf{A}}$ and $\bar{\mathbf{S}}$ are the average values over the element subdomain. This is an alternative to numerical integration, which is equivalent when using linear shape functions. Similarly the coefficient matrix \mathbf{L}_e is found to be

$$\mathbf{L}_e = \left(\frac{l_e}{6} - \frac{\Delta t l_e}{12} \bar{\mathbf{S}}^n \right) \begin{bmatrix} 2 & 1 \\ 1 & 2 \end{bmatrix} + \frac{\Delta t}{4} \bar{\mathbf{A}}^n \begin{bmatrix} -1 & -1 \\ 1 & 1 \end{bmatrix} \quad (13.42)$$

For the flux term, the contributions from the Taylor-Galerkin terms are not included since these arise from the numerical technique and will be zero on the boundaries. Thus, for the elements at the boundaries (if applicable),

$$\mathbf{f}_e = \begin{Bmatrix} \tilde{\mathbf{F}}_a^n \\ -\tilde{\mathbf{F}}_b^n \end{Bmatrix} \quad (13.43)$$

The system can then be implemented by assembling and substituting Eqs. (13.37) and (13.41)–(13.43) into Eq. (13.36) and adding the boundary conditions (see Section 13.2.3). Assuming that $u \ll c$, it can be shown that the stability condition for the characteristic system in Section 13.2.2 is [15, 20]

$$\Delta t_{max} \approx \frac{\Delta x_{min}}{c_{max}} \quad (13.44)$$

although for a nonzero source term (\mathbf{Q}) this will be slightly lower. Experience has shown that Eq. (13.44) with a small safety factor (i.e., using $\Delta t = 0.9 \Delta t_{max}$) works well for the coupled system [Eq. (13.5)].

13.2.5 Some results

Only two simple examples are provided in this subsection. The practical application of one-dimensional fluid–structure interaction is discussed for a human arterial system in Chapter 14.

Example 13.2. Pulse propagation in a single uniform vessel

Figure 13.3 shows the propagation of a Gaussian pressure pulse in a single vessel with uniform initial area $A_0 = 1.0 \text{ cm}^2$ and $\beta = 229674 \text{ dynes/cm}^3$. Note that the width of this pulse (0.03 s) is very short. In Fig. 13.3a it can be seen that for a relatively low amplitude pulse (10^3 dynes/cm^2) and inviscid conditions ($\mu = 0$), the pulse propagates with little distortion. Introducing viscous effects ($\mu = 0.035 \text{ P}$) leads to the gradual decay of the pulse as energy is lost due to viscous friction. For a larger amplitude pressure pulse (10^4 dynes/cm^2), there is significant distortion

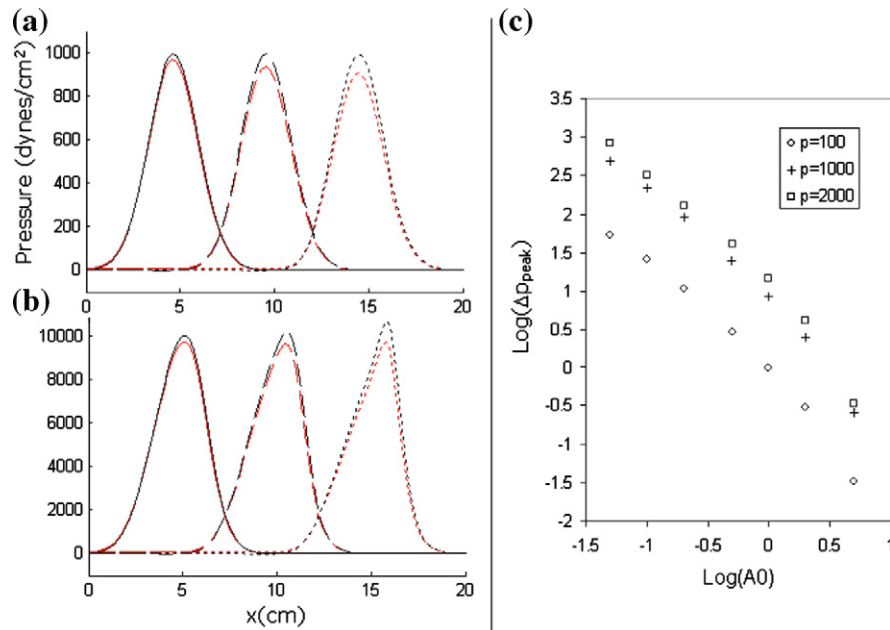


FIGURE 13.3

Propagation of a short (a) small and (b) large amplitude pressure pulse in a single vessel for inviscid (higher amplitude) and viscous flow (lower amplitude), with snapshots taken at $t = 0.03 \text{ s}$ (solid lines), 0.045 s (dashed lines), and 0.06 s (dotted lines). For small amplitude pulses, propagation is approximately linear and the pulse does not distort. For large amplitude pulses, nonlinear effects distort the pulse and lead to shock formation. (c) Log-log plot of pressure peak decay Δp_{peak} over 20 cm due to viscosity with different vessel cross-sectional areas (A_0) and for initial pulse amplitudes of 100, 1000, and 2000 dynes/cm².

(Fig. 13.3b) due to both viscous effects and nonlinear effects. As discussed in Section 13.2.1, the pressure peak propagates faster than its foot, which is predicted from Eq. (13.10). The result is that, given enough time, the high pressure peak will catch up with the low pressure foot, thus forming a shock. Since the foot propagates at c_0 and from Eq. (13.13) the peak propagates at $u_{peak} + c_{peak}$, the approximate distance at which a shock will form is 182 cm for the pulse in Fig. 13.3a and 18.4 cm for pulse in Fig. 13.3b. Fig. 13.3c shows that the attenuation of the pressure pulse due to viscosity is dependent on vessel cross-sectional area. As predicted from Eq. (13.3), the decay of the pressure peak (Δp_{peak}) is greater for small vessels or for large amplitude pulses.

Example 13.3. Discontinuities

Figure 13.4a shows the effect of a sudden decrease in A_0 . Since this corresponds to an increase in characteristic impedance, there is a partial positive reflection. The linear reflection coefficient may be calculated using the characteristic impedance or admittance. Defining the characteristic impedance as

$$Z_0 = \frac{1}{Y_0} = \frac{\rho c_0}{A_0} \quad (13.45)$$

where Y_0 is the characteristic admittance, the reflection coefficient may now be computed using

$$R = \frac{Y_{0p} - \sum_{i=1}^n Y_{0i}}{Y_{0p} + \sum_{i=1}^n Y_{0i}} \quad (13.46)$$

where p indicates the starting vessel before the change in area, properties, or topology and n is the number of branching daughter vessels. This is only applicable when pipe or arterial networks (see Chapter 14) are considered.

The reflection coefficient calculated for the problem shown in Fig. 13.4a is $R = 0.25$, while the transmission coefficient (from transmission line theory, $T = 1 + R$) is $T = 1.25$. The amplitudes of the reflected and transmitted waves approximately

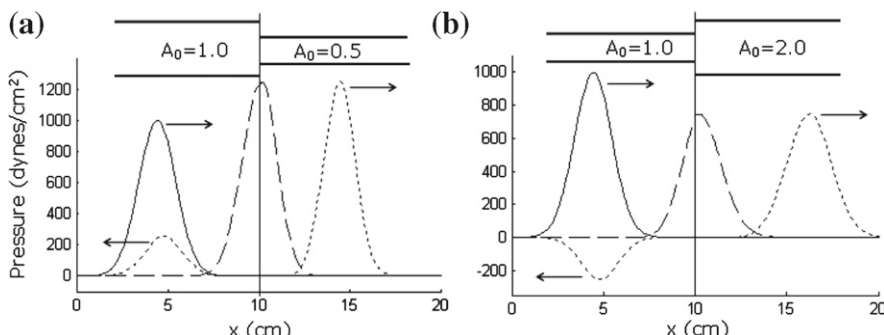
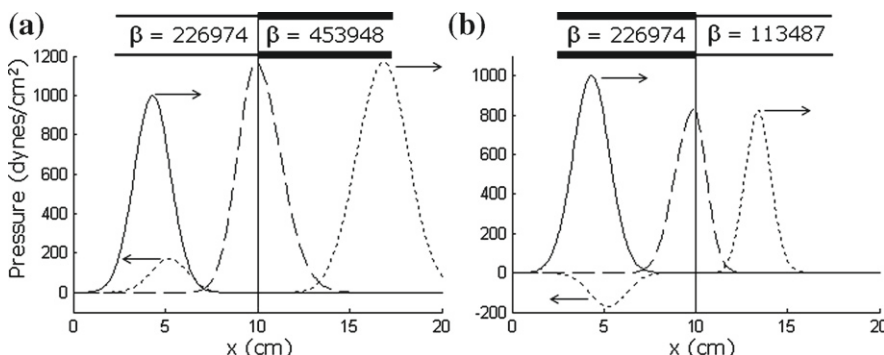


FIGURE 13.4

Reflected and transmitted waves in a single vessel due to (a) a step decrease and (b) a step increase in A_0 .

**FIGURE 13.5**

Reflected and transmitted waves in a single vessel due to (a) a step increase and (b) a step decrease in β with constant A_0 .

represent these values, and while the concept of reflection coefficient is not strictly valid for the nonlinear system, small pulses do approach the linear behavior. Conversely, Fig. 13.4b demonstrates that there is a partial negative reflection when A_0 is increased (with $R = -0.25$ and $T = 0.75$).

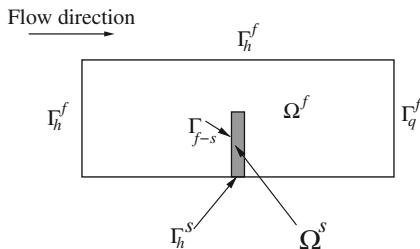
Another possible type of discontinuity is in β . Assuming A_0 is constant, this reflects a sudden change in material properties (Young's modulus or wall thickness) of the vessel [see Eq. (13.7)]. Figure 13.5 shows reflected and transmitted waves for a single reflection site where β doubles or halves. Note that wave speed increases or decreases along with β [Eq. (13.10)] as shown by changes in the width of the pulse.

13.3 Multidimensional problems

In the one-dimensional problem discussed in the previous section, the mesh points are fixed and the material is allowed to pass through the fixed mesh. This Eulerian approach simplified the presentation dramatically. However, in multidimensions the issue is more complicated due to an explicit interface which was absent for one-dimensional problems. Since this interface in multidimensions is not fixed, the problem for fluid dynamics becomes a moving boundary problem. In addition the interface forces should be exchanged between the two media in a sensible way to couple the two domains. In the following sections we use an incompressible fluid as a model problem to describe the fluid–structure interaction. The methods presented are equally valid for compressible flows.

13.3.1 Equations and discretization

With reference to Fig. 13.6, the incompressible flow equations governing the flow inside the fluid domain may be written in nonconservation form and in arbitrary

**FIGURE 13.6**

Schematic of a fluid–structure interaction problem. Superscripts f and s respectively indicate the fluid and solid and subscripts h , q , and $f - s$ respectively indicate a Dirichlet, Neumann, and fluid–structure interface boundary.

Lagrangian and Eulerian (ALE) frame as follows (refer to [Chapter 6](#)):

$$\rho_f \left(\frac{\partial u_i}{\partial x_i} + (u_j - u_j^g) \frac{\partial u_i}{\partial x_j} \right) = - \frac{\partial p}{\partial x_i} + \frac{\partial \tau_{ij}}{\partial x_j} \quad (13.47)$$

is the momentum equation with the deviatoric stresses τ_{ij} expressed as

$$\tau_{ij} = \mu \left(\frac{\partial u_i}{\partial x_j} + \frac{\partial u_j}{\partial x_i} \right) \quad (13.48)$$

and the conservation of mass equation in the domain is given as

$$\frac{\partial u_i}{\partial x_i} = 0 \quad (13.49)$$

The flow problem is completed using the following boundary conditions:

$$\begin{aligned} u_i &= \bar{u}_i \quad \text{on } \Gamma_h^f \\ t_i^f &= \tau_{ij} n_j - p n_i = \bar{t}_i^f \quad \text{on } \Gamma_q^f \\ u_i &= \frac{dd_i}{dt} = \dot{d}_i \quad \text{on } \Gamma_{f-s} \end{aligned} \quad (13.50)$$

where t_i are the components of traction, quantities with the overbar are assumed to be known, and d_i are the components of displacement at the fluid–solid interface. This condition applied at the interface is referred to as the kinematic condition.

For simplicity, in the treatment of the solid body we consider only the small deformation form described in [Ref. \[26\]](#). This includes all the salient features of the fluid–structure interaction problem without the need to treat the more complex finite deformation effects. Accordingly, the momentum equation for the solid may be written as

$$\rho_s \frac{\partial^2 d_i}{\partial t^2} - \frac{\partial \sigma_{ij}}{\partial x_j} = f_i \quad (13.51a)$$

in which the stress σ_{ij} for a linear isotropic elastic material is related to strains as

$$\sigma_{ij} = \lambda\delta_{ij}\frac{\partial d_k}{\partial x_k} + \mu\left(\frac{\partial d_i}{\partial x_j} + \frac{\partial d_j}{\partial x_i}\right) \quad (13.51b)$$

where λ, μ are the Lamè elastic constants, δ_{ij} is the Kronecker delta, ρ_s is the density of the solid, and f_i are the body force components. The boundary conditions for the solid domain may now be written as

$$\begin{aligned} d_i &= \bar{d}_i \quad \text{on } \Gamma_h^s \\ t_i^s &= \sigma_{ij}n_j = \bar{t}_i^s \quad \text{on } \Gamma_q^s \\ (\sigma_{ij}n_j)^s - (\tau_{ij}n_j - pn_i)^f &= 0 \quad \text{or} \quad t_i^s + t_i^f = 0 \quad \text{on } \Gamma_{f-s} \end{aligned} \quad (13.52)$$

The condition imposed at the interface in Eq. (13.52) is often referred to as the dynamic condition. Equations (13.47)–(13.52) form the governing equation system for fluid–structure interaction.

13.3.1.1 Finite element formulation of fluid equations

The finite element algorithms and spatial discretization are extensively discussed in Chapters 2 and 3. Although any of the standard fluid dynamics algorithm can be used, we use the CBS scheme as the basis to explain the monolithic form [27–30]. In order to establish this, we use Section 3.6 of Chapter 3. Assuming that the flow is unsteady, Eq. (3.51) (Step 1 of the CBS scheme) may be written for a generic incompressible flow with implicit time discretization as

$$\frac{\Delta\tilde{\mathbf{U}}^*}{\Delta t} = -\mathbf{M}_u^{-1} \left[(\mathbf{C}_u\tilde{\mathbf{U}} + \mathbf{K}_\tau\tilde{\mathbf{u}} - \mathbf{f}) - \Delta t(\mathbf{K}_u\tilde{\mathbf{U}} + \mathbf{f}_s) \right]^{n+1} \quad (13.53)$$

Similarly Steps 2 [Eq. (3.56)] and 3 [Eq. (3.59)] are written as (with $\theta_1 = 1$ and $\theta_2 = 1$)

$$(\Delta t\mathbf{H})\tilde{\mathbf{p}}^{n+1} = [\mathbf{G}\tilde{\mathbf{U}}^* - \mathbf{f}_p] \quad (13.54)$$

and

$$\frac{\Delta\mathbf{U}^{**}}{\Delta t} = \frac{\Delta\tilde{\mathbf{U}} - \Delta\tilde{\mathbf{U}}^*}{\Delta t} = -\mathbf{M}_u^{-1} \left[\mathbf{G}^T(\tilde{\mathbf{p}}^{n+1}) + \frac{\Delta t}{2}\mathbf{P}\tilde{\mathbf{p}}^{n+1} \right] \quad (13.55)$$

Although various other time integration schemes are possible, for the sake of simplicity we use $\Delta\mathbf{U}^* = \mathbf{U}^* - \mathbf{U}^n$ and $\Delta\mathbf{U} = \mathbf{U}^{n+1} - \mathbf{U}^n$. We get the following equation by substituting Eq. (13.55) into Eq. (13.53):

$$\begin{aligned} \mathbf{M}_u\tilde{\mathbf{U}}^{n+1} - \mathbf{M}_u\tilde{\mathbf{U}}^n + \left[(\mathbf{C}_u\tilde{\mathbf{U}} + \mathbf{K}_\tau\tilde{\mathbf{u}} - \mathbf{f}) - \Delta t(\mathbf{K}_u\tilde{\mathbf{U}} + \mathbf{f}_s) + \mathbf{G}^T(\tilde{\mathbf{p}}^{n+1}) \right. \\ \left. + \frac{\Delta t}{2}\mathbf{P}\tilde{\mathbf{p}}^{n+1} \right]^{n+1} = 0 \end{aligned} \quad (13.56)$$

Similarly, substituting Eq. (13.55) into (13.54) gives

$$\mathbf{G}\tilde{\mathbf{U}}^{n+1} + \Delta t\mathbf{GM}_u^{-1} \left[\mathbf{G}^T(\tilde{\mathbf{p}}^{n+1}) + \frac{\Delta t}{2}\mathbf{P}\tilde{\mathbf{p}}^{n+1} \right] - \Delta t\mathbf{H}\tilde{\mathbf{p}}^{n+1} - \tilde{\mathbf{f}}_p = \mathbf{0} \quad (13.57)$$

Equations (13.56) and (13.57) may be written in matrix form as

$$\begin{bmatrix} \mathbf{M}_u + \mathbf{K}_\tau/\rho + \mathbf{C}_u - \Delta t\mathbf{K}_u & \mathbf{G}^T + \frac{\Delta t}{2}\mathbf{P} \\ \mathbf{G} & \Delta t[\mathbf{GM}_u^{-1}(\mathbf{G}^T + \frac{\Delta t}{2}\mathbf{P}) - \mathbf{H}] \end{bmatrix} \begin{Bmatrix} \tilde{\mathbf{U}} \\ \tilde{\mathbf{p}} \end{Bmatrix}^{n+1} = \begin{Bmatrix} \mathbf{f}_1 \\ \mathbf{f}_2 \end{Bmatrix} \quad (13.58)$$

Here \mathbf{f}_1 and \mathbf{f}_2 terms are the forcing terms. In the context of fluid–structure interaction, the interface dynamic condition should be included within the formulation. Thus the interface condition in Eq. (13.50) may be integrated along the interface as a Lagrange multiplier constraint and gives a functional term

$$\tilde{\lambda}^T \int_{\Gamma_{f-s}} \mathbf{N}_\lambda^T (\mathbf{u} - \dot{\mathbf{d}})^{n+1} d\Gamma_{f-s} = 0 \quad (13.59)$$

in which λ is discretized along the interface as

$$\lambda = \mathbf{N}_\lambda \tilde{\lambda} \quad (13.60)$$

Assuming that $\mathbf{d} = \mathbf{N}_d \tilde{\mathbf{d}}$ and with $\mathbf{u} = \mathbf{N}_u \tilde{\mathbf{u}}$, the above equation may be written for the interface nodes as

$$\tilde{\lambda}^T \left(\mathbf{M}_{\lambda u}^\Gamma \tilde{\mathbf{u}}^{n+1} - \mathbf{M}_{\lambda d}^\Gamma \tilde{\mathbf{d}}^{n+1} \right) = 0 \quad (13.61)$$

where

$$\begin{aligned} \mathbf{M}_{\lambda u}^\Gamma &= \int_{\Gamma_{f-s}} \mathbf{N}_\lambda^T \mathbf{N}_u d\Gamma_{f-s} \\ \mathbf{M}_{\lambda d}^\Gamma &= \int_{\Gamma_{f-s}} \mathbf{N}_\lambda^T \mathbf{N}_d d\Gamma_{f-s} \end{aligned} \quad (13.62)$$

In the case of fluid–structure interaction problems, the variation of (13.59) with respect to the fluid velocity should be added to (13.56). To put together the full system of simultaneous equations for a fluid–structure system, we need to discretize (13.51a) along with the interface condition given in (13.52).

13.3.1.2 Finite element formulation of solid dynamics

Following Chapter 12 of Ref. [26], we can write the semi-discrete form of the equation governing the solid dynamics as

$$\mathbf{M}_d \tilde{\ddot{\mathbf{d}}} + \mathbf{C}_d \tilde{\dot{\mathbf{d}}} + \mathbf{K}_d \tilde{\mathbf{d}} + \mathbf{f}_d = 0 \quad (13.63)$$

These may be discretized in time using several alternative methods. For one-step methods the form of (13.63) becomes

$$(c_3 \mathbf{M}_d + c_2 \mathbf{C}_d + c_1 \mathbf{K}_d) \tilde{\mathbf{d}}^{n+1} + \mathbf{f}_d^{n+1} = \mathbf{0} \quad (13.64)$$

For example in the Newmark procedure [26,31,32], the solution is advanced using

$$\begin{aligned}\tilde{\mathbf{d}}^{n+1} &= \tilde{\mathbf{d}}^n + \Delta t \dot{\tilde{\mathbf{d}}}^n + \left(\frac{1}{2} - \beta\right) \Delta t^2 \ddot{\tilde{\mathbf{d}}}^n + \beta \Delta t^2 \ddot{\tilde{\mathbf{d}}}^{n+1} \\ \dot{\tilde{\mathbf{d}}}^{n+1} &= \dot{\tilde{\mathbf{d}}}^n + (1 - \gamma) \Delta t \ddot{\tilde{\mathbf{d}}}^n + \gamma \Delta t \ddot{\tilde{\mathbf{d}}}^{n+1}\end{aligned}$$

where β and γ are parameters controlling accuracy and stability and the c_i parameters are given by

$$c_1 = 1, \quad c_2 = \frac{\gamma}{\beta \Delta t} \quad \text{and} \quad c_3 = \frac{1}{\beta \Delta t^2}$$

Discretization of the dynamic boundary condition at the interface given in (13.52) may be performed similar to (13.59). However, one can show that the Lagrange multiplier in (13.59) is the fluid traction (see, for example, Chapter 3 of Ref. [26]) and, thus, may be used also on the solid interface to enforce nodally the dynamic boundary condition.

13.3.1.3 Monolithic fluid–structure interaction formulation

The monolithic form of a fluid–structure interaction system may now put together using Eqs. (13.58), (13.61), and (13.64) as

$$\begin{bmatrix} \mathbf{K}_{11} & \mathbf{K}_{12} & \mathbf{0} & \mathbf{K}_{14} \\ \mathbf{K}_{21} & \mathbf{K}_{22} & \mathbf{0} & \mathbf{0} \\ \mathbf{0} & \mathbf{0} & \mathbf{K}_{33} & \mathbf{K}_{34} \\ \mathbf{K}_{41} & \mathbf{0} & \mathbf{K}_{43} & \mathbf{0} \end{bmatrix} \begin{Bmatrix} \tilde{\mathbf{U}} \\ \tilde{\mathbf{p}} \\ \tilde{\mathbf{d}} \\ \tilde{\lambda} \end{Bmatrix}^{n+1} = \begin{Bmatrix} \mathbf{f}_1 \\ \mathbf{f}_2 \\ \mathbf{f}_3 \\ \mathbf{f}_4 \end{Bmatrix} \quad (13.65)$$

where the nonzero entries of the above equation may be written as

$$\begin{aligned}\mathbf{K}_{11} &= \mathbf{M}_u + \frac{1}{\rho} \mathbf{K}_\tau + \mathbf{C}_u - \Delta t \mathbf{K}_u \\ \mathbf{K}_{12} &= \mathbf{G}^T + \frac{\Delta t}{2} \mathbf{P} \\ \mathbf{K}_{21} &= \mathbf{G} \\ \mathbf{K}_{22} &= \Delta t \left[\mathbf{G} \mathbf{M}_u^{-1} \left(\mathbf{G}^T + \frac{\Delta t}{2} \mathbf{P} \right) - \mathbf{H} \right] \\ \mathbf{K}_{33} &= c_3 \mathbf{M}_d + c_2 \mathbf{C}_d + c_1 \mathbf{K}_d \\ \mathbf{K}_{14} &= \mathbf{M}_{\lambda u}^{\Gamma, T} \\ \mathbf{K}_{34} &= \mathbf{M}_{\lambda d}^{\Gamma, T} \\ \mathbf{K}_{41} &= \mathbf{M}_{\lambda u}^\Gamma \\ \mathbf{K}_{43} &= \mathbf{K}_{\lambda d}^\Gamma\end{aligned} \quad (13.66)$$

It is important to note that various stabilization components including the pressure stabilization part \mathbf{K}_{22} in the above equation may be replaced with different methods

of stabilization to obtain different stabilized formulations. The monolithic form, Eq. (13.65), may also be written in a single residual form as

$$\mathbf{R}(\mathbf{W}) = 0 \quad (13.67)$$

where \mathbf{R} is the sum of all residuals of Eq. (13.65) and \mathbf{W} are the unknowns of Eq. (13.65). In theory Eq. (13.67) can be solved using a Newton method to obtain a solution. The solution procedure may take the following form:

- Start with an initial guess for \mathbf{W} equal to \mathbf{W}^n at the n th time iteration.
- Using the initial guess calculate the residual at the n th time iteration as $\mathbf{R}(\mathbf{W}^n)$ and the Jacobian (or tangent) matrix $\mathbf{A} = \frac{\partial \mathbf{R}}{\partial \mathbf{W}}(\mathbf{W}^n)$
- Solve for the correction of $\Delta \mathbf{W}$ by solving the set of simultaneous equations $\mathbf{A} \Delta \mathbf{W} = \mathbf{R}(\mathbf{W}^n)$.
- Update the solution using $\mathbf{W}^{n+1} = \mathbf{W}^n + \gamma \Delta \mathbf{W}$, where γ is an optimal parameter that determines the step size. The process of determining this parameter is referred to as line search.

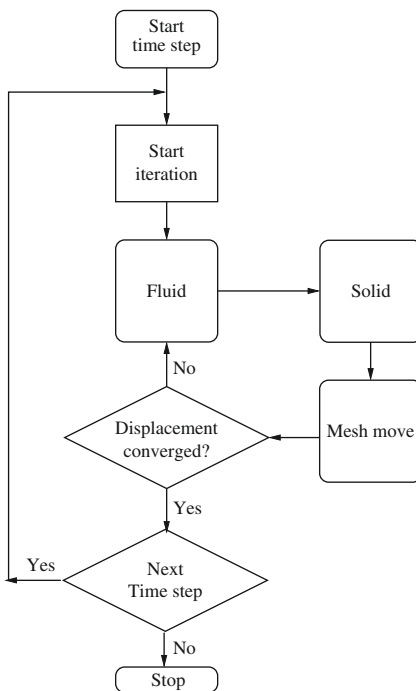
For more details on approximate Newton methods and the line search algorithm, readers are referred to Chapter 3 of Ref. [32].

13.3.2 Segregated approach

Although the monolithic approach discussed above is a natural and strongly coupled way of solving the FSI problems, it poses several difficulties in practice. In addition to convergence issues associated with the monolithic form, the implementation issues can also be cumbersome. The implementation difficulties are often posed by the fact that fluid and solid solvers in general are independently developed and tested. Thus, it is more practical to implement a segregated approach that combines the established fluid and solid algorithms. In such segregated approaches, the coupling is carried out through the dynamic and kinematic conditions at the interface. This provides us with two alternatives. The first one is the so-called loosely coupled approach in which the interface conditions may or may not be fully satisfied. Such loosely coupled approaches are sometime applied in aeroelasticity calculations. The second approach is the so-called strongly coupled approach in which the interface conditions are more accurately satisfied. The loosely coupled approach can be unstable for many applications, especially applications in which the solid and fluid density values are close [27]. The strong coupling may be achieved through different methods. Figure 13.7 shows a typical coupling routine. As seen, this provides a large number of different options to couple the fluid and structure [28–30, 33–39].

When the fluid and solid solvers are separately available (see Fig. 13.7), the coupling between them may be carried out via Dirichlet–Neumann coupling. To understand such a coupling let us assume that the discrete form of fluid equation, Eq. (13.58), and fully discrete form of solid equation, Eq. (13.64), are

$$\mathbf{K}^f \mathbf{u}^f = \mathbf{F}^f \quad (13.68)$$

**FIGURE 13.7**

Strong coupling of fluid and structure solvers using a staggered approach.

and

$$\mathbf{K}^s \mathbf{d}^s = \mathbf{F}^s \quad (13.69)$$

respectively. To couple the two equations strongly, start the iteration with the initial solutions of solid and fluid variables and solve the fluid equation (13.68) to determine the new fluid variables and fluid forces at the interface. This is followed by solution to Eq. (13.69) to determine the displacements within the solid domain, calculation of fluid velocity at the interface from the interface displacements and determination of new mesh position. Now, check whether or not interface displacements converged. If not, using the interface velocity values solve the flow equation, Eq. (13.68). Continue this iteration between fluid, solid, and mesh until interface displacements are converged. The interface displacements are often converged quickly using relaxation methods.

13.3.3 Mesh moving procedures

In a majority of fluid–structure interaction problems the mesh of both solid and fluid domains is altered in one way or another. Often the solid domain is treated using a Lagrangian form of mesh movement and the fluid domain is subjected to the so-called

arbitrary Lagrangian-Eulerian (ALE) method. In an ALE formulation, the mesh is allowed to move independently of the material points. This independent motion of the mesh to maintain mesh quality in general is not necessarily always straightforward. The reason is that sophisticated methods of mesh motion are often computationally expensive. The simple methods on the other hand are not very useful for calculating large deformation of meshes. For really complex problems of practical interest, preserving the topology of the mesh and avoiding remeshing may not be possible. Thus, in addition to remeshing algorithms, a robust interpolation method to transfer variables from the original mesh to new mesh is also required. This approach is widely adopted in adaptive remeshing (see Chapters 4 and 5).

Since it is very common to use topology-preserving mesh moving algorithms in fluid–structure interaction applications, we provide a brief overview on some of the mesh moving algorithms. In a simple problem of fluid–structure interaction such as membrane–fluid interaction, often a one-dimensional membrane movement is assumed (no stretching). In such problems, assuming linear distribution of membrane movement in the direction of displacement is sufficient. For more complex problems and unstructured meshes, a horde of different methods are available. They include simple methods such as a spring analogy and Delaunay-based mapping to using solid mechanics equations to find out the mesh displacement. Some of them are briefly presented below.

13.3.3.1 Spring analogy

In this method the edges connecting two nodes are assumed to be connected by a spring that maintains equilibrium [40,41]. To find the position of a node a , the total force between node a and nodes connected to a is equal to zero to maintain equilibrium, i.e.,

$$\sum_{b=1}^{n_E} \mathbf{F}_{ab} = 0 \quad (13.70)$$

where n_E is the number of edges connected to node a . This may be written for a patch of elements as

$$\sum_{b=1}^{n_E} \mathbf{t}_{ab}^T k_{ab} \mathbf{t}_{ab} (\mathbf{u}_{ab}) = 0 \quad (13.71)$$

where k_{ab} is the spring constant connecting nodes a and b , which is often taken equal to the inverse of the square of the edge length ($= 1/l_{ab}^2$), \mathbf{t}_{ab} is the edge vector of edge ab given in two dimensions as

$$\begin{aligned} \mathbf{t}_{ab} &= [t_{a1} \ t_{a2} \ t_{b1} \ t_{b2}]^T = \left[\frac{\partial l_{ab}}{\partial x_{a1}} \ \frac{\partial l_{ab}}{\partial x_{a2}} \ \frac{\partial l_{ab}}{\partial x_{b1}} \ \frac{\partial l_{ab}}{\partial x_{b2}} \right]^T \\ &= [-\cos \alpha \ -\sin \alpha \ \cos \alpha \ \sin \alpha]^T \end{aligned} \quad (13.72)$$

where subscripts 1 and 2 indicate the two Cartesian coordinate directions, and \mathbf{u}_{ab} are the displacements and may be written for an edge as

$$\mathbf{u}_{ab} = [u_{a1} \ u_{a2} \ u_{b1} \ u_{b2}]^T \quad (13.73)$$

Although Eq. (13.71) is valid for a patch, the common practice is to solve the system for the whole mesh so that the boundary conditions can be easily applied on global boundaries. It is common to use a Gauss-Seidel method to solve a global equilibrium equation that puts all the patches together in the form

$$\mathbf{K}\mathbf{u} = \mathbf{0} \quad (13.74)$$

with known values of displacements along the boundaries. Here $\mathbf{K} = \mathbf{t}^T \mathbf{k} \mathbf{t}$. The above method of spring analogy is a good method for small displacements and fairly uniform meshes. However, the linear spring analogy discussed above has no control over the angle between edges. For keeping the angles between edges under control, the method needs to be modified by incorporating the torsional effects as well to the total force. The torsional force may be written for a node a as (assuming a triangle abc)

$$\mathbf{F}_{abc}^t = \mathbf{K}_{abc} \mathbf{u}_{abc} = 0 \quad (13.75)$$

The element stiffness matrix \mathbf{K}_{abc} is now modified to incorporate the effects of torsion in terms of the angle between edges. This may be written as [following Eq. (13.71)]

$$\mathbf{K}_{abc} = \mathbf{R}_{abc}^T C_{abc} \mathbf{R}_{abc} \quad (13.76)$$

where \mathbf{R}_{abc} is the rotation matrix and C_{abc} is the spring stiffness. The rotation matrix may be written as

$$\mathbf{R}_{abc} = \begin{bmatrix} \frac{\partial \theta_a}{\partial \mathbf{x}_a} & \frac{\partial \theta_a}{\partial \mathbf{x}_b} & \frac{\partial \theta_a}{\partial \mathbf{x}_c} \end{bmatrix}^T \quad (13.77)$$

and the spring stiffness is given as

$$C_{abc} = \left(\frac{1}{1 - \cos \theta_a} \right) \left(\frac{1}{1 + \cos \theta_a} \right) = \left(\frac{1}{\sin^2 \theta_a} \right) \quad (13.78)$$

where θ_a is the angle between edges ab and ac . The stiffness is expressed in terms of $\sin \theta^2$ to restrict θ from reaching a value close to either 0° or 180° . What remains to be done is to compute the rotation matrix \mathbf{R}_{abc} . To compute this matrix for a triangle abc , we can write

$$\sin \theta_a = \frac{2A}{l_{ab} l_{ac}} \quad (13.79)$$

where A is the area of the triangle. Differentiating equation (13.79) with respect to any coordinate direction gives the following relation:

$$\frac{\partial \sin \theta_a}{\partial \mathbf{x}} = \cos \theta_a \frac{\partial \theta_a}{\partial \mathbf{x}} = \sin \theta \left[\frac{1}{A} \frac{\partial A}{\partial \mathbf{x}} - \frac{1}{l_{ab}} \frac{\partial l_{ab}}{\partial \mathbf{x}} - \frac{1}{l_{ac}} \frac{\partial l_{ac}}{\partial \mathbf{x}} \right] \quad (13.80)$$

Computing $\frac{\partial \theta_a}{\partial \mathbf{x}}$ using the above equation, the rotation matrix can be easily computed. The solution to the equilibrium equation can now be carried out using any standard procedure. It is also possible to sum the lineal force and torsional force together when applying the spring analogy to a problem in two or three dimensions.

13.3.3.2 Mapping using background mesh (Delaunay graph method)

This method follows a one-to-one mapping between the nodes and a background element [42]. The method starts with generation of a background mesh followed by allocation of the nodes of a finite element mesh to the background elements. A finite element node should only belong to one background element. As the structure moves within a fluid, the background mesh is moved with the structural movement. This is followed by the mapping of the nodes to the new position of the background element using simple finite element interpolation using barycentric (area) coordinates. Thus, the new position of a point within a background mesh may be written in terms of area coordinates as

$$\mathbf{x}_a = \sum_{b=1}^3 L_b \mathbf{x}_b \quad (13.81)$$

where L_b is the barycentric (area) coordinate of the background mesh calculated based on the original position of the node and the new position of the background element. For linear triangular elements this can simply be replaced with the shape functions. Although simple and robust for a problem with fairly uniform movement, certain difficulties are faced by the method if element nodes are shared between two background elements. For instance if two adjacent background elements are moving at much different rates, the element shared by these two background elements may be stretched or compressed excessively to create entanglement. Since the background mesh is often generated using the initial Delaunay triangulation, this method is sometimes referred as the Delaunay graph method.

13.3.3.3 Solution to partial differential equations

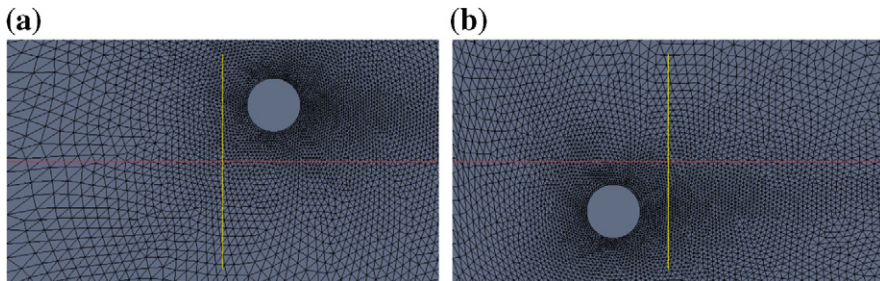
Though expensive, moving a mesh by solving an equilibrium equation appears to be robust [39]. The most general form of equation used in moving a mesh is an equation of elasticity. This is logical with displacement boundary conditions prescribed on the boundaries of a domain. The discrete form of the elasticity equation may be written as

$$\int_{\Omega_t} \mathbf{B}^T \mathbf{D} \mathbf{B} (\tilde{\mathbf{u}}^{n+1} - \tilde{\mathbf{u}}^n) d\Omega = \mathbf{F} \quad (13.82)$$

where \mathbf{B} is the matrix that contains the derivatives of shape functions (Chapter 3), \mathbf{D} is the elasticity matrix, $\tilde{\mathbf{u}}$ is the vector of displacements within the fluid domain, and \mathbf{F} contains the prescribed displacements on the solid surface. The matrix \mathbf{D} may be simplified to $\frac{1}{A_e} \mathbf{I}_m$ with A_e being the area of elements and \mathbf{I}_m is given for 3D as

$$\mathbf{I}_m = \begin{bmatrix} 1 & & \\ & 1 & \\ & & 1 \\ & 0 & \\ & 0 & \\ & 0 & \end{bmatrix}.$$

This simplification reduces Eq. (13.82) to the vector form of a Laplace-type equation. This may be employed to move a fluid mesh as shown in Fig. 13.8. This figure shows the movement of a rigid cylinder within a fluid domain. The

**FIGURE 13.8**

Artificially moved mesh surrounding a circular cylinder by solving the Laplace equation. (a) Cylinder moved to a position above and (b) below the original position.

cylinder here is artificially displaced to check the validity of the mesh moving method. As seen extreme movement of the mesh is possible for simple problems of this type. However, when the problem is complex and displacement is large, remeshing may be required to avoid mesh entanglement. Due to prohibitive cost involved with the remeshing, preserving topology is preferred in fluid–structure interaction problems.

13.3.3.4 Other methods of mesh moving

One of the very simple methods used for small displacements is the method of Laplacian smoothing. In this method the coordinate of a node is taken equal to the average of the coordinates surrounding that node, i.e.,

$$\mathbf{x}_a = \frac{1}{n_c} \sum_{b=1}^{n_c} \mathbf{x}_b \quad (13.83)$$

where n_c is the number of nodes connected to node a . This method works well if the displacement is much smaller than the element size. Often this method combined with a more general method provides better quality elements (see Fig. 13.9). On its own this method is unsuitable for boundary layer meshes and very fine meshes close to solid surfaces.

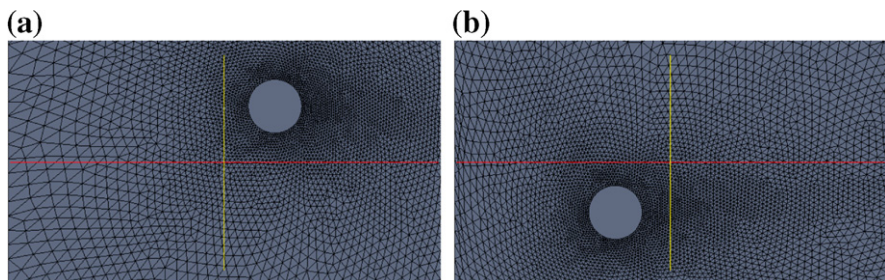
Another method for improving mesh quality used by researchers is minimization of the ratio between circumscribed and inscribed radii of a triangle (spheres in three dimensions), i.e., minimizing [33]

$$R_m = \sum_{ie=1}^{n_e} \left(\frac{r_{out}}{r_{in}} \right) \quad (13.84)$$

where n_e is the total number of elements in a mesh. Minimization may be carried out by differentiating R_m with respect to the nodal coordinates of the mesh, i.e.,

$$\frac{\partial R_m}{\partial \mathbf{x}_a} = 0 \quad (13.85)$$

with subscript a indicating all the nodes within the mesh.

**FIGURE 13.9**

Artificially moved mesh surrounding a circular cylinder by solving the Laplace equation and applying Laplace smoothing. (a) Cylinder moved to a position above and (b) below the original position.

13.4 Concluding remarks

This chapter was intended as an introduction to the coupled problem of fluid–structure interaction. Although it is ideal to have a monolithic scheme for solving fluid–structure interaction, for various practical reasons a staggered approach is often preferred. However, for problems with added mass, it appears that monolithic schemes are as competitive as strongly coupled staggered approaches. Due to the evolving nature of this area, currently it is difficult to provide a firm conclusion. We hope that further progress will be made in this area in the next few years to get answers to some of the emerging questions on speed, accuracy, and robustness of solution methods for fluid–structure interaction problems.

References

- [1] J.K. Raines, M.Y. Jaffrin, A.H. Shapiro, A computer simulation of arterial dynamics in the human leg, *J. Biomech.* 7 (1) (1974) 77–91.
- [2] K.S. Rammos, G.J. Koulias, T.J. Papou, A.J. Bakas, P.G. Panagopoulos, S.G. Tsangaris, A computer model for the prediction of left epicardial coronary blood flow in normal, stenotic and bypassed coronary arteries, by single or sequential grafting, *Cardiovascular Surgery* 6 (6) (1998) 635–648.
- [3] L. Formaggia, J.F. Gerbeau, F. Nobile, A. Quarteroni, On the coupling of 3D and 1D Navier-Stokes equations for flow problems in compliant vessels, *Comput. Methods Appl. Mech. Eng.* 191 (2001).
- [4] L. Formaggia, F. Nobile, A. Quarteroni, A one dimensional model for blood flow: application to vascular prosthesis, in: I. Babuska, T. Miyoshi, P.G. Ciarlet (Eds.), *Mathematical Modeling and Numerical Simulation in Continuum Mechanics*,

- Lecture Notes in Computational Science and Engineering, Springer-Verlag, Berlin, 2002.
- [5] L. Formaggia, D. Lamponi, A. Quarteroni, One-dimensional models for blood flow in arteries, *J. Eng. Math.* 47 (2003) 251–276.
 - [6] S.A. Urquiza, P.J. Blanco, M.J. Vénere, R.A. Feijóo, Multidimensional modelling for the carotid artery blood flow, *Comput. Methods Appl. Mech. Eng.* 195 (33–36) (2006) 4002–4017.
 - [7] C. Sheng, S. Sarwal, K. Watts, A. Marble, Computational simulation of blood flow in human systemic circulation incorporating an external force field, *Med. Biol. Eng. Comput.* 33 (1) (1995) 8–17.
 - [8] S.J. Sherwin, L. Formaggia, J. Peiró, V. Franke, Computational modelling of 1D blood flow with variable mechanical properties and its application to the simulation of wave propagation in the human arterial system, *Int. J. Numer. Methods Fluids* 43 (6–7) (2003) 673–700.
 - [9] S.J. Sherwin, V. Franke, J. Peiró, K. Parker, One-dimensional modelling of a vascular network in space-time variables, *J. Eng. Math.* 47 (3) (2003) 217–250.
 - [10] J. Wan, B. Steele, S.A. Spicer, S. Strohband, G.R. Feijóo, T.J.R. Hughes, C.A. Taylor, A one-dimensional finite element method for simulation-based medical planning for cardiovascular disease, *Comput. Methods Biomed. Eng.* 5 (3) (2002) 195–206.
 - [11] M.S. Olufsen, Structured tree outflow condition for blood flow in larger systemic arteries, *Am. J. Physiol.* 276 (1) (1999) H257–H268.
 - [12] M.S. Olufsen, C.S. Peskin, W.Y. Kim, E.M. Pedersen, A. Nadim, J. Larsen, Numerical simulation and experimental validation of blood flow in arteries with structured-tree outflow conditions, *Ann. Biomed. Eng.* 28 (2000) 1281–1299.
 - [13] S. Čanić, E.H. Kim, Mathematical analysis of the quasilinear effects in a hyperbolic model blood flow through compliant axi-symmetric vessels, *Math. Methods Appl. Sci.* 26 (14) (2003) 1161–1186.
 - [14] N.P. Smith, A.J. Pullan, P.J. Hunter, An anatomically based model of transient coronary blood flow in the heart, *SIAM J. Appl. Math.* 62 (3) (2002) 990–1018.
 - [15] S.J. Payne, Analysis of the effects of gravity and wall thickness in a model of blood flow through axisymmetric vessels, *Med. Biol. Eng. Comput.* 42 (2004) 799–806.
 - [16] G. Porenta, D.F. Young, T.R. Rogge, A finite-element model of blood flow in arteries including taper, branches, and obstructions, *J. Biomech. Eng.* 108 (2) (1986) 161–167.
 - [17] N. Stergiopoulos, D.F. Young, T.R. Rogge, Computer simulation of arterial flow with applications to arterial and aortic stenoses, *J. Biomech.* 25 (12) (1992) 1477–1488.
 - [18] A.H. Shapiro, Steady flow in collapsible tubes, *J. Biomech. Eng.* 99 (1977) 126–147.

- [19] C. Guiot, G. Pianta, C. Cancelli, T.J. Pedley, Prediction of coronary blood flow with a numerical model based on collapsible tube dynamics, *Am. J. Physiol.* 258 (1990) H1606–H1614.
- [20] B.S. Brook, S.A.E.G. Falle, T.J. Pedley, Numerical solutions for unsteady gravity-driven flows in collapsible tubes: evolution and roll-wave instability of a steady state, *J. Fluid Mech.* 396 (1999) 223–256.
- [21] P.J. Reuderink, H.W. Hoogstraten, P. Sipkema, B. Hillen, N. Westerhof, Linear and nonlinear one-dimensional models of pulse wave transmission at high Womersley numbers, *J. Biomech.* 22 (8–9) (1989) 819–827.
- [22] T. Kitawaki, M. Shimizu, Flow analysis of viscoelastic tube using one-dimensional numerical simulation model, *J. Biomech. Sci. Eng.* 1 (1) (2006) 183–194.
- [23] L. Formaggia, F. Nobile, A. Quarteroni, A. Veneziani, Multiscale modelling of the circulatory system: a preliminary analysis, *Comput. Visual. Sci.* 2 (2) (1999) 75–83.
- [24] C. Hirsch, *Numerical Computation of Internal and External Flows. II: Computational Method for Inviscid and Viscous Flows*, Wiley Series in Numerical Methods in Engineering, John Wiley and Sons, Chichester, UK, 1990.
- [25] M. Anliker, R.L. Rockwell, E. Ogden, Nonlinear analysis of flow pulses and shock waves in arteries. Part I: Derivation and properties of mathematical model, *Z. Angew. Math. Phys.* 22 (2) (1971) 217–246.
- [26] O.C. Zienkiewicz, R.L. Taylor, J.Z. Zhu, *The Finite Element Method: Its Basis and Fundamentals*, seventh ed., Elsevier, Oxford, 2013.
- [27] P. Causin, J.F. Gerbeau, F. Nobile, Added-mass effect in the design of partitioned algorithms for fluid–structure problems, *Comput. Methods Appl. Mech. Eng.* 194 (2005) 4506–4527.
- [28] M. Heil, A.L. Hazel, J. Boyle, Solvers for large-displacement fluid–structure interaction problems: segregated versus monolithic approaches, *Comput. Mech.* 43 (2008) 91–101.
- [29] J. Degroote, K.-J. Bathe, J. Vierendeels, Performance of a new partitioned procedure versus a monolithic procedure in fluid–structure interaction, *Comput. Struct.* 87 (2009) 793–801.
- [30] U. Küttler, M. Gee, Ch. Förster, A. Comerford, W.A. Wall, Coupling strategies for biomedical fluid–structure interaction problems, *Int. J. Numer. Methods Biomed. Eng.* 26 (2010) 305–321.
- [31] N. Newmark, A method of computation for structural dynamics, *J. Eng. Mech., ASCE* 85 (1959) 67–94.
- [32] O.C. Zienkiewicz, R.L. Taylor, *The Finite Element Method for Solid and Structural Mechanics*, sixth ed., Elsevier, Oxford, 2005.
- [33] W. Dettmer, D. Perić, A computational framework for fluid–structure interaction: finite element formulation and applications, *Comput. Methods Appl. Mech. Eng.* 195 (2006) 5754–5779.

- [34] T.E. Tezduyar, S. Sathe, Modelling of fluid–structure interactions with the space-time finite elements: solution techniques, *Int. J. Numer. Methods Fluids* 54 (2007) 855–900.
- [35] W.A. Wall, S. Genginger, E. Ramm, A strong coupling partitioned approach for fluid–structure interaction with free surfaces, *Comput. Fluids* 36 (2007) 169–183.
- [36] U. Küttler, W.A. Wall, Fixed-point fluid–structure interaction solvers with dynamic relaxation, *Comput. Mech.* 43 (2008) 61–72.
- [37] T. Klöppel, A. Popp, U. Küttler, W.A. Wall, Fluid–structure interaction for non-conforming interfaces based on a dual mortar formulation, *Comput. Methods Appl. Mech. Eng.* 200 (2011) 3111–3126.
- [38] D.C. Sternal, M. Schäfer, M. Heck, S. Yigit, Efficiency and accuracy of fluid–structure interaction simulations using an implicit partitioned approach, *Comput. Mech.* 43 (2008) 103–113.
- [39] Y. Bazilevs, K. Takizawa, T.E. Tezduyar, *Computational Fluid–Structure Interaction Methods and Applications*, Wiley, 2013.
- [40] C. Farhat, C. Degand, B. Koobus, M. Lesoinne, Torsional springs for two-dimensional dynamics unstructured fluid meshes, *Comput. Methods Appl. Mech. Eng.* 163 (1998) 231–245.
- [41] C.O.E. Burg, A robust unstructured grid movement strategy using three-dimensional torsional springs, in: AIAA Paper 2004-2529, 2004.
- [42] X. Liu, N. Qin, H. Xia, Fast dynamic grid deformation based on Delaunay graph mapping, *J. Comput. Phys.* 211 (2006) 405–423.

Biofluid Dynamics

14

14.1 Introduction

Biofluid dynamics encompasses the topics of fluid flow, fluid–structure interaction, and heat and mass transfer in mammalian systems and in medical devices. Unlike standard engineering applications, understanding human body biofluid dynamics is extremely complex. This is due to the fact that *in vivo* experiments are not easy to perform and *in vitro* experiments may not always reflect the reality. Noninvasive experiments on humans are useful but do not always give the desired result. Thus, both theoretical and computational biofluid dynamics play a major role in the understanding of human body biofluid dynamics. The extracorporeal systems, such as blood pumps, can be experimentally tested. However, computational fluid dynamics is very useful at the early stages of design and development. The topics covered in this chapter are divided into one-dimensional systemic circulation and multidimensional subject-specific studies. These two topics are selected as they are realistic and provide useful information to understand diseases. Flow in model geometry and extracorporeal systems needs no special fluid dynamics treatment and thus the techniques discussed in the previous chapters may directly be applied to such problems.

14.2 Flow in human arterial system

A one-dimensional flow model is a useful tool for gaining a better understanding of blood flow in a systemic circulation¹ and how it is influenced by various interventions or diseases. At present, 3D modeling of the entire human arterial tree is not feasible within a reasonable amount of time. Apart from the unavailability of precise information regarding 3D geometry and material properties, the computational time required to model such an extensive network of branching vessels, including the fluid–structure interaction between blood and vessel walls, is simply too great. It has long been recognized that the wavelengths of the pressure-flow waves produced by the heart are much greater than the diameter of the vessels, thus it is valid to consider flow in the arteries to be quasi-one-dimensional [1–4]. The one-dimensional equations of flow are expressed in terms of vessel cross-sectional area A , velocity u , and

¹ Systemic circulation consists of all arteries and veins.

pressure p as discussed in the previous chapter. Pressure is related to A via the chosen nonlinear elastic wall law (i.e., $p = p(A)$). There are indeed several to choose from (for example, see Ref. [5]) which reflects the fact that the wall law is an empirical and/or mathematical simplification of the true mechanics of vessel walls, which are anisotropic and not perfectly cylindrical. It is also well known [6–8] that the arterial wall is a viscoelastic material and thus pressure is determined not only by A but its time derivatives also, although usually these effects are generally considered small enough to be ignored [9]. Another consideration is the treatment of blood viscosity. While various approximations have been used [3,4,10], most authors [9,11–13] calculate its effects in 1D by using an assumption of fully developed Newtonian steady flow with a parabolic velocity profile over a given cross-section (Poiseuille flow).

A typical human arterial network is shown in Fig. 14.1. Table 14.1 presents details on the majority of physical artery models available in the literature. The starting point of the physical model usually is the left ventricle.² A base pressure signal of two fused sigmoid functions is the input into the ventricle. The aortic valve then (see Fig. 14.1b) regulates and directs the flow into the aorta. The pulsatile flow is then naturally allowed to pass through the arteries until the location where the network is truncated to obtain a manageable flow network. At the point of truncation, appropriate resistance should be included to represent the microcirculation.

Although a one-dimensional fluid–structure interaction model has been presented in the previous chapter, there are some additional issues that need to be addressed before the flow in the systemic arterial circulation can be fully studied. The additional information required includes representation of the left ventricle, aortic valve, bifurcations, and boundary conditions at the truncation points.

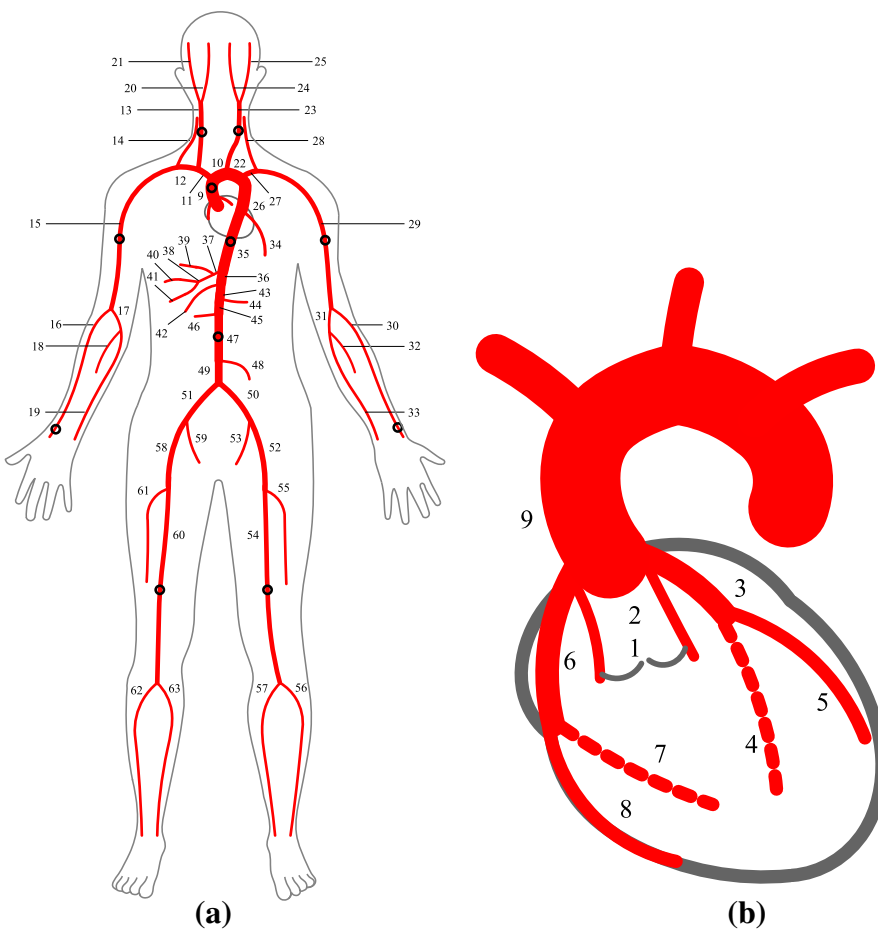
14.2.1 Heart

The heart model requires an appropriate representation of left ventricular pressure, aortic valve and coronary arteries. All arteries usually are modeled as circular cross-sectional tubes with flexible walls.

14.2.1.1 Ventricle

In the ventricle, a normal heart cycle consists of four phases: (1) In the *isovolumic contraction phase*, the ventricle begins to contract but the valve is closed. During this time there is a rapid increase in ventricular pressure since the ventricle is a closed cavity. (2) The *ejection phase* begins when ventricular pressure rises above aortic pressure, causing the valve to open. Further contraction causes ventricular pressure to rise above aortic pressure resulting in flow output, but this pressure difference is relatively small since (under normal conditions) there is little resistance to flow. (3) In the *isovolumic relaxation phase*, the heart muscle relaxes causing a drop in pressure and flow in both the ventricle and aorta. When aortic flow reaches zero, the valve closes, but there is often a small amount of reverse aortic flow before the valve is fully

²Left part of the heart from where oxygenated blood is pumped into the aorta.

**FIGURE 14.1**

(a) A typical human systemic arterial circulation network. (b) Representation of the heart within a one-dimensional framework.

closed. After the valve closes, ventricular pressure continues to fall rapidly to near zero pressure. (4) The final phase is *diastolic filling*, where the heart muscle is relaxed and, similar to a compliant balloon, increases in volume but with little increase in pressure. All these four stages can be mathematically represented using pressure variations.

As mentioned previously, the heart (left ventricle) is the input to the network model. A realistic pressure waveform within the ventricle may be generated using two sigmoid functions fused at mid-ejection (see Fig. 14.2). Each sigmoid has the form

$$p_{sig}(t) = a_1 + \frac{(a_2 - a_1)}{1 + e^{(a_3 - t)/a_4}} \quad (14.1)$$

Table 14.1 Major Arteries Used in the Present Study. The ID Numbers and Name Correspond to Those in [Figure 14.1](#).

ID	Vessel	L (cm)	r ₀ (cm)	r ₀ Taper	h (cm)	E × 10 ⁶	E Taper
						(dyne/cm ²)	
1	LV Outflow Tract	1.0	1.494	—	0.168	4.0	—
2	Aortic Root	1.0 ^a	1.494 ^a	—	0.168 ^a	4.0 ^a	—
3	Left Coronary Artery	3.0 ^a	0.259 ^a	—	0.080 ^a	8.0 ^a	—
4	Left Subendocardial	7.0 ^a	0.195 ^a	-0.293	0.080 ^a	8.0 ^a	—
5	Left Subepicardial	7.0 ^a	0.195 ^a	-0.293	0.080 ^a	8.0 ^a	—
6	Right Coronary Artery	3.0 ^a	0.239 ^a	—	0.080 ^a	8.0 ^a	—
7	Right Subendocardial	7.0 ^a	0.181 ^a	-0.293	0.080 ^a	8.0 ^a	—
8	Right Subepicardial	7.0 ^a	0.181 ^a	-0.293	0.080 ^a	8.0 ^a	—
9	Ascending Aorta	4.0 ^a	1.470 ^a	-0.020	0.163 ^d	4.0 ^a	—
10	Aortic Arch I	2.0 ^a	1.120 ^a	—	0.126 ^d	4.0 ^a	—
11	Brachiocephalic	3.5 ^c	0.650 ^c	-0.046	0.080 ^d	4.5 ^c	—
12	Right Subclavian I	3.5 ^c	0.425 ^c	-0.042	0.067 ^d	3.0 ^c	—
13	Right Carotid	9.4 ^b	0.675 ^b	-0.481	0.063 ^d	7.5 ^b	-0.467
14	Right Vertebral	13.5 ^c	0.200 ^c	—	0.045 ^d	6.5 ^c	—
15	Right Subclavian II	39.8 ^c	0.407 ^c	-0.435	0.067 ^d	3.0 ^c	-0.333
16	Right Radial	22.0 ^c	0.175 ^c	-0.200	0.043 ^d	6.5 ^c	-0.154
17	Right Ulnar I	6.7 ^c	0.215 ^c	—	0.046 ^d	6.0 ^c	—
18	Right Interosseous	7.0 ^c	0.100 ^c	—	0.028 ^d	14.0 ^c	—
19	Right Ulnar II	17.0 ^c	0.203 ^c	-0.113	0.046 ^d	11.0 ^c	-0.091
20	Right Internal Carotid	17.8 ^b	0.285 ^b	-0.246	0.045 ^d	6.5 ^b	-0.231
21	Right External Carotid	10.2 ^b	0.250 ^b	-0.300	0.042 ^d	6.5 ^b	-0.231
22	Aortic Arch II	3.9 ^a	1.070 ^a	—	0.115 ^d	4.0 ^a	—
23	Left Carotid	13.9 ^b	0.600 ^b	-0.500	0.063 ^d	7.0 ^b	-0.500
24	Left Internal Carotid	17.8 ^b	0.265 ^b	-0.226	0.045 ^d	6.5 ^b	-0.231
25	Left External Carotid	10.2 ^b	0.235 ^b	-0.255	0.042 ^d	6.5 ^b	-0.231
26	Thoracic Aorta I	5.2 ^a	0.999 ^a	—	0.110 ^d	4.0 ^a	—
27	Left Subclavian I	3.5 ^c	0.425 ^c	-0.042	0.066 ^d	3.0 ^c	—
28	Left Vertebral	13.5 ^c	0.200 ^c	—	0.045 ^d	6.5 ^c	—
29	Left Subclavian II	39.8 ^c	0.407 ^c	-0.435	0.067 ^d	3.0 ^c	-0.333
30	Left Radial	22.0 ^c	0.175 ^c	-0.200	0.043 ^d	6.5 ^c	-0.154
31	Left Ulnar I	6.7 ^c	0.215 ^c	—	0.046 ^d	6.0 ^c	—
32	Left Interosseous	7.9 ^c	0.100 ^c	—	0.028 ^d	14.0 ^c	—
33	Left Ulnar II	17.0 ^c	0.203 ^c	-0.113	0.046 ^d	11.0 ^c	-0.091
34	Intercostals	8.0 ^a	0.620 ^a	-0.250	0.049 ^d	4.0 ^a	-0.250
35	Thoracic Aorta II	10.4 ^a	0.675 ^a	-0.044	0.100 ^d	4.0 ^a	—
36	Abdominal Aorta I	5.3 ^a	0.610 ^a	—	0.090 ^d	4.0 ^a	—
37	Celiac I	1.0 ^a	0.390 ^a	-0.487	0.064 ^d	4.0 ^a	—
38	Celiac II	1.0 ^a	0.200 ^a	—	0.064 ^d	4.0 ^a	—
39	Hepatic	6.6 ^a	0.220 ^a	—	0.049 ^d	4.0 ^a	—
40	Gastric	6.3 ^a	0.180 ^a	—	0.045 ^d	4.0 ^a	—
41	Splenic	7.1 ^a	0.275 ^a	—	0.054 ^d	4.0 ^a	—
42	Superior Mesenteric	5.9 ^a	0.300 ^a	—	0.069 ^d	4.0 ^a	—
43	Abdominal Aorta II	1.0 ^a	0.590 ^a	—	0.080 ^d	4.0 ^a	—

(continued)

Table 14.1 (Continued)

ID	Vessel	<i>L</i> (cm)	<i>r</i> ₀ (cm)	<i>r</i> ₀ Taper	<i>h</i> (cm)	<i>E</i> × 10 ⁶	<i>E</i> Taper
						(dyne/cm ²)	
44	Left Renal	3.2 ^a	0.260 ^a	–	0.053 ^d	4.0 ^a	–
45	Abdominal Aorta III	1.0 ^a	0.590 ^a	–	0.080 ^d	4.0 ^a	–
46	Right Renal	3.2 ^a	0.260 ^a	–	0.053 ^d	4.0 ^a	–
47	Abdominal Aorta IV	10.6 ^a	0.580 ^a	-0.055	0.075 ^d	4.0 ^a	–
48	Inferior Mesenteric	5.0 ^a	0.160 ^a	–	0.043 ^d	4.0 ^a	–
49	Abdominal Aorta V	1.0 ^a	0.520 ^a	–	0.065 ^d	4.0 ^a	–
50	Left Common Iliac	5.8 ^a	0.400 ^c	-0.075	0.060 ^d	4.0 ^a	–
51	Right Common Iliac	5.9 ^a	0.400 ^c	-0.075	0.060 ^d	4.0 ^a	–
52	Left External Iliac	14.4 ^a	0.370 ^c	-0.152	0.053 ^d	8.0 ^a	–
53	Left Internal Iliac	5.0 ^a	0.200 ^c	–	0.040 ^d	16.0 ^a	–
54	Left Femoral	44.3 ^a	0.314 ^c	-0.124	0.050 ^d	8.0 ^a	–
55	Left Deep Femoral	12.6 ^a	0.200 ^c	–	0.047 ^d	8.0 ^a	1.000
56	Left Posterior Tibial	32.1 ^a	0.175 ^c	–	0.045 ^d	16.0 ^a	–
57	Left Anterior Tibial	34.3 ^a	0.275 ^c	-0.091	0.039 ^d	16.0 ^a	–
58	Right External Iliac	14.5 ^a	0.370 ^c	-0.152	0.053 ^d	8.0 ^a	–
59	Right Internal Iliac	5.0 ^a	0.200 ^c	–	0.040 ^d	16.0 ^a	–
60	Right Femoral	44.4 ^a	0.314 ^c	-0.124	0.050 ^d	8.0 ^a	–
61	Right Deep Femoral	12.7 ^a	0.200 ^c	–	0.047 ^d	8.0 ^a	1.000
62	Right Posterior Tibial	32.2 ^a	0.175 ^c	–	0.045 ^d	16.0 ^a	–
63	Right Anterior Tibial	34.4 ^a	0.275 ^c	-0.091	0.039 ^d	16.0 ^a	–

*Vessel Length (L) and Wall Thickness (h), Proximal Radius (*r*₀), and Young's Modulus (E), Both with the Degree of Linear Tapering Shown in Fractional Decrease (Negative Values) or Increase (Positive Values).^{a-d}*

^a Mynard and Nithiarasu [14].

^b Reymond et al. [15].

^c Liang et al. [16, 17].

^d Wang and Parker [18].

where

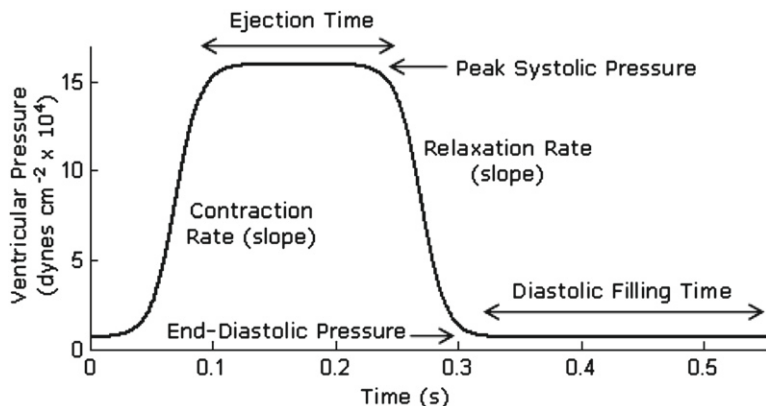
$$a_1 = p_{ed} - 9.11 \times 10^{-4} p_{peak}$$

$$a_2 = p_{peak}$$

$$a_3 = 7t_c$$

$$a_4 = t_c$$

Here, *p*_{ed} is end-diastolic pressure, *p*_{peak} is peak pressure, and *t*_c is a time constant that determines the slope of the isovolumic upstroke or downstroke. From end-diastole to peak pressure (i.e., the first sigmoid) Eq. (14.1) is used as is, but from peak pressure onwards (the second sigmoid) the relation is calculated backwards in time and applied forwards in time. Where the two sigmoids join (peak pressure), an iterative technique is used to ensure the pressures of the adjacent points are similar to within a threshold. This avoids a jump in pressure that would occur when fusing two sigmoids that

**FIGURE 14.2**

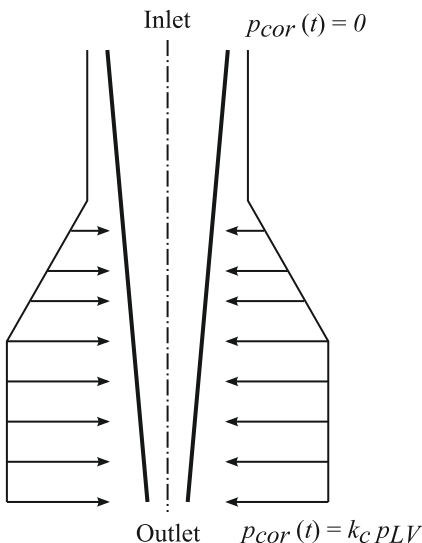
An example of a realistic ventricular pressure constructed using two sigmoid functions and used (in combination with a valve model) as the input to the arterial model. Important physiological features are labeled.

have different shapes (for example, when using a different value of t_c for isovolumic contraction and relaxation). The benefit of this input is that important features of real ventricular pressures can be emulated and manipulated independently. These features are end-diastolic pressure, peak pressure, ejection time, contraction rate, relaxation rate, and diastolic filling time as shown in Fig. 14.2, as well as heart rate, which results from a combination of the other parameters.

14.2.1.2 Coronary flow

Coronary arteries supply blood to the heart muscle. There are two inlets to the coronary circulation (the left and right coronary arteries, LCA and RCA, respectively) and these are located behind two of the three cusps of the aortic valve. It is well known [19] that the majority of coronary flow to the LV occurs during diastole when the valve is closed. This is because during systole, the contracting muscle compresses the subendocardial coronary arterioles and capillaries, which reduces or even reverses total left coronary flow. However, during diastole the heart muscle is relaxed and there is no restriction to flow.

The situation is somewhat different in the right coronary artery which feeds the RV. Since the pressure generated by the RV is lower than the LV, there is less compression of the subendocardial coronary vessels and thus greater systolic flow. Similar to Wang and Parker [20], the effect of coronary flow on arterial flow can be approximated by assuming there is no coronary flow during systole, and by making $R_{Vr} < 1$ when the valve is fully closed (see below). It is also possible to model regional coronary flow explicitly [14], with LCA and RCA both branching into two “equivalent” vessels that represent the lumped behavior of the left and right coronary arterial circulations, respectively. Each of these equivalent vessels have a linear taper in A_0 . This is a

**FIGURE 14.3**

Representation of external pressure distribution on the coronary artery induced by the heart.

similar approach to that taken by Rumberger [21], who used an equivalent vessel with an elastic taper (i.e., taper of β rather than A_0) to represent the coronary circulation. Thus in the current model, blood flows from the ventricle (input) into the aortic root, where a trifurcation is formed from the two coronary equivalent vessels and ascending aorta (see Fig. 14.1b). Furthermore, and similar to Guiot et al. [22], the effect of the surrounding heart muscle on the subendocardial vessels is simulated by applying a time-varying external pressure $p_{ext}(t)$ to the distal part (Fig. 14.3). More precisely,

$$p_{ext}(x, t) = \begin{cases} 0 & x < \frac{L_c}{3} \\ k_c p_{LV}(t) \left(\frac{3x}{L_c} - 1 \right) & \frac{L_c}{3} \leq x \leq \frac{2L_c}{3} \\ k_c p_{LV}(t) & x > \frac{2L_c}{3} \end{cases} \quad (14.2)$$

where $p_{LV}(t)$ is the time-varying LV pressure (see Fig. 14.2), $L_c = 7$ cm is the length of the equivalent coronary vessel, x is assumed to be zero at the inlet, and k_c is a constant that determines the proportion of ventricular pressure to be applied as external pressure. For the left subendocardial equivalent vessel, $k_c = 1$, while $k_c = 0.2$ for the right subendocardial vessel, thus reflecting the fact that the right coronary arteries undergo less compression than the left. The cross-sectional area of the LCA and RCA at the inlet was taken as 0.21 and 0.18 cm^2 , respectively, which is slightly larger than measurements performed *in vivo* at more distal sites, where the cross-sectional area would be somewhat smaller than at the coronary inlet [23,24]. The value of β for LCA and RCA was found by using the Young's modulus of the femoral artery [23] and a wall thickness of 0.08 cm.

14.2.2 Reflections

Before proceeding to understand how the aortic valve is embedded into the arterial network, it is useful to understand how reflections work within the network. It was shown in [Chapter 13](#) that whenever there is a change in characteristic impedance due to changes in vessel properties or branching, wave reflections occur. The characteristic impedance of a vessel relates the velocity or flow of a wave to the applied pressure (and is therefore analogous to Ohm's Law, i.e., $Z_0 = \frac{p}{Q}$) and may be expressed as

$$Z_0 = \frac{1}{Y_0} = \frac{\rho c_0}{A_0} \quad (14.3)$$

Considering [Eq. \(13.9\)](#), it can be seen that Z_0 depends only on vessel geometric and material properties. Y_0 is called the characteristic admittance. The reflection coefficient (R) is commonly used to express the ratio of the amplitudes of incoming and reflected waves and is given by [using the same subscripts as in [\(13.46\)](#)]

$$R = \frac{Y_{0p} - \sum_{i=1}^n Y_{0i}}{Y_{0p} + \sum_{i=1}^n Y_{0i}} \quad (14.4)$$

For a dead end terminal (i.e., $\sum Y_{0i} = 0$), there is a total positive reflection ($R = 1$) and for an opening with no downstream resistance ($\sum Y_{0i} \rightarrow \infty$), there is a total negative reflection ($R \rightarrow -1$), while for a well-matched branching no reflection occurs ($R = 0$). While [Eq. \(14.4\)](#) is strictly valid only in a linear model, it is useful for verifying the results of a nonlinear model and to make general predictions about reflections at discontinuities or vessel branching points. A reflection coefficient can also be used to set boundary conditions of simple resistance terminal vessels (see [Section 14.2.4](#)).

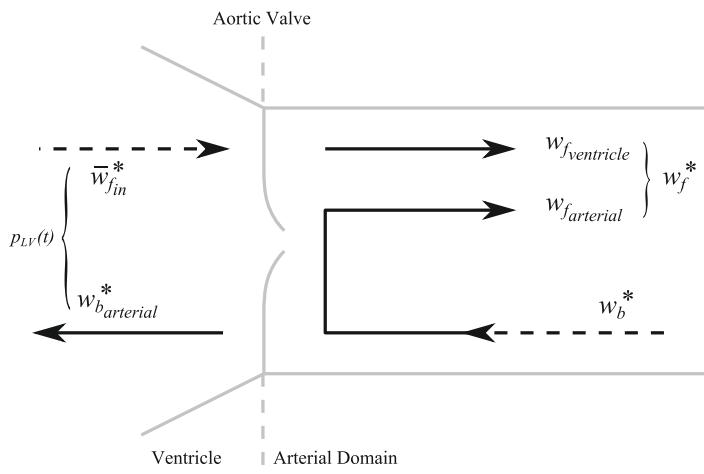
14.2.3 Aortic valve

The schematic describing the coupling between left ventricle (LV) and aortic valve (AV) is shown in [Fig. 14.4](#). The forward left ventricular pressure is generated using two sigmoid functions fused at the mid-ejection period as discussed previously. The left ventricle contraction gives rise to a forward characteristic variable and backward characteristic variable due to arterial effects while propagating through the arterial system as illustrated in [Fig. 14.4](#). The total forward characteristic variable, including the contribution from the aortic valve, can be written as

$$w_f^{*(n+1)} = w_{f_{ventricle}}^{(n+1)} + w_{farterial}^{(n+1)} \quad (14.5)$$

where $w_{f_{ventricle}}$ represents the forward characteristic variable of the ventricular pressure, which can be expressed as

$$w_{f_{ventricle}}^{(n+1)} = (1 - R_{av}) \bar{w}_{fin}^{*(n+1)} \quad (14.6)$$

**FIGURE 14.4**

A simple ventricular-valve model describing the transformation of the characteristic variables at the aortic valve.

where R_{av} denotes the aortic valve reflection coefficient and $(1 - R_{av})$ is known as the time-varying aortic valve transmission coefficient T_{av} . This transmission coefficient allows the forward characteristic variable to partially ($0 < T_{av} < 1$) or completely ($T_{av} = 1$) transmit through or completely reflect ($T_{av} = 0$) due to the presence of the aortic valve.

An exponential variation is appropriate for axial displacement waveforms of leaflet tips in normal aortic valves [25]. The valve function $V(t)$ used may therefore be expressed as

$$V(t) = B \left(e^{-kt} - 1 \right) \quad (14.7)$$

where $0 < t < 1$, while the constants are $B = 1/(e^{-k} - 1)$ and $k = 3$. This expression results in variation between 0 and 1 over 1 s. A scaled (in time or amplitude) and/or reversed version of this expression is then applied (in the form of reflection coefficient) to the opening or closing valve as necessary.

The term $w_{b,arterial}$ is associated with the backward characteristic variable which is completely transmitted ($R_{av} = 0$), or partially ($0 < R_{av} < 1$) or completely reflected ($R_{av} = 1$) from the aortic valve which yields

$$w_{f,arterial}^{(n+1)} = -R_{av} w_b^{*(n+1)} \quad (14.8)$$

Expanding $w_{f,b}^*$ gives the final form (Note that $w^* = w - w^0$)

$$w_f^{(n+1)} = w_f^0 + (1 - R_{av}) \left(\bar{w}_{fin}^{(n+1)} - w_f^0 \right) - R_{av} \left(w_b^{(n+1)} - w_b^0 \right) \quad (14.9)$$

where \bar{w}_f is calculated from the prescribed forward pressure using Eq. (13.28).

14.2.3.1 Afterload-corrected ventricular pressure

Afterload can be described as the pressure in the aorta that the heart needs to overcome in order to eject blood out of the heart. If the aortic pressure increases, the ventricular pressure increases and maintains the amount of blood that needs to be pumped through the arterial system. The afterload-corrected ventricular pressure can be described by rearranging Eq. (13.28) as

$$p_{LV}(t) = p_{ext} + \frac{\rho}{32} \left(\bar{w}_{fm}^{(n+1)} - w_{arterial}^{(n+1)} \right)^2 - \beta \sqrt{A_0} \quad (14.10)$$

where the backward characteristic variable w_b is caused by the backward-propagating waves transmitted into the left ventricle illustrated in Fig. 14.4 and can be obtained through

$$w_{arterial}^{*(n+1)} = (1 - R_{av}) w_b^{*(n+1)}$$

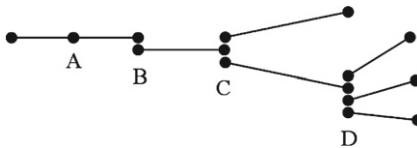
Expanding w_b^* gives (see Chapter 13)

$$w_{arterial}^{(n+1)} = w_b^0 + (1 - R_{av}) \left(w_b^{(n+1)} - w_b^0 \right) \quad (14.11)$$

14.2.4 Vessel branching

The arterial circulation has the structure of a tree, where blood from the LV is pumped into the aortic trunk, and major branches direct blood to all parts of the body, feeding fractal-like asymmetric networks [26] of small arteries, arterioles, and finally capillaries where oxygen and carbon dioxide transfer occurs. Deoxygenated blood then continues to the venous circulation, where small venules connect to progressively larger veins and finally return blood to the right side of the heart. The pulmonary circulation may be treated as a separate circulation, fed from the RV, which provides blood flow to the lungs. This circulation has a fractal structure [27,28] due to the rapid and almost immediate branching network that ends in the pulmonary capillaries. Here, blood is reoxygenated and completes its journey back to the left heart via the pulmonary venous circulation.

Modeling part or all of the circulation, therefore, requires consideration of branching points such as bifurcations or trifurcations. In one dimension, branching points are a type of discontinuity in cross-sectional area and vessel material properties (β). Figure 14.5 shows a variety of possible node connections. Type B has two nodes sharing the same location and the adjacent elements are therefore not connected in any intrinsic way. The benefit of such a connection is that unlike type A connections, true discontinuities can be realized, since for example, the co-located nodes can have different values of A_0 or β . In a similar way, bifurcations are formed by a connection of type C, with three co-located nodes belonging to the three weakly connected elements. A trifurcation would be of type D and indeed, any number of branches is possible.

**FIGURE 14.5**

Various possible nodal branching/connection types.

To transmit information between co-located nodes, the characteristic solutions will again be used. (Note: The following treatment is a generalization of that given in Refs. [29,30].) Consider a parent vessel p with N daughter vessels. Each of the $N + 1$ co-located nodes is treated as boundaries and the boundary conditions (i.e., values of A and u for each node) will be set using upstream and downstream information. There are therefore $2(N + 1)$ unknowns and as many equations required to solve the system. Half of these equations can be determined from the outgoing characteristics as discussed in [Section 13.2.2](#). The known value of the characteristic can then be related to the primitive variables for the nodes as follows:

$$w_{1p} = u_p + 4A_p^{1/4} \sqrt{\frac{\beta_p}{2\rho}} \quad (14.12)$$

for the parent vessel and

$$w_{2i} = u_i - 4A_i^{1/4} \sqrt{\frac{\beta_i}{2\rho}} \quad (14.13)$$

for the i th daughter vessel. Note that it is possible to have multiple “parent” vessels, but for this example only a single parent vessel branching to multiple daughter vessels is considered. Next, equations are used that ensure continuity of mass flow and total pressure. These provide the necessary remaining information and so, in this case, the incoming characteristics are not needed. Conservation of mass provides one equation and requires that

$$Q = A_p u_p = \sum_{i=1}^N A_i u_i \quad (14.14)$$

Continuity of total pressure [i.e., dynamic pressure ($\rho u^2/2$) + static pressure Eq. (13.6)] provides the remaining N equations, where for the i th daughter vessel,

$$\frac{\rho u_p^2}{2} + p_{ext(p)} + \beta (\sqrt{A_p} - \sqrt{A_{p0}}) = \frac{\rho u_i^2}{2} + p_{ext(i)} + \beta (\sqrt{A_i} - \sqrt{A_{i0}}) \quad (14.15)$$

This set of nonlinear equations may then be solved using the Newton-Raphson method [31].

14.2.5 Terminal vessels

The number of branches in the arterial tree increases dramatically toward the periphery, which includes approximately 2.7×10^9 capillaries [19]. While the vast number of small vessels and capillaries cannot be modeled individually, their combined effect may be approximated and imposed at the terminal boundaries of a model of larger arteries. Many investigators [2, 3, 6, 29, 32] have treated the downstream effects on flow as being purely resistive, that is, there is no phase difference between reflected pressure and flow, and the reflection coefficient is the same for all frequency harmonics. In this case, the change in the incoming characteristic could be determined from the change in the outgoing characteristic. For a wavefront traveling in the $+x$ direction the terminal reflection coefficient is

$$R_t = -\frac{\Delta w_2}{\Delta w_1} = -\frac{w_2^{n+1} - w_2^0}{w_1^{n+1} - w_1^0} \quad (14.16)$$

The value of w_1 for the next time step ($t = n + 1$) can be determined via extrapolation (see [Section 13.2.3](#)), while w_1^0 and w_2^0 are the initial values of the characteristic variables. The unknown (w_2^{n+1}) can then be determined by simply rearranging [Eq. \(14.16\)](#):

$$w_2^{n+1} = w_2^0 - R_t(w_1^{n+1} - w_1^0) \quad (14.17)$$

The drawback of the simple resistance terminal is that the arterial bed is known to have capacitive as well as resistive properties. This leads to a phase lag between reflected pressure and velocity and this means that higher frequency harmonics undergo smaller reflections. Thus the reflection coefficient is frequency dependant and complex [$R = R(j\omega)$]. This has led others [9–11, 13] to use the Windkessel element (which consists of two resistors and a capacitor) as vessel terminals. Here, the input impedance and reflection coefficient spectra have peaks at zero frequency, fall rapidly over the first several harmonics, and remain small and relatively constant at high frequencies [33]. While this model is a vast improvement, Olufsen [33] points out that the Windkessel element does not take into account the effects of wave propagation in a branching network. The shortcoming is that in real branching networks there are ripples in the input impedance spectrum (and thus reflection coefficient) after the low frequency peak [2, 26].

An alternative is to apply the input impedance of a generalized branching network model at the terminals [26, 33]. While this produces ripples in the input impedance and input reflection coefficient spectra, the method relies on an assumption of linearity and is difficult to apply in a nonlinear time-domain model.

14.2.5.1 Tapering vessels as terminal elements

Another possible approach is to use a tapering vessel as the terminal element. Consider a vessel with multiple step decreases in A_0 or step increases in β . Each step corresponds to a local increase in characteristic impedance (Z_0) and thus reflections will occur at each stepping point. Since these reflections occur at different distances

along the vessel, backward-running waves will reach the start of the vessel at different times. Note however that waves traveling back toward the inlet will also experience partial and negative re-reflections, since in this direction there are step decreases in characteristic impedance. Thus, from the perspective of the inlet, reflections that occur at more distant reflection sites have a smaller effect. This is similar to what occurs in the arterial system. Forward-traveling waves undergo relatively small reflections at branching points, but backward-traveling waves undergo relatively large negative re-reflections. In the limit where there is an infinite number of very small steps, there will be an infinite number of small reflections and re-reflections at every point along the vessel. It is thus possible to approximate the behavior of a branching network at its input with a single tapering vessel. In fact, several investigators [34–37] have modeled the input characteristics of the entire arterial tree with some success using only one or two tapering vessels. These models predict an input impedance spectrum with ripples which is similar to the input characteristics of branching networks. An exact solution to the Riccati equation which governs the input impedance of a tapering vessel has only recently been formulated [38]. This and other approximate solutions [35–37] assume linearity and ignore viscous effects, which become important in small vessels. No known analytical solution exists for the input impedance of a tapering vessel for nonlinear viscous flow. An empirical approach has thus been taken in the study described in this chapter and the relationship between input reflection coefficient, vessel length, and taper gradient (a linear taper is assumed throughout) has been investigated. The frequency-dependent input reflection coefficient, $R_{in}(j\omega)$, of both a fourth-generation branching network and various tapering vessels was determined by prescribing sinusoidal forward pressures of various frequencies at the inlet (1–10 Hz in steps of 1 and 12, 15, 20, 25 Hz). Since this input was a time-varying *forward* pressure, the time-varying backward pressure (which arises from reflections) was determined by subtracting the actual (or assigned) value of pressure (see [Section 13.2.3](#)) at the inlet from the forward pressure. Thus for each sinusoidal inlet forward pressure, the inlet backward pressure was calculated, which, after an initial stabilization period, was also sinusoidal with the same frequency as the forward pressure. The magnitude of the effective input reflection coefficient was then calculated for each frequency as the ratio of the amplitudes of the forward and backward sine waves. The phase was also determined via the time delay between the occurrence of peaks in the forward and backward sine waves. The results are then compared to get the most suitable tapering vessel.

Note that a boundary condition still needs to be specified at the end of the tapering vessel. This boundary condition can be set by using a pure resistance or a Windkessel impedance (as discussed above). For simplicity, the terminal (or load) impedance of each tapering vessel has been chosen to provide good matching. To achieve this, a reflection coefficient of zero is applied according to [Eq. \(14.16\)](#). While using a Windkessel load impedance at the output would result in more degrees of freedom for adjusting the input characteristics of the tapering vessel, setting a zero reflection coefficient at the output means that the input characteristics of the tapering vessel can be determined entirely by the length of the vessel and the gradient (or severity) of the taper [14].

14.2.6 Numerical solution

The fluid dynamics equations and solution procedure are identical to that explained in Chapter 13. The difference here is that the one-dimensional fluid–structure interaction method is applied to a network of one-dimensional tubes along with appropriate properties, initial conditions, boundary conditions, and other conditions, mentioned previously. The step-by-step procedure of model integration is given below.

14.2.6.1 Initialization

1. Using the ventricular input waveform calculate the incoming characteristic wave at the inlet for each time step [Eq. (13.28)].
2. Calculate the valve opening and closing function [Eq. (14.7)].
3. Calculate an external pressure weighting factor for each node in the subendocardial coronary “equivalent” vessels [Eq. (14.2)].

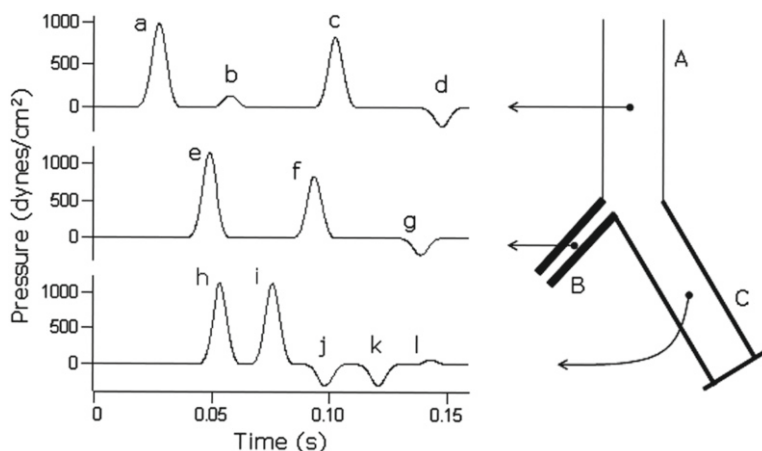
14.2.6.2 The main processing within the time-stepping loop follows

1. Using the value of afterload-corrected ventricular pressure (p_{LV}) from the previous time step (or initial value for the first iteration), calculate the external pressure for each node of the subendocardial coronary vessels [Eq. (14.2)].
2. Solve the governing equations using the method presented in the previous chapter.
3. Calculate the outgoing characteristic wave at the inlet [Eq. (13.28)].
4. Based on the values of pressure and flow in the previous time step, calculate the valve reflection and transmission coefficients (R_{Vr} and T_{Vp}) (see Section 14.2.3).
5. Using the prescribed incoming (ventricular) characteristic wave (Step 1) and the valve coefficients (Step 7), calculate the incoming (aortic) characteristic wave [Eq. (14.5)].
6. Based on the incoming and outgoing characteristics, calculate and assign the boundary conditions at the inlet (see Section 13.2.3).
7. Calculate the afterload-corrected ventricular pressure [Eq. (14.10)].
8. For each discontinuity or branching point (i.e., bifurcation, trifurcation, etc.), calculate the conditions for all co-located nodes (see Section 14.2.4).
9. For all tapering terminal vessels, calculate the outgoing characteristic [Eq. (13.27)]. Using a reflection coefficient of zero, calculate the incoming characteristic and the boundary conditions for each outlet.

The examples below are generated using the steps discussed above.

Example 14.1. Vessel branching

The branching nature of the arterial tree and the fact that parent and daughter branches are not perfectly matched [Eq. (14.4)] gives rise to a great number of reflections, re-reflections, and so on throughout the system. To illustrate this, Fig. 14.6 shows the propagation of a short pressure pulse in a single bifurcation. The parent vessel (A) ($A_0 = 4$, $\beta_A = 113487$, $L = 10$) branches into a narrow open-ended branch (B) ($A_0 = 0.5$, $\beta_B = 4\beta_A$, $L = 5$) and a larger close-ended branch (C) ($A_0 = 0.35$, $\beta_B = 2\beta_A$, $L = 10$). When pressure is monitored midway along each

**FIGURE 14.6**

Pulse propagation in a single bifurcation. The pulse propagates from parent branch A to daughter branches B (with a terminal reflection coefficient $R_t = 0$) and C ($R_t = 1$). Pressure is monitored at the midpoint of each vessel and plotted against time, showing the primary and reflected waves that occur (see text for explanation). The line thickness of the vessels signifies wall stiffness (i.e., $\beta_B = 4\beta_A = 2\beta_C$).

branch, it can be seen that a single input pulse (*a*) gives rise to several reflected waves in each segment in addition to the primary wave. The first reflection occurs when the wave reaches the bifurcation, partly reflecting back along A (wave *b*) and partly transmitting to both daughter branches (*e* and *h*). In branch B, wave *e* arrives at the monitoring point before wave *h* in branch C, due to the shorter distance and greater wave speed in B. Since B is well matched to any downstream vessels (that is, the terminal reflection coefficient is zero), there are no further reflections of wave *e*. Conversely, wave *h* in C reflects completely at the closed end, producing *i*, which has the same magnitude. This backward-running wave then propagates toward the bifurcation, reflecting once again to produce the forward-running wave *j* in C, the backward-running wave *c* in A, and the forward-running wave *f* in B. Note that the effective reflection coefficient of the bifurcation from the perspective of C is negative (since the combined characteristic impedance of A and C is less than that of B), causing wave *j* to be negative. This re-reflected wave is reflected again at the terminal of C producing *k*, which is then partially reflected once again as *l* and transmitted as waves *g* and *d*.

Several points should be noted. First, the input pulse is very short to enable clear view of backward- and forward-running waves without overlap. The heart pulse however is much longer making individual waves more difficult to distinguish. It is then important to note that the principle of superposition, where the overlapping waves can simply be considered as the sum of individual waves, is only valid in a linear model. In nonlinear models, this is not the case and will only hold approximately. This is because linear models assume a constant wave speed whereas nonlinear

models do not. Thus a wave traveling by itself will propagate at a different speed to the same wave when it encounters other waves [39]. Therefore, forward-running waves do in fact influence backward-running waves, although this effect is small. Secondly, the results in Fig. 14.6 are for inviscid flow. For viscous flow there would be some attenuation of the waves which, in turn, would lead to a slightly lower peak wave speed. However since the signals in Fig. 14.6 are small, these effects are negligible.

Example 14.2. Normal “at rest” state

Figure 14.7 shows various waveforms for a normal adult at rest. The model produces waveforms that contain all the well-known features that are obtained from

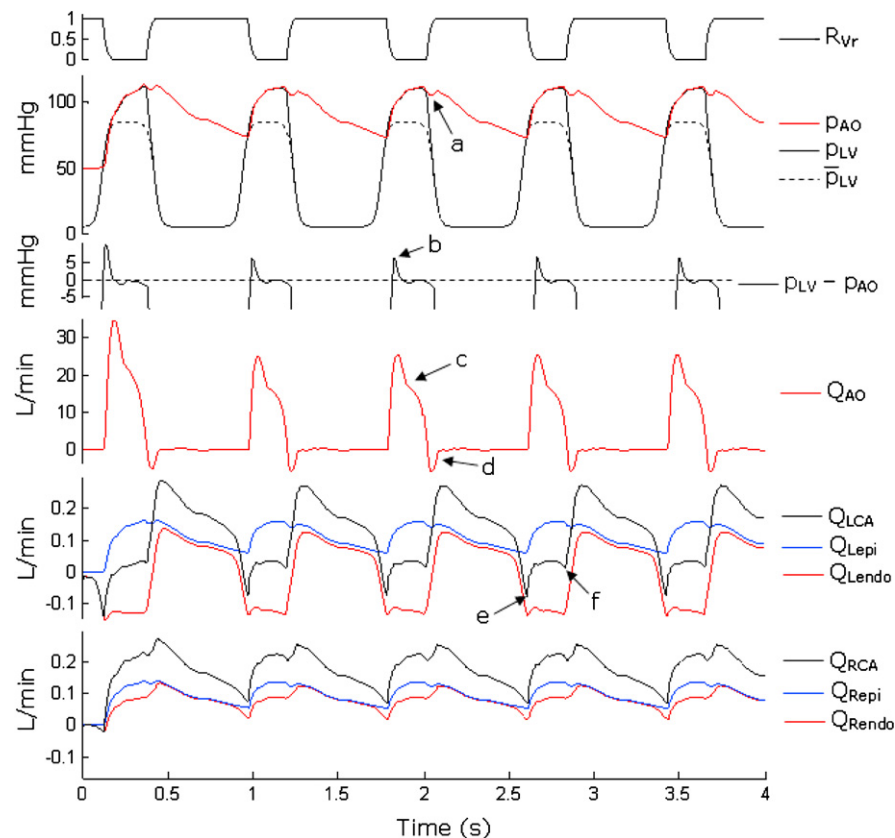


FIGURE 14.7

Waveforms produced by the model representing a normal human adult at rest. Marked features are (a) the dicrotic notch, (b) early systolic ventricule-aorta pressure gradient, (c) the reduction in blood flow due to reflected waves in mid-systole, (d) aortic backflow during valve closure, and (e) the first and (f) second local minima of left coronary flow (see text for explanations).

in vivo measurements, with regularity arising after the first beat. The plot of aortic valve reflection coefficient (R_{Vr}) shows that the valve opens and closes at the appropriate times based on local hemodynamics as discussed in Section 14.2.3. Prescribed (\bar{p}_{LV}) and afterload adjusted (p_{LV}) LV pressure are shown along with ascending aortic pressure (p_{AO}) and aortic flow (Q_{AO}), all of which display normal morphologies [40,41]. It can be seen that during systole, afterload has the effect of increasing ventricular pressure. Also during systole, p_{AO} is almost equal to p_{LV} , with a small positive pressure difference ($p_{LV} - p_{AO}$) in early systole (marked feature b) which drives forward flow, and a small negative pressure difference in mid-to-late systole caused by backward-running waves and the relaxing ventricle, which cause reductions in aortic flow and lead to valve closure. Relatively early in systole, there is a pressure-increasing and flow-decreasing hump in p_{AO} and Q_{AO} (feature c). This is the well-known pressure augmentation [42] that is due to reflected waves arriving at the aorta and causes the shape of p_{LV} and p_{AO} waveforms to depart from that of \bar{p}_{LV} . Valve closure is associated with the dicrotic notch in p_{AO} (feature a). This jump in pressure can be explained by noting that the valve reflection coefficient is rapidly increasing during this time and thus backward-running waves begin to reflect from the valve. At this time there is also a small amount of reverse flow across the valve. During diastole, Q_{AO} is effectively zero while p_{AO} gradually declines. This decline is governed by reflected waves. Using the data shown in Fig. 14.7, the common hemodynamic measures of systolic/diastolic(mean) aortic pressures of 110/73(94), cardiac output (CO = mean Q_{AOroot}) of 4.5 L/min, contractility index (maximum dp_{LV}/dt) of 1179 mmHg/s, and systemic vascular resistance (SVR = mean p_{AO}/CO with central venous pressure taken to be zero) of 1671 dynes/s/cm⁵ would all be considered normal for an adult human at rest.

The morphology of coronary flow also accords with *in vivo* data. Mean flow in the LCA and RCA was 0.127 and 0.181 L/min, respectively, with total coronary flow accounting for 6.8% of cardiac output, which again is in the range of normal values. In the LCA, the majority of flow (Q_{LCA}) occurs during diastole [19,43,44] and there are two well-defined local minima [19,22]. To explain these features, it is helpful to observe that Q_{LCA} is equal to the sum of subepicardial and subendocardial flows (Q_{Lepi} and Q_{Lendo}). Q_{Lepi} has a similar morphology to aortic pressure which shows that forward-running waves are predominant throughout the cardiac cycle. In contrast, Q_{Lendo} reveals a large amount of backflow during systole when the heart squeezes blood out of the subendocardial equivalent vessel, while during diastole when there is almost no external pressure applied, Q_{Lendo} follows Q_{Lepi} . Such large subendocardial backflows have been observed in [45]. The first minimum (feature e) in Q_{LCA} occurs in early systole and is caused by the fall in Q_{Lendo} . The presence of reverse flow in Q_{LCA} thus depends on whether the negative Q_{Lendo} outweighs the positive end-diastolic Q_{Lepi} . The Q_{LCA} second minimum occurs at the time of valve closure and is accompanied by decreases in both Q_{Lepi} and Q_{Lendo} . This is most likely associated with the fact that Q_{AO} falls rapidly just before the external pressure is removed and Q_{Lendo} begins to rise. In the right coronary circulation, Q_{RCA} , Q_{Rep_i} , and Q_{Rendo} always remain positive [46], since the external pressure

exerted on subendocardial vessels is less pronounced. The effect of external pressure is seen, however, by the reduced flow in Q_{Rendo} compared with Q_{Repi} during systole.

Example 14.3. Exercise and disease conditions

Exercise is characterized by an increase in heart rate, force of ventricular contraction, and peak pressure. Systemic vascular resistance also drops because more small blood vessels are recruited for oxygen transfer [47]. To simulate moderate exercise, the model parameters were adjusted as follows: HR = 115 bpm, $\bar{p}_{LV} = 115/5$ mmHg, and RVOT = RVCT = 35 ms. Vascular resistance was reduced by decreasing the taper severity of terminal elements so that $A_0(L) = 0.1 \text{ cm}^2$ or $0.9A_0(0)$, whichever was smaller. Figure 14.8b shows a regular beat under these conditions and may be compared to the “at rest” case in Fig. 14.8a. Of particular note is a 3.3-fold increase in cardiac output and an associated increase in coronary flow. There is also an increase in peak $pAO - pLV$ to 17.8 mmHg (compared with 6.7 mmHg at rest). Contractility also increased by 133%. These results accord well with *in vivo* measurements [47].

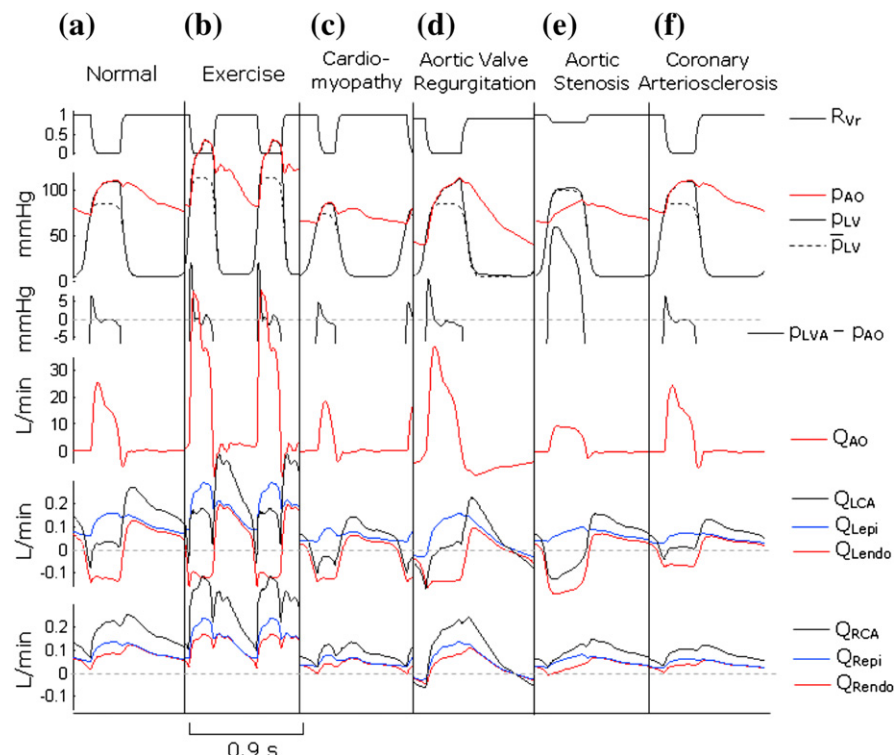


FIGURE 14.8

Sample steady-state beats from simulations of various normal and disease states.

Cardiomyopathy may take several forms but is generally characterized by a reduction in the capacity of the heart to generate force. Accordingly, peak \bar{p}_{LV} was reduced to 60 mmHg, while the isovolumic contraction and relaxation times were increased by 30% compared with the normal “at rest” case. Figure 14.8c shows that cardiomyopathy has the opposite effect to exercise in a normal heart, with cardiac output dropping to 1.79 L/min, contractility dropping by 47% and $p_{AO} - p_{LV}$ dropping by 43%. Similar trends have been observed in [48]. While [48] showed only small reductions in left coronary flow, the model predicted a 64% decrease. This may reflect that the amount of external pressure applied by the failing heart is actually less than applied in the model.

Compromise of the structural integrity of the aortic valve can lead to leakage of blood from aorta to ventricle during diastole. To model mild valve regurgitation, the maximum valve reflection coefficient was set to $R_{Vr}(\text{max}) = 0.9$. This led (Fig. 14.8d) to sustained Q_{AO} backflow during the whole period of diastole, and although peak Q_{AO} was higher, cardiac output fell by 37%. Valve leakage also led to a small amount of negative flow in Q_{Lepi} as well as both right coronary flows. End-diastolic and mean p_{AO} fell while peak p_{AO} was preserved [40/114(76)] and peak $p_{AO} - p_{LV}$ increased by 64%. These findings are in good agreement with [49].

Aortic valve stenosis (or just “aortic stenosis”) is a narrowing of the aortic valve which impedes systolic flow. This leads to a significant pressure gradient between the LV and the aorta, and to compensate, the LV must generate much greater pressures to maintain adequate arterial pressures and flows. This may be modeled with a reduced maximum valve transmission coefficient or nonzero reflection coefficient during systole as well as an increased \bar{p}_{LV} . Using $R_{Vr}(\text{min}) = 0.8$ and $\bar{p}_{LV} = 100/5$, Fig. 14.8e reveals a large ventricular-aortic pressure gradient (peak $p_{AO} - p_{LV}$ of 26 mmHg compared with 6.7 mmHg in the normal state) which lasts for all of systole. Despite the increased ventricular pressure, aortic pressure is lower [64/89(77)], and this leads to compromised coronary flow. Due to increased external pressure during systole, there is a greater negative Q_{Lendo} which overcomes Q_{Lepi} and is revealed in Q_{LCA} as a sustained systolic backflow. These trends have been observed by Kenny et al. [50] and Sabbah et al. [51].

Coronary arteriosclerosis is a stiffening of the coronary vessel walls due to the deposition of lipids, lipid by-products, and calcium. To provide a basic model of arteriosclerosis, Young’s modulus of the coronary vessels was increased by a factor of 4. Since this is equivalent to a reduction in characteristic admittance (see Section 14.2.2), mean Q_{LCA} and Q_{RCA} fell by 52% and 46%, respectively (Fig. 14.8f) [19], although there was little change to the morphology of coronary flow. Systemic hemodynamics did not change significantly, although in reality, the reduced coronary flow would lead to compromised ventricular function and thus hemodynamics in general. To model this interaction, cardiac metabolism and gas transport between myocardium and coronary capillaries would need to be accounted for.

In summary, various normal and disease states have been simulated. While the model does not account for all physiological interactions or physical characteristics

of the diseases, the waveforms obtained from the model are consistent with *in vivo* measurements and suggest that the model is physiologically relevant.

14.3 Image-based subject-specific flow modeling

The general structure of any subject-specific blood flow modeling framework consists of mainly image segmentation, meshing, and solution stages. The image segmentation is normally followed by a meshing stage in which a domain discretization is carried out. The connection between the image processing and meshing is established via a geometry definition step. The majority of the efforts during the mesh generation process goes toward establishing a valid and high-quality surface mesh that is a close representation of the geometry. The surface meshing in general is followed by the boundary layer mesh construction and artery wall meshing (when applicable). The boundary layer and arterial wall volume discretizations are followed by automatic volume meshing of the central flow domain of the artery with unstructured meshes. The flow solver is then used along with appropriately generated boundary conditions to complete the pipeline. The solver may include rigid geometry, flow and structure coupling, and Newtonian or non-Newtonian approximation and may also include multiscale mechanics or turbulence.

One of the main challenges in the computational modeling of hemodynamics is the accurate reconstruction of a blood vessel geometry. Anatomically accurate geometric models of the lumen are essential for realistic flow simulations and analysis. The anatomical information used to reconstruct the geometries are usually provided in the form of medical image datasets (scans) from imaging modalities such as computed tomography (CT) and magnetic resonance (MR) imaging. Manual reconstruction of the geometries can be tedious and time consuming. There is also the issue of variability between the geometries extracted manually by different individuals, and variability of geometries extracted by the same individual on different occasions. In order to allow computational flow modeling to be efficiently applied as a diagnostic or predictive tool, the amount of user intervention required in the process should be reasonably small. Therefore, a robust and efficient method that can be used to accurately segment the geometry from medical image datasets can be very useful and advantageous in the modeling process.

Assuming that a reasonably accurate reconstruction of the geometry is possible, the next stage of the modeling pipeline would be to generate a surface mesh or meshes to accurately discretize the surface or surfaces of the geometry. Unlike well-defined standard engineering geometries, the reconstructed subject-specific, arterial geometries are often defined by binaries. Thus, an alternative approach is required to that of standard engineering applications. Once a valid mesh is generated, appropriate flow conditions from either measurements or assumed data should be generated before flow algorithm is applied to get a solution.

14.3.1 Image segmentation

Extracting geometry from 3D scan data is a prerequisite for many computational modeling applications in cardiovascular fluid dynamics. Ideally, it should be carried out with minimum user interference and should robustly handle variations and noise interference that exist in the imaging data. Although a large number of procedures are available for image segmentation, a level set based image segmentation technique [52,53] to extract arterial geometries is adopted. An overview of this method and implementation details are given below. Let $I(\mathbf{x})$ denote the 3D gray image, where $\mathbf{x} = [x, y, z]^T$ is a point in the image domain \mathcal{D} . Let Ω be an object to be segmented from this image. We employ the level set method in which the object boundary $\partial\Omega(t)$ is defined through the level set function $\Phi(\mathbf{x}, t)$:

$$\partial\Omega(t) = \{\mathbf{x} : \Phi(\mathbf{x}, t) = 0\} \quad (14.18)$$

To compute the level set function, we numerically solve the following PDE for $\Phi(\mathbf{x}, t)$ [52,53]:

$$\frac{\partial\Phi}{\partial t} = \alpha g(\mathbf{x})\kappa(\mathbf{x}, t)\|\nabla\Phi\| - (1 - \alpha)(\mathbf{F}(\mathbf{x}) \cdot \nabla\Phi) \quad (14.19)$$

where α is a tuning parameter, $g(\mathbf{x}) = 1/(1 + |\nabla I|)$ is an edge stopping function, $\kappa(\mathbf{x}, t) = \nabla \cdot (\nabla\Phi/|\nabla\Phi|)$ is the mean curvature of the surface $\Phi = \text{const}$, and $\mathbf{F}(\mathbf{x}) = [F_x, F_y, F_z]^T$ is the flow function determined by image I . The flow function, which is derived from the image data, acts as an external force on the deformable model, and it is the most critical component in this kind of deformable model formulation.

14.3.2 Geometrical potential force (GPF)

The geometrical potential force (GPF) [52,53] is defined as

$$\mathbf{F}(\mathbf{x}) = \pm \frac{\nabla\Phi(\mathbf{x})}{|\nabla\Phi(\mathbf{x})|} G(\mathbf{x}) \quad (14.20)$$

where the scalar potential G is represented by a convolution of the form

$$G(\mathbf{x}) = P.V. \frac{\mathbf{x}}{|\mathbf{x}|^{\lambda+1}} * \nabla I(\mathbf{x}) = P.V. \iint_{\mathbf{x}' \in \mathcal{D}} \frac{\mathbf{x} - \mathbf{x}'}{|\mathbf{x} - \mathbf{x}'|^{\lambda+1}} \cdot \nabla I(\mathbf{x}') d\mathbf{x}' \quad (14.21)$$

Here $P.V.$ denotes the principle value and parameter λ depends on the domain dimension: $\lambda = 3$ for a 3D domain and \mathbf{x}' indicates a deformable model. Force, \mathbf{F} , acts in the direction of the gradient of Φ , i.e., always normal to the active surface $\Phi(\mathbf{x}, t) = 0$. It is possible to show that in the 2D case, with $\lambda = 2$, this force coincides with a magnetic-active force [54], but in contrast to magnetic force the GPF can be defined and applied to images of any dimension (even to 4D, i.e., time-varying 3D scans).

A discrete analog of the convolution kernel in the Eq. (14.21) takes the form

$$P.V.\frac{\mathbf{x}}{|\mathbf{x}|^{\lambda+1}} = \begin{cases} \mathbf{x}/|\mathbf{x}|^{\lambda+1} & \mathbf{x} \neq \mathbf{0} \\ \mathbf{0} & \mathbf{x} = \mathbf{0} \end{cases} \quad (14.22)$$

The fastest way to evaluate convolution (Eq. 14.21) and compute the potential $G_{ijk} = G(x_i, y_j, z_k)$ is to apply the 3D fast Fourier transform (FFT) method. It can be computed prior to the level set function calculation.

14.3.3 Numerical solution, initial and boundary conditions

Equation 14.19 may be solved using any standard method discussed in Chapter 2. The obvious and direct choice of numerical method is the finite difference method due to the fact that a regular mesh exists in the form of scan voxels. However, the finite element method can also be used on these regular meshes.

To set the initial condition, we have to define the initial surface S_0 somewhere in the vicinity of the blood vessel being investigated. An initial level set function is defined as a signed distance $D[S_0]$ from the initial surface S_0 , i.e.,

$$\Phi(x_i, y_j, z_k, 0) = D[S_0]$$

The signed distance can be computed efficiently using the algorithm described in Ref.[55]. At the boundaries of the image domain, zero Neumann boundary conditions are imposed. The narrow band approach described in [56] is used to reduce the computational cost in updating the level set function.

During the calculation, the function Φ may become irregular. Therefore, it is periodically reinitialized to the signed distance surface set from the current zero level set (surface of the deformable body), $S(t) = \{\mathbf{x} : \Phi(\mathbf{x}, t) = 0\}$. Hence, Φ can be redefined as $\Phi(\mathbf{x}, t) = D[S(t)]$, which is a smooth function with $S(t)$ being the surface with zero level set.

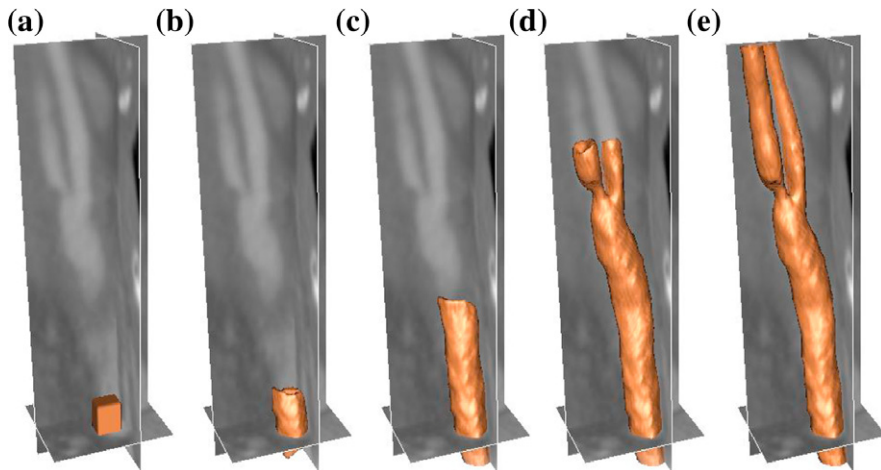
Example 14.4. Segmentation of a carotid artery

Here, a CT scan (DICOM dataset) of a human carotid artery is used to demonstrate the GPF-based segmentation method. The progression of the level set function is depicted in Fig. 14.9. Note that the initial model is positioned across the object boundaries to illustrate the capability of the deformable model to handle arbitrary cross-boundary initializations. The final solution is independent of the initial surface shape (example: sphere, parallelepiped, etc.). The position of the center of the initial surface S_0 is prescribed manually, which is the only manual operation in the segmentation process.

14.3.4 Domain discretization

14.3.4.1 Surface meshing

The surface mesh generation procedure has the following steps. The level set functions calculated by the image segmentation method are used to determine the skeleton of the

**FIGURE 14.9**

Segmentation of a carotid artery using GPF-based deformable model: (a) initial surface S_0 , after (b) 11, (c) 81, (d) 187, and (e) 241 time steps.

given artery first. This involves determining the approximate axis of the artery and its branches. This is followed by the procedure of generating a valid surface triangulation using again the final level set functions generated by the image segmentation. After carefully applying cosmetics to the surface mesh, it is clipped at the required length, orthogonal to the vessel axis.

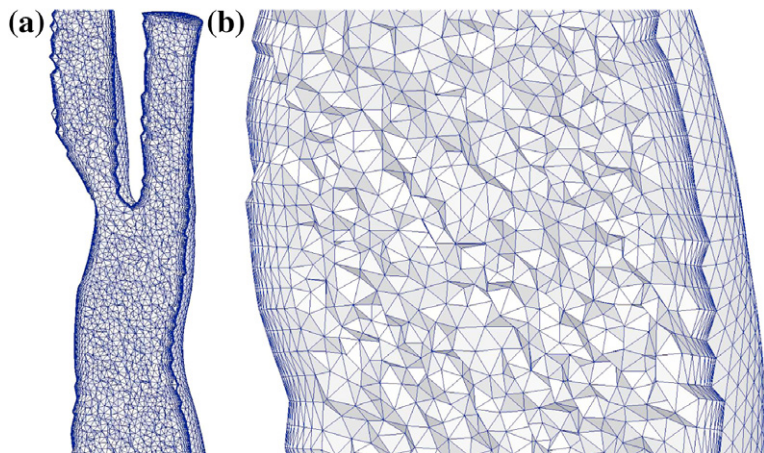
14.3.4.2 Boundary layer meshing

Often a boundary layer mesh is required close to the walls to capture high velocity gradients. This is generally carried out by growing inward normals from the surface triangles to create prism elements within the boundary layers. These prisms are then divided into tetrahedron elements if required.

14.3.5 Flow solution

In this section, analysis of flow in a moderately stenosed (blocked) carotid artery is presented. Any standard incompressible flow solver is sufficient to obtain a flow solution. Here, we recommend the CBS method and its variants. The geometry used here is generated using the image segmentation method presented in [Section 14.3.1](#), and the surface and volume meshes are obtained by employing all the techniques discussed in [Section 14.3.4](#). The transient flow boundary conditions are generated using the methods outlined in [Ref.\[57\]](#).

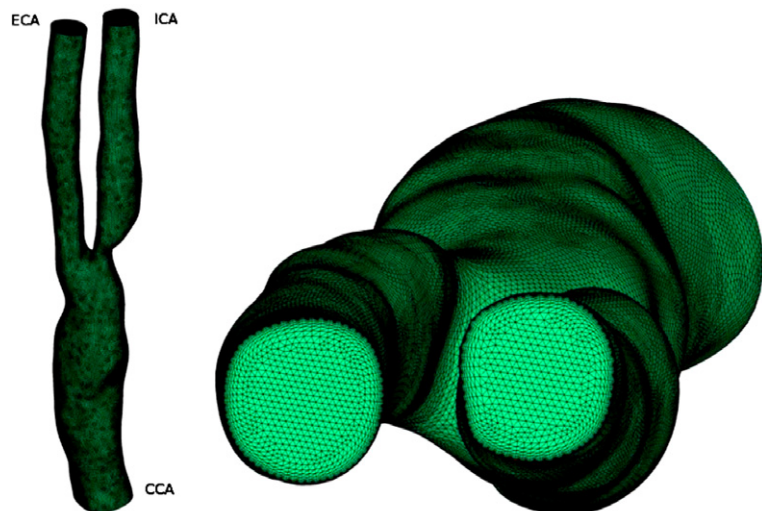
The carotid artery geometry used here was obtained from the Heart and Lung Centre, at Wolverhampton Hospital. This artery contains a moderate stenosis within the internal carotid artery (ICA) immediately downstream of the bifurcation. For the

**FIGURE 14.10**

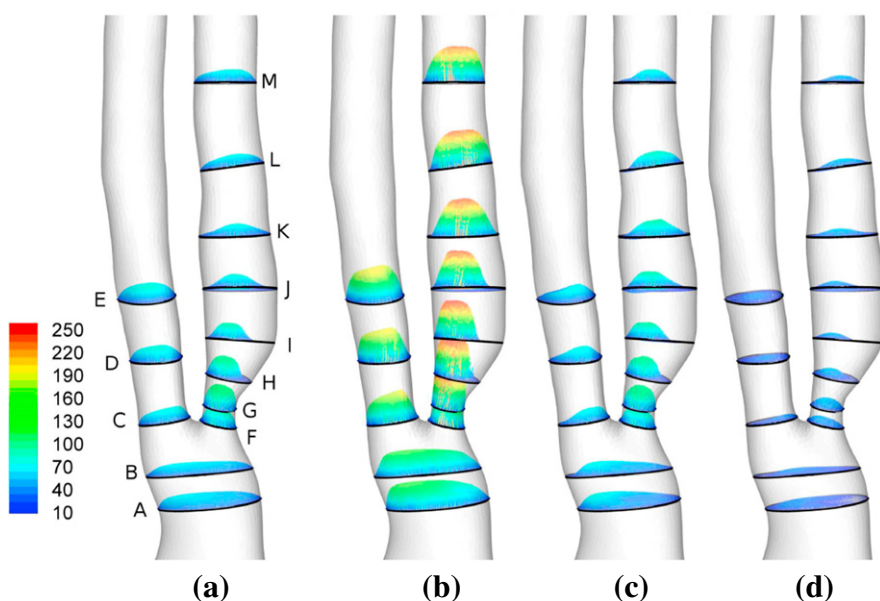
Volume mesh generated for a carotid artery.

numerical simulation, the mesh is clipped at the mid-height of the common carotid artery and maximal lengths of both internal and external carotid arteries are retained (see Fig. 14.10a). The final mesh is depicted in Fig. 14.11. This mesh consists of 4,126,777 linear tetrahedral elements and 708,191 nodes with 10 structured boundary layers. The stenosis occludes approximately 65% of the ICA. The common carotid artery (CCA) and the external carotid artery (ECA), however, are typical healthy arteries. A flow division of 50–50% between ECA and ICA is assumed. In normal circumstances, a flow division of 40–60% between ECA and ICA may be used. Since the ICA is partially occluded in the geometry used here, we assumed a 50–50% flow division.

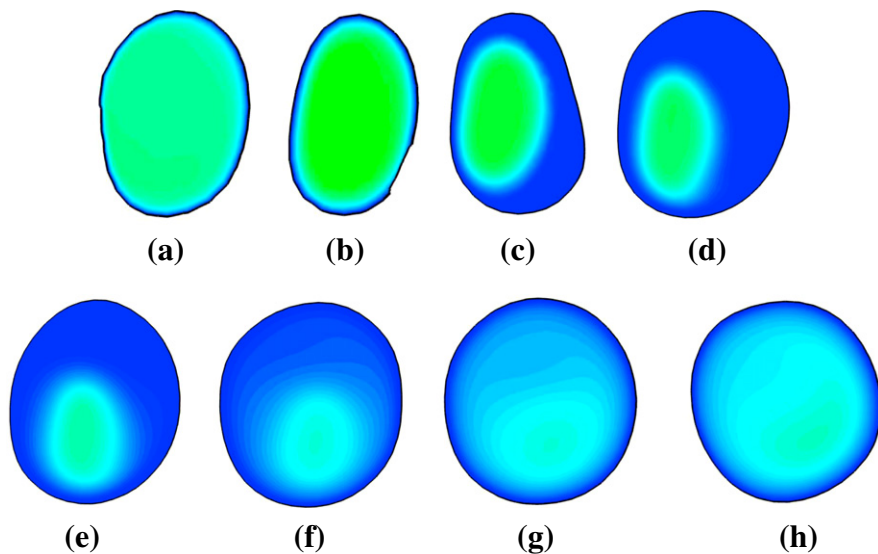
To examine the complex flow patterns within the stenosed artery and bifurcation in greater detail, the flow is visualized through a number of slices in Fig. 14.12. Here, the velocity vectors for the representative phases of the cardiac cycle (mid-acceleration, peak flow, mid-deceleration, dicrotic notch) are shown. From the figure, it is clear that the stenosis has a strong influence on the downstream flow. This is shown by the flow separation and recirculation between the bifurcation and at least up to slice J. As a result, low wall shear stress (WSS) would be expected downstream of the stenosis, marking a potential region of further plaque formation. This is in good agreement with Smedby [58] who found that plaque was more likely to grow downstream of a stenosis. Within the CCA and ICA, the flow at mid-acceleration and peak flow is typically well distributed within the slice, although in the ECA the flow is skewed toward the inner wall. It is during deceleration that the skewed nature becomes more obvious, with larger velocity values found closer to the inner wall in the ECA. To further establish the flow conditions within the ICA, the slices are now presented for three time instances. The mid-acceleration time instance is presented in Fig. 14.13, peak flow in Fig. 14.14, and during deceleration in Fig. 14.15. From the three figures, it is possible to see the evolution of the flow during systole. During the mid-acceleration

**FIGURE 14.11**

Mesh used for the computation.

**FIGURE 14.12**

3D velocity distribution within 13 slices (cm/s): (a) mid-acceleration; (b) peak; (c) mid-deceleration; (d) dicrotic notch.

**FIGURE 14.13**

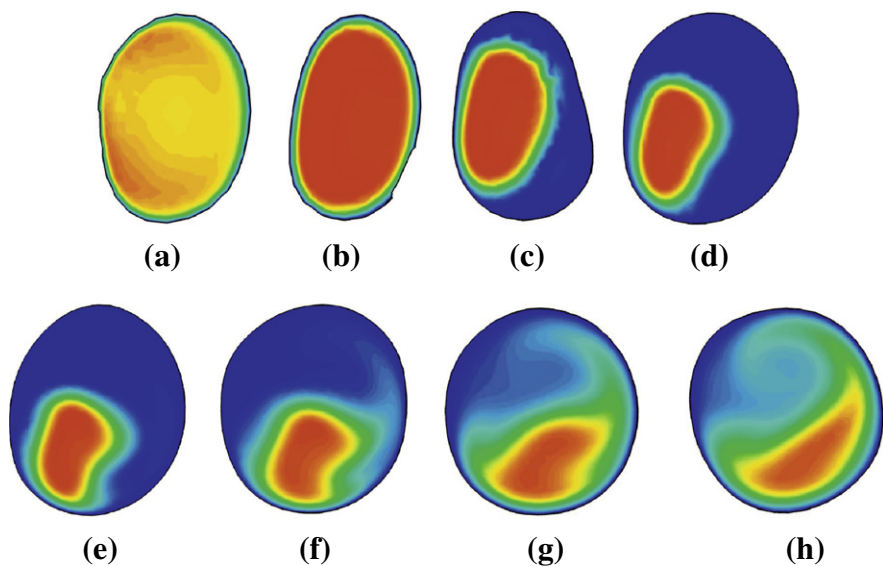
Streamline velocity magnitude at eight cross-sections within the ICA at mid-acceleration (cm/s): (a) slice F; (b) slice G; (c) slice H; (d) slice I; (e) slice J; (f) slice K; (g) slice L; (h) slice M.

stage, flow maintains a strong jet from slice F to slice J, before it begins to diffuse, and by slice M reattachment has occurred. In contrast, during peak flow the length of the jet has extended such that it impacts the posterior wall and flow is skewed toward this wall even in slice M. During peak flow, the predicted overall peak velocity is 266 cm/s within slice G and even in slice M, the velocity readily exceeds 200 cm/s. Within the deceleration phase, the influence of the jet is still strong, although secondary flow is observed downstream of the stenosis.

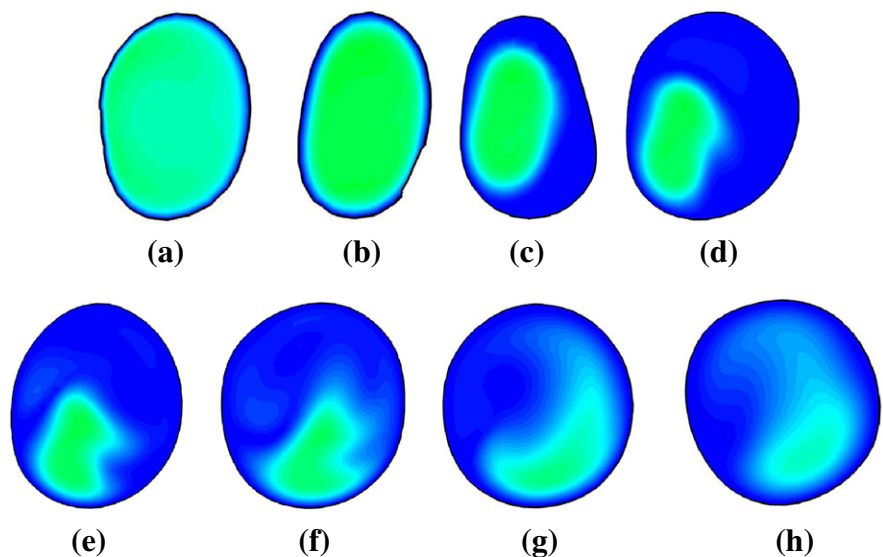
Low WSS is one of the indicators of the location of atherogenesis [59–66]. The work [67] defines the low shear stress as any value less than 5 dyne/cm² and this work also defines an athero-protective region as the region where the wall shear stress exceeds 25 dyne/cm². While instantaneous WSS values can provide individual snapshots of potential atherogenesis and athero-protective regions, the time-averaged WSS is employed to provide information over the full cardiac cycle. The time-averaged WSS can be determined using

$$\tau_{abs} = \frac{1}{T} \int_0^T |\mathbf{t}_s| dt \quad (14.23)$$

where $\mathbf{t}_s = \mathbf{t} - (\mathbf{t} \cdot \mathbf{n})\mathbf{n}$ is the surface traction vector and the traction vector \mathbf{t} is calculated from the Cauchy stress tensor σ and the surface normal vector \mathbf{n} using $\mathbf{t} = \sigma \cdot \mathbf{n}$. The oscillatory shear index (OSI), originally introduced in [59] and adapted for general three-dimensional use in [68], is also used here to quantify the transient

**FIGURE 14.14**

Streamline velocity magnitude at eight cross-sections within the ICA at peak flow (cm/s): (a) slice F; (b) slice G; (c) slice H; (d) slice I; (e) slice J; (f) slice K; (g) slice L; (h) slice M.

**FIGURE 14.15**

Streamline velocity magnitude at eight cross-sections within the ICA at mid-deceleration (cm/s): (a) slice F; (b) slice G; (c) slice H; (d) slice I; (e) slice J; (f) slice K; (g) slice L; (h) slice M.

shear stress dynamics experienced by the endothelial cells. The OSI is a ratio of the absolute wall shear stress and the mean wall shear stress. The mean wall shear stress is calculated as the magnitude of the time-averaged surface traction vector $\tau_{mean} = \left| \frac{1}{T} \int_0^T \mathbf{t}_s dt \right|$ and the oscillatory shear index is defined as [68]

$$OSI = \frac{1}{2} \left(1 - \frac{\tau_{mean}}{\tau_{abs}} \right) \quad (14.24)$$

The logarithmic time-averaged WSS distribution is given in Fig. 14.16 along with the OSI distribution. As expected, the peak time-averaged WSS occurs within the ICA in the vicinity of the flow divider. The predicted peak WSS of 805 dyne/cm^2 is exceptionally high and damaging. Upstream of the stenosis apex lies a band of high time-averaged WSS, across the ICA ($400\text{--}500 \text{ dyne/cm}^2$). This is also greater than the threshold value of 315 dyne/cm^2 that according to Holme et al. [69] was sufficient to induce platelet activation and enhanced platelet thrombus formation. Immediately downstream of the stenosis lies a small region experiencing time-averaged WSS of

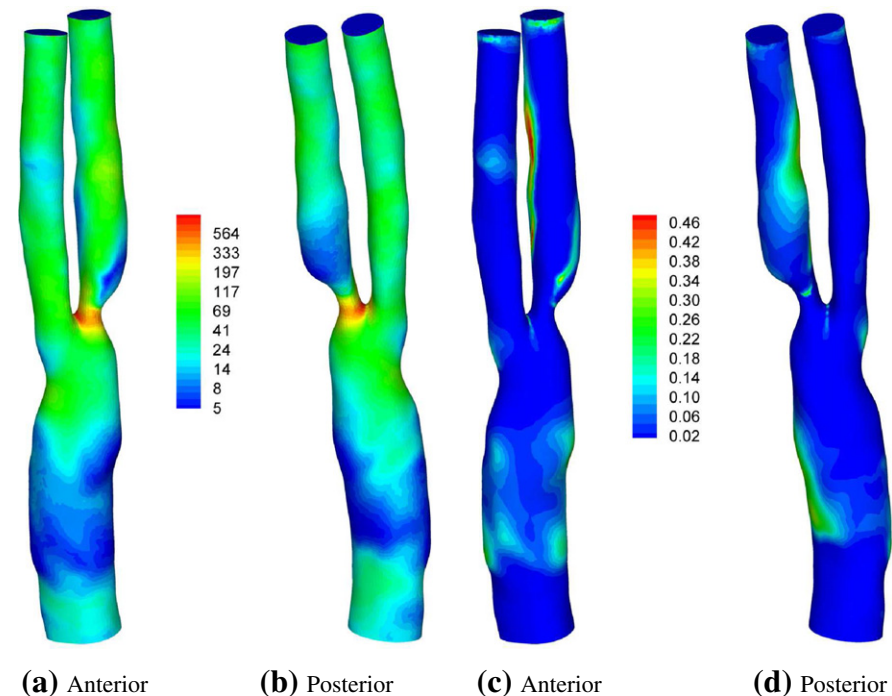


FIGURE 14.16

Hemodynamic wall parameter distributions: (a) and (b) time-averaged WSS [dyne/cm^2]; (c) and (d) OSI.

less than 5 dyne/cm² and a bigger region experiencing less than 10 dyne/cm². This region is indicative of a potential location for further plaque formation and it corresponds to the region experiencing flow separation. Away from the stenosis, the majority of the ICA experiences a WSS value less than 40 dyne/cm², although some regions experience values exceeding 100 dyne/cm² along the posterior wall. In the ECA, the time-averaged WSS values range between 20 and 50 dyne/cm². In contrast, approximately 20% of the CCA is predicted to experience a time-averaged WSS of less than 5 dyne/cm² with the vast majority experiencing less than 25 dyne/cm².

The OSI distribution indicates that the regions experiencing low time-averaged WSS in the CCA are coincident with the elevated OSI values. In the ICA, the regions of elevated or high OSI are extensive. A region extends from above the stenosis down the entire length of the inner wall to the ICA outlet. Another region of elevated OSI extends from near the stenosis apex along the outer wall of the ICA. In the ECA, only a small region experiences elevated OSI although this is located distal to the flow divider along the outer wall, which is reminiscent of the regions experiencing low time-averaged WSS in three out of four of the carotids studied by Kaazempur-Mofrad et al. [62]. This region experiences time-averaged WSS of between 5 and 7 dyne/cm².

14.4 Concluding remarks

In this chapter a brief overview on biofluid dynamics modeling within one-dimensional and three-dimensional cardiac frameworks was presented. The vast amount of work done in this area including fluid–structure interaction, mass transport, and other biofluid dynamics problems including human respiratory systems is indicative of the importance of this area. Unfortunately, it is very difficult to cover the entire subject of biofluid dynamics within one chapter. The objective was to provide sufficient information on the fundamentals of two important approaches in biofluid dynamics. We believe we have provided readers with a strong foundation that may be employed in various biofluid dynamics problems.

References

- [1] V.L. Streeter, W.F. Keitzer, D.F. Bohr, Pulsatile pressure and flow through distensible vessels, *Circ. Res.* 13 (1) (1963) 3–20.
- [2] N. Westerhof, F. Bosman, C.J. De Vries, A. Noordergraaf, Analog studies of the human systemic arterial tree, *J. Biomech.* 2 (2) (1969) 121–134.
- [3] B.W. Schaaf, P.H. Abbrecht, Digital computer simulation of human systemic arterial pulse wave transmission: a nonlinear model, *J. Biomech.* 5 (4) (1972) 345–364.

- [4] A.H. Shapiro, Steady flow in collapsible tubes, *J. Biomech. Eng.* 99 (1977) 126–147.
- [5] W. Ruan, M.E. Clark, M. Zhao, A. Curcio, Global solution to a hyperbolic problem arising in the modeling of blood flow in circulatory systems, *J. Math. Anal. Appl.* 331 (2007) 1068–1092.
- [6] A. Avolio, Multi-branched model of the human arterial system, *Med. Biol. Eng. Comput.* 18 (6) (1980) 709–718.
- [7] R. Holenstein, R.M. Nerem, P.F. Niederer, On the propagation of a wave front in viscoelastic arteries, *J. Biomech. Eng.* 106 (2) (1984) 115–122.
- [8] I. Larrabide, P.J. Blanco, S.A. Urquiza, G.R. Feijóo, Sensitivity of blood flow in stenosed carotid bifurcation, in: H. Rodrigues et al. (Eds.), II International Conference on Computational Bioengineering, Lisbon, Portugal, 2005.
- [9] J.K. Raines, M.Y. Jaffrin, A.H. Shapiro, A computer simulation of arterial dynamics in the human leg, *J. Biomech.* 7 (1) (1974) 77–91.
- [10] N. Stergiopoulos, D.F. Young, T.R. Rogge, Computer simulation of arterial flow with applications to arterial and aortic stenoses, *J. Biomech.* 25 (12) (1992) 1477–1488.
- [11] S.A. Urquiza, P.J. Blanco, M.J. Vénere, R.A. Feijóo, Multidimensional modelling for the carotid artery blood flow, *Comput. Methods Appl. Mech. Eng.* 195 (33–36) (2006) 4002–4017.
- [12] P.J. Reuderink, H.W. Hoogstraten, P. Sipkema, B. Hillen, N. Westerhof, Linear and nonlinear one-dimensional models of pulse wave transmission at high womersley numbers, *J. Biomech.* 22 (8–9) (1989) 819–827.
- [13] G. Porenta, D.F. Young, T.R. Rogge, A finite-element model of blood flow in arteries including taper, branches, and obstructions, *J. Biomech. Eng.* 108 (2) (1986) 161–167.
- [14] J.P. Mynard, P. Nithiarasu, A 1D arterial blood flow model incorporating ventricular pressure, aortic valve and regional coronary flow using the locally conservative Galerkin (LCG) method, *Commun. Numer. Methods Eng.* 24 (2008) 367–417.
- [15] P. Reymond, F. Merenda, F. Perren, D. Rufenacht, N. Stergiopoulos, Validation of a one-dimensional model of the systemic arterial tree, *Am. J. Phys. Heart Circ. Phys.* 297 (2009) H208–H222.
- [16] F.Y. Liang, S. Takagi, R. Himeno, H. Liu, Multi-scale modeling of the human cardiovascular system with applications to aortic valvular and arterial stenoses, *Med. Biol. Eng. Comput.* 47 (2009) 743–755.
- [17] F.Y. Liang, S. Takagi, R. Himeno, H. Liu, Biomechanical characterization of ventricular-arterial coupling during aging: a multi-scale model, study, *J. Biomech.* 42 (2009) 692–704.
- [18] J.J. Wang, K.H. Parker, Wave propagation in a model of the arterial circulation, *J. Biomech.* 37 (2004) 457–470.
- [19] R.M. Berne, M.N. Levy, *Cardiovascular Physiology*, The Mosby Physiology Monograph Series, eighth ed., Mosby, Inc., Missouri, USA, 2001.

- [20] J.J. Wang, K.H. Parker, Wave propagation in a model of the arterial circulation, *J. Biomech.* 37 (4) (2004) 457–470.
- [21] J.A. Rumberger, R.M. Nerem, A method-of-characteristics calculation of coronary blood flow, *J. Fluid Mech.* 82 (3) (1977) 429–448.
- [22] C. Guiot, G. Pianta, C. Cancelli, T.J. Pedley, Prediction of coronary blood flow with a numerical model based on collapsible tube dynamics, *Am. J. Phys.* 258 (1990) H1606–H1614.
- [23] B.S. Gow, C.D. Hadfield, The elasticity of canine and human coronary arteries with reference to postmortem changes, *Circ. Res.* 45 (5) (1979) 588–594.
- [24] C. Cuspidi, L. Lonati, L. Sampieri, L. Valagussa, I. Michev, G. Leonetti, A. Zanchetti, Lack of correlation between left ventricular mass and diameter of left coronary artery main trunk in hypertensive patients, *Am. J. Hypertens.* 12 (12) (1999) 1163–1168.
- [25] A. Ranga, O. Bouchot, R. Mongrain, P. Ugolini, R. Cartier, Computational simulations of the aortic valve validated by imaging data: evaluation of valve-sparing techniques, *Inter. Cardiovasc. Thorac. Surg.* 5 (4) (2006) 373–378.
- [26] D.J. Brown, Input impedance and reflection coefficient in fractal-like models of asymmetrically branching compliant tubes, *IEEE Trans. Biomed. Eng.* 43 (7) (1996) 715–722.
- [27] R.W. Glenny, H.T. Robertson, Fractal properties of pulmonary blood flow: characterization of spatial heterogeneity, *J. Appl. Phys.* 69 (2) (1990) 532–545.
- [28] G.S. Krenz, J.H. Linehan, C.A. Dawson, A fractal continuum model of the pulmonary arterial tree, *J. Appl. Phys.* 72 (6) (1992) 2225–2237.
- [29] S.J. Sherwin, L. Formaggia, J. Peiró, V. Franke, Computational modelling of 1D blood flow with variable mechanical properties and its application to the simulation of wave propagation in the human arterial system, *Int. J. Numer. Methods Fluids* 43 (6–7) (2003) 673–700.
- [30] C. Sheng, S. Sarwal, K. Watts, A. Marble, Computational simulation of blood flow in human systemic circulation incorporating an external force field, *Med. Biol. Eng. Comput.* 33 (1) (1995) 8–17.
- [31] G.H. Golub, C.F. Van Loan, *Matrix Computations*, John Hopkins University Press, Baltimore, 1996.
- [32] J. Wan, B. Steele, S.A. Spicer, S. Strohband, G.R. Feijóo, T.J.R. Hughes, C.A. Taylor, A one-dimensional finite element method for simulation-based medical planning for cardiovascular disease, *Comput. Methods Biomed. Eng.* 5 (3) (2002) 195–206.
- [33] M.S. Olufsen, Structured tree outflow condition for blood flow in larger systemic arteries, *Am. J. Phys.* 276 (1) (1999) H257–H268.
- [34] M. Anliker, R.L. Rockwell, E. Ogden, Nonlinear analysis of flow pulses and shock waves in arteries, part I: derivation and properties of mathematical model, *Z. Angew. Math. Phys.* 22 (2) (1971) 217–246.
- [35] S. Einav, S. Aharoni, M. Manoach, Exponentially tapered transmission line model of the arterial system, *IEEE Trans. Biomed. Eng.* 35 (5) (1988) 333–339.

- [36] K.-C. Chang, T.-S. Kuo, Exponentially tapered T-tube model in the characterization of arterial non-uniformity, *J. Theor. Biol.* 183 (1) (1996) 35–46.
- [37] R. Fogliardi, R. Burattini, K.B. Campbell, Identification and physiological relevance of an exponentially tapered tube model of canine descending aortic circulation, *Med. Eng. Phys.* 19 (3) (1997) 201–211.
- [38] L.J. Myers, W.L. Capper, Exponential taper in arteries: an exact solution of its effect on blood flow velocity waveforms and impedance, *Med. Eng. Phys.* 26 (2) (2004) 147–155.
- [39] M. Anliker, M.B. Histand, E. Ogden, Dispersion and attenuation of small artificial pressure waves in the canine aorta, *Circ. Res.* 23 (4) (1968) 539–551.
- [40] M.P. Spencer, F.C. Greiss, Dynamics of ventricular ejection, *Circ. Res.* 10 (1962) 274–279.
- [41] M.I. Noble, The contribution of blood momentum to left ventricular ejection in the dog, *Circ. Res.* 23 (5) (1968) 663–670.
- [42] R. Kelly, C. Hayward, A. Avolio, M. O'Rourke, Noninvasive determination of age-related changes in the human arterial pulse, *Circulation* 80 (6) (1989) 1652–1659.
- [43] W.M. Chilian, M.L. Marcus, Phasic coronary blood flow velocity in intramural and epicardial coronary arteries, *Circ. Res.* 50 (6) (1982) 775–781.
- [44] T. Matsumoto, F. Kajiyama, Coronary microcirculation: physiology and mechanics, *Fluid Dynam. Res.* 37 (2005) 60–81.
- [45] E. Toyota, Y. Ogasawara, O. Hiramatsu, H. Tachibana, F. Kajiyama, S. Yamamori, W.M. Chilian, Dynamics of flow velocities in endocardial and epicardial coronary arterioles, *Am. J. Phys.* 288 (4) (2005) H1598–H1603.
- [46] H.S. Lowensohn, E.M. Khouri, D.E. Gregg, R.L. Pyle, R.E. Patterson, Phasic right coronary artery blood flow in conscious dogs with normal and elevated right ventricular pressures, *Circ. Res.* 39 (6) (1976) 760–766.
- [47] E.M. Khouri, D.E. Gregg, C.R. Rayford, Effect of exercise on cardiac output, left coronary flow and myocardial metabolism in the unanesthetized dog, *Circ. Res.* 17 (5) (1965) 427–437.
- [48] L.A. Nikolaidis, A. Doverspike, R. Huerbin, T. Hentosz, R.P. Shannon, Angiotensin-converting enzyme inhibitors improve coronary flow reserve in dilated cardiomyopathy by a bradykinin-mediated, nitric oxide-dependent mechanism, *Circulation* 105 (23) (2002) 2785–2790.
- [49] D.M. Griggs, C.C. Chen, Coronary hemodynamics and regional myocardial metabolism in experimental aortic insufficiency, *J. Clin. Invest.* 53 (1974) 1599–1606.
- [50] A. Kenny, C.R. Wisbey, L.M. Shapiro, Profiles of coronary blood flow velocity in patients with aortic stenosis and the effect of valve replacement: a transthoracic echocardiographic study, *Br. Heart J.* 71 (1994) 57–62.
- [51] H.N. Sabbah, P.D. Stein, Effect of aortic stenosis on coronary flow dynamics: studies in an in-vitro pulse duplicating system, *J. Biomech. Eng.* 104 (1982) 221–225.

- [52] S.Y. Yeo, X. Xie, I. Sazonov, P. Nithiarasu, Geometric potential force for the deformable model, in: British Machine Vision Conference, 2009.
- [53] S.Y. Yeo, X. Xie, I. Sazonov, P. Nithiarasu, Geometrically induced force interaction for three-dimensional deformable models, in: IEEE Transactions of Image Processing, 2010.
- [54] X. Xie, M. Mirmehdi, MAC: magnetostatic active contour model, *IEEE Trans. Pattern Anal. Mach. Intell.* 30 (4) (2008) 632–647.
- [55] P.F. Felzenszwalb, D.P. Huttenlocher, Distance transforms of sampled functions, Cornell Computing and Information Science, TR2004-1963, 2004.
- [56] J.A. Sethian, *Level Set Methods and Fast Marching Methods: Evolving Interfaces in Computational Geometry, Fluid Mechanics, Computer Vision, and Material Science*, Cambridge University Press, Cambridge, UK, 1999.
- [57] I. Sazonov, S.Y. Yeo, R.L.T. Bevan, X. Xie, R. van Loon, P. Nithiarasu, Modelling pipeline for subject-specific arterial blood flow – a review, *Int. J. Numer. Methods Biomed. Eng.* 27 (2011) 1868–1910.
- [58] O. Smedby, Do plaques grow upstream or downstream? An angiographic study in the femoral artery, *Arterioscl. Thromb. Vascul. Biol.* 17 (1997) 912–918.
- [59] D.N. Ku, D.P. Giddens, C.K. Zarins, S. Glagov, Pulsatile flow and atherosclerosis in the human carotid bifurcation – positive correlation between plaque location and low and oscillating shear-stress, *Atherosclerosis* 5 (3) (1985) 293–302.
- [60] F.P. Glor, Q. Long, A.D. Hughes, A.D. Augst, B. Ariff, S.A. McG, Thom P.R. Verdonck, X.Y. Xu, Reproducibility study of magnetic resonance image-based computational fluid dynamics prediction of carotid bifurcation flow, *Ann. Biomed. Eng.* 31 (2003) 142–151.
- [61] P. Papathanasopoulou, S. Zhao, U. Köhler, M.B. Robertson, Q. Long, P. Hoskins, MRI measurement of time-resolved wall shear stress vectors in a carotid bifurcation model, and comparison with CFD predictions, *J. Magn. Reson. Imag.* 17 (2003) 153–162.
- [62] M.R. Kaazempur Mofrad, A.G. Isasi, H.F. Younis, R.C. Chan, D.P. Hinton, G. Sukhova, G.M. LaMuraglia, R.T. Lee, R.D. Kamm, Characterization of the atherosclerotic carotid bifurcation using MRI finite element modeling, and histology, *Ann. Biomed. Eng.* 32 (2004) 932–946.
- [63] S.A. Urquiza, P.J. Blanco, M.J. Vénere, R.A. Feijóo, Multidimensional modelling for the carotid artery blood flow, *Comput. Methods Appl. Mech. Eng.* 195 (2006) 4002–4017.
- [64] A.D. Jeays, P.V. Lawford, R. Gillott, P. Spencer, D.C. Barber, K.D. Bardhan, D.R. Hose, Characterisation of the haemodynamics of the superior mesenteric artery, *J. Biomech.* 40 (2007) 1916–1926.
- [65] K.E. Lee, K.H. Parker, C.G. Caro, S.J. Sherwin, The spectral/hp element modelling of steady flow in non-planar double bends, *Int. J. Numer. Methods Fluids* 57 (2008) 519–529.

- [66] K.T. Nguyen, C.D. Clark, T.J. Chancellor, D.V. Papavassiliou, Carotid geometry effects on blood flow and on risk for vascular disease, *J. Biomech.* 41 (2008) 11–19.
- [67] A.M. Malek, S.L. Alper, S. Izumo, Hemodynamic shear stress and its role in atherosclerosis, *JAMA* 282 (1999) 2035–2042.
- [68] X. He, D.N. Ku, Pulsatile flow in the human left coronary artery bifurcation: average conditions, *J. Biomech. Eng.* 118 (1996) 74–82.
- [69] P.A. Holme, U. Orvim, M.J.A.G. Hamers, N.O. Solum, F.R. Brosstad, R.M. Barstad, K.S. Sakariassen, Shear-induced platelet activation and platelet microparticle formation at blood flow conditions as in arteries with a severe stenosis, *Arterioscl. Thromb. Vascul. Biol.* 17 (1997) 646–653.

Computer Implementation of the CBS Algorithm*

15

15.1 Introduction

In this chapter we consider some essential steps in the computer implementation of the CBS algorithm on structured or unstructured finite element grids. Only linear triangular elements are used and the description given here is intended for a two-dimensional version of the program. The program source and user manual along with several solved problems are available at the website

<http://www.zetacomp.com>

free of charge. Readers also will find documentation of the code and other details on this website including new results and corrections.

The program can be used to solve the following different categories of fluid mechanics problems:

1. Compressible viscous and inviscid flow problems
2. Incompressible viscous flows
3. Incompressible flows with heat transfer

With further simple modifications, many other problems such as turbulent flows, solidification, mass transfer, free surfaces, etc., can be solved. The procedures presented are largely based on the theory presented in [Chapter 3](#). The program is written in Fortran and it is assumed that the reader is familiar with coding and finite element procedures discussed in this book [\[1,2\]](#).

We call the present program CBSflow since it is based on the CBS algorithm discussed in [Chapter 3](#) of this volume. We prefer to keep the compressible and incompressible flow codes separate to avoid any confusion. However an experienced programmer can incorporate both parts into a single code without much difficulty. Each program listing is accompanied by some model problems which may be used to validate an installation. In addition to the model inputs to programs, a complete user manual is available to describe each part of the program in detail. Any error reported by users will be corrected and the program will be continuously updated by the authors.

*Dr Rhodri Bevan's assistance in writing and improving the code is gratefully acknowledged.

The modules are (1) the data input module with preprocessing; (2) the solution module; and (3) the output module. The CBSflow program contains the source statements to solve transient Navier-Stokes (or Euler-Stokes) equations iteratively. Here there are many possibilities such as fully explicit forms, semi-implicit forms, quasi-implicit forms, and fully implicit forms as presented in [Chapter 3](#). We concentrate mainly on the first two forms which require small memory and simple solution procedures compared to other forms.

In both the compressible and incompressible flow codes, only nondimensional equations are used. The reader is referred to the appropriate chapters ([Chapters 3, 4](#), and [5](#)) for different nondimensional parameters.

In [Section 15.2](#) we describe the essential features of data input to the program. Here either structured or unstructured meshes can be used to divide the problem domain into finite elements. [Section 15.3](#) explains how the steps of the CBS algorithm are implemented. In that section, we briefly remark on the options available for shock capturing, various methods of time stepping, and different procedures for equation solving. In [Section 15.4](#), the output generated by the program and postprocessing procedures are considered.

15.2 The data input module

This part of the program is the starting point of a calculation where the input data for the solution module are prepared. Here an appropriate input file is opened and the data are read from it. The mesh generators are provided separately. By suitable coupling, the reader can implement various adaptive procedures as discussed in [Chapters 4](#) and [6](#). Either structured or unstructured mesh data can be given as input to the program. Readers are referred to the user manual for further details.

15.2.1 Mesh data: Nodal coordinates and connectivity

Once the nodal coordinates and connectivity of a finite element mesh are available from a mesh generator, they are allotted to appropriate arrays. The coordinates are allotted to $coord(i, j)$ with i defining the appropriate Cartesian coordinates $x_1(i = 1)$ and $x_2(i = 2)$ and j defining the global node number. Similarly the global node numbers describing the connectivity are allotted to an array $intma(k, l)$. Here k is the local node number and l is the global element number. It should be noted that the material code normally used in heat conduction and stress analysis is not used but can be introduced if necessary.

15.2.2 Boundary data

In CBSflow we mostly use the edges to store the information on boundary conditions. Some situations require boundary nodes (e.g., pressure specified in a single node) and in such cases corresponding node numbers are supplied to the solution module.

15.2.3 Other necessary data and flags

In addition to the mesh data and boundary information, the user needs to input a few more parameters used in flow calculations. For example, compressible flow computations need the values of nondimensional parameters such as the Mach number, Reynolds number, Prandtl number, etc. Here the reader may consult the nondimensional equations and parameters discussed in [Section 3.1, Chapter 3](#), and in [Chapter 4](#). Further details are available in the user manual.

Several flags for boundary conditions, shock capture, etc., need to be given as inputs. For a complete list of such flags, the reader is referred to the user manual and program listing www.zetacomp.com.

15.2.4 Preliminary subroutines and checks

A few preliminary subroutines are called before the start of the time iteration loop. Establishing the surface normals, element area (for direct integration), mass matrix calculation and lumping, and some allocation subroutines are necessary before starting the time loop.

15.3 Solution module

The solution module primarily contains the following steps (explicit time stepping):

```

pre-processing
do iter = 1, number of time steps
    call alotim ! allot appropriate time step value
    call shock ! calculate shock capturing viscosity
    call step1 ! intermediate momentum
    call step2 ! calculate density/pressure
    call step3 ! correct momentum
    call energy ! energy equation
    call press ! relate density and pressure using energy
    call bound ! apply boundary conditions
    call check ! check steady state criterion
enddo !iter
post-processing

```

The time iteration is carried out over the steps of the CBS algorithm and over many other subroutines such as the local time step and shock capture calculations. As mentioned, the energy can be calculated after the velocity correction. However, for a fully explicit form of solution, the energy equation can be solved in step 1 along with the intermediate momentum variable if preferred.

Most of the routines within the time loop are further branched into several other subroutines. For instance, convection and diffusion are treated using separate routines within each step.

15.3.1 Time step

In general, three different ways of establishing the time steps are possible. In problems where only the steady state is of importance, so-called “local time stepping” is used ([Chapter 3](#)). Here a local time step at each and every nodal point is calculated and used in the computation.

When we seek accurate transient solution of any problem, the so-called “minimum step” value is used. Here the minimum of all local time step values is calculated and used in the computation.

Another and less frequently used option is that of giving a “fixed” user-prescribed time step value. Selection of such a quantity needs considerable experience from solving several flow problems.

The time loop starts with a subroutine where the above-mentioned time step options are available (`alotim`). If the last option of the user-specified fixed time step is used, the local time steps are not calculated.

15.3.2 Shock capture

The CBS algorithm introduces naturally some terms to stabilize the oscillations generated by the convective acceleration. However, for compressible high-speed flows, these terms are not sufficient to suppress the oscillations in the vicinity of shocks and some additional artificial viscosity terms need to be added ([Chapter 7](#)). We have given two different forms of artificial viscosities based on the second derivative of pressure in the program. Another possibility is to use anisotropic shock capturing based on the residual of individual equations solved. However we have not used the second alternative in the program as the second derivative-based procedures give quite satisfactory results for all high-speed flow problems.

In the first method implemented, we need to calculate a pressure switch ([Chapter 7](#)) from the nodal pressure values. We calculate the inner nodal switch as ([Fig. 15.1](#))

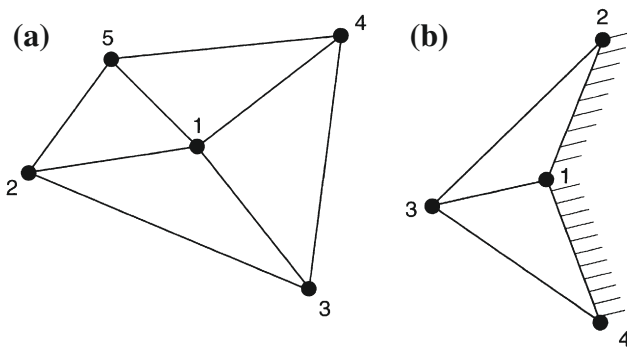
$$S_1 = \frac{|4p_1 - p_2 - p_3 - p_4 - p_5|}{|p_1 - p_2| + |p_1 - p_3| + |p_1 - p_4| + |p_1 - p_5|} \quad (15.1)$$

and for the boundary node we calculate

$$S_1 = \frac{|5p_1 - 2p_2 - p_3 - 2p_4|}{2|p_1 - p_2| + |p_1 - p_3| + 2|p_1 - p_4|} \quad (15.2)$$

The nodal quantities calculated in a manner described above are averaged over elements.

In the next option available in the code, the second derivative of pressure is calculated from the smoothed nodal pressure gradients ([Chapter 4](#)) by averaging. Other approximations to the second derivative of pressure are described in [Chapter 4](#). The user can employ those methods to approximate the second derivative of pressure if desired.

**FIGURE 15.1**

Typical element patches: (a) interior node; (b) boundary node.

15.3.3 CBS algorithm: Steps

In the subroutine `step1` we calculate the temperature-dependent viscosity at the beginning according to Sutherland's relation (see [Chapter 7](#)). The averaged viscosity values over each element are used in the diffusion terms of the momentum equation and dissipation terms of the energy equation. The diffusion, convective and stabilization terms are integrated over elements and assembled appropriately to the RHS vector. The integration is carried out directly. Finally the RHS vector is divided by the lumped mass matrices and the values of intermediate momentum variables are established.

In step 2, in explicit form, the density/pressure values are calculated. The subroutine `step2` is used for this purpose. Here the option of using different values of θ_1 and θ_2 is available. In explicit form θ_2 is identically equal to zero and θ_1 varies between 0.5 and 1.0. For compressible flow computations, the semi-implicit form with θ_2 greater than zero has little advantage over the fully explicit form. For this reason we have not given the semi-implicit form for compressible flow problems in the program.

The third step is the one where the intermediate momentum variables are corrected to get the real values of the intermediate momentum. In all three steps, mass matrices are lumped if the fully explicit form of the algorithm is used. As mentioned in earlier chapters, this is the best way to accelerate the steady-state solution along with local time stepping. However, in problems where transient solutions are of importance, either a mass matrix correction as given in [Chapter 2](#) or simultaneous solution using a consistent mass matrix may be necessary. The dual time stepping approach used in [Chapter 3](#) may also be used.

15.3.4 Boundary conditions

As explained before, the boundary edges are stored along with the elements to which they belong. Also in the same array `inside(i, j)` the flags necessary to inform the solution module about the type of boundary conditions are stored. In this array

$i = 1, 2$ correspond to the node numbers of any boundary side of an element, $i = 3$ indicates the element to which the particular edge belongs, and $i = 4$ is the flag which indicates the type of boundary condition (a complete list is given in the user manual available at the web page). Here j is the boundary edge number.

15.3.5 Solution of simultaneous equations: Semi-implicit form

The simultaneous equations need to be solved for the semi-implicit form of the CBS algorithm. Two types of solvers are provided. The first one is a banded solver which is effective when structured meshes are used. For this the half-bandwidth is necessary in order to proceed further. The second solver is a conjugate gradient solver. The latter can be used to solve both structured and unstructured meshes. The details of procedures for solving simultaneous equations can be found in Ref. [3].

15.3.6 Different forms of energy equation

In compressible flow computations only the fully conservative form of all equations ensures correct position of shocks. Thus in the compressible flow code, the energy equation is solved in its conservative form with the variable being the energy. However for incompressible flow computations, the energy equation can be written in terms of the temperature variable and the dissipation terms can be neglected. In general for compressible flows, Eq. (3.14) is used, and Eq. (4.6) is used for incompressible flow problems.

15.3.7 Convergence to steady state

The residuals (difference between the current and previous time step values of parameters) of all equations are checked at every few user-prescribed number of iterations. If the required convergence (steady state) is achieved, the program stops automatically. The aimed residual value is prescribed by the user. The program calculates the L_2 norm of the residual of each variable over the domain. The user can use them to fix the required accuracy.

15.4 Output module

If the imposed convergence criteria are satisfied then the output is written into a separate file. The user can modify the output according to the requirements of the postprocessor employed. The formats for Tecplot [4] and ParaView [5] are provided.

References

- [1] I. Smith, D.V. Griffiths, Programming the Finite Element Method, Wiley, Chichester, 1998.
- [2] D.R. Willé, Advanced Scientific Fortran, Wiley, Chichester, 1995.

- [3] O.C. Zienkiewicz, R.L. Taylor, J.Z. Zhu, *The Finite Element Method: Its Basis and Fundamentals*, seventh ed., Elsevier, Oxford, 2013.
- [4] Tecplot, Inc., Bellevue, Washington, Tecplot: Visualization software. <www.tecplot.com>.
- [5] Sandia National Laboratories, Paraview: Visualization software. <www.paraview.org>.

Self-Adjoint Differential Equations

A

Let us consider the following system of linear partial differential equation to demonstrate the property of self-adjointness:

$$\mathbf{A}(\mathbf{u}) = \mathcal{L}\mathbf{u} + \mathbf{b} = \mathbf{0} \quad (\text{A.1})$$

where \mathcal{L} is a linear differential operator. For the above equation to be self-adjoint the operator \mathcal{L} requires

$$\int_{\Omega} \psi^T (\mathcal{L}\gamma) d\Omega = \int_{\Omega} \gamma^T (\mathcal{L}\psi) d\Omega + \text{b.t} \quad (\text{A.2})$$

for any two functions ψ and γ . In the above equation b.t stands for boundary integral terms.

B

Nonconservative Form of Navier-Stokes Equations

To derive the Navier-Stokes equations in their nonconservative form, we start with the conservative form.

Conservation of mass:

$$\frac{\partial \rho}{\partial t} + \frac{\partial(\rho u_i)}{\partial x_i} = \frac{\partial \rho}{\partial t} + \rho \frac{\partial u_i}{\partial x_i} + u_i \frac{\partial \rho}{\partial x_i} = 0 \quad (\text{B.1})$$

Conservation of momentum:

$$\frac{\partial(\rho u_i)}{\partial t} + \frac{\partial(u_j \rho u_i)}{\partial x_j} - \frac{\partial \tau_{ij}}{\partial x_j} + \frac{\partial p}{\partial x_i} = 0 \quad (\text{B.2})$$

Conservation of energy:

$$\frac{\partial(\rho E)}{\partial t} + \frac{\partial(u_j \rho E)}{\partial x_j} - \frac{\partial}{\partial x_i} \left(k \frac{\partial T}{\partial x_i} \right) + \frac{\partial(u_j p)}{\partial x_j} - \frac{\partial(\tau_{ij} u_j)}{\partial x_j} = 0 \quad (\text{B.3})$$

Rewriting the momentum equation with terms differentiated as

$$\rho \frac{\partial u_i}{\partial t} + u_i \left(\frac{\partial \rho}{\partial t} + \rho \frac{\partial u_j}{\partial x_j} + u_j \frac{\partial \rho}{\partial x_j} \right) + \rho u_j \frac{\partial u_i}{\partial x_j} - \frac{\partial \tau_{ij}}{\partial x_j} + \frac{\partial p}{\partial x_i} = 0 \quad (\text{B.4})$$

and substituting the equation of mass conservation [Eq. (B.1)] into the above equation gives the reduced momentum equation

$$\frac{\partial u_i}{\partial t} + u_j \frac{\partial u_i}{\partial x_j} - \frac{1}{\rho} \frac{\partial \tau_{ij}}{\partial x_j} + \frac{1}{\rho} \frac{\partial p}{\partial x_i} = 0 \quad (\text{B.5})$$

Similarly as above, the energy equation [Eq. (B.3)] can be written with differentiated terms as

$$\begin{aligned} E & \left(\frac{\partial \rho}{\partial t} + \rho \frac{\partial u_j}{\partial x_j} + u_j \frac{\partial \rho}{\partial x_j} \right) + \rho \frac{\partial E}{\partial t} + \rho u_j \frac{\partial E}{\partial x_j} - \frac{\partial}{\partial x_i} \left(k \frac{\partial T}{\partial x_i} \right) \\ & + \frac{\partial(u_i p)}{\partial x_i} - \frac{\partial(\tau_{ij} u_j)}{\partial x_i} = 0 \end{aligned} \quad (\text{B.6})$$

Again substituting the continuity equation into the above equation, we have the reduced form of the energy equation

$$\frac{\partial E}{\partial t} + u_j \frac{\partial E}{\partial x_j} - \frac{1}{\rho} \frac{\partial}{\partial x_i} \left(k \frac{\partial T}{\partial x_i} \right) + \frac{1}{\rho} \frac{\partial (u_i p)}{\partial x_i} - \frac{1}{\rho} \frac{\partial (\tau_{ij} u_j)}{\partial x_i} = 0 \quad (\text{B.7})$$

Some authors use Eqs. (B.1), (B.5), and (B.7) to study compressible flow problems. However these nonconservative equations can result in multiple or incorrect solutions in certain cases. This is true especially for high-speed compressible flow problems with shocks. The reader should note that such conservative equations are not suitable for simulation of compressible flow problems.

Computing the Drag Force and Stream Function



C.1 Drag calculation

The drag force is the resistance offered by a body which is equal to the force exerted by the flow on the body at equilibrium conditions. The drag force arises from two different sources. One is from the pressure p acting in the flow direction on the surface of the body (form drag) and the second is due to the force caused by viscosity effects in the flow direction. In general the drag force is characterized by a drag coefficient, defined as

$$C_d = \frac{D}{A_f \frac{1}{2} \rho_a u_a^2} \quad (\text{C.1})$$

where D is the drag force, A_f is the frontal area in the flow direction, and the subscript a indicates the free stream value. The drag force D contains the contributions from both the influence of pressure and friction, i.e.,

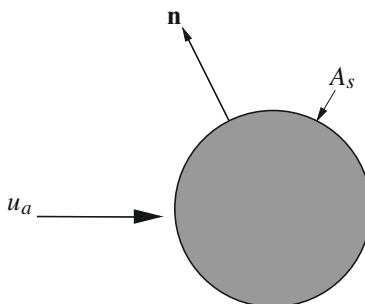
$$D = D_p + D_f \quad (\text{C.2})$$

where D_p is the pressure drag force and D_f is the friction drag force in the flow direction. The pressure drag, or form drag, is calculated from the nodal pressure values. For a two-dimensional problem, the solid wall may be a curve or a line and the boundary elements on the solid wall are one-dimensional with two nodes if linear elements are used. The pressure may be averaged over each one-dimensional element to calculate the average pressure over the boundary element. If this average pressure is multiplied by the length of the element, then the normal pressure acting on the boundary element is obtained. If the pressure force is multiplied by the direction cosine in the flow direction, we obtain the local pressure drag force in the flow direction. Integration of these forces over the solid boundary gives the drag force due to pressure D_p .

The viscous drag force D_f is calculated by integrating the viscous traction in the flow direction, over the surface area. The relation for the total drag force in the x_1 direction may be written for a two-dimensional case as

$$D_{x_1} = \int_{A_s} [(-p + \tau_{11})n_1 + \tau_{12}n_2] dA_s \quad (\text{C.3})$$

where n_1 and n_2 are components of the surface normal \mathbf{n} as shown in Fig. C.1.

**FIGURE C.1**

Normal gradient of velocity close to the wall.

C.2 Stream function

In most two-dimensional fluid dynamics and convection heat transfer problems, it is often easier to understand the flow results if the streamlines are plotted. In order to plot these streamlines, or flow pattern, it is first necessary to calculate the stream function values at the nodes. Lines with constant stream function values are referred to as streamlines. The stream function is defined by the following relationships:

$$\begin{aligned} u_1 &= -\frac{\partial \psi}{\partial x_2} \\ u_2 &= \frac{\partial \psi}{\partial x_1} \end{aligned} \quad (C.4)$$

where ψ is the stream function. If we differentiate the first relation with respect to x_2 and the second with respect to x_1 and then sum, we get the differential equation for the stream function as

$$\frac{\partial^2 \psi}{\partial x_2^2} + \frac{\partial^2 \psi}{\partial x_1^2} = \frac{\partial u_2}{\partial x_1} - \frac{\partial u_1}{\partial x_2} \quad (C.5)$$

A solution to the above second order equation is straightforward for any numerical procedure. This equation is similar to Step 2 of the CBS scheme and an implicit procedure immediately gives the solution. Unlike the pressure equation of Step 2, the stream function of a solution needs to be calculated only once.

Convection-Diffusion Equations: Vector-Valued Variables

D

D.1 The Taylor-Galerkin method used for vector-valued variables

The only method which adapts itself easily to the treatment of vector variables is that of the Taylor-Galerkin procedure. Here we can repeat the steps of [Section 2.7](#) but now addressed to the vector-valued equation with which we started [Chapter 2](#) ([Eq. 2.1](#)), which we rewrite here for convenience. Accordingly,

$$\frac{\partial \Phi}{\partial t} + \frac{\partial \mathbf{F}_i}{\partial x_i} + \frac{\partial \mathbf{G}_i}{\partial x_i} + \mathbf{Q} = \mathbf{0} \quad (\text{D.1})$$

Noting that now Φ has multiple components, expanding Φ by a Taylor series in time we have [\[1,2\]](#)

$$\Phi^{n+1} = \Phi^n + \Delta t \frac{\partial \Phi}{\partial t} \Big|_n + \frac{\Delta t^2}{2} \frac{\partial^2 \Phi}{\partial t^2} \Big|_{n+\theta} \quad (\text{D.2})$$

where θ is a number such that $0 \leq \theta \leq 1$.

From [Eq. \(D.1\)](#),

$$\left[\frac{\partial \Phi}{\partial t} \right]_n = - \left[\frac{\partial \mathbf{F}_i}{\partial x_i} + \frac{\partial \mathbf{G}_i}{\partial x_i} + \mathbf{Q} \right]_n \quad (\text{D.3a})$$

and differentiating

$$\left[\frac{\partial^2 \Phi}{\partial t^2} \right]_{n+\theta} = - \frac{\partial}{\partial t} \left[\frac{\partial \mathbf{F}_i}{\partial x_i} + \frac{\partial \mathbf{G}_i}{\partial x_i} + \mathbf{Q} \right]_{n+\theta} \quad (\text{D.3b})$$

In the above we can write

$$\frac{\partial}{\partial t} \left(\frac{\partial \mathbf{F}_i}{\partial x_i} \right) \equiv \frac{\partial}{\partial x_i} \left(\frac{\partial \mathbf{F}_i}{\partial \Phi} \frac{\partial \Phi}{\partial t} \right) = - \frac{\partial}{\partial x_i} \left[\mathbf{A}_i \left(\frac{\partial \mathbf{F}_j}{\partial x_j} + \frac{\partial \mathbf{G}_j}{\partial x_j} + \mathbf{Q} \right) \right] \quad (\text{D.3c})$$

where $\mathbf{A}_i \equiv \partial \mathbf{F}_i / \partial \Phi$.

If $\mathbf{Q} = \mathbf{Q}(\Phi, x)$ and $\partial \mathbf{Q} / \partial \Phi = \mathbf{S}$, then

$$\frac{\partial \mathbf{Q}}{\partial t} = \frac{\partial \mathbf{Q}}{\partial \Phi} \frac{\partial \Phi}{\partial t} = - \mathbf{S} \left(\frac{\partial \mathbf{F}_i}{\partial x_i} + \frac{\partial \mathbf{G}_i}{\partial x_i} + \mathbf{Q} \right) \quad (\text{D.3d})$$

and we can therefore approximate Eq. (D.2) as

$$\begin{aligned}\Delta\Phi^n &\equiv \Phi^{n+1} - \Phi^n \\ &= -\Delta t \left[\frac{\partial \mathbf{F}_i}{\partial x_i} + \frac{\partial \mathbf{G}_i}{\partial x_i} + \mathbf{Q} \right]_n + \frac{\Delta t^2}{2} \left\{ \frac{\partial}{\partial x_i} \left[\mathbf{A}_i \left(\frac{\partial \mathbf{F}_j}{\partial x_j} + \frac{\partial \mathbf{G}_j}{\partial x_j} + \mathbf{Q} \right) \right] \right. \\ &\quad \left. + \frac{\partial}{\partial t} \frac{\partial \mathbf{G}_i}{\partial x_i} + \mathbf{S} \left(\frac{\partial \mathbf{F}_j}{\partial x_j} + \frac{\partial \mathbf{G}_j}{\partial x_j} + \mathbf{Q} \right) \right\}_{n+\theta}\end{aligned}\quad (\text{D.4})$$

Omitting the second derivatives of \mathbf{G}_i and interpolating the $n+\theta$ between n and $n+1$ values and applying $n+\theta$ to \mathbf{G}_i term we have

$$\begin{aligned}\Delta\Phi &\equiv \Phi^{n+1} - \Phi^n \\ &= -\Delta t \left[\frac{\partial \mathbf{F}_i}{\partial x_i} + \mathbf{Q} \right]_n - \Delta t \left(\left[\frac{\partial \mathbf{G}_i}{\partial x_i} \right]_{n+1} \theta + \left[\frac{\partial \mathbf{G}_i}{\partial x_i} \right]_n (1-\theta) \right) \\ &\quad + \frac{\Delta t^2}{2} \left[\frac{\partial}{\partial x_i} \left\{ \mathbf{A}_i \left(\frac{\partial \mathbf{F}_j}{\partial x_j} + \mathbf{Q} \right) \right\} + \mathbf{S} \left(\frac{\partial \mathbf{F}_j}{\partial x_j} + \mathbf{Q} \right) \right]_{n+1} \theta \\ &\quad + \frac{\Delta t^2}{2} \left[\frac{\partial}{\partial x_i} \left\{ \mathbf{A}_i \left(\frac{\partial \mathbf{F}_j}{\partial x_j} + \mathbf{Q} \right) \right\} + \mathbf{S} \left(\frac{\partial \mathbf{F}_j}{\partial x_j} + \mathbf{Q} \right) \right]_n (1-\theta)\end{aligned}\quad (\text{D.5})$$

At this stage a standard Galerkin approximation is applied which will result in a discrete, time-stepping scheme. As the explicit form is of particular interest we shall only give the details of the discretization process for $\theta = 0$. Writing as usual

$$\Phi \approx \mathbf{N}\tilde{\Phi}$$

we have

$$\begin{aligned}\left(\int_{\Omega} \mathbf{N}^T \mathbf{N} d\Omega \right) \Delta\tilde{\Phi} &= -\Delta t \left[\int_{\Omega} \mathbf{N}^T \left(\frac{\partial \mathbf{F}_i}{\partial x_i} + \frac{\partial \mathbf{G}_i}{\partial x_i} + \mathbf{Q} \right) d\Omega \right. \\ &\quad \left. - \frac{\Delta t}{2} \int_{\Omega} \mathbf{N}^T \frac{\partial}{\partial x_i} \left\{ \mathbf{A}_i \left(\frac{\partial \mathbf{F}_j}{\partial x_j} + \frac{\partial \mathbf{G}_j}{\partial x_j} + \mathbf{Q} \right) \right\} d\Omega \right. \\ &\quad \left. - \frac{\Delta t}{2} \int_{\Omega} \mathbf{N}^T \mathbf{S} \left(\frac{\partial \mathbf{F}_j}{\partial x_j} + \frac{\partial \mathbf{G}_j}{\partial x_j} + \mathbf{Q} \right) d\Omega \right]_n\end{aligned}\quad (\text{D.6})$$

This can be written in a compact matrix form similar to Eq. (2.107) as

$$\mathbf{M} \Delta\tilde{\Phi} = -\Delta t [(\mathbf{C} + \mathbf{K}_u + \mathbf{K}) \tilde{\Phi} + \mathbf{f}]^n \quad (\text{D.7a})$$

in which, with

$$\mathbf{G}_i = -k_{ij} \frac{\partial \Phi}{\partial x_j}$$

we have (on omitting the third derivative terms and the effect of \mathbf{S}) matrices of the form of Eq. (2.108), i.e.,

$$\begin{aligned}\mathbf{C} &= \int_{\Omega} \mathbf{N}^T \mathbf{A}_i \frac{\partial \mathbf{N}}{\partial x_i} d\Omega \\ \mathbf{K}_u &= \int_{\Omega} \frac{\partial \mathbf{N}^T}{\partial x_i} \left(\mathbf{A}_i \mathbf{A}_j \frac{\Delta t}{2} \right) \frac{\partial \mathbf{N}}{\partial x_j} d\Omega \\ \mathbf{K} &= \int_{\Omega} \frac{\partial \mathbf{N}^T}{\partial x_i} k_{ij} \frac{\partial \mathbf{N}}{\partial x_j} d\Omega \\ \mathbf{f} &= \int_{\Omega} \left(\mathbf{N}^T + \frac{\Delta t}{2} \mathbf{A}_i \frac{\partial \mathbf{N}^T}{\partial x_i} \right) \mathbf{Q} d\Omega + \text{boundary terms} \\ \mathbf{M} &= \int_{\Omega} \mathbf{N}^T \mathbf{N} d\Omega\end{aligned}\tag{D.7b}$$

With $\theta = 1/3$ it can be shown that the order of approximation increases and for this scheme a simple iterative solution is possible [3]. We note that with the consistent mass matrix \mathbf{M} the stability limit for $\theta = 1/3$ is increased to $C = 1$.

Use of $\theta = 1/3$ apparently requires an implicit solution. However, similar iteration to that used in Eq. (2.118) is rapidly convergent and the scheme can be used quite economically.

D.2 Two-step predictor-corrector methods: Two-step Taylor-Galerkin operation

There are of course various alternative procedures for improving the temporal approximation other than the Taylor expansion used in the previous section. Such procedures will be particularly useful if the evaluation of the derivative matrix \mathbf{A}_i can be avoided. In this section we shall consider two predictor-corrector schemes (of the Runge-Kutta type) that avoid the evaluation of this matrix and are explicit.

The first starts with a standard Galerkin space approximation being applied to the basic Eq. (D.1). This results in the form

$$\mathbf{M} \frac{d\tilde{\Phi}}{dt} \equiv \mathbf{M} \dot{\tilde{\Phi}} = \mathbf{P}_C + \mathbf{P}_D + \mathbf{f} = \Psi\tag{D.8}$$

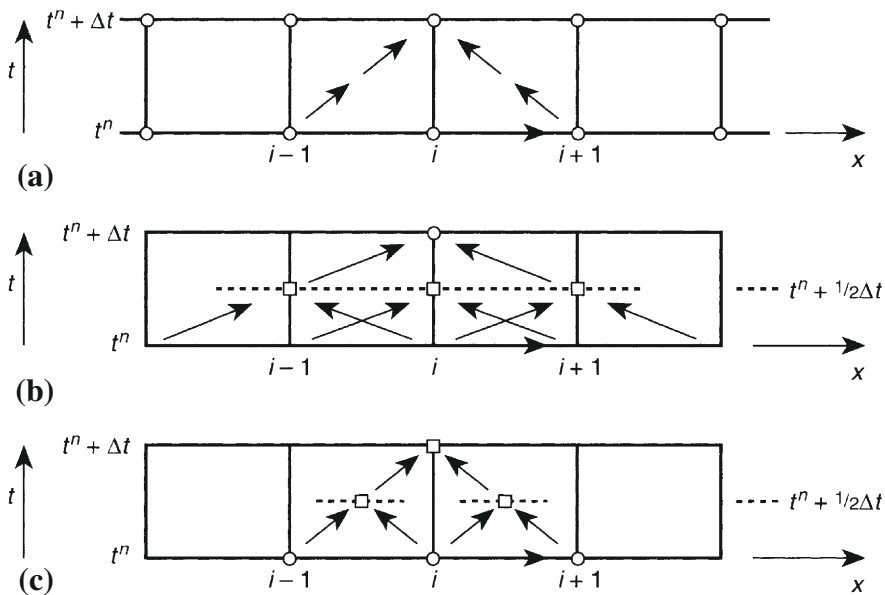
where again \mathbf{M} is the standard mass matrix, \mathbf{f} the prescribed “forces,” and

$$\mathbf{P}_C(\Phi) = \int_{\Omega} \mathbf{N}^T \frac{\partial \mathbf{F}_i}{\partial x_i} d\Omega\tag{D.9a}$$

represents the convective “forces,” while

$$\mathbf{P}_D(\Phi) = \int_{\Omega} \mathbf{N}^T \frac{\partial \mathbf{G}_i}{\partial x_i} d\Omega\tag{D.9b}$$

are the diffusive ones.

**FIGURE D.1**

Progression of information in explicit one- and two-step schemes: (a) single-step explicit; (b) standard predictor-corrector; (c) local predictor-corrector (two-step Taylor-Galerkin).

If an explicit time integration scheme is used, i.e.,

$$\mathbf{M}\Delta\Phi \equiv \mathbf{M}(\tilde{\Phi}^{n+1} - \tilde{\Phi}^n) = \Delta t \Psi^n \quad (\text{D.10})$$

the evaluation of the right-hand side does not require the matrix product representation and \mathbf{A}_i does not have to be computed.

Of course the scheme presented is not accurate for the various reasons previously discussed, and indeed becomes *unconditionally unstable* in the absence of diffusion and external force vectors.

The reader can easily verify that in the case of the linear one-dimensional problem the right-hand side is equivalent to a central difference scheme with $\tilde{\Phi}_{i-1}^n$ and $\tilde{\Phi}_{i+1}^n$ only being used to find the value of $\tilde{\Phi}_i^{n+1}$, as shown in Fig. D.1a.

The scheme can, however, be recast as a two-step, predictor-corrector operation and conditional stability is regained. Now we proceed as follows:

Step 1. Compute $\tilde{\Phi}^{n+1/2}$ using an explicit approximation of Eq. (D.10), i.e.,

$$\tilde{\Phi}^{n+1/2} = \tilde{\Phi}^n + \frac{\Delta t}{2} \mathbf{M}^{-1} \Psi^n \quad (\text{D.11})$$

and

Step 2. Compute $\tilde{\Phi}^{n+1}$ inserting the improved value of $\tilde{\Phi}^{n+1/2}$ in the right-hand side of Eq. (D.10), giving

$$\tilde{\Phi}^{n+1} = \tilde{\Phi}^n + \Delta t \mathbf{M}^{-1} \Psi^{n+1/2} \quad (\text{D.12})$$

This is precisely equivalent to the second-order Runge-Kutta scheme being applied to the ordinary system of differential equations (D.8). Figure D.1b shows in the one-dimensional example how the information “spreads,” i.e., that now $\tilde{\Phi}_i^{n+1}$ will be dependent on values at nodes $i - 2, \dots, i + 2$.

It is found that the scheme, though stable, is overdissusive and numerical results are poor.

An alternative is possible, however, using a two-step Taylor-Galerkin operation. Here we return to Eq. (D.1) and proceed as follows in semi-discrete form

Step 1. Find an improved value of $\Phi^{n+1/2}$ using only the convective and source parts. Thus

$$\Phi^{n+1/2} = \Phi^n - \frac{\Delta t}{2} \left(\frac{\partial \mathbf{F}_i^n}{\partial x_i} + \mathbf{Q}^n \right) \quad (\text{D.13a})$$

which of course allows the evaluation of $\mathbf{F}_i^{n+1/2}$.

We note, however, that we can also write an approximate expansion as

$$\begin{aligned} \mathbf{F}_i^{n+1/2} &= \mathbf{F}_i^n + \frac{\Delta t}{2} \frac{\partial \mathbf{F}_i^n}{\partial t} = \mathbf{F}_i^n - \frac{\Delta t}{2} \mathbf{A}_i^n \frac{\partial \Phi^n}{\partial t} \\ &= \mathbf{F}_i^n - \frac{\Delta t}{2} \mathbf{A}_i^n \left(\frac{\partial \mathbf{F}_j}{\partial x_j} + \frac{\partial \mathbf{G}_j}{\partial x_j} + \mathbf{Q} \right)^n \end{aligned} \quad (\text{D.13b})$$

This gives

$$\mathbf{A}_i^n \left(\frac{\partial \mathbf{F}_j}{\partial x_j} + \frac{\partial \mathbf{G}_j}{\partial x_j} + \mathbf{Q} \right)^n = -\frac{2}{\Delta t} (\mathbf{F}_i^{n+1/2} - \mathbf{F}_i^n) \quad (\text{D.13c})$$

Step 2. Substituting the above into the Taylor-Galerkin approximation of Eq. (D.6) we have

$$\begin{aligned} \mathbf{M} \Delta \tilde{\Phi} &= -\Delta t \left[\int_{\Omega} \mathbf{N}^T \left(\frac{\partial \mathbf{F}_i}{\partial x_i} + \frac{\partial \mathbf{G}_i}{\partial x_i} + \mathbf{Q} \right)^n d\Omega \right. \\ &\quad \left. + \int_{\Omega} \mathbf{N}^T \frac{\partial}{\partial x_i} (\mathbf{F}_i^{n+1/2} - \mathbf{F}_i^n) d\Omega + \int_{\Omega} \mathbf{N}^T \mathbf{S} (\mathbf{F}_i^{n+1/2} - \mathbf{F}_i^n) d\Omega \right] \end{aligned} \quad (\text{D.13d})$$

and after integration by parts of the terms with respect to the x_i derivatives we obtain simply

$$\begin{aligned} \mathbf{M}\Delta\tilde{\Phi} = -\Delta t & \left\{ -\int_{\Omega} \frac{\partial \mathbf{N}^T}{\partial x_i} (\mathbf{F}_i^{n+1/2} + \mathbf{G}_i^n) d\Omega \right. \\ & \left. + \int_{\Omega} \mathbf{N}^T [\mathbf{Q} + \mathbf{S}(\mathbf{F}^{n+1/2} - \mathbf{F}^n)] d\Omega + \int_{\Gamma} \mathbf{N}^T (\mathbf{F}_i^{n+1/2} + \mathbf{G}_i^n) \mathbf{n}_i d\Gamma \right\} \end{aligned} \quad (\text{D.14})$$

We note immediately that:

1. The above expression is identical to *using a standard Galerkin approximation on Eq. (D.1)* and an explicit step with \mathbf{F}_i values updated by the simple Eq. (D.13a).
 2. The final form of Eq. (D.14) does not require the evaluation of the matrices \mathbf{A}_i resulting in substantial computation savings as well as yielding essentially the same results. Indeed, some omissions made in deriving Eq. (D.7a) did not occur now and presumably the accuracy is improved.
- A further practical point must be noted:
3. In nonlinear problems it is convenient to interpolate \mathbf{F}_i directly in the finite element manner as

$$\mathbf{F}_i = \mathbf{N}\tilde{\mathbf{F}}_i$$

rather than to compute it as $\mathbf{F}_i(\tilde{\Phi})$.

Thus the evaluation of $\mathbf{F}_i^{n+1/2}$ need only be made at the quadrature (integration) points within the element, and the evaluation of $\tilde{\Phi}^{n+1/2}$ by Eq. (D.13a) is only done on such points. For a linear triangle element this reduces to a single evaluation of $\tilde{\Phi}^{n+1/2}$ and $\mathbf{F}^{n+1/2}$ for each element at its barycenter, taking of course $\tilde{\Phi}^{n+1/2}$ and $\mathbf{F}^{n+1/2}$ as the appropriate interpolation average there.

In the simple one-dimensional linear example the information progresses in the manner shown in Fig. D.1c. The scheme, which originated at Swansea, can be appropriately called the *Swansea two step* [4–14], and has found much use in the direct solution of compressible high-speed gas flow equations. We presented some of the results obtained by this procedure in Chapter 7. In Chapter 3 we discussed an alternative which is more general and has better performance. It is of interest to remark that the Taylor-Galerkin procedure can be used in contexts other than direct fluid mechanics. The procedure has been used efficiently by Morgan et al. [15] in solving electromagnetic wave problems.

D.2.1 Multiple wave speeds

When ϕ is a scalar variable, a single wave speed will arise in the manner in which we have already shown at the beginning of Part II of Chapter 2. When a vector variable is considered, the situation is very different and in general the number of wave speeds

will correspond to the number of variables. If we return to the general equation (D.1), we can write this in the form

$$\frac{\partial \Phi}{\partial t} + \mathbf{A}_i \frac{\partial \Phi}{\partial x_i} + \frac{\partial \mathbf{G}_i}{\partial x_i} + \mathbf{Q} = \mathbf{0} \quad (\text{D.15})$$

where \mathbf{A}_i is a matrix of the size corresponding to the variables in the vector $\tilde{\Phi}$. This is equivalent to the single convective velocity component $A = U$ in a scalar problem and is given as

$$\mathbf{A}_i \equiv \frac{\partial \mathbf{F}_i}{\partial \Phi} \quad (\text{D.16})$$

This in general may still be a function of Φ , thus destroying the linearity of the problem.

Before proceeding further, it is of interest to discuss the general behavior of Eq. (D.1) in the absence of source and diffusion terms. We note that the matrices \mathbf{A}_i can be represented as

$$\mathbf{A}_i = \mathbf{X}_i \Lambda_i \mathbf{X}_i^{-1} \quad (\text{D.17})$$

by a standard eigenvalue analysis in which Λ_i is a diagonal matrix.

If the eigenvector matrices \mathbf{X}_i are such that

$$\mathbf{X}_i = \mathbf{X} \quad (\text{D.18})$$

which is always the case in a single dimension, then Eq. (D.15) can be written (in the absence of diffusion or source terms) as

$$\frac{\partial \Phi}{\partial t} + \mathbf{X} \Lambda_i \mathbf{X}^{-1} \frac{\partial \Phi}{\partial x_i} = \mathbf{0} \quad (\text{D.19})$$

Premultiplying by \mathbf{X}^{-1} and introducing new variables (called Riemann invariants) such that

$$\phi = \mathbf{X}^{-1} \Phi \quad (\text{D.20})$$

we can write the above as a set of decoupled equations in components ϕ of Φ and corresponding Λ of Λ :

$$\frac{\partial \phi}{\partial t} + \Lambda_i \frac{\partial \phi}{\partial x_i} = 0 \quad (\text{D.21})$$

each of which represents a wave-type equation of the form that we have previously discussed. A typical example of the above results from a one-dimensional elastic dynamics problem describing stress waves in a bar in terms of stresses (σ) and velocities (v) as

$$\begin{aligned} \frac{\partial \sigma}{\partial t} - E \frac{\partial v}{\partial x} &= 0 \\ \frac{\partial v}{\partial t} - \frac{1}{\rho} \frac{\partial \sigma}{\partial x} &= 0 \end{aligned}$$

This can be written in the standard form of Eq. (D.1) with

$$\Phi = \begin{Bmatrix} \sigma \\ v \end{Bmatrix} \quad \mathbf{F} = \begin{Bmatrix} Ev \\ \sigma/\rho \end{Bmatrix}$$

The two variables of Eq. (D.20) become

$$\phi_1 = \sigma - c v \quad \text{and} \quad \phi_2 = \sigma + c v$$

where $c = \sqrt{E/\rho}$ and the equations corresponding to (D.21) are

$$\begin{aligned} \frac{\partial \phi_1}{\partial t} + c \frac{\partial \phi_1}{\partial x} &= 0 \\ \frac{\partial \phi_2}{\partial t} - c \frac{\partial \phi_2}{\partial x} &= 0 \end{aligned}$$

representing respectively two waves moving with velocities $\pm c$.

Unfortunately the condition of Eq. (D.18) seldom pertains and hence the determination of general characteristics and therefore decoupling is not usually possible for more than one space dimension. This is the main reason why the extension of the simple, direct procedures is not generally possible for vector variables. Because of this in Chapter 3 we only used the upwinding characteristic-based procedures on scalar systems for which a single wave speed exists and this retains justification of any method proposed.

References

- [1] J. Donea, A Taylor-Galerkin method for convective transport problems, *Int. J. Numer. Methods. Eng.* 20 (1984) 101–119.
- [2] V. Selmin, J. Donea, L. Quattrapelle, Finite element method for non-linear advection, *Comput. Methods. Appl. Mech. Eng.* 52 (1985) 817–845.
- [3] L. Bottura, O.C. Zienkiewicz, Experiments on iterative solution of the semi-implicit characteristic Galerkin algorithm, *Commun. Appl. Numer. Methods* 6 (1990) 387–393.
- [4] O.C. Zienkiewicz, R. Löhner, K. Morgan, S. Nakazawa, Finite elements in fluid mechanics—a decade of progress, in: R.H. Gallagher, et al. (Eds.), *Finite Elements in Fluids*, vol. 5, John Wiley & Sons, Chichester, 1984, pp. 1–26.
- [5] J. Peraire, A finite method for convection dominated flows, Ph.D. Thesis, University of Wales, Swansea, 1986.
- [6] R. Löhner, K. Morgan, J. Peraire, O.C. Zienkiewicz, L. Kong, Finite element methods for compressible flow, in: K.W. Morton, M.J. Baines (Eds.), *Numerical Methods in Fluid Dynamics*, vol. II, Clarendon Press, Oxford, 1986, pp. 27–52.
- [7] J. Peraire, K. Morgan, O.C. Zienkiewicz, Convection dominated problems, in: *Numerical Methods for Compressible Flows—Finite Difference, Element and Volume Techniques*, vol. AMD 78, ASME, New York, 1987, pp. 129–147.

- [8] O.C. Zienkiewicz, J.Z. Zhu, Y.C. Liu, K. Morgan, J. Peraire, Error estimates and adaptivity. From elasticity to high speed compressible flow, in: J. Whiteman (Ed.), *The Mathematics of Finite Elements and Applications*, vol. VII, Academic Press, London, 1988, pp. 483–512.
- [9] J. Peraire, J. Peiro, L. Formaggia, K. Morgan, O.C. Zienkiewicz, Finite element Euler computations in three dimensions, in: AIAA 26th Aerospace Sciences Meeting, Reno, NV, Paper AIAA-87-0032, January 1988.
- [10] J. Peraire, J. Peiro, L. Formaggia, K. Morgan, O.C. Zienkiewicz, Finite element Euler computations in three dimensions, *Int. J. Numer. Methods. Eng.* 26 (1988) 2135–2159.
- [11] R. Löhner, K. Morgan, J. Peraire, M. Vahdati, Finite element, flux corrected transport (FEM–FCT) for the Euler and Navier–Stokes equations, *Int. J. Numer. Methods. Fluids* 7 (1987) 1093–1109.
- [12] R. Löhner, K. Morgan, O.C. Zienkiewicz, The use of domain splitting with an explicit hyperbolic solver, *Comput. Methods. Appl. Mech. Eng.* 45 (1984) 313–329.
- [13] R. Löhner, K. Morgan, An unstructured multigrid method for elliptic problems, *Int. J. Numer. Methods. Eng.* 24 (1987) 101–115.
- [14] O.C. Zienkiewicz, Explicit or semi-explicit general algorithm for compressible and incompressible flows with equal finite element interpolation, Technical Report Report 90/5, Chalmers Technical University, Gothenborg, 1990.
- [15] K. Morgan, O. Hassan, J. Peraire, A time domain unstructured grid approach to simulation of electromagnetic scattering in piecewise homogeneous media, *Comput. Methods. Appl. Mech. Eng.* 134 (1996) 17–36.

Integration Formulae

E

E.1 Linear triangles

Let i , j , and k be the nodes of a triangular element. Integrating over the triangular area gives

$$A = \int dx_1 dx_2 = \frac{1}{2} \begin{vmatrix} 1 & x_{1i} & x_{2i} \\ 1 & x_{1j} & x_{2j} \\ 1 & x_{1k} & x_{2k} \end{vmatrix} \quad (\text{E.1})$$

where A is the area of the triangle. For a linear triangular element (shape functions are the same as local coordinates), the integration of the shape functions can be written as

$$\int_{\Omega} N_i^a N_j^b N_k^c d\Omega = \frac{a!b!c!2A}{(a+b+c+2)!} \quad (\text{E.2})$$

On the boundaries

$$\int_{\Gamma} N_i^a N_j^b d\Gamma = \frac{a!b!l}{(a+b+1)!} \quad (\text{E.3})$$

Note that $i - j$ is assumed to be the boundary side. The above equation is identical to the integration formula of a one-dimensional linear element. In the above equation l is the length of a boundary side.

E.2 Linear tetrahedron

Let i , j , k , and m be the nodes of a linear tetrahedron element. Integrating over the volume gives

$$V = \int dx_1 dx_2 dx_3 = \frac{1}{6} \begin{vmatrix} 1 & x_{1i} & x_{2i} & x_{3i} \\ 1 & x_{1j} & x_{2j} & x_{3j} \\ 1 & x_{1k} & x_{2k} & x_{3k} \\ 1 & x_{1m} & x_{2m} & x_{3m} \end{vmatrix} \quad (\text{E.4})$$

where V is the volume of a tetrahedron. For linear shape functions, the integration formula can be written as

$$\int_{\Omega} N_i^a N_j^b N_k^c N_m^d d\Omega = \frac{a!b!c!d!6V}{(a+b+c+d+3)!} \quad (\text{E.5})$$

On the boundaries

$$\int_{\Gamma} N_i^a N_j^b N_k^c d\Gamma = \frac{a!b!c!2A}{(a+b+c+2)!} \quad (\text{E.6})$$

Note that the above formula is identical to the integration formula of triangular elements within the domain. In the above equation A is the area of a triangular face.

Edge-Based Finite Element Formulation

F

Edge-based data structures have been used in many finite element formulations for flow problems. As mentioned in [Section 7.9, Chapter 7](#), this formulation has many advantages such as smaller storage, etc. To explain the formulation we shall consider the Euler equations and a few assembled linear triangular elements on a two-dimensional finite element mesh as shown in [Fig. F.1](#). From [Eq. \(1.25\)](#) we rewrite the following Euler equations:

$$\frac{\partial \Phi}{\partial t} + \frac{\partial \mathbf{F}_i}{\partial x_i} = \mathbf{0} \quad (\text{F.1})$$

where Φ are the conservation variables. If the element-based formulation for the above equation omits the stabilization terms, the weak form can be written we get

$$\int_{\Omega} \mathbf{N}^T \frac{\Delta \Phi}{\Delta t} d\Omega = - \int_{\Omega} \mathbf{N}^T \frac{\partial \mathbf{F}_i}{\partial x_i} d\Omega \quad (\text{F.2})$$

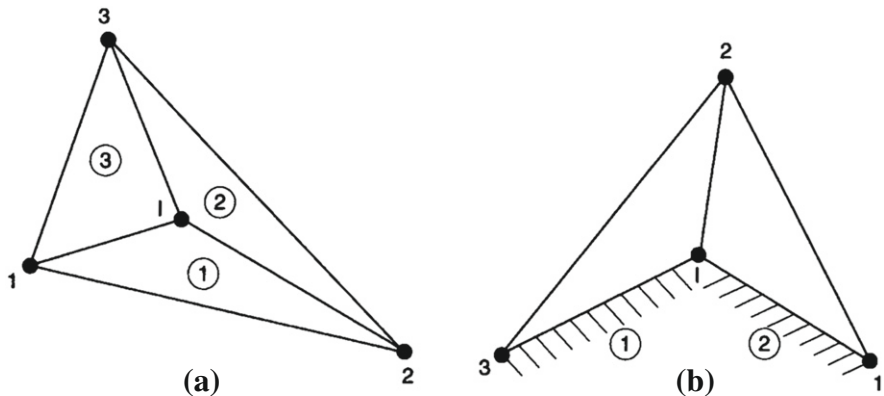
In a fully explicit form of solution procedure, the left-hand side becomes $\mathbf{M}(\Delta \Phi / \Delta t)$ and here \mathbf{M} is the consistent mass matrix (see [Chapter 3](#)). We can write the RHS of the above equation for an interior node I ([Fig. F.1a](#)) by interpolating \mathbf{F}_i in each element and after applying Green's theorem we get

$$\sum_{E \in I} \int_{A_E} \frac{\partial N_I}{\partial x_i} \sum_k (N_k \mathbf{F}_i^k) d\Omega = \sum_{E \in I} \left[\frac{A_E}{3} \frac{\partial N_I}{\partial x_i} \right]_E (\mathbf{F}_i^I + \mathbf{F}_i^J + \mathbf{F}_i^K) \quad (\text{F.3})$$

where A_E is the area and I , J , and K are the three nodes of the element (triangle) E . This is an acceptable added approximation which is frequently used in the Taylor-Galerkin method (see [Chapter 2](#)). In another form, the above RHS can be written as ([Fig. F.1a](#))

$$\frac{A_1}{3} \frac{\partial N_I}{\partial x_i} (\mathbf{F}_i^I + \mathbf{F}_i^1 + \mathbf{F}_i^2) + \frac{A_2}{3} \frac{\partial N_I}{\partial x_i} (\mathbf{F}_i^I + \mathbf{F}_i^2 + \mathbf{F}_i^3) + \frac{A_3}{3} \frac{\partial N_I}{\partial x_i} (\mathbf{F}_i^I + \mathbf{F}_i^3 + \mathbf{F}_i^1) \quad (\text{F.4})$$

where A_1 , A_2 , and A_3 are the areas of elements 1, 2, and 3, respectively. For integration over the boundary on the RHS, we can write the following in the element formulation:

**FIGURE F.1**

Typical patch of linear triangular elements: (a) inside node; (b) boundary node.

$$\sum_{B \in I} \int_{\Gamma_B} N_I(N_k \mathbf{F}_i^k) d\Gamma \mathbf{n}_B = \sum_{B \in I} \left[\frac{\Gamma_B}{6} (2\mathbf{F}_i^I + \mathbf{F}_i^J) \mathbf{n} \right]_B \quad (\text{F.5})$$

where \mathbf{n} is the boundary normal. The above equation can be rewritten for the node I in Fig. F.1b as

$$\frac{\Gamma_{B1}}{6} (2\mathbf{F}_i^I + \mathbf{F}_i^3) \mathbf{n}_1 + \frac{\Gamma_{B2}}{6} (2\mathbf{F}_i^I + \mathbf{F}_i^1) \mathbf{n}_2 \quad (\text{F.6})$$

where Γ_{B1} and Γ_{B2} are appropriate edge lengths.

The above Eqs. (F.3) and (F.5) can be reformulated for an edge-based data structure. In such a procedure, (Eq. F.3) can be rewritten as (for an interior node I)

$$\sum_{E \in I} \int_{\Omega_E} \frac{\partial N_I}{\partial x_i} (N_k \mathbf{F}_i^k) d\Omega = \sum_{S=1}^{m_s} \left\{ \sum_{E \in II_s} \left[\frac{A_E}{3} \frac{\partial N_I}{\partial x_i} \right]_E (\mathbf{F}_i^I + \mathbf{F}_i^{I_s}) \right\} \quad (\text{F.7})$$

where m_s is the number of edges in the mesh which are directly connected to the node I and the summation $\sum_{E \in II_s}$ extends over those elements that contain the edges II_s . The coefficient in Eq. (F.7) is

$$C_i^{II_s} = \sum_{E=II_s} \frac{A_E}{3} \left[\frac{\partial N_I}{\partial x_i} \right]_E \quad (\text{F.8})$$

It can be easily verified that

$$\sum_{S=1}^{m_s} C_i^{II_s} = 0 \quad (\text{F.9})$$

for all i . The user can now readily verify that the above equation is identically equal to the standard element formulation of Eq. (F.4) if we consider the node I in Fig. F.1(a). For the boundary nodes, however, Eq. (F.9) is not satisfied and thus the element formulation is not reproduced. For the boundary edges, in addition to Eqs. (F.6) and (F.7) the following addition is necessary

$$-\left[\frac{\Gamma_{B1}}{6} \mathbf{n}_1 + \frac{\Gamma_{B2}}{6} \mathbf{n}_2 \right] \mathbf{F}_i^I \quad (\text{F.10})$$

Boundary Layer–Inviscid Flow Coupling

G

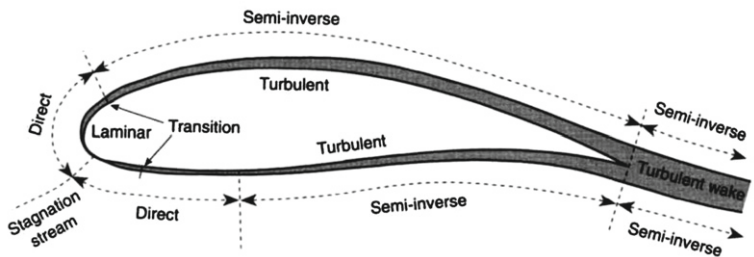
A few references on the topic of boundary layer–inviscid flow coupling are given in [Chapter 7](#). In this appendix we shall briefly explain a simple procedure of this flow coupling procedure. To understand the process of coupling the Euler and integral boundary solutions we shall consider a typical flow pattern around a wing as shown in [Fig. G.1](#). Both turbulent and laminar regimes are shown in this figure.

We summarize the procedure as follows.

- Step 1** Solve the Euler equations in the domain considered around the aerofoil. Here any mesh can be used independently of the mesh used for the boundary layer solution. The solution thus obtained will give a pressure distribution on the surface of the wing.
- Step 2** Solve the boundary layer using an integral approach over an independently generated surface mesh. If the surface nodes do not coincide with the Euler mesh, the pressure needs to be interpolated to couple the two solutions. The laminar portion near the boundary ([Fig. G.1](#)) is calculated by the “Thwaites compressible” method and the turbulent region is predicted by the “lag-entrainment” integral boundary layer model.
- Step 3** The Euler and integral solutions are coupled by transferring the outputs from one solution to the other. As indicated in [Fig. G.1](#), direct and semi-inverse couplings can be used for different regions. The semi-inverse coupling is introduced here mainly to stabilize the solution in the turbulent region close to separation. [Fig. G.2](#) shows the flow diagrams for the present boundary layer–inviscid coupling.

Further details on the Thwaites compressible method and semi-inverse coupling can be found in the references discussed in [Section 7.13, Chapter 7](#) (Le Balleur and coworkers).

In [Fig. G.2](#), C_p is the coefficient of pressure; s is the coordinate along the surface; δ is the boundary layer thickness; θ is the momentum thickness; C_f is the skin friction coefficient; H is the velocity profile shape parameter; ρ is the density; V_N is the transpiration velocity; K^* is a factor developed from stability analysis; the subscript v marks the viscous boundary layer region; δ^* is the displacement thickness; the superscript i indicates the inviscid region; and the superscript m indicates the current iteration.

**FIGURE G.1**

Flow past an aerofoil. Typical problem for boundary layer–inviscid flow coupling.

Following are useful relations for some of the above quantities:

$$H = \frac{\delta^*}{\theta}, \quad \delta^* = \int_0^\infty \left(1 - \frac{\rho u}{\rho_v u_v}\right) dn, \quad K^* = \frac{\beta \lambda}{2\pi\theta}, \quad \beta = \sqrt{1 - M^2} \quad (\text{G.1})$$

where n is the normal direction from the wing surface.

We have the following equations to be solved in the integral boundary layer lag-entrainment model.

Continuity

$$\theta \frac{d\bar{H}}{ds} = \frac{d\bar{H}}{dH} \left[C_e - H_1 \left(\frac{C_f}{2} - (H+1) \frac{\theta}{u_v} \frac{du_v}{ds} \right) \right] \quad (\text{G.2})$$

Momentum

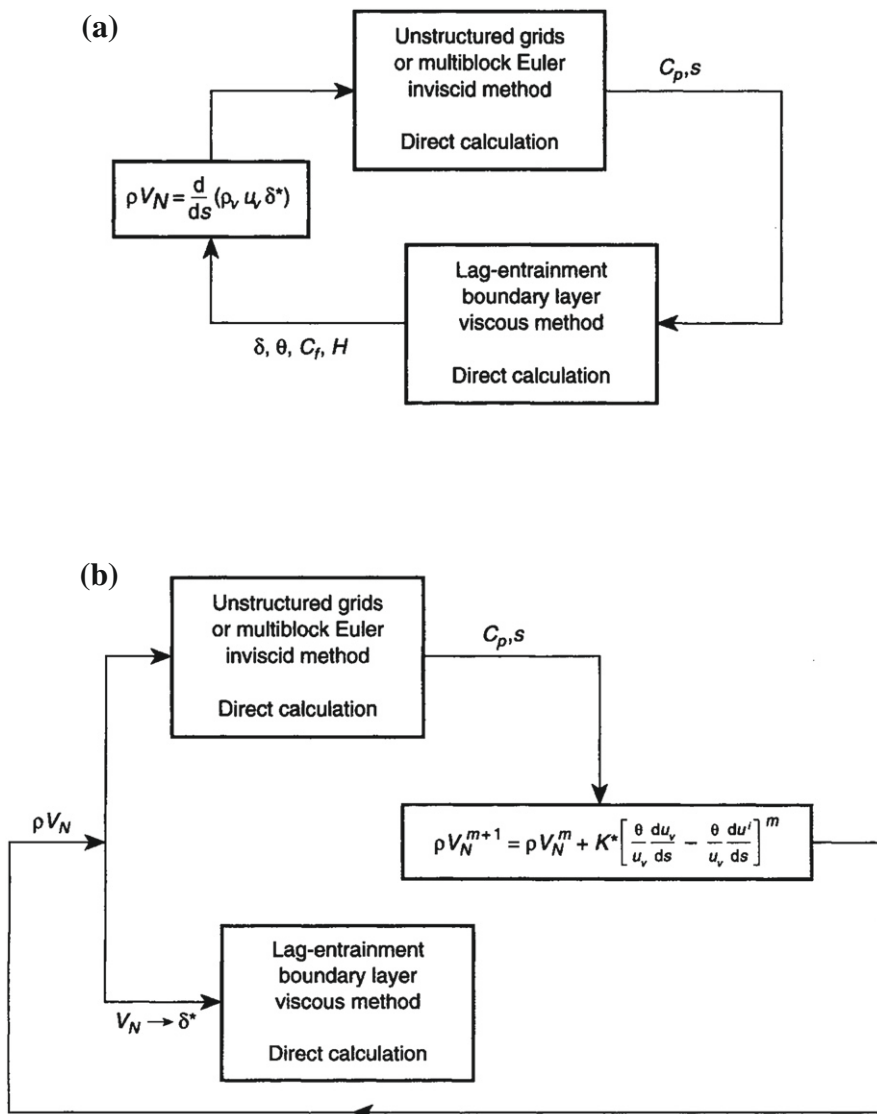
$$\frac{d\theta}{ds} = \frac{C_f}{2} - (H+2-M^2) \frac{\theta}{u_v} \frac{du_v}{ds} \quad (\text{G.3})$$

Lag-entrainment

$$\begin{aligned} \theta \frac{dC_e}{ds} &= F \left[\frac{2.8}{H+H_1} \left((C_\tau)_{EQ_0}^{0.5} - \lambda C_f^{0.5} \right) + \left(\frac{\theta}{u_v} \frac{du_v}{ds} \right)_{EQ} \right. \\ &\quad \left. - \frac{\theta}{u_v} \frac{du_v}{ds} (1 + 0.075M^2) \frac{(1 + 0.2M^2)}{(1 + 0.1M^2)} \right] \end{aligned} \quad (\text{G.4})$$

where F is a function of C_e and C_f and given as

$$F = \frac{\left(0.02C_e + C_e^2 + \frac{0.8C_f}{3} \right)}{(0.01 + C_e)} \quad (\text{G.5})$$

**FIGURE G.2**

Coupling techniques: (a) direct; (b) semi-inverse.

In the above equations, \bar{H} and H_1 are the velocity profile shape parameters defined as

$$\bar{H} = \frac{1}{\theta} \int_0^\infty \left(1 - \frac{u}{u_v} \right) dn, \quad H_1 = \frac{\delta - \delta^*}{\theta} \quad (G.6)$$

C_e is the entrainment coefficient; u_v is the mean component of the streamwise velocity at the edge of the boundary layer; M is the Mach number; C_τ is the shear stress coefficient; λ is the scaling factor on the dissipation length; and the subscripts EQ and EQ_o denote, respectively, the equilibrium conditions and equilibrium conditions in the absence of secondary influences on the turbulence structure.

Once the above equations are solved, the transpiration velocity V_N is calculated as shown in Fig. G.2, added to the standard Euler boundary conditions on the wall, and plays the role of a surface source. The coupling continues until convergence. In practice, in one coupling cycle, several Euler iterations are carried out for each boundary layer solution.

Multigrid Method

H

It is intuitively obvious that whenever iterative techniques are used to solve a finite element or finite difference problem it is useful to start from a coarse mesh solution and then to use this coarse mesh solution as a starting point for iteration in a finer mesh. This process repeated on many meshes has been used frequently and obviously accelerates the total convergence rate. This acceleration is particularly important when a hierarchical formulation of the problem is used. We have indeed discussed such hierarchical formulations in Chapter 6 of Ref. [1] and the advantages are pointed out there.

The simple process which we have just described involves going from coarser meshes to finer ones. However it is not useful if no return to the coarser mesh is done. In hierarchical solutions such returning is possible as the coarser mesh matrix is embedded in the finer one with the same variables and indeed the iteration process can be described entirely in terms of the fine mesh solution. The same idea is applied to the multigrid form of iteration in which the coarse and fine mesh solution are suitably linked and use is made of the fact that the fine mesh iteration converges very rapidly in eliminating the higher frequencies of error while the coarse mesh solution is important in eliminating the low frequencies.

To describe the process let us consider the problem of

$$\mathcal{L}\phi = f \quad \text{in } \Omega \quad (\text{H.1})$$

which we discretize incorporating suitable boundary conditions. On a coarse mesh the discretization results in

$$\mathbf{K}^c \tilde{\boldsymbol{\phi}}^c = \mathbf{f}^c \quad (\text{H.2})$$

which can be solved directly or iteratively and generally will converge quite rapidly if $\tilde{\boldsymbol{\phi}}^c$ is not a big vector. The fine mesh discretization is written in the form

$$\mathbf{K}^f \tilde{\boldsymbol{\phi}}^f = \mathbf{f}^f \quad (\text{H.3})$$

and we shall start the iteration after the solution has been obtained on the coarse mesh. Here we generally use a *prolongation* operator which is generally an interpolation from which the fine mesh values at all nodal points are described in terms of the coarse mesh values. Thus

$$\boldsymbol{\phi}_i^f = \mathbf{P} \boldsymbol{\phi}_{i-1}^c + \Delta \boldsymbol{\phi}_i^f \quad (\text{H.4})$$

where $\Delta\phi_i^f$ is the increment obtained in direct iteration. If the meshes are nested then of course the matter of obtaining \mathbf{P} is fairly simple but this can be done quite generally by interpolating from a coarser to a finer mesh even if the points are not coincident. Obviously the values of the matrices \mathbf{P} will be close to unity whenever the fine mesh points lie close to the coarse mesh ones. This leads to an almost hierarchical form. Once the prolongation to ϕ^f has been established at a particular iteration i the fine mesh solutions can be attempted by solving

$$\mathbf{K}^f \Delta\tilde{\phi}^f = \mathbf{f}^f - \mathbf{R}_i^f \quad (\text{H.5})$$

where the residual \mathbf{R} is easily evaluated from the actual equations. We note that the solution need not be complete and can well proceed for a limited number of cycles after which a return to the coarse mesh is again made to cancel out major low frequency errors. At this stage it is necessary to introduce a matrix \mathbf{Q} which transforms values from the fine mesh to the coarse mesh. We now write for instance

$$\tilde{\phi}_i^c = \mathbf{Q}\tilde{\phi}_i^f \quad (\text{H.6})$$

where one choice for \mathbf{Q} is, of course, \mathbf{P}^T . In a similar way we can also write

$$\mathbf{R}_i^c = \mathbf{Q}\mathbf{R}_i^f \quad (\text{H.7})$$

where \mathbf{R}_i are residuals. The above interpolation of residuals is by no means obvious but is intuitively at least correct and the process is self-checking as now we shall start a coarse mesh solution written as

$$\mathbf{K}^c(\tilde{\phi}_{i+1}^c - \tilde{\phi}_i^c) = \mathbf{R}_i^c \quad (\text{H.8})$$

At this stage we solve for $\tilde{\phi}_{i+1}^c$ using the values of previous iterations of $\tilde{\phi}_i^c$ and putting the collected residuals on the right-hand side. This way of transferring residuals is by no means unique but has established itself well and the process is rapidly convergent.

In general more than two mesh subdivisions will be used and suitable operators \mathbf{P} and \mathbf{Q} have to be established for transition between each of the stages. The total process of solution is vastly accelerated and proceeds well as shown by the many papers cited in [Chapter 7](#).

Reference

- [1] O.C. Zienkiewicz, R.L. Taylor, J.Z. Zhu, *The Finite Element Method: Its Basis and Fundamentals*, seventh ed., Elsevier, Oxford, 2013.

Mass-Weighted Averaged Turbulence Transport Equations

I

I.1 Turbulence models

In this appendix we provide two turbulence models commonly employed in the compressible flow calculations. Before discussing these models we write the Reynolds stress term and turbulent heat flux term in terms of turbulent eddy viscosity as

$$\tau_{ij}^R = \mu_T \left(\frac{\partial \tilde{u}_i}{\partial x_j} + \frac{\partial \tilde{u}_j}{\partial x_i} - \frac{2}{3} \frac{\partial \tilde{u}_k}{\partial x_k} \delta_{ij} \right) - \frac{2}{3} \rho \kappa \delta_{ij} \quad (\text{I.1})$$

and

$$q_j^R = -\mu_T \frac{c_p}{Pr_T} \frac{\partial \bar{T}}{\partial x_j} \quad (\text{I.2})$$

One of the following turbulence models may be employed to calculate the turbulent viscosity

I.1.1 Spalart-Allmaras model

In this model the turbulent eddy viscosity is calculated as

$$\nu_T = \frac{\mu_T}{\rho} = \tilde{\nu} f_{v1} \quad (\text{I.3})$$

where

$$f_{v1} = \frac{X^3}{X^3 + C_{v1}^3} \quad (\text{I.4})$$

with

$$X = \frac{\tilde{\nu}}{\nu} \quad (\text{I.5})$$

The viscosity variable $\tilde{\nu}$ is calculated from

$$\begin{aligned} \frac{\partial \tilde{\nu}}{\partial t} + \tilde{u}_j \frac{\partial \tilde{\nu}}{\partial x_j} &= c_{b1}[1 - f_{t2}] \tilde{S} \tilde{\nu} + \frac{1}{\sigma} \left[\frac{\partial}{\partial x_j} \left\{ (\nu + \tilde{\nu}) \frac{\partial \tilde{\nu}}{\partial x_j} \right\} \right. \\ &\quad \left. + c_{b2} \frac{\partial \tilde{\nu}}{\partial x_j} \frac{\partial \tilde{\nu}}{\partial x_j} \right] - \left[c_{w1} f_w - \frac{c_{b1}}{K^2} f_{t2} \right] \left[\frac{\tilde{\nu}}{y} \right]^2 + f_{t1} \Delta \tilde{u}^2 \end{aligned} \quad (\text{I.6})$$

The parameters used in the above equation are written as

$$\begin{aligned}
 \tilde{S} &= \tilde{\omega} + \frac{\tilde{v}}{K^2 y^2} f_{v2} \\
 f_{v2} &= 1 - \frac{X}{1 + X f_{v1}} \\
 f_w &= g \left[\frac{1 + c_{w3}^6}{g^6 + c_{w3}^6} \right]^{1/6} \\
 g &= r + c_{w2}(r^6 - r) \\
 r &= \min \left(\frac{\tilde{v}}{\tilde{S} K^2 d^2}, 10 \right) \\
 f_{t2} &= c_{t3} \exp(-c_{t4} X^2) \\
 f_{t1} &= c_{t1} g_t \exp \left(-c_{t2} \frac{\tilde{\omega}_t^2}{\Delta \tilde{u}^2} [y^2 + g_t^2 y_t^2] \right) \\
 g_t &= \min \left(0.1, \frac{\Delta \tilde{u}}{\tilde{\omega}_t \Delta x} \right)
 \end{aligned} \tag{I.7}$$

where y is the distance from a given node to the nearest wall, $\tilde{\omega}$ is the vorticity given as

$$\tilde{\omega} = \left[\left(\frac{\partial u_3}{\partial x_2} - \frac{\partial u_2}{\partial x_3} \right)^2 + \left(\frac{\partial u_1}{\partial x_3} - \frac{\partial u_3}{\partial x_1} \right)^2 + \left(\frac{\partial u_2}{\partial x_1} - \frac{\partial u_1}{\partial x_2} \right)^2 \right]^{1/2} \tag{I.8}$$

$\Delta \tilde{u}$ is the difference in velocity between the point and trip, y_t is distance from a node to a trip point or curve, $\tilde{\omega}_t$ is the vorticity magnitude at the trip point or curve, and Δx is the surface grid spacing at the trip. Other constants used in the model are $c_{b1} = 0.1355$, $c_{b2} = 0.622$, $\sigma = 2/3$, $K = 0.41$, $c_{w1} = c_{b1}/K^2 + (1 + c_{b2})/\sigma$, $c_{w2} = 0.3$, $c_{w3} = 2$, $c_{v1} = 7.1$, $c_{t1} = 1$, $c_{t2} = 2$, $c_{t3} = 1.1$, and $c_{t4} = 2$.

The major difference between the model given here and the one used in Section 8.2 is that here we have a trip curve (3D) or trip point (2D) to trigger turbulence. The trip curve is often defined at a 3% distance from the leading edge of a solid surface.

1.1.2 κ - ω model

The basic idea of the κ - ω model arises from the fact that vorticity is directly proportional to κ^2/l , i.e.,

$$\omega = c \frac{\kappa^2}{l} \tag{I.9}$$

where c is a constant. The eddy viscosity may therefore be written as

$$\mu_T = \rho \frac{\kappa}{\omega} \tag{I.10}$$

The transport equations for κ and ω may be written as

$$\frac{\partial}{\partial t}(\bar{\rho}\kappa) + \frac{\partial}{\partial x_i}(\bar{\rho}\kappa\tilde{u}_i) = \frac{\partial}{\partial x_i}\left(\mu_\kappa \frac{\partial \kappa}{\partial x_i}\right) + \frac{\partial}{\partial x_i}(\bar{\tau}_{ij}\tilde{u}_j) - \beta^*\bar{\rho}\kappa\omega \quad (\text{I.11})$$

and

$$\frac{\partial}{\partial t}(\bar{\rho}\omega) + \frac{\partial}{\partial x_i}(\bar{\rho}\omega\tilde{u}_i) = \frac{\partial}{\partial x_i}\left(\mu_\omega \frac{\partial \omega}{\partial x_i}\right) + \alpha \frac{\omega}{\kappa} \frac{\partial}{\partial x_i}(\bar{\tau}_{ij}\tilde{u}_j) - \beta \bar{\rho}\omega^2 \quad (\text{I.12})$$

where $\mu_\kappa = \mu + \mu_T/\sigma_\kappa$ and $\mu_\omega = \mu + \mu_T/\sigma_\omega$. The constants are $\alpha = 5/9$, $\beta = 3/40$, $\beta^* = 9/100$, $\sigma_\kappa = \sigma_\omega = 2$.

If necessary the turbulence models discussed in this section can be non-dimensionalized as discussed in [Section 8.2](#).